Universiteit Antwerpen

Universitaire Instelling Antwerpen

Departement Scheikunde

Eindverslag: Addenda A t.e.m. C

Studie van de geochemische cycli van particulaire zware metalen en organische micropolluenten in het Noordzeemilieu

Oktober 1992- september 1996

R. Van Grieken, promotor
W. Jambers
L. De Bock
K. Torfs
K. Gysels
J. Injuk
H. Struyf
S. Hoornaert
H. Van Malderen

Eindverslag in het kader van het Impulsprogramma Zeewetenschappen, voor rekening van de Belgische Staat - Diensten van de Eerste Minister - Federale Diensten voor Wetenschappelijke, Technische en Culturele Aangelegenheden
(contract MS/06/050)

Oktober 1996

Universiteit Antwerpen

Universitaire Instelling Antwerpen

Departement Scheikunde

Eindverslag: Addenda A t.e.m. C

Studie van de geochemische cycli van particulaire zware metalen en organische micropolluenten in het Noordzeemilieu

Oktober 1992- september 1996

R. Van Grieken, promotor
W. Jambers
L. De Bock
K. Torfs
K. Gysels
J. Injuk
H. Struyf
S. Hoornaert
H. Van Malderen

Eindverslag in het kader van het Impulsprogramma Zeewetenschappen, voor rekening van de Belgische Staat - Diensten van de Eerste Minister - Federale Diensten voor Wetenschappelijke, Technische en Culturele Aangelegenheden
(contract MS/06/050)

Oktober 1996

Addendum A

Atmospheric concentrations and deposition of heavy metals into the North Sea:
a literature review

University of Antwerp (UIA)
Micro- and Trace Analysis Centre

ATMOSPHERIC CONCENTRATIONS AND DEPOSITION OF HEAVY METALS INTO THE NORTH SEA:

a literature review

Jasna Injuk
René Van Grieken

Report prepared in the framework of the Impulse Programme in Marine Sciences, supported by the Belgian State - Prime Minister's Service - Science Policy Office (contract MS/06/050)

March 1993

Contents

1. Introduction

Quantitative data on the heavy metals emissions, concentrations levels in air and accumulation and transfer in the North Sea ecosystem have not been systematically gathered and intercompared hitherto. It is the purpose of this report to examine available data, in order to see if there is a basis for a systematic approach capable of describing the environmental cycle and impact of heavy metals in the North Sea.

Today, there is much discussion on the sources and abatement policies of pollution to the sea. Atmospheric transport and deposition of pollutants over long distances have received attention, particularly in connection with the acid rain problem, and the photochemical oxidants and ozone formation, and more recently the global climatic effects. It is only relatively up-to-date that it has become possible to estimate the amounts of material entering the oceans via the atmosphere. Further, as the calculations have become less crude, for some substances the atmospheric route seems to have gained in importance relative to the other paths, like those borne by rivers and direct discharge. Though the pollution of the oceans is not a new phenomenon, a question of how important role the atmosphere plays in this was addressed only a decade ago (NAS,1978).

There are various sources which emit trace metals into the atmosphere, i.a. volcanic activity, vegetation, soil erosion, man-made pollution and aerosol formation from sea-spray. The concentrations of so-called anthropogenic pollutants in the atmosphere are mainly due to the volatility of these elements at the high temperatures of fossil fuel combustion, and many other high-temperature industrial processes, particularly the extraction of non-ferrous metals from sulphides. Among other industrial sources, waste incineration is becoming increasingly important, particularly in Western Europe, due to the emissions of Cd, Pb and other trace elements and a need to incinerate increasing amounts of wastes. A first preliminary review of the atmospheric emissions of various trace elements from anthropogenic sources in Europe, for 1979/1980, was provided by Pacyna (1983). The earlier surveys were concerned with either a single metal (van Enk, 1980; Hutton, 1982) or certain types of emission sources, e.g. fossil fuel combustion. As such, they were very valuable for the control strategies, but less applicable for modelling of the long-range transport of air pollutants and their migration through the environment. The survey of Pacyna has recently been updated and improved. In Table 1, the estimates of Pacyna (1987) of trace element emissions from all sources in countries bordering the North Sea are compared with

Table 1: Comparison of the 1982 survey of trace element emission by Pacyna (1987) with national emission data (tons y^{-1}) for countries bordering the North Sea

Country	Cd	As	Pb	Zn	Reference
U.K.	30.6	117.4	8614	2230	Pacyna, 1987
	14	315	7590	-	Hutton and Symon, 1986
Belgium	12	85	2100	700	Pacyna, 1987
	-	-	-	-	-
The Netherlands	5.5	34	2200	290	Pacyna, 1987
	3.8	-	-	-	Kendall et al., 1985
Germany	79.9	351.2	5562	6663.3	Pacyna, 1987
	79*	500	7590	10000	*Schladot and Nürnberg, 1982 Braun et al., 1984
Denmark	6.3	7	650	130	Pacyna, 1987
	5	-	-	-	Murkherje, 1986
Sweden	16.4	183.4	1053	425.6	Pacyna, 1987
	12	130	950	1200	Naturvardsverket, 1982
Norway	2.1	41	730	120	Pacyna, 1987
	1.7-2.7	-	-	-	Naturvardsverket, 1982

the countries' own estimates. The former estimates are based on the emission factors, calculated separately for each of the countries, on statistics on the consumption of raw materials, and on the production of various industrial goods in 1982.

Any expectations with respect to changes in future emissions are primarily related to innovations in production technology and modernisation of environmental protection installations. As there is no significant change in the production of Pb, Cu, Zn and Ni in Europe, the emissions of As, Cd, Pb and Zn from European smelters estimated in Table 1, will continue to be valid for the next 5 years at least. The emission trends in coal and oil consumption are difficult to predict, since they rely on the export-import movements of fossil fuels. The present increase of the coal use in European electric-power plants of approximately 2% per year is due to the increasing demand for electricity in Europe (1% per year). The expected increase of air pollution from coal combustion in the future may be compensated by the tendency to extend the use of dual-fired installations with natural gas in Europe. Thus, also the As, Cd, Pb, and Zn emissions from the European electric power plants are not likely to be changed in the near future (Semb and Pacyna, 1988).

2. Data on trace metal concentrations in air

There is quite a detailed data base of concentration measurements for trace metals in aerosols over the European regional seas (GESAMP, 1989). Table 2 gives an overview of literature values for the particulate Cd, Cr, Cu, Pb and Zn concentrations in the marine troposphere concerning the North Sea and adjacent areas. The data set covers a relatively long time period, over 19 years. The oldest data, supplied by Peirson et al. (1973), Kretzschmar and Cosemans (1979) and Van Aalst et al. (1983) (who give a list of concentrations measured between 1974 and 1981 at coastal stations in Great Britain, Belgium and The Netherlands), are generally higher than the other reported values in Table 2. The use of less accurate techniques in those days may be one reason, but these values were also obtained from coastal or even inland measurements, i.e. closer to the emission sources. Van Daalen (1991) measured the concentrations over the province of South-Holland in the Netherlands and although his sampling sites were not very far removed from the North Sea coast, his data show clearly high concentrations. The rest of the coastal values in Table 1 seem to agree very well with the exception of the Belgian ones from Ostende, due to very high concentrations measured in the continental air masses (factor 2 to 5 higher compared to the values for the eastern and western air-masses). Although not explicitly North Sea coastal measurements, the data collected by Flament et al. (1987) at the French coast in the Channel and those reported by Schneider (1987) in the Kiel Bight offer a good basis for intercomparison of results.

In contrast with measurements performed at coastal stations around the North Sea, much less data are available on experimental determinations of airborne elemental concentrations in samples taken on the North Sea itself. Results from the West Hindler light-ship station located off the Belgian coast were reported by Baeyens and Dedeurwaerder (1991), Dedeurwaerder (1988), and ATMOS (1984). The West-Hinder results are generally higher than comparable ones for the southern North Sea. One possible explanation is that ship West-Hindler is only separated from the coastline by a relatively small distance and is located at a very dense traffic channel (100 ships per day) on the North Sea. The aircraft-measured values (Injuk et al., 1992) agree well with those of the cruise with the R/V Belgica (Otten et al., 1989). Values reported by Otten et al. (1989), predominantly based on measurements done in the northern part of the North Sea, during north-westerly winds, can be considered as background values for the North Sea area. And when the values reported for the North Sea are considered, a concentration gradient from the southern North Sea (high

Table 2 : Measured airborne concentrations over the North Sea and adjacent areas in ng m^{-3} (s- or n- preceding an area means southern or northern, respectively)

Area	Period	Cd	Cr	Cu	Pb	Zn	Remarks	References
United Kingdom	'72	<4-<18	1.0-14	<1-55	35-380	64-415	range for 7 sites	Peirson et al. (1973)
United Kingdom	'75	4-6	-	13-15	20-120	15-300	range for 2 sites	Cawse (1974)
Holland	'84-'88	0.3-2	1.7-14	3.7-23	36-178	18-200	-	van Daalen (1991)
North Sea (coast)	'72-'81	0.5-2.5	0.5-5	<5-25	20-200	10-100	-	van Aalst et al. (1983)
The Netherlands (coast)	'87	0.8	-	5.5	45	59	Hage	Cambray et al. (1975)
The Netherlands (coast)	'84-'85	0.7	1.3	3.3	39	40	Pellworm	Steiger (1991)
The Netherlands (coast)	'83	0.6	1.6	3.0	41	30	Tange	Kemp (1984)
Belgium (coast)	'72-'77	8	-	19	278	300	Ostende	Kretzschmar and Cosemans (1979)
Belgium (coast)	'81-'84	3.4	-	12.8	77	174	-	ATMOS (1984)
Norway (coast)	'78-'79	0.3	1	7	19	-	-	Pacyna et al. (1984)
Norway (coast)	'85-'86	0.14	1.1	1.6	18	15	Birkenes	Amundsen et al. (1992)
England (coast)	'87-'88	1.1	-	-	34	41	-	Yaaqub et al. (1991)
England (coast)	'72-'73	-	7.0	-	168	155	Leiston	Cambray et al. (1975)
German Bight	'86	1.9	1.9	4.7	52.6	46	island	Kersten et al. (1991)
Kiel Bight	'81-'83	-	-	40	53	57	lighthouse	Schneider (1987)
East Channel	'87	3	-	20	56	100	-	Flament et al. (1987)
North Sea	'86-'90	1.6	1.5	3.5	20.2	38	Helgoland	Kriews (1992)
North Sea	'87	0.9	-	3.9	28.5	42	FPN	Steiger (1991)
North Sea	71'-'73	-	4.8	-	155	161	Gasplatform	Cambray et al. (1975)
North Sea	'88-'89	1.4	-	11	55	67	flights	Injuk et al. (1992)
North Sea	'84-'88	-	-	11	39	54	cruise	Otten et al. (1989)
sNorth Sea	'81-'84	2.9	-	9	104	94	West-Hindler	ATMOS (1984)
sNorth Sea	'84-'85	0.7	-	3	39	41	-	Stoeßel (1987)
sNorth Sea	'80-'85	4	-	17	150	150	West-Hindler	Dedeurwaerder (1988)
sNorth Sea	'84-'88	-	-	17	62	86	cruise	Otten et al. (1989)
sNorth Sea	'80-'85	2.8	-	14.7	96	67	West-Hindler & cruises	Baeyens and Dedeurwaerder (1991)
nNorth Sea	'72-'73	-	1.4	20	21	32	Collafirth	Cambray et al. (1975)
nNorth Sea	'84-'88	-	-	2	2	2	cruise	Otten et al. (1989)
North Sea	'91	0.2	2.0	1.9	4.5	30	Gullfaks"C"	Dannecker et al. (1992b)

concentrations) to the northern part (low concentration) is observed.

Under the Paris Convention, an international commission (PARCOM-ATMOS) has been established to assess the state of the marine environment and formulate the policy to eliminate or reduce existing pollution. With regard to atmospheric pollution, a dual approach has been proposed: a monitoring programme at a number of coastal stations and a modelling programme for which an emission database is being set up. The monitoring programme of PARCOM-ATMOS includes measuring concentrations in precipitation of Pb, Cd, Cu, Zn, Cr, Hg, Ni, NH_4^+ and NO_3^- and some of these species in air. In Tables 3 and 4, the basic description of the stations monitoring heavy metals in air and in precipitation, and annual mean aerosol concentration values are given. From the summarized results in Table 4, it is obvious that only data from the Belgian stations (B1 and B2b) are not comparable with the others, due to high values for Cu, Ni, Pb and Zn. But these results agree well with reported ones for the same region by Kretzschmar and Cosemans (1979), indicating a high level of pollution for this region. In Figure 1, the North Sea area with the stations which take part in the PARCOM-ATMOS monitoring program is given.

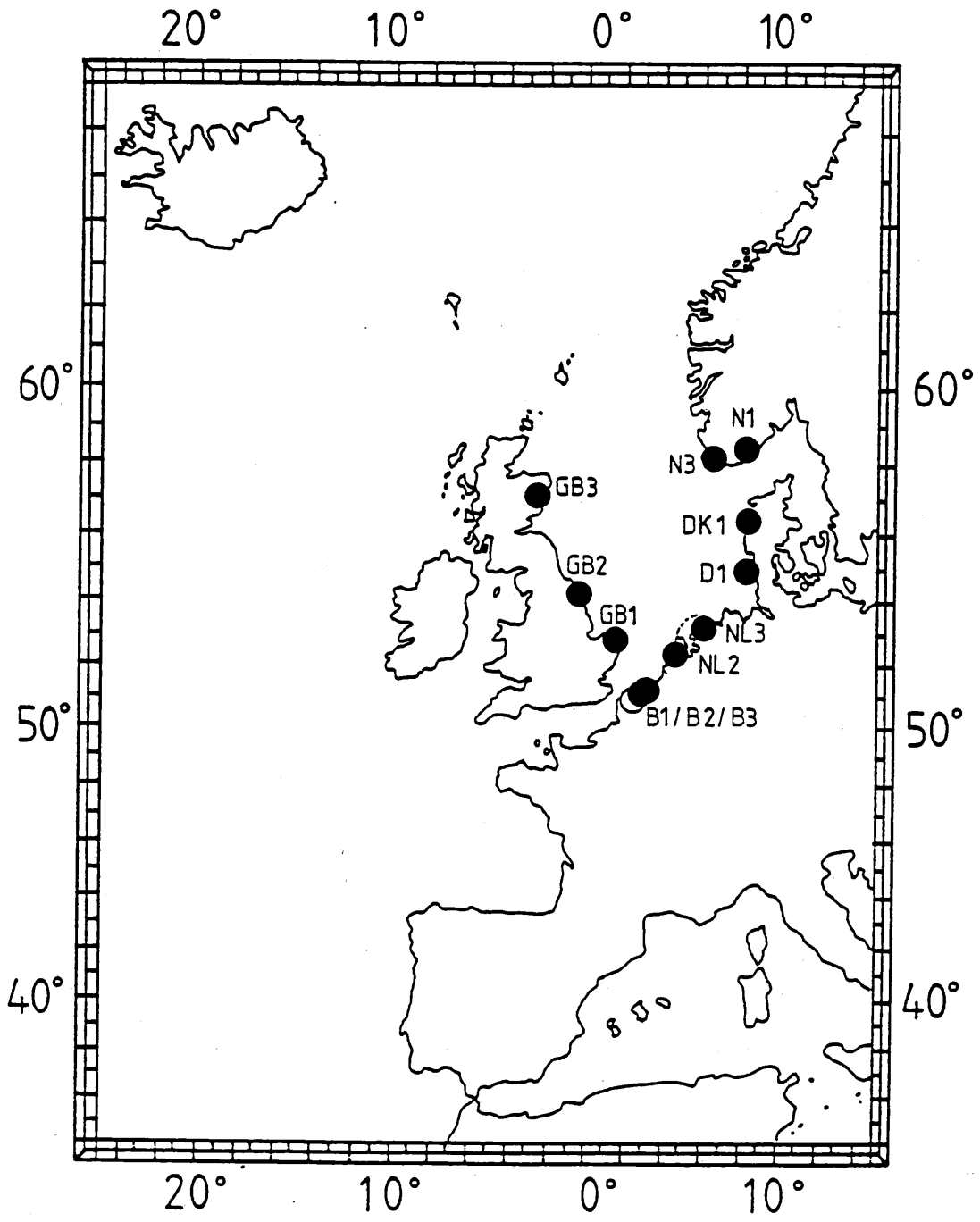

Figure 1: The North Sea area with the stations which take part in the PARCOM Comprehensive Atmospheric Monitoring Programme (CAMP)- so called "Central North Sea Stations"

Table 3. Coastal measuring stations participating in Paris Commision Comprehensive Atmospheric Monitoring Programme (CAMP)

Number Country	Name	Latitude Longitude	Elevation	Distance from the sea	Parameters measured
B1 Belgium	Houtem	51°01'N 2°35'E	sea level	9 km	Pb,Zn- in air
B2b Belgium	Bredene	51°14'N 2°57'E	<< 10 m	2 km	Cu,Ni,Pb,Zn- in air
B3a Belgium	Brugge	51°15'N 3°11'E	<< 10 m	8 km	Cd,Cu,Pb,Zn- in precipitation
GB1 Great Britain	East Ruston	52°48'N 1°28'E	5 m	8 km	Cd,Cr,Cu,Ni,Pb,Zn- in air Cd,As,Cr,Cu,Ni,Pb,Zn- in precipitation
GB2 Great Britain	Staxton Wold	54°11'N 0°26'W	170 m	10 km	Cd,Cr,Cu,Ni,Pb,Zn- in air Cd,As,Cr,Cu,Ni,Pb,Zn- in precipitation
GB3 Great Britain	Banchory	57°5'N 2°32'W	120 m	26.5 km	Cd,Cr,Cu,Ni,Pb,Zn- in air Cd,As,Cr,Cu,Ni,Pb,Zn- in precipitation
DK1 Denmark	Ulborg	56°17'N 8°26'E	40 m	20 km	Cd,As,Cr,Cu,Ni,Pb,Zn- in air Cd,Cu,Pb,Zn- in precipitation
D1 Germany	Westerland	54°53'N 8°19'E	5 m	2 km	Cd,Cu,Pb- in air Cd,As,Cr,Cu,Ni,Pb,Zn- in precipitation
NL3 The Netherlands	Kollumerwaard	53°20'N 6°16'E	0-5 m	10 km	Cd,As,Pb,Zn- in air Cd,Cu,Ni,Pb,Zn- in precipitation
NL2 The Netherlands	Leiduin	52°20'N 4°35'E	0-5 m	6.3 km	Cd,Cr,Cu,Ni,Pb,Zn- in precipitation
N1 Norway	Birkenes	58°23'N 8°15'E	190 m	20 km	Cd,Pb,Zn- in precipitation
N3 Norway	Lista	58°06'N 6°34'E	13 m	-	Cd,Cr,Cu,Ni,Pb,Zn- in precipitaion

Table 4. An overview of the data submitted to PARCOM-ATMOS as regards elemental concentrations (ng m^{-3}) in aerosols for 1988, 1989, 1990 and 1991, measured at "CAMP" stations

Station	Period	Cd	As	Cr	Cu	Ni	Pb	Zn
B1	'90	-	-	-	-	-	104	351
B2b	'89	-	-	-	-	-	112	150
	'91	-	-	-	23	15	86	222
DK1	'88	0.3	1.6	2.3	1.2	1.9	19.2	23.7
	'89	0.3	-	1.0	2.29	1.66	21.8	25.8
	'90	-	-	1.48	1.6	1.7	17	24
	'91	-	-	2.5	2.3	2	17	23
D1	'88	0.4	-	-	3.4	-	23.3	-
	'89	0.42	-	-	2.69	-	20.4	-
	'90	0.30	-	-	3.10	-	17.3	-
	'91	0.36	-	-	1.5	-	18	-
NL3	'90	0.33	0.78	-	-	-	27	52
	'91	0.4	1.48	-	-	-	30.2	51
GB1	'88	0.5	-	0.7	3.7	2.0	35.4	27.7
	'89	0.43	-	0.82	3.85	2.30	31.3	27.5
	'90	0.33	-	0.65	2.77	1.75	21	23
	'91	0.66	-	0.72	3.36	3.27	26.1	73.9
GB2	'88	0.5	-	1.2	4.6	3.1	22.3	111.3
	'89	0.64	-	1.33	3.62	2.5	27.2	59
	'91	1.9	-	0.79	3.06	2.36	17	50.7
GB3	'88	0.1	-	0.2	0.9	0.5	7.9	8.3
	'89	0.12	-	0.31	1.24	0.74	7.6	7.3
	'90	0.13	-	1.19	1.97	2.60	6.8	16.2
	'91	0.12	-	0.3	1.58	0.81	7.02	10.5

3. The atmospheric input of trace elements to the North Sea

3.1. Introduction

Because of the recent research efforts, it is now possible to assess the atmospheric fluxes of many materials to the sea waters. The first major studies of the deposition of heavy metals from the atmosphere started in the United Kingdom at the beginning of the 1970's (Cawse, 1974). The concentrations of some 40 elements were determined in dry and wet deposition at seven non-urban sites, while the water soluble and insoluble fractions of the total deposition were analyzed separately. At the same time, analyses of the deposition of heavy metals were made in Norway (Breekke, 1976), in the USA (Andren et al.,1975; Feely et al., 1976) and in the FRG (Ruppert, 1975). The routine monitoring of trace elements in precipitation began in Sweden in 1983 (Ross, 1987) with the aim to determine the atmospheric wet deposition of Cd, Cu, Fe, Mn, Pb and Zn. In 1987, Barrie et al. have reviewed literature data on the trace element concentrations in remote precipitation. This information is very important to assess the contribution of long-range transport of pollutants in comparison with their background concentrations. Authors have notified that the concept of typical remote concentrations should be qualified by the distance from sources and the prevailing meteorological air masses.

For many years, research on pollution of the North Sea marine environment has focused on the most obvious inputs, those borne by rivers and direct discharges of wastes. In the work of Goldberg (1973) and Cambray et al. (1975), a first indication can be found that the atmospheric input might also be a significant contributor of trace elements to the North Sea. More recently, van Aalst et al. (1983) employed a simple model to compare the long-term average concentrations of various elements in the sea, and to determine the atmospheric input of a large group of contaminants into the North Sea. They have compared their results with information on the other inputs into the North Sea and concluded that atmospheric deposition was a relatively important source of contamination with Cu, Pb, Ni and Zn, and to a lesser extent with Cd and Cr. A first international attempt to estimate the input of various elements to the sea by atmospheric deposition and via other pathways was made by a European group of experts on behalf of the International Council for the Exploration of the Sea (ICES, 1978).

Since trace elements are removed from the atmosphere by dry deposition (sedimentation, interception and impaction) and by wet deposition (rainout, washout), in the further text a literature overview concerning both processes is given separately.

3.2. Dry deposition fluxes to the North Sea

Dry deposition of particles to the sea surface is the sum of all physical removal processes that take place when there is no form of precipitation (rain, snow or hail). Pollutants in aerosol form may reach the sea surface by a number of processes, such as gravitational settling, turbulent diffusion, Brownian diffusion or impaction. In general terms it can be stated that small particles (<0.1 μm) are removed mainly by Brownian diffusion and large particles (>10 μm) by gravitational settling. In the intermediate size range, impaction and interception are important. The loss of particles to the sea surface is frequently described in terms of a dry deposition velocity, which is the ratio between the deposition rate per unit area, and the ambient concentration. The dry deposition velocity of particles is strongly dependent on particle size, wind velocity and surface characteristics. Both theoretical considerations and field experiments show that the deposition velocity is small for particles with aerodynamic diameter less than 1 μm, typically of the order of 0.1 cm s^{-1}, while for the large particles it reaches a value of a few cm s^{-1}. Due to the very high deposition velocities of the large particles in comparison with deposition velocities of submicrometer particles, they contribute above 80% in total dry flux, although they account for a few per cent in the total mass collected.

Transport fluxes across the air-sea interface can be determined by theoretical or semi-empirical relations (Sehmel and Hodgson, 1978; Slinn and Slinn, 1980; Williams, 1982; Friedlander et al., 1986; Main and Friedlander, 1990). Dry deposition velocities can be also evaluated by direct measurements of actual dry fluxes and particle concentrations in the air. Although the performance characteristics of air sampling equipment is quite well known, the properties of dry deposition collectors, as well as the structure of the laminar boundary layer above the collector and the collection efficiency still remain uncertain. It is not still clear how comparable the deposition to the surrogate surface is with the deposition to the natural sea surface. Another practical limitation, in the case when the deposited mass is measured, is that the results are strongly affected by the deposition of only few large particles. Since the gravitational settling velocity is roughly proportional to the square of the particle diameter and the particle mass is proportional to the cube of the particle diameter, the

deposited mass is a function of diameter to the 5th power. A single 10 μm particle will therefore contribute as much to the total deposited mass as roughly 100,000 particles of 1 μm. This makes direct measurements of the dry deposition extremely difficult.

Only a few experimentalists have tried to measure directly the dry deposition of trace metals to the North Sea. Cambray et al. (1975) used a Whatman 541 cellulose filter, which was placed on a gas platform (53°5'N, 2°21'E). Samples were collected on a monthly basis. The high values found were explained by the authors as due to the possible contamination by resuspended sea water or by the platform itself, what is more likely.

Baeyens et al. (1990) measured dry deposition fluxes in a direct way with vasilinated plexiglass plates, in 14-days exposed intervals. Sampling was carried out throughout one year, at the West-Hindler lightvessel (51°23'N,2°21'W) and during several cruises on the North Sea with the R/V Mechelen and the R/V Belgica. The collector plates were used horizontally and vertically. Directly measured dry deposition values were compared with the fluxes calculated by the adopted model of Slinn and Slinn (1980) and from a large set of *in situ* measured particle size distributions and their elemental concentrations. Despite the large uncertainties on the calculated dry deposition fluxes, results generally agree fairly well for both methods. The collection surfaces provide higher values, except for Mn and K, while the largest difference between both methods was observed for Pb, for factor of 2.3.

Estimated dry deposition fluxes at the west coast of Sweden by Selin et al. (1991) were derived from trace element concentrations in the air in the winter of 1990 and from experimentally obtained deposition velocities.

Aircraft-based aerosol sampling in the lower troposphere was performed between September 1988 and October 1989 (Otten, 1991), above the Southern Bight of the North Sea. The dry deposition fluxes of Cd, Cu, Pb and Zn were calculated from size-differentiated atmospheric concentrations as a function of wind direction and dry deposition velocities obtained with the Slinn and Slinn model.

The dry deposition fluxes reported by Kriews (1992) are based on arithmetic mean values of atmospheric elemental concentrations, measured at Helgoland (54°10'N,7°53'E) in period from 1986-1990, and deposition velocities followed by Slinn and Slinn model.

Atmospheric fluxes reported by ATMOS (1992) are based on mean aerosol concentration values measured at all the CAMP stations monitoring heavy metals in air during '88, 89', '90 and '91 and dry deposition velocities of 0.1 cm s^{-1} (Table 5). However, this value is far from being generally accepted.

As follows from Table 6, dry deposition fluxes to the North Sea show certain

variations, rendering the estimated quantification of the overall annual atmospheric input of heavy metals into the sea very difficult. In Table 7 the dry deposition velocities, used by different authors for estimation of the dry deposition fluxes above the North Sea, are given. Considering the complex interaction of processes involved in particle deposition it is, perhaps, not surprising that inconsistencies have been evident in the reported research. Some of these inconsistencies are likely to indicate a real variability in environmental influences since an important number of factors influence the dry deposition processes. Meteorological data such as friction velocity, the aerodynamic surface roughness and the atmospheric stability are related to the deposition of particles. Humidity gradients and rainfall characteristics all affect the deposition of particles too. Furthermore, pollutant properties which vary with temperature, humidity and electrostatic gradients at the sea surface will result in a variation of the deposition characteristics of particles.

Table 5: The annual mean aerosol concentration (ng m^{-3}) and estimated dry deposition fluxes (kg km^{-2} y^{-1}) based on measurements at "CAMP" stations

Period	Param.	Cd	As	Cr	Cu	Ni	Pb	Zn
'88	conc.	0.36	1.6	1.1	2.76	1.87	21.6	42.7
	flux	0.01	0.05	0.04	0.09	0.06	0.73	1.45
'89	conc.	0.38	-	0.87	2.7	1.8	21.6	29.9
	flux	0.01	-	0.03	0.09	0.06	0.68	0.95
'90	conc.	0.27	0.78	1.1	2.4	2.0	32.2	93.2
	flux	0.01	0.03	0.03	0.07	0.06	1.0	3.0
'91	conc.	0.58	1.14	1.24	5.09	4.01	25.5	62.2
	flux	0.02	0.04	0.04	0.16	0.13	0.8	1.96

Table 6: Dry deposition fluxes (kg km^{-2} y^{-1}) to the North Sea - comparison with the literature data

	Cambray et al. (1975) Gasplatform	Dedeurwaerder et al. (1982) West-Hindler	Bayens et al. (1990) West-Hindler&ship		Selin et al. (1991) Sweden-west coast	Otten (1991) aircraft	ATMOS (1991) CAMP-stations	Kriews (1992) Helgoland
			model exp.					
S	-	-	-	-	275	-	-	-
Cr	-	-	-	-	-	-	0.04	0.34
Mn	6.8	1.2	3.5	3.0	-	-	-	1.68
Fe	290	69	82	180	-	-	-	76
Ni	-	-	-	-	0.5	-	0.13	0.23
Cu	30	0.6	2.8	3.5	-	1.9	0.16	0.29
Zn	420	3.4	6.2	13	1.9	10.3	1.96	3.69
As	-	-	-	-	-	-	0.04	0.11
Pb	24	4.5	3.3	7.5	0.4	4.23	0.80	1.06
Cd	-	-	-	-	-	0.28	0.02	-

Table 7: Dry deposition velocities (cm s^{-1}), used by different authors for estimation of dry deposition fluxes

	Van Jaarsveld et al. (1986)	Krell and Roeckner (1988)	Dulac et al. (1989)	Steiger et al. (1989)	Baeyens et al. (1990)	Selin et al. (1991)	Otten (1991)	ATMOS (1992)	Kriews (1992)
S	-	-	-	-	-	1.0	-	-	-
Cr	-	-	-	-	-	-	-	0.1	0.69
Mn	-	-	-	-	0.49	-	-	-	0.75
Fe	-	-	-	-	0.56	-	-	-	1.0
Ni	-	-	-	-	-	0.84	-	0.1	0.28
Cu	0.22	-	-	-	0.53	-	0.48	0.1	0.26
Zn	0.22	-	-	-	0.41	0.34	0.35	0.1	0.31
As	-	-	-	-	-	-	-	0.1	0.19
Pb	0.22	0.2	0.04	0.14	1.35	0.12	0.25	0.1	0.17
Cd	0.22	0.2	0.05	-	0.53	-	0.39	0.1	-

As follows from Table 7, the main subject of discrepancy in the results concerning dry deposition velocities relies in the size distribution of the collected aerosols. Indeed, Van Aalst (1988) states that dry deposition velocities might vary in the range between 0.1 to 1 cm s^{-1}, and that most of this spread is caused by the lack of knowledge of the atmospheric particulate matter size distribution. Even though elements like Pb are more abundant in the sub-micrometer size range, these particles can coagulate with sea salt aerosols and reach super-micrometer dimensions. In order to give a quantitative idea on how important relatively large particles can be in the whole deposition process, Table 8 shows the percentage of the dry deposition flux accounted for by a given particle size class. Here only particle diameters larger than 1 μm are tabulated since the contribution of the sub-micrometer particles can be considered as negligible (Rojas et al., 1993). It is seen from this table that 98% of the dry deposition velocity for Cd is accounted for by particles larger than 4 μm while for Cu, Pb and Zn, this percentage corresponds to 95, 96 and 97%, respectively. For the same North Sea area, Baeyens et al. (1990) concluded that the first stages of their cascade impactor, i.e. particles larger than 4 μm, were responsible for 82% of the deposition of Pb. In the Mediterranean Sea, Dulac et al. (1989) reported that only 20% of the total deposition of Cd and Pb is accounted for by particles with sizes larger than 7 μm.

Table 8: Relative contribution of the particle size classes in the determination of dry deposition fluxes for the Southern Bight of the North Sea (Rojas et al., 1993)

	Contribution to the dry deposition in %			
Diameter (μm)	Cd	Cu	Pb	Zn
1 - 2	1.1	1.5	1.1	0.4
2 - 4	0.4	3.1	1.4	1.7
4 - 8	2.2	6.3	14	11
8 - 16	50	5.7	39	27
> 16	46	83	43	59

3.3. Wet deposition fluxes to the North Sea

Wet deposition is the combination of rainfout (in-cloud scavenging of particles) and washout (below-cloud scavenging of particles). Capture of particles by cloud droplets does not automatically lead to removal of the particles from the atmosphere, since cloud droplets may evaporate on their way to the earth's surface. This merely results in redistribution of the aerosol.

The amount of micropollutants which is deposited to the oceans over a certain period of time can be determined either directly or indirectly. In the direct way the wet atmospheric fluxes are determined by collecting rainwater in rain collectors over a certain period of time and measuring the concentrations of the substances involved. For particles, the wet flux F_w can be calculated with the following formula:

$$F_w = \sum_i C_{p,i} P_i$$

or the flux F_w is the sum over all individual rain events i of the product of the concentration of particles in rainwater ($C_{p,i}$) times the amount of precipitation per unit area and time (P_i). Because it is difficult to sample rainwater at each single rain event, the above equation is usually approximated. The most common approximation is as follows:

$$F_w = \overline{C_p} P$$

where the annual wet flux F_w is expressed as the product of the average rainwater concentration (C_p) and the yearly precipitation rate P. However, there are some major difficulties arising from the determining the wet deposition to the sea surface directly. Practically, collection of atmospheric material by the rain water samplers should be avoided during dry periods (Ruijgrok et al., 1990), so wet-only samplers need to be used. Additional problems include sea-spray and contamination or deterioration of the samples prior to or during analysis by material sampling and handling, particularly if one deals with trace amounts (Ross, 1984; Buijsman et al., 1991). Also, the statistical relevance of such direct measurements is doubtful. Firstly, precipitation is a discontinuous process and secondly, there is a natural variability of the concentrations of trace substances in precipitation. This means that a large number of rain events

must be covered before meaningful average wet fluxes can be obtained, which is expensive and time-consuming. Also, these measurements are very much determined by the sampling location and time, which is problematic if one wants to investigate the deposition over a larger area and over a considerable period of time (Smith, 1991). For this reason, indirect approaches are often preferred. The limited amount of directly measured data is then used to check the results of these indirect approaches. For indirect measurements, the wet deposition flux of material to the ocean surface can be written as:

$$F_w = WPC_a$$

where C_a is the concentration of the substance in air, P is the yearly precipitation rate and W is the washout ratio - also called scavenging ratio - which is the ratio of the concentration of a substance in rainwater to the concentration of the same substance in air (both concentrations measured in the same volume units, e.g. $\mu g\ m^{-3}$).

This equation can be modified in a number of ways. Some authors for instance, add the density of air ρ as an extra factor (GESAMP, 1989):

$$F_w = WPC_a\rho^{-1}$$

In this case the resulting washout ratios are temperature and pressure dependent and about a factor of 1200-1300 smaller. An alternative method to calculate the wet flux is the use of scavenging rates. This subject was extensively described by Slinn (1983).

3.3.1. Data on precipitation

The existing estimates of surface precipitation (rain, snow, hail,...) over the seas and oceans are based on a very limited data set. A serious problem with the measurement of precipitation, both on the ground and aloft, is its great variability in time and space. Moreover, the total amount of rainfall at any location can be a combination of a small number of very intense showers (of convective origin) together with comparatively extended periods of light rainfall from stratiform clouds. The overall contributions of these two kinds of precipitation are often comparable (Browning, 1990). Even for a relatively small area as the North Sea, an accurate value for annual

average rainfall is not available at present. It is, however, generally recognized that less rain falls over sea than over land (see e.g. Cambray et al., 1979; Baeyens et al., 1990). By measurements on a gas platform, the rainfall there was observed to be about 55% of that at land-based stations at similar latitude on either side of the North Sea (Cambray et al., 1975). Taking this observation into account, a mean rainfall value of 438 mm per year was calculated for the North Sea on the basis of measurements of seventeen stations situated on adjacent land. This value was seen as a kind of "standard" value. However, this value was adjusted to 475 mm annually on the basis of measurements at seven stations surrounding the North Sea (Cambray et al., 1979). Van Aalst et al. (1983) disagree with Cambray's value, claiming that the difference between the amount of precipitation on land and at sea is lower than assumed before. Baeyens et al. (1990) measured the yearly precipitation volume at the West-Hinder light vessel; the mean value, based on a period of two years, amounts to 430 mm per year. They also indicated that, in general, there is less precipitation above the sea. They found an average ratio West-Hindler/De Blankaert (a Belgian coastal station) of 0.72 and a ratio of 0.60 for West-Hindler/all Belgian meteorological stations. Krell and Roeckner (1988) used a model to simulate the atmospheric input of Pb and Cd into the North Sea, and used yet another annual precipitation rate, namely 558 mm.

According to Balls (1989), the uncertainty in the amount of rainfall is the most important single error source in flux estimations. It is obvious that more reliable values are urgently needed in order to be able to calculate more accurate wet deposition fluxes. In the future, space-based techniques for measuring global rainfall will provide us with data with a good resolution and accuracy. Radars and/or radiometers, installed on satellites, will be able to measure the instantaneous intensity of the rain or hail that is falling, from which an estimation can be made of how much rain has fallen in a particular area over a certain amount of time, and all of this will happen on a routine basis (Bowler, 1990; Kedem et al., 1990; Scofield, 1991).

3.3.2. Concentrations in precipitation

In Table 9 an overviev of data concerning measured precipitation concentrations over the North Sea and adjacent areas is given. It is obvious that the Swedish concentrations measured by Ross (1987 and 1990) are lower than those reported for The Netherlands (van Jaarsveld and Onderlinden, 1986; van Daalen, 1991). On the other hand, the values of Jickells et al. (1992) for Scottish snow and the wet-only values for Sweden (Ross, 1990) agree very well. The coastal values listed by van Aalst et al. (1983) show rather large variations, probably because they were obtained

Table 9: Measured precipitation concentrations (µg l^{-1}) over the North Sea and adjacent areas (s- preceding an area means southern)

Area	Period	Cd	Cr	Cu	Pb	Zn	Remarks	References
The Netherlands	'82-'83	0.26-0.36	0.21-0.8	1.8-4.9	8.9-20	18-32	bulk	van Jaarsveld and Onderlinden (1986)
The Netherlands	'86-'88	0.5-0.9	1.4-1.8	6.7-8.0	13-20	21-31	wet-only	van Daalen (1991)
Sweden	'84-'85	0.033-0.15	-	0.46-1.5	2-9	4.2-16	bulk	Ross (1987)
Sweden	'87-'88	0.04-0.12	0.06-0.16	0.85-2.32	1.84-3.75	4.1-10.2	wet-only	Ross (1990)
Scotland (Highlands)	'87	0.16	-	1.2	1.6	6.4	snow (Cd, Pb dissolved only)	Jickells et al. (1992)
North Sea (coast)	'72-'81	0.3-1.2	0.2-4	4-30	10-35	20-160	literature range	van Aalst et al. (1983)
Norway (coast)	'78-'79	0.27	-	-	11	15	weekly bulk	Pacyna et al. (1984)
Norway (coast)	'80-'84	0.37	-	-	7.1	9.2	-	S&TWG (1987)
Scotland (coast)	'87-'88	0.68	-	2.3	4	13	wet-only	Balls (1989)
sNorth Sea	'81	3	-	39.5	13	194	wet-only	Dedeurwaerder et al. (1985)
sNorth Sea	'74-'85	0.5-9.5	-	2.5-77	10-29	26-490	literature range	GESAMP (1989)
sNorth Sea	'84-'87	10	-	77	29	500	wet-only	Baeyens et al. (1990)

by different operators using other sampling methods at different sites and over other time intervals. However, the lowest values of these ranges agree very well with the concentrations measured at the North Sea coasts of Norway (Pacyna et al., 1984; S&TWG, 1987) and in Scotland (Balls, 1989). Ross (1987) observed that the concentrations in southern Sweden were higher and that the wet deposition fluxes were higher than the Swedish anthropogenic emissions, so a long range transport of the pollutants was postulated. Clearly, the southern North Sea concentration values included in Table 9 are very high compared to the other values. The inconsistency of those mentioned in the GESAMP report (1989) is ascribed to sampling problems (e.g. not all measurements were wet-only) and difficult analysis associated with this kind of measurements. Also, at the West-Hindler station (and during several cruises) rainwater samples were collected (Dedeurwaerder et al., 1985; Baeyens et al., 1990). Although the sampling was done only when precipitation occurred and precautions were taken to avoid contamination, the concentration values reported are very high compared to the other values in Table 9. The results of the ATMOS report (1984) point out that the heavy metal concentrations in rainwater above the sea are higher than above land (this is the "maritime effect" as reported by Cambray, 1975). Cambray (1975) thought that the maritime effect was caused by bubble bursting processes, which bring aerosols coming from an enriched sea surface layer into the atmosphere. However, Balls (1989) concluded on the basis of measurements of the enrichment factor in surface water that this process is not a significant contributor to the "maritime effect". Possible alternative processes are thought to be enhanced solubility of the metals above the sea due to aging of the aerosols emitted by land based sources and/or different physico-chemical characteristics of rainwater above land and water (ATMOS, 1984).

Trace metal concentrations in precipitation collected from "CAMP" stations, around the North Sea (Table 10) are quite variable from year to year, probably due to orographic effects. Also, they show much less consistency, undoubtely because of the greater sampling and analytical problems associated with such measurements. Therefore the results have not been used to calculate deposition fluxes directly, but whenever was possible on the measurement-based calculation.

Table 10: An overview of the data submitted to PARCOM-ATMOS as regards elemental concentrations (µg l^{-1}) in precipitation for 1988, 1989, 1990 and 1991, measured at "CAMP" stations

Station	Period	Cd	As	Cr	Cu	Ni	Pb	Zn
B3A	'91	0.1	-	-	1.26	-	2.7	8.16
DK1	'88	0.08	-	-	1.4	-	4.2	12.1
	'89	0.10	0.45	0.46	1.1	0.45	3.93	15.58
	'90	0.10	-	0.28	0.99	0.50	2.73	9.10
	'91	-	-	0.17	1.42	0.35	2.72	13.50
D1	'89	0.25	0.21	0.52	2.89	3.34	4.24	11.39
	'90	0.15	0.31	0.49	1.05	0.71	2.43	11.47
NL2	'88	0.19	-	-	2.9	-	6.4	-
	'89	0.12	-	-	2.62	0.35	10.18	14.95
	'90	0.16	-	-	2.45	-	5.91	11.26
	'91	0.16	-	0.40	2.97	0.51	6.41	14.52
NL3	'90	0.16	-	-	2.53	-	2.78	12.56
	'91	0.13	-	-	3.36	0.77	6.84	13.82
GB1	'88	0.28	-	-	3	-	8.7	16.1
	'89	0.23	0.78	1.93	4.65	1.42	7.67	25.08
	'90	0.40	0.70	0.75	2.00	1.46	4.93	16.8
	'91	0.16	0.42	0.50	6.50	1.70	7.70	18.70
GB2	'88	(0.58)	-	-	6.5	-	22.7	46.1
	'89	0.57	1.11	1.68	7.85	3.28	22.79	61.33
	'90	0.36	1.10	1.04	3.52	2.66	10.65	33.45
	'91	0.46	1.18	0.90	7.60	5.50	19.00	49.50
GB3	'88	0.20	-	-	2.4	-	7.5	8.3
	'89	0.13	0.59	0.68	3.06	1.31	5.25	9.66
	'90	0.13	-	0.25	1.94	0.74	3.04	8.98
	'91	0.14	0.26	0.30	4.30	0.70	4.00	8.10
N1	'88	0.11	-	-	-	-	7.4	14.1
	'89	0.11	-	-	-	-	5.45	11.43
N3	'91	0.06	-	0.60	2.50	0.10	7.00	14.20

3.3.3. Estimated wet deposition fluxes to the North Sea

As explained at the beginning of this section the wet flux of trace metals can be estimated either directly or indirectly. In Table 11 wet and total fluxes to the North Sea and its coasts are given. The results will depend on the area considered to constitute the North Sea and the used value for the annual precipitation rate are included, as well as on the method used (direct or indirect measurement).

It is very difficult to compare any data in the Table 11, because the authors used different rainfall rates and methods, and because both total fluxes and wet fluxes are listed. The estimated fluxes to the coast of southern Norway (S&TWG, 1987) and of Scotland (Balls, 1989) are reported to be lower than the other coastal values. And for the North Sea itself, the West-Hindler values are either relatively high (except for Pb) (ATMOS, 1984; Baeyens et al., 1990) or very low (Dedeurwaerder et al., 1985). Baeyens et al. (1990) reported that the wet flux to the North Sea is clearly higher than that at a Belgian coastal station. It should be noted that the input values reported by Otten (1991) are based on sampling flights and that they were calculated using scavenging rates.

As far as wet fluxes are concerned, the uncertainties are far from being known. The theoretical approach to wet deposition is rather crude in the sense that the mechanisms by which atmospheric particulate matter is scavenged by rain, are not yet fully understood. For indirect estimations of the wet flux, the washout ratio used in the calculations is of considerable importance. In Table 12 some relatively recent values for trace metals are listed. They are again, very difficult to compare. The values used in the GESAMP (1989) report and by Otten (1991) are "best estimates" based on published washout ratios for trace metals above the North Sea. In the ATMOS report (1984), it is stated that values for Cu, Zn and Cd above the sea are up to 5 times larger than above land.

To assess the environmental effect of the atmospheric input of heavy metals into the North Sea, it is important to know whether a distinction can be made between the amount of a certain trace metal that reaches the surface of the earth in a dissolved or in a particulate form. For instance, dissolved metals are much more readily available to be incorporated by organisms. Flament et al. (1984) investigated the metal distribution over the solid and liquid phases in rain at some French coastal sites. They found the following percentages of dissolved material: Pb (21-31%), Cd (53-78%), Cu (63-94%) and Zn (68-87%). Losno et al. (1988) observed that Zn partitioning is governed by adsorption/desorption processes on existing particles, which are pH

Table 11: Total (dry + wet) or wet flux to the North Sea in kg km^{-2} y^{-1} (s- preceding an area means southern)

Area	Rain (mm y^{-1})	Cd	Cr	Cu	Pb	Zn	Method	Remarks	References
coastal stations	438	-	1.4	10.5	11	31	direct	wet	Cambray et al. (1979)
coastal stations	778-1028	0.3-1.4	-	6.1-16.2	5.6-13.5	20.6-55.6	direct	total	Flament et al. (1984)
coastal stations	-	0.09-1.7	0.58	0.8-27	5.1-14	9.3-156	-	total	PARCOM (1987)
Scotland (coast)	-	0.39	-	1.3	2.3	7.6	direct	wet	Balls (1989)
sNorway (coast)	1399	0.48	-	-	9.2	12	direct	total	S&TWG (1987)
Dutch Continental Shelf	-	0.06-0.11	0.15-0.30	0.28-0.55	4.8-9.6	2.4-4.8	-	total	S&TWG (1987)
North Sea	680	0.1-0.5	-	1-4.4	4-23	5-23	indirect	total	GESAMP (1989)
North Sea	430	2.9	-	25	7	170	direct	wet (dissolved)	Baeyens et al. (1990)
North Sea	500	0.35	-	2.68	6.5	15.1	indirect	total	Otten (1991)
sNorth Sea	-	1.6	-	24.9	9.4	143	-	wet	ATMOS (1984)
Southern Bight	458	0.0002	-	0.0026	0.0014	0.015	direct	total	Dedeurwaerder et al. (1985)
Southern Bight	500	0.43	-	2.5	8.8	19.7	indirect	wet	Otten (1991)
Southern Bight	500	0.71	-	5.36	12.9	30.2	indirect	total	Otten (1991)
German Bight	677	-	0.43	1	5.7	4.3	indirect	wet	Kriews (1992)

Table 12: Washout ratios for trace metals

Cd	Cr	Cu	Pb	Zn	Remarks	References
125-500	150	140-751	76-169	179-1000	literature range	Schroeder et al. (1987)
-	-	-	-	1226	value measured	Jaffrezo and Colin (1988)
200-1000	-	200-1000	200-1000	200-1000	range used	GESAMP (1989)
150	-	150	150	150	value used	Otten (1991)
-	200-1280	60-3800	20-1350	280-11500	value measured (snow)	Cadle et al. (1990)

dependent. Nevertheless, Colin et al. (1990) state that the nature of the particles is also important. Jickells et al. (1992) conclude that the solubility of an element is the result of the complex interplay of several factors and cannot be simply assigned to one factor such as pH.

3.4. Total deposition fluxes to the North Sea

The amount of material deposited to the North Sea as reported by several authors, is given in Table 13. The atmospheric flux reported in the ATMOS (1984) report is significantly higher than the other total fluxes, except for Pb. The range calculated by van Aalst et al. (1983) is also relatively high but the other total flux values agree fairly well. They were assessed at totally different points in time, with other methods and concentration measurements to start from (coastal precipitation vs. airborne concentrations), and even the area taken into consideration is different. The annual estimation of atmospheric fluxes reported by ATMOS are based on measurements during '88,'89,'90 and '91 at the so-called "Central North Sea stations", but taking into account concentration gradients from land to sea due to removal processes or due to dilution. For each station a bulk gradient correction factor (defined as the ratio of the average deposition at the certain station to the average deposition over the total North Sea area) was derived from model calculations developed by RIVM (van Jaarsveld et al.,1986a; van Jaarsveld et al., 1991). It is evident that, for a number of elements, the estimated depositions reported for '91 (ATMOS, 1992) are higher than those calculated for '90 (ATMOS, 1991). The estimated increases in Pb (30%) and Cu (40%) are higher due to high concentrations at UK stations.

If deposition to the total North Sea area is estimated from observations at coastal stations, one has to deal with the problem of how representative those observations are for larger areas. The problem can be split into a problem of representativeness of precipitation amounts and a problem of representativeness of measured concentrations. The first problem can be solved reasonably by using a precipitation which varies from year to year. Taking a precipitation amount which is 70% of the median precipitation amount of all the coastal stations could be a way to derive such a value for a specific year for the North Sea area. The second problem can be solved only when knowledge about atmospheric residence times is included in the method. A combined method based on observations and model calculations can therefore be expected to give the most realistic results.

As far as the relative importance of dry and wet deposition goes, most authors seem to agree on the fact that, for the trace metals, the wet flux is more important than the dry flux, except perhaps for Pb, where some authors consider both fluxes to be of about the same magnitude. However, on the extent of this difference, opinions vary very widely (Galloway et al., 1982; ATMOS, 1984; Schroeder et al., 1987; GESAMP, 1989; Martin et al., 1989; Baeyens et al., 1990; Otten, 1991; Remoudaki

Table 13: Total (dry + wet) atmospheric input of trace metals into the North Sea in tons y^{-1}

Area x 10^5 (km^2)	Rain ($mm\ y^{-1}$)	Cd	Cr	Cu	Pb	As	Zn	Method	References
-	-	-	740	5600	5800	460	1600	indirect	Cambray et al. (1979)
5.25	685	110-430	70-1400	1400-10000	3600-13000	220-720	7200-58000	direct	van Aalst et al. (1983)
5.25	-	-	100-530	380-1600	1800-6400	150-510	3900-12000	indirect	Stössel (1987)
-	-	45-240	300-900	400-1600	2600-7400	40-120	4900-11000	direct	PARCOM (1987)
5.3	-	900	-	13542	7367	-	77566	-	ATMOS (1984)
5.25	500	47	205	620	1900	95	4600	indirect	ATMOS (1990)
5.25	520	32	88	321	958	95	2740	indirect	ATMOS (1991)
5.25	650	27	94	610	1241	83	3099	indirect	ATMOS (1992)
5.3	680	50-250	-	500-2300	2300-12000	130-580	2700-12000	indirect	GESAMP (1989)
5.35	600	158	-	1348	3670	-	7409	indirect	Injuk et al. (1990)
5.25	677	-	-	-	3500	160	-	indirect	Dannecker et al. (1992)
5.25	677	-	530	5100	3200	160	-	direct	Schulz in Dannecker et al. (1993)
5.25	677	-	400	670	3500	160	4200	indirect	Kriews (1992)

et al., 1991). Martin et al. (1989) remark that the ratio of wet to dry deposition is controlled by many meteorological factors and also by the distance between the sampling site and the emission source (see also Migon et al., 1991; Remoudaki et al., 1991).

Whenever the deposition of micropollutants to a water surface is estimated, attention should be paid to the reverse fluxes (from the water to the atmosphere) as well. According to the ATMOS report (1984), for which the heavy metal content in the sea surface microlayer was determined, the maximum water-to-air fluxes are at least 30 times smaller than the total input fluxes. The authors of the GESAMP (1989) report state that, although the atmospheric concentrations of trace metals associated with large (resuspended) sea salt particles constitute only a minor fraction of the total atmospheric concentration, this fraction may well account for a significant part of the gross dry deposition flux. This complicates the assessment of the "real" deposition fluxes to the sea.

3.5. Deposition fluxes based on model calculations

3.5.1. Introduction

An alternative way of determining the deposition of micropollutants from the atmosphere to the sea involves atmospheric transport models. Basically, one uses emission data for a certain source area (e.g. Europe) in combination with a long range transport model (which requires a number of input data) to simulate the dispersion and deposition of a substance for a determined receptor area (e.g. the North Sea). Model calculations can provide independent estimates for atmospheric inputs which can be compared to input estimates from measurements. Moreover, the calculations may indicate the spatial variation of the deposition, and allow the evaluation of the representativeness of measurements at coastal stations. In this section the results of calculations performed using relatively recent models which have been applied to the calculation of the total deposition of heavy metals to the North Sea will be discussed and compared to the values obtained from field measurements.

3.5.2. Literature data on the deposition fluxes based on model calculations

In the 1980's, van Aalst et al. (1983) employed a simple model to compare the long-term (ca. 1 year) average concentrations of various elements, and wet and dry deposition for an area of 1000x1000 km^2 of the North Sea. The total air concentrations at the receptor were calculated as the sum of the contributions from the different emission areas (the "cells" of the emission grid) weighted by the probability that the wind would blow from that emission cell. The results showed good agreement between measurements and calculations. The data from this and other works (PARCOM, 1985) were recently reviewed by van Aalst and Pacyna (PARCOM, 1986) in order to assess the atmospheric inputs of trace elements to the North Sea.

A more advanced 3-dimensional trajectory model based on the Monte-Carlo method was recently employed to estimate the long range transport and deposition of Pb to the North Sea (Krell et al., 1986). The emission data used were the numbers from Pacyna (1985). Results from the first model calculation show that the calculated and measured monthly mean depositions and surface concentrations of Pb over the sea differ by about a factor of 2. In 1988, Krell and Roeckner used more a distinguished trajectory model to estimate the dry and wet deposition of Pb and Cd into the North Sea. The input of Pb and Cd was simulated with a long range transport

model using gridded data of the respective anthropogenic emissions in Europe and the relevant meteorological data. Krell and Roeckner's model is particularly designed for episode studies.

The total annual atmospheric input of Pb to the North Sea was determined for all the months of 1980 to be ca. 1440 tons by Petersen (1987). A relatively large contribution on the order of 50% was estimated for the UK. The Netherlands, France and Germany contributed about 12% each, Belgium 5%, Sweden 1.5%, Denmark 1% and Norway even less. However, conclusions from this work should be taken with caution. The results are based only on a one year period, which shows a significant month-to-month variability of the deposition. More recently the same author estimated the annual input of Pb to be 2300 tons (Petersen et al., 1988).

The TREND model was developed at the Dutch National Institute of Public Health and Environmental Protection in order to calculate long term averaged concentrations and depositions (van Jaarsveld et al., 1986). It is a statistical long-range version of the Gaussian plume model, what means that the dispersion from a source is assumed to follow the prevailing wind direction and wind speed within a sector of 30% in the horizontal plane. The vertical dispersion is limited by the earth surface and the top of a mixing layer. Due to wet and dry deposition and chemical reactions, atmospheric concentrations decrease during the transport; this process is also taken into account. The model assumes homogeneous climatology and boundary characteristics over whole Europe. The occurring meteorological situations are grouped in a limited number of classes and the calculations are carried out separately for 5 size classes from < 0.95 μm to > 20 μm particles, each of which has its own deposition characteristics. This model has been successfully applied to a period of a month, but even shorter periods yielded reasonable results.

The model of Graßl et al. (1989) is very similar to the model of Krell and Roeckner.

The model of Warmenhoven et al. (1989) is, in fact, an elaborated version of the van Jaarsveld model, but instead of applying it to trace metals solely, a number of organic compounds like PAHs, PCBs, pesticides, etc. were also taken into consideration. The model assumes the same meteorology, surface characteristics and deposition velocities over the whole surface area.

The main problem concerning model based calculation is in estimating the emissions. Though, for some countries, there were explicit data on emissions of pollutants, generally the annual emissions from all countries have been estimated on the basis of industrial and agricultural activities within the countries. All the models used almost similar emission data as input to their model.

There are only a few studies on the deposition into the North Sea based on models. The total atmospheric input of some pollutants into the North Sea is given in Table 14. The values were calculated with the models discussed in the previous section. Included is also the "best" estimate defined as the value obtained when emissions are multiplied with the average ratio measured/modelled air concentration. It can be seen that there is a general agreement between the results of the different models. Taking into account that all models use more or less the same emission data, this agreement confirms the idea that the influence of the different model assumptions is not very large, at least not in the case of the total deposition into the North Sea.

For the reported trace elements, the model values are consistently lower than the values obtained from field measurement data in Table 13. Krell and Roeckner (1988) claim that this discrepancy can be explained as follows: the extrapolation of coastal measurements, on which most deposition estimates up until 1988 were based, cannot be justified, because there is no reason to believe that the high precipitation intensities/volumes measured along the southern and western coasts are representative for the whole of the North Sea. The authors find a strong argument in the life-time of clouds which is not more than a few hours for a precipitating one: in this way, most of the pollutant material is likely to be washed out within about 100 km from the coast. Their model simulations (and those by van Jaarsveld et al. (1986)) reveal a substantial decrease of the deposition across the southern and western coasts. Van Jaarsveld et al. (1986) state that the discrepancy might partly be due to less accurate sampling and analysis of rainwater as well.

3.5.3. Validation of the models

Van Jaarsveld et al. (1986) note that there are some assumptions inherent to their model, which do not agree very well with reality. For instance, it is not correct to assume that transport and dispersion over sea are analogous to those over land. The stability over sea is mainly determined by the temperature difference between the air and the seawater, and shows hardly any diurnal variation. Also, in the coastal zone complicated transition phenomena occur, which are not accounted for in the model. However, the authors do not think that a more realistic model would yield largely different results.

Krell and Roeckner (1988) had difficulties to validate their model because of the lack of comparison material for the North Sea. Therefore, they were obliged to simulate air and precipitation concentrations at certain sites and for certain periods (e.g. a month) for which measurements were made, and their results agreed fairly well

Table 14: Comparison of the total deposition (tons y^{-1}) to the North Sea calculated with different models

Reference	Cd	Cr	Cu	Pb	Zn	As
Earlier estimates review in PARCOM (1985)	110-430	70-1400	1400-10000	3600-13000	7200-58000	220-720
PARCOM (1986)	14	70	130	2600	1200	42
Van Jaarsveld et al. (1986)	11	58	100	2000	940	-
Petersen (1987)	-	-	-	1440	-	-
Petersen et al. (1988)	-	-	-	2300	-	-
Krell and Roeckner (1988)	11	-	-	1200	-	-
Graßl et al. (1989)	-	-	-	2300	-	-
Warmenhoven et al. (1989)	15	72	110	1900	930	-
Van Jaarsveld (1991)	10	-	-	960	600	-
ATMOS (1990)-"best" estimates (model/measurements)	13	-	-	870	1800	-

with the measured values.

Warmenhoven et al. (1989) estimate that the results concerning the heavy metal deposition are the most reliable ones. In general, the validity of this model is mainly governed by the quality of the emission data and the choice of the emission grid (because some materials are so stable in the atmosphere, that a much larger emission area should be taken into consideration). As a result of this, the real deposition of these elements should be higher than predicted by the model. Finally, the assumption that the North Sea is a well-mixed tank, without any inflow or outflow except from rivers (and the atmosphere), has an influence on the deposition estimates. In this concept it would be more realistic to include the dynamics of the North Sea in the model.

4. Relative contribution of atmospheric deposition of trace metals to the total input into the North Sea

Apart from atmospheric pollution, the North Sea is subject to a number of other sources of pollution as well: e.g. input via rivers, direct discharges from industries into the estuaries, dumping of industrial wastes, dredging sludge and sewage sludge, and drainage of sewage (van Aalst et al., 1983). It is very difficult to evaluate the relative importance of the various input sources as most input estimates are subject to considerable uncertainty arising from analytical and sampling problems. Moreover, the actual quantity of pollutants entering the North Sea varies from year to year, depending on factors like natural variations in river flows and water exchange with adjacent sea areas, economic variations (industrial expansion and reorganization, large strikes), changing legislation (emission and dumping restrictions), atmospheric conditions (wind flow patterns, rainfall intensity) and unforeseen circumstances (accidents).

Although, in a number of publications, estimates of the non-atmospheric input are given (e.g. Cambray et al., 1979; van Aalst et al., 1983; ATMOS, 1984), we chose to use the recent data as given by Warmenhoven et al. (1989). They use the figures reported during the Second International Conference on the Protection of the North Sea in 1987, which are based on information obtained from the countries concerned. For the contaminants which are not included in the report of the Conference, the total fluxes are estimated on the basis of data on the total loading through the Rhine and the Meuse (Folkertsma, 1989). These authors point out, however, that the values calculated in this way can only serve as an indication of the order of magnitude. Also, the contamination of the water entering the North Sea from the English Channel, the Baltic Sea and the North Atlantic is not included in the estimates. And the river catchment areas are also subject to atmospheric deposition (Warmenhoven et al., 1989). In Table 15 the estimates for non-atmospheric deposition of metals are given. By comparing the non-atmospheric input to the atmospheric input fluxes discussed earlier, it is possible to get an idea of the relative importance of both pathways for the input of pollutants to the North Sea. In Table 16, the non-atmospheric values with the measured and modeled atmospheric data are compared. We used the values calculated by the model of Warmenhoven et al. (1989) and flux values reported by ATMOS (1992). The most important pathway for each compound seems the same for measurements and model. Based on this data, non-atmospheric input is more

important for all the elements. GESAMP (1989) notes that, for particulate trace elements, the major source is usually the rivers. However, particulate riverine material is likely to be deposited close to the source regions, while atmospheric input can more easily occur to remote oceanic areas. Still according to the GESAMP report, the global atmospheric and riverine inputs are comparable for dissolved Cu, while for Zn and Cd atmospheric inputs appear to dominate. The atmospheric input of Pb is expected to decrease over the next decade, due to the growing use of unleaded gasoline. Martin et al. (1989) state that the atmospheric input to the Mediterranean Sea is predominant over the river input, either dissolved or particulate. For organic contaminants as well, the riverine flux may influence only the nearshore areas, while atmospheric input is supposed to have a much wider impact over regional seas (GESAMP, 1989).

However, it must be emphasized that the accuracy of the estimations of both the atmospheric and non-atmospheric input sources is still very poor. Thus the reliability of the comparison of both pathways is very uncertain.

Table 15: Total input into the North Sea (tons y^{-1}) by non-atmospheric sources. The input of water from the English Channel, the Baltic Sea and the North Sea is not included (Warmenhoven et al., 1989)

Element	Input
Cd	95
Cr	4000
Cu	2800
Pb	3500
Zn	17000

Table 16: Relative contribution of atmospheric deposition to the total loading of the North Sea, in percent

Element	**Atmospheric-measured** ATMOS (1992)	**Non-atmospheric** Warmenhoven et al. (1989)	**Atmospheric-modelled** Warmenhoven et al. (1989)	**Non-atmospheric** Warmenhoven et al. (1989)
Cd	22	78	14	86
Cr	2	98	2	98
Cu	18	82	4	96
Pb	26	74	35	65
Zn	15	85	5	95

5. Conclusion

From this study several important gaps in the knowledge of the atmospheric deposition to the North Sea have become apparent.

For aerosols, the presently available concentrations data need to be improved, on the basis of airborne mass size distributions. The dependence of the deposition velocity upon the particle size requires further investigation and better knowledge of the kinetic parameters as deposition/transfer velocity. It should be stressed that the success of any further research in this field, particularly that regarding dry deposition to natural waters, should focus on accurate determinations of the size distribution of airborne particulate matter since this is directly controlling the deposition rates.

It is obvious that current knowledge about the wet deposition of trace elements to the North Sea is insufficient. For the trace metals, which were dealt with in this report, a number of specific problems like the lack of accurate washout ratios for the North Sea area or the contribution of resuspension to the observed pollutant concentrations still have to be solved. Reported washout or scavenging ratios for a particular element vary substantially. Part of the problem relies on the method by which scavenging ratios are determined; usually they are computed from rain and air concentrations measured on samples that were not collected contemporaneously. Therefore, it is absolutely necessary to work out a global measurement strategy for the North Sea area which would include precipitation and air sampling, preferably simultaneously at a large number of sites (islands, cruises, platforms, coastal stations) and over a considerable period of time, in order to be able to calculate the scavenging rates from really paired rain and air samples. The considerable expansion of the geographical coverage of rain sampling programmes should eliminate the uncertainties on the temporal distributions of precipitations events for the North Sea area.

The results of different studies on the atmospheric input of trace elements into the North Sea are still indicating large uncertainties. A combined model and monitoring approach seems to be most useful for the determination of atmospheric fluxes to large surface waters. Model studies give much lower values than the studies based on measurements. The major uncertainty in model studies is the quality and completeness of the emission data and the different size distributions used in the models. Furthermore, none of the models takes into account particle growth due to high relative humidities.

Emission estimates for Cd and Zn currently in use are most probably too low. Cd emissions in 1982-1989 over a whole region, should be at least 30% higher. For Zn, the general underestimating is at least a factor of 3. Therefore, research on emission processes and identification of unknown emission categories is urgently needed for heavy metals (Van Jaarsveld, 1991).

6. References

Amundsen, C.E., Hanssen, J.E., Semb, A. and Steinnes, E. (1992) Long-range atmospheric transport of trace elements to Southern Norway. Atmos. Environ., **26A**, 1309-1324.

Andren, A.W., Lindberg, S.E., and Bate, L.C. (1975) Atmospheric input and geochemical cycling of selected trace elements in Walker Branch Watershed. Oak Ridge, TN, Oak Ridge National Laboratory, ORNL Report NSF-EATC-13.

ATMOS (1984) Working group on the atmospheric input of pollutants to convention waters. Heavy metal input from the atmosphere into the North Sea. ATMOS report 4/4-E.

ATMOS (1990) Working group on the atmospheric input of pollutants to convention waters. ATMOS report 8/12/1-E.

ATMOS (1991) Working group on the atmospheric input of pollutants to convention waters. ATMOS report 9/18/1-E.

ATMOS (1992) Working group on the atmospheric input of pollutants to convention waters. ATMOS report 10/4/2-E.

Baeyens, W., Dehairs, F. and Dedeurwaerder, H. (1990) Wet and dry deposition fluxes above the North Sea. Atmos. Environ. **24A**, 1693-1703.

Baeyens W. and Dedeurwaerder H. (1991) Particulate trace metals above the Southern Bight of the North Sea - I. Analytical procedures and average aerosol concentrations. Atmos. Environ. **25A**, 293-304.

Balls, P.W. (1989) Trace metal and major ion composition of precipitation at a North Sea coastal site. Atmos. Environ. **23**, 2751-2759.

Barrie, L.A., Lindberg, S.E., Chan, W.H., Ross, H.B., Arimoto,R., and Church, T.M. (1987) On the concentration of trace metals in precipitation. Atmos. Environ., **21**, 1133-1135.

Bowler, S. (1990) Radar network watches where the wind blows. New Scientist, **24** March, 30-31.

Braun, H., Vogg, H., Halbritter, G., Bräutigam, K.R. and Katzer, H. (1984) Comparison of the stack emissions from waste incineration facilities and coal fired heating power stations. Recycling International. **1**, 1-2.

Breekke, F.H. (1976) Impact of acid precipitation forest and fresh-water ecosystems in Norway. SNSF Project Research Report, Phase 1, 1972-75. Oslo, Norwegian Institute for Forest Research.

Browning, K.A. (1990) Rain, rainclouds and climate. Q.J.R. Meteorol. Soc. **116**, 1025-1051.

Buijsman, E., Jonker P.J., Asman W.A.H. and Ridder T.B. (1991) Chemical composition of precipitation collected on a weathership on the North Atlantic. Atmos. Environ. **25A**, 873-883.

Cadle, S.H., VandeKopple, R., Mulawa,P.A. and Muhlbaier Dasch,J. (1990) Ambient concentrations, scavenging ratios, and source regions of acid related compounds and trace metals during winter in northern Michigan. Atmos. Environ., **24A**, 2981-2989.

Cambray, R.S., Jefferies, D.F., and Topping, G. (1975) An estimate of the input of atmospheric trace elements into the North Sea at Clyde sea (1972-73). AERE Harwell, England (AERE Report R 7733).

Cambray, R.S., Jefferies, D.F. and Topping, G. (1979) The atmospheric input of trace elements to the North Sea. Mar. Sci. Comm. **5**, 175-194.

Cawse, P.A. (1974) A survay of atmospheric trace elements in the U.K. (1972-73). AERE Harwell, England, AERE Report R 7669.

Colin, J.L., Jaffrezo, J.L. and Gros, J.M. (1990) Solubility of major species in precipitation: factors of variation. Atmos. Environ. **24A**, 537-544.

Dannecker, W., Bredthauer, U., Kriews, M., Rebers, A., Selke, K. and M. Shulz (1992) Preliminary report of atmospheric pollutant measurements in the northern North Sea region. University of Hamburg, Germany.

Dannecker, W., Hinzpeter, H., Kriews, M., Naumann, K., Schulz, M., Schwikowski, M., Steiger, M. and Terzenbach, U. (1993) Atmospheric transport of contaminants, their concentrations and input into the North Sea. In: Circulation and Contaminant Fluxes in the North Sea. Sündermann J. (ed.), Springer Verlag Berlin, Heidelberg, New York, (in press).

Dedeurwaerder, H., Dehairs, F., Xian, Q. and Nemery, B. (1985) Heavy metals transfer from the atmosphere to the sea in the Southern Bight of the North Sea. In Proceedings "Progress in Belgian Oceanographic Research" (edited by R. Van Grieken and R. Wollast), pp. 170-177. University of Antwerp (UIA), Belgium.

Dedeurwaerder H.L. (1988) Study of the dynamic transport and the fall-out of some ecotoxicological heavy metals in the troposphere of the Southern Bight of the North Sea. Ph.D. thesis, University of Brussels (VUB), Belgium.

Dulac, F., Buat-Ménard, P., Ezat, U., Melki, S. and Bergametti, G. (1989) Atmospheric input of trace metals to the Western Mediterranean: uncertainities in modelling dry deposition from cascade impactor data. Tellus **41B**, 362-378.

Feely, H.W., Volchok, H.L., and Toonkel, L. (1976) Trace metals in atmospheric deposition, New York, U.S. ERDA, Health and Safety Laboratory (Environmental Quarterly Report HASL-308).

Flament, P., Noël S., Auger Y., Leman G., Puskaric E. and Wartel M. (1984) Les retombées atmosphériques sur le littoral Nord-Pas-de-Calais. Pollution Atmosphérique oct.-déc. 1984, 262-270.

Flament, P., Lepretre, A., Noel, S. and Auger, Y. (1987) Aerosols cotiers dans le nord de la Manche. Ocean. Acta **10**, 49-61.

Folkertsma, F. (1989) Nationale rapportage Noordzee-Aktieprogramma deel A: inventarisatie van emissies van geselecteerde stoffen in Nederland in 1985. Dienst Binnenwateren, RIZA, Lelystad, The Netherlands.

Friedlander, S.K., Turner, J.R. and Hering, S.V. (1986) A new method for estimating dry deposition velocities for atmospheric aerosols. Atmos. Environ. **17**, 240-244.

Galloway, J.N., Thornton, J.D., Norton S.A., Volchok, H.L. and McLean, R.A.N. (1982) Trace metals in atmospheric deposition: a review and assessment. Atmos. Environ. **16**, 1677-1700.

GESAMP (1989)-IMO/FAO/UNESCO/WMO/WHO/IAEA/UN/UNEP Joint Group of Experts on the Scientific Aspects of Marine Pollution. The atmospheric input of trace species to the world ocean. Reports and Studies GESAMP-WMO 38.

Goldberg, E.D. (1973) North Sea Science. Cambridge, MS. MIT Press.

Graßl, H., Eppel, D., Pettersen, G., Schneider, B., Weber, H., Gandraß, J.G., Reinhardt, K.H., Wodarg, D. and Fließ, J. (1989) Stofeintrag in Nord-und Ostsee über die Atmosphäre. GKSS-Forschungszentrum, GKSS-89/E/8.

Hutton, M. and Symon, C. (1986) The quantities of cadmium, lead, mercury and arsenic entering the U.K. environment from human activities. Sci.Total Environ., **57**, 129-150.

Hutton, M. (1982) Cadmium in the European Community, London. Monitoring and Assessment Research Centre (MARC Report 26).

ICES (1978) Input of pollutants to the Oslo Commission area, Cooperative Research 77. Charlottenlund, Denmark. Int. Council for the Exploration of the Sea.

Injuk, J., Otten, Ph., Rojas, C., Wouters, L. and Van Grieken, R. (1990) Atmospheric deposition of heavy metals (Cd, Cu, Pb and Zn) into the North Sea. Final report, NOMIVE*2 task No DGW-920. University of Antwerp, Belgium.

Injuk, J., Otten, Ph., Laane, R., Maenhaut, W. and Van Grieken, R. (1992) Atmospheric concentrations and size distributions of aircraft-sampled Cd, Cu, Pb and Zn over the Southern Bight of the North Sea. Atmos. Environ., **26A**, 2499-2508.

Jaffrezo, J.L. and Collin, J.L. (1988) Rain-aerosol coupling in urban area: scavenging ratio measurement and identification of some transfer processes. Atmos. Environ., **5**, 929-935.

Jickells, T.D., Davies, T.D., Tranter, M., Landsberger, S. and Jarvis, K. (1992) Trace elements in snow samples from the Scottish Highlands: sources and dissolved/particulate distributions. Atmos. Environ. **26A**, 393-401.

Kedem, B., Chiu, L.S. and North, G.R. (1990) Estimation of mean rain rate: application to satellite observations. J. Geophys. Res. **95**, 1965-1972.

Kemp, K. (1984) Long Term Analysis of Marine and Nonmarine Transported Aerosols. Nucl. Inst. and Methods, B3, **470**.

Kersten, M., Kriews, M. and Förstner, U. (1991) Partitioning of trace metals released from polluted marine aerosols in coastal seawater. Mar. Chem. **36**, 165-182.

Kendall, P.M.H., Bevington, C.F.P. and Pearse, D.J. (1985) Atmospheric cadmium emission and deposition in the Netherlands. Kockengen, Metra Consulting B.V.

Krell, U., Lehmhaus, J. and Roeckner, E. (1986) Atmospheric input of heavy metals into the North Sea: Firs results of a 3-dimensional trajectory model. In: Proc. WMO Conf. on Air Pollution Modelling and Its Application, Leningrad, USSR, 18-24 May.

Krell, U. and Roeckner, E. (1988) Model simulation of the atmospheric input of lead and cadmium into the North Sea. Atmos. Environ. **22**, 375-381.

Kretzschmar, J.G. and Cosemans, G. (1979) A five year survey of some heavy metal levels in the air at the Belgian North Sea coast. Atmos. Environ, **13**, 267-277.

Kriews, M. (1992) Charakterisierung mariner Aerosole in der Deutschen Bucht sowie Prozessstudien zum Verhalten von Spurenmetallen beim Ubergang Atmosphare/Meerwasser. Ph.D. Thesis, University of Hamburg, Germany.

Losno, R., Bergametti, G. and Buat-Menard, P. (1988) Zinc partitioning in Mediterranean rainwater. Geophys. Res. Lett. **15**, 1389-1392.

Main, H.H. and Friedlander, S.K. (1990) Dry deposition of atmospheric aerosols by dual tracer method-I. Area source. Atmos. Environ. **24A**, 103-108.

Martin, J.-M., Elbaz-Poulichet, F., Guieu C., Loije-Pilot M.-D. and Han, G. (1989) River versus atmospheric input of material to the Mediterranean Sea: an overview. Mar. Chem. **28**, 159-182.

Migon, C., Morelli, J., Nicolas, E. and Copin-Montegut, G. (1991) Evaluation of total atmospheric deposition of Pb, Cd, Cu and Zn to the Ligurian Sea. Sci. Total Environ. **105**, 135-148.

Mukherje, A.B. (1986) The discharge of lead, cadmium and mercury into the ecosystem in relation to Finnish industry. Helsinki University of Technology (SF-02150)

Naturvardsverket (1982) Monitor 1982. Tungmetaller och organiska miljögifter i svensk natur.

NAS (1978) The tropospheric transport of pollutants and other substances to the oceans. National Academy of Sciences Press, Washington, D.C., 194 pp.

Otten, P., Storms, H., Xhoffer C. and Van Grieken, R. (1989) Chemical composition, source identification and quantification of the atmospheric input into the North Sea. In Progress in Belgian Oceanographic Research (edited by G. Pichot), pp. 413-422. Prime Minister's Services of Science Policy Office & Ministry of Public Health and Environment, Brussels.

Otten, P. (1991) Transformation, concentrations and deposition of North Sea aerosols. Ph.D. thesis, University of Antwerp (UIA), Belgium.

Pacyna, J.M. (1983) Trace element emission from anthropogenic sources in Europe. Lillestrøm, Report of the Norwegian Institute for Air Resarch, NILU TR 10/82.

Pacyna, J.M., Semb, A. and Hanssen, J.E. (1984) Emission and long-range transport of trace elements in Europe. Tellus **36B**, 163-178.

Pacyna, J.M. (1985) Spatial distribution of the As, Cd, Cu, Pb, V and Zn emissions in Europe within a 1.5 grid net. Lillestrøm, Norwegian Institute for Air Research, NILU OR 60/85.

Pacyna, J.M. (1987) Atmospheric emissions of arsenic, cadmium, mercury and zinc in Europe in 1982. Lillestrøm, Norwegian Institute for Air Research (EMEP/CCC-Rept.3/86).

PARCOM (1985) Sixth Annual Report of the Paris Commission, Annex 6. London.

PARCOM (1986) Report from the Fourth Meeting of the Working Group on the Atmospheric Input of Pollutants to Convention Waters, Oslo 28-30 October.

PARCOM (1987) Current estimates of atmospheric inputs to the North Sea. Ninth Annual Report on the Activities of the Paris Commission, Annex pp.38-42.

Peirson, D.H., Cawse, P.A., Salmon, L. and Cambray, R.S. (1973) Trace elements in the atmospheric environment. Nature **241**, 252-256.

Petersen, G. (1987) Methodology for model calculations of the atmospheric input of trace metals into the North Sea and Baltic Sea. In: Proc. PARCOM Meeting, ATMOS-5, Berlin, 10-12 November.

Petersen, G., Weber, H. and Grassl, H. (1988) Modelling the Transport of Trace Metals from Europe to the North Sea and Baltic Sea. In: Control and Fate of Atmospheric Trace Metals. Pacyna, J.M. and Ottar, B. (eds.), NATO ASI Series, Kluwer Academic Publishers, Dordrecht, The Netherlands.

Remoudaki, E., Bergametti, G. and Losno, R. (1991) On the dynamic of the atmospheric input of copper and manganese into the western Mediterranean Sea. Atmos. Environ. **25A**, 733-744.

Rojas, C.M., Injuk, J., Laane, R.W. and Van Grieken, R. (1993) Dry and wet deposition fluxes of Cd, Cu, Pb and Zn into the Southern Bight of the North Sea. Atmos. Environm. **27A**, 251-259.

Ross, H.B. (1984) Methodology for the collection and analysis of trace metals in atmospheric precipitation. Report CM-67, International Meteorological Institute in Stockholm/Dept. of Met., University of Stockholm.

Ross, H.B. (1987) Trace metals in precipitation in Sweden. Water, Air, and Soil Poll. **36**, 349-363.

Ross, H.B. (1990) Trace metal wet deposition in Sweden: insight gained from daily wet only collection. Atmos. Environ. **24A**, 1929-1938.

Ruijgrok, W., Visser H. and Römer F.G. (1990) Comparison of bulk and wet-only samplers for trend detection in wet deposition. Proceedings International Workshop on Cloud Chemistry and Wet Deposition, Utrecht, The Netherlands, April 1990, pp. 34-40.

Ruppert, J. (1975) Geochemical investigations on atmospheric precipitation in a medium-sized city (Göttingen, FRG), Water, Air and Soil Poll., **4**, 447.

Schladot, J.D. and Nürnberg, H.W. (1982) Report Jülich, Nuclear Research Center.

Schneider, B. (1987) Source characterization for atmospheric trace metals over Kiel Bight. Atmos. Environ. **21**, 1275-1283.

Schroeder, W.H., Dobson, M., Kane, D.M. and Johnson, N.D. (1987) Toxic trace elements associated with airborne particulate matter: a review. J. Air Poll. Control Ass. **37**, 1267-1284.

Scofield, R.A. (1991) Operational estimation of precipitation from satellite data. Palaeogeography, Palaeoclimatology, Palaeoecology (Global and Planetary Change Section) **90**, 79-86.

Sehmel, G.A. and Hodgson, W.J. (1978) A Model for Predicting Dry Deposition of Particles and Gases to Environmental Surfaces. Battelle, Pacific Northwest Laboratory, Richland, WA., PNL-SA-6721.

Selin, E., Mnubi, A., Isakson, J. and Foltescu, V. (1991) Transport and Deposition of Particulate Pollution to the Wast Coast of Sweden. Preliminary report.

Semb, A. and Pacyna, J.M. (1988) Toxic trace elements and chlorinated hydrocarbons: sources, atmospheric transport and deposition. Environmental Report 1988:10. Nordic Council of Ministers, Copenhagen, ISBN Denmark.

Slinn, S.A. and Slinn, W.G.N.(1980) Predictions for particle deposition on natural waters. Atmos. Environ., **16**, 1785-1794.

Slinn, W.G.N. (1983) Air-to-sea transfer of particles. In: Air-sea Exchange of Gases and Particles. Liss, P.S. and Slinn, W.G.N. (eds.) pp. 299-405. D. Reidel, Dordrecht.

Smith, F.B. (1991) Deposition processes for airborne pollutants. The Meteorological Magazine **120**, 173-182.

S&TWG Scientific and Technical Working Group (1987) Quality status of the North Sea. Second International Conference on the Protection of the North Sea, London, November 1987, Vol. **5**, p. T8 and Vol. 6, pp. 6-10.

Steiger, M., Schulz, M., Schwikowski, M., Naumann, K. and Dannecker, W. (1989) Variability of aerosol size distribution above the North Sea and its implication to the dry deposition estimates. J. Aerosol. Sci., **20**, 1229-1232.

Steiger, M. (1991) Die anthropogenen und naturlichen Quellen urbaner und mariner Aerosole charakterisiert und quantifiziert durch Multielementanalyse und chemische Receptormodelle. Ph.D. Thesis. University of Hamburg. Germany.

Stöessel, R. (1987) Untersuchungen zu Naß- und Trockendeposition von Schwermetallen auf der Insel Pellworm. Ph.D. thesis, University of Hamburg, Germany.

van Aalst, R.M., van Ardenne, R.A.M., de Kreuk, J.F. and Lems, Th. (1983) Pollution of the North Sea from the atmosphere. TNO report CL 82/152, Delft, The Netherlands.

van Aalst, R.M. (1988) Input from the atmosphere. In: Pollution of the North Sea: An Assessment. Salomons et al. (eds.), Springer-Verlag, Berlin Heidelberg, Germany.

van Daalen, J. (1991) Air quality and deposition of trace elements in the province of South-Holland. Atmos. Environ. **25A**, 691-698.

van Enk, R.H. (1980) The pathway of cadmium in the European Community. European Appl.Res.Rept.Environ. and Nat.Res.Sec.,1:1.

Van Jaarsveld, J.A., van Aalst, R.M. and Onderdelinden, D. (1986) Deposition of metals from the atmosphere into the North Sea: Model calculations. RIVM, Bilthoven, Report 842015002.

Van Jaarsveld, J.A. and Onderlinden, D. (1986) Modelmatige beschrijving van concentratie en depositie van kolen relevante componenten in Nederland, veroorzaakt door emissies in Europa. Nationaal Onderzoeksprogramma Kolen (NOK), deelrapport 4, April 1986, PEO, Utrecht, The Netherlands.

Van Jaarsveld, J.A. (1991) Estimating Atmospheric inputs of Trace constituents to the North Sea: Methods and Results. 19th NATO/CCMS-ITM on Air Pollution Modelling and its Application. 29 September - 4 October 1991, Ierapetra, Greece.

Warmenhoven, J.P., Duiser, J.A., de Leu, L.Th. and Veldt, C. (1989) The contribution of the input from the atmosphere to the contamination of the North Sea and the Dutch Wadden Sea. TNO Report R 89/349A, Delft, The Netherlands.

Williams, R.M. (1982) A model for the dry deposition of particles to natural water surfaces. Atmos. Environ. **16**, 1933-1938.

Yaaqub R.R., Davies T.D., Jickells T.D. and Miller J.M. (1991) Trace element in daily collected aerosols at a site in southeast England. Atmos. Environ. **25A**, 985-996.

Addendum B

Data Quality Assurance Report

University of Antwerp (UIA)
Micro- and Trace Analysis Centre

Data Quality Assurance report

Wendy Jambers
René Van Grieken

Report prepared in the framework of the Impulse Programme in Marine Sciences, supported by the Belgian State - Prime Minister's Service - Science Policy Office (contract MS/06/050)

May 1993

Table of contents

Chapter 1: Introduction

In this project, much emphasis is on micro-analysis techniques which can give information concerning origin, transport, reactivity, transformation reactions and impact of environmental particles. Since only a limited number of researchers work on environmental micro-analysis, no international guidelines are available. The analysis and quality assurance methods described in this report are based on in-house experience and on the few articles already published about environmental micro-analysis.

For sampling and storing of inorganic particulate matter suspended in seawater and in rain samples, international recommendations are also nonexisting. Since these do exist for the collection and storing of dissolved trace metals in seawater, we can base ourselves on these guidelines taking into account that contamination is not as critical. For marine aerosols we base ourselves on the sampling methods given in articles about isokinetic sampling.

The micro-analysis techniques used in this work are electron probe X-ray micro-analysis (EPXMA), micro-proton induced X-ray emission (micro-PIXE), secondary ion mass spectrometry (SIMS) and Fourier transform laser microprobe mass spectrometry (FT-LMMS). SIMS and FT-LMMS have seldom been used on environmental particles and will have to be tested for their potential.

Anodic stripping voltammetry (ASV) and total reflection X-ray fluorescence (TXRF) are two bulk techniques which will be further optimised for the determination of trace elements. Atomic absorption spectrometry (AAS) will be used for those elements for which more information is necessary.

In this report we discuss the procedure for sampling, storage and analysis that have been selected in the framework of contract MS/06/050 of the Impulse Programme in Marine Sciences, and the ways in which the quality of these procedures has been or will be guaranteed for the study of aerosols, aqueous suspensions and rainwater from the North Sea. As a base to this, the QUASIMEME (Quality Assurance of Information in Marine Environmental Monitoring Programmes in Europe) report (Topping et al., 1993) was followed.

Reference

Topping G., Wells D. E. and Griepink B., Quality Assurance of Information in Marine Environmental Monitoring Programmes in Europe (QUASIMEME): Guidelines on Quality Assurance for Marine Measurements, BCR EC, 1993

Chapter 2: Sample collection procedures

2.1. Sampling of aerosols above the North Sea

Sampling strategy and devices

Isokinetic sampling is necessary to obtain representative aerosol samples and is very important for the collection of giant aerosol particles, because these can easily escape collection when the wind direction and speed deviate significantly relative to the air inlet speed of the sampling device (Lodge, 1991). High-quality isokinetic sampling is accomplished by using a wind tunnel, designed at the university of Essex (Vawda et al., 1989), which is a 1.2 m thin-walled tube with a diameter of 0.25 m. By using a ventilator which produces an air flow at the same speed as air is sucked into the sampling device by the pump, isokinetic sampling is assured. Since the air is sensitive to the rotation movement of the ventilator, a laminar flow is created by placing a honeycomb between the sampling orifice and the main body of the impactor. To be sure that the opening of the tunnel is always directed to the wind, a metal plate is mounted at the back of the tunnel as a wind vane.
The wind tunnel is mounted on the highest deck of the research vessel at an altitude of 11 m above the sea level. Mostly two sampling devices are placed in the wind tunnel, namely a cascade impactor and a filter unit (NASA, 1969; Bond et al., 1972). Air is sucked through the sampling devices by using two pumps with the same pumping volume. As a precaution to avoid local contamination from the vessel, the power to the pump is cut off during unfavourable wind speed and wind direction relative to the ship. During the first sampling campaign from 15 till 19 February 1993 samples were taken simultaneously in and out the wind tunnel. The results of these tests will prove that sampling with the tunnel is necessary for the collection of giant aerosols.

For the sampling of the total aerosol, a 47 mm diameter Nuclepore 0.4 µm aerosol-grade polycarbonate filter is mounted in a Sartorius SM 16598 filter device which is supplied with a stainless steel inlet tube.

To obtain aerosol samples as a function of their particle size, size-fractionating devices called 'cascade impactors' are used. The cascade impactor is horizontally mounted in the tunnel, because this gives the best collection efficiency (May, 1975). Since the ideal method of sample preparation for particle analysis is to collect the particles directly onto the substrate which will be analyzed (Russell and Hutchings, 1978), different cascade impactors and substrates are used for different analysis techniques.

Collection substrates

For EPXMA, micro-PIXE and ASV, samples are taken with a May cascade impactor on 47 mm diameter Nuclepore 0.4 µm (micro-PIXE and ASV) or 8 µm (EPXMA and ASV) aerosol-grade polycarbonate filters which are fixed on microscope glasses by gluing the sides of the filter to the glass with a glue-spray. To reduce the 'bounce-off' effect in the impactor, Apiezon-coated Nuclepore filters are used for the collection. For the single particle analyzing techniques (EPXMA and micro-PIXE), it is important that the particles on the filter do not touch. Overloading of the filters with the smallest fractions is avoided by replacing them after 3 hours by an empty microscope glass. Sampling of the largest fractions takes about 6 hours. ASV is a bulk technique; therefore high loadings are preferred. For this reason samples are taken for 12 hours or more.

Sampling for TXRF is done on 30 mm diameter and 3 mm thick highly polished quartz disks (Synsil) which are placed in a Batelle cascade impactor. To reduce 'bounce-off', these disks are siliconised with a silicon solution (SERVA) according to the manufacturers' instructions (see Muia, 1991). Previous to sampling the disks are cleaned using the following procedure:

1. Remove the remainder of the last measurement mechanically.
2. Rinse in de-ionized 'Milli Q' water.
3. Heat in a detergent bath (RBS-50) for 2 hours.
4. Rinse in de-ionized 'Milli Q' water.
5. Rinse in 0.1 N ultra-pure nitric acid.
6. Soak 1 night in 0.1 N ultra-pure nitric acid.
7. Rinse in de-ionized 'Milli Q' water.
8. Siliconise with silicon solution (SERVA).
9. Dry under reduced pressure in an exsiccator.

Next to this, collection for TXRF is also done on 25 mm diameter Nuclepore 0.1 µm aerosol-grade polycarbonate filters which are glued on PE rings fitting in the Batelle impactors. Since TXRF is also a bulk technique, collection is done over 12 hours.

For SIMS, a special very small Batelle cascade impactor is used. Three different collection materials will to be tested. The first is pure indium-foil, the two others are 700 mesh copper microscope grids covered with carbon-foil or formvar-carbon-foil. The sampling time for SIMS will be around 6 hours.

FT-LMMS samples will be taken with a Batelle impactor and different metal-foils will be tested as collection material.

Blanks are regularly taken, i.e. a collection substrate is brought into the sampling device without sucking air through it, for subsequent analyses.

2.2. Sampling of aqueous suspension from the North Sea

Sampling strategy and device

Samples are taken with a 10 litre PTFE Niskin bottle on a stainless steel wire which is free from rust (Topping et al., 1993). The messenger is made of bronze. The unfiltered sub-samples are tapped in 1 litre PE bottles which have been washed with acid (see section 3.2) and rinsed with sample water. Since it is important to minimize the time between sampling and filtration, as interactions between the dissolved and particulate phases may occur in the temporary storage bottles (Yeats, 1987), filtration is done immediately after collection.

Sampling substrate

The suspended matter is filtered on 47 mm diameter Nuclepore 0.4 µm aerosol-grade polycarbonate filters by using a Sartorius SM 16510 polycarbonate filter holder. Before use, the filter holder and all the glass labware are cleaned with the same procedure used for storage bottles (see section 3.2). As the samples are used for single particle analysis, the loading of the filters is kept sufficiently low so that the particles on the filter do not touch; hence the quantity of seawater filtered (about 100 ml in open sea) depends on the turbidity of the water. To remove the freshly crystallized sea salt, the filters are washed three times with 50 ml of de-ionized 'Milli Q' water (Yeats, 1990).

A blank is obtained by putting a filter in the filter holder and adding three times 50 ml of de-ionized 'Milli Q' water.

2.3. Sampling of suspension in rain from above the North Sea

Sampling strategy and device

Rainwater is collected on the highest deck of the research vessel at an altitude of 10 m above the sea surface. The collector consists of a 633 cm^2 PVC funnel (ASTM, 1988) which is well fitted on the 2 l PE collection bottle (Galloway and Likens, 1976). It is supported by a stainless steel framework which is fastened at the railing of the highest deck and is covered by the 60° slopes of the funnel.

Before use the funnels and collection bottles are acid cleaned with the same procedure as for the storing bottles (see section 3.2). The funnel is protected from dry deposition with a well fitting plastic bag. At the beginning of each rain shower the funnel is manually uncovered. Immediately after the shower the collection bottle is emptied in a 250 ml acid cleaned PE bottle and the funnel is rinsed with de-ionized 'Milli Q' water (Laquer,1990).

Sampling substrate

Immediately after collection, the suspended matter is filtered on 25 mm diameter Nuclepore 0.4 μm aerosol-grade polycarbonate filters by using a Sartorius SM 16306 25 mm glass vacuum filter holder with 30 ml funnel and with glass frit filter support. These small filters are used because the collected quantity of rain and the number of suspended particles in rain water are small in comparison with sea water. Before use, the filter holder and all the glass labware are cleaned with the same procedure used for storage bottles (see section 3.2).

Blanks are taken by placing a filter in the filter holder and adding 50 ml of de-ionized 'Milli Q' water.

2.4. References

ASTM, Standard practice for handling of ultra pure water samples, Annual book of ASTM standards 11.01, method D4453-85, 1988

Bond R. G., Straub C. P. and Prober R., CRC Handbook of environmental control Volume I: Air pollution Chapter 1.5, CRC press, Ohio, 1972

Galloway J. N. and G. E. Likens, Calibration of collection procedures for the determination of precipitation chemistry, Water Air Soil Pollut. 6, 1976, 241

Guisti L., Yang Y.-L., Hewitt C. N., Hamilton-Taylor J. and Davison W., The solubility and partitioning of atmospherically-derived trace metals in artificial and natural waters - A review (in press)

Laquer F. C., Sequential precipitation samplers: a literature review, Atmos. Environ. 24A, 1990, 2289

Lodge J. P. Jr., Methods of air sampling and analysis 3th ed., Lewis Publishers Inc., Michigan, 1991

May K. R., An 'ultimate' cascade impactor for aerosol assessment, J. Aerosol Sci. 6, 1975, 413

Muia L. M., Influence coefficient and total reflection methods in EDXRF: Methodology and applications in the analysis of geological and environmental samples, Ph. D. thesis at the University of Antwerp (UIA), Antwerp, 1991

NASA SP-5076 Technology Utilization Division, Contamination control handbook, National Aeronautics and Space Administration, Washington D. C., 1969, V-22

Russell P. A. and Hutchings A. E., Electron microscopy and X-ray applications to environmental and occupational health analysis, Ann Arbor Science Publishers Inc., Michigan, 1978

Topping G., Wells D. E. and Griepink B., Quality Assurance of Information in Marine Environmental Monitoring Programmes in Europe (QUASIMEME): Guidelines on Quality Assurance for Marine Measurements, Chapter 13, BCR EC, 1993

Vawda Y., Colbeck I., Harrison R. M. and Nicholson K. W.,The effect of particle size on deposition rates, J. Aerosol Sci. 20, 1989, 1155

Yeats P. A., Techniques in Marine Environmental Sciences No.2: Trace metals in sea water: Sampling and Storage methods, ICES, Denmark, 1987

Yeats Y. A., Techniques in Marine Environmental Science No.7: Suspended particulate matter: Collection methods for gravimetric and trace metal analysis, ICES, Denmark, 1990

Chapter 3: Sample storage procedures

3.1. Storage of aerosol samples

Filters, quartz disks and metal-foils with aerosol deposits are stored in petri dishes while microscope grids are kept in grid boxes.

3.2. Storage of aqueous suspension samples

The filters loaded with suspended matter from sea water are air dried in Millipore petri dishes (Yeats, 1990) and stored in a deep-freezer. In case something should go wrong with the filters, some of the water is stored in 250 ml PE bottles. The storage bottles, filter holder and all the labware are cleaned using the following procedure:

1. Rinse in de-ionized 'Milli Q' water.
2. Soak 3 nights in 10 % nitric acid (pro analysis).
3. Rinse in de-ionized 'Milli Q' water.
4. Soak 3 nights in 10 % nitric acid (pro analysis).
5. Rinse in de-ionized 'Milli Q' water.
6. Soak 3 nights in de-ionised 'Milli Q' water.
7. Rinse in de-ionized 'Milli Q' water.
8. For storage the bottles are kept closed, the filter holder is closed and wrapped in protective paper and the labware is also wrapped in paper (Topping et al., 1993).

Water samples are generally preserved for storage by either acidification or freezing or both. As the pH influences the solubility of material (Guisti et al., 1993) freezing is the only possible way to store our samples.

3.3. Storage of suspension samples from rain

The filters loaded with suspended matter from rain are air dried in Millipore petri dishes and stored in a deep-freezer.

3.4. References

Guisti L., Yang Y.-L., Hewitt C. N., Hamilton-Taylor J. and Davison W., The solubility and partitioning of atmospherically-derived trace metals in artificial and natural waters - A review (in press)

Topping G., Wells D. E. and Griepink B., Quality Assurance of Information in Marine Environmental Monitoring Programmes in Europe (QUASIMEME): Guidelines on Quality Assurance for Marine Measurements, Chapter 13, BCR EC, 1993

Yeats Y. A., Techniques in Marine Environmental Science No.7: Suspended particulate matter: Collection methods for gravimetric and trace metal analysis, ICES, Denmark, 1990

Chapter 4: Analysis procedures

4.1. EPXMA

Single particle analyses on the aerosol, aqueous suspension and rainwater suspension samples are performed by EPXMA (Electron Probe X-ray Micro-Analysis). Contamination is minimized by sample preparation in a laminar-flow clean bench (Russell and Hutchings, 1978). A small piece of the filter is cut off and mounted with double face tape on a clean plastic ring. To prevent charging of the sample, it is coated with 50 nm of carbon in a Balzer Carbon Evaporation Device 010 and fitted into a copper sample holder.

The instrument used is a JEOL Superprobe JXA-733, equipped with a Tracor Northern TN-2000 and a LSI 11/23 minicomputer. The home-made 733B automatic particle analysis program (Nullens, 1986) is used to locate and analyze the particles. This differs from the Tracor Northern particle recognition and characterization software (Fritz, 1982) in the particle searching and sizing methodology. The main advantages of the 733B program are the faster searching mode and the more accurate sizing routine (Bernard, 1989).

This 733B program has been tested with standard materials with respect to accuracy of particle size measurement and X-ray spectrum acquisition (Raeymaekers, 1986). The quality of the particle size measurement depends on the threshold setting of the backscattered image signal and the magnification used. If the guidelines for these two parameters, given by Raeymaekers (1986), are followed, the accuracy of the size measurement is good. Results of the tests regarding X-ray spectrum acquisition for single particles are : (a) for particles in the size range 1-100 µm, an acquisition time of 10 to 20 s yields spectra with satisfactory signal to noise ratio, (b) optimum detectability for most elements is obtained with a voltage between 20 and 25 keV, (c) an electron beam current of 1 Na offers a good compromise between the count rate and the resolution requirements of the electron beam and (d) a star scanning pattern is representative for the acquisition of the spectra of the whole particle.

In the 733B program the peak intensities are calculated with the fast deconvolution technique called Fast Filter Algorithm (Op de Beeck and Hoste, 1975). Tests on clay mineral standards have shown that this algorithm gives good results but that deconvolutions with the slower off-line Analytical X-ray analysis by Iterative Least squares (AXIL)-program (Van Espen et al., 1977; Nullens et al., 1979) are better (Bernard, 1989). However, taking into account the required computer time, FFA is by necessity the method of choice for the deconvolution of enormous amounts of spectra.

The Data Processing Program (DPP) developed by Van Espen (1984) is used to cluster the relative X-ray intensities, i.e. to define types or groups of particles of a certain similarity. The hierarchical Ward's classification gives the best compromise between describing the large

data set using a minimum number of groups and maintaining a maximum of geochemically relevant information while avoiding the fusion of geochemically important groups (Bernard et al., 1986). Indeed, test results from mixtures of mineral standards show that the Ward's method has the highest probability of correct classification (Bernard, 1989). Selection criteria for different particle types are derived from the mean relative X-ray intensities of several characteristic particle types found in riverine suspension (for marine aqueous particles) and in air masses above the North Sea during either pure marine or continental sampling conditions (for aerosols). The particle types, as defined by these selection rules, act as a replacement for the hierarchically obtained centroids. Since these guidelines are the same for all samples, no further classification routines are necessary (Xhoffer,1993). In the course of this project, alternative particle classification procedures, such as nonlinear mapping and fuzzy clustering, will be evaluated.

By applying specific ZAF-corrections (i.e. corrections for differences between samples and standards with respect to average atomic number, Z, X-ray absorption, A, and secondary X-ray fluorescence, F) for spherical particles (Raeymaekers, 1986), the composition of particle types in weight percentages is obtained. These corrections are done on the average composition of the groups obtained by clustering, and not on the individual particles, because it has been proven that there is no significant difference between correcting before or after hierarchical clustering (Bernard, 1989). However, since no rigorously exact ZAF-correction for particles exists, care has to be taken when interpreting these results; the accuracy will often not be better than 30% but this is sufficient to identify the different particle types.

Manual EPXMA with spot analysis will be applied to investigate the internal heterogeneity of the largest particles.

Jeol reference materials, available for Mg, Al, Si, Ti, Cr, Fe, Ni, Cu, Zn, W, Zr and Au, are frequently analyzed to insure a good accuracy and precision. The detection limit varies with the elements present in the sample, the sample itself, instrumental set-up and the goal of the analysis. For EPXMA on environmental particles, the detection limit is on the average 1000 ppm.

4.2. Micro-PIXE

For micro-PIXE, the scanning nuclear microprobe instrument at the Central Bureau for Nuclear Measurements (CBNM) in Geel is used (Lövestam et al., 1991). The accelerator is a KN-3.7 MV vertical single stage Van de Graaff, with a radio-frequency ion source generating H^+, D^+ or He^+ ions. The entire beam line, from the object slits to the target chamber, is mounted on a granite bench carried by active pneumatic insulators, and connected to the high energy side of the accelerator via a bellow. As focusing device, a quadrupole doublet from Microscope Associates Inc., is used (Martin and Goloskie, 1983). Using a new focusing procedure (Swietlicki et al., in press), utilizing the grid shadow method (Jamieson

and Legge, 1988), a 2.5 x 2.5 μm^2 proton beam spot with a beam current of 100 pA is achieved. The beam scanning is performed by applying a voltage to the electrically insulated poles in the quadrupole focusing magnets. Corresponding high voltage power supplies are controlled by a VMEbus computer system (Lövestam, 1989; Tapper et al., 1987) giving a maximum scanning speed of 10,000 pixels per second. For the collection of PIXE-data, a Si(Li) detector connected to a VMEbus/μVax-II/ND-9900 data acquisition system is used (Tapper et al., 1987; Lövestam and Swietlicki, submitted article).

For PIXE, no specific sample preparation is necessary; the sample is placed in the Al sample holder and analyzed. Peak intensities are calculated with Sesam X-software developed by Wätjen. Calibration curves made with Micromatter thin film standards are used to calculate the concentrations.

The detection limit for analysis of environmental particles with micro-PIXE is about 100 fg, which, for a particle of a few μm, corresponds to ca. 10 ppm.

4.3. SIMS

Secondary ion mass spectrometry (SIMS) will be done with a Cameca IMS 3F/4F. Since SIMS has almost never been used on environmental particles, a testing period will be necessary. Glass particles will be used to calibrate the sensitivity, accuracy and precision of SIMS for single particle analysis. These particles are made by crushing small parts of the standards NBS 1412 (multicomponent glass) and NBS 1411 (soft borosilicate glass) (Satoh, 1991).

The detection limit of analysis of environmental particles with SIMS is often about 1 ppm, but this can vary very much among the different elements.

4.4. FT-LMMS with external ion source

The instrument used for Fourier-transform laser microprobe mass spectrometry is a prototype built in 1991. It exists of a Quanta-Ray DCR 2,10 Nd:YAG laser (E = 25 mJ/pulse, λ = 266 nm and τ = 10 ns) and a Spectrospin CMS 47X MicroFocus mass spectrometer (Spectrospin AG, Switzerland) (Van Vaeck et al., in press). Since the machine has only recently been acquired, it still has to be tested intensively to explore all the possibilities and characteristics. Analysis of environmental samples will only be possible after this testing period.

4.5. ASV

The measurement of toxic metals in airborne particles by anodic stripping voltammetry (ASV) has been proven to be a rapid, accurate and sensitive technique, if sufficient care is given to several sources of serious errors (Lodge, 1991). The filter is cut from the microscope glass with a Pt knife to avoid contaminations. To decrease the negative effect of the organic compounds, filter material and organic matter content of the airborne particles are destroyed by micro-waves. This destruction is done in a Parr Microwave Acid Digestion Bomb (Type 4782) which is heated in a 800 W micro-wave oven. Before destruction, the teflon cup of the bomb is cleaned by boiling 1 hour in a 1/3 nitric acid solution. The combination of ultra pure acids (0.5 ml HF, 3 ml HNO_3 and 1 ml $HClO_4$) and the high temperature destroys all the organic material and brings the metal ions in solution. To prevent overheating of the bomb, it is twice heated and cooled for two minutes followed by eight times one minute heating and cooling. After complete cooling, the bomb is opened and the solution is reduced to one drop by evaporation. This drop is quantitatively diluted with de-ionized 'Milli Q' water to a 100 ml solution. All glassware is kept clean by soaking it at least 24 h in diluted hydrochloric or nitric acid and rinsing it thoroughly with de-ionized 'Milli Q' water.

The voltammetric measurements are done with a microprocessor-controlled PAR polarograph analyzer model 264 (E. G. and G. Princeton Applied Research). This device controls a PAR model 303 static mercury drop electrode system (SMDE) and magnetic stirrer and an x-y recorder. The SMDE is provided with a 10 ml glass or teflon sample cup and a three-electrode system including an Ag/AgCl reference electrode, a teflon covered Pt auxiliary electrode and a mercury working electrode, which is used in the hanging drop mode (HMDE) to minimize interferences (Lodge, 1991). The metals Zn, Cd, Pb and Cu are determined in 10 ml portions. Zn is measured at pH 3 (ultra pure HNO_3), Cd, Pb and Cu are detected at pH 1. After de-aeration for 4 minutes with N_2, these metals are deposited at a potential of -1.2 V with deposition times of 4 minutes. After a rest period of 30 seconds, the HMDE is polarized in the differential-pulse mode in the anodic direction (Van Alsenoy, 1993). Most of these instrumental parameters were optimized by Vos et al. (1986).

To minimize matrix effects, concentrations are calculated by using a standard addition method (standards from Servi-lab: Labo De Leersnyder, Wakken, Dentergem, Belgium) and by correction for the blanks. To test the efficiency of the micro-wave destruction method, the CBR Fly Ash standard N 38-N 106 (fly ash from pulverised coal) was added to a non-coated and an apiezon-coated Nuclepore polycarbonate filter, destructed and measured. The observed recoveries were acceptable, but further optimization is necessary (Verrecken, 1993).

The detection limit for ASV is well below 1 ppb for Zn, Cd, Cu and Pb in the final solution to be analyzed.

4.6. TXRF

Since collection for total reflection X-ray fluorescence (TXRF) is done on two different substrates, two different sample preparations have to be used. When aerosols are collected on the highly polished quartz disks, one drop (5 µl) of a 5 ppm Ga solution (Servi-lab: Labo De Leersnyder, Wakken, Dentergem, Belgium) is brought on the aerosol spot as an internal standard. The liquid is evaporated under reduced pressure and the remaining thin circular sample film is analyzed immediately. When collection is done on filters, destruction of this filter is necessary. This destruction is performed by the same procedure as for ASV (see section 4.5) with the only difference that 5 ppm Ga is added as internal standard. The preconcentrated drop is quantitatively diluted to a 10 ml solution. Five µl of this solution is put on a quartz disk, the liquid is evaporated and the remaining sample film is analyzed immediately. A recent experimental optimization of the procedure has shown that Ga is more suitable as an internal standard than Y or Ge; indeed, EPXMA has shown that the evaporation deposits are spatially more homogeneous in this case, and that better accuracies can be obtained. For further analyses of aerosol samples, collection on quartz disks was preferred because of the short preparation time, the low cost and the better detection limit.

The equipment used consists of a 2 kW (PW 2225/20) Mo fine focus tube from Philips and a modified TXRF module obtained from the Atom Institute in Vienna. Spectral data are collected with a Kevex Si(Li) detector. Peak intensities are calculated with the AXIL-program (Van Espen et al., 1977 and Nullens et al., 1979).

The efficiency of the microwave destruction method was tested by destructing a fly ash standard (BCR N 38-N 106 fly ash from pulverised coal) which was added to a non-coated Nuclepore polycarbonate filter. The recovery for all elements was quantitative within the usual standard deviation of 20%.

To insure a good accuracy and precision, a home-made standard for Cr, Co, Zn and Ga is measured before and after every series of aerosol samples. An extra quality check will be done by analyzing three sets of five samples with the Atomika Extra II A TXRF-module of the Institüt für Spektrochemie und angewandte Spektroskopie (ISAS) in Dortmund.

The detection limit for TXRF on environmental particles collected on quartz disks is about 1 ng or somewhat better; for a 5 µl final solution drop, this corresponds to 200 ppb.

4.7. AAS

Atomic absorption spectrometry (AAS) has become the most widely used analytical technique for quantitative trace metal analysis (Lodge, 1991). Since it is a solution-based technique, the filters have to be destroyed and the metal ions have to be brought in solution. This is done by the same procedure as described for ASV (section 4.5).

A Perkin Elmer 3030 AAS unit equipped with a AS 40 sampler and a PR 100 printer is used to measure Zn and Fe by flame AAS. Cd, Cu, Pb and Ni are measured electrothermally by using a Perkin Elmer HGA 600 and a Perkin Elmer PE 5100 spectrometer with Zeeman background correction.

Concentrations are calculated through calibration curves which are constructed with a diluted 1000 ppm Merck solution or with a diluted 1000 ppm certified standard solution from Johnson & Matthey.

To minimize contamination, preconcentration of the metals is done by extraction in a closed flow injection analyzing (FIA) system. A specific reagent which complexates the metal ions is added to the sample by a pumping system. The complexes are retained on a C_{18}-column and eluted from the column with ultra-pure ethanol. This technique is at this moment tested for Cd, Pb and Cu (Van Mol, publication in preparation). After specific reagents for other metal ions will have been examined, further development will follow.

In 1992, we participated in an international certification for metals in sea water, organized by the Community Bureau of Reference of the Commission of the European Communities, for As, Mn, Fe and Zn. Since there were not enough participants for Mn and Fe, only Zn was accepted for certification while As was allowed as an indicative value (Quevauviller et al., 1992). The project also included Cd, Cu, Mo and Ni, but because these concentrations were so low that preconcentration in ultra clean conditions was needed, no application was done for these elements. At this moment an application is done for an international intercalibration exercise on estuarine water, organized by the Community Bureau of Reference of the Commission of the European Communities. Results of the closed extraction method for Cd, Pb and Cu are included in the application. A certification for estuarine water will follow in 1994.

For flame AAS the detection limit is about 100 ppb. The detection limit for AAS with Zeeman background correction is ca. 1 ppb.

4.8. References

Bernard P. C., Van Grieken R. E., Eisma D., Classification of estuarine particles using automated electron microprobe analysis and multivariate techniques, Environ. Sci. Technol. 20, 1986, 467

Bernard P. C., Automated electron probe X-ray micro-analysis combined with multivariate analysis for application in marine research, Ph. D. thesis at the University of Antwerp (UIA), Antwerp, 1989

Fritz G., Particle recognition and characterization (TN-1912), Tracor Northern Inc.,1982

Jamieson D. N. and Legge G. J. F., Nucl. Instr. and Meth. B30, 1988, 235

Lodge J. P. Jr., Methods of air sampling and analysis 3th ed., Lewis Publishers Inc., Michigan, 1991

Lövestam N. E. G., Nucl. Instr. and Meth. B36, 1989, 455

Lövestam N. E. G., Swietlicki E., Wätjen U., Breitenbach L. and Rietveld P., The CBNM scanning nuclear microprobe for materials analysis, Presented at 10th international conference on ion beam analysis (Eindhoven July 1991) and accepted for publication in Nucl. Instr. and Meth. B

Lövestam N. E. G. and Swietlicki E., Off-line data evaluation of elemental maps obtained from scanning proton microprobe analysis, submitted to Scanning Microscopy

Martin F. W. and Goloskie R., IEEE Trans. on Nucl. Sci. NS-30, 1983, 1472

Nullens H., Unpublished software developed at the University of Antwerp (UIA), Antwerp, 1986

Nullens H., Van Espen P. and Adams F., Linear and non-linear peak fitting in energy-dispersive X-ray fluorescence, X-Ray Spectrometry 8, 1979, 104

Op de Beeck J. P. and Hoste J., Gamma-ray spectrometry data-collection and -reduction by single computer systems, Atomic Energy Review 13, 1975, 743

Quevauviller P., Kramer K. J. M., Vercoutere K., Griepink B., The certification of the contents of Cd, Cu, Pb, Mo, Ni and Zn in sea water CRM 403, bcr information: reference materials Report EUR 14061 EN, Commission of the European Communities: Community Bureau of Reference, 1992

Raeymaekers B., Characterization of particles by automated electron probe micro-analysis, Ph. D. thesis at the University of Antwerp (UIA), Antwerp, 1986

Russell P. A. and Hutchings A. E., Electron microscopy and X-ray applications to environmental and occupational health analysis, Ann Arbor Science Publishers Inc., Michigan, 1978

Satoh H., Owari M. and Nihei Y., Quantitative analysis of small particles by submicron secondary ion mass spectrometry, Anal. Sci. 7 suppl., 1991, 533

Swietlicki E., Lövestam N. E. G. and Wätjen U., The grid shadow technique as a tool for beam focusing in nuclear microprobes, Nucl. Instr. and Meth. B, in press

Tapper U. A. S., Lövestam N. E. G., Karlsson E. and Malmqvist K. G., Nucl. Instr. and Meth. B28, 1987, 317

Van Alsenoy V., Concentration and partitioning of heavy metals in the Scheldt estuary, Ph. D. thesis at the University of Antwerp (UIA), Antwerp, 1993

Van Espen P., Nullens H. and Adams F., A computer analysis of X-ray fluorescence spectra, Nucl. Instr. and Meth. 142, 1977, 243

Van Espen P., A program for the processing of analytical data (DPP), Anal. Chim. Acta 165, 1984, 31

Van Mol W., Private communication

Van Vaeck L., Van Roy W., Struyf H., Adams F. and Caravatti P., Development of a laser microprobe Fourier transform mass spectrometer with external ion source, Rapid Communications in Mass Spectrometry, in press

Verrecken S., Optimalisatie van de bepaling van Cd, Pb, Cu en Zn met anodische heroplossingsvoltammetrie na microgolfovendestructie, Thesis aan Hoger Instituut voor Technische en Paramedische Wetenschappen, Hoger Instituut der Kempen, Geel, 1993

Vos L., Komy Z., Reggers G., Roekens E. and Van Grieken R., Determination of trace metals in rain water by differential pulse stripping voltammetry, Anal. Chim. Acta 184, 1986, 271

Wätjen U., Unpublished software developed at the Central Bureau for Nuclear Measurements (CBNM), Geel

Xhoffer C., Chemical characterization of individual particles by electron probe X-ray micro-analysis and electron energy-loss spectrometry, Ph. D. thesis at the University of Antwerp (UIA), Antwerp, 1993

Chapter 5: Personnel

In principle, all samples are taken by the person who will carry out the analyses, usually a Ph.D. student responsible for a well defined fraction of the programme. Sometimes, e.g. when not sufficient places on board are available, sampling is done according to the instructions of the person who will do the analyses.

Unskilled new Ph.D. students are trained on the job by more experienced scientists and technicians.

To get an optimal use of the available equipment, major servicing is done by the manufacturer's service engineers.

Addendum C

Gepubliceerde Artikels

Lijst met alle artikels gepubliceerd in het kader van dit project gedurende de periode oktober 1992- september 1996 (kopie van reprints bijgevoegd).

1. Struyf H., Van Roy W., Van Vaeck L., Van Grieken R., Gijbels R. en Caravatti P., Laser microprobe Fourier transform mass spectrometer with external ion source for organic and inorganic microanalysis, Anal. Chim. Acta, 1993, **283**, 139-151.

2. Treiger B., Injuk J., Bondarenko I., Van Espen P., Van Grieken R., Breitenbach L., en Wätjen U., Nonlinear mapping of microbeam proton-induced X-ray emission data for source identification of North Sea aerosols, Spectrochim. Acta, 1994, **49B**, 345-353.

3. Injuk J., Breitenbach L., Wätjen U. en Van Grieken R., Individual aerosol particle analysis with the nuclear microprobe, Mikrochim. Acta, 1994, **114/115**, 313-321.

4. De Bock L.A., Van Malderen H. en Van Grieken R., Individual aerosol particle composition variation in air masses crossing the North Sea, Environ. Sci Techn., 1994, **28**, 1513-1520.

5. Struyf H., Van Roy W., Van Vaeck L., Van Grieken R. en Caravatti P., The Fourier transform laser microprobe mass spectrometer with external ion source as a tool for inorganic micro-analysis, Rapid Communications in Mass Spectrometry, 1994, **8**, 32-39.

6. Van Roy W., Struyf H., Van Vaeck L., Gijbels R. en Caravatti P., Desorption-ionization of organic compounds studies by Fourier-transform laser microprobe mass spectrometry, Rapid Communications in Mass Spectrometry, 1994, **8**, 40-45.

7. Van Put A., Vertes A., Wegrzynek D., Treiger B. en Van Grieken R., Quantitative characterization of individual particle surfaces by fractal analysis of scanning electron microprobe images, Fresenius J. Anal. Chem., 1994, **350**, 440-447.

8. Berghmans P., Injuk J., Van Grieken R. en Adams F., Microanalysis of atmospheric particles and fibres by electron energy loss spectrometry, electron spectroscopic imaging and scanning proton microscopy, Anal. Chim. Acta, 1994, **297**, 27-42.

9. Otten P., Injuk J. en Van Grieken R., Elemental concentrations in atmospheric particulate matter sampled on the North Sea, Science of the Total Environment, 1994, **155**, 131-149.

10. Injuk J. en Van Grieken R., Atmospheric concentrations and deposition of heavy metals over the North Sea: a literature review, J. Atmos. Chem., 1995, **20**, 179-212.

11. Jambers W., De Bock L. en Van Grieken R., Recent advances in analysis of individual environmental particles, Analyst, 1995, **120**, 681-692.

12. Xhoffer C., Jacob W., Buseck P.R. en Van Grieken R., Problems in quantitatively analyzing individual salt aerosol particles using electron energy loss spectroscopy, Spectrochim. Acta B, 1995, **50**, 1281-1292.

13. Treiger B., Bondarenko I., Van Malderen H. en Van Grieken R., Elucidating the composition of atmospheric aerosols through the combined hierarchical, non-hierarchical and fuzzy clustering of large electron probe microanalysis data sets, Anal. Chim. Acta, 1995, **317**, 33-51.

14. Injuk J. en Van Grieken R., Optimisation of total reflection X-ray fluorescence for aerosol analysis, Spectrochim. Acta B, 1995, **50**, 1787-1803.

15. Van Roy W., Struyf Herbert, Kennis P., Van Vaeck L., Van Grieken R. en Andrle C., Assessement of local analysis by Fourier transform laser microprobe mass spectrometry with external ion source, Mikrochim. Acta, 1995, **120**, 121-137.

16. Jambers W. en Van Grieken R., Present and future applications of beam techniques in environmental micro-analysis, TrAC, 1996, **15**, 114-122.

17. Struyf H., Van Vaeck L. en Van Grieken R., Desorption/ionization of inorganic compounds in Fourier transform laser microprobe mass spectrometry with external ion source, Rapid Comm. Mass Spectrom., 1996, **10**, 551-561.

18. Van Malderen H., Hoornaert S. en Van Grieken R., Identification of individual aerosol particles containing Cr, Pb and Zn above the North Sea, Environ. Sci. Technol., 1996, **30**, 489-498.

19. Jambers W., De Bock L. en Van Grieken R., Applications of micro-analysis to individual environmental particles, Fresenius J. Anal. Chem., 1996, **355**, 521-527.

20. Hoornaert S., Van Malderen H. en Van Grieken R., Gypsum and other calcium-rich aerosol particles above the North Sea, Environ. Sci. Technol., 1996, **30**, 1515-1520.

21. Jambers W. en Van Grieken R., A message in the dust, Analysis Europa, 1996, Jan/Febr, 25-29.

22. Schelles W., Maes K.J.R., De Gendt S. en Van Grieken R.E., Glow discharge mass spectrometric analysis of atmospheric particulate matter, Anal. Chem., 1996, **68**, 1136-1142.

Analytica Chimica Acta, 283 (1993) 139–151
Elsevier Science Publishers B.V., Amsterdam

Laser microprobe Fourier transform mass spectrometer with external ion source for organic and inorganic microanalysis

H. Struyf, W. Van Roy, L. Van Vaeck, R. Van Grieken and R. Gijbels

Department of Chemistry, University of Antwerp (UIA), Universiteitsplein 1, B-2610 Wilrijk (Belgium)

P. Caravatti

Spectrospin AG, Industriestrasse 26, CH-8117 Fällanden (Switzerland)

(Received 8th September 1992; revised manuscript received 27th January 1993)

Abstract

The earlier laser microprobe (LM) mass spectrometer with a time-of-flight (TOF) analyser showed that the irradiation of solids by a focused UV laser represents an interesting means of performing local analysis. However, the subsequent measurement of the generated ions is done under low-resolution conditions. The characterization of heterogeneous samples and the occurrence of poorly understood ion formation mechanisms motivated the development of an instrument with superior mass spectrometric performance. Specifically, Fourier transform (FT) mass spectrometry potentially provides the required high mass resolution and accurate mass determination in combination with adequate sensitivity. In this work an FT-LM mass spectrometer with an external source was developed. Analysis is performed in the reflection mode with a 5-μm spot from a Q-switched Nd:YAG laser. Transfer of ions from the external source into the cell is performed by static electrical fields. The resulting mass separation imposes limitations on the panoramic spectrum registration in the case of pulsed laser microbeam ionization of solids, producing ion bunches over not more than a few hundred microseconds. This paper addresses instrument design and performance with respect to sensitivity, spatial resolution and accuracy of m/z determination and the problem of panoramic registration. Attention is focused on the comparison of results from FT- and TOF-LM mass spectrometry in relation to the determination of the speciation of inorganic compounds and diagnostic analysis of organic molecules.

Keywords: Mass spectrometry; Laser microprobe

Laser microprobe (LM) mass spectrometry (MS) is a relatively recent technique for the measurement of organic and inorganic constituents at the surface of solids with a spatial resolution of the order of a few μm. A microvolume is irradiated by a focused laser and the ions produced are mass analysed. The local excitation of the sample by means of a photon beam eliminates the charging problems. The first commercial instruments were time-of-flight (TOF) LM mass spectrometers [1–3]. The high transmission ensured good sensitivity and no scanning was needed, so that complete mass spectra could be obtained from each single laser interaction. The applicability of TOF-LMMS to a wide range of research problems from science and industry has been demonstrated [4–6].

The results indicated the analytical potential of laser microbeam irradiation for inorganic and organic local analysis, but also revealed the limi-

Correspondence to: L. Van Vaeck, Department of Chemistry, University of Antwerp (UIA), Universiteitsplein 1, B-2610 Wilrijk (Belgium).

tations of the TOF instrument for mass analysis. On the one hand, fine speciation capabilities are offered while the mass spectra for organic compounds usually yield molecular weight information and numerous fragments to characterize the functionalities in the molecule. However, mass resolution of TOF-LMMS is limited to less than 1000 [7,8]. Hence the exact chemical composition of the detected ions cannot be derived, which is a prerequisite because of the lack of knowledge about the ion formation under laser microbeam irradiation of heterogeneous solids. Additionally, TOF-MS relies on prompt ion formation, which essentially occurs during the laser pulse. Organic compounds tend to form ions for a long time after the laser pulse [9].

The well known capabilities of Fourier transform (FT) MS with respect to high mass resolution, accurate m/z determination and spectrum registration without scanning and the additional use of ion–molecule reactions and multiple MS experiments to elucidate the ion structure makes the idea of FT-LMMS particularly appealing on the condition that the sensitivity is sufficient to detect the extremely small number of ions generated from the irradiated microvolume.

The feasibility of the FT-LMMS approach has been evidenced by the experimental set-ups developed at the University of Metz (France) and the IBM Laboratories (San Jose, CA, and Endicott, NY, USA) [10–12]. These instruments used laser microbeam ionization of the samples *inside* the FT-MS cell. Hence, the optical systems for laser focusing, sample observation and illumination and the micropositioner of the specimen have to be mounted at least partially within the narrow bore of the superconducting magnet. This often makes the design complicated. Moreover, preliminary results suggested that ion formation inside the magnetic field is responsible for second-order interactions between the orbiting ions and the slowly pumped-off neutral species [13]. This could explain at least in part the observed differences between FT- and TOF-LMMS of, e.g., polymers.

In this work, the development of FT-LMMS with an external ion source was investigated. The first reason was the accessibility and roominess around the sample so that the implementation of the laser focusing and viewing optics and the sample positioning system could be fully optimized. Additionally, the ion lenses required to guide the ions into the ion transfer system can offer the possibility of studying the kinetics and characteristics of the generated species with respect to, e.g., energy distribution and gas-phase vs. surface ionization. The short residence time of the ions in the laser-generated micro-cloud just above the sample surface should minimize the ion–molecule interactions. Second, a high vacuum is maintained in the cell, even when, *e.g.*, post-chemical ionization would be used in the source, and hence good mass resolution can be expected.

However, the use of an external source in FT-MS also implies the problem of ion transfer. Specifically, the injection of ions through the inhomogeneous fringing field of the magnet is not trivial [14,15]. Tandem quadrupoles have been used [16,17], the first acting as a mass filter while the second is used as a lens in the r.f.-only mode. Also, mass selection by tandem quadrupoles has been combined with an electrostatic lens to guide the ions through the fringing field into the cell [18]. However, a single quadrupole-based FT mass spectrometer has been proved to show excellent sensitivity and resolution [19]. Alternatively, the use of static electrical fields allows high transmission efficiency in combination with simple construction [20]. Purely electrostatic lenses have been applied to inject the ions from a metal cluster beam [21]. The retention of the ions in the low trapping field of the cell is not obvious because this conflicts with the relatively high kinetic energy of the ions required for efficient ion transfer [22]. Some accumulation effects occur during ion trapping, e.g., collisional deceleration of injected ions by the neutral species in the cell [22], ion–molecule reactions [23] or possibly deflection of injected ions by radial magnetic field inhomogeneities induced by the trap plates [24].

The purpose of this paper is to describe the FT-LM mass spectrometer and to illustrate the basic specifications with respect to sensitivity and spatial and mass resolution. Analysis is performed in the reflection mode by a frequency-

quadrupled Nd:YAG laser beam, which is focused to 5 μm. Post-ionization of the laser-generated neutral species can be performed using a 70-eV electron beam. With laser microbeam irradiation of solids, ion formation occurs over less than a few hundred microseconds. The time dispersion of the laser-generated ion bunches in the electrostatic transfer line conflicts with the simultaneous registration of ions within a wide m/z range. It will be shown, however, that this problem may provide interesting clues to the basic ion formation mechanisms induced by laser microbeam irradiation of organic vs. inorganic solids. Subsequently, attention will be devoted to representative results in relation to the speciation analysis of inorganic compounds and structural analysis of organic molecules. Comparative data from FT-LMMS and TOF-LMMS show characteristic differences, which will be tentatively interpreted in terms of the ion formation mechanism.

EXPERIMENTAL

Figure 1 shows a schematic diagram of the MicroFocus™ instrument, based on a Spectrospin CMS 47X with a 4.7-T superconducting magnet and a single cylindrical cell of 60 mm length and 60 mm diameter (Spectrospin, Fällanden, Switzerland). Instrument control and data acquisition are performed using an Aspect 3000 computer upgraded with a 20-MHz, 9-bit fast ADC and 256K memory. A full description of the basic instrumentation is available elsewhere [25]. The ion source–ion transfer–cell assembly is mounted on a movable vacuum cart to facilitate maintenance.

Ionization is performed by a frequency Q-switched Nd:YAG laser (Quanta-Ray DCR-2A, Spectra-Physics, San Jose, CA), delivering 20 mJ per pulse of 4–5 ns at 266 nm and equipped with fill-in optics for a Gaussian beam profile. The laser head is flashlamp-pumped at 10 Hz. The

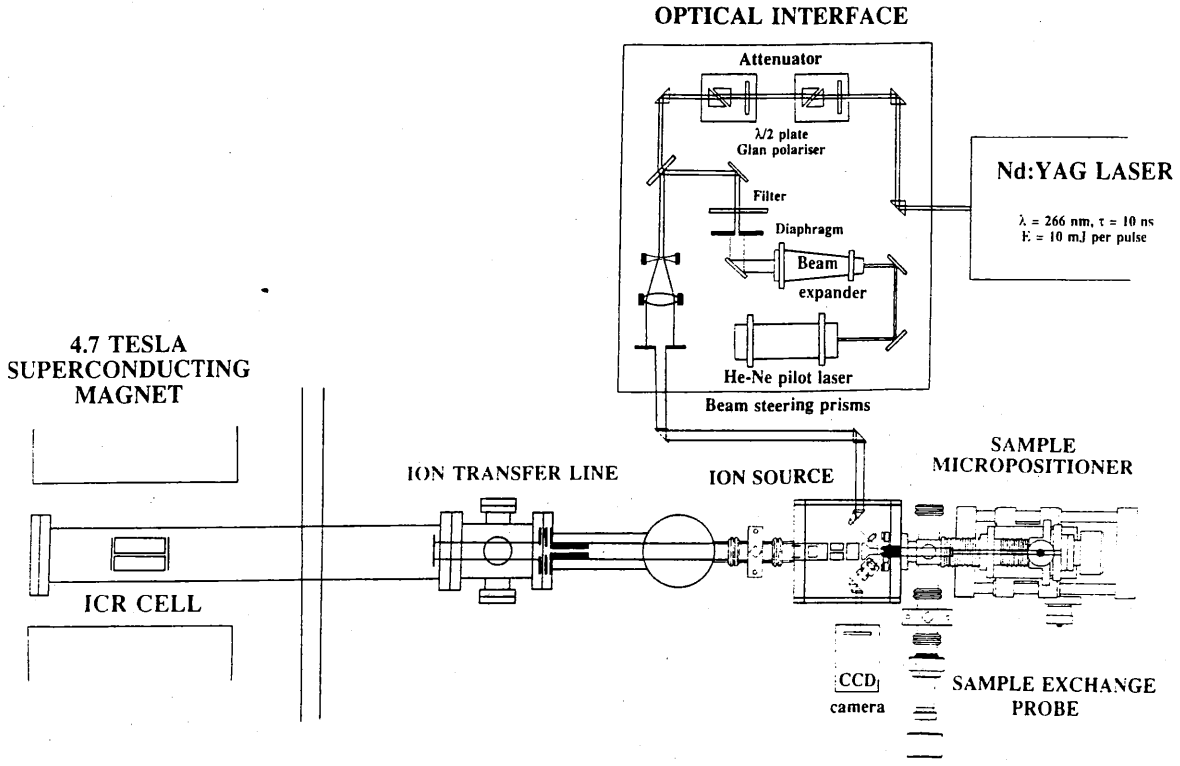

Fig. 1. Schematic diagram of the developed FT-LM mass spectrometer with the external source.

Pockell cell is controlled by a special interface board, triggered by the ionization pulse. The internal clock of the Aspect computer is disabled until the next flashlamp event. The analyses were performed under the so-called threshold conditions, involving the use of less than 100 nJ per shot.

Apart from the obvious diaphragms, filters and steering prisms, the optical interface essentially contains an expanded He–Ne laser, coupled collinearly with the UV beam at a 45° quartz plate, a 2.5 × Galilean-type beam expander and two sets of $\lambda/2$ waveplates in front of Glan air-spaced polarizers for rough and fine attenuation of the UV beam. A 15 × microscope lens (OFR, NJ) inside the vacuum performs the final focusing. The laser irradiates the sample in reflection under 45° over an ellipsoid spot, of which the long side is 5μm. All UV optics are anti-reflection coated and adjustable for tilt around two orthogonal axes, except for the beam expander lenses. The front optic is fixed and the exit optic is adjustable for tilt and in the x, y, z-directions. The number of steering prisms is optimized to permit partial readjustment when the laser or the ion source is being maintained.

The sample viewing system consists of a microscope objective with ultra-long working distance (M Plan SLWD 20X, Nikon, Tokyo) inside the vacuum, a CCD camera (CCD 500; Bischke, Switzerland), and a high-resolution monitor (TVM 12HI; Bischke) for display. The final magnification is 700 ×, so 1 mm on the screen represents 1.4 μm on the specimen. The depth-of-focus (DOF) permits the position of the sample surface to be assessed critically within the waist of the ionizing laser. The observation under 45° with a high-magnification microscope lens means that the sample is only imaged over 12 μm. A complementing low-magnification (10–63 ×) binocular (Nikon SMZ-2T), mounted outside the vacuum chamber, permits an overview of the sample. An area of 4 mm diameter is illuminated by a common halogen light source (Intralux; Volpi, Switzerland) outside the manifold and by prisms inside the vacuum.

The sample holder is designed for specimen with a size up to 20 × 20 × 10 mm. Micropositioning of the sample is performed by means of a commercial x, y, z-manipulator (Huntington, CA) with a 1-μm precision and 25-mm travel. The additional chamber with appropriate interlock and probe allows the exchange of the sample within 5 min without interruption of the vacuum in the ion source.

The standard configuration of the electrodes in the ion source and at the beginning of the transfer line has been redesigned. The sample is electrically isolated from the manifold and can be used as a repeller electrode. The first extracting electrode consists of a perforated cone of 6 mm diameter and 9 mm length, placed 2 mm above the sample surface. Post-ionization in the external source by 70 eV of laser-generated neutral species is feasible. Additional details of the system are described elsewhere [26].

Comparative results were recorded on a LAMMA 500 transmission-type instrument (Leybold Heraeus, Germany). Powdered particles of about 1–3 μm were attached to a Formvar film over a usual electron microscopy grid. The mass spectra were registered using the described procedure for threshold mode analysis [27].

Samples

Most samples were applied to a polished stainless-steel sample holder by evaporating a 10-μl aliquot of a solution, typically containing 2 mg of material per 100 ml methanol or water. Gold coatings were made by sputtering with Ar^+ under vacuum.

RESULTS AND DISCUSSION

Basic performance

Routinely, the mass resolution is over 100 000 for m/z values up to 500. Naturally, in the lower range higher values are attained. Figure 2 shows a few examples of the signals. Determination of m/z values yields results which lie within 1 ppm around the values calculated by calibration on perfluorotributylamine, which was introduced through the gas inlet and ionized with 70-eV electrons.

The sensitivity of the instrument in the laser ionization mode depends on the compound under consideration. Consumption of less than 1 pg of coronene gives a fairly intense signal in the narrow-band mode with a signal-to-noise ratio (S/N) of 7.5 at a resolution of 240 000. In general, the detectability of FT-LMMS allows the recording of at least the base peak from a single shot with a 5-μm spot size. Irradiation of a gold layer of less than 100 nm thickness with a 5-μm spot yields a very prominent signal for the positive elemental ions with $S/N > 100$ and a resolution of 1.2×10^6. Under these conditions, the crater depths exceeds the thickness of the upper layer. However, the total amount of evaporated material only contains about 1.2×10^{10} gold atoms.

An interesting feature of the LM irradiation under threshold conditions is the very limited information depth, i.e., the recorded mass spectral data only issue from the upper 100 nm whereas the crater goes several μm deeper. This makes the method appealing as a surface technique. No iron ions could be detected during the irradiation of stainless steel covered with a gold layer of about 100 nm. In principle, this phenomenon depends on the relative ionization yield of the upper and underlying component on the condition that the ion characteristics are comparable with respect to, e.g., energy distribution and formation time. Of course, the broadband mode is less sensitive than the high-resolution mode, by a factor of at least 50, depending on the ion trapping procedure (see the next section).

The availability of post-electron impact (EI) in the external ion source has been demonstrated to be a substantial asset for particular organic compounds. For structures giving the same ions with laser ionization and post-EI, e.g., coronene, the detection limit improves by a factor of five or more. Alternatively, post-EI can be applied to overcome the poor ionization efficiency of the laser for certain molecules. Finally, post-EI allows the generation of additional fragment peaks, which increase the diagnostic information of the registered mass spectra. Figure 3 illustrates several aspects in the spectra of methylene blue obtained by FT-LMMS. The TOF-LMMS results are included for comparison. The latter method detects the intact cations with virtually no fragmentation. The situation is more or less comparable for the laser-only mode in FT-LMMS, but still some small additional peaks are present. Ionization of the laser-generated neutral species yields a substantial increase in the signal at m/z 268 in the presence of the corresponding fragments. The latter peaks certainly increase the information

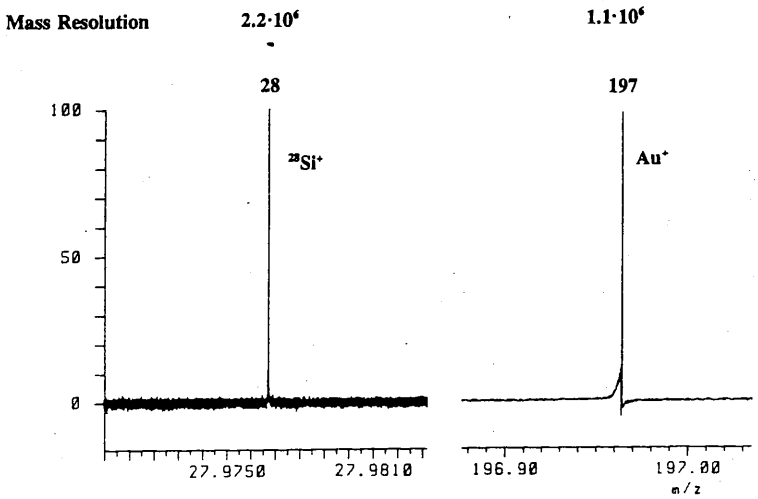

Fig. 2. Typical high-resolution measurements by FT-LMMS of the elemental ions from a silicon wafer (left) and a 100-nm gold layer (right).

content of the spectra and allow the description of the functionalities in the molecule, which is hardly feasible from the laser-only mode data. Moreover, the signal at m/z 149 is related to the phthalate contamination of the sample, which is almost inevitable although not detected in the laser-only mode. For some reason, this compound is not very sensitive under laser microbeam irradiation conditions, in spite of its aromatic functionality.

Panoramic registration

Depending on the application, local analysis research may involve the localization of a given

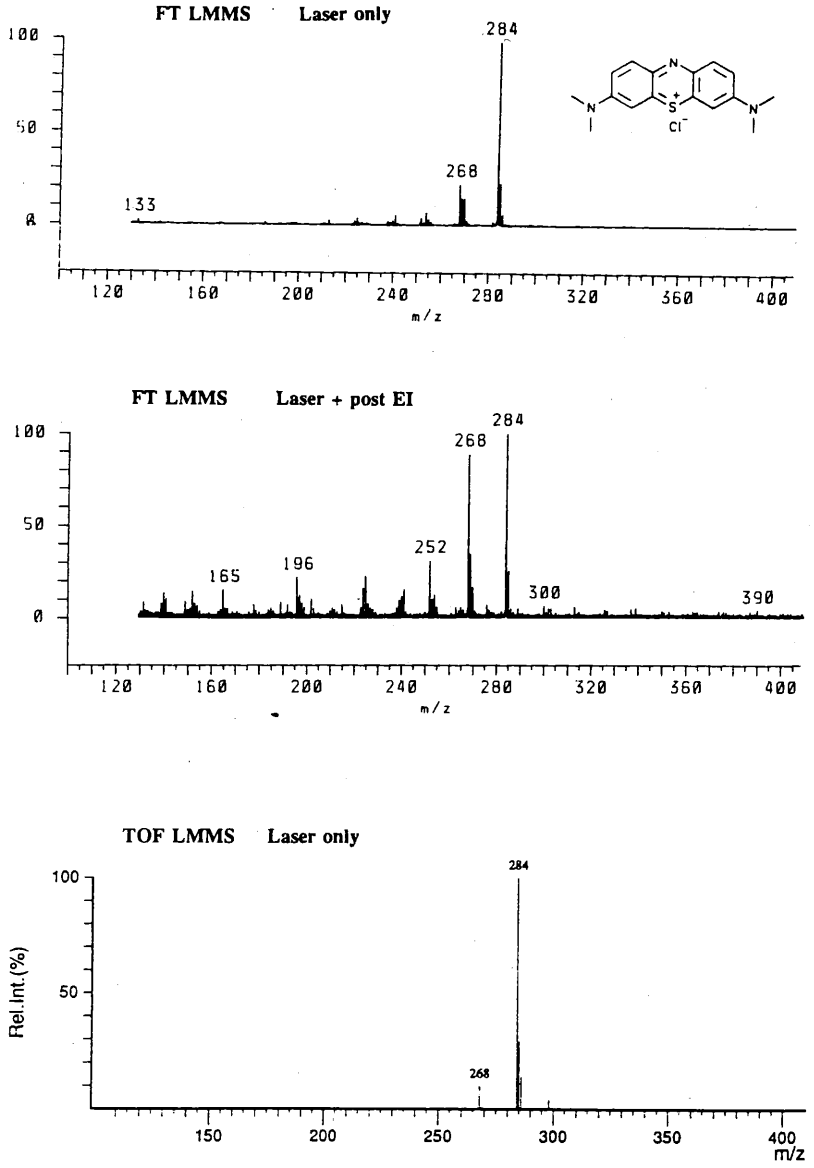

Fig. 3. Positive-ion detection mode mass spectra of methylene blue recorded by TOF-LMMS and FT-LMMS with or without post-electron ionization.

target or the identification of an unknown substance in, e.g., a microscopic heterogeneity. In the former case, single ion monitoring in the high-resolution mode can be considered as an adequate means, because the m/z accuracy and the available mass resolution in FT-LMMS make the determination of the compound under consideration almost unambiguous in practice. However, multiple ion monitoring would be desirable to allow the localization of several components in the same shot. In the latter case, a mass spectrum over a wide m/z range is required.

Whenever an external source is coupled to the FT-MS analyser cell over static electrical fields, a mass-dependent time separation occurs during the ion transfer. Hence, the low-m/z ions arrive

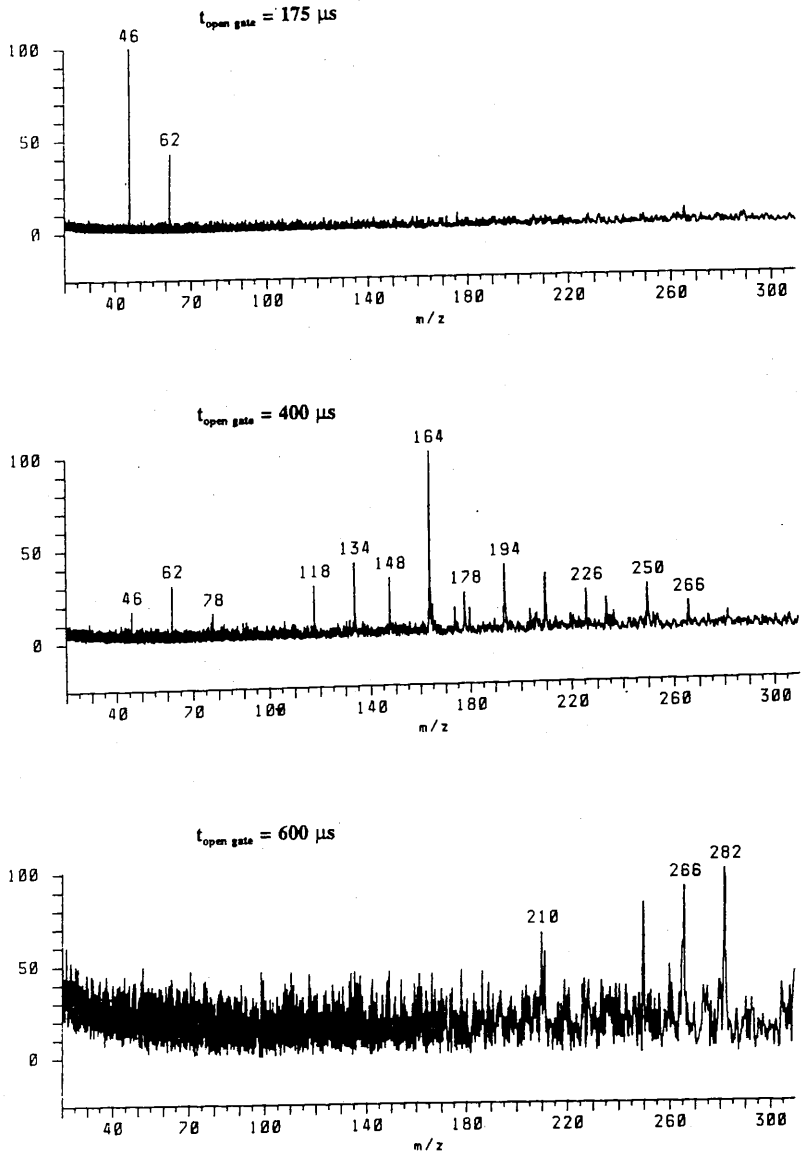

Fig. 4. Negative-ion mass spectra of calcium nitrate recorded by FT-LMMS a function of the duration of the ionization pulse ($t_{\text{open gate}}$).

first at the "cell gate". These ions are allowed to enter the cell when the repulsing field situated in the central perforation of the first trapping electrode is reduced to zero. Subsequently, the ions are reflected by the second trapping plate. Obviously, the repelling field in the front electrode has to be restored before the ions have returned. At the same time, the higher m/z ions which arrive later can no longer enter the cell. Stated differently, to determine the mass range for panoramic registration one has to consider the lowest m/z to be recorded. The trap residence time (i.e., the period in which the ions travel from one trap plate to the other) of these ions, which arrive first, determines the time during which the cell can be opened for the slower, higher m/z ions. These effects have been extensively described [15,28]. Note that these problems arise whenever the ionization method used produces ion bunches within extremely short time periods. When, for instance, EI is applied to a continuous sample supply, ions can be produced at a fairly constant rate over thousands of μs, i.e., several times the flight time of even the heaviest ions. Hence the TOF effect is rules out completely because, at each moment, the cell contains ions that were generated at different times. Further, the use of two half-electrodes in front of the first trapping plate, permitting the repulsing trapping field to be compensated upon entering, partially prevents the escape of the ions from the cell. As a result, ions are accumulated in the cell [29]. Of course, in the present instance this is not feasible.

Figure 4 shows a few broadband spectra of calcium nitrate as a function of the duration of the ionization pulse. The indicated times refer to the ionization pulse time, which roughly corresponds to the time between the laser firing and the disabling of the half-electrodes in front of the cell. The assignment of the signals shown in Fig. 4 is summarized in Table 1 and will be discussed later.

It is clear, however, that the TOF effect causes severe problems but the situation can be dealt with on the condition that the considered m/z range can be limited, especially with respect to the low mass limits. A coverage of the m/z range from 100 to 500 is acceptable for practical applications. Note that the elemental ions in the low-mass range require different laser ionization conditions than the organic compounds and the higher mass ion clusters used for speciation analysis of inorganic compounds.

Hence it is worth comparing the mentioned times for the ionization pulse with the values in Table 2, which were calculated using the SIMION program (Idaho National Engineering Laboratory), for the flight times and the trapping residence times. The former were calculated for the voltages on the transfer optics as used in the present experiments. This essentially involves a stepwise acceleration up to 3 kV followed by a gradual decrease to 550 V in the last flight tube, ending about 50 cm before the cell. The ions then drift through a zero-voltage tube towards the cell. The trapping residence times are calculated for a

TABLE 1

Assignment of the major signals in the negative-ion mass spectrum of calcium nitrate

m/z	Species	m/z	Species
46	NO_2^-	178	$CaO \cdot NO_2 \cdot NO_2 \cdot NO^-$
62	NO_3^-	192	$CaO \cdot CaO \cdot H_2O \cdot NO_3^-$
118	$CaO \cdot NO_3^-$	194	$Ca(NO_3)_2 \cdot NO^-$
134	$CaO \cdot O_2 \cdot NO_2^-$	205	$CaO \cdot HNO_2 \cdot CaO \cdot NO_2^-$
148	$CaO \cdot NO_2 \cdot NO_2^-$	210	$Ca(NO_3)_2 \cdot NO_2^-$
149	$CaO \cdot HNO_2 \cdot NO_2^-$	221	$CaO \cdot HNO_2 \cdot CaO \cdot NO_3^-$
164	$CaO \cdot NO_2 \cdot NO_3^-$	226	$Ca(NO_3)_2 \cdot NO_3^-$
165	$CaO \cdot HNO_2 \cdot NO_3^-$	234	$CaO \cdot NO_2 \cdot CaO \cdot NO_2 \cdot NO^-$
174	$CaO \cdot CaO \cdot NO_3^-$	237	$Ca(NO_3)_2 \cdot CaO \cdot OH^-$
176	$CaO \cdot CaO \cdot H_2O \cdot NO_2^-$	250	$Ca(NO_3)_2 \cdot CaO \cdot NO^-$

TABLE 2

Calculation of flight times and trapping residence times for ions at different m/z in FT-LMMS with external source

m/z	Flight time (T_{fl}) (μs)	Trapping residence time (T_{tr}) (μs)	Optimum time calculated ($T_{fl} + T_{tr}$) (μs)
20	46	52	98
50	72	82	154
100	102	116	218
250	161	183	344
500	227	259	486
1000	321	366	687

trap potential of 1.5 V and ions arriving with 0.3–1.4 eV in the cell. The spread of the trapping residence time for ions with different energies in that range is about 2.4%.

Assume that abstraction can be made from the time dispersion resulting from the initial velocity and angular emission spread of the ions and that all ions are generated within 5 ns. If one uses an ionization pulse time of 344 μs, i.e., the sum of the flight time and the trap residence time for the ions at m/z 250, it should be possible to trap all ions (i.e., up to m/z 1000) that arrive at the "cell gate" within that time. At the same time, however, all ions below m/z 100 arrive sooner and have a shorter trap residence time and hence will have escaped from the cell by then. As a result, the TOF effects are particularly annoying when the low-mass range is aimed at. For organic compounds, it is often sufficient to record the spectral information from ions between m/z 150 and 500. In order to overcome these TOF effects the instrumentation will be modified with respect to the ion transfer and/or trapping system, according to the results of Beu and Laude [28].

Comparison of FT-LMMS with TOF-LMMS

For convenience, let us discuss the possible reasons for the differences between mass spectra obtained in TOF- and FT-LMMS.

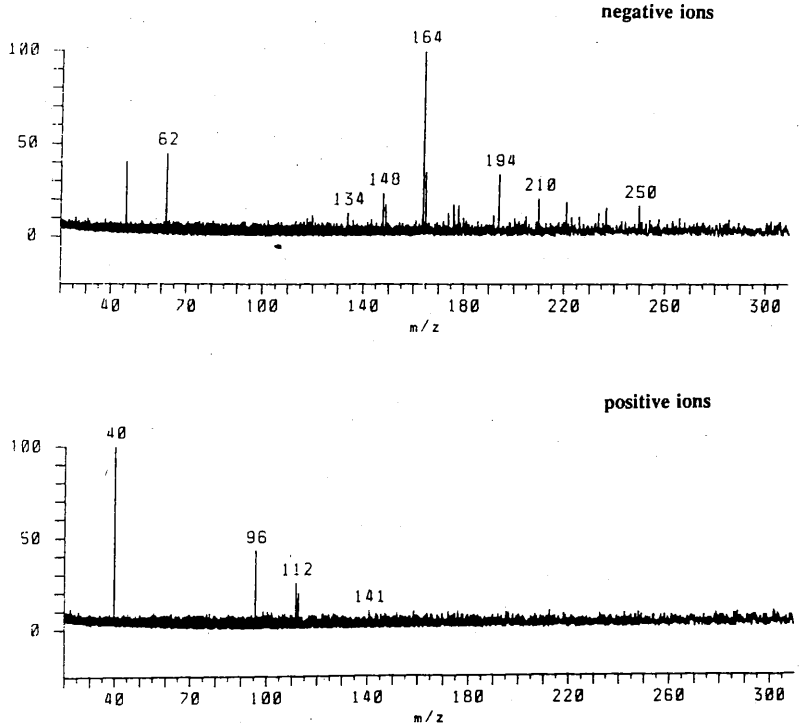

Fig. 5. Positive- and negative-ion mass spectra of calcium nitrate recorded by FT-LMMS.

Laser microbeam irradiation. The power density distribution within the irradiated area can be different simply because of the spot size. Further, it is difficult to reproduce the irradiate conditions exactly on two different instruments because the energy in the final spot cannot be measured. Finally, the proposed FT-LM mass spectrometer uses reflection geometry, i.e., the laser impinges on the sample and the ions are extracted from the same side, whereas the TOF-LM mass spectrometer works in transmission geometry, i.e., the laser beam and spectrometer are on the same axis but at opposite sides of the thin sample.

Time domain for ion collection. The TOF instrument deals essentially with the prompt ions whereas the FT-LM spectrometer allows the measurement of the total ion current, generated within a fraction of a millisecond, unless special precautions are taken.

Duration of the experiment. In TOF-LMMS there is a period of only 500 μs between ion generation and registration. In FT-LMMS the basic duty cycle of even a simple experiment lies in the range of milliseconds.

Kinetic energy acceptance. This is high in TOF-LMMS where only the distribution width matters as long as the average ion velocity allows preservation of the calibration. The kinetic energy acceptance is low in FT-LMMS, depending on the trapping potential and the characteristics of the ion transfer system.

Extraction field. This is high in TOF-LMMS, hence the residence time within the laser microplasma is minimal. There is a low to very low or even repelling field in the external source of the FT-LM mass spectrometer, which causes a longer residence time. It is better, however, than in the alternative set-ups, using laser microbeam irradiation of the sample inside the cell [13].

Inorganic speciation analysis. The positive- and negative-ion mode mass spectra of calcium nitrate in Fig. 5 illustrate the features one expects from LMMS for measurement of speciation. Note that the intensity of the elemental ions in the positive-ion mass spectrum is possibly underestimated because of the TOF effect. The same is true for the negative ions below m/z 100 in the negative-ion mass spectrum. The main information that can be derived from the positive ions comes from cations in the form of elemental ions and oxides in the case of oxo salts (see Table 3). Depending on the structure, higher clusters consist of these units attached to one or more neutral entities. The low-m/z ions in the negative ion mode usually characterize the anionic moiety by means of the base peak (cf., Table 1). Highly relevant in this respect is the presence of intense signals referring to the combination of the salt ionic pair with a stable anionic moiety. Sometimes, however, higher clusters are not detected, depending on the compound studied. The combination of all of these signals clearly allows the identification of a salt in a very obvious way. In this respect, laser microbeam irradiation has been proved superior to, e.g., secondary ion MS or other microprobe methods.

TABLE 3

Assignment of the major signals in the positive-ion mass spectrum of calcium nitrate

m/z	Species
40	Ca^+
96	$CaO \cdot Ca^+$
112	$CaO \cdot CaO^+$
113	$CaO \cdot CaO \cdot H^+$
152	$CaO \cdot CaO \cdot Ca^+$

The LM irradiation conditions are kept identical in both the TOF and FT-LM instruments as far as possible, but there is no absolute guarantee that this is really the case. Owing to the extreme dependence of the spectral intensities on the exact irradiation conditions, i.e, focusing, particle size, etc., it is justified to classify the signals in three or four intensity ranges. From comparison of the two methods, it is clearly observed that the FT-LMMS data contain in general fewer peaks than the corresponding TOF spectra; the main diagnostic information is preserved but the spectra look cleaner.

The interpretation of this observation is not yet clear. One of the reasons is the lack of knowledge on the ion formation mechanisms. In principle, desorption as an ion pair and subsequent association with a charged species or dissociation into the detected low-m/z ions can occur in

competition with direct emission of the registered ions from the solid. A relevant observation in this respect concerns the fact that the detection of higher clusters in FT-LMMS is favoured if one increases the residence time of the ions in the first part of the ion transfer system. This can be achieved by increasing the voltage on the first extraction lens, which is very near to the sample surface, above that on the sample holder, which consequently ceases to act as a real repeller. In contrast, elemental ions still pass through when there is a small accelerating field between the extractor and repeller. Also, the experimentally optimized pulse ionization times agree better with the calculated values for elemental ions, compared with the higher clusters. This may point to prompt ionization processes for the former ions and delayed mechanisms for the latter.

So far, little is known about the possible fragmentation rates of inorganic ions. Exploration of this field using the capabilities of FT-LMMS for ion decomposition studies of laser-generated ions provides an exciting research topic for the near future.

Organic compounds. Figure 6 compared the TOF- and FT-LMMS results for haloperidol in the positive-ion detection mode [30]. The general trend with respect to the relative ion intensities concerns the fact that the base peak is more dominant over the other signals in FT- than in

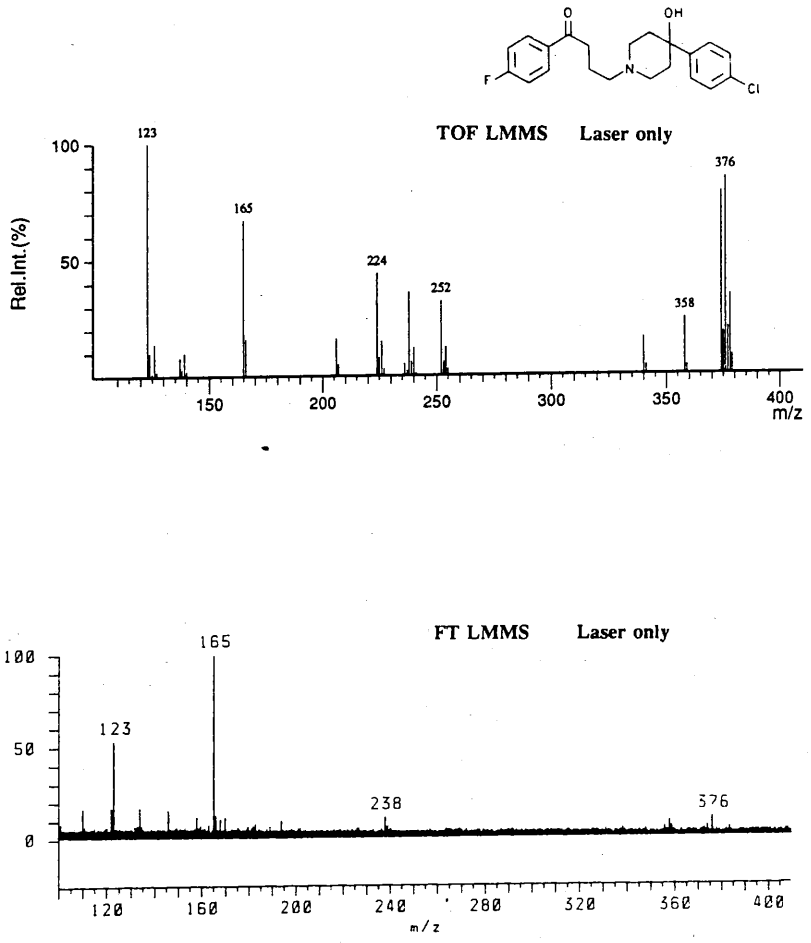

Fig. 6. Positive-ion detection mode mass spectra of haloperidol recorded by TOF-LMMS and FT-LMMS.

TOF-LMMS. The abundance of the stable fluorobenzoyl fragment ion "suppresses" the other signals in the former instance. Qualitatively, TOF-LMMS produces more signals, e.g., the ions at m/z 252 and 224, which are not detected in FT-LMMS. The tentative rationalization of the observed differences is straightforward. The effect of sampling the total ion bunch and not only the promptly generated species in FT-LMMS results in a lower energy distribution for the ion population. This hypothesis can be deduced, for instance, from the draw-out pulse measurements on a TOF instrument [9]. The later generated ions have smaller energy distributions and undergo less fragmentation down to none at all.

The FT-LMMS data remain adequate for localization of this target in a mixture or a complex sample. One should bear in mind that the signals still remain structure specific and that the peaks can be measured in high resolution. It was also noted that the $[M - H]^+$ signal is consistently lower in FT-LMMS than in TOF-LMMS, which may be due to a relative increase in the $[M + H]^+$ ions in FT-LMMS.

A substantially longer pulse ionization time is required in comparison with the SIMION calculations for the ions in the molecular region, which points to a prevalent formation process after the laser pulse.

Conclusions

Preliminary results have shown the feasibility of the developed FT-LMM mass spectrometer with an external ion source to perform high mass resolution measurements of the ions, generated from a 5-μm spot on organic and inorganic samples. At least the base peak can be detected in the single shot mode. The high mass resolution and accurate m/z determination provide valuable identification possibilities for the localization of the target, depending, of course, on its structure. The benefits from the application of post-EI on the laser-generated neutral species also depend on the structure studied. If the laser ionization yields ions at the same m/z as post-EI, the sensitivity is improved by a factor of five. On the other hand, the fragmentation caused by post-EI disperses the additional ion yield over several m/z signals. To overcome this problem, the ion source is currently modified to perform post-CI on laser-desorbed neutral species. There are some differences between FT- and TOF-LMMS data, which are tentatively interpreted in terms of ion formation mechanisms, but further research is required. There is evidence for the occurrence of thermal degradation during the analysis. It can be concluded that the sensitivity of FT-LMMS is sufficient to register the base peak but it still remains a factor of 100 lower than in TOF-LMMS. In the authors' opinion, the price to be paid for the higher mass resolution with FT-LMMS system is very reasonable. At present, panoramic spectrum registration by FT-LMMS is hindered by the time-of-flight problem. Under these conditions, only limited m/z ranges can be recorded in the broadband mode. The comparison of experimental and SIMION-calculated data suggest that the situation is aggravated by the delayed ion formation. This problem will be dealt with in the immediate future. FT-LMMS results for inorganic compounds are characterized by fewer lines in comparison with TOF-LMMS data, but the main diagnostic information is preserved. It is not yet clear which factor is responsible for this, e.g., kinetic energy distribution or time scale. FT-LMMS fulfills the expectations for inorganic and organic analysis, with fine speciation analysis capabilities in the former field and good structural characterization information for the latter application.

Luc Van Vaeck and Wim Van Roy are indebted to the National Science Foundation, Belgium (NFWO) as research associate and research assistant, respectively. Eng. R. Saelens is acknowledged for technical support. This work was partially sponsored by the Belgian Ministry of Public Health and the Environment and by the Belgian Prime Minister's Services, Science Policy Office, in the framework for the Impulse Programme on Marine Sciences.

REFERENCES

1 H. Vogt, H.J. Heinen, S. Meier and R. Wechsung, Fresenius' Z. Anal. Chem., 308 (1981) 195.

2 H.J. Heinen, S. Meier, H. Vogt and R. Wechsung, Int. J. Mass Spectrom. Ion Phys., 47 (1983) 19.
3 J.C. Ruckman, R. Davey and N.S. Clarke, Vacuum, 34 (1984) 911.
4 A.H. Verbueken, F.J. Bruynseels, R. Van Grieken and F. Adams, in F. Adams, R. Gijbels and R. Van Grieken (Eds.), Inorganic Mass Spectrometry, Wiley, New York, 1988, p. 173.
5 L. Van Vaeck and R. Gijbels, Fresenius' J. Anal. Chem., 337 (1990) 743.
6 L. Van Vaeck and R. Gijbels, Fresenius' J. Anal. Chem., 337 (1990) 755.
7 R. Kaufmann, F. Hillenkamp, R. Wechsung, H.J. Heinen and M. Schurmann, Scanning Electron Microsc., 2 (1979) 279.
8 L. Van Vaeck, J. Claereboudt, P. Van Espen, F. Adams, R. Gijbels and W. Cautreels, Adv. Mass Spectrom., 9B (1986) 957.
9 R.J. Cotter and J.C. Tabet, Int. J. Mass Spectrom. Ion Phys., 53 (1983) 151.
10 M. Pelletier, G. Krier, J.F. Muller, D. Weil and M. Johnston, Rapid Commun. Mass Spectrom., 2 (1988) 146.
11 J.T. Brenna, W.R. Creasy, W. McBain and C. Soria, Rev. Sci. Instrum., 59 (1988) 873.
12 R.B. Cody, A. Bjarnason and D.A. Weil, in D. Lubman (Ed.), Lasers in Mass Spectrometry, Oxford University Press, New York, 1990, p. 316.
13 J.T. Brenna, in P.E. Russell (Ed.), Microbeam Analysis–1989, San Francisco Press, San Francisco, 1989, p. 306.
14 P. Köfel and T.B. McMahon, Int. J. Mass Spectrom. Ion Processes, 98 (1990) 1.
15 P. Köfel, M. Alleman, H. Kellerhals and K.P. Wanczek, Int. J. Mass Spectrom. Ion Processes, 72 (1986) 53.
16 R.T. McIver, Jr., R.L. Hunter and W.D. Bowers, Int. J. Mass Spectrom. Ion Processes, 64 (1985) 67.
17 D.F. Hunt, J. Shabanowitz, J.R. Yates, III, P.R. Griffin and N.-Z. Zhu, Anal. Chim. Acta, 225 (1989) 1.
18 W.G. Millen, J.T. Meek, G.W. Stockton, M.L. Thomson and R.S. Wayne, in Proceedings of 36th ASMS Conference on Mass Spectrometry and Allied Topics, San Francisco, CA, June 5–10, 1988, p. 1247.
19 C.B. Lebrilla, I.J. Amster and R.T. McIver, Jr., Int. J. Mass Spectrom. Ion Processes, 87 (1989) R7.
20 P. Köfel, M. Alleman, H. Kellerhals and K.P Wanczek, Int. J. Mass Spectrom. Ion Processes, 65 (1985) 97.
21 J.M. Alford, P.E. Williams, D.J. Trevor and R.E. Smalley, Int. J. Mass Spectrom. Ion Processes, 72 (1986) 33.
22 S.C. Beu and D.A. Laude, Int. J. Mass Spectrom. Ion Processes, 97 (1990) 295.
23 D.F. Hunt, J. Shabanowitz, R.T. McIver, R.L. Hunter and J.E.P. Syka, Anal. Chem., 57 (1985) 765.
24 M. Bamberg and K.P. Wanczek, in Proceedings of the 37th ASMS Conference on Mass Spectrometry and Allied Topics, Miami Beach, FL, May 21–26, 1989, p. 456.
25 P. Grossmann, P. Caravatti, M. Alleman and H. Kellerhals, in Proceedings of the 36th ASMS Conference on Mass Spectrometry and Allied Topics, San Francisco, CA, 1988, p. 616.
26 L. Van Vaeck, W. Van Roy, H. Struyf, F. Adams and P. Caravatti, Rapid Commun. Mass Spectrom., in press..
27 L. Van Vaeck, J. Bennett, W. Lauwers, A. Vertes and R. Gijbels, Mikrochim. Acta, III (1990) 283.
28 S.C. Beu and D.A. Laude, Jr., Int. J. Mass Spectrom. Ion Processes, 104 (1991) 109.
29 P. Caravatti, US Pat., 4 924 089 (1990).

Pergamon

Spectrochimica Acta, Vol. 49B, No. 4, pp. 345–353, 1994

0584-8547/94 $6.00 + .00

0584-8547(93)E0018-C

Non-linear mapping of microbeam proton-induced X-ray emission data for source identification of North Sea aerosols

BORIS TREIGER,* JASNA INJUK, IGOR BONDARENKO,* PIET VAN ESPEN, RENÉ VAN GRIEKEN
Department of Chemistry, University of Antwerp (UIA), B-2610 Antwerpen-Wilrijk, Belgium

LOTHAR BREITENBACH and UWE WÄTJEN
CEC-JRC, Institute for Reference Materials and Measurements, B-2440 Geel, Belgium

(*Received* 6 *July* 1993; *accepted* 6 *December* 1993)

Abstract—A multivariate statistical evaluation technique, non-linear mapping, is proposed to extract information from a multielement microbeam proton-induced X-ray emission data set. Individual aerosol particles, collected in the North Sea troposphere, were classified according to their composition. Several groups of particles were identified and suggestions were made for their sources.

1. INTRODUCTION

MICROBEAM particle-induced X-ray emission (micro-PIXE) is a powerful method for the determination of spatially resolved trace-element compositions. The basic characteristic features of micro-PIXE are low detection limits and detailed elemental mapping capability over spatial intervals of a few micrometres. Therefore it can be used to evaluate the nature of the particles responsible for the environmentally important atmospheric input of heavy metals into the North Sea.

Estimations of the impact of sources of atmospheric aerosols on a specific receptor site can be made by several methods. Usually deterministic dispersion [1], hybrid [2] or receptor models [3] can be used for this purpose. The present paper deals with the latter group of methods, which relate the chemical and physical properties of the aerosol observed at the receptor site to the known properties of the source aerosols, and estimate the impact of each source at the site. The receptor models are generally divided into chemical mass balance (CMB) models and multivariate models. CMB models have the advantage of being able to make an apportionment based on only one aerosol sample, but on the other hand the composition and the number of sources affecting the receptor site have to be known beforehand. The multivariate models require a large number of samples to be taken and analysed for several relevant components. The number as well as the composition of the sources can be inferred from the covariation between the components of the aerosol. The methods most commonly used are principal component (or factor) analysis (PCA) and cluster analysis (CA). Factor models primarily yield only qualitative results. Among them one can mention the absolute factor models [4–6] and the target transformation factor analysis [7]. The factor models are ambiguous in the sense that several solutions can be obtained even when subjected to reasonable physical constraints [8]. The validity of results is thus to a large extent determined by the skill and experience of the modeller.

PCA is representative of a large group of graphical multivariate methods, which enable the analytical chemist to explore data thoroughly, to look for relationships, to confirm or disprove the expected, and to discover new phenomena [9–13]. However, with the exception of PCA, graphical methods that are already commonly used for

* On leave from Pedagogical Institute, Kirovograd, Ukraine.

classification in social and life sciences are practically without use in natural sciences. The aim of the present paper is to show how the application of graphical multivariate methods can enhance the usefulness of micro-PIXE in environmental applications.

2. THEORETICAL

2.1. *Graphical representation of multivariate chemical data*

There are two main groups of methods for the graphical display of multivariate data. The first is the direct display of the data, and the second lies in displaying quantities derived from the data. The direct display of multivariate data is rather complicated, although there are some useful methods, e.g. draftsman's display (for review see, e.g. Ref. [14]). Display of quantities derived from the original data can also be made in two main ways, namely qualitative and quantitative displays. The qualitative ones can show qualitative differences among multivariate data sets; no quantitative information can be obtained from them. Methods such as Chernoff faces, linear, circular and star profiles, Kleiner–Hartigan trees, and Andrews' Fourier representations belong to this group. These methods are extensively used in social sciences, but they are almost useless for computation (see e.g. Ref. [15]). Among quantitative displays (in other words, dimensionality reduction methods), are linear and non-linear projections of multivariate data. A typical method for linear dimensionality reduction is PCA, which is a very powerful method in cases when the real dimensionality of the N-dimensional data (the rank of data matrix) is less than N. However, with PCA one can obtain the graphical visualization of the N-dimensional data structure in one step (i.e. the reduction of dimensionality to two or three) only in cases when the rank of the data matrix is also two or three. Unfortunately, such a situation does not occur often and in the cases when the real dimensionality of data is more than three, the application of only one PCA plot can lead to incorrect results. That is why the application of alternative non-linear methods (not instead of PCA but, rather, along with it!) offers good perspectives to improving visually obtained information.

2.2. *Non-linear mapping*

The main idea of all non-linear methods is to represent the original data elements as points in a space with reduced dimensions so that the distance between the points in the space corresponds to the differences between the data points in the initial space. In other words, the data structure in N-dimensional space can be preserved if the relative distances between the points in the initial space and their projections in the space with reduced dimensions are kept the same. Under such an approach, no error is made and it is clear that this is an ideal situation. In practice, non-linear methods try to minimize the possible error:

$$\sum_{i<j} \frac{(d_{ij}-d_{ij}^*)^2}{d_{ij}}$$

where d_{ij} are the original distances between the objects and d_{ij}^* are the new distances in a two-dimensional space (see e.g. Ref. [16]).

Among the most famous non-linear methods are non-linear mapping (NLM) and multidimensional scaling (MDS). Both are similar in concept. The main difference is that NLM can be applied only to quantitative data (i.e. it uses only a dissimilarity matrix containing some types of distances) whereas MDS is free of this constraint. On the other hand, NLM is somewhat simpler than MDS, although the computational realization of both methods is rather complicated (see e.g. Ref. [17]). But there exists a simple approach [18, 19] which can be described as follows. First, choose reference points in N-dimensional space. Then find a transformation of N-dimensional space into 2 or 3 dimensions that preserves, not the relative distances between any points

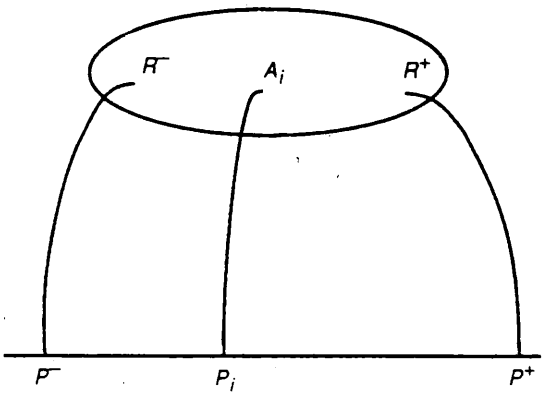

Fig. 1. An illustration of the procedure of NLM using a pair of reference points.

in N-dimensional space, but the relative distances between the data points and the reference points. That is, if we have a pair of the reference points (say, R^- and R^+) and a data point A_i in N-dimensional space and a pair of corresponding reference points (P^- and P^+) and a point P_i (image of the point A_i) on a straight line (see Fig. 1), the invariance of the relative distances between the reference and data points can be expressed as:

$$\frac{|R^+A_i|}{|R^-A_i|} = \frac{|P^+P_i|}{|P^-P_i|}.$$

If we know the reference points and the rule for the calculation of the distance between the points in N-dimensional space, we can obtain the coordinates of the projections of the data points on a straight line. The choice of reference points can be done in various ways since it is an arbitrary matter.

Let us discuss the choice of the reference points in some detail. Here, three pairs of reference points are selected for NLM. These points are chosen so that all data points must in a sense "lie between" them. Indeed, if we choose a pair of reference points in N-dimensional space and a pair of corresponding points on a straight line, it really means that we try to project N-dimensional space on a straight line. But the points on a straight line are ordered, i.e. one of the three lies between two others. Thus if one tries to get a meaningful projection, one has to choose reference points in the way described above. Thus the first step in the procedure for choosing reference points is construction of artificial sets representing the minimal and maximal "data points". This is done as follows. The sorting of all N columns of the data matrix in ascending order is done. Then, the first row is an artificial point, of which the coordinates are the minimal values of coordinates of all data points along all coordinate axes; this point will be referred to as reference point R_1^-. Reference point R_1^+ is constructed from the maximal values.

To introduce the next pair of reference points, we take the minimal value of the coordinates of R_1^- (designate it as min) and maximal value of the coordinates of R_1^+ (designate it as max). Let us calculate the parameters a and b from the equation of the straight line $y = ax + b$ given the requirements: $x = 0$, $y = \min$; and $x = N-1$, $y = \max$. One can easily calculate that the equation has the form:

$$y = \frac{\max - \min}{N-1} x + \min.$$

Consequently, we can introduce the second pair of reference points:

$$R_2^- = \left\{\min, \frac{\max-\min}{N-1}1 + \min, \frac{\max-\min}{N-1}2 + \min, \ldots, \max\right\}$$

$$R_2^+ = \left\{\max, \frac{\min-\max}{N-1}1 + \max, \frac{\min-\max}{N-1}2 + \max, \ldots, \min\right\}.$$

They represent the "crossing lines" in N-dimensional space. The last pair of reference points is chosen in such a way as to represent the symmetrical "crossing parabolas":

$$R_3^- = \left\{\min, \ldots, \frac{\min-\max}{\left(\frac{N-1}{2}\right)^2}\left(i - \frac{N-1}{2}\right)^2 + \max, \ldots, \max\right\}$$

$$R_3^+ = \left\{\max, \ldots, \frac{\max-\min}{\left(\frac{N-1}{2}\right)^2}\left(i - \frac{N-1}{2}\right)^2 + \min, \ldots, \min\right\}$$

where $i = 0, \ldots N-1$.

As mentioned above, the introduction of reference points in NLM makes this method computationally very simple; furthermore, the method becomes more flexible. One can choose reference points to solve specific problems.

Why do we use just three pairs of reference points? This can be explained by the following considerations. The projection of an N-dimensional space into a straight line must lead to a distortion of the projected data structure in comparison with the initial one. Simultaneous use of two or three projections can decrease the level of distortion. At the same time the three-dimensional projection is still a visual one. However, if one wishes to reduce the dimensionality to two, one can apply PCA to these three-dimensional NLM results. This is the procedure used in the present paper.

3. EXPERIMENTAL

3.1. *Sampling*

Aerosol samples were taken during the "North Sea" experiment of the EUROTRAC ASE program, which was set up from 1–22 September 1992, on the Research Platform *Nordsee* (54°42′N, 7°10′E). Size-segregated airborne particulate matter was taken by means of a wind tunnel which orients itself continuously towards the wind direction and has a forced internal air flow by a ventilator; this allows quantitative collection of the large and giant particles (aerodynamic diameter above 4 μm) without problems of variable cut-off with wind direction and wind speed [20]. The samples were collected under diverse meteorological conditions using a multistage May cascade impactor [21]. Every stage has a single slot-shaped jet and the impaction stages are glass slides. We covered these slides with Nuclepore filters (0.4 μm pore size) to reduce re-entrainment and bounce-off. The cut-off diameters of the stages range between 20 and 0.5 μm at a flow rate of 20 l min^{-1} [22].

3.2. *Analytical procedure*

The major elements of individual size-segregated aerosol particles were identified by means of micro-PIXE at the scanning proton microprobe (SPM) facility at the Institute for Reference Materials and Measurements (CEC-JRC) in Geel, Belgium [23]. The microbeam line is mounted in the target hall of the KN-3.7 MV vertical single-stage Van de Graaff accelerator. The accelerator is equipped with a radio frequency ion source to produce H^+ or He^+ ions. The energy spread of the accelerator is about 0.07%, while the brightness has been measured on the beam line to be 3.5 pA·$mrad^{-2}$·μm^{-2} at a proton energy of 2 MeV. A lateral resolution of 2.5 × 2.5 μm^2 was routinely achieved at a beam current of 100 pA. In the Geel SPM, a flexible front-end computer is used together with a powerful host computer. A VMEbus system acts as a front-end computer that controls the beam scanning and the acquisition of data from a maximum of four detectors and from the beam charge monitor. The host computer is a MicroVax-II, equipped with a Nuclear Data ND9900 multiparameter MCA system.

The aerosol samples were analysed by scanning the beam over a fairly large, square region, usually 128 × 128 μm^2 in a 64 × 64 pixel scanning pattern. The X-rays induced by the proton beam were continuously recorded and sorted by the data acquisition system, producing X-ray

intensity images of selected elements. From these maps, clusters of particles deposited on the backing were located. The time of analysis varied between 30 and 60 min, depending on the elements present and their respective amounts. Elements ranging from S to Ca normally yield high X-ray count rates and are detected within a short counting time. Higher-Z elements have lower X-ray production cross-sections and consequently require longer irradiation times for adequate detection. No corrections were made for particle shapes or absorption of X-rays in the particles, so that the defined concentrations have only a relative meaning. The off-line spectrum analysis and quantification of present elements were performed with the fast linear least-squares spectrum evaluation code SesamX.

4. Results and Discussion

The elemental composition of 58 aerosol particles in the size range of 8–16 μm (Table 1) shows a rather complex and not easily interpretable structure, since the detected total amounts for S, Cl, K, Ca, Ti, V, Cr, Fe, Ni and Zn vary significantly for different aerosol particles. To resolve the underlying structure of the displayed results, the data set was autoscaled [12] and processed by PCA and NLM.

The plot of the first two principal components after PCA processing is shown in Fig. 2. It is seen that the data have no clear structure, although the points 46 and 49 (enriched with S, K, Ca, Ti, Fe and Zn) stand alone from the main group. A rather separated group consisting of the points 3, 4, 7, 8 and 52 (enriched with Cl) is also seen.

At the same time the results of NLM of the data, shown in Fig. 3 (3-D NLM data are projected to 2-D through PCA), possess a more evident structure. Three main groups of particles can be distinguished:

(1) particles with high concentrations of Cl, K, S and Ca (probably sea salts, transformed or aged sea salt, and gypsum);

(2) particles with low Cl, but with a clear presence of the metals Cr, Fe, Ni, Zn, V and Ti (probably fly ash); and

(3) particles containing mainly Cl, K and Cr (mixed or aggregated marine/continental aerosol).

It is apparent that the North Sea aerosol is a mixture of many components, some derived from the sea itself and some having descended from above. The presence of sea salts in marine air is expected. Gypsum particles have frequently been observed in both the North Sea and remote marine atmosphere [24, 25]. Fly ash particles are known to be abundant over the North Sea under certain atmospheric conditions [26, 27], e.g. when the sampled air masses are influenced by Eastern European emissions, as was the case during this sampling campaign (wind direction 124°; possible impact of air masses from Eastern Germany, Poland and the Czech Republic).

The common feature of Figs 2 and 3 is the relative separation of the points 46 and 49 from the main group of points.

Summarizing, the application of NLM may reveal the structure of environmental data (in the present case: to make suggestions about the sources of aerosol samples) even when the routine PCA does not give satisfactory results.

NLM can also be used for the analysis of relations among the variables (in the present case: between the chemical elements of which aerosol particles consist). This may be of interest in cases when the set of chemical elements can be split into fairly homogeneous clusters. Then if we choose one chemical element from each such cluster, a simplified set of elements can be compiled which will provide roughly the same amount of information on the particles under study as the original set. It can be also of interest when one deals with the interaction of different chemical elements in aerosol particles. This information may be obtained if we simply transpose the initial data matrix.

The results of the application of such a procedure to the initial set of micro-PIXE determinations of 10 elements in 58 aerosol particles are given in Fig. 4. Three different sets of variables are clearly seen here: one, consisting of variables S, Cl, K

Table 1. The elemental composition of 58 aerosol particles (in pg)

N	S	Cl	K	Ca	Ti	V	Cr	Fe	Ni	Zn
1	20	29	1.14	1.04	0.00	0.00	1.79	0.00	0.00	0.00
2	1.36	55	1.51	5.29	0.00	0.00	0.00	0.00	0.00	0.00
3	4.56	258	4.69	3.98	0.15	0.00	2.61	0.38	0.00	0.00
4	13	176	4.24	2.81	0.00	0.00	1.71	0.00	0.00	0.00
5	13	113	3.03	2.64	0.00	0.00	0.00	0.00	0.00	0.00
6	8.71	129	1.75	2.44	0.00	0.00	0.31	0.00	0.00	0.00
7	0.00	392	6.62	7.63	0.00	0.00	0.00	0.00	0.00	0.00
8	34	145	1.97	3.19	0.00	0.00	0.00	0.00	0.00	0.00
9	0.00	71	0.00	1.83	0.00	0.00	0.00	0.00	0.00	0.00
10	0.00	110	2.33	2.71	0.00	0.00	0.00	0.00	0.00	0.00
11	0.00	52	0.00	4.74	0.00	0.00	0.00	0.42	0.00	0.00
12	0.00	211	0.00	1.23	0.00	0.00	0.00	0.00	0.00	0.00
13	20	20	5.13	4.32	0.17	0.00	0.79	0.00	0.00	0.00
14	0.00	64	1.94	0.15	0.61	0.06	0.86	0.00	0.00	0.00
15	8.84	58	0.00	0.00	0.00	0.00	0.78	0.00	0.00	0.00
16	13	25	4.83	4.19	0.13	0.00	0.37	0.00	0.00	0.00
17	0.00	40	0.75	0.88	0.00	0.00	0.21	0.00	0.00	0.00
18	6.15	45	3.47	3.75	0.00	0.00	1.22	0.00	0.00	0.00
19	18	23	4.58	1.22	0.00	0.00	0.94	0.00	0.00	0.00
20	4.39	68	1.15	0.95	0.00	0.00	0.17	0.00	0.00	0.00
21	0.00	44	0.79	0.68	0.00	0.00	0.00	0.00	0.00	0.00
22	0.00	53	1.18	0.89	0.00	0.00	0.00	0.00	0.00	0.00
23	0.00	86	1.43	0.87	0.00	0.00	0.24	0.00	0.00	0.00
24	0.00	43	0.51	0.77	0.00	0.00	0.10	0.00	0.00	0.00
25	1.98	72	1.13	1.15	0.00	0.00	0.07	0.00	0.00	0.00
26	2.35	70	1.22	1.34	0.16	0.04	0.41	0.00	0.00	0.00
27	10	49	1.26	1.82	0.44	0.14	0.59	0.10	0.00	0.00
28	2.62	30	0.89	0.95	0.10	0.07	0.27	0.03	0.00	0.00
29	5.30	103	2.36	1.94	0.32	0.03	1.79	0.59	0.00	0.00
30	2.36	35	1.25	1.23	0.00	0.00	0.12	0.00	0.00	0.00
31	1.99	42	1.19	1.19	0.03	0.00	0.31	0.00	0.00	0.00
32	0.14	60	1.42	1.33	0.16	0.00	0.14	0.00	0.00	0.00
33	2.35	70	1.61	1.61	0.08	0.00	0.14	0.06	0.00	0.00
34	3.93	72	1.46	1.94	0.26	0.00	0.45	0.12	0.00	0.00
35	0.00	53	0.94	1.44	0.11	0.00	0.31	0.00	0.00	0.00
36	0.00	51	0.97	1.35	0.16	0.00	0.18	0.05	0.00	0.00
37	4.72	52	1.39	1.39	0.00	0.00	0.08	0.00	0.00	0.00
38	0.85	0.19	0.26	0.24	0.26	0.00	0.09	0.38	0.00	0.00
39	0.16	0.09	0.03	0.09	0.17	0.00	0.05	0.09	0.00	0.00
40	0.29	0.15	0.20	0.17	0.47	0.00	0.05	0.16	0.00	0.00
41	0.91	1.32	0.09	0.11	0.02	0.00	0.28	0.19	0.03	0.01
42	0.48	28	0.58	0.70	0.03	0.00	0.10	0.02	0.01	0.01
43	1.01	27	0.45	0.52	0.05	0.00	0.15	0.07	0.01	0.00
44	0.00	0.09	0.09	0.14	0.17	0.00	0.12	0.42	0.04	0.00
45	0.00	0.28	0.35	0.86	1.30	0.00	0.19	0.42	0.00	0.00
46	0.00	56	17.11	5.47	1.79	0.00	0.48	1.10	0.00	0.52
47	0.00	8.09	2.56	1.30	1.42	0.00	0.47	0.87	0.00	0.00
48	0.00	5.50	2.79	1.50	1.22	0.00	0.21	0.26	0.00	0.11
49	21	54	15.87	6.92	3.84	0.00	0.54	0.59	0.10	0.34
50	0.00	23	0.42	0.65	0.89	0.00	0.57	0.59	0.08	0.00
51	0.00	34	1.27	0.92	0.03	0.00	0.36	0.00	0.00	0.00
52	0.00	260	4.11	6.19	0.22	0.14	0.29	0.08	0.00	0.00
53	0.00	40	0.89	0.58	0.00	0.00	0.00	0.00	0.00	0.00
54	0.00	28	1.19	0.54	0.00	0.00	0.00	0.00	0.00	0.00
55	0.00	7.85	1.24	1.07	0.78	0.00	0.38	0.21	0.02	0.02
56	0.00	2.10	0.55	0.55	0.25	0.05	0.32	0.06	0.00	0.02
57	0.00	3.92	0.54	0.43	0.16	0.00	0.01	0.02	0.00	0.00
58	0.00	48	1.22	0.89	0.41	0.02	0.07	0.07	0.00	0.00

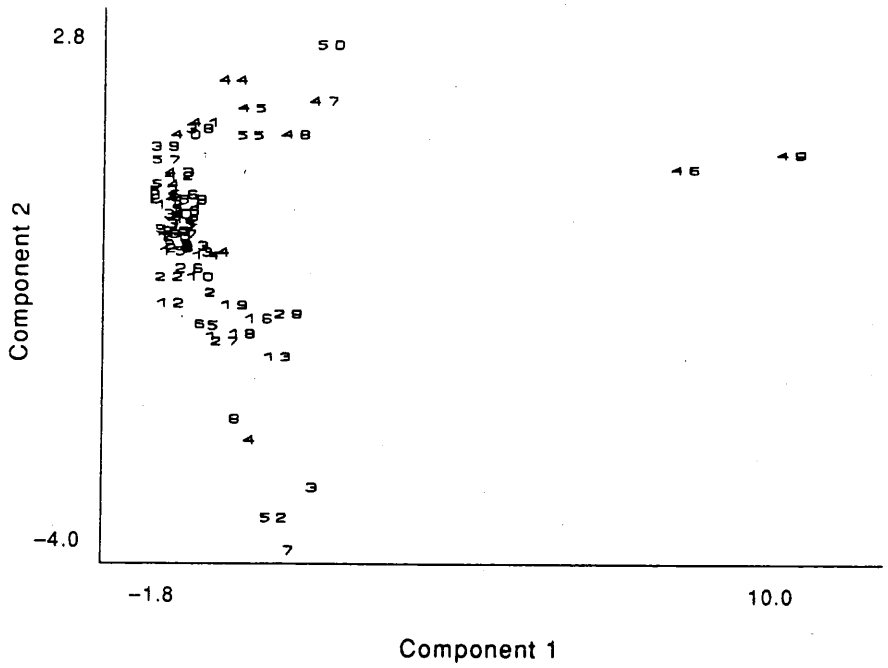

Fig. 2. The results of PCA of the micro-PIXE data of 58 aerosol samples.

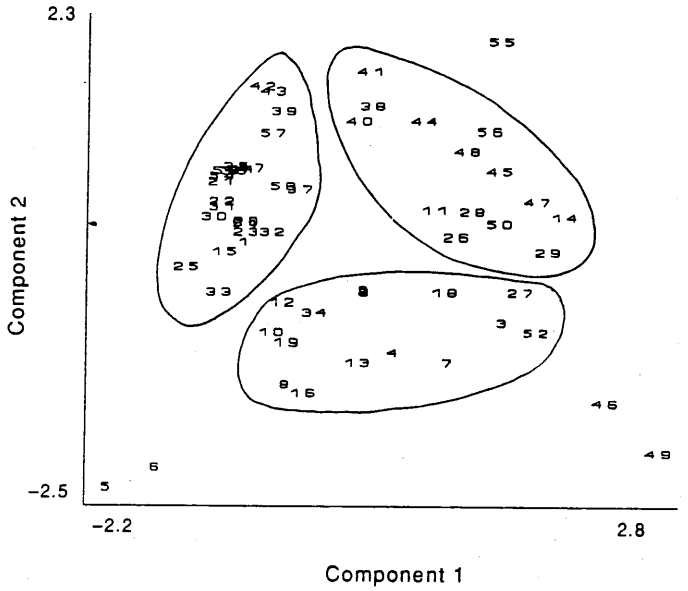

Fig. 3. Projection of the results of NLM processing of the micro-PIXE data of 58 aerosol particles on the plane of the first two principal components.

and Cr; the second, consisting of Ca; and the third, consisting of Ti, V, Fe, Ni and Zn. Fly ash particles (group 2 of Fig. 3) often contain these elements. This can be considered as being in satisfactory agreement with the results presented in Fig. 3.

5. Conclusion

The application of NLM to the processing of micro-PIXE data can enlarge the amount of information obtained by this analytical method. The combined application

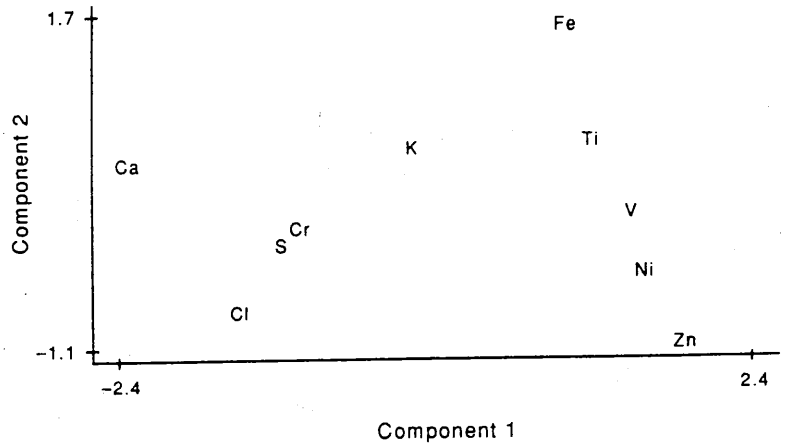

Fig. 4. Projection of the results of NLM of the 10 elements on the plane of the first two principal components.

of NLM and micro-PIXE to individual particle analysis shows the internal heterogeneity of the aerosols as a consequence of their different production mechanisms or sources.

Acknowledgements—One of the authors (B.T.) is indebted to the National Science Foundation of Belgium (NFWO) for financial support during his stay at UIA. This work was partially supported by the Belgian State Prime Minister's Service—Science Policy Office, in the framework of EUROTRAC program (contract EU 7/08) and the Impulse Programme in Marine Sciences (contract MS/06/050).

REFERENCES

[1] G. Petersen, H. Weber and H. Grabl, in *Control and Fate of Atmospheric Trace Metals*, Eds J. M. Pacyna and B. Ottar, NATO Advanced Science Institutes Series C, Vol. 268, p. 57. Kluwer, Amsterdam (1989).
[2] G. J. Keeler and P. J. Samson, in *Control and Fate of Atmospheric Trace Metals*, Eds J. M. Pacyna and B. Ottar, NATO Advanced Science Institutes Series C, Vol. 268, p. 115. Kluwer, Amsterdam (1989).
[3] R. C. Henry, C. W. Lewis, P. K. Hopke and H. J. Williamson, *Atmos. Environ.* **18**, 1507 (1984).
[4] G. D. Thurston and J. D. Spengler, *Atmos. Environ.* **19**, 9 (1985).
[5] K. Keiding, F. Palmgren Jensen and N. Z. Heidam, *Anal. Chim. Acta* **22**, 763 (1986).
[6] K. Keiding, J. Pedersen and F. Palmgren Jensen, *Atmos. Environ.* **22**, 763 (1988).
[7] P. K. Hopke, *Receptor Modelling in Environmental Chemistry*. Wiley, New York (1985).
[8] R. C. Henry, *Atmos. Environ.* **21**, 1815 (1987).
[9] P. C. Bernard and R. E. Van Grieken, *Anal. Chim. Acta* **267**, 81 (1992).
[10] H. Van Malderen, C. Rojas and R. E. Van Grieken, *Environ. Sci. Technol.* **26**, 750 (1992).
[11] C. M. Rojas and R. E. Van Grieken, *Atmos. Environ.* **26A**, 1231 (1992).
[12] T. W. Shattuck, M. S. Germani and P. R. Buseck, *Anal. Chem.* **63**, 2646 (1991).
[13] C. Xhoffer, L. Wouters and R. Van Grieken, *Environ. Sci. Technol.* **26**, 2151 (1992).
[14] J. M. Chambers, W. S. Cleveland, B. Kleiner and P. A. Tukey, *Graphical Methods for Data Analysis*. Wardsworth, Belmont (1983).
[15] P. C. C. Wang (Ed.) *Graphical Representation of Multivariate Data*. Academic Press, New York (1978).
[16] M. A. Sharaf, D. L. Illman and B. R. Kowalski, *Chemometrics*. Wiley, New York (1986).
[17] P. M. Mather, *Computational Methods of Multivariate Analysis in Physical Geography*. Wiley, London (1976).
[18] B. A. Treiger, G. N. Dolenko, T. I. Guzhavina and L. N. Mazalov, *Comput. Enhanced Spectrosc.* **3**, 153 (1986).
[19] V. V. Rezvitskii, B. A. Treiger, I. I. Bondarenko and L. N. Mazalov, *Analyst* **117**, 803 (1992).
[20] Y. Vawda, I. Colbeck, R. M. Harrison and K. W. Nicholson, *J. Aerosol Sci.* **23**, 233 (1992).
[21] K. R. May, *J. Aerosol Sci.* **6**, 413 (1975).
[22] J. Injuk, H. Van Malderen, R. Van Grieken, E. Swietlicki, J. M. Knox and R. Schofield, *X-Ray Spectrom.* **22**, 220 (1993).
[23] N. E. G. Lövestam, E. Swietlicki, U. Wätjen, E. Louwerix, A. Perujo and P. Rietveld, *Nucl. Instrum. Meth.* **B69**, 463 (1992).

[24] P. Artaxo, H. Storms, F. Bruynseels, R. Van Grieken and W. Maenhaut, *J. Geophys. Res.* **93**, 1605 (1988).
[25] M. O. Andreae, R. J. Charlson, F. Bruynseels, H. Storms, R. Van Grieken and W. Maenhaut, *Science* **232**, 1620 (1986).
[26] C. Xhoffer, P. Bernard, R. Van Grieken and L. Van der Auwera, *Environ. Sci. Technol.* **25**, 1470 (1991).
[27] H. Van Malderen, C. Rojas and R. Van Grieken, *Environ. Sci. Technol.* **26**, 750 (1992).

Mikrochim. Acta 114/115, 313–321 (1994)

Mikrochimica Acta

Performance of a Nuclear Microprobe to Study Giant Marine Aerosol Particles

Jasna Injuk[1], Lothar Breitenbach[2], René Van Grieken[1], and Uwe Wätjen[2,*]

[1] University of Antwerp (UIA), Deptartment of Chemistry, Universiteitsplein 1, B-2610 Antwerpen-Wilrijk, Belgium

[2] CEC–JRC, Institute for Reference Materials and Measurements (IRMM) (formerly CBNM), Retieseweg, B-2440 Geel, Belgium

Abstract. The scanning nuclear microprobe analytical facility of the IRMM was used to determine with PIXE major, minor and trace elements in individual giant marine aerosol particles, collected above the North Sea (particle size > 5 μm ∅). The instrumentation is briefly described, and the experimental parameters chosen for these analyses are discussed. Elements with atomic numbers $Z > 15$ could be determined. Detection limits observed under the prevailing experimental conditions reached down to 50 fg in the case of Ti, V or Cr, corresponding to a mass content of 10 μg/g in particles of 15 μm size. Quantitative evaluation of the acquired spectra revealed basically three aerosol types in these samples: sea salt particles, sea salt combined with high contents of S, K and Ca, and particles rich in heavier elements (Ti, Cr, Fe, Ni). The agglomeration of several large particles forming a giant one could be visualised directly through the heterogeneity found in the elemental maps of such a particle.

Key words: scanning nuclear microprobe, individual aerosol particle analysis, elemental composition, detection limits, PIXE analysis, giant marine aerosol, elemental heterogeneity of agglomerates.

The importance of the heavy metal contamination of large water bodies, among them the North Sea, through atmospheric input relative to more obvious inputs such as pollution borne by rivers or direct waste discharge, has been under investigation since the late 1970s. For the determination of atmospheric parameters describing the heavy metal flux especially into the North Sea, physical aerosol size distributions and also elemental size distributions were measured and deposition velocities were calculated [1, 2]. However, a review by Kersten et al. [3] showed that there are large uncertainties still in the estimation of the heavy metal input from the atmosphere to the North Sea. Steiger et al. [4] pointed out the dominating contribution of the largest particles (aerodynamic diameter > 3 μm) to the dry deposition flux, placing utmost importance on the representative collection of large

* To whom correspondence should be addressed

particles. Not only dry but also wet deposition of heavy metals is determined by giant particles [5, 6].

Several analytical methods have been used to determine the atmospheric metal concentrations based on size-segregated bulk samples of aerosol: AAS, ICP-OES, XRF (also as total reflection X-ray fluorescence TXRF), NAA, PIXE and electrochemical methods. In order to distinguish between different particle compositions in the same size range, and thus between different sources of aerosol, individual particle analysis has been performed with laser microprobe mass analysis (LAMMA) and especially with electron probe X-ray microanalysis (EPXMA). Whereas ten thousands of particles were analysed with the latter [5, 6], only few particles were analysed so far (<100 in each study) with the scanning nuclear microprobe (SNM) combined with proton-induced X-ray emission (PIXE) [7, 8] in spite of the much better detection limits of this method. The intrinsic analytical advantage of PIXE for heavy metals is based on its orders of magnitude lower intensity of bremsstrahlung background.

This work is aiming at an improved determination of elemental aerosol size distributions above the North Sea. This will contribute to a more reliable estimation of the heavy metal inputs into the North Sea via the atmospheric route. The new approaches are an improved sampling scheme, avoiding the loss of very large particles at the sampler inlet, and the complementary use of TXRF for bulk aerosol samples and EPXMA and scanning nuclear microprobe-PIXE (SNM-PIXE) for a more detailed characterization of individual particles. In the present paper we concentrate on the detection limits achieved with the SNM under practical analytical conditions, the analytical details of quantifying elemental fingerprints of individual particles and the study of the elemental heterogeneity of particle agglomerates.

Experimental

Sampling

A sampling campaign was set up on the Research Platform "Nordsee" (54°42′ N, 7°10′ E) from September 1–22, 1992. A wind tunnel sampler, incorporating a multistage May cascade impactor [9], was used for the efficient collection of marine aerosols. The main problem in nearly all aerosol deposition studies over the North Sea in the past was that the large particles were not adequately assessed. Difficulties of sampling these particles in a representative way can arise because the collection efficiency of the instrument is affected by the ratio of the intake velocity to the ambient wind velocity (i.e. isokinetic sampling is necessary) and by a variable angle between the sampler inlet and the wind direction. By taking samples by means of a wind tunnel, this problem is overcome since it allows quantitative collection of big particles without problems of a variable cut-off with wind direction and wind speed. The tunnel is directed into the ambient wind by means of a light wind vane and, as a ventilator produces a constant forced air stream inside the tunnel, the linear velocity of the particles in the air can be made exactly the same as the intake velocity in the sampling device. Since isokinetic sampling conditions are set up at the orifice of the impactor probe, 100% aspiration efficiency from the tunnel air stream into the impactor probe may be assumed for all particle sizes [10].

Other sources of error in aerosol sampling are particle losses on the orifices and internal walls of the impactor and in the inlet nozzle. In the cascade impactor designed by May negligible internal wall losses have been reported [9]. Each impactor stage consists of a single slot-shaped orifice and a glass slide, covered with an Apiezon-coated Nuclepore filter (0.4 μm pore size) to reduce reentrainment and bounce-off. The cut-off diameters of the stages range between 0.5 to 20 μm at a flow rate of 20 l min^{-1}.

Analytical Method

Details of the SNM analytical facility of IRMM (formerly CBNM) are published elsewhere [11]. We summarize here only the main features of the instrumentation and describe the actual experimental parameters during this work. H^+ or He^+ ions of 2 to 3.5 MeV kinetic energy, produced in an electrostatic Van de Graaff accelerator, are employed as incident projectiles. A microbeam is formed with a magnetic quadrupole doublet lens system from a variable slit assembly serving as object. With an object distance of 405 cm and an image distance of 12 cm, a typical beam spot size of 2.5 × 2.5 μm^2 to 3 × 3 μm^2 at 100 pA ion current is achieved. We devised a very efficient focusing procedure [12], based on grid shadows cast on a ZnS scintillation screen 1 m behind a Cu grid (2000 mesh). The scanning of the microbeam over the target surface is accomplished by electrostatic deflection, making use of the insulated poles of the focusing magnets as electrodes. Ionisation of target atoms and ion scattering from target nuclei are exploited with PIXE and Rutherford backscattering spectrometry (RBS), implemented as main analytical methods.

During the course of this work, we focused protons of 2 and 2.5 MeV down to beam spots of approximately 3 × 3 μm^2. Ion currents in this focus were varying between 30 and 140 pA, the former leading to extended irradiation times of up to 3 h in a scanning frame (0.5–1.0 h is normal). With scanning steps (distances between adjacent pixels) chosen between 5 and 1 μm the scanning frames ranged from 320 × 320 μm^2 down to 64 × 64 μm^2, allowing a reliable detection of giant particles. A 125 μm thick mylar foil in front of the Si(Li) detector (60 mm^2 effective surface area, $\Delta\Omega$ = 120 msr) absorbed X-rays of very low energy. This made determination of elements with $Z \geq 16$ possible, however, at strongly reduced counting rates (and high detection limits) for sulphur and chlorine.

Data Acquisition and Normalization

Our SNM data acquisition system [11, 13] is characterized by a versatility which is unknown from electron microprobes or scanning Auger systems. During analysis—in parallel with real-time mapping from selected energy windows—data are stored on the large discs of the μVAX II computer either in a time-sequential event-by-event format, or as sorted spectra in three-dimensional data sets (x-position, y-position, spectrum). The former allows to retrieve retrospectively the complete experiment as it evolved in time; no data are lost. This mode is very valuable to investigate a possible instability of samples under microbeam irradiation or specimen damage. On the other hand, storing energy spectra for each pixel has the great advantage of fast manipulations and displays of various cross-sections through the data set [13]. Thus elemental maps can be quickly calculated (a matter of seconds) from

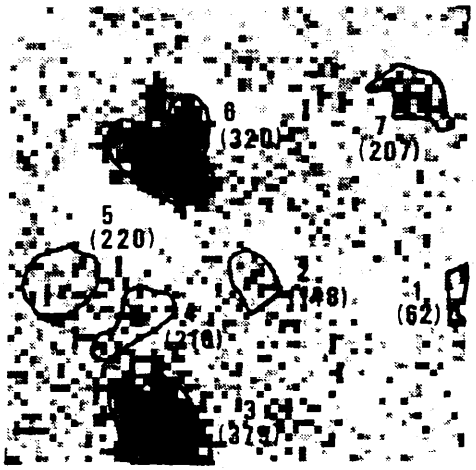

a

Fig. 1. a Distribution of total X-ray intensity in a scanning frame of 128 × 128 μm^2 with seven regions of interest selected for further analysis. Number of pixels given in brackets. **b** Set of PIXE spectra extracted from the total map and the seven ROIs defined in (**a**)

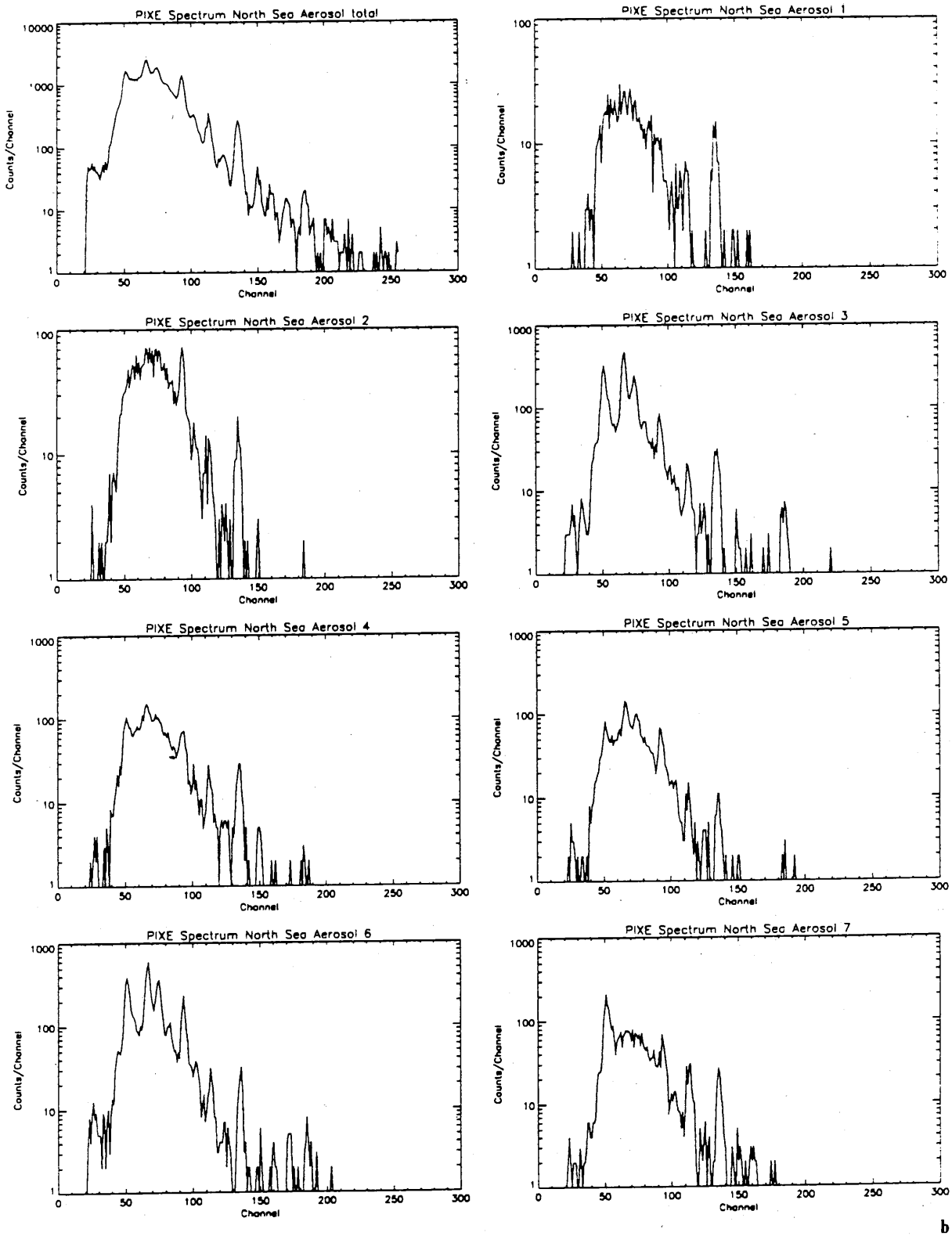
PIXE Spectrum North Sea Aerosol total
PIXE Spectrum North Sea Aerosol 1
PIXE Spectrum North Sea Aerosol 2
PIXE Spectrum North Sea Aerosol 3
PIXE Spectrum North Sea Aerosol 4
PIXE Spectrum North Sea Aerosol 5
PIXE Spectrum North Sea Aerosol 6
PIXE Spectrum North Sea Aerosol 7
Counts/Channel
Channel

b

Fig. 1 (cont.)

any energy window of the complete set of spectra, or spectra from several pixels making up a region of interest (ROI) in any selected map can be summed up. Furthermore, elemental histograms obtained from line scans can be displayed, or spectrum profiles, useful for presenting depth profiles along a line scan with RBS. The only disadvantage of storing a complete set of spectra is its limitation to scanning frames of 64 × 64 pixels. Since this posed no practical problems in this work, we used the latter format of data storage.

How spectra are extracted from ROIs (with a mouse at the display system) is visualized in Fig. 1. Either intensity distributions of the total X-ray signal, which represent roughly the distribution of aerosol mass in the scanned area, or a specific elemental map serve to define ROIs, each outlining a detected large particle. From the number of pixels, making up a ROI, the ion charge accumulated in that particle is determined. The sum spectrum, normalized to the respective ion charge, is then quantitatively evaluated off-line—with the PIXE-specific evaluation code SESAMX [14]—for the elemental masses in the enclosed particle.

Results and Discussion

Detection Limits

A practical criterion for detection limits applicable to microprobe analysis is chosen. Since affordable analysis times limit the achievable analytical precision in those microdistributional applications where the background signal is negligible we consider here detection limits demanding only ~30% relative precision as minimum. This corresponds to a signal of at least 10 events in a background-free spectrum part. Thus, the common criterion for detecting a peak of N_x net events above a background signal $N_{B,x}$ (taken within 1 FWHM of the respective peak) is supplemented with the condition of 10 events minimum:

$$N_x \geq \max\{3 \cdot \sqrt{N_{B,x}}, 10\}.$$

On the basis of experimental parameters observed during this work, we calculate the detection limits given in Table 1. 50 fg of Ti, V or Cr corresponds to a mass content of only 10 μg/g in particles of 15 μm $\varnothing$ (assuming $\rho = 3\ \mathrm{g \cdot cm^{-3}}$, corresponding to a total particle mass of about 5 ng).

In quasi background-free spectra, as is the case for heavy metals (cf. Fig. 1(b)), the mass detection limits MDL are scaling simply according to

$$\mathrm{MDL} \propto Q^{-1} \cdot \Delta\Omega^{-1},$$

where Q is the accumulated charge of incident ions and $\Delta\Omega$ is the detector solid angle. This accentuates the utmost importance of a very good beam alignment for

Table 1. Practical detection limits observed and calculated for individual particles of 15 μm size, scanned with a beam spot of 3 × 3 μm²

Element	S	Cl	Ca	Cr	Ni	Zn	Pb
Detection limit [fg]	1000	200	50	50	100	150	1100

2.5 MeV protons, 10 nC accumulated in 15 × 15 μm² scanned area, 140 s analysis time, 125 μm mylar absorber.

highest possible ion currents, and the need for detectors with large surface areas combined with a close distance between target and detector.

Elemental Composition of Aerosol Particles

About 60 giant particles found in 10 scanning frames have so far been analysed quantitatively for up to 12 elements : S, Cl, K, Ca, Ti, V, Cr, Mn, Fe, Ni, Cu and Zn. The results of S, Cl, K and Ca still have to be corrected for grain size effects in the giant particles, which reduce the X-ray yields due to the energy loss of protons and the attenuation of X-radiation. Corrections up to a factor of 2 are estimated for S and Cl. Since the particle sizes and shapes are not dramatically different, however, the analytical results obtained so far also for these elements can be compared among each other. The composition of another 50 particles was qualitatively determined without normalizing to absolute mass values. As an example for the results obtained so far, Fig. 2 displays an elemental "fingerprint" histogram of the seven giant particles defined above (cf. Fig. 1). In this data representation three aerosol types sampled in the air masses influenced by Eastern European emissions can easily be distinguished:

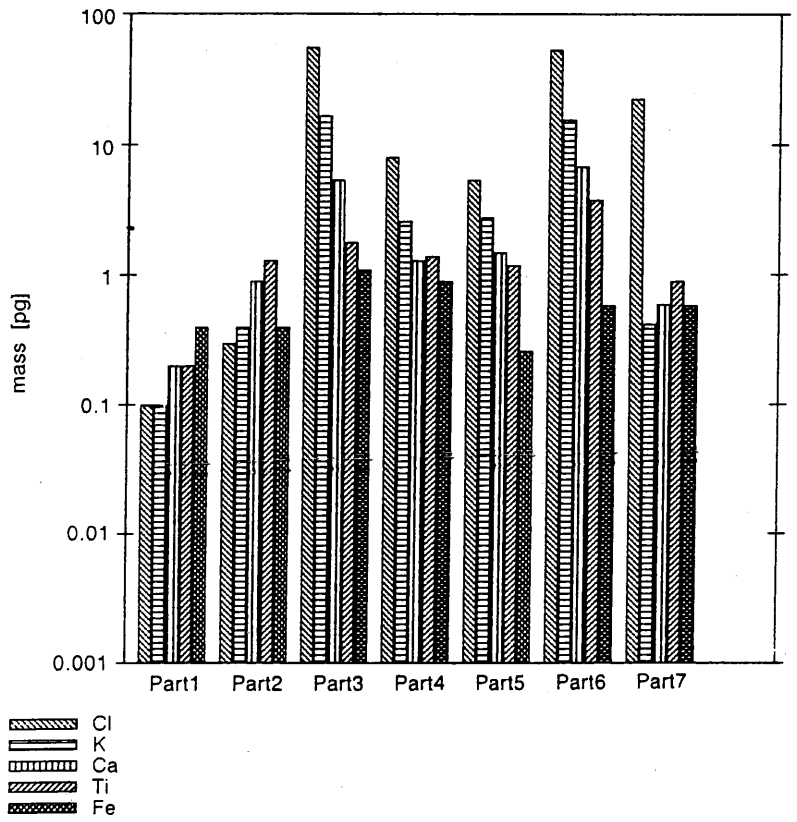

Fig. 2. Elemental "fingerprints" of seven particles in a scanning frame (only elements common to all particles are displayed). For the approximate sizes of the particles see Fig. 1(a)

—sea salt particles dominated by (Na)Cl (particle #7);
—sea salt combined with high contents of S (not shown in Fig. 2), K and Ca (probably representing sea salt and gypsum, #3 to #6);
—particles of low Cl, but relatively high metal contents such as of Ti, Fe, Cr, Ni (#1 and #2). (One has to keep in mind the comparatively small size of these two particles (see Fig. 1 a).

This rough aerosol classification was confirmed by a much more powerful multivariate statistical method, making use of nonlinear mapping combined with principal component analysis [15]. After more particles are analysed, multivariate statistics will render more in-depth information from these data sets.

Particle Agglomerates

Internally mixed particles, composed of giant sea salt and mineral particles rich in heavy metals, were already observed earlier in remote marine atmospheres based

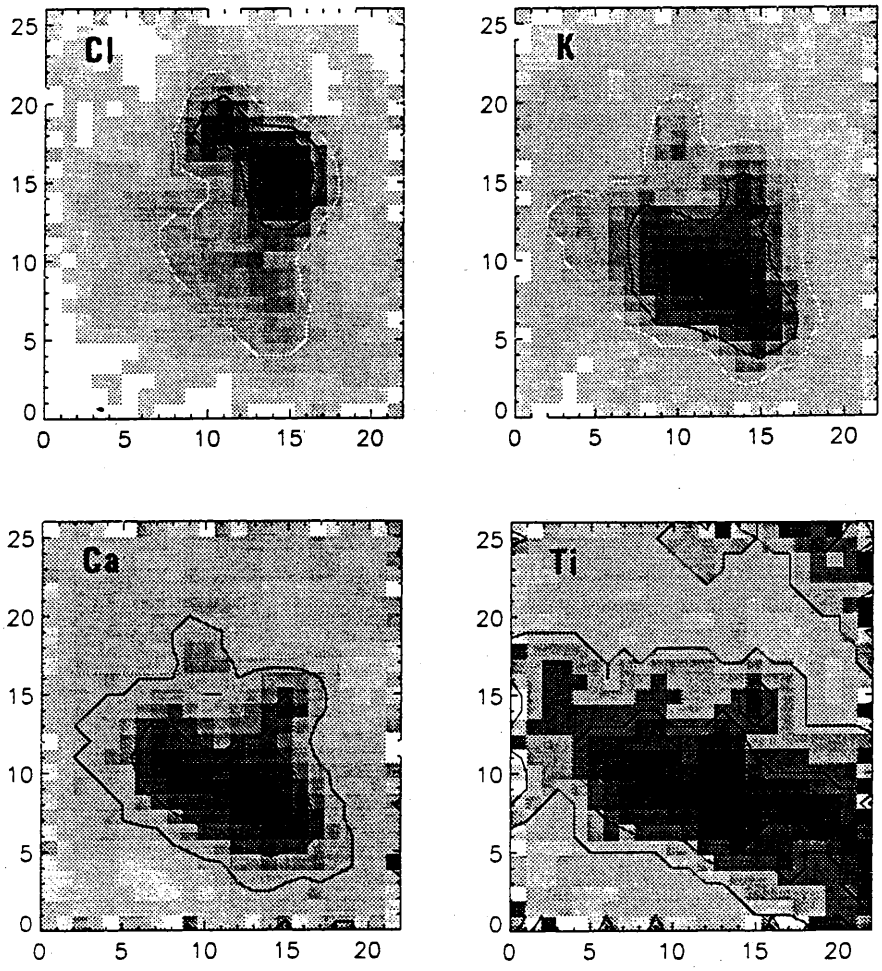

Fig. 3. Elemental distributions in a particle agglomerate of about 20 μm size, the width of the indicated scanning steps is 2 μm. Total scanning widths: 44 μm in the horizontal and 52 μm in the vertical directions

on secondary electron imaging [16]. Complementary to such SEM observations, the SNM is able to show the agglomeration of particles directly through the elemental heterogeneity within a scanned area. An important property of heavy charged particles such as protons is used to advantage here: when penetrating into material protons do not undergo the scattering and other deflections by large angles such as electrons do, which renders a widened beam after only short distances in the case of electrons (about 3 μm wide after only 1 μm depth [17]). With protons the original beam width remains almost unchanged such that the lateral ion beam resolution of, for example, 3 μm, although inferior to a SEM for the topmost surface layers, remains practically constant throughout the sample or—in this case—large aerosol particle. Figure 3 shows such an agglomerate of two giant particles. The one in the top half is obviously a sea salt particle taken from the Cl distribution, whereas the other one is a pollution particle containing metals such as Ti and Fe, but also Cr, Cu and Zn barely above the detection limits (the latter elements are not mapped in Fig. 3).

Conclusions

The SNM combined with PIXE was successfully applied to the analysis of individual giant aerosol particles for their elemental composition ($Z \geq 16$) down to absolute masses of 50 fg for some metals. Three aerosol types could be identified in these samples from the marine atmosphere above the North Sea. Exploiting the very straight paths of protons in matter, the lateral elemental distribution within giant particles was characterized with a constant resolution of 3 μm throughout the depth of the particles. This way several agglomerates of large particles showing completely different composition were determined. Considering the low detection limits of 50 fg achievable for metals, sample contamination in all stages from preparation for aerosol sampling to irradiation in the microbeam laboratory has clearly to be regarded as a risk to accurate microanalysis and reliable interpretation of micro-distribution results.

Acknowledgements. We have to thank the operators of the Van de Graaff accelerator, P. Falque and J. Leonard, for always providing a stable beam of high current from the machine. Part of this work was supported by the Belgian State Prime Minister's Service—Science Policy Office, in the framework of EUROTRAC Programme (Contract EU 7/08) and the Impulse Programme in Marine Sciences (Contract MS/06/050).

References

[1] S. A. Slinn, W. G. N. Slinn, *Atmos. Environ.* **1980**, *14*, 1013.

[2] C. M. Rojas, P. M. Otten, R. E. Van Grieken, R. W. Laane, in: *Proc. 18th International Technical Meeting of NATO-CCMS on Air Pollution* (H. Van Dop, R. Steyn, eds.), Plenum, New York, 1991.

[3] M. Kersten, M. Dicke, M. Kriews, K. Naumann, D. Schmidt, M. Schulz, M. Schwikowski, M. Steiger, in: *Pollution of the North Sea* (W. Salomons, B. L. Bayne, E. K. Duursma, U. Förstner, eds.), Springer, Berlin, 1988.

[4] M. Steiger, M. Schulz, M. Schwikowski, K. Naumann, W. Dannecker, *J. Aerosol Sci.* **1989**, *20*, 1229.
[5] H. Van Malderen, C. M. Rojas, R. E. Van Grieken, *Environ. Sci. Technol.* **1992**, *26*, 750.
[6] C. M. Rojas, J. Injuk, R. E. Van Grieken, R. W. Laane, *Atmos. Environ.* **1993**, *27A*, 251.
[7] P. Artaxo, M. L. C. Rabello, F. Watt, G. Grime, E. Swietlicki, *Nucl. Instrum. Meth.* **1993**, *B75*, 521.
[8] J. Injuk, H. Van Malderen, R. Van Grieken, E. Swietlicki, J. M. Knox, R. Schofield, *X-Ray Spectrom.* **1993**, *22*, 220.
[9] K. R. May, *J. Aerosol Sci.* **1975**, *6*, 413.
[10] Y. Vawda, I. Colbeck, R. M. Harrison, K. W. Nicholson, *J. Aerosol Sci.* **1992**, *23*, 233.
[11] N. E. G. Lövestam, E. Swietlicki, U. Wätjen, E. Louwerix, A. Perujo, P. Rietveld, *Nucl. Instrum. Meth.* **1992**, *B69*, 463.
[12] E. Swietlicki, N. E. G. Lövestam, U. Wätjen, *Nucl. Instrum. Meth.* **1991**, *B61*, 230.
[13] N. E. G. Lövestam, E. Swietlicki, *Scann. Microsc.* **1992**, *6*, 607.
[14] U. Wätjen, *Nucl. Instrum. Meth.* **1987**, *B22*, 29.
[15] B. Treiger, J. Injuk, I. Bondarenko, P. Van Espen, R. Van Grieken, L. Breitenbach, U. Wätjen, *Spectrochim. Acta B.* **1994** (in press).
[16] M. O. Andreae, R. J. Charlson, F. Bruynseels, H. Storms, R. Van Grieken, W. Maenhaut, *Science* **1986**, *232*, 1620.
[17] D. E. Newbury, D. C. Joy, P. Echlin, C. E. Fiori, J. I. Goldstein, *Advanced Scanning Electron Microscopy and X-ray Microanalysis*, Plenum, New York, 1986.

Reprinted from ENVIRONMENTAL SCIENCE & TECHNOLOGY, Vol. 28, 1994

Individual Aerosol Particle Composition Variations in Air Masses Crossing the North Sea

Lieve A. De Bock,* Hans Van Malderen, and René E. Van Grieken

Department of Chemistry, University of Antwerp, Universiteitsplein 1, B-2610 Antwerp-Wilrijk, Belgium

Single-particle analysis on North Sea aerosol and rainwater samples was performed by electron-probe X-ray microanalysis (EPXMA). The analysis was mainly focused on the determination of the inorganic composition of giant particles with diameters above 1 μm. Multivariate techniques were used for the reduction of the data set and for source apportion. Based on the relative abundances found by hierarchical cluster analysis according to the Ward error sum method, three to eight different aerosol types were distinguished. Crossing the North Sea, the changes in air mass composition appeared as a decrease in the abundance for the aluminosilicate particles and a relative increase for NaCl and seawater crystallization products. Principal factor analysis revealed four different aerosol sources: aluminosilicates and NaCl, seawater crystallization products as a marine source, and two industrial sources. Relations between the particle composition, origin, and shape were studied by manual EPXMA, and for most of the particle types, a characterization based on their shape was obtained.

Introduction

It has been shown that atmospheric deposition represents a major input route to the North Sea for some pollutants, like heavy metals (*1*). Within the scope of the EUROTRAC Project "Air–Sea Exchange", aerosol and rainwater samples were collected above the North Sea on board two research vessels continuously positioned downwind from each other. The aim of this project was to study variations in the composition of air masses crossing the North Sea due to air–sea exchange processes in the lower troposphere. The two major exchange processes considered to be responsible for possible changes in air mass composition are dry deposition, such as sedimentation or gravitational fallout and impaction, and wet deposition, such as rainout, snowout, and washout. A decrease in particle concentration could also be the result of vertical dilution of the air masses. Obviously, chemical and physical reactions in the atmosphere as well as parameters like wind speed, relative humidity, and temperature affect these processes.

The single-particle analysis in the present study was performed by electron probe X-ray microanalysis (EPXMA), one of the most commonly used nondestructive microanalytical techniques. In spite of its unfavorable detection limits (0.1%), automated EPXMA is, in combination with multivariate techniques, a powerful method for the determination of the chemical composition and characterization of a large number of individual particles in a very short time. The determination of the chemical composition could provide assignment to specific sources while the particle group abundance characterizes the source strength. Manual EPXMA, on the other hand, offers the possibility of morphological studies and element mapping.

Bulk and alternative individual single-particle analyses have been performed on the same samples by energy-dispersive X-ray fluorescence and electron proton microprobe analyses, respectively (*2*).

The aerosol analysis in this work was mainly focused on aerosol particles with diameters above 1 μm, the so-called giant aerosols. Although the number of these giant particles in the lower troposphere is very low compared to the condensation-mode particles, their contribution to the atmospheric deposition is of extreme importance (*3–5*). Due to the slow realization of the importance of giant aerosol particles in the atmosphere together with sampling difficulties and measurement errors, many questions still remain unanswered, and further research will be necessary.

Experimental Procedures

Sampling Strategy. A sampling campaign was organized for September 15–27, 1991. During this campaign, two research vessels, F.S. *Alkor* and R.V. *Belgica*, were positioned on a circle, with a 200-km diameter, continuously downwind from each other in the central area of the North Sea (Figure 1). Sampling started on the F.S. *Alkor* (upwind ship) on the 16th at 1 a.m. and stopped on the 25th at 11 a.m. Sampling on the R.V. *Belgica* (downwind ship) was delayed according to the calculated air mass travel time, based on the actual wind speed aboard the F.S. *Alkor* and the R.V. *Belgica*. A wind speed of 10 m/s^{-1} and a distance of 200 km resulted in a transport time of ca 5.5 h by which the downwind ship had to delay its sampling interval. Every 8 h new positions were taken on the circle. When achieved, the ships were holding position within a few miles facing the wind for undisturbed sampling conditions. In this way, the same air mass was sampled with an interval of 200 km. During the travel time to reach the new position, sampling was stopped. The result of this campaign gave an idea about the changes in composition that aerosols and rainwater undergo during air mass travel.

Meteorological data were provided by radiosonde inspection aboard the F.S. *Alkor* every 8 h. The whole sampling campaign was characterized by stormy weather. Due to prevailing southwesterly winds, the United Kingdom was the main source region for anthropogenic and soil-derived components.

Aerosols were collected on the main deck using a cascade impactor and filter units, both positioned inside a wind tunnel, for single-particle and bulk analyses, respectively. In a cascade impactor, aerosols are segregated in size based on their inertial characteristics. Microscope slides covered with special coated Nuclepore filters (COSTAR Europe Ltd. Nuclepore Filtration Products) were used as the impaction surface. The special coating is necessary to reduce effects like "bounce off" and "reentrainment", which

* Address correspondence to this author; e-mail address: debockl@schs.uia.ac.be.

0013-936X/94/0928-1513$04.50/0

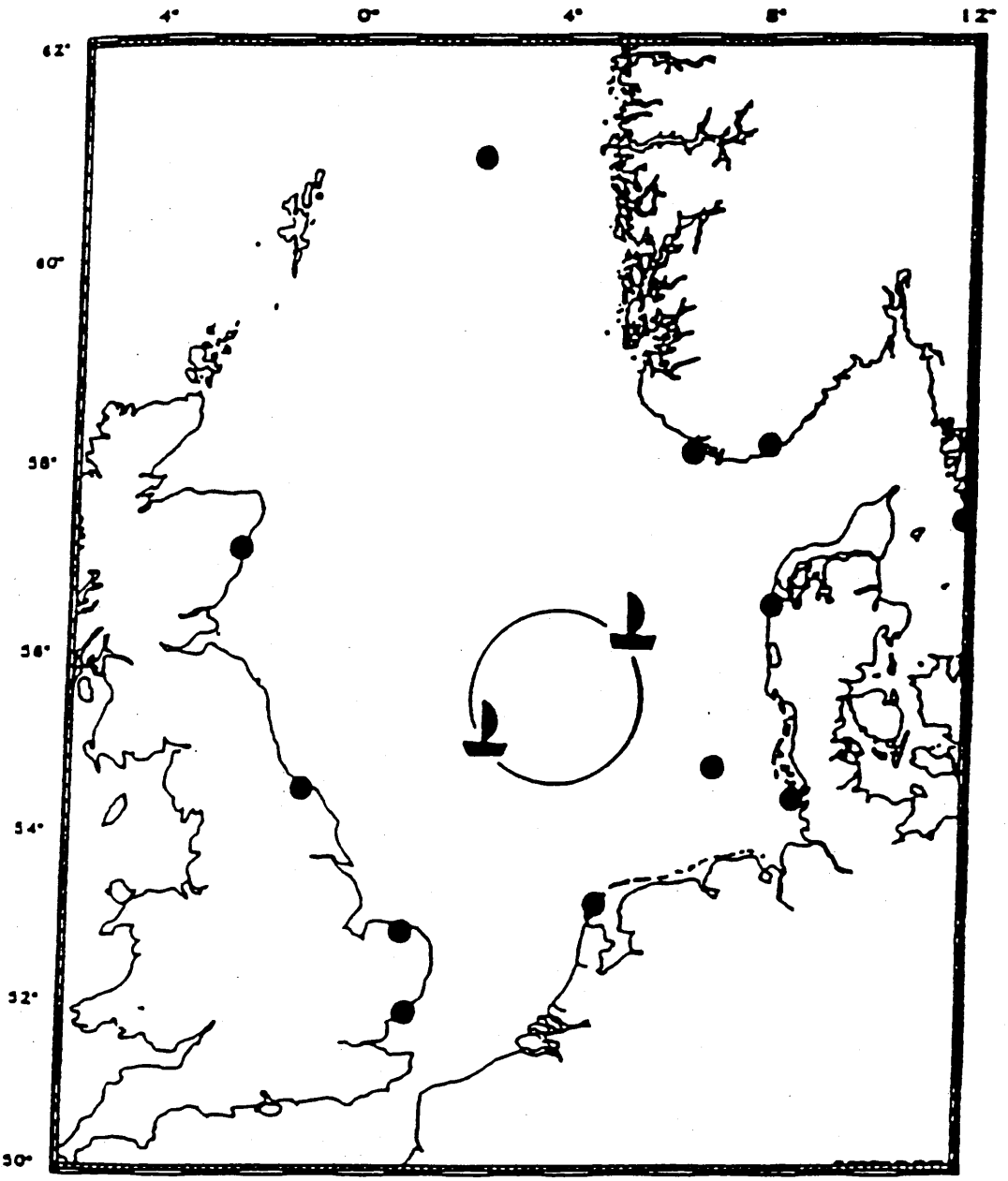

Figure 1. North Sea map with indication of the sampling sites on a circle of 200 km, around 55.0° N and 4.0° E.

influence the collection efficiency and change the apparent size distribution. The type of cascade impactor applied during this campaign was based on the design of May (*6*). It offers a very good resolution of particle size due to sharp cutoffs at different stages (20, 8, 4, 2, 1, and 0.5μm), minimal internal losses, the possibility for quantitative analyses at sampling speeds of 20 L/min, easy handling due to its compactness and fast dismantlement, and stainless steel composition to prevent corrosion. To collect the total airborne particulate matter, filter units were also applied. Because no size segregation is required, the Nuclepore filters were not coated.

A representative sampling of atmospheric aerosols is only possible when isokinetic conditions are fulfilled. This means that there cannot be any kind of disturbance of the air stream at the inlet of the impactor, resulting in a nongradual translation of the aerosol particles into the impactor nozzle. The wind tunnel used, designed at the University of Essex (*7*), consists of a 1.2-m thin-walled tube with a diameter of 0.25 m. In the middle of the tube immediately behind a honeycomb structure, which creates a laminar flow, the impactor and filter unit are positioned. At the end, a ventilator sucks air into the tunnel at the same speed as it is sucked into the sampling device by the pump, which guarantees isokinetic sampling. To keep the inlet of the tunnel in the prevailing wind direction, it is provided with a 1-m^2 wind vane. Due to the suppressing effect of a portable wind tunnel on airstream fluctuations around the impactor and the filter unit, isokinetic sampling is possible, and giant particles can quantitatively be collected also.

For the collection of rainwater, a PVC funnel was connected to a low-density polyethylene barrel on the main deck. The barrels were first treated with ultrapure nitric acid during 1 month and washed with Milli-Q water afterwards. After each rain shower, the funnel was closed, and the collected rainwater was frozen to prevent microorganism growth. In the lab, the bottles were thawed, and each time 100 mL of rainwater was filtered on a Nuclepore membrane.

Instrumentation. A set of 75 size-segregated aerosol samples and five rainwater samples was analyzed by EPXMA. The automated analyses of 27 500 particles was performed on a JEOL 733 Superprobe equipped with a Tracor Northern TN-2000 system, using the particle analysis program 733B written in Fortran (*8*). For every impactor stage, 300 particles were analyzed, and 500 particles were analyzed for each rainwater sample. The analysis was carried out at an acceleration voltage of 25 kV and a beam current of 1 nA. The energy-dispersive X-ray spectra accumulation time was fixed at 20 s to obtain satisfactory signal/noise ratios. In the 733B program, the localization of a particle is performed by successive horizontal line scans with the electron beam, followed by saving the contour pixel of the particle. After saving all the contour pixels, the area, perimeter, and diameter of the particles are calculated, and the X-ray spectrum is accumulated. All the information is stored on disks for off-line data processing on a Unix computer. Reducing the data set was performed by multivariate techniques.

To study the relations between the particle composition, origin, and shape and obtain even a possible characterization of particles based on their shape, over 200 giant aerosol particles were manually analyzed by EPXMA using the 733A program. The particles were collected for single-particle analysis on a Nuclepore filter in the wind tunnel. The only difference with 733B is that the particles are localized manually and the X-ray spectrum accumulation time was 100 s. ZAF corrections were performed on these spectra for the following elements: Na, Cl, Mg, Al, Si, P, S, K, Ca, Fe, Ti, Ni, Cu, and Zn, resulting in normalized concentrations for each element expressed in weight percentages. The sensitivity of a conventional EPXMA instrument is poor for Na; even at relatively high concentrations, Na may escape detection.

Matrix Correction and Multivariate Techniques. EPXMA is a fast method for element identification. However to obtain quantitative information about the elements present, a very complex procedure is needed, called ZAF correction. Due to electron–sample interactions, processes occur which influence the production and collection of X-rays. The ZAF procedure performs a correction for the atomic number effect (Z), the absorption effect (A), and the fluorescence effect (F). Z represents the difference in electron scattering and retardation in the sample and the standard. Loss of X-rays due to absorption in the sample is represented by A, and the artificial increase of X-ray intensity of an element due to ionization by X-rays originating from an other element is corrected by F. Without correction, errors in excess of 10% could result. After a ZAF correction, the element concentrations present are normalized and expressed in weight percentages.

Reduction of the data set was performed by hierarchical cluster analysis on each of the aerosol and rainwater samples (*9*), producing a classification into groups of particles with chemically similar composition. A hierarchical cluster analysis starts with n particles or clusters from which the most similar ones are joined successively into new clusters. Different strategies are possible to join two clusters; Ward's error sum method is the one we applied because it provides a maximum internal homogeneity into the separated groups (*10*).

Principal factor analyses (PFA) with orthogonal varimax rotation was used to discover the interrelation of 13 variables (Na, Mg, Al, Si, P, S, Cl, K, Ca, Ti, Fe, Ni, and Zn) in our aerosol data set, which led to the identification of different sources of giant aerosols. This multivariate technique splits the data set into subsets of strongly correlated variables. The rotation of these subsets or 'factors' provides a better factor loading. Elements were considered to be detected if the X-ray intensities were found above the detection limit in one of the 300 analyzed particles, for each air sample. Elements like Cu, Pb, Mn, Cr, Ba, Pt, and V were occasionally detected in particles. These elements were found in particles which contributed less than 0.5% of the total aerosol abundance, and therefore, they were further excluded from the data matrix. The major problem in PFA is the choice of the number of factors P that should be taken into account in the model or how many factors are required to estimate the communalities. The value of P was determined by the following criteria (*11*): the number of factors should be significantly less than the number of variables, a large fraction of both the total variance of the variables and the individual variable variance has to be explained by the factor variation, which means that the communalities should be close to 1 and factors that contribute with a variance less than 1 should be excluded from the model. Considering these criteria, the appropriate number of factors is established.

Table 1. Varimax Rotated Factor Loading Matrix for 75 North Sea Giant Aerosol Samples[a]

variable	factor 1	factor 2	factor 3	factor 4	communality	SD
Na	−0.34		−0.81		0.792	0.15
Mg		**0.82**			0.708	0.18
Al	**0.91**				0.851	0.15
Si	**0.87**	0.16	0.17		0.826	0.15
P	0.31			**0.87**	0.854	0.15
S		**0.85**	−0.40		0.872	0.12
Cl	−0.72		−0.23	0.31	0.678	0.21
K	0.17	**0.80**	0.30	0.25	0.824	0.15
Ca		**0.79**	−0.33		0.747	0.18
Ti	**0.83**	0.16		0.30	0.813	0.15
Fe	**0.93**		0.13		0.878	0.12
Ni	−0.18	0.12	**0.48**	**0.81**	0.933	0.09
Zn	**0.59**		**0.73**	0.18	0.912	0.12
eigenvalue	5.05	2.83	1.78	1.02		
% variance explained	38.5	21.6	13.6	7.8		

[a] Only values greater than three times their standard deviation were reported.

Results and Discussion

Automated EPXMA. *Principal Factor Analyses.* By performing PFA on the correlation matrix of the data set, four eigenvalues greater than 1 were produced (5.05, 2.83, 1.78, and 1.02); the fifth value was 0.86. Because no standard procedure exists for the selection of the number of factors, factor matrices with four and five eigenvalues were calculated. After comparing the two varimax rotated matrices, the solution with four factors was preferred, and the varimax rotated factor matrix is represented in Table 1 (the most important values are shown in bold).

To facilitate factor interpretation, factor loadings smaller than three times the standard deviation were rejected because they are considered to be not statistically significant (*11*). The four factors explain together 81.4% of the total variance of the variables, and communality values for most of the variables are high, situated between

0.74 and 0.93, except for Mg, Ca, and Cl. The first factor is determined by high loadings of Al, Si, Fe, Ti, Zn and Na and Cl. Explaining 63.7% of the total variance this factor provides the two major particle types: marine sea-salt particles and aluminosilicates such as fly ash and soil dust with a continental or anthropogenic origin. The inverse correlation between both group concentrations is expressed by the minus sign of the Na and Cl loading. The combination of the seven elements in those two element groups is confirmed by an additional factor analysis. Factor two contains mainly Mg, K, S, and Ca which indicates the presence of seawater crystallization products such as different combinations of $CaCO_3$, $CaSO_4$, K_2SO_4, $MgSO_4$, and dolomite. The NaCl crystals, which should represent the main crystallization product [70% of the total dissolved solids inside a seawater droplet (*16*)], were probably classified in the first factor due to their dominance as compared to the other crystallization salts. Recalculations of the data set by choosing three factors instead of four confirms this. The loadings of Na and Cl increase, but the communalities that describe how well the factor analysis reproduces the reality are lower. The solution with four factors is therefore more appropriate. Factors three and four can be associated mainly with industrial origins because of high loadings for Ni and Zn, inversely correlated with Na, and for Ni and P, respectively. Elements like Ni and V are released by oil combustion processes in power plants due to oil-fired furnaces. Because the low contribution of natural sources to the total emission of Ni and V, respectively 14% and 16% (*12, 13*), Ni and V are used as indicator elements of oil-fired power plants and oil combustion sources in numerous industries. Iron, steel, and ferro alloy plants are responsible for the release of Zn. The emissions are distributed evenly over Europe, but large emission areas are located in the United Kingdom, Spain, and Italy. The occurrence of P in the presence of Fe can be assigned to anthropogenic emissions because of its use in ferro alloy.

Hierarchical Clustering. Particle classification into different groups based on their chemical composition was achieved by hierarchical cluster analysis. Correct interpretation of the cluster analysis results was possible by taking into account the exact ship positions and meteorological data like wind speed, wind direction, and relative humidity during sampling periods. From September 15 to September 27, wind speed fluctuated between 3.4 and 14.5 m/s, and the prevailing wind direction was southwest, characterizing the samples by both continental and marine influences. The results of the hierarchical clustering of 300 particles for each of the five impactor stages collected on September 18 are shown in Tables 2 and 3, on the upwind and downwind ship, respectively. The stage number corresponds to the theoretical cutoff diameter of the particles collected on a certain stage. For each particle type the percent of abundance in a group of 300 particles is given as well as its average diameter (μm) and its composition. Clustering results for aerosol and rainwater samples will be discussed separately.

Aerosols. Depending on the sample, three to eight different aerosol types were distinguished. Due to stormy weather and high wind speeds, the concentration of sea-salt particles is very high in all the impactors, ranging from 10 to 90% of the total aerosol abundance. In a marine atmosphere, sea spray particles are mainly produced by the bubble-bursting mechanism. Due to breaking waves, air is captured and released as bubbles at the sea surface. Bubble breaking results in the ejection of film and jet drops into the atmosphere. This process is more effective with increasing wind speeds. Experiments performed by Deleeuw (*14*) concerning vertical profiles of giant sea spray particles deduced from their size distribution close above the sea surface confirm that particle concentration and

Table 2. Hierarchical Clustering Results of Five Aerosol Samples Taken on the F.S. *Alkor* (Upwind Ship) on September 18, 1991

stage	abundance (%)	av diameter (μm)	composition
1, $d > 20$ μm	49	6.8	NaCl
	24	5.3	organic
	6.0	4.0	Al, Si, Fe
	6.0	4.5	Cr-rich
	4.0	6.7	KCl
2, 8 μm $< d <$ 20 μm	72	3.1	NaCl
	16	4.6	NaCl, $CaSO_4$
	3.3	1.7	$CaSO_4$, Cl
	3.0	3.6	Al, Si, Fe
	2.0	3.5	Fe, Cl
3, 4 μm $< d <$ 8 μm	75	1.3	Cl-rich
	12	1.2	organic
	7.0	1.8	NaCl
	2.3	1.7	Al, Si, Fe
	1.0	1.2	Fe-rich
	1.0	2.2	Si, Cl
4, 2 μm $< d$ 4 μm	74	2.0	NaCl
	7.7	2.1	Na-rich
	6.3	2.4	$CaSO_4$, NaCl
	3.4	1.8	organic
	3.0	1.5	$CaSO_4$
	3.0	3.2	NaCl, Al, Si
5, 1 μm $< d <$ 2 μm	70	2.2	organic
	18	1.7	Cl-rich
	3.0	1.8	Si-rich

Table 3. Hierarchical Clustering Results of Five Aerosol Samples Taken on the R.V. *Belgica* (Downward Ship) on September 18, 1991, from Same Air Mass with Delay of 6 h

stage	abundance (%)	av diameter (μm)	composition
1, $d > 20$ μm	55	4.9	NaCl
	14	5.0	NaCl, $CaSO_4$
	13	5.3	Cl-rich
	11	4.0	organic
	4.3	3.6	$CaSO_4$, Cl
	2.0	5.0	Al, Si, Fe
2, 8 μm $< d <$ 20 μm	43	5.0	NaCl
	27	3.1	$CaSO_4$, Cl
	8.0	2.4	Al, Si, Fe
	7.6	4.0	Mg, S, Cl, K
	6.0	2.9	Al, Si, Fe
	5.3	2.6	Na-rich
3, 4 μm $< d <$ 8 μm	77	1.5	Cl-rich
	16	2.0	NaCl
	9.3	1.7	organic
	1.0	2.8	$CaSO_4$
	1.0	1.5	Si, Cl
4, 2 μm $< d <$ 4 μm	50	3.0	NaCl
	30	2.2	organic
	7.0	2.2	$CaSO_4$
	3.3	2.7	Al, Si, Fe
	3.3	1.7	S-rich
	2.6	2.6	Si-rich
5, 1 μm $< d <$ 2 μm	31	1.5	NaCl
	31	1.6	Cl-rich
	21	1.4	organic
	5.0	1.5	Na-rich
	4.0	1.5	Al, Si, Fe
	2.0	1.1	Fe-rich
	2.0	1.6	S, Cl

variation of sampling height are strongly influenced by wind speed. At sampling heights of 11 m, the increase in particle number concentration of 11-μm particles per particle diameter increment could be up to a factor of 10 if the wind speed increases from 2 to 16 m/s. During transport in the atmosphere, pure NaCl particles can react with sulfuric acid or SO_2 to produce transformed or aged sea-salt particles. In some of the samples, high concentrations of these sulfur-rich particles were detected, but mostly their abundance was low. This can be explained by the limited time the particles possess to react with sulfur-containing compounds, between their creation and sampling. All samples are also characterized by high abundances (3-33%) of Ca- and S-rich particles. These particles can have a marine or a continental origin and are identified as $CaSO_4$. Responsible mechanisms (*15*) could be a fractional crystallization from seawater, interaction between $CaCO_3$ aerosols and atmospheric SO_2 or H_2SO_4, release of gypsum from flue gas in desulfurization processes, and limestone building deteriorating due to air pollution. The first two mechanisms are positively influenced by high relative humidity. Seawater crystallization products such as KCl, $MgCl_2$, $MgSO_4$, and K_2SO_4 are found in 43% of the samples, and abundances are below 19%. Crystallization of successive salts appears by evaporation of seawater drops and is subdivided in four stages (*16*). The first is characterized by the crystallization of $CaCO_3$ and dolomite. $CaSO_4$ and NaCl precipitate respectively the second and third stage. Finally, sodium, potassium, and magnesium sulfates and potassium and magnesium chloride precipitate. Sometimes aluminosilicates such as fly ash and soil dust account for 30% of the total aerosol abundance. Major elements detected in these particles are Si, Al, K, Mg, Fe, and S, which are seldom accompanied by minor elements such as Ti, Cu, Zn, Cr, and Mn. Sometimes high concentrations of S and Ca were found, pointing out the existence of secondary reactions with anthropogenic emissions of SO_2 and H_2SO_4. Until now, no significant difference in composition could be found between fly ash and soil dust particles; only morphological differences appeared. Fly ash is often spherically shaped, and it is emitted by high-temperature combustion processes in power plants; on the other hand, soil dust particles are irregularly shaped and the result of soil erosion. A few times Si- and Fe-rich particles were observed. Si-rich particles originate from quartz or from the decomposition of aluminosilicates confirmed by lower concentrations of elements such as Al, Mg, S, K, and Fe. Combustion processes could also be a possible Si source, but the associated diameters should be smaller than 1 μm (*15*), which is not the case for our samples. The abundance of Fe-rich particles mainly results from metallurgical processes. Organic particles were also present in significant concentrations and probably correspond to biological materials like pollen, bacteria, bird excrements, etc. In EPXMA, the detection is limited to elements with an atomic number ≥ 11, due to the presence of a Be window in front of the Si–Li detector. The X-rays of elements like C, O, and N are too low energy to penetrate this window, and therefore during EPXMA, a particle is classified as organic if no X-rays are collected. Particle diameters were observed to be smaller, especially for large particles, than the cutoff aerodynamic diameters of the May impactor stages. In a marine environment, this can be attributed to four different effects: particle density above 1, splintering of large particles into pieces upon impaction, collection of wet particles which are reduced in volume after drying, or fractional crystallization occurring after evaporation of the water present leading to many small particles. The appearance of NaCl in low concentrations in all the hierarchical clustering tables (except for pure NaCl or transformed NaCl) can be explained as a NaCl coating. This kind of coating can be established in different ways (*17*). The two major mechanisms responsible for a possible NaCl coating at North Sea aerosols are the evaporation of seawater present in particles originating from sea spray and the collision or coalescence of particles with NaCl-containing cloud droplets. According to Andreae (*17*), if the surface of a mineral dust particle has a coating of water-soluble material (the result of a chemical reaction or the residue from a rain shower), it will probably act as a cloud condensation nucleus (CCN). Due to the adsorption of droplets at its surface, the CCN increases in size. On the other hand, if the particle is hydrophobic because lack of soluble material on its surface or because of a nonpolar organic coating, then it might not be a CCN. These particles can collide and coalescence with cloud droplets and develop possibly into CCN. If the cloud droplets disappear by evaporation instead of rainout, crystallization of the solute could appear as a coating on the particle surface.

By investigating possible changes between the samples collected during six sampling periods on board the *Alkor* and the *Belgica* (positioned at 200 km downwind from each other), the following conclusions were made: (a) No significant decrease in particle diameter was observed; the average diameter of particle "types" for each stage remains more or less constant. (b) The abundance of seawater crystallization products increases during traveling across the sea for the first two stages (particles with diameters above 20 μm and between 20 and 8 μm, respectively), with a factor 2.2 and 2.4, respectively. The discrimination between different element combinations seems to be more difficult for the *Belgica* samples. (c) In stages with particle diameters above 4 μm, a decrease in aluminosilicate abundance was noticed. (d) 48% of the analyzed samples did not contain organic particles. If present, no clear changes in relevant abundance could be discovered between samples from the two research vessels. (e) An increase in freshly produced NaCl particles was observed at the first three stages; aged sea salt almost disappears at large particle stages, and its abundance is replaced by pure NaCl. The determination of changes in diameter for each stage is very difficult because sometimes groups disappear or their composition becomes very complex. Diameters fluctuate: in some of the samples they increase, in others they decrease during air mass travel. A marine climate like the North Sea is characterized by high atmospheric concentrations of marine-derived components and a very high relative humidity, which offers particles the possibility of water absorption during their atmospheric residence. Water uptake is caused by deliquescence of soluble salt present in the particle (*18*). Each salt is associated with its critical humidity at which it is transformed from the crystal form into the liquid phase. At very high relative humidity, a mixed salt particle can even be transformed into a droplet. As mentioned above, the evaporation of water can lead to a recrystallization. Compared with the initial salt composition, different combinations can be possible after this recrystallization

process. These facts probably explain the high abundance of seawater crystallization products and their difficult compositional interpretation. The decrease and sometimes total disappearance of aluminosilicate particles in the largest particle size fractions can be interpreted as a result of the short residence time of those large and giant particles in the atmosphere due to their higher sensitiveness compared with small or Aitken particles for removal mechanisms like sedimentation, impaction, rainout, and washout. The apparent increase in pure NaCl concentration and marine crystallization products could be explained by considering the following facts. The concentration is inversely correlated with height, and the difference in concentration is very clear by comparing sampling at 0.2 and 11 m height. Concentration differences between the sampling at 11 m on board the *Alkor* and at 15 m on board the *Belgica*, however, decrease very rapidly for particle diameters smaller than 20 μm. Therefore, the main reason for the difference in sea-salt concentration and marine crystallization products on both vessels is the increasing marine influence during air mass travel over the sea; the different sampling height will be of minor importance. Due to their dominant concentrations, both particle groups suppress all other particle types. Collection close to the sea implies a shorter time between creation and sampling, which decreases the possibility for reactions with other compounds like SO_2, as mentioned before.

Wet Deposition. To study the changes in the composition of rainwater particles above the North Sea, rainwater samples were collected on board the *Alkor* and the *Belgica*. Comparing the hierarchical cluster analysis results of the rainwater suspension samples from both vessels, showed a few differences. First, a significant difference in composition was distinguished. Samples collected on board the *Alkor* contained beside aluminosilicates and Si-rich particles high abundances of S, P, Fe, and Cr in contrast with the *Belgica* samples, which contained only high abundances of aluminosilicates and Si-rich particles. These high abundances of S, P, Fe, and Cr are probably the result of the downward mixing of anthropogenic plumes of SO_2 and Fe- and Cr-rich particles from U.K. power plants. Due to the dilution of the air masses over a 200-km distance, the abundance of those elements probably decreases or even disappears. The occurrence of Cr serves as indicator for iron and steel industries (*19*), which is confirmed by the presence of Fe. In addition, a high abundance of organic material was detected in the *Alkor* samples. The exact composition of the organic material cannot be determined by EPXMA due to detection limitations. The only possible explanation for the high abundance of organic material can be either microorganism growth due to the thawing of rainwater during transport or the presence of bird excrements. Second, differences in particle diameters could be noticed. For the rain samples collected on September 16, the mean particle diameter of the *Alkor* sample was significantly larger compared with that from the *Belgica* sample. The difference between the two samples collected on September 22 was not so pronounced. A decrease in mean particle diameter could be the result of the removal of several giant and large particles from the air mass by washout and rainout during air mass travel.

Non-Automated EPXMA. North Sea aerosols are a mixture of different components, some derived from the sea itself and some supplied by the wind, sometimes from very distant places (*20*). The abundance of particle types is influenced by meteorological conditions and obviously by the sampling site. Based on their composition, seven groups of giant particles were manually analyzed: NaCl, aluminosilicates, Si-rich, S- and K-rich, Fe-rich, Ca- and S-rich particles, and particles with a high contribution of heavy metals.

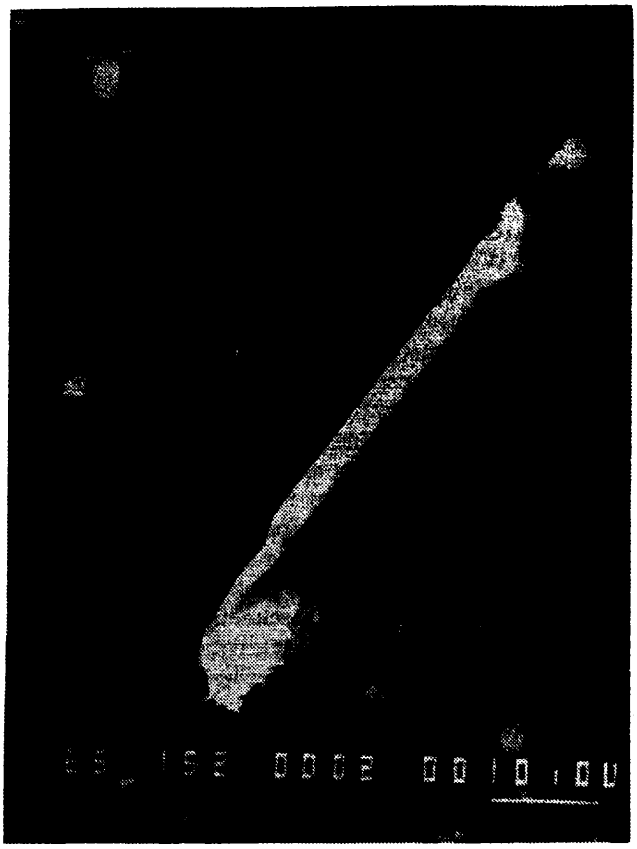

Figure 2. Linearly shaped particle rich in Na and Cl at the end a Si-rich particle.

The first class of particles, sea salt, was subdivided in two groups: freshly produced sea salt and transformed or aged sea salt. In addition to the cubic shape typical for halite and the irregularly shaped NaCl particles (probably agglomerated halite crystals) described in the literature, linearly shaped particles were observed with lengths ranging from 7 to 37 μm (Figure 2). In 58% of the linearly shaped particles, higher concentrations of Cl were detected. The stoichiometry and mineral types of these NaCl-rich particles are not clear. Transformed or aged sea-salt particles were irregularly shaped with diameters varying from 4 to 9 μm. Low concentrations of Al, Si, Mg, K, and P indicate the presence of soil dust particles.

Si-rich particles and K- and S-rich particles were irregularly shaped with corresponding diameters of 3–7 and 3–9 μm, respectively. Consistent with the literature (*15*), spherical fly ash particles and irregularly shaped soil dust particles were detected. The fly ash particles, with diameters of 3–5 μm, were sometimes enriched in S, likely originating from secondary reactions with anthropogenic S compounds, and in agreement with experimental results of Kaufer (*21*), the variations in Ti and Mg concentrations were independent of particle size. Ni, Cu, and Zn were rejected from the tables because of too low concentrations. Beside the higher S concentrations, 25% of the soil dust particles contained also higher concentrations of Ca. A possible explanation could be the occurrence of reactions

between H_2SO_4 and aluminosilicate–mineral particles. Concentrations of Ni, Cu, and Zn could also be neglected. The presence of S- and K-rich particles results as described above from seawater crystallization products, and high concentrations of K may refer to a pollution or biological source.

Fe-rich particles can be spherical or irregularly shaped. The ones we examined were mainly irregularly shaped with diameters ranging from 3 to 7 μm. Beside the pure Fe-rich particles, Fe particles with enriched S concentrations were detected. S enrichment could be the result of the metallurgic processes.

Based on their shape, Ca- and S-rich particles could be divided in two groups. The irregularly shaped $CaSO_4$ particles vary in diameter from 3 to 12 μm, and lower concentrations of Si, K, Fe, Mg, and Al refer to the presence of soil dust. The second group contains apparently diamond and elongated hexagonally shaped particles with diameters from 3 to 10 μm, and no characteristic aluminosilicate elements were present. These two shapes belong to the same crystal type called gypsum. By observing the crystalline form from the top view and then from the front view, the elongated hexagonal shape (Figure 3, top) followed by the diamond shape (Figure 3, bottom) were distinguished. Particles with enriched concentrations of Ti, Zn, and Cu belong to the seventh group and are irregularly shaped with varying diameters of 3–9 μm. Compared to submicrometer particles (*22*), only low concentrations of heavy metals could be found. Due to industrial high-temperature combustion processes, gases are released which mainly convert by sudden cooling into submicrometer particles. Condensation can also occur on the surface of already existing particles. These kinds of composite particles may of course also arise from the coagulation of small particles onto large ones. Finally, we could conclude that, compared with the literature, only for NaCl and Ca- and S-rich particles were different shapes detected; the other ones matched those described in earlier published articles by different authors.

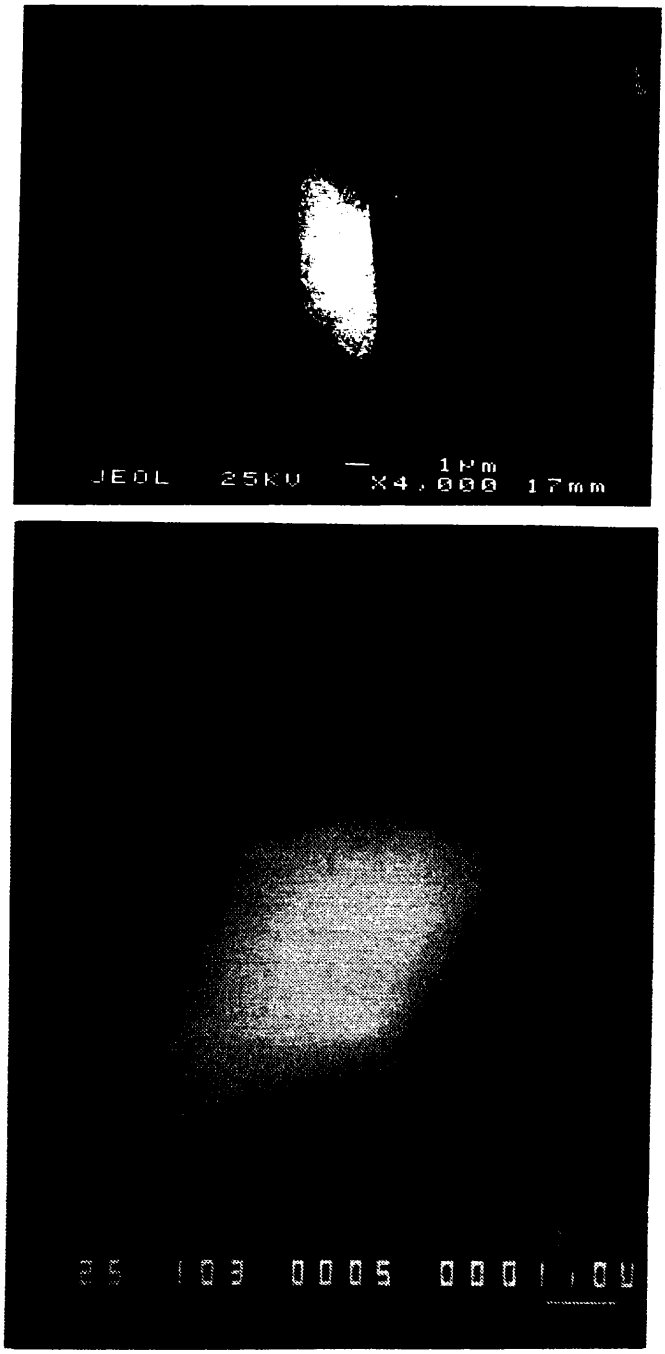

Figure 3. (Top) An elongated, hexagonally shaped $CaSO_4$ particle. (Bottom) Diamond shaped $CaSO_4$ particle.

Conclusion

To study variations in composition of air masses crossing the North Sea due to air–sea exchange processes in the lower troposphere, aerosol and rainwater samples were collected on two research vessels positioned 200 km apart downwind from each other. Single-particle analysis was achieved by EPXMA.

The identification of the particle origin was possible by performing PFA on the data set resulting in four different giant aerosol sources: aluminosilicates and sea salt, seasalt crystallization processes, and two industrial sources. The classification of particles into groups of chemically similar composition was accomplished by a hierarchical cluster analyses according to Ward's error sum method. A total of eight different aerosol types could be distinguished: freshly produced and aged NaCl particles; Ca- and S-rich particles; seawater crystallization products like $NaSO_4$, K_2SO_4, KCl, and $MgCl_2$; aluminosilicates as fly ash and soil dust; Si-rich particles; Fe-rich particles; and organic particles.

By comparing aerosol clustering results of the two research vessels, three differences in composition were found after crossing a large distance above the sea: the abundance of crystallization products increases at the first two stages, leading to difficulties in the interpretations of salt compositions; the aluminosilicate abundance in the first three stages in the samples decreased; and in some of the samples, the aged sea-salt abundance decreases or sometimes disappears at higher stages in favor of pure NaCl. No significant decrease in particle diameter was observed. Compositional as well as size differences appeared in the collected rainwater samples of both research vessels.

Manual EPXMA was performed to investigate the relations between particle composition, origin, and shape. Based on their chemical composition, seven groups were determined: NaCl particles, Si-rich particles, aluminosilicates, Fe-rich particles, S- and K-rich particles, Ca- and S-rich particles, and particles with a high contribution of heavy metals. All shapes matched with those described

in literature, and only for NaCl and $CaSO_4$ were unexpected shapes detected.

Acknowledgments

This work was partially financed by the Belgian State-Prime Minister's Services-Science Policy Office, in the framework of the EUROTRAC program (under Contract EU7/08) and in the framework of the Impulse Programme on Marine Sciences (under Contract MS/06/050). We thank M. Schulz for coordinating the North Sea sampling campaign. L.D.B. acknowledges financial support by the Belgian Instituut ter bevordering van het Wetenschappelijk Onderzoek in Nijverheid en Landbouw (IWONL).

Literature Cited

(1) Rojas,C. M.; Injuk, J.; Van Grieken, R. *Atmos. Environ.* **1993**, *27A*, 251–259.
(2) Injuk, J.; Van Malderen, H.; Van Grieken, R.; Swietlicki, E.; Knox, J. M.; Schofield, R. *X-Ray Spectrom.* **1993**, *22*, 220–228.
(3) Jaenicke, R. *Ann. N.Y. Acad. Sci.* **1980**, *338*, 317–322.
(4) Jaenicke, R. In *Chemistry of the Unpolluted and Polluted Troposphere*, 1st ed.; Georgii, W., Jaeschke, W., Eds.; D. Reidel Publishing Co.: Dordrecht, The Netherlands, 1982; pp 341–374.
(5) Dedeurwaerder, H. L. Ph.D. Dissertation, Free University of Brussels, 1988.
(6) May, K. R. *J. Aerosol. Sci.* **1975**, *6*, 1–7.
(7) Vawda, Y.; Colbeck, I.; Harrison, R. M.; Nicholson, K. W. *J. Aerosol Sci.* **1989**, *20*, 1155–1158.
(8) Raeymaekers, B. Ph.D. Dissertation, University of Antwerp, 1986.
(9) Van Espen, P. *Anal. Chim. Acta* **1984**, *165*, 31–49.
(10) Bernard, P. C.; Van Grieken, R. E.; Eisma, D. *Environ. Sci. Technol.* **1986**, *20*, 467–473.
(11) Heidam, N. Z. *Atmos. Environ.* **1982**, *16*, 1923–1931.
(12) Nriagu, J. O. *Nature* **1979**, *279*, 409–411.
(13) Pacyna, J. M. Trace element emission from anthropogenic sources in Europe. Technical Report No. 10/82; The Norwegian Institute for Air Research: Lillestrom, 1982.
(14) Deleeuw, G. *Tellus* **1986**, *38B*, 51–61.
(15) Xhoffer, C.; Bernard, P.; Van Grieken, R. *Environ. Sci. Technol.* **1991**, *25*, 1470–1478.
(16) Bochert, H. *Chemical Oceanography*; Academic Press: London,1965.
(17) Andreae, M. O.; Charlson, R. J.; Bruynseels, F.; Storms H.; Van Grieken, R.; Maenhaut, W. *Science* **1986**, *232*, 1620–1632.
(18) Winkler, P. *Phys. Scr.* **1988**, *37*, 223–230.
(19) Pacyna, J. M. *Atmos. Environ.* **1984**, *18*, 41–50.
(20) Betzer, P. R. *Nature* **1988**, *336*, 569–571.
(21) Kaufer, N. *Environ. Sci. Technol.* **1984**, 18, 544–547.
(22) Van Malderen, H.; Rojas, C.; Van Grieken, R. *Environ. Sci. Technol.* **1992**, *26*, 750–756.

Received for review December 6, 1993. Revised manuscript received April 11, 1994. Accepted April 27, 1994.

• Abstract published in *Advance ACS Abstracts*, June 1, 1994.

RAPID COMMUNICATIONS IN MASS SPECTROMETRY, VOL. 8, 32–39 (1994)

The Fourier-transform Laser Microprobe Mass Spectrometer with External Ion Source as a Tool for Inorganic Micro-analysis†

Herbert Struyf, Wim Van Roy, Luc Van Vaeck* and René Van Grieken
Department of Chemistry, University of Antwerpen (UIA), Universiteitsplein 1, B-2610 Wilrijk, Belgium

Pablo Caravatti
Spectrospin AG, Industriestrasse 26, CH-8117 Fällanden, Switzerland

Focused-laser ionization of solids and subsequent analysis of the generated ions by Fourier-transform mass spectrometry is suitable for the characterization of inorganic and organic constituents. This paper describes selected examples to illustrate the capability of structural characterization of inorganic substances and the problems associated with the critical nature of the energy deposition phenomena which can complicate the use of the method. Selected examples from practical problem solving in material applications are presented to evidence the feasibility of local analysis by Fourier-transform laser microprobe mass spectrometry.

Laser microprobe mass spectrometry (LMMS) is a recent technique for local analysis of solids. A focused UV beam of a high-power laser is employed for the one-step vaporization and ionization of a microvolume of the specimen. The ions produced are then mass analysed.[1]

Local analysis techniques determine the chemical composition on the micrometre scale. In this way, the microscopic sample morphology can be correlated with the actual constituents. The information usually remains confined to major components. Apart from the analysis of micro-objects such as single aerosol particles, local analysis is intensively applied in material research. Faulty processing procedures often result in the formation of μm-sized heterogeneities, which cannot be dealt with, even by so-called trace analysis methods.

Laser ionization of solids provides attracting features in both elemental and organic mass spectrometry. The photon beam is easily directed onto the sample in the confined space of an ion source and neither disturbs the electric fields nor induces sample charging of non-conducting solids. The initially developed LMMS instruments, employing a time-of-flight (TOF) mass analyser, were appreciated for selected organic and inorganic applications.[2–5] However, the use of TOF LMMS for practical solving was handicapped by the limitations of the mass analyser.[6] Recently, the Fourier-transform mass spectrometer (FT MS) has been advocated as the analyser of choice for LMMS.[7,8] We developed an FT LMMS instrument with an external ion source.[9]

One of the on-going projects aims at determining the possibilities and limitations of FT LMMS for inorganic micro-analysis. Although TOF and FT LMMS instruments share the basic step of focused laser irradiation, there still remains a considerable difference between the two approaches as a result of the specific features of the mass analyser used. The first of this paper will present selected examples to highlight the detailed nature of the spectra for speciation purposes. Speciation is used in the present sense to mean the structural characterization of inorganic components as opposed to merely monitoring of a given element. Additionally, selected data will illustrate the problems associated with the critical nature of the energy-deposition phenomena which may complicate the use of the method. A comparative evaluation of features such as mass resolution, mass accuracy, mass range and specificity of the signals, will be made between FT and TOF LMMS. The second part of the paper will deal with practical problem-solving tasks. Specifically, the analysis of a floppy disc represents an interesting test case to study the heterogeneous distribution of elements in an organic matrix. Another real-life application comes from the photographic industry and involves the study of local defects on AgBr and polyethylene terephthalate (PET) layers.

EXPERIMENTAL

The LMMS instrumentation is based on a Spectrospin CMS 47X (Spectrospin AG, Fällanden, Switzerland) with a 60 mm diameter single cell in a 4.7 T superconducting magnet. The Infinity Cell™ has been recently installed.[10] Differential pumping in the ion transfer line between the ion source and the cell maintains a pressure of 5×10^{-10} Torr in the cell while that in the source is 1×10^{-8} Torr. Ion transfer is performed by electrostatic fields. Instrument control and data acquisition are performed using an ASPECT 3000 computer upgraded with a 20 MHz 9 bit fast ADC and 256 kword memory. A full description of the basic instrumentation is available elsewhere.[11]

The ionization of solid samples is performed with a frequency quadrupled Nd:YAG laser (Quanta-Ray™ DCR-2A, Spectra Physics, Mountain View, CA, USA) delivering up to 20 mJ per pulse of 4–5 ns at 266 nm. The laser is equipped with filling-in optics for a Gaussian beam profile. Attenuation is performed by two sets of λ/2 plates and air-spaced Glan polarizers. The reflection geometry is used, i.e. laser impinges at 45° on the sample on the side from which the ions are extracted perpendicularly. The sample holder accomo-

† Contribution from the 2nd European FTMS Workshop, Antwerp, Belgium, September 1993.
* Author for correspondence.

0951–4198/94/010032–08 $09.00

Received 18 October 1993
Accepted 9 November 1993

dates a specimen up to $20 \times 20 \times 10$ mm, while a flat specimen can be attached by double-sided tape. The sample can be positioned with a resolution of 1 μm in three orthogonal directions. Sample exchange can be performed in only five minutes without interruption of the vacuum in the ion source.

The sample viewing system comprises a microscope objective with ultra-long working distance (Nikion M Plan SLWD 20 X, Japan) inside the vacuum and a charge-coupled device (CCD) camera with high resolution monitor (Bischke, Switzerland) for display. The final magnification of 700× means that 1 mm on the screen represents 1.4 μm on the specimen. Additionally, a binocular eyepiece (3-63 Nikon, Japan) is mounted to permit an overview of the sample. Full details of the instrument are reported elsewhere.[9]

Samples of pure products are applied as thin coatings, by spraying a 10^{-3}% solution into a cascade impactor system, in which a sample holder is mounted, in order to collect the microdroplets of an equivalent aerodynamic diameter larger than 0.1 μm. Alternatively, a finely ground powder can be adhered directly to the stainless steel sample support. The samples of TiW on silicon were obtained through collaboration with the Interuniversitary Micro-Electronics Center (IMEC, Leuven, Belgium). The preparation was based on vacuum deposition. The malachite analysed was part of a mineralogical collection.

RESULTS AND DISCUSSION

1. Time, energy and emission angle acceptance of FT LMMS with external source

A mass spectrometer samples the ions produced in the ion source more or less quantitatively. It is well known that, for instance, energy selection in ion lens systems means that the energy distribution of the detected ion population is different from that of the ion population initially made by ionization. To facilitate the understanding of the results presented later, it may be profitable to discuss first the limits imposed by the combination of ion transfer line and cell to the emission angle, initial kinetic energy and formation time of the ions.

The first features were evaluated by means of SIMION (Idaho National Engineering Laboratory, Idaho Falls, ID, USA) ion-trajectory simulation studies. Both the electrostatic field and the inhomogeneous fringing field from the 4.7 T magnet were introduced into the calculations. It was observed that (for the currently used instrumental parameters) ions up to 2 eV and 3° can be trapped in the cell. The low kinetic energy limit is not uncommon in FTMS, where the ions are trapped by typically 1–2 V. Nevertheless, it has to be noted that the emission angles and initial kinetic energies of elemental ions, generated by focused-laser irradiation of solids, can be substantially higher than the values mentioned above.[12]

Although the principle of FTMS requires the generation of ion bunches, extremely short ion production processes pose a problem, specifically when an instrument with external ion source is used. Assuming that ions of m/z 20 and 500 are generated from the sample within 10 ns, it can be calculated by SIMION that their respective flight times (T_{flight}) up to the entrance of the cell amount to 46 μs and 227 μs respectively. When the first trapping plate is biased to allow entrance of the ions into the cell, they will travel through the cell until reflection occurs against the potential barrier of the second trapping plate. Again SIMION permits one to calculate that these ions return to the entrance trapping plate after respectively 52 μs and 259 μs (T_{cell}). To be able to measure these ions, the first trapping plate has to be rebiased to trapping voltage value in order to prevent ions from escaping from the cell. From that moment onwards, the ions arriving from the ions source can no longer enter the cell. Summarizing the cycle for the ions of m/z 20, the first cell plate has to be 'closed' before $46 + 52 = 98$ μs. The time elapsed between the laser pulse and the closure of the 'gate' is denoted as $T_{\text{open gate}}$. Even at the maximal $T_{\text{open gate}}$ for the ions of m/z 20, those of m/z 500 are still in the middle of their flight ($T_{\text{flight}} = 227$ μs). However, the picture becomes more diffuse if the spread in time of formation and initial kinetic energy is taken into account. The latter parameter can be neglected in a first approximation because the acceptance of the electrostatic lenses in the ion transfer system is relatively low. However, it will be shown that the time duration of the ion formation process is important and certainly more so than is generally assumed in LMMS. This applies not only to organic compounds but also to inorganic constituents. To facilitate the discussion of the results, the concept of an 'ion formation window' is defined as:

$$T_{\text{window}} = T_{\text{open gate}} - T_{\text{flight}}(-T_{\text{cell}}).$$

It is clear that the time spent during the reflection of the ions inside the cell determines the width of the window.

At present, the value of T_{cell} limits the time resolution with which the ion formation can be investigated to windows (depending on the m/z value) of 50 μs to 200 μs wide for m/z 20 and m/z 300, respectively. Further refinement is planned for the near future by gating the electrode in front of the sample. Dividing up the laser-generated ion bunch by the use of increasingly smaller time windows implies a decreasing number of ions available for detection. Hence the attainable time resolution will be limited by the sensitivity of FT LMMS.

2. Speciation capabilities

Figure 1 illustrates the positive- and negative-ion mass spectra of $InCl_3$, recorded by FT LMMS. In spite of the timing problem with ions of different m/z, In^+ at m/z 115 is accompanied by a small signal at m/z 265 due to $InCl.In^+$. The calculated values for T_{flight} and T_{cell} are 109 μs and 124 μs for m/z 115, and are 165 μs and 188 μs for m/z 265. As a result, Fig. 1 shows that the generation of In^+ still continues between 67 and 191 μs after the laser pulse. Hence, the corresponding signal can be detected together with the $InCl.In^+$ ions. The situation is different for the negative ions. The Cl^- signal dominates for a $T_{\text{open gate}}$ of 175 μs while the structurally most relevant ions $InCl_3.Cl^-$ and $InCl.Cl^-$ are detected with $T_{\text{open gate}} = 400$ μs. Note that the employed $T_{\text{open gate}}$ of 175 μs corresponds to the experimentally optimized setting. Calculations ($T_{\text{flight}} = 60$ μs and $T_{\text{cell}} = 69$ μs) show that the maximal ion current for Cl^- again is due to post-laser ion formation processes, at least under the conditions (with respect to kinetic energy and emission

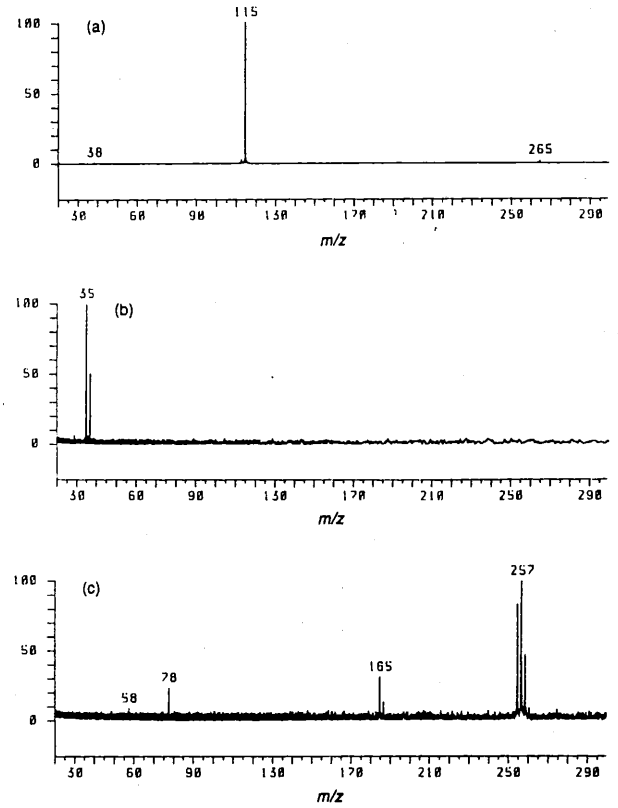

Figure 1. Diagnostic mass spectra in the positive- and negative-ion detection mode recorded by FT LMMS from indium chloride. The peak at m/z 78 is due to electronic noise. (a) Positive ions, $T_{\text{open gate}} = 300\ \mu s$; (b) negative ions, $T_{\text{open gate}} = 175\ \mu s$ and (c) negative ions, $T_{\text{open gate}} = 400\ \mu s$.

angle) as applied in our FT LMMS system with external ion source and ion transfer using static electric fields.

Apart from the information on the ion formation, it is important to stress that the abundant signal from $InCl_3.Cl^-$ or in general $MX_n.X^-$ becomes a striking asset of FT LMMS for speciation purposes. This generally applicable feature allows us to identify LiCl quite unambiguously although our instrument is only equipped for detection of ions from m/z 15 onwards. Hence, Li^+ cannot be detected, though the diagnostic ions $LiCl.Li^+$ and $LiCl.Cl^-$ are detectable (see Fig. 2).

Techniques such as Auger spectroscopy, electron probe X-ray micro-analysis (EPXMA) and secondary ion mass spectrometry (SIMS) essentially determine the composition of the inorganic molecule from the relative abundances of the individual elements. The former two methods measure the elements individually, while in SIMS it is assumed that the average composition of the observed clusters corresponds to the original composition of the sample. In contrast, LMMS permits the generation of ions, the composition of which clearly reflects the structural moieties in the analysed molecules. Specifically, FT LMMS data obtained from salts systematically show the following features. For binary salts (MX_n), prominent signals are usually due to $(MX_n)_mM^+$ or $(MX_n)_mX^-$. For oxy-salts (MOX) on the other hand, combinations of MO and X serve as building blocks for the clusters $(MO)_nX_m.MO^+$ and $(MO)_nX_m.X^-$. The negative-ion mass spectrum of sodium nitrate is shown in Fig. 3 as a representative example. The main signals are due to $NaO.NO_2.NO^-$ and $NaO.NO_2.NO_2^-$ (m/z 115 and 131 respectively). Other examples have been described elsewhere.[13] The speciation capabilities of FT LMMS have been exploited to determine the oxidation state of chromium.[14]

3. Layer of TiW on Si: the role of energy deposition

FT LMMS is also very surface sensitive: a TiW layer of 50 nm thickness is sufficient to obtain intense signals at a mass resolution of 1.5×10^6 for W^+ in the absence of an Si^+ signal. The crater depth however clearly exceeds 50 nm.

However, the adjustment of the laser irradiation power density on the sample is extremely critical. Figure 4(a)–(c) gives the broadband spectra as a function of laser energy. Under threshold conditions, both elements are detected. At a power density level of 2.5 times the threshold value, the W^+ signal disappears, and at 5 times threshold the Ti^+ peak shows a tendency to vanish into the noise. The explanation is quite obvious. It is hard to assume that the more energy that is applied, the fewer ions are made. Consequently, it is clear that fewer ions can be transferred into the cell and/or trapped. It can be readily conceived that the ions generated under higher energy conditions exhibit energies and emission angles exceeding the SIMION values mentioned in Section 1. This problem does not exist in TOF LMMS.[12] Note however that the power densities required for element detection are significantly higher than those required to detect the cluster ions, which are most useful for speciation.

4. Malachite: the role of energy deposition and time window

Malachite is a mineral with an average composition of $Cu(OH)_2.CuCO_3$ and consists of compacted layers of different shades of green. Figure 5 gives the positive-ion mass spectra recorded with values of $T_{\text{open gate}}$ of 400 μs and 600 μs corresponding to respectively ion

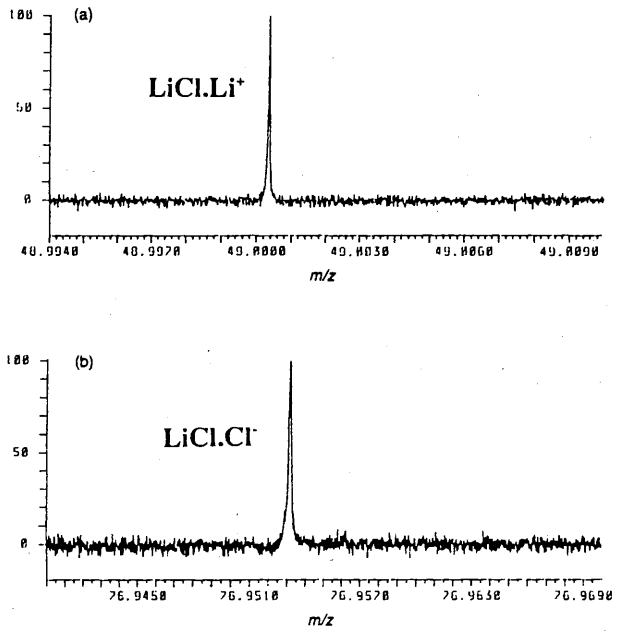

Figure 2. Diagnostic signals in the (a) positive- and (b) negative-ion detection mode recorded by FT LMMS from lithium chloride at a resolving power of 1 270 000.

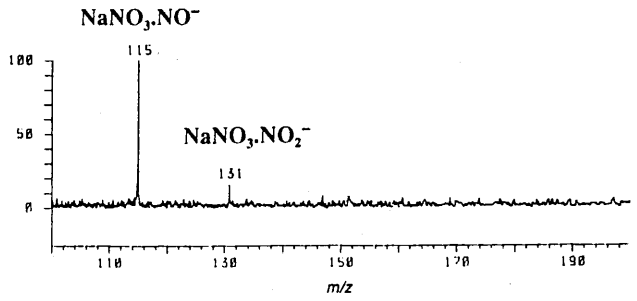

Figure 3. Negative-ion mass spectrum recorded by FT LMMS from sodium nitrate.

formation windows of 227 to 319 μs and 427 to 519 μs for m/z 63 and to windows of 0 to 210 μs and 194 to 410 μs for m/z 349. In the light-coloured zone, the relative intensity of higher m/z clusters—taking the ions at m/z 207 as a reference—increases with a longer $T_{\text{open gate}}$, which points to a post-laser generation process. The Cu^+ signal is absent but can be detected with a shorter $T_{\text{open gate}}$ of 200 μs. The prevalent formation of Cu^+ ions soon after the laser pulse is not unexpected. However, in the dark region, the Cu^+ signal is strikingly present at a $T_{\text{open gate}}$ of 400 μs, which means that there is a significant post-laser formation of elemental ions between 227 μs and 319 μs. Additionally, the clusters from m/z 250 to higher masses show up with much higher intensity at a $T_{\text{open gate}}$ of 600 μs than in the lightly coloured region. The elemental composition of the main ions is given in Table 1.

The differences in peak intensities and ion formation times for both regions cannot yet be interpreted unambiguously. It is possible that the chemical composition in each zone is different as to the major components. The same cluster ions were detected, which means that one of the constituents is not characterized in the spectrum. This is possible because the energy selectivity can be substantial. At low energy, one can ionize Mn^+ from stainless steel while no Fe^+ peak occurs in the spectrum. In this case, the speciation capabilities of FT LMMS are limited by the laser power-density selection. Alternatively, the chemical composition could be almost identical except for trace element concentrations. The physical properties of the matrix can however affect the energy deposition of the laser irradiation and in this way affect the duration of ion formation and the relative abundances of the generated clusters. Also, this effect means that speciation in FT LMMS requires careful tuning of the laser energy to the material under study and explains why, in our view, quantitation is a long term goal.

5. Single-ion monitoring versus full mass spectra in LMMS

By its principle, TOF LMMS records complete mass spectra. Due to the use of an external ion source, FT LMMS broadband spectra can be taken over limited mass ranges only.[9] Additionally, the deviations from relative peak abundances of different naturally occurring isotopes can amount to 40% in routine conditions, i.e. without ejection. Moreover, the best sensitivity is obtained in the high resolution mode, which—in practice—almost means single-ion monitoring in the low m/z range. The mass accuracy lies in the low ppm

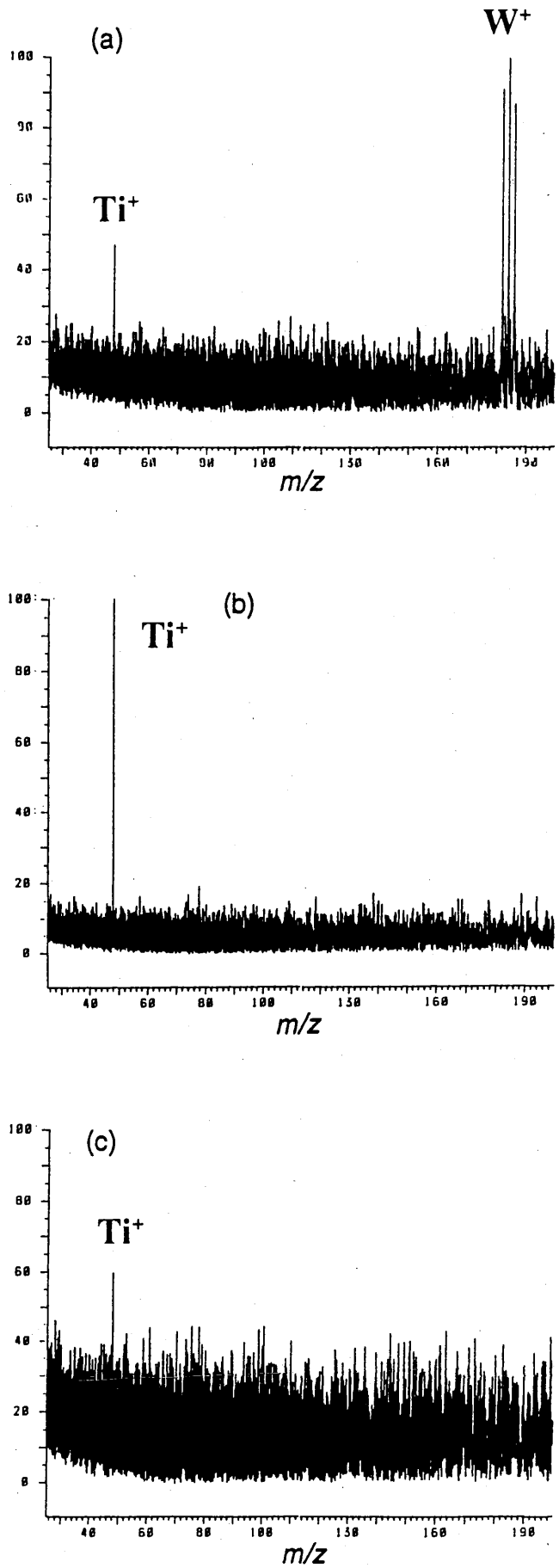

Figure 4. Effect of the laser irradiation energy on the positive-ion mass spectra recorded by FT LMMS from a 50 nm TiW layer on silicon with a value of $T_{\text{open gate}}$ of 200 μs; (a) was obtained at threshold energy, (b) at 2.5 times threshold and (c) at 5 times threshold.

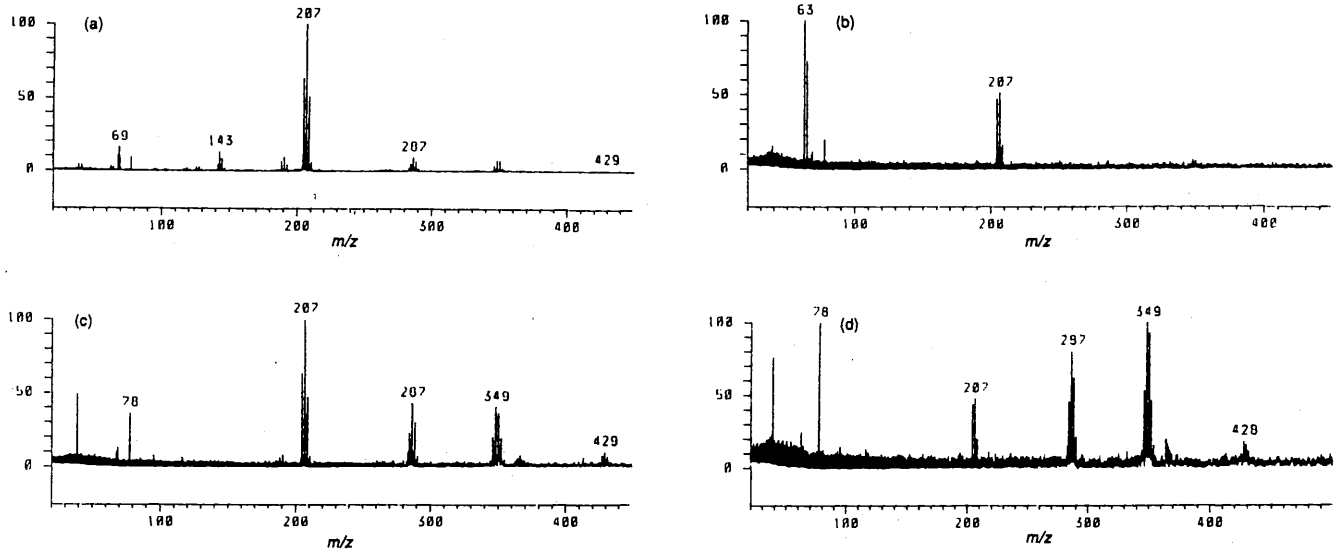

Figure 5. Typical positive-ion mass spectra recorded by FT LMMS from the light and dark zones of malachite. (a) corresponds to the light zone and (b) to the dark zone, both with a value of $T_{\text{open gate}}$ of 400 μs. (c) and (d) also correspond to the light and dark zones respectively, but with a value of $T_{\text{open gate}}$ of 600 μs. The peak at m/z 78 is due to electronic noise.

range and allows unambiguous determination of the chemical composition of the detected ions (cf. Table 1). Equally important is that in practice a high mass resolution is needed to separate the ions from sodium oxysalts at m/z 62, usually assigned to Na_2O^+ but actually corresponding to $Na.K^+$. The high mass separating power and the good mass accuracy make the detection of correct isotope ratios less essential for diagnostic analysis.

6. Polyethylene terephthalate (PET)

PET is one of the most widely used polymers in modern technology. As a result, no scientist attempting to solve material processing problems can ignore this material. We were confronted with this material in most of the subsequently described applications. Figure 6 shows the positive-ion mass spectra recorded from a pure PET sample at different values of $T_{\text{open gate}}$. A full discussion of the effect of the $T_{\text{open gate}}$ on the organic mass spectra has been given.[16] Apart from the trivial observation that longer $T_{\text{open gate}}$ allows one to measure ions of higher m/z, these spectra also evidence the unexpectedly late formation of some ions of low m/z. Specifically, the fragments at m/z 105, detected with $T_{\text{open gate}}$ of 700 μs, show that their formation continues up to between 500 and 600 μs after the laser pulse ($T_{\text{flight}} = 104$ μs and $T_{\text{cell}} = 119$ μs for m/z 105).

The structural assignment of the major ions in Fig. 7 was elaborated on the basis of the measured elemental compositions (cf. Table 2). Note the dramatic progress of FT LMMS analysis in comparison with TOF LMMS. In the latter case, the ions are only separated according to nominal mass so that time-consuming comparative studies on different compounds are necessary to support tentative interpretations.

Table 1. Exact mass measurement of diagnostic cations detected by FT LMMS from malachite

Measured m/z	Elemental composition	Absolute error (ppm)
62.929	^{63}Cu	0.9
125.859	$^{63}Cu_2$	1.0
188.788	$^{63}Cu_3$	0.8
188.832	$^{63}Cu_2C_2K$	0.8
204.783	$^{63}Cu_3O$	1.2
206.781	$^{63}Cu_2{}^{65}CuO$	1.1
286.713	$^{63}Cu_3{}^{65}CuO_2H$	1.3
288.712	$^{63}Cu_2{}^{65}Cu_2OH$	0.2
346.637	$^{63}Cu_5O_2$	0.7
364.630	$^{63}Cu_4{}^{65}CuO_3$	0.1
428.566	$^{63}Cu_5{}^{65}CuO_3H$	5.4
429.558	$^{63}Cu_4{}^{65}Cu_2O_3$	1.0
431.557	$^{63}Cu_3{}^{65}Cu_3O_3$	0.5

7. Floppy disc

Figure 8 shows a selection of typical positive-ion mass spectra from a floppy disc, recorded with different values of $T_{\text{open gate}}$. Figure 8(a) and (b) show the mass

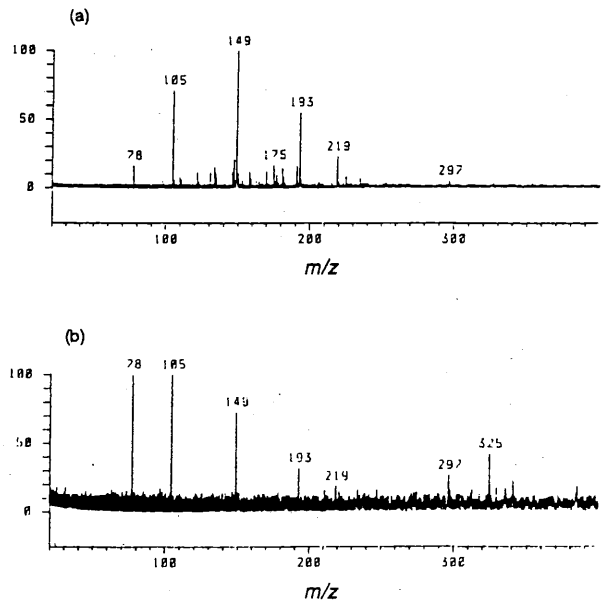

Figure 6. Positive-ion mass spectra recorded by FT LMMS from a polyethylene terephthalate reference sample. (a) $T_{\text{open gate}} = 400$ μs; (b) $T_{\text{open gate}} = 700$ μs. The peak at m/z 78 is due to electronic noise.

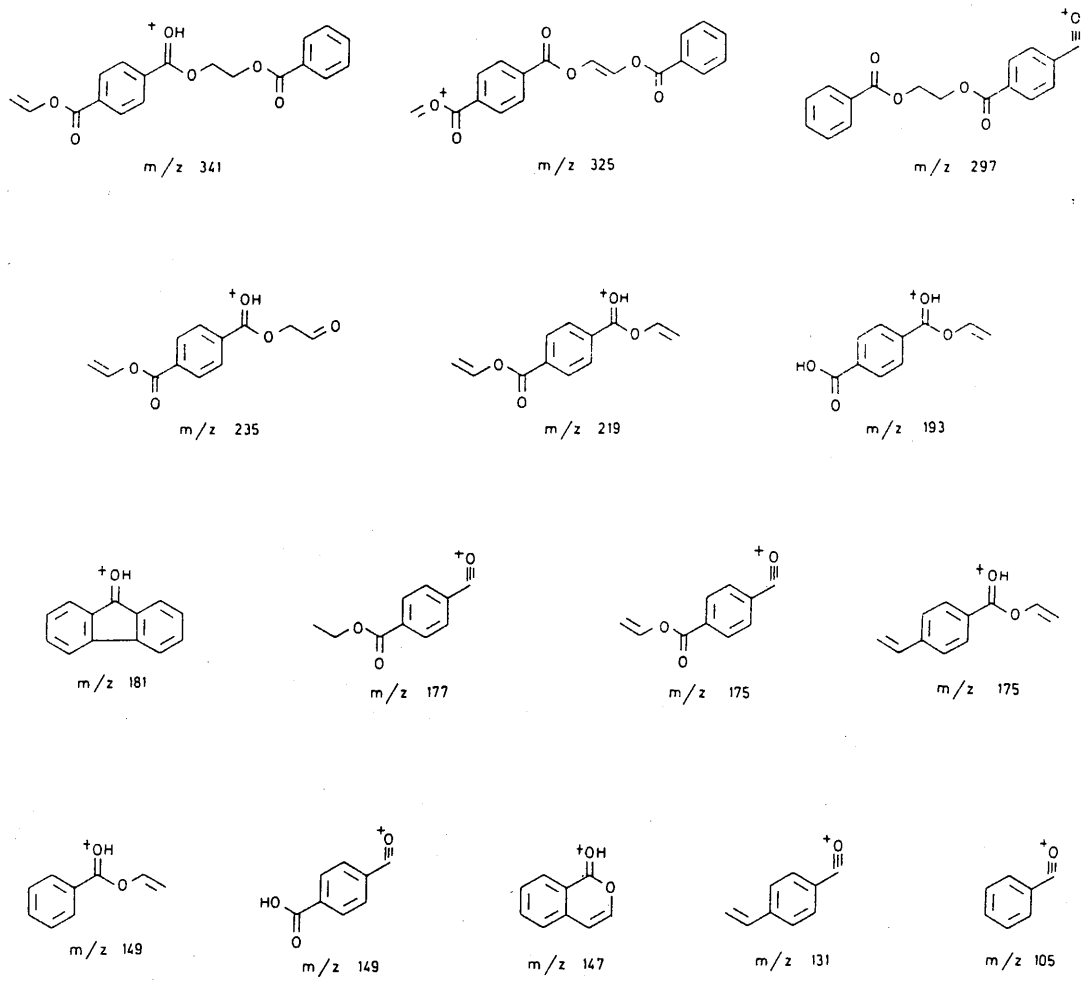

Figure 7. Structure of the major ions in the positive-ion mass spectra from a polyethylene terephthalate reference sample. The assignment is based on the exact elemental composition deduced from accurate mass measurements made by FT LMMS.

spectra, recorded under the optimized $T_{\text{open gate}}$ conditions for the low-mass and high-mass ions respectively. However, the spread on the ion distributions allows the capture of both low- and high-mass ions in one spectrum, albeit with some loss of sensitivity at the ends of the window. A selection of representative spectra in Fig. 8(c)–(e) permit the characterization of the distribution of the elements Fe and Mn in the PET layer of the disc. First of all, the majority of spectra show the signals from Fe together with those from PET. Secondly, there are areas of the order of 50 μm in diameter where Mn and no Fe is embedded in the PET matrix. Finally, some similarly sized regions show a spectrum with Fe and no organic ions, pointing to areas of poor dispersion of the elemental component in the matrix. It has to be noted that there is a difference in the laser power density to be applied to organic constituents and that for elements. In this respect, Fe and Mn represent a favourable case because these elements can be ionized with relatively low energy, i.e. completely in the range commonly used for organic products. The same applies for the time of ion formation. Additionally, the post-laser ionization of Fe ($T_{\text{flight}} = 76$ μs, $T_{\text{cell}} = 87$ μs), i.e. 80 and 220 μs, also helps the capture of the elemental ions together with the PET fragments in the cell.

Table 2. Exact mass measurement of diagnostic cations detected by FT LMMS from a polyethylene terephthalate reference sample

Measured *m/z*	Elemental composition	Absolute error (ppm)
105.033	C_7HO	2.6
131.049	C_9H_7O	0.9
147.044	$C_9H_7O_2$	1.4
149.023	$C_8H_5O_3$	0.6
149.060	$C_9H_9O_2$	0.8
175.039	$C_{10}H_7O_3$	0.1
175.075	$C_{11}H_{11}O_2$	1.7
176.616	$C_{10}H_8O_3$	0.3
181.065	$C_{13}H_9O$	1.2
193.049	$C_{10}H_9O_4$	0.9
219.066	$C_{12}H_{11}O_4$	1.6
235.060	$C_{12}H_{11}O_5$	0.5
297.076	$C_{17}H_{13}O_5$	0.4
325.070	$C_{18}H_{13}O_6$	1.1
341.101	$C_{19}H_{17}O_6$	1.8

8. Defect in photographic film

The results described in this section concern a practical problem of a photographic film showing areas where the upper emulsion layer was depleted in AgBr. These areas were about 50 μm in diameter. Two possible causes were put forward: the spreading of the emulsion on the PET support had been disturbed physically or

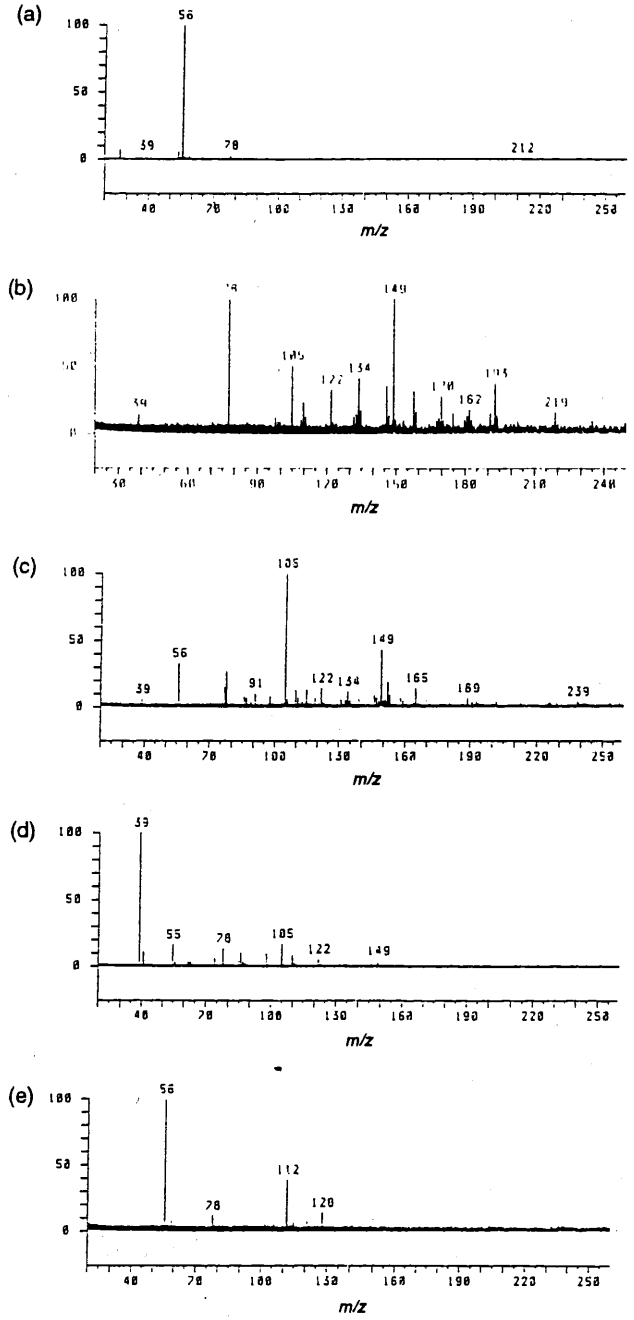

Figure 8. Typical positive-ion mass spectra recorded by FT LMMS from a floppy disc. Spectra (a) and (b) were recorded using the optimum $T_{\text{open gate}}$ values of 175 μs and 400 μs for low- and high-mass ions respectively. Spectra (c), (d) and (e) are from different regions of the PET layer of the disc, all with $T_{\text{open gate}} = 300$ μs. The peak at m/z 78 is due to electronic noise.

mechanically; or the local presence of an unknown chemical substance, most likely an organic product, had caused this defect. This problem illustrates an application of choice for the LMMS in general and FT LMMS with its superior identification capabilities in particular.

Figure 9 surveys typical positive-ion mass spectra recorded from the central spot of the defect, from the peripheral ring, where the residue of any contaminant would be most likely concentrated, and from the unaffected film itself. The latter spectra are of course dominated by the Ag^+ peak with a $T_{\text{open gate}}$ of 200 μs while a longer $T_{\text{open gate}}$ yields the appearance of several AgBr-related higher m/z clusters. As expected, no signals are shared with the previously described spectra of ions on the PET reference sheet. In the middle of the depletion area, some Ag^+ is still detected but the signal-to-noise ratio shows that the quantity is minor. Of course, longer $T_{\text{open gate}}$ removes the Ag^+ almost completely but also permits the observation of the characteristic PET fragments at m/z 105 and 149 (cf. Table 2). The mass spectra of the peripheral ring correspond in detail to a superposition of the PET and AgBr spectra.

In conclusion, FT LMMS data did not reveal the presence of unexpected contaminants in or around the depleted areas. The possibility that the emulsion manufacturing process was disturbed by an unwelcome chemical is not very likely.

CONCLUSION

The application of FT LMMS with external ion source provides access to the time of ion formation with respect to the laser pulse. It has been demonstrated that ion formation continues up to several hundreds of microseconds after the laser pulse, in the case of inorganic compounds. This delayed ion formation for inorganic ion clusters is not expected on the basis of TOF LMMS results. Since the conditions for laser ionization are comparable, the observed differences between TOF and FT LMMS results can be explained in part by the specific characteristics of the mass analysers with respect to the initial kinetic energy of the ions and the emission angle from the sample.

The data presented show that FT LMMS permits detailed speciation of inorganic substances. Specifically, prominent signals in the positive and negative mass spectra do refer to structural moieties in the analyte. Binary salts (MX_n) yield diagnostic ions such as $(MX_n)_mM^+$ or $(MX_n)_mX^-$. Oxy-salts (MOX) on the other hand, produce cluster ions for which combinations of MO and X serve as building blocks.

The analysis of a 50 nm TiW layer on silicon shows the small information depth. Although the crater depth clearly exceeds 50 nm, only the peaks from the components in the upper layer are detected and no silicon signal appears. However, the adjustment of the laser irradiation power density on the sample is extremely critical. Increase of the energy regime can remove elemental ions from the spectrum. This is explained by the fact that the ions generated under these conditions possess energies and emission angles exceeding the acceptance of the mass analyser.

The different zones of malachite yield mass spectra that differ by the relative peak intensities of the higher clusters and the ion formation time of Cu^+ ions. This observation is tentatively related to the physical properties of the matrix affecting the energy-deposition of the laser irradiation, and in this way also the duration of the ion formation and the relative abundance of the different generated clusters. This means that speciation in FT LMMS requires careful tuning of the laser energy to the material under study.

The second part of this paper demonstrates the capabilities of FT LMMS for local analysis of materials. It is important to note that most of the practical problem-solving applications are not confined either to organic or inorganic constituents. One of the major assets of LMMS is that the method characterizes both

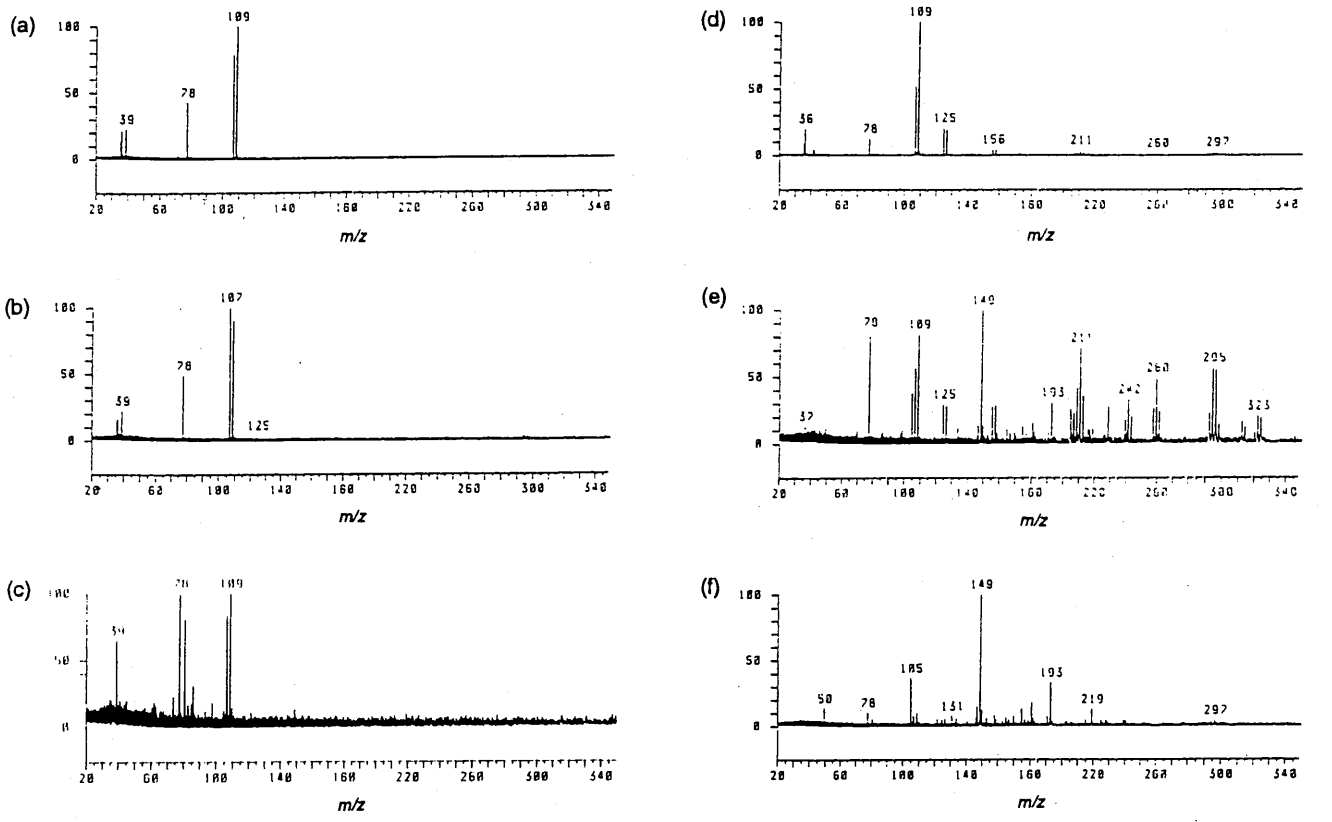

Figure 9. Typical positive-ion mass spectra recorded by FT LMMS from photographic film. Spectra (a) and (b) are of undamaged film, (c) and (d) are from the periphery of an affected area and (e) and (f) are from the centre of a defect. (a), (c) and (e) correspond to a $T_{\text{open gate}}$ value of 200 μs and (b), (d) and (f) to 500 μs. The peak at *m/z* 78 is due to electronic noise.

types of components. In this way, the heterogeneous distribution of iron and manganese and the extent of dispersion in the embedding PET matrix in a floppy disc is shown. Similarly, FT LMMS characterization of a 50 μm defect in a photographic emulsion shows the absence of unexpected contaminants, organic or inorganic in nature. As a result, it is deduced that the emulsion processing was disturbed by mechanical or physical processes.

Acknowledgements

Wim Van Roy and Luc Van Vaeck are indebted to the National Science Foundation, Belgium, (NFWO) as research assistant and research director respectively. Herbert Struyf acknowledges the 'Impulse Programme in Marine Sciences', supported by the Belgian State—Prime Minister's Services—Science Policy Office (contract MS/06/050). W. Vandervorst (IMEC) is thanked for providing the metal-coated silicon samples.

REFERENCES

1. A. H. Verbueken, F. J. Bruynseels, R. Van Grieken and F. Adams, in *Organic Mass Spectrometry*, ed. by F. Adams, R. Gijbels and R. Van Grieken, p. 173, Wiley, New York, 1988.
2. L. Van Vaeck and R. Gijbels, *Fresenius J. Anal. Chem.* **337**, 743 (1990).
3. L. Van Vaeck and R. Gijbels, *Fresenius J. Anal. Chem.* **337**, 755 (1990).
4. R. Holm and D. Holtkamp, in *Microbeam Analysis—1989*, ed. by P. E. Russell, p. 325, San Francisco Press, San Francisco, 1989.
5. D. Holtkamp, G. Bayer and R. Holm, *Mikrochim. Acta*, **I**, 245 (1991).
6. L. Van Vaeck, J. Bennett, W. Lauwers, A. Vertes and R. Gijbels, *Mikrochim. Acta*, **III**, 283 (1990).
7. M. Pelletier, G. Krier, J. F. Muller, D. Weil and M. Johnston, *Rapid Commun. Mass Spectrom.* **3**, 146 (1987).
8. J. T. Brenna, W. R. Creasy, W. McBain and C. Soria, *Rev. Sci. Instrum.* **59**, 873 (1988).
9. L. Van Vaeck, W. Van Roy, H. Struyf, F. Adams and P. Caravatti, *Rapid Commun. Mass Spectrom.* **7**, 323 (1993).
10. P. Caravatti and M. Alleman, *Org. Mass Spectrom.* **26**, 514 (1991).
11. P. Grossmann, P. Caravatti, M. Alleman and H. Kellerhals, in *Proceedings of the 36th Annual Conference on Mass Spectrometry and Allied Topics, San Francisco, CA*, ASMS, East Lansing, 1988.
12. M. De Wolf, T. Mauney, E. Michiels and R. Gijbels, *Scanning Electron Microsc.* **III**, 799 (1986).
13. W. Van Roy, H. Struyf, L. Van Vaeck, R. Van Grieken, R. Gijbels and P. Caravatti, *Analusis* (in press).
14. A. Hachimi, E. Poitevin, G. Krier, J. F. Muller, J. Pironon and F. Klein, *Analusis*, **21**, 77 (1993).
15. L. Van Vaeck, P. Van Espen, W. Jacob, R. Gijbels and W. Cautreels, *Biomed. Environ. Mass Spectrom.* **16**, 113 (1988).
16. W. Van Roy, H. Struyf, L. Van Vaeck, R. Gijbels and P. Caravatti, *Rapid Commun. Mass Spectrom.* **8**, 40 (1994).

RAPID COMMUNICATIONS IN MASS SPECTROMETRY, VOL. 8, 40–45 (1994)

Desorption–Ionization of Organic Compounds Studied by Fourier-transform Laser Microprobe Mass Spectometry†

Wim Van Roy, Herbert Struyf, Luc Van Vaeck* and Renaat Gijbels
Department of Chemistry, University of Antwerp, Universiteitsplein 1, B-2610 Wilrijk, Belgium

Pablo Caravatti
Spectrospin AG, Industriestrasse 26, CH-8117 Fällanden, Switzerland

The recently developed FT LMMS with an external ion source has been applied to selected organic molecules. Some aspects of the ion formation processes from solids under focused laser irradiation at 266 nm were investigated. Specifically, the effect of laser energy and the time profile of ion production were studied. First, the generation of intact cations, fragments and thermal decomposition products from a quaternary ammonium salt were evaluated at distinct times after the laser pulse. The mass spectra of phenol red in its neutral and salt form were recorded under different conditions with respect to laser irradiation power density conditions and ion formation after the laser pulse. The results allow the refinement of previous concepts about ionization in LMMS.

Laser microprobe mass spectrometry (LMMS) is a recent technique for local analysis of solids. A focused UV beam of a high power laser is employed for the one-step vaporization and ionization of a microvolume of the specimen prior to mass analysis.

The initially developed instruments used time-of-flight (TOF) analysers. Literature data demonstrate the capability of the technique to cope with the localization and characterization of organic and inorganic constituents in both conducting and dielectrical samples.[1,2] While several complementary techniques are available for inorganic and elemental analysis on a microscopic scale, laser microprobes have triggered a particular interest because of their potential for achieving local analysis of organics by means of structurally relevant information. Apart from the localization aspect, laser irradiation of solids allows the analysis of non-volatile, polar and/or high molecular weight compounds such as polymers, organic salts etc. As a result, the LMMS principle offers the potential to deal with a wide variety of practical problems, ranging from the measurement of micro-objects such as aerosol particles, to the localization of natural products in biological material and to the characterization of μm-sized heterogeneities due to faulty material processing.[3,4] The wide applicability of this technique motivates the research efforts to overcome the limitations of the previously used TOF mass analysers in LMMS. Specifically, a much higher mass resolution and mass accuracy is mandatory to fully exploit the potential of focused laser ionization of solids.[5] As a result, Fourier-transform mass spectrometry (FT-MS) has become advocated as an analyser of choice for LMMS.[6,7] We started the development of an FT LMMS instrument with external ion source.[8]

One of the basic problems in LMMS is that ion formation by focused laser irradiation of solids appears to represent extremely complicated processes, involving several competitive time- and energy-dependent mechanisms.[9] A better understanding of the ionization processes is essential to optimize the LMMS technology so that it can be routinely applied to heterogeneous samples. On the basis of a systematic study of organic molecules by means of TOF LMMS, we have attempted to elaborate a tentative model for desorption and ionization (DI), allowing the rationalization of the formation of the detected ions in terms of time, energy and local pressure.[5]

This paper describes the study of selected compounds by means of FT LMMS in order to verify and/or refine some aspects of these concepts. In particular, the effect of laser energy and the time profile of ion production will be illustrated by representative examples of non-ionic and ionic compounds. Part of this research has issued from local analysis applications, one of which is described in an accompanying paper.[10]

EXPERIMENTAL

The developed FT LMMS instrument is based on a Spectrospin CMS 47X now commercially available as MicroFocus™ (Spectrospin AG, Fällanden, Switzerland). The instrument is equipped with an external ion source, modified to permit focused laser irradiation at 266 nm in the reflection geometry. More details are given in the accompanying paper[11] and a full description of the system was reported previously.[8]

The application of laser irradiation and ion extraction in the reflection geometry requires minimal sample preparation. For instance, crystals of pure products can be simply applied to the sample support by adhesion. Also double-sided adhesive tape can be used. The bias voltage on the sample holder has to be tuned between ± 15 V according to the thickness of the sample and the presence or absence of a non-conducting interlayer. Hence, to improve comparability of the results for different compounds, products have been applied as thin coatings on the stainless-steel sample support by spotting 10 μL of a concentrated methanol solution or by spraying a 10^{-3}% solution into a cascade impactor system, in which a sample holder is mounted to collect the microdroplets of an equivalent aerodynamic diameter above 0.1 μm directly.

† Contribution from the 2nd European FTMS Workshop, Antwerp, Belgium, September 1993.
* Author for correspondence.

0951–4198/94/010040–06 $08.00

Received 18 October 1993
Accepted 8 November 1993

RESULTS AND DISCUSSION

1. Time of ion formation

To facilitate the discussion of the results, it may be profitable to summarize the differences between FT and TOF LMMS with respect to the ion formation period vs. the laser pulse, i.e. prompt or delayed ionization, and the acceptance of the systems for ions, according to their initial kinetic energies and emission angles.

It is generally assumed that ion formation by focused laser irradiation of organic solids is almost instantaneous or 'prompt', i.e. within about 25–50 ns. As a result, extraction of the ions into a TOF analyser without gating the electrode in front of the drift tube can be applied and still separation of nominal masses up to m/z 500 is feasible in a two metre long TOF system with reflector. Although this only means that there is at least a bunch of promptly formed ions, it has become a general notion that all ion formation in LMMS is prompt.[12] Otherwise stated, the focused laser irradiation of solids would not be expected to lead to a substantial number of ions later on by the so-called post-laser DI processes. As a result, there would be a real difference in the ion formation by focused and non-focused laser irradiation of solids, the latter mode having been exploited for a long time as 'laser desorption' mass spectrometry (LDMS).[13–15] Several literature reports demonstrated that the ion formation in LDMS continues over several hundreds of μs after the laser pulse but most of these experiments were conducted with different laser systems than the ones used in LMMS.[6,17] The experiments described in this paper, however, were perfomed with a UV pulsed laser system: this means the same power density regime on the sample as currently used in TOF LMMS.

The information about the time of ion formation relative to the laser pulse is deduced from the experiments by FT LMMS with the external ion source as follows:

$$T_{\text{window}} = T_{\text{gate}} - T_{\text{flight}}(-T_{\text{cell}})$$

where T_{window} refers to the ion formation time window, T_{gate} denotes the time period during which ions can enter or escape the cell, T_{flight} is the time period between the ion formation and its arrival at the cell (transfer through electrostatic fields from ion source to cell), and T_{cell} refers to the time spent by an ion during the reflection back and forth in the cell. A full description of these parameters is given in the previous paper.[11] In practice, the present FT LMMS system with external ion source permits slicing of the ion formation window by periods of about 200 μs. Gating of the electrode in front of the sample will be carried out to obtain a better resolution and, possibly, complete separation of the prompt and delayed ion formation processes with a 25–50 ns resolution. However, a limit will be imposed by the sensitivity of the system since the fractional ion current can be expected to be proportional to the window width.

As to the comparison with the ion optics in current TOF LMMS instruments, it has to be remembered that the FT LMMS with external source is quite selective as to the enegy and emission angle of the detectable ions. SIMION calculations reveal that ions up to 2 eV and 3° can be trapped in the cell. These values were determined taking the inhomogeneous magnetic field into account. Current TOF optics accept ions up to 50 eV and 45°.[18]

2. DI of a non-ionic compound

In order to determine to what extent our approach allows fine interpretation of differences between mass spectra, Fig. 1 represents the positive-ion mass spectra of 2-hydroxy-4-n-octyloxy-benzophenone recorded at different power densities. The data in Fig. 1(a) and (b) were recorded under closely similar conditions with respect to laser irradiation power density. The relative intensities of the $[M+H]^+$ signal at m/z 327 and the different daughter-ion signals agree closely, and the signal-to-noise ratios are comparable. These spectra were taken from ground powder, adhering directly to the metal sample support, which is in principle not ideal for comparability purposes. The structural assignment of the fragments is discussed elsewhere.[19] The positive-ion mass spectrum in Fig. 1(c) was obtained using a 6 times lower power density for laser irradiation. The overall intensity is lower as is apparent from the signal-to-noise ratio while the relative contribution from the protonated molecules to the total ion current decreases significantly. This tendency is generally observed in FT LMMS and can be interpreted consistently with the concepts of the tentative DI model, namely that most of the adduct ions are due to a process separate from the one responsible for the generation of fragments. Otherwise, it would be hard to rationalize the fact that the more excitation that is pumped into the solid, the lower the relative contribution of fragments becomes. Finally, attention has to be given to the fact that the T_{gate} is 500 μs. The latter setting is selected to optimize

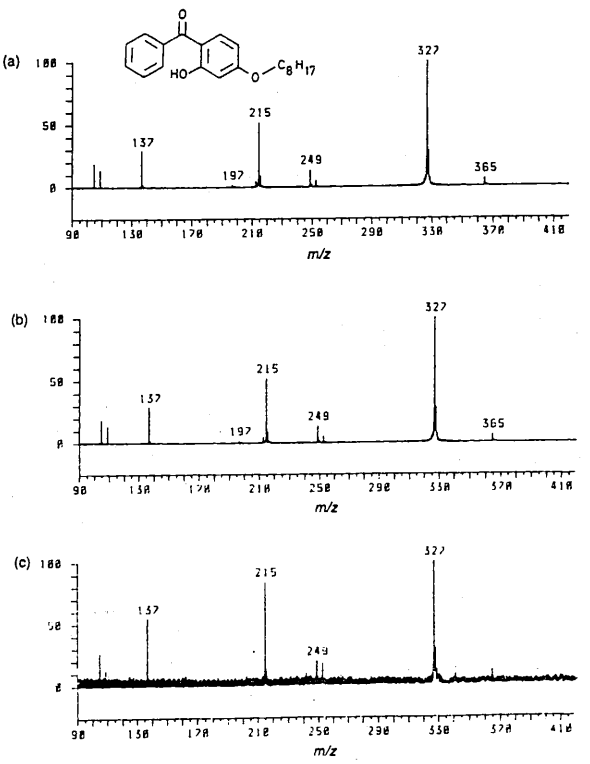

Figure 1. Positive-ion mass spectra recorded by FT LMMS from 2-hydroxy-4-n-octyloxy-benzophenone at laser power densities of (a) 1.5×10^7 W cm^{-2}; (b) 2×10^7 W cm^{-2} and (c) 3×10^6 W cm^{-2}.

the ion current at m/z 327. Given that the T_{flight} is 184 μs for m/z 327 and 104 μs at m/z 105, and that the values of T_{cell} are 209 μs and 119 μs respectively, the spectra characterize ion formation windows of 107 μs to 316 μs and of 277 μs to 396 μs respectively on the condition that abstraction is made from the time spread arising from the width of the ion distributions in the cell. In conclusion, it can be stated that the detected ions refer to an ion formation window, starting about 100 μs or longer after the laser pulse. Note that the ions from the prompt formation process are not measured under these conditions since these ions have already escaped from the cell.

3. DI of a quaternary ammonium salt: hexadecyltrimethylammonium bromide

In view of the Literature data on LDMS,[12,17] it is readily conceived that the generation of cationized molecules in particular, and possibly also protonated molecules, occurs as a post-laser process under focused laser irradiation conditions. Whenever preformed ions from organic salts are released from the solid state, these species are already charged and need no further ion/molecule interaction within the micro-plume above the sample. To date, their detection in TOF LMMS has contributed to the generally accepted idea that preformed ions refer exclusively to prompt ion formation mechanisms. Because of the thermolabile nature of the compounds, it is implicitly assumed that the post-laser ion formation does not occur.

Hexadecyltrimethylammonium bromide was selected as a test case to verify the time window of ion formation in FT LMMS. Figure 2(a) and (b) represent the positive-ion mass spectra recorded by FT LMMS with T_{gate} values of 200 μs and 500 μs. The latter value corresponds to the maximum ion current for m/z 284. The ion formation time windows for a T_{gate} of 200 μs are between 0 and 29 μs for ions of m/z 284 and between 31 μs and 121 μs for m/z 60 ions while a T_{gate} of 500 μs results in a window of from 134 μs to 329 μs for m/z 284 and from 331 μs to 421 μs for m/z 60. Hence, the results with T_{gate} of 200 μs in FT LMMS include the promptly formed ions in the high-mass range. As a result, the comparison of Fig. 2(a) with the TOF LMMS data[20] in Fig. 2(c) becomes particularly interesting. Both mass spectra are largely comparable indeed, except for the substantially higher intensity of the ions at m/z 60 in FT LMMS. However, if the post-laser processes are sampled using a T_{gate} of 500 μs by FT LMMS, the mass spectrum shows important differences. The signal from the intact cations becomes the base peak while the ions at m/z 60 dominate over the fragments at m/z 58. The interpretation is quite obvious. Intact cations are predominantly generated at a relatively long time after the laser pulse. The observed maximum of ion production lies in the range measured using a CO_2 laser.[16]

An important conclusion from Fig. 2 is that ion formation process contributions within the first 29 μs after the laser pulse produce only a relatively small fraction of the total number of intact cations that a focused laser generates from the solid. This is consistent with the fact that the intact cations are detected in TOF LMMS as a base peak for the lower analogs and that the intensity systematically decreases for the higher analogs. As to the formation of low-mass ions

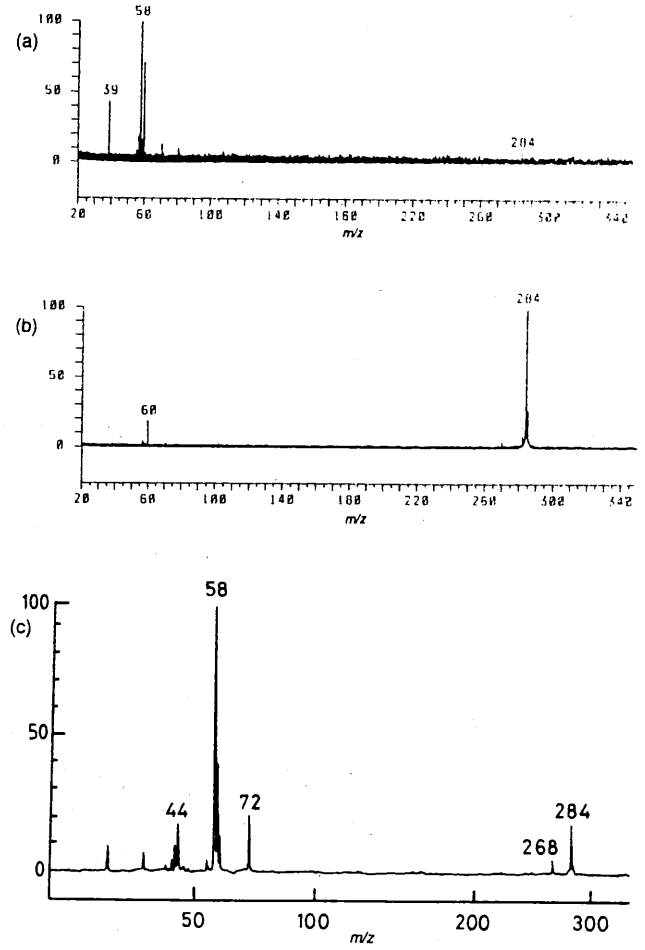

Figure 2. Positive-ion mass spectra recorded by FT LMMS at T_{gate} values of (a) 200 μs and (b) 500 μs and (c) by TOF LMMS from hexadecyltrimethylammonium bromide. The latter data are reprinted with permission of Springer Verlag from Reference 20.

detected in FT LMMS, the data does not yet permit an unambiguous explanation. The ions at m/z 58 must be reasonably related to fragmentation of the intact cations but the situation is less clear for the ions at m/z 60.[21] Either it is assumed that the ions at m/z 60 correspond to the protonated form of the most likely thermal degradation product, i.e. trimethylamine, or that these ions actually correspond to daughters of the parents at m/z 284. The intensity ratio of the ions at m/z 60 to those at m/z 58 suggests that the thermal degradation route gains importance at longer times. Alternatively. if the second explanation is preferred, this means that the internal energy distribution of the cations, generated promptly, is different from that of the parent ions, released later on. Further research will be required to fully elucidate these phenomena.

4. Comparison of DI for neutral and salt

As previous results indicate, the study of organic salts is useful for revealing some aspects of the DI process. Specifically, the comparison of compounds existing in the neutral and salt form has been initiated in TOF LMMS.[5,22] It is straightforward to conduct similar experiments on FT LMMS. Phenol red in its neutral and salt form will be discussed here as a representative example.

Figure 3(a) and (b) compare the negative-ion mass spectra, recorded for the neutral form by FT LMMS at

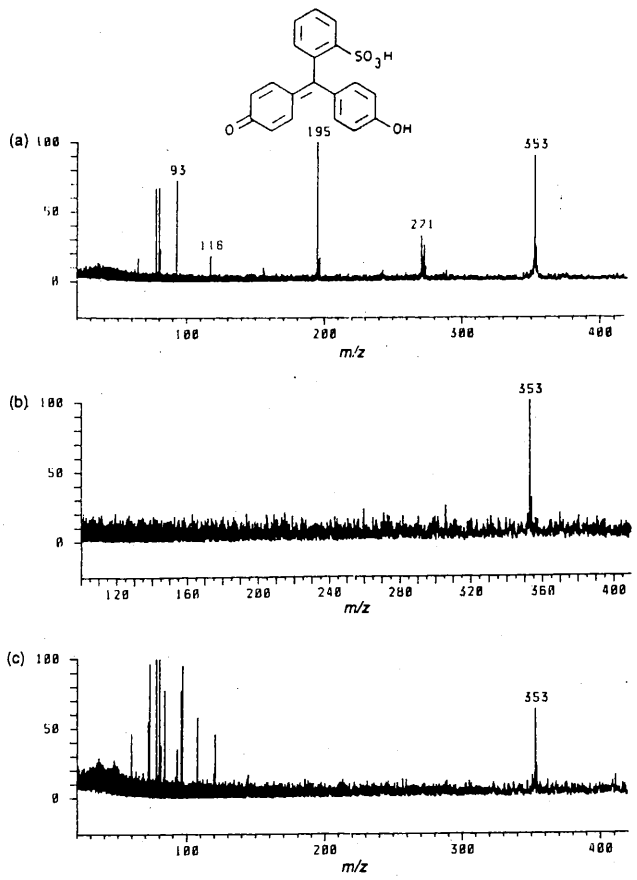

Figure 3. Negative-ion mass spectra recorded by FT LMMS at different T_{gate} and laser power densities from phenol red in the neutral form: (a) $T_{gate} = 400\ \mu s$, laser power density $3 \times 10^6\ W\ cm^{-2}$; (b) $T_{gate} = 600\ \mu s$, laser power density $3 \times 10^6\ W\ cm^{-2}$ and (c) $T_{gate} = 600\ \mu s$, laser power density $1.1 \times 10^7\ W\ cm^{-2}$. The signal at m/z 78 is due to electronic noise.

different T_{gate} settings under identical threshold laser irradiation power density conditions. The T_{flight} of the anions at m/z 353 is about 190 μs and the value of T_{cell} is 217 μs. Hence, the mass spectra recorded at a T_{gate} of 400 μs and 600 μs characterize an ion formation time window of 0–210 μs and 193–410 μs respectively for m/z 353. The mass spectra reflect the initial formation of the deprotonated molecules and show structurally relevant fragments at m/z 271 and 195. FT LMMS permits determination of the exact chemical composition by accurate mass measurements made to within 1 ppm. The fragment at m/z 271 ($C_{19}H_{11}O_2$, error 0.1 ppm) arises from the loss of the sulphonic acid group from the anion at m/z 353 while the one at m/z 195 ($C_{13}H_7O_2$, error 0.9 ppm) arises from the elimination of the sulphonated phenylring and cyclization. The elemental composition of the ions at m/z 195 contradicts the previously reported tentative assignment based on TOF LMMS analysis.[22] This highlights the need for high resolution mass spectrometry capabilities in this kind of work.

After an additional 200 μs, $[M-H]^-$ ions but no fragments still reach the cell, as can be seen from Fig. 3(b). If the laser power density during the irradiation is increased three to four times (Fig. 3(c)), abundant C_mH_n-type ($m = 1, 2, 3, \ldots$; $n = 1, 2, 3, \ldots$) cluster signals are detected but no structural fragments. Note that an additional time period elapses between the generation of the intact anions and the observed C_mH_n-clusters, detected simultaneously in the cell. The C_mH_n-clusters have to be generated at least 150 μs later in order to arrive in the cell at the same time as the ions of m/z 353. Using the values of the previous Section for m/z 60, the ion formation window becomes 431–521 μs vs. 193–410 μs for m/z 60 and 353 respectively. The mass spectra suggest that the additional input of laser energy cannot be used to increase the internal energy of the intact anions and to induce fragmentation. It is hard to believe that ladder-type mechanisms would become active after delays of over 100 μs—the laser pulse only being 10 ns long—and therefore, simple pyrolysis due to slow heating of the bulk is assumed to be responsible for the C_mH_n-cluster formation.

Figure 4(a)–(c) represent the negative-ion mass spectra of phenol red in the salt form recorded at different T_{gate} and laser power densities. The ion bunch trapped with a T_{gate} of 450 μs is composed primarily of fragments of m/z 271 with only a minority of $[A + Na - H]^-$ ions (A denotes the anionic moiety without sodium, corresponding to the $[M-H]^-$ ions of the neutral form) at m/z 375 and daughter ions at m/z 243. The corresponding ion formation time windows are 92–283 μs for m/z 271 and 29–353 μs for m/z 375. No C_mH_n-clusters are detected due to keeping the laser irradiation power density strictly at the threshold level. Increase of the power density by about 30% gives rise to an impressive series of C_mH_n-clusters, bearing however no structural

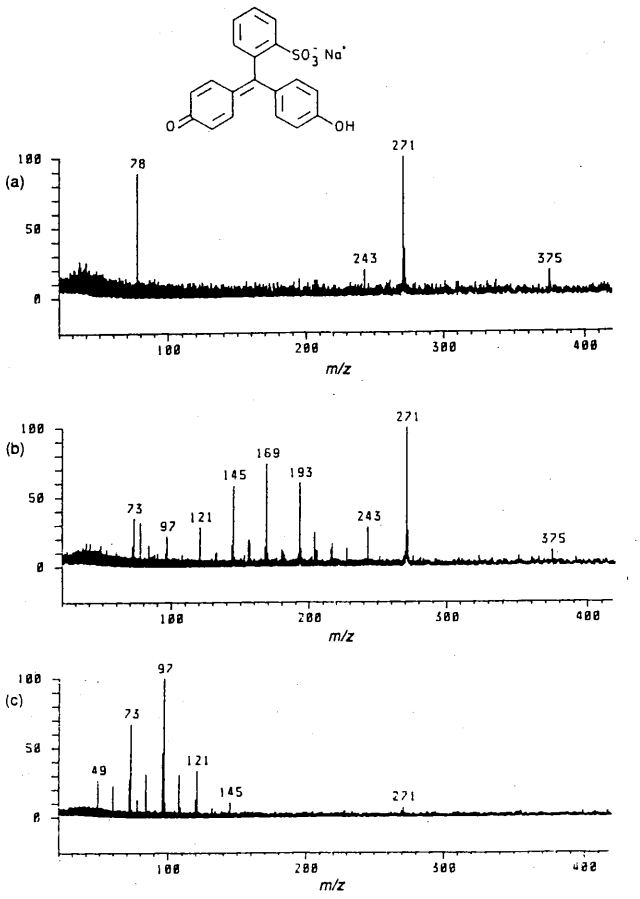

Figure 4. Negative-ion mass spectra recorded by FT LMMS at different T_{gate} and laser power densities from phenol red in the salt form: (a) $T_{gate} = 450\ \mu s$, laser power density $5 \times 10^6\ W\ cm^{-2}$; (b) $T_{gate} = 450\ \mu s$, laser power density $7 \times 10^6\ W\ cm^{-2}$ and (c) $T_{gate} = 600\ \mu s$, laser power density $6 \times 10^6\ W\ cm^{-2}$. The signal at m/z 78 is due to electronic noise.

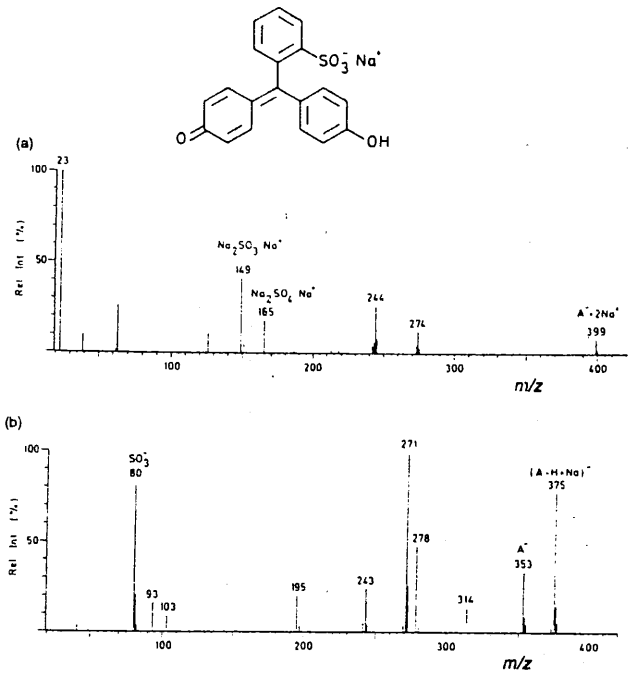

Figure 5. Positive- (a) and negative- (b) ion mass spectra recorded by TOF LMMS from phenol red in the salt form. The data are reprinted with permission of John Wiley & Sons Ltd from Reference 22.

information. The critical adjustment of the laser irradiation power density on the sample with a very small range is typical for ionic compounds LMMS, as opposed to the corresponding neutrals.[5] For the longer T_{gate} (cf. Fig. 4(c)), the low-mass range C_mH_n-clusters appear even under threshold laser irradiation conditions. Increase of the energy regime does not change the picture. The high-mass-range anions are completely absent.

For comparison purposes, Fig. 5 shows the negative- and positive-ion mass spectra taken by TOF LMMS from the salt form of phenol red.[22] The negative-ion mass spectrum in Fig. 5(b) shows striking differences from the spectra in Fig. 4(a) and (b). TOF LMMS apparently yields a clean mass spectrum without C_mH_n-clusters and a much higher contribution from the parent ions. Interestingly, the additional fragment at m/z 195 is observed in FT LMMS for the neutral form but not for the salt.

Figure 6 summarizes the positive-ion mass spectra of phenol red in the salt form recorded by FT LMMS. A substantially higher power density (4×10^7 W cm^{-2}) than for the negative ions from the salt is required. With the short time window, only sulfonate clusters (m/z 149, $Na_2SO_3.Na^+$, and m/z 165, $Na_2SO_4.Na^+$) and a series of low-mass inorganic ions are detected. In contrast, three modest signals are observed above m/z 200 in TOF LMMS (cf. Fig. 5(a)) and assigned to the cationized salt molecule and radical fragments.[22] When FT LMMS samples the ions generated later with a T_{gate} of 600 μs, corresponding to a ion formation time window of 154–392 μs at m/z 421, ions of m/z 421 and 317 are observed. The former signal refers to the cationized salt structure, bearing a Na^+ on the sulfonate and one on the phenolic group. The ions at m/z 317 formally correspond to the loss of sodium sulfonate.

No radical ions are detected by FT LMMS for this product as opposed to the mass spectrum recorded by TOF LMMS and shown in Fig. 5(a). Additionally, the parent ions are found at m/z 399 in the TOF LMMS and m/z 421 in FT LMMS. It is not clear whether this is due to the measurement of a different sample or to a more fundamental reason. First of all, there is the ion formation window. The shortest possible window in FT LMMS is limited by the T_{cell} and inevitably continues over 100 μs or longer. The typical TOF LMMS ion formation window is only 25 ns. As a result, there is an obvious dilution effect of the initial promptly formed ion bunch with the processes starting later. If radical ion formation in TOF LMMS prevails only during and shortly after the laser pulse, then this might explain why FT LMMS does not detect radical ions here and TOF LMMS does. Clearly, further research on this issue is needed.

CONCLUSION

The presented data show that the use of FT LMMS with external ion source gives access to the time profile of the ion production process. Specifically, the effect of the laser power density and the time profile of ion production could be monitored. It has been shown that the reproducibility is sufficient to permit a detailed interpretation of observed peak intensities. It is demonstrated that the relative contribution of the protonated molecules to the total ion current increases with the laser power density while the fragments follow the opposite trend. This effect is interpreted as an indication that distinct processes are involved in the generation of fragments and of $[M+H]^+$ ions. Also, intact cations from quaternary ammonium salts yield an optimal signal long after the laser pulse. Thermal degradation is observed to become important about 300–400 μs after the laser pulse. The fundamentally different behaviour of salts and the corresponding neutral analog under laser microbeam irradiation of solids is shown. As to the negative ions, continuing ion formation suppresses the structural fragments from the mass spectrum of the neutral form, generating the $[M-H]^-$ base peak. Increase of the laser power density on the sample does not yield structural daughters but non-specific C_mH_n-clusters appear. In contrast, the salt form gives prominent C_mH_n-cluster signals slightly above the

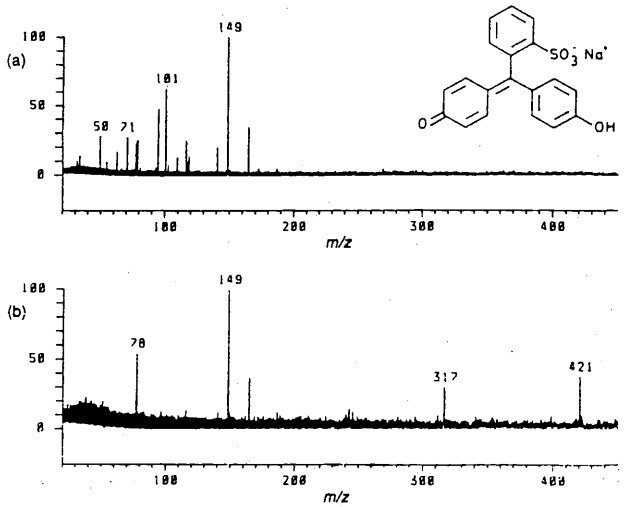

Figure 6. Positive-ion mass spectra recorded by FT LMMS at a laser power density of 4×10^7 W cm^{-2} and at T_{gate} values of (a) 400 μs and (b) 600 μs from phenol red in the salt form. The signal at m/z 78 is due to electronic noise.

threshold while the structurally relevant ions disappear from the spectrum at longer ion formation times after the laser pulse. As to the positive mass spectra of the salt form, optimal ion currents of structural ions are observed long after the laser pulse. Hence, the FT LMMS data demonstrate the importance of the post-laser contribution to the total ion formation from organic solids under laser microbeam irradiation, as opposed to the general concepts arising from the previous TOF LMMS investigations. However, to compare these results with the ones of TOF LMMS, it has to be considered that ions detected in the used FT LMMS with external ion source, must have initial kinetic energies less than 2 eV and emission angles of less than 3°.

Acknowledgements

Wim Van Roy and Luc Van Vaeck are indebted to the National Science Foundation of Belgium (NFWO) as research assistant and research director. Herbert Struyf acknowledges the 'Impulse Programme in Marine Sciences', supported by the Belgian State—Prime Minister's Services—Science Policy Office (contract MS/06/050).

REFERENCES

1. A Verbueken, F. Bruynseels, R. Van Grieken and F. Adams, *Inorganic Mass Spectrometry*, ed. by F. Adams, R. Gijbels and R. Van Grieken, p. 173, Wiley, New York, 1988.
2. L. Van Vaeck, W. Van Roy, R. Gijbels and F. Adams, *Laser Ionization Mass Analysis*, ed. by A. Vertes, R. Gijbels and F. Adams, p. 7, Wiley, New York, 1993.
3. L. Van Vaeck and R. Gijbels, *Fresenius' Z. Anal. Chem.* **337**, 743 (1990).
4. L. Van Vaeck and R. Gijbels, *Fresenius' Z. Anal. Chem.* **337**, 755 (1990).
5. L. Van Vaeck, J. Bennett, W. Lauwers, A. Vertes and R. Gijbels, *Mikrochim. Acta* **3**, 283 (1990).
6. J. Brenna, W. Creasy, W. McBain and C. Soria, *Rev. Sci. Instrum.* **59**, 873 (1988).
7. M. Pelletier, G. Krier, J. F. Muller, D. Weil and M. Johnston, *Rapid Commun. Mass Spectrom.* **2**, 146 (1988).
8. L. Van Vaeck, W. Van Roy, H. Struyf, F. Adams and P. Caravatti, *Rapid Commun. Mass Spectrom.* **7**, 323 (1993).
9. L. Van Vaeck, W. Van Roy, R. Gijbels and F. Adams, *Laser Ionization Mass Analysis*, ed. by A. Vertes, R. Gijbels and F. Adams, p. 177, Wiley, New York, 1993.
10. A. Mathey, W. Van Roy, L. Van Vaeck, G. Eckhardt and W. Steglich, *Rapid Commun. Mass Spectrom.* **8**, 46 (1994).
11. H. Struyf, W. Van Roy, L. Van Vaeck, R. Van Grieken and P. Caravatti, *Rapid Commun. Mass Spectrom.* **8**, 32 (1994).
12. R. J. Cotter, *Anal. Chem.* **56**, 485A (1984).
13. P. G. Kistemaker, M. M. Lens, G. J. Q. Van der Peyl and A. J. H. Boerboom, *Adv. Mass Spectrom.* **8A**, 928 (1979).
14. R. J. Cotter, *Anal. Chim. Acta* **195**, 45 (1987).
15. F. Hillenkamp, *Int. J. Mass Spectrom. Ion Phys.* **45**, 305 (1982).
16. R. B. Van Breemen, M. Snow and R. J. Cotter, *Int. J. Mass Spectrom. Ion Phys.* **49**, 35 (1973).
17. G. J. Q. Van der Peyl, K. Isa, J. Haverkamp and P. G. Kistemaker, *Int. J. Mass Spectrom. Ion Phys.* **47**, 11 (1983).
18. M. De Wolf, T. Mauney, E. Michiels and R. Gijbels, *Scanning Electron Microsc.* **III**, 799 (1986).
19. L. Van Vaeck, J. Claereboudt, J. De Waele, E. Esmans and R. Gijbels, *Anal. Chem.* **57**, 2194 (1985).
20. L. Van Vaeck, J. De Waele and R. Gijbels, *Mikrochim. Acta* **III**, 237 (1984).
21. H. H. Gierlich, F. W. Röllgen, F. Borchers and K. Levsen, *Org. Mass Spectrom.* **12**, 387 (1977).
22. L. Van Vaeck, J. Bennett, P. Van Espen, E. Schweikert, R. Gijbels, F. Adams and W. Lauwers, *Org. Mass Spectrom.* **24**, 797 (1989).

Fresenius J Anal Chem (1994) 350:440–447

Fresenius' Journal of

Quantitative characterization of individual particle surfaces by fractal analysis of scanning electron microscope images

Annick Van Put[1], Akos Vertes*, Darek Wegrzynek[2], Boris Treiger, René Van Grieken[1]**

[1] Department of Chemistry, University of Antwerp (UIA), B-2610 Antwerp-Wilrijk, Belgium
[2] Institute of Physics and Nuclear Techniques, Academy of Mining and Metallurgy, PL-30059 Krakow, Poland

Received: 7 May 1994/Revised: 12 July 1994/Accepted: 25 July 1994

Abstract. Morphological characterization of individual particle surfaces was explored by off-line image processing of data obtained by scanning electron microscope – microanalyzer. The fractal geometry was studied by two methods, the power spectrum and the variogram approach. Both methods were evaluated, theoretically by a series of numerically simulated surface profiles and experimentally on a set of pre-recorded secondary electron images of particle surfaces exposing characteristic textures. It was shown that the fractal approach could stand as a base of the methods enlarging the application of electron probe X-ray microanalyzers for individual particle characterization.

Introduction

Electron probe X-ray microanalysis (EPXMA) has for long been extensively used for quantitative measurements of the elemental composition of individual particles. Scanning electron microscopy (SEM) has been used for their visual morphological examination. Quantitative interpretation of surface textures has also been applied for various purpose (see, e.g. [1]). However several facets of texture ougth to be mastered quantitatively, a discipline in which so far little progress has been made [2]. Texture quantification would not only lead to reliable surface characterization, it would also extend the knowledge on relating structure with surface properties (i.a. adsorption) and with shaping processes (i.a. physical and chemical weathering). In this respect, direct measurements are becoming increasingly important through the availability of sophisticated image analysis systems and associated software. The recent introduction of fractal analysis as a refinement on the conventional roughness parameters provides a powerful tool capable of revealing systematic differences in texture.

The surface characteristic of particles are important since they are really their 'fingerprints'. Indeed, the particle surface texture itself results from a combination of alternating chemical and physical processes, leaving markings that reflect more or less the origin of the particles. So far, SEM exoscopic studies [3] allowed, to a certain extent, the reconstruction of the history of individual suspended particles based on their surface texture. An example can be found in the study of suspended quartz grains in the Loire river [4]. This method is however very time consuming which makes the need of an automated direct method through a quantitative description of texture even more necessary. Therefore an attempt was made to extract information on surface morphology of individual microscopic particles by mathematical processing of SEM images. The interpretation of SEM images is clearly of paramount importance if conclusions are to be drawn about the morphological nature of individual particles. A quantitative description of surface texture, based on digital images of surfaces, could eventually contribute to the classification of particles of different morphology, origin or history. In the first instance, this can be done by incorporating the surface descriptors in a form suitable for computer processing off-line. In a later stage on-line processing may become possible.

Up till now the problem of texture quantification essentially lay in the fact that it is very difficult to grasp a concept such as texture and evaluate it by a single parameter, as we intuitively view texture as a measure of several properties such as smoothness, coarseness, heterogeneity and regularity. However, the introduction of a fractal geometry provided a tool to tackle the problem of describing the concept texture. Theoretically a fractal can be defined as a set for which the only consistent illustration of its metric properties requires a dimension value D (called fractal dimension) larger than the standard topological dimension (T):

Dedicated to Professor Dr. Dieter Klockow on the occasion of his 60th birthday

* *Present address:* Department of Chemistry, George Washington University, Washington, DC 20052, USA
** *On leave from:* State Pedagogical Institute, Kirovograd, Ukraine

Correspondence to: R. Van Grieken

$$D = T + (1 - H)$$

where the parameter H is commonly referred to as the codimension. This practically means that curves can have their ruggedness described by allocating a fractal number between one and two establishing the space filling ability of the curves. Similarly, the concept of fractal dimension can be extended to higher dimensions, e.g. a rugged surface can be given a number between 2 and 3. Assigning fractal dimension values to rugged surfaces therefore allows the texture to be mastered quanitatively rather than qualitatively. Several methods may be applied to obtain the codimension H and thus the fractal dimension D.

In a first method the fractal dimension of the function z(x) may be defined in terms of the Fourier power spectrum $P(\omega)$ of the function, as the Fourier power spectrum falls off with increasing frequency ω [5], proportional to:

$$P(\omega) \approx \omega^{-(2H+1)}$$

By using a linear regression on the log-log plot of the observed power spectrum (PWS) as a function of frequency, the codimension H and the fractal dimension D can be determined. This method of surface analysis in terms of the power spectrum appears to be so far little explored in the microscopic domain [6] in comparison with the Fourier approach of macroscopic surfaces such as landscapes and environmental topographies [7].

Another method for fractal dimension calculation that was implemented is the so-called variogram method. This method can be defined in terms of how the variance of interpixel differences changes with distance. The fractal dimension of the function z(x) may then be estimated from a log-log plot of the variance of increments versus increments:

$$\mathrm{Var}(x) \approx x^{2H}$$

The resulting graph is called a variogram, from which the name variogram method of this fractal dimension calculation procedure originates. The variogram method has been extensively adapted to analyze a number of environmental data (from anemones to rainfall). A review of the applications has been given by Burrough [8].

Other experimental methods for fractal-based characterization of surface texture exist, but are more complicated being mainly based on the different sectional approaches and are beyond the intention of this paper. The vertical section method comprehends for example the structured walk technique [9] or the box dimension approach [10] on vertical sections to the fracture plane, whereas the slit island technique [6] makes use of sequentially prepared sections parallel to the fracture plane and is based on the perimeter-area relation.

Experimental

Image acquisition

The images are recorded and stored with the Tracor Northern TN 2000 and TN 1310 automating system of a JEOL 733 electron microprobe. The images collected for our purposes were 256 analysis pixels in both x and y directions. All images were collected in the secondary electron mode because the secondary electron images generally show very low noise level and a sharp contrast with high spatial resolution [11]. The absolute signal intensity at each analysis pixel was converted from an analogue to a digital signal by an 8 bit resolution analogue to a digital converter (ADC). The system is thus capable of coding the images in as much as 256 brightness levels. Since the system does not offer adequate bulk storage and processing facilities, the images are stored on floppy disk or on tape and transferred to VAX/VMS minicomputer for further processing.

Image processing

To constraint the processing time and to simplify the interpretation for the power spectrum method, the one-dimensional version of the fast Fourier transform (FFT) was preferentially applied. In this one-dimensional approach, the FFT was run consecutively on the 256 transsect lines composing the image. The PWS was calculated by recombining the imaginary and real part of the transform to establish real data. Subsequently the 256 power spectra, taken from serial sections, were averaged to reduce the influence of microstructure and statistical artefacts. This average PWS was finally transformed into a log-log plot before exercising a linear regression fit routine. The fractal dimension was estimated from the slope, considering the following equation:

$$P(\omega) \approx \omega^{-(5-2D)}$$

The variogram method of measuring the fractal dimension has the advantage that it is an easy method in application, which does not involve too difficult mathematics and which does not require any preceding data adaptation. Additionally, it was based on good statistics since the method was applied in its two-dimensional version, i.e. on the whole data matrix simultaneously. Hence the occurrence of possible problems due to directionality of the surface is also excluded. Since it is more convenient, the standard deviation was calculated and used instead of the variance. Nevertheless, the term variogram will be maintained because it is commonly used in the literature. For this method, it was sufficient to scan the whole 256×256 matrix, to calculate the differences in image intensity, in the horizontal and the vertical direction. Starting with a pixel step size equal to 1, the procedure was repeated for successively increasing pixel step increments (up to 200). The distributions of the intensity differences were approximately Gaussian, with zero mean, for all increment settings. The standard deviation $\sigma(k)$ value corresponding with a certain pixel step k was calculated by recombining the individual sums of squared differences respectively for the x and y directions. The whole procedure was repeated for a limited number of pixel distance up to 200, because for higher pixel distances the statistics readily deteriorate. Also at higher pixel steps, only differences in the boundaries will be measured. Subsequently the standard deviation was plotted as a function of the pixel step in a log-log graph. From the linear least-

squares fit of the data the fractal dimension could be calculated as:

$$\sigma(k) \approx k^{2(3-D)}$$

with T = 2.

Results and discussion

Fractal Brownian function simulation

First the fractal dimension calculation methods based on power spectrum and variogram were tested on fractal Brownian motions (FBM) with controlled fractal dimensions. For this purpose, a set of FBM's were generated by the successive random addition algorithm [12]. These fractal Brownian functions have the same properties as the conventional fractal Brownian function, namely a power spectrum $P(\omega)$ that varies with $\omega^{-(5-2D)}$ and a variogram that varies with $(x)^{2H}$.

In Figs. 1–4, four fractal Brownian functions with theoretical fractal dimensions varying from 1.2 to 1.8 with increments of 0.2 (A) together with the PWS (B) and variogram (C) evaluation of the fractal dimensions are shown. This set of functions covers nearly the whole possible range of fractal dimensions. The functions were generated with 4096 points. A comparison between the theoretical and the experimental dimension values shows that both methods provide fair estimates of the fractal dimension values in the relatively broad range.

Observations on natural surfaces

Images of real particle surfaces were collected with SEM in view of an evaluation of their dimensionality by both fractal dimension calculation procedures. However before engaging ourselves with the fractal calculations, we acknowledged the necessity to verify the applicability of the methods on the intensity images of these surfaces rather than on the surfaces themselves. Pentland [13] proved, in this respect, that the fractal dimension methods can be used on particular image data as a representative of the actual three dimensional fractal surface. Moreover the obtained fractal dimension for the intensity surface agrees with that of the real three dimensional surface.

The two naturally occurring particle surfaces that will be represented were chosen so that they clearly demonstrate which information their PWS or variograms provide. In addition they also allow a simple and illustrative interpretation of this information. Two silicon dioxide particles were chosen for this purpose. The first particle was a radiolaria particle, one out of two possible SiO_2 (opal) forms of biogenic origin, the round shaped radiolaria and the oblong shaped diatoms. The second particle was a quartz particle of lithogenic origin, selected from a suspended matter sample from the Scheldt estuary (Belgium). These two surfaces were processed with both PWS and variogram methods. The 3d representations of the morphology of these particles (at the magnification 3000×) are shown in Fig. 5A and 6A.

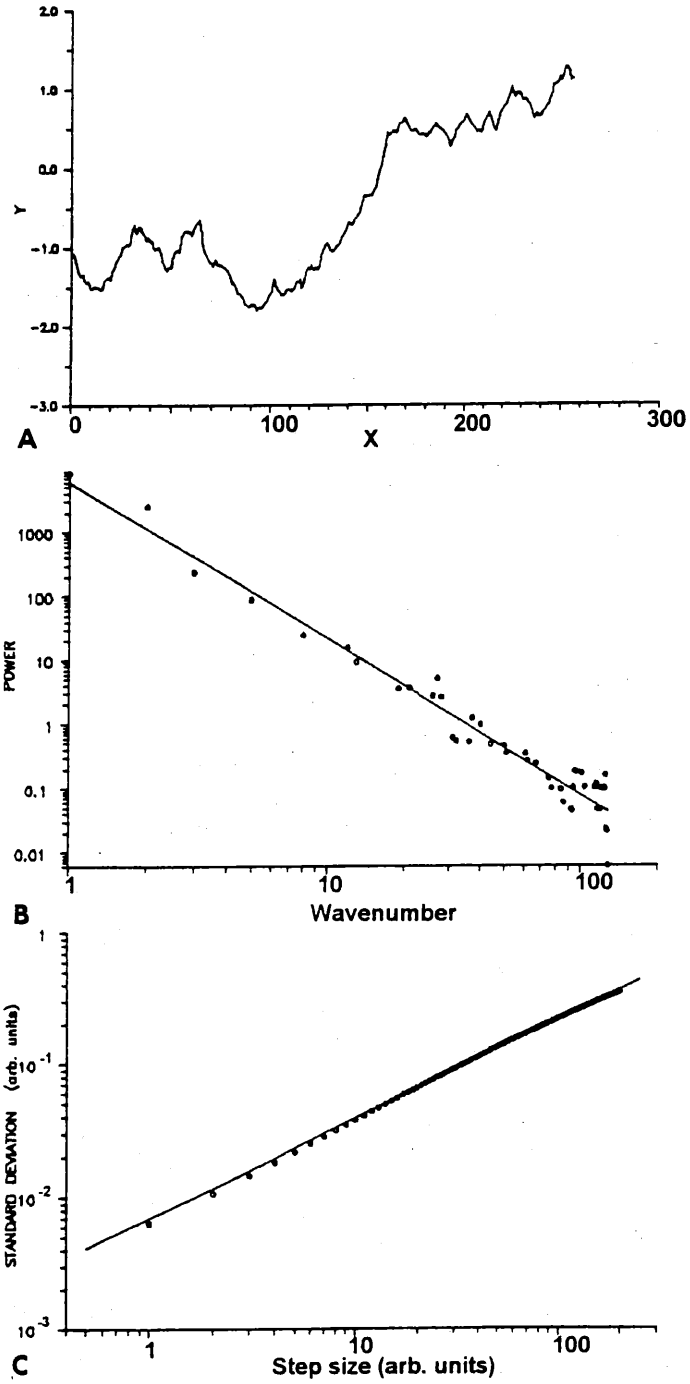

Fig. 1A–C. Fractal Brownian function, generated by the successive random addition algorithm, with theoretical fractal dimension 1.2 (**A**) together with the PWS (**B**) and variogram (**C**) evaluation of fractal diameter

Biogenic silicon dioxide particles

Since all radiolaria (and diatoms) reveal a regular surface pattern and overall structure, it is apparent that any attempt to differentiate biogenic from lithogenic SiO_2 particles has primarily to be based on differences in morphology rather than on differences in composition. Many studies tried to use morphology based parameters such as the shape factor. But no exclusive selection can be estab-

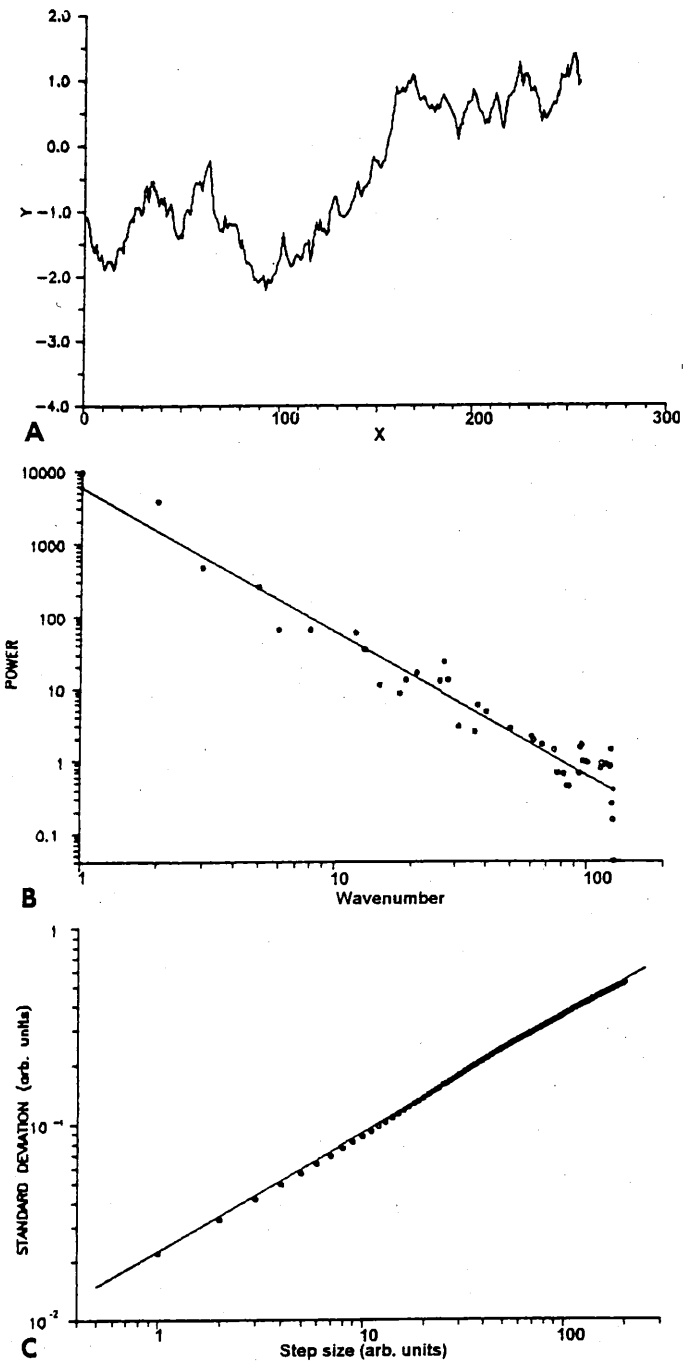

Fig. 2 A–C. Fractal Brownian function, generated by the successive random addition algorithm, with theoretical fractal dimension 1.4 (**A**) together with the PWS (**B**) and variogram (**C**) evaluation of fractal diameter

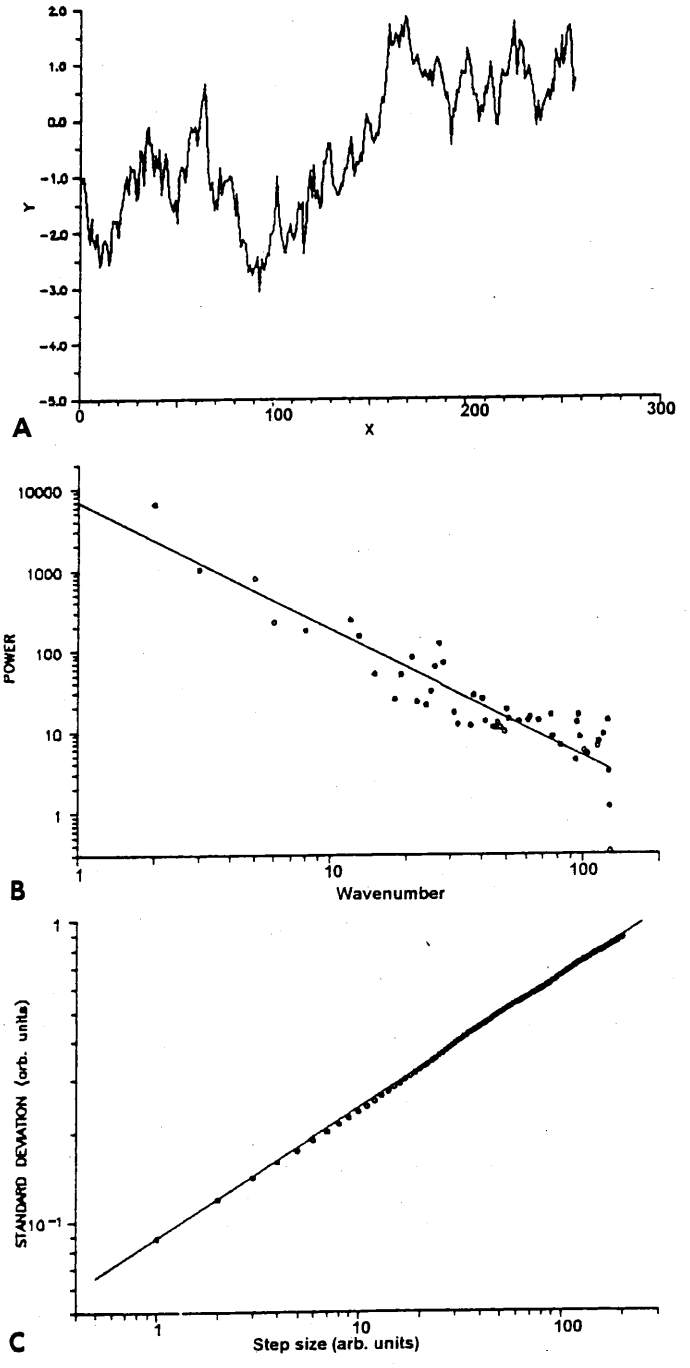

Fig. 3 A–C. Fractal Brownian function, generated by the successive random addition algorithm, with theoretical fractal dimension 1.6 (**A**) together with the PWS (**B**) and variogram (**C**) evaluation of fractal diameter

lished because the shape factor is generally not sensitive enough. Obviously an alternative solution may be found in the application of the technique which picks up and reflects periodicity. In this respect Fourier transform based methods have proven their applicability. The FFT is ideally suited for describing the periodicity, as the fundamental spatial period of the pattern will appear as distinguishable prominent peaks in the PWS at locations corresponding with the frequency of the pattern.

The PWS for the radiolaria exhibits a broad peak at an average wavelength of 1.2 μm as it is an average of 256 line scans with mutually slight different periodicity (see Fig. 5 B). The practical meaning of this dominant wavelength of 1.2 μm is that the average distance between the middle points of two neighbour holes on the surface of radiolaria is 1.2 μm. The same perception can be made from the variogram where the distance between the middlepoints of the holes corresponds with a minimum in the

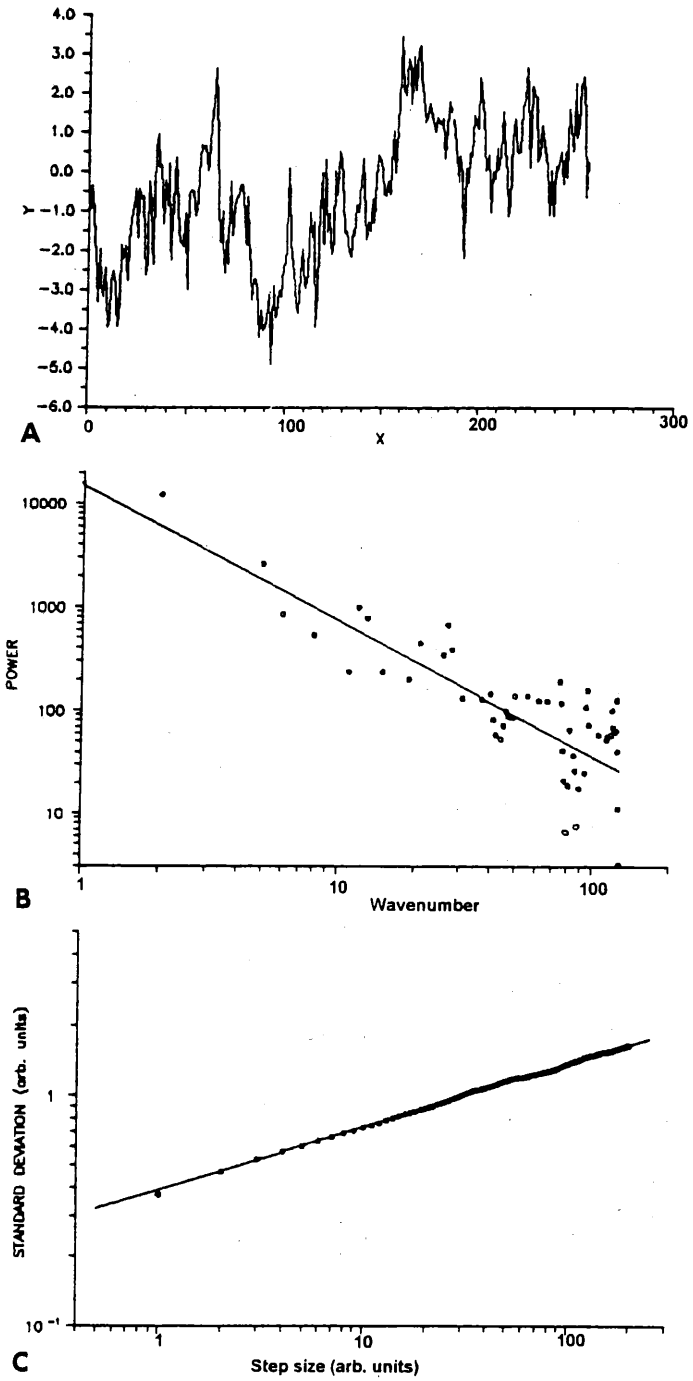

Fig. 4A–C. Fractal Brownian function, generated by the successive random addition algorithm, with theoretical fractal dimension 1.8 (**A**) together with the PWS (**B**) and variogram (**C**) evaluation of fractal diameter

plot (see Fig. 5C). This minimum reflects the narrow variance for the distribution for the step size equal to 1.2 μm.

It must however be stated that the correspondence between the PWS and the variogram for the scaling of the microstructure is not so straightforward as suggested. The variogram scales the surface structure in increments whereas the FFT expresses the same surface morphology in wavelengths. To relate the pixel size increments with the PWS wavelengths a factor of two should be incorporated. Therefore, to avoid any confusion, it would have been better to relate the maximum power peak with the maximum in the variogram (at 0.6 μm) taking into consideration that the scaling of the microstructure by the two methods differs by a factor of 2.

So surface structures with periodic structure can have their pattern characteristics extracted and differentiated by both the PWS and variogram methods. Not only will, for example, the appearance of a peak in the PWS and variogram allow the recognition of biogenic particles, the position of peak maxima may also be characteristic for the radiolaria/diatom type. In case that the positions differ significantly, it may be sufficient to perform a single line scan over the surface of the biogenic particle in the automatic routine (at a specified constant magnification) to specify the radiolaria/diatom types by performing FFT (or variogram) routine. The problem associated with the directionality of the periodicity – the diatoms have their periodicity directed along their longest axis, whereas radiolaria do not expose any directionality of their surface pattern – can be solved by letting the line scans coincide with the direction of the maximum diameter. One major drawback is that not all opal particles have their periodicity aligned along a length axis; some radiolaria have a rotational symmetry. In these cases a more complicated rotational PWS routine can provide a solution. Nevertheless, this solution would implicate a compilation of adaptations, making it practically unattractive.

It should be emphasized that the problem of differentiating and characterizing biogenic particles is not restricted to silicon dioxide particles only. It is equally hard to differentiate, based on composition solely, between calcite/aragonite particles and coccolith/foraminifera organisms.

Lithogenic quartz particle

Careful analysis of the PWS plot (Fig. 6B) for the quartz particles indicates that the spectrum splits up into 3 distinct subregions, each characterized by a different fractal value. The short distance part is sensitive to the discrete approach imposed for the computation of the PWS as it is subjected to large statistical noise. This is manifested by the fractal dimension value for this range, which exceeds 2. Such a value has neither a physical nor a fractal meaning as it depicts the unnatural case of increasing amplitudes with increasing frequency. Such a noise event can impossibly be accounted for by fractal Brownian functions, as such a situation cannot be caused by Brownian processes. This range is also far too short and no lower limit distance could be determined. To determine, as yet, the lower limit distance, higher magnification examination of the sample has to be performed [14].

The intermediate range between approximately 9.3 and 0.82 μm is characterized by a fractal dimension equal to 1.29. The question is now, over how many orders of magnitude a power law should hold in order to give rise to an effective surface dimension greater than 1. Normally it is believed that reliable estimates of the dimen-

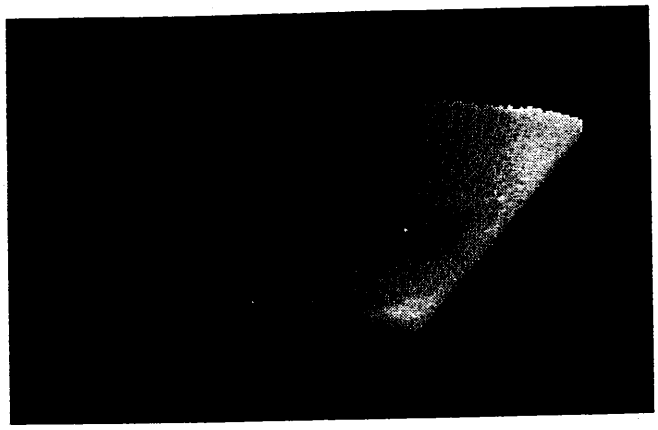

A

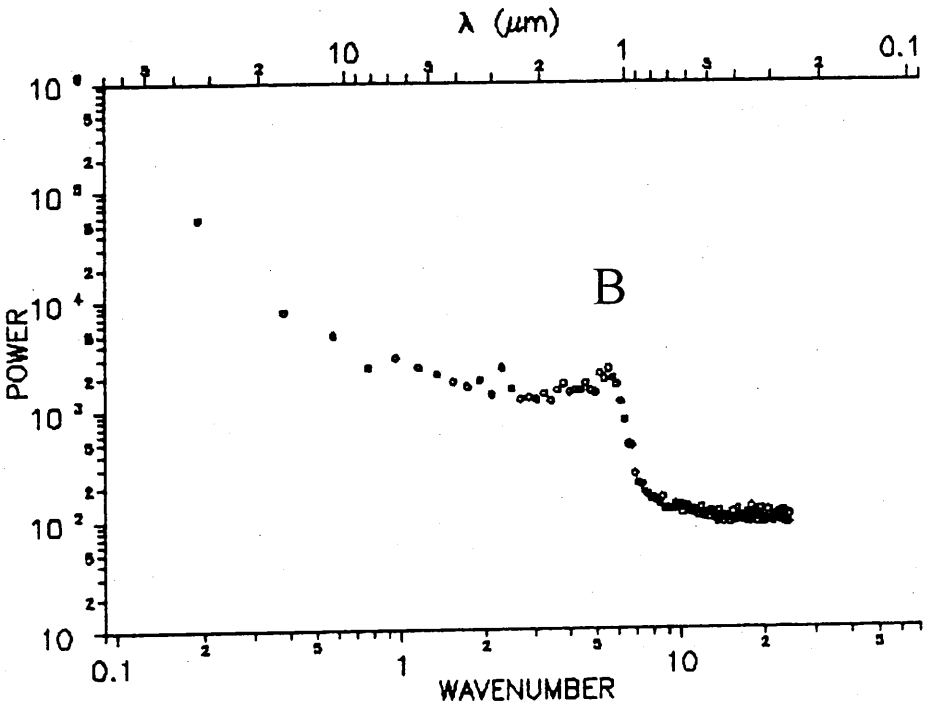

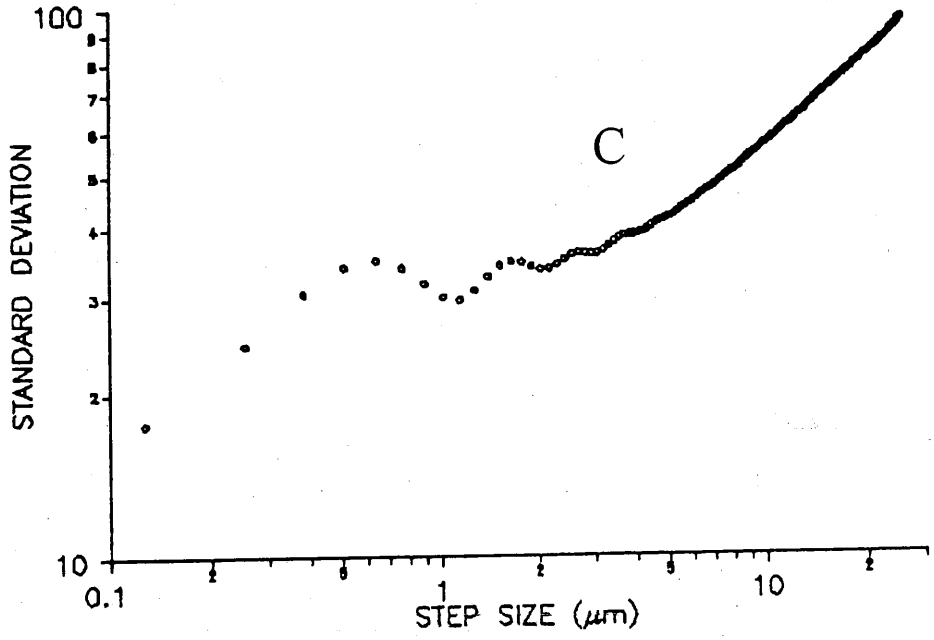

Fig. 5A–C. Three dimensional representation (A) of the secondary electron image of a biogenic SiO_2 particle (radiolaria) at magnification 3000× along with PWS (B) and variogram (C)

A

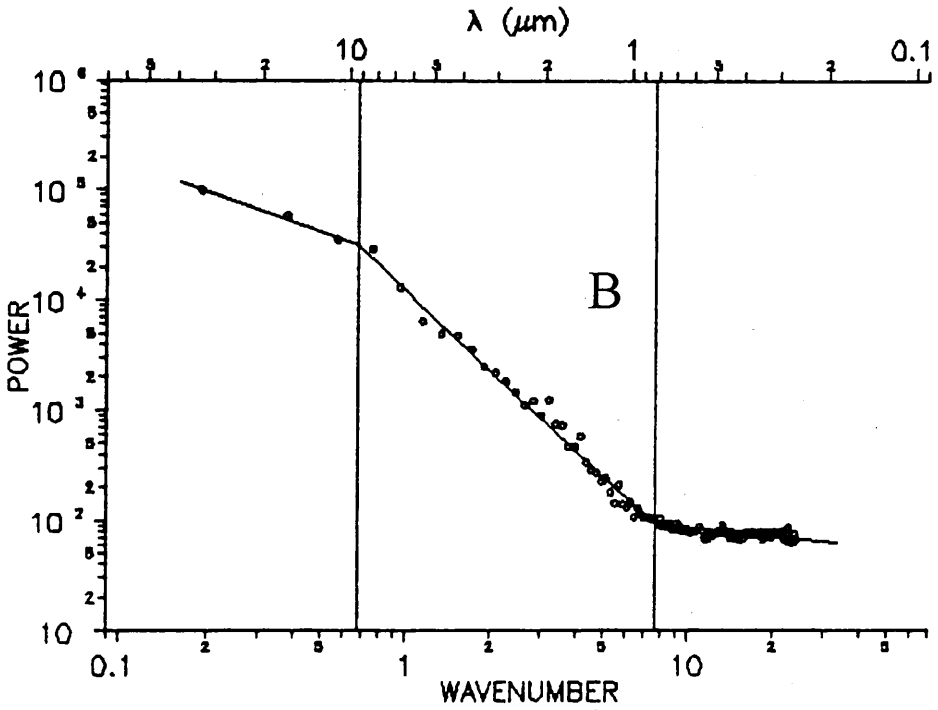

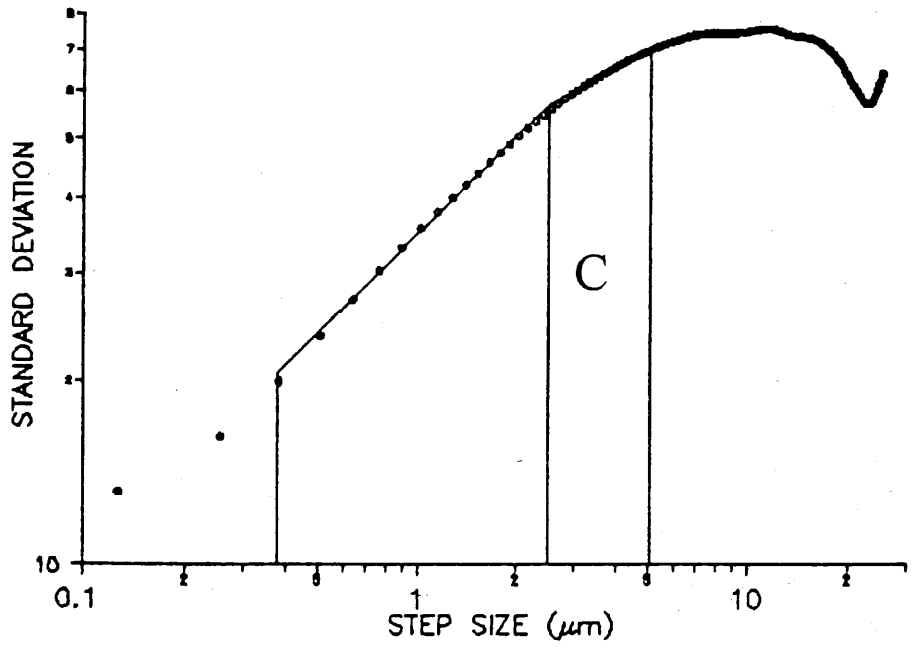

Fig. 6A–C. Three dimensional representation (**A**) of the secondary electron image of a lithogenic quartz particle, originating from the Scheldt estuary, at magnification 3000× along with PWS (**B**) and variogram (**C**)

sion can only be obtained when the power law extends over at least two decades [15]. This stringent criterion, however, has not been met so far in the discussion of fractal surfaces or in environmental data. Mandelbrot himself [6], for instance, has focused his fractal dimension evaluation of fractured surfaces of metals on the central straight portion of the PWS which hardly stretched over a range of approximately 1.5 decades. Besides, real images cannot be true mathematical fractals, defined to exist at all scales [16]. Therefore, with necessary caution, it can be specified that the fractal dimension of the particle surface shows fractal properties over a range of 1 decade. The long distance range is built on an insufficient amount of data to reveal any relevant fractal property.

The results for the variogram method are shown in Fig. 6C. The dimension for the variogram has been estimated through a value between 2 and 3 as the method was applied to the whole surface rather than to transsect lines. The standard deviation in the variogram does not increase without limit, but attains a more or less constant value from a certain step size on. This range corresponds most likely with the spatial structure of the surface. The short distance range (first 5–6 points approximately) should also be excluded from the fractal evaluation as it is not relevant to the fractal determination [17]. Besides the long and the short distance region, the variogram was characterized by two additional ranges covering a transition zone, which was as such preferentially approached by a multiple fit. These two central ranges jointly coincide remarkably well with the fractal range in the PWS, as they together cover 1 decade of the microstructure, between approximately 0.76 and 10.2 μm. There is, however, slight inconsistency with average values obtained by PWS and variogram results. In the variogram method the values of fractal dimensions were 2.47 for the range from 0.38 to 2.52 μm and 2.69 for the range 2.52 to 5.08 μm. This difference is explained by the different grounds of the both methods; still it is not essential.

Burrough [8] interpreted the sets of dimensions for restricted ranges in his variograms as the result of the variety of natural phenomena having their levels of variability clustered at particular scales and to a certain degree displayed over multiple spatial scales. Therefore, the subdivision of the central region for the suspended particle surface may be interpreted in the same way, namely as a compilation of two fractal impacts.

Conclusions

The fractal based characterization of texture by means of SEM reveals systematic differences in texture and is more detailed than the conventional roughness parameters. Both the PWS and variogram method are sensitive enough for surface roughness evaluation and moreover they coincide with the human concept of roughness. Generally we can decide that the central region satisfying the fractal power law for about one decade in scale is the most appropriate zone for fractal characterization. The contribution of noise can than be considered to be minimal. Moreover, this region is well defined both by the PWS and variogram method. Herewith it should be recognized that the fractal description will not only allow to characterize the microstructure of a surface. It may also be possible that the fractal dimension in combination with the range over which a certain process (e. g. weathering) operates is sensitive to the type of processes and to the extent they had an impact on the surface. As such the fractal description may prove its value for future quantitative approaches of the impact of a variety of processes on the surface structure and in any research field concerned with physical and chemical properties related with surface structure. Final dimension calculation methods may also be very useful tools to be incorporated in routine procedures for individual particle analysis when the automation system is extended with a powerful image processing system. It could complement the particle classification procedure, based generally on composition only, and it could contribute to the differentiation of the particles, which cannot be differentiated on the basis of their composition alone.

Acknowledgements. The work was carried out within the Impulse Programme on Marine Sciences, supported by the Belgian State – Prime Minister's Services – Scientific Policy Office under contract MS/06/050.

References

1. Bull P (1987) In: Goudie A (ed) Geomorphological techniques. Allen and Urwin, London, pp 206–211
2. Von Lutz G (1990) Z Geol Wiss 18:615–635
3. Le Ribault L (1975) L'exoscopie. Méthode et application. Mém Compagnie Française des Pétroles (ed) Paris, pp 232–239
4. Manickam S, Barbaroux L (1987) Sedimentology, 34:495–510
5. Falconer K (1990) Fractal geometry, mathematical foundations and applications. Wiley, Chichester
6. Mandelbrot B, Passoja D, Paullay A (1984) Nature 308:721–722
7. Sayles R, Thomas T (1978) Nature 271:431–434
8. Burrough P (1981) Nature 294:240–242
9. Dauskardt R, Haubensak F, Ritchie E (1990) Acta Metall Mater 38:143–159
10. Chesters S, Wen H, Lundin M, Kaper G (1989) Appl Surf Sci 40:185–192
11. Goldstein J, Newbury D, Echlin P, Joy D, Fiori C, Lifshin E (1984) Scanning electron microscopy and X-ray microanalysis. Plenum Press, New York
12. Voss R (1985) In: Earnshaw R (ed) Fundamental algorithms in computer graphics, Spinger, Berlin Heidelberg New York, pp 805–835
13. Pentland P (1984) SRI Technical note 280
14. Van Put A (1991) Ph D Dissertation, University of Antwerp
15. Feder J (1988) Fractals. Plenum Press, New York
16. Pfeifer P (1984) Appl Surf Sci 18:146–164
17. Naudts J (1990) Personal communication

ELSEVIER

Analytica Chimica Acta 297 (1994) 27–42

ANALYTICA CHIMICA ACTA

Microanalysis of atmospheric particles and fibres by electron energy loss spectroscopy, electron spectroscopic imaging and scanning proton microscopy

Patrick Berghmans, Jasna Injuk, Rene Van Grieken and Freddy Adams

Department of Chemistry, University of Antwerp (UIA), Universiteitsplein 1, B-2610 Antwerp-Wilrijk (Belgium)

Received 23rd April 1993, revised manuscript received 8th July 1993

Abstract

Some aspects of micro- and surface-analytical beam techniques for studies of individual airborne particulates are reviewed. Applications of the microanalysis techniques of electron spectroscopic imaging, secondary ion imaging and proton induced x-ray-micro analysis (micro-PIXE) for the characterization of individual particles in environmental samples and chemically modified asbestos fibres are discussed.

Keywords: Asbestos fibres; Atmospheric particles; Electron spectroscopic imaging; Secondary ion imaging; Micro-PIXE

The present drive for analytical developments enabling spatial, depth, point and bulk analysis methods for surface elements can be credited to their increasing importance in many areas of science and technology. In environmental chemistry, microscopical surface characterization is particularly relevant. The composition and structure of microscopically sized environmental particles are important parameters for their persistence and fate in the environment, their toxicology and for inferring the assignment of particles to specific sources of pollution. Chemical analysis has also shown the presence of unique surface layers on environmental particles. In addition, elemental concentration levels in individual particles often show substantial variations from the average, even if the particles are morphologically similar. This indicates that various particles, even within a narrow size range, may be derived from different emission sources or formation mechanisms. Micro-analysis can reveal whether a specific element or compound is uniformly distributed over all the particles of a population or whether it is a component of only a specific group of particles. In rare cases the lateral and depth distribution of elements within one particle has been inferred. With such data, one can more easily interpret, pinpoint and eventually control sources of particulate pollution, and more refined information about source mechanisms and heterogeneous surface reactions can be derived.

Correspondence to: F. Adams, Department of Chemistry, University of Antwerp (UIA), Universiteitsplein 1, B-2610 Antwerp-Wilrijk (Belgium).

SSDI 0003-2670(93)E0401-R

Microscopical particle characterization is nowadays one of the more challenging aspects of microbeam analysis because it requires microprobe capabilities, which enable the generation of compositional maps that establish the lateral distribution of an element. Many of the available microscopic techniques permit analysis of microscopic particles or individual fibres, but have the disadvantages of sampling error problems, they suffer from excessive lengths of time required to obtain the data and require extensive sample preparation. Little research has been done, however, on the direct characterization of the microscopic variation of element concentrations, including trace species, within individual particles. Quantitative analysis is often difficult because of the uncertainty in defining a precise analytical volume. Also, with techniques involving energetic beam interactions, the sample may be altered because of chemical reactions, selective volatilization of elements or migration in the solid. Finally, the analytical signals often depend in a complex way on the instrumental and sample parameters.

Several analytical techniques have been used to study surface layers and/or to analyze elemental concentrations as a function of depth for a collection of particles without lateral spatial resolution. These techniques include x-ray photoelectron spectroscopy (XPS), Auger electron spectroscopy (AES), photoacoustic spectroscopy (PAS), and conventional secondary ion mass spectroscopy (SIMS).

In order to reduce the effects of the intrinsic limitations associated with some techniques (such as reduced sensitivity for some classes of substances, owing to the very small analytical vol-

Table 1
Methods for surface analysis used in studies of microparticulate solids

Probe	Analytical signal	Technique	Acronym	Resolution	
				Lateral	Surface
Electrons	Electrons	Auger electron spectroscopy	AES	50 nm	1–2 nm
	Electrons	Electron energy loss spectroscopy	EELS	10 nm	thin sample
	X-rays	Energy dispersive x-ray spectrometry	EDXRS	0.2 μm	2 μm
X-ray photons	Electrons	X-ray photoelectron spectroscopy	XPS	10 μm (tube)	nm
	Electrons	X-ray absorption near edge spectroscopy	XANES	1 μm (synchrotron)	nm
Low energy ions	Ions	Ion scattering spectrometry	ISS	none	nm
keV ions	Ions	Secondary ion mass spectroscopy (dynamic)	SIMS	0.1 μm	3 nm
	Ions	Secondary ion mass spectroscopy (static)	SSIMS	1 μm	nm
IR photons	Photons	Fourier transform infrared spectroscopy	FTIR	20 μm	μm
UV photons (laser)	Ions	Laser microprobe mass analysis/Fourier transform laser microprobe mass spectrometry	LAMMA/ FT-LMMS	1–5 μm	50 nm
X-rays (synchrotron)	X-rays	Fluorescence x-rays	SRXRF	1 μm	none
Protons	X-rays	Micro-proton induced x-ray micro-analysis	micro-PIXE	1–10 μm	thin sample

umes sampled), the combined use of different analytical and visualization techniques is necessary. This allows a much more complete and detailed study of individual particles. For example, the morphological resolution and the large depth of focus associated with scanning electron microscopy (SEM) is useful in morphological analysis, while SIMS is useful in the determination of the chemical composition, because of its high sensitivity. The techniques are complementary and are very powerful when used together.

Some aspects of micro- and surface-analytical techniques for environmental studies as well as microanalysis applied to individual environmental particles have previously been reviewed [1–3]. Table 1 gives an overview of the main analytical features of some micro- and surface-analytical beam techniques for the characterization and analysis of environmental particles. The techniques are classified by the type of probe used to obtain the observed analytical signal and also the limitations in surface and lateral resolution of each type are summarized.

Heterogeneities in the composition in single particles are frequently observed from site to site, and SIMS offers special capabilities for particulate analysis. The inherent depth profiling capabilities of SIMS, along with its high sensitivity and full periodic table elemental coverage, its capability to measure isotope ratios and finally its ion imaging potential of specific constituents, make it uniquely suited to the study of intraparticle trace element concentration gradients. For studies of the depth distribution of trace elements, SIMS can be successfully applied to individual particles [4]; yet, irregular topography of particles can degrade the depth resolution considerably. When the imaging capabilities of a secondary ion microprobe or microscope are employed, an image depth profile can be generated which yields information on three-dimensional elemental distributions within single, micrometer-sized particles [5,6]. With an ion microscope, such information can be acquired simultaneously for a group of individual particles present in an image field typically on the order of 100 μm in diameter. The limiting lateral resolution is about 0.5 μm for the ion microscope and less than 0.1 μm for the scanning ion microprobe. When molecular information of particles is needed, both laser microprobe mass spectrometry (LMMS) [7,8] and SIMS can be used since they exhibit qualitatively the same positive ions. The speciation capabilities of LMMS and time of flight (TOF) LMMS have been exploited successfully, e.g., in the study of polyaromatic compounds in particulate samples [9,10].

SEM has allowed the compositional analysis of particles down to μm diameters using energy dispersive x-ray analysis (EDX). However, it is unsuitable in the majority of cases for the analysis of smaller particles. The scanning transmission electron microscope (STEM) extends the size range of EDX analysis to the nm region, as a fine electron probe and thin specimens lead to increased spatial resolution. However the low collection rate of x-rays from small sample volumes becomes a limiting factor, leading to long data acquisition times. An alternative analytical method in the STEM is electron energy loss spectroscopy (EELS). EELS seems to have promising potential as an analytical technique in the chemical characterization of airborne particulates, but thus far few applications to single particle analysis have been reported. Combined with EDX for heavy element quantification, and with electron diffraction, where appropriate, the STEM seems highly suited to aerosol analysis.

Whereas Auger electron spectroscopy (AES), x-ray emission spectroscopy, and many other techniques are concerned with the analysis of the several possible processes induced by the de-excitation of the atom which received the energy lost by the incident electron, EELS deals with the energy loss (ΔE) distribution of the electron probe at the exit surface of the thin specimen. It is beyond the scope of this paper to give a complete review of these techniques and of their applications to chemical analysis of particulate and fibrous material; several hundreds of articles are published every year in various journals or conference proceedings. In order of glance through some recent publications, we have only selected a few papers dealing with EELS [11–13], AES [14,15], x-ray emission spectroscopy [16]. A brief discussion of applications of AES and x-ray

photoelectron spectroscopy (XPS) to single particle analysis is given by Powel [17]. Cox III and Linton [18] already discussed extensively the aspects of environmental applications of XPS involving airborne particle chemistry. Small et al. [19] and Gordon et al. [20] reported on the use of Fourier transform infrared spectroscopy (FTIR) to study atmospheric pollutants and to characterize organic substances in aerosols.

The use of focused MeV ion microprobes for studies of materials samples has increased rapidly during the last decade. Today, about 40 available nuclear microprobes are used around the world for material analysis. The scanning proton microprobe (SPM) utilises a well-focused beam of high energy protons (1 to 3 MeV) or other light ions, to scan a specimen. In its operation, it is similar to the SEM. After the incident MeV ion beam enters the target, most of the particles penetrate the specimen and roughly retain their incident directions. Part of the energy transferred to the target as the impinging ions decelerate produce many types of radiation, each of them containing information about the atoms and nuclei in the matrix. A variety of signals that can be collected and processed are used to obtain unique information on the composition of the sample. It uses PIXE (proton induced x-ray emission), RBS (Rutherford backscattering) or RFS (Rutherford forward scattering) and NRA (nuclear reaction analysis) for elemental or isotopic analysis.

In what follows we will illustrate the potential of microscopical characterization of fibrous and environmental particles with two examples from recent laboratory experience. First we give examples of the characterization of surface modified asbestos particles using SIMS and EELS. Then we treat the application of the SPM for the characterization of the North Sea aerosol.

1. Surface characterization of chrysotile asbestos fibres

In order to reduce the cytotoxic and long term haemolytic activity of asbestos fibres, there have been many efforts to modify the surface reactivity. The use of $TiCl_3$ as a modifier provokes a modification of the surface properties specific to the mineral concerned [21,22]. Also, the gas phase reaction of chrysotile with organosilane compounds has led to thermally and chemically stabilized asbestos fibres [23]. For a better understanding of specific surface structures and reactivity of the modified fibres, in relation to their biological reactivity, knowledge about the spatial distribution of reaction products is necessary. The inhomogeneity on the microscopical level of the composition of the asbestos fibres and the small fibre size require the use of highly sensitive microanalytical techniques providing high lateral resolution. Given these constraints, EELS, in conjunction with electron spectroscopic imaging (ESI), is a very suitable analytical method to address this problem. As will be demonstrated, these techniques offer the possibility of detecting differences in surface composition and mapping the reaction products on the modified chrysotile surfaces down to the sub-micrometer level.

The elemental distributions measured with ESI are processed with a commercial digital image-processing unit (IBAS 2000, Zeiss/Kontron, Eching, Germany), operated at an image size of 512 $\times$ 512 pixels and a 8 bit grey value resolution. The images as acquired from a TV camera (SIT 66, Dage-MTI) are automatically analyzed. The EELS instrument (ZEISS EM 902, Oberkochen, Germany) is used nearly in the original version completed by a digital control of the photomultiplier detector with the computer (IEEE 488) interface system and an image-processing system with some special image processing programs (Zeiss/Kontron). The analyses were performed at electron optical magnifications of 50 000 to 140 000, corresponding to a selected area of approximately 200–100 nm in diameter (with the filter entrance aperture of 100 μm acting as a selected-area aperture). The optimal signal-to-noise ratios of the elements of interest were obtained with an objective aperture of 60 μm. In all cases, the energy-selecting slit was set to a width of 10 eV.

One of the severest limitations of the usual procedures for processing energy-filtered images is the difficulty in obtaining accurate data on the net elemental intensity. First, it is necessary to

define an analytical model for the background estimation. The background intensity usually decreases smoothly with energy loss ΔE, approximating to the power-law form $I_b = A\Delta E^{-R}$, where A and R are constants which can be determined by examining the energy dependence of I_b at energy losses just below the ionization threshold. Unfortunately, both A and R may vary across the specimen as a result of local changes in thickness and chemical composition, both of which affect background intensity and its energy dependence. Therefore the background estimation procedure must be performed separately for every pixel point of the image. Generally a three-image procedure is used, where two images are taken before the charateristic edge and one image at the specific edge, but in some critical situations the application of this procedure does not yield reliable results. Indeed, for high-resolution mapping of elements with relatively low concentration, the signal-to-background ratio is generally quit low, putting severe constraints on procedures which rely on the extrapolation of the background using two measurements in the vicinity of the edge.

A perforated supporting film of polyvinyl formaldehyde (Formvar) on 700 mesh electron microscope grids is used to mount the modified fibres. The deposited fibres become electrostatically attached to the supporting film. To avoid measuring carbon from the support material, only the portion of the asbestos fibres that are not lying directly on the support material are selected and analyzed.

For obtaining cross sectional information, the fibres are embedded in a Spurr (epoxy) resin and thin sections (ca. 35–45 nm thick) are cut across the fibre axis using an ultramicrotome (LKB Ultrotome III, LKB-Products AB, Bromma, Sweden). The cross-sectioned samples appear to yield more insights into morphological details, and offer the ability to obtain spatial information on the submicroscopical level with recognition of fine structure.

ESI of organosilane coated chrysotile

The first step in the analysis procedure is the recording of energy loss spectra to survey the possible elements of interest. Fig. 1 shows a typical EEL spectrum of a chrysotile fibre treated with trimethyl chlorosilane. The characteristic carbon K-edge is located at $\Delta E = 284$ eV. The observed carbon jump ratio (peak-to-background) ratios range between 1.1 and 1.3.

ESI of carbon distributions are carried out with serial ESI acquisition, which means that the different energy-filtered images are acquired successively, using the three-window method, to re-

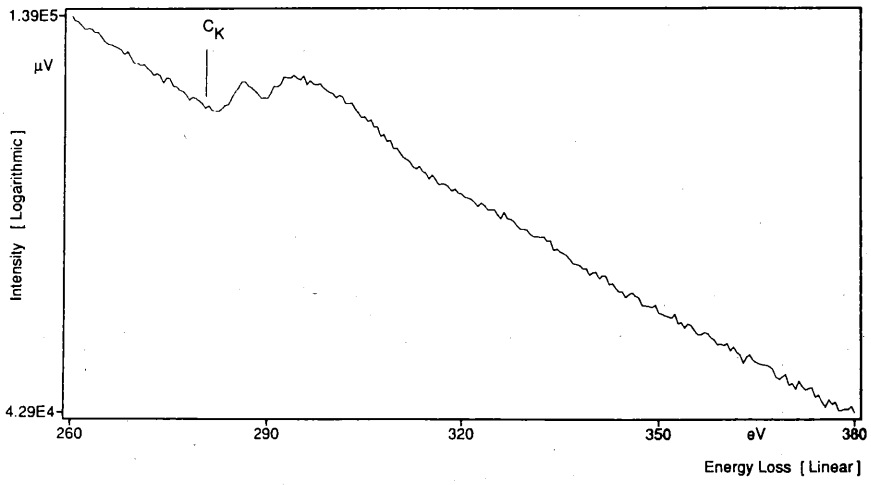

Fig. 1. Electron energy loss spectrum of asbestos fibres treated with organosilane taken between 260 and 380 eV energy loss showing the carbon K-edge at 284 eV.

move the background contribution from the image recorded above the ionisation edge, at the maximum signal intensity. This is performed as follows: two background images are obtained with a SIT Vidicon camera just prior to the ionisation edge ($\Delta E = 250$ and 270 eV) and one image at the ionisation edge (energy loss $\Delta E = 300$ eV) and recorded with a Kontron SEM/IPS image processing unit. The processed images were segmented interactively by expanding the grey values of the processed images over the whole grey range and raising the threshold until all background noise was cut off, in order to minimize the signals present in structures other than the specimen.

Initially, the power law background extrapolation procedure is evaluated for its effectiveness as a background correction, by inspecting the region below the carbon edge in the ESI mode. Therefore, the validity of the image processing is verified for a set of "ghost" images from and around a hypothetical edge, with the third image taken at an enery loss position just below the characteristic edge. The non-characteristic signal, observed in the net distribution, results from extrapolation errors and camera artifacts, and is used as a cut-off threshold for subtracting the noise contribution in order to obtain a more statistically valuable net image. No filtering techniques are employed in the image processing in order to avoid these supplementary, non-controllable artifacts. Only contrast enhancement is performed on the low contrast net images by expanding the set of grey values to the full range available.

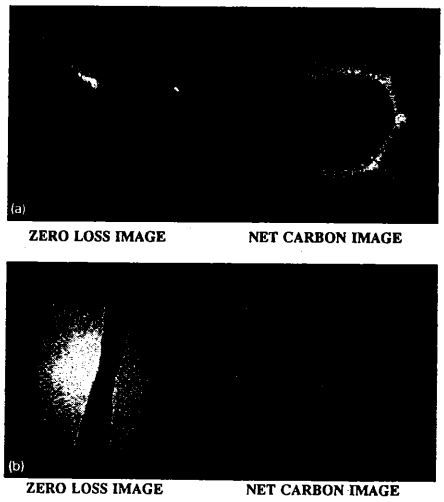

Fig. 2. Carbon mapping of organosilane treated chrysotile fibres, mounted on a perforated carbon foil, with the zero-loss image (left) and the net carbon-image (right).

ESI images for carbon in trimethyl chlorosilane modified chrysotile, supported on a perforated carbon foil are depicted in Fig. 2, with the net carbon distribution image (right) and the con-

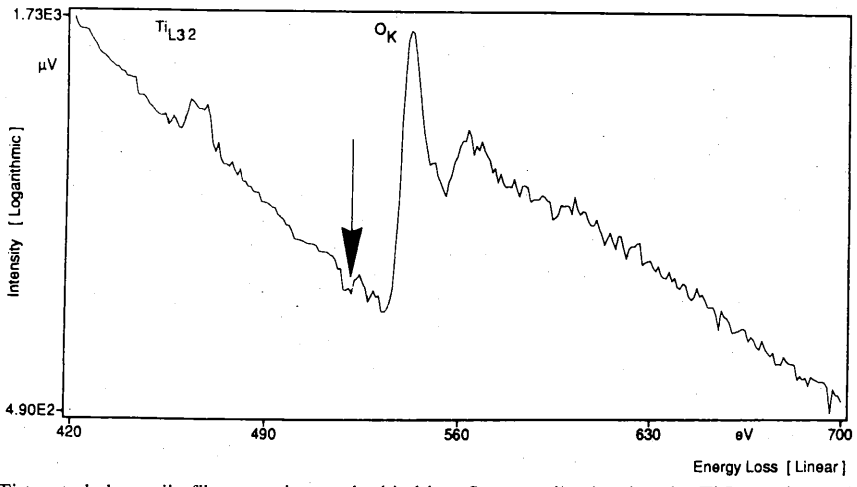

Fig. 3. EELS of a Ti-treated chrysotile fibres section, embedded in a Spurr resin, showing the Ti-$L_{3,2}$ edge at 455 eV and the O-K edge at 530 eV.

ventional zero-loss image (left), respectively. All images were acquired with a magnification of 50 000 ×. The use of a conducting perforated carbon foil is advantageous since the stability of such electrically insulating asbestos fibres under the electron beam is increased. This allows the operation of the electron microscope at greater magnifications without sacrificing beam intensity.

From such carbon maps it could be concluded that the organosilane coating is not homogeneously distributed over the fibres. Some fibres do not seem to have been affected by the organosilane treatment, which indicates that the carbon layer does not completely encompasses each and every fibre. This means that the surface modification is only partially effective.

EELS and ESI study of $TiCl_3$-treated chrysotile

In the following example we have investigated the asbestos fibres' condition after their chemical modification process with $TiCl_3$, especially in view of a possible penetration of titanium in the first layer and a localised built-up of species of the modification reaction inside the tubes of the fibres.

Before performing chemical mapping, the extended area of interest of the section was examined by recording a typical energy-loss spectrum. A part of one of these EEL spectra from an area (250 nm × 200 nm) within the chrysotile fibril of the modified asbestos is shown in Fig. 3, and it reveals the presence of titanium with the Ti-$L_{2,3}$ edge at 455 eV. The Ti $L_{3,2}$ threshold peak shows two dissimilar peaks with multiplet structures at both L_3 and L_2. The sharpness of these peaks makes the Ti edge easily recognizable even at low Ti contents. The pre-edge, preceding the oxygen edge, is assigned to a manifestation of the bond between oxygen and titanium, arising from transitions to the $2t_{2g}$ and $3e_g$ anti-bonding orbitals of the Ti–O bonds [24]. The appearance of this shoulder at the onset of the oxygen edge is an indication that the titanium chloride has chemically reacted with the chrysotile fibres and is not chemisorbed.

While for EELS analysis a relatively large area of an ultrathin fibre section is selected, the localization of titanium is possible with ESI in very small areas, restricted only by the spatial resolution of the electron microscope. Taking into account that the jump ratio for Ti is sufficiently high for imaging, first the three-image method was used for the collection of the electron spectroscopic images.

Lateral elemental Ti maps (magnification of 140 000 ×) obtained with ESI analysis of the cross-sectioned treated fibres demonstrate unambiguously the presence of titanium inside the

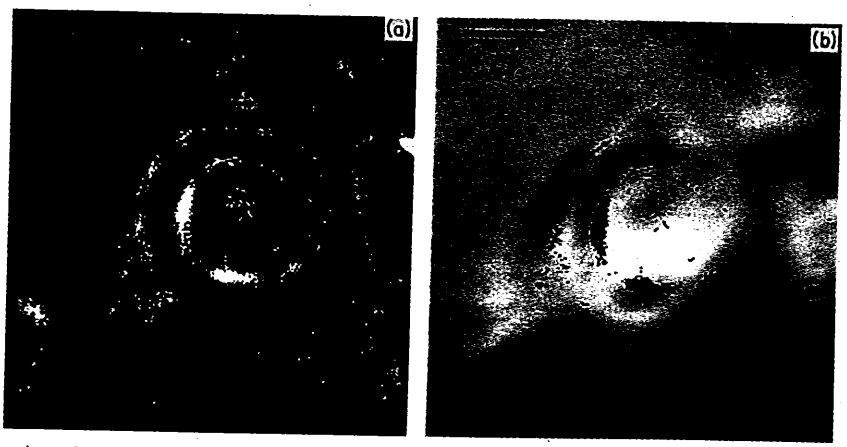

Fig. 4. Elemental mapping of Ti in a cross section of a $TiCl_3$-treated fibre embedded in a Spurr resin. (a) The net-titanium image is obtained by subtracting an extrapolated image at 450 eV (calculated from the 435 eV and 445 eV images) from the 460 eV image, (b) combination of binary titanium distribution image (black) and the grey reference electron specific image at 435 eV (Scale bar = 25 nm).

hollow tubes of the fibres as well as on the external surface of the fibres, which shows that the Ti distribution forms a non-complete encapsulation around the material. The superposition of the titanium map (in black) on the grey reference area depicted in Fig. 4 indicates that the

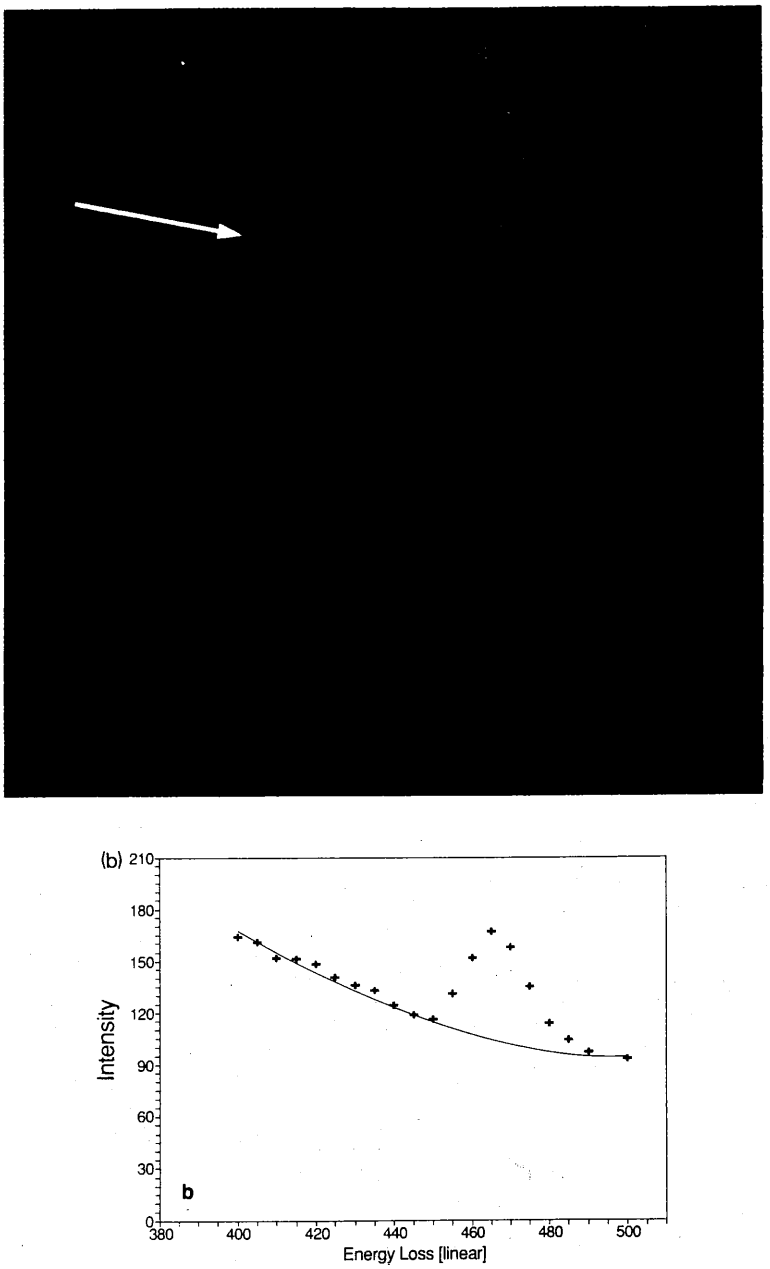

Fig. 5. Zero-loss image of a cross section of $TiCl_3$-treated chrysotile fibres embedded in a Spurr resin (full picture is 200 nm) showing the Ti-signal in overlay (a); Datapoints (+) of a selected part of the EEL spectrum generated from the images, at one pixel location near the surface of fibril. The background curve was modelled by fitting the 10 pre-edge points (+) to the power law curve (b).

modification follows the spiral curvature of the chrysotile asbestos.

In addition to the inaccuracies which are obtained using the three-image procedure, statistical noise plays an important role in the background estimation. Hence, in this typical situation, it is difficult to distinguish the true characteristic signal from background and noise. Therefore we investigated the use of a point-by-point processing of the spectrum through increasing the number of images before and after the edge, attempting a significant progress in accuracy for the restoration of the net image from the three-dimensional data set, by taking into account the local thickness variations and increasing the accuracy in the A and R determination. To calculate the background counts beneath the characteristic core edge, a least-squares fitting procedure, using a data-analysis program, PV ~ WAVE (Precision Visuals, Colorado), is performed in parallel for all pixels in the series of images.

This multi-image procedure can be easily modified to take the statistical uncertainty on the intensities in the original images into account, in order to differentiate between variations due to noise limitations or real elemental data. In this way, next to the net image, also a corresponding uncertainty image can be calculated which allows the identification of the area in the image with a net intensity significantly different from zero. At different locations in the net image, the EEL-spectrum, its background and the intensity distributions across the X and Y directions through the net image at those locations can be interactively inspected.

The WAVE processing routine allows the operator to display an EEL spectrum at each selected pixel position in the image. The number of

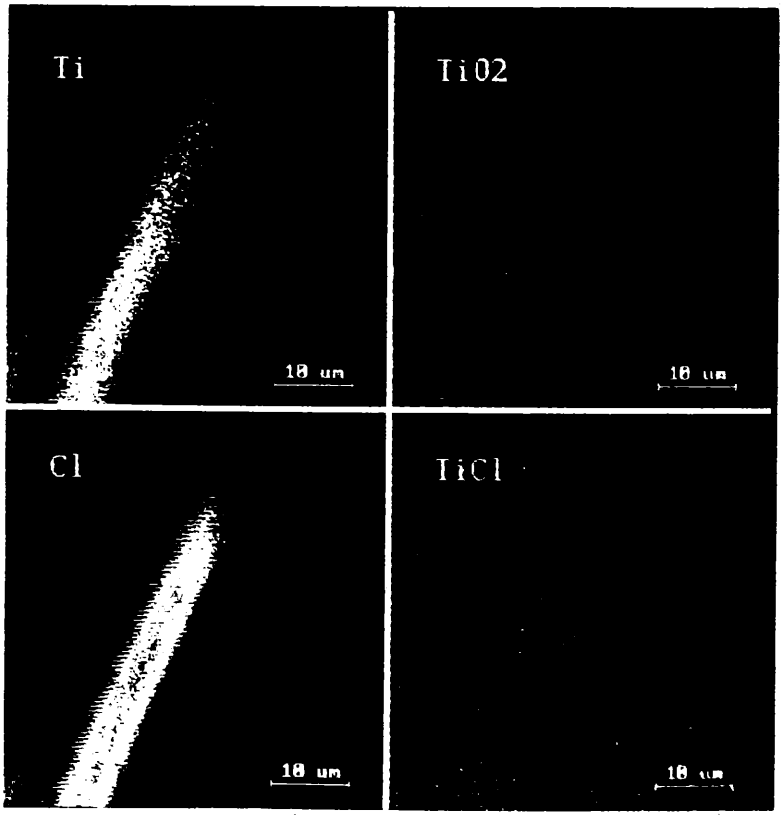

Fig. 6. Negative secondary ion images for Ti^-, TiO_2^-, Cl^- and $TiCl^-$ of $TiCl_3$-treated chrysotile fibres deposited on a GaAs wafer. The diameter of the imaged area is 25 μm.

data points selected for construction of this spectrum corresponds to the number of images collected (in this case 20). The resulting statistically significant net-distributing of titanium is presented in Fig. 5a, showing the Ti-signal in overlay. The image spectrum for one pixel position located on the fibre section, as indicated by the arrow, is presented in Fig. 5b, showing a clear edge of Ti-$L_{2,3}$ above the extrapolated background.

The use of a multi-image ESI procedure at different electron energies, for processing the net-element distribution, has demonstrated its utility in cases where low element concentrations are analyzed. In general, one has to be aware that the multi-image method is very sensitive to radiation damage and specimen drift occuring during the image collection. These effects, arising from the high intensity level of the electron beam required for high magnification electron microscopy, mostly can be avoided by using cryo-cooling in order to stabilize the sample prior to image collection. In comparison with the three-image method, significant increase for the yield in characteristic net-signal is obtained, while the statistical uncertainty on the intensities for every pixel position decreases. The calculation with the use of the WAVE procedure ensures that the images represent a true Ti distribution and not mass thickness variations.

Secondary ion imaging of titanium coated fibres

An ion microprobe (CAMECA IMS 4F) was used for the SIMS measurements. The lateral resolution of this equipment is limited to about 0.2 μm. The achieved primary beam current densities are kept rather low to make feasible three-dimensional distribution analysis in a reasonable time. Therefore we mainly deal with the two-dimensional lateral distribution analysis. For this purpose the CAMECA 4F was furnished with a SEM-box which controls the deflection raster plates of the primary beam and collects synchronously the signal from the electron multiplier to send it to an image-processing unit, an IBAS 2000 unit, described above.

In order to reach sufficiently high counting rates, a primary beam of mass filtered Cs^+ ions at a net 10.0 kV and approximately 100 pA is rastered over a 5 μm × 5 μm area. Ion images (25 μm^2 imaged field), mass spectra and energy distributions of negative secondary ions are obtained. Because of the drastic deterioration of the electrical parameters of the asbestos, the samples are prepared from a suspension in hexane that had been spotted on an ultra-pure GaAs-wafer. This resulted in clumps of fibres dried on the GaAs-wafer. The energy distributions that are obtained for each sample dried on a GaAs-wafer show that no significant amount of electrical charge had accumulated within the area of analysis.

The lateral elemental maps of the major secondary ion species present, Ti^-, TiO_2^-, Cl^-, and $TiCl^-$ are shown in Fig. 6. The diameter of the imaged area is 25 μm in all the elemental maps. A pixel time of $t_d = 0.5$ or 1 ms was used for collection of these images, having 256 × 256 pixels.

It is clear that the secondary ion images of Ti and TiO may be used to selectively indicate the contour of the asbestos fibre. The titanium ion images show that, within the lateral resolution of the ion microprobe, the titanium has reacted fairly evenly over the selected area of the chrysotile surface, and no evidence of any significant built up of localized titanium containing compounds is observed. The $TiCl^-$ map does not show any contribution, hence we assume the absence of $TiCl_x$ species on the $TiCl_3$-treated fibres. This is an extra indication that $TiCl_3$ has reacted fully with the chrysotile structure. Microstructures on these fibres, however, cannot be studied with the ion micro-probe image-processing combination using a Cs^+ primary ion beam, as the dimension of these structures are ca. 0.1 μm or smaller and so below the limit of resolution of this technique.

2. Characterization of the north sea aerosols by spm

Atmospheric transport and deposition of pollutants over long distances have received attention, particularly in connection with the acid rain

problem, the photochemical oxidants and ozone formation, and, more recently, the global climatic effects. Though the pollution of the oceans is not a new phenomenon, the question of how important a role the atmosphere plays in this was addressed only a decade ago [25]. A number of studies conducted at the end of the 1970s and the beginning of the 1980s (e.g., [26–28]) revealed direct deposition from the atmosphere as a potentially major input source for contaminants.

Due to a large number of limitations, direct measurements of pollutant fluxes over the sea are scarce [29]. In order to overcome this problem, several authors have proposed, as an alternative, the use of mathematical models to predict the atmospheric input of particulate matter to the large water surfaces [30] or to calculate deposition indirectly, based on measured airborne concentrations and kinematic parameters which control the rate of mass transfer [31].

Regarding to the pollution of coastal and shelf systems of the North Sea, there has been a growing concern especially since Weichart in 1973 concluded that the southern North Sea is one of the most heavily polluted areas [32]. Because of its relevance, since quite some years our laboratory has studied the North Sea environment intensively; we focused our efforts primarily on the heavy metal deposition and concentrations, and physical and chemical characterization of individual North Sea particles responsible for this flux. Previous studies showed that some 95% of the total deposition is explained by fluxes of particles with a diameter larger than 4 μm i.e. the so-called "giant particles"; this emphasizes the accuracy of size-determinations of large particles as the limiting factor in the estimation of total fluxes. The following example gives a quantitative idea on how important relatively large particles are in the whole deposition process. Since the gravitational settling velocity is roughly proportional to the square of the particle diameter and the particle mass is proportional to the cube of the particle diameter, the deposited mass is a function of diameter to the 5th power. Therefore one single 10 μm particle contributes as much to the total deposited mass as 100 000 particles of 1 μm.

In the above-stated context, an attempt was made to demonstrate the potential usefulness of the flexible SPM system in a quite novel approach: to estimate quantitatively from field measurements the atmospheric input of heavy metals into the North Sea and to evaluate the nature of aerosol particles, especially the "giant" particles, responsible for this flux. The basic reason for the use of a focused proton beam is the high sensitivity of PIXE in a small sample mass allowing the determination of fingerprinting trace elements, and the potential for elemental concentration mapping over spatial intervals of a few microns permitting studies of the internal heterogeneity of giant aerosol particles.

The aerosol samples were taken in the frame of EUROTRAC Air-Sea Exchange experiment, on the research platform "Nordsee" (54°10′, 7°53′E). As a follow-up of previous experiments on the North Sea [33], isokinetic collection of size-segregated aerosols on Nuclepore filters (0.4 μm pore size) was carried out in a continuous forced air flow within a wind tunnel, which directs itself continuously towards the wind with a wind-vane. The major problem in all previous aerosol deposition studies over the North Sea in the past, was that the giant aerosols have not been adequately assessed, because of difficulties in sampling these particles in a representative way. Indeed, the linear velocity of the particles in the air should exactly be the same as the inlet speed in the sampling device. By taking samples with the means of a wind tunnel, this problem is overcome since it allows quantitative collection of giant particles without problems of a variable cut-off with wind direction and wind speed.

The micro-PIXE measurements were done at the Central Bureau for Nuclear Measurements (CBNM) in Geel, Belgium [34]. The microbeam line is mounted in the target hall of the KN-3.7 MV vertical single stage Van de Graaff accelerator. The accelerator is equipped with a radio-frequency ion source used to produce H^+ or He^+ ions. The energy spread of the accelerator is about $\pm 0.07\%$, a typical value for single ended machines, while the brightness has been measured on the beam line to be 3.5 pA/(mrad^2 μm^2) at a proton energy of 2 MeV. The distance from the object slits to the target position is 425

cm. The entire beam line is resting on a 420 cm long and 500 kg heavy granite bench carried by four active pneumatic vibration insulators. The beam line is equipped with the two pairs of stainless steel "Heidelberg"-type slits, which are electrically insulated and equipped with cable connections to enable monitoring of the beam current striking each individual slit. This option has proven useful during the start-up procedure. As the beam focusing element, a magnetic quadrupole lens doublet is chosen. The lenses are mounted on the granite bench beam line support, in direct contact with the chamber. Therefore, the lenses cannot be moved relative to the chamber, what requires a very precise beam line alignment. The copper-grid shadow pattern was used to facilitate the focusing and the size of the ion beam. A lateral resolution of $2.5 \times 2.5\ \mu m^2$ was routinely achieved at a beam current of 100 pA. In the Geel SPM, a flexible front computer is used together with a powerful host computer. A VMEbus system acts as a front-end computer which controls the beam scanning and the acquisition of data from a maximum of four detectors and from the beam charge monitor. The host computer is a MicroVax-II, equipped with a Nuclear Data ND9900 multiparameter MCA system.

The aerosol samples were analyzed by scanning the beam over a fairly large square region, mostly of $128 \times 128\ \mu m^2$ in a 64×64 pixels scanning pattern. The x-rays induced by the proton beam were continuously recorded and sorted by the data acquisition system, producing x-ray intensity images of selected elements on a graphics terminal. From these maps, clusters of particles deposited on the backing were located. The time of analysis varied between 30 and 60 min, depending on the elements present and their respective amounts. Elements ranging from S to Ca

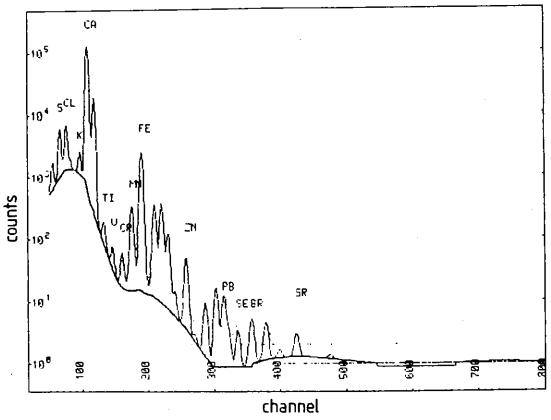

Fig. 7. PIXE spectrum obtained from from the analysis of a single aerosol particle-summed spectrum from all 4096 irradiated pixels in the scanning frame.

normally yield high x-ray count rates and were detected within a short counting time. Higher-Z elements have lower x-ray production cross sections and consequently require longer irradiation times for adequate detection.

The off-line spectrum analysis was performed by using a linear least-squares fitting procedure and the corresponding mass of the trace elements was then calculated from a calibration library. A PIXE spectrum obtained from the analysis of one single aerosol particle is given in Fig. 7.

By using the scanning proton beam, it was possible to reveal elemental distributions within a single aerosol particle structure. Detected total amounts for S, Cl, K, Ca, Ti, V, Cr, Fe, Ni and Zn were in the range of 0.01 (Zn) to 390 (Cl) pg, and these would have been difficult to quantify using other microprobe techniques (Table 2). The accuracy is estimated to be around 10%.

The elemental distributions on the individual particle level have demonstrated the heteroge-

Table 2
The range of elemental concentrations (pg) for the two representative particle groups found in the North Sea troposphere

Group	S	Cl	K	Ca	Ti	V	Cr	Fe	Ni	Zn
Marine aerosols	10–33	20–390	5–17	1–4	–	–	–	–	–	–
Agglomerated aerosols	2–20	8–100	1–16	1–7	0.1–3.8	0.1–0.3	0.2–2.6	0.2–1.1	0.01–0.08	0.01–0.52

neous structure of marine aerosols (Fig. 8). Especially in the case of agglomerates of particles, a distinct difference in elemental composition was found. Commonly in the presence of a high load of airborne sea-salt particles, a large fraction of the heavy metal rich particles were found to be

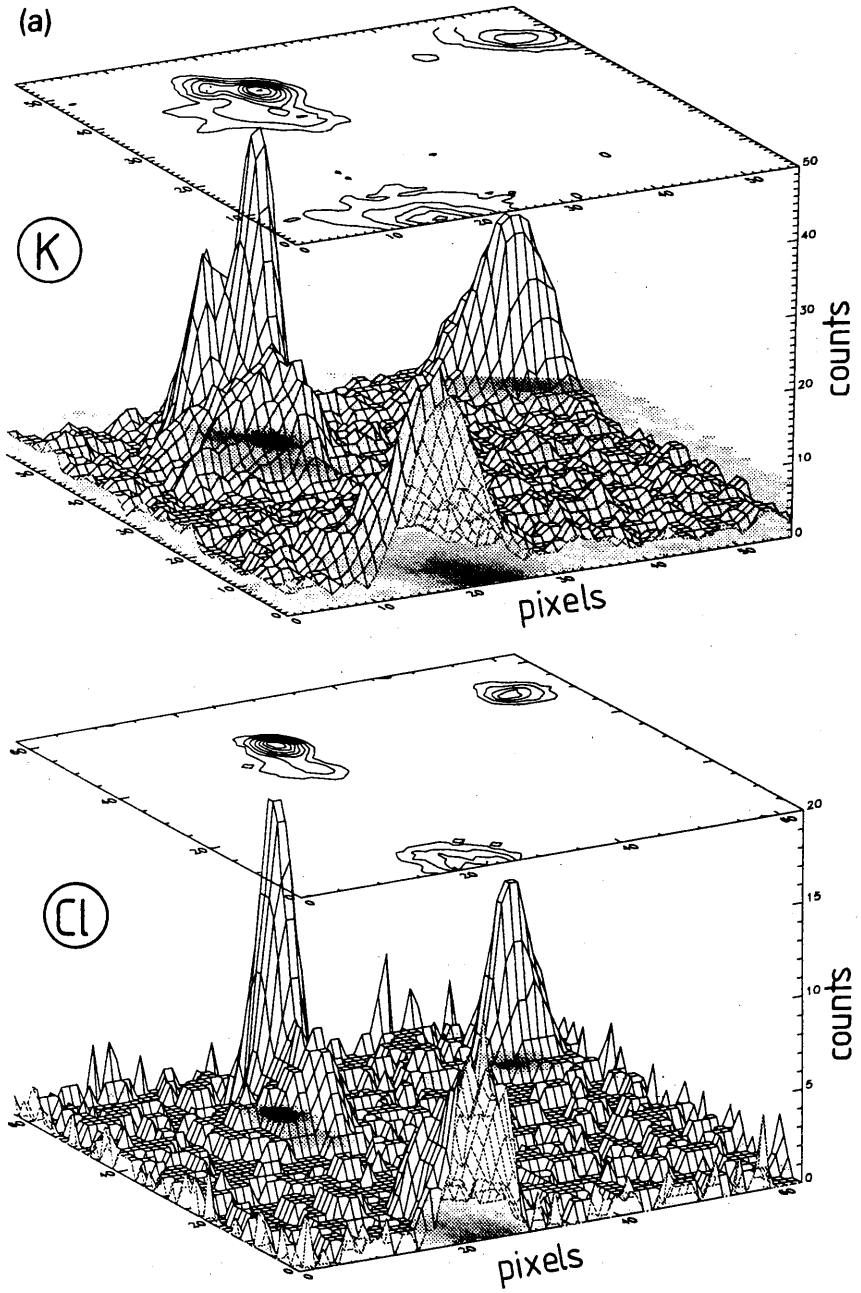

Fig. 8. Elemental mapping of Cl, K, Ca and Ti, obtained from the analysis of North Sea aerosol particles. The heterogeneous structure of the marine particles is evident. The total scanning area is about $64 \times 46\ \mu m^2$.

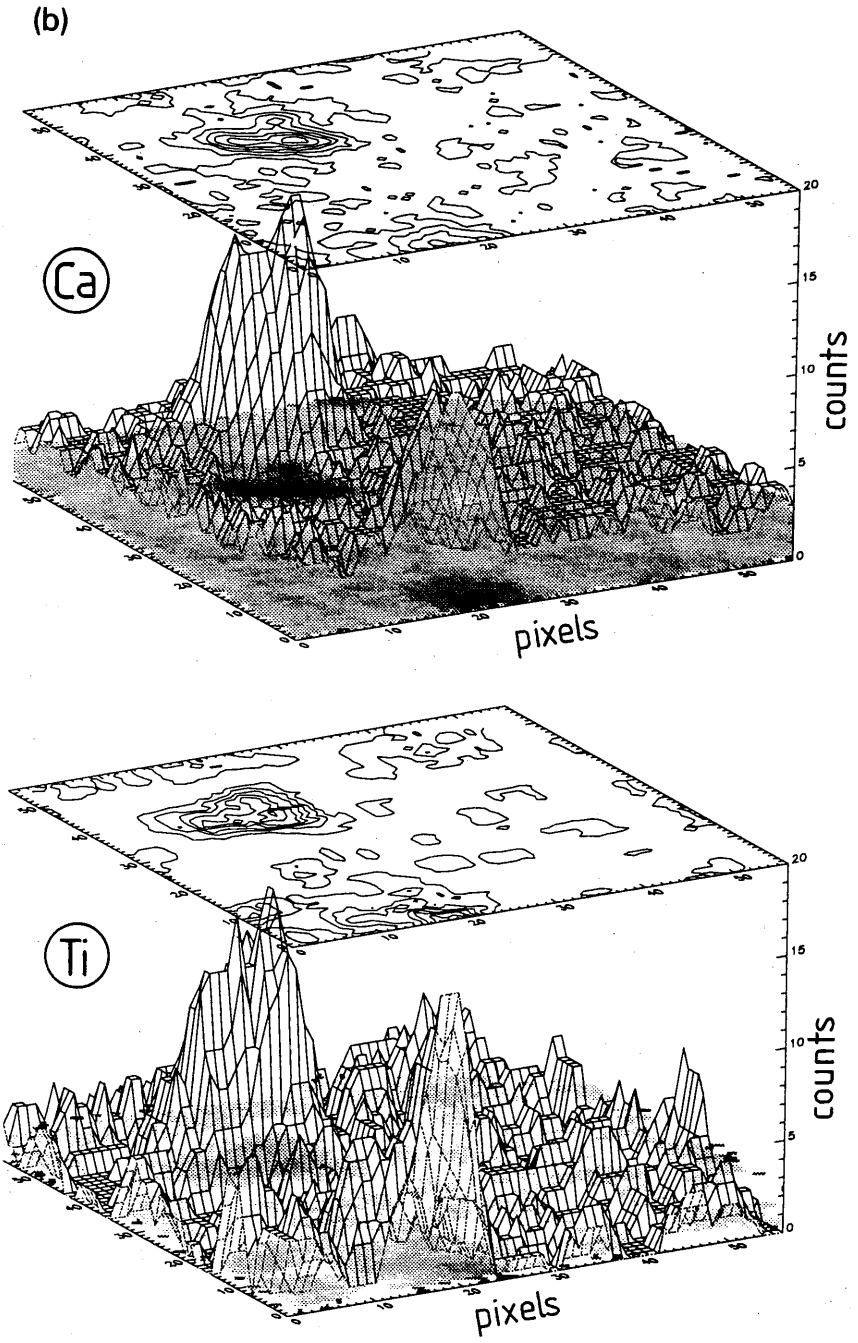

Fig. 8 (continued).

internally mixed, forming the coarse marine aerosol fraction with diameter above 5 μm. Hence, while elements like V, Cr, Ni, Zn are usually more abundant in the sub-micrometer size range in polluted air, it was demonstrated that these particles can coagulate with the sea-salt

aerosols and reach super-micrometer dimensions. Elemental maps taken during the scanning analysis of a few aerosol particles are shown in Fig. 8.

From an environmental prospect, it was also of interest to relate the elemental aerosol compositions to their sources, i.e., to identify source profiles of the North Sea aerosols. Therefore we have analyzed the variability of the 10 elemental concentrations. The principal sources for most particulate trace elements in the marine troposphere of the North Sea appear to be sea-salt generation (oceanic source) and a variety of mainly high-temperature combustion processes (anthropogenic sources). The predominant particle groups were particles with a high loading of marine elements (Cl, S, K) and agglomerated particles containing simultaneously sea-salt and trace elements ascribable mostly to anthropogenic processes (Ti, V, Cr, Fe, Ni, Zn).

This work was sponsored by NFWO/FNRS Brussels, Belgium and by the Belgian Prime Minister's Service for the Programmation of Science Policy under the Programme Interuniversity Attraction Poles (IUAP), the Eurotrac Project EU7/08 and the Impulse Programme on Marine Sciences (contract MS/06/050). We thank Dr. U. Wätjen and Ing. L. Braitenbach, from the CEC-JRC, Central Bureau for Nuclear Measurements, Geel, for the micro-PIXE analyses.

References

[1] M. Grasserbauer, Mikrochim. Acta, III (1983) 415.
[2] R. Van Grieken and C. Xhoffer, J. Anal. Atom. Spectrom., 7 (1992) 81.
[3] C. Xhoffer, L. Wouters, P. Artaxo, A. Van Put and R. Van Grieken, in J. Buffle and H.P. Van Leeuwen (Eds.), Environmental Particles, Vol. I, Lewis Publishers, Boca Raton, FL, 1992, 107.
[4] M. Van Craen, D.F.S. Natusch and F. Adams, Anal. Chem., 54 (1982) 1786.
[5] G. Morrison and G. Slodzian, Anal. Chem., 47 (1975) 932A.
[6] X.B. Cox III, S.R. Bryan and R.W. Linton, Anal. Chem., 59 (1987) 2018.
[7] E. Denoyer, R. Van Grieken, F. Adams and D.F.S Natusch, Anal. Chem., 54 (1982) 26a.
[8] L. Van Vaeck and R. Gijbels, Fresenius' J. Anal. Chem., 337 (1990) 743.
[9] T. Mauney and F. Adams, Sci. Total Environ., 36 (1984) 215.
[10] Ro Chul-Un, I.H. Musselman, R.W. Linton, in P.E. Russel (Ed.), Microbeam analysis-1989, San Francisco Press, San Francisco, CA, 1989, 293.
[11] A.D. Maynard and L.M. Brown, J. Aerosol Sci., 23 (1992) 433.
[12] C. Xhoffer, P. Berghmans, I. Muir, W. Jacob, R. Van Grieken and F. Adams, J. Microsc., 162 (1991) 179.
[13] C. Colliex, J.L. Maurice and D. Ugarte, Ultramicroscopy, 29 (1989) 31.
[14] J. Chazelas, J. Cazaux, G. Gillmann, J. Linch and R. Szymanski, Surface Interface Anal., 12 (1988) 45.
[15] A. Erdemir and C.C. Cheng, Ultramicroscopy, 29 (1989) 266.
[16] P. Dravid, C.E. Lymam, M.R. Notis and A. Revcolevschi, Ultramicroscopy, 29 (1989) 60.
[17] C.J. Powell, in K. Heinrich (Ed.), Characterization of Particles, Proc. of the Particle Analysis Session of the 13th Int. Conf. of Microbeam Analysis Society, Ann Arbor, MI, 1980, p. 131.
[18] X.B. Cox III and R.W. Linton, in K.R. Spurny (Ed.), Physical and Chemical Characterization of Individual Airborne Particles, Wiley Sons, New York, 1986, p. 341.
[19] G. Small, R. Kroutil, J. Ditillo and W. Loerop, Anal. Chem., 60 (1988) 264.
[20] R. Gordon, N. Trivedi and B. Singh, Environ. Sci. Technol., 22 (1988) 672.
[21] D. Cozak, C. Barbeau, F. Gauvin, J.-P. Barry, C. DeBlois, R. De Wolf and F. Kimmerle, Can. J. Chem., 61 (1983) 2753.
[22] F.M. Kimmerle and P. Roberge, Titanium Coated Asbestos Fiber, U.S. Pat., 4,388,149 (1983).
[23] A. Van Meerbeek and E. Ruiz-Hitzky, Coll. Polym. Sci., 257 (1979) 178.
[24] L.A. Grunes, R.D. Leapman, C.N. Wilker, R. Hoffmann and A.B. Kunz, Phys. Rev. B, 25 (1982) 7157.
[25] NAS, The Tropospheric Transport of Pollutants and Other Substances to the Oceans, National Academy of Sciences Press, Washington, DC, 1978, p. 194.
[26] NAS, The Tropospheric Transport of Pollutants and Other Substances to the Oceans, National Academy of Sciences Press, Washington, DC, 1978, p. 243.
[27] R.M. Van Aalst, R.A.M. Van Ardenne, J.F. de Kreuk and Th. Lems, Pollution of the North Sea from the Atmosphere, TNO Report CL 82/152, Organization for Applied Scientific Research, Netherlands, 1982, p. 124.
[28] H. Rodhe, R. Soederlund and J. Ekstedt, Ambio, 9 (1980) 168.
[29] R.M. Van Aalst, in Schneider et al., (Eds.), Dry Deposition of Aerosol Particles: Aerosols, Lewis Publishers, Chelsea, MI, 1986.
[30] J.A. Van Jaarsveld, R.M. Van Aalst and D. Onderdelinden, Deposition of Metals from the Atmosphere into the

North Sea: Model Calculations, Report RIVM 842015002, Bilthoven, Netherlands, 1986, p. 21.
[31] S.A. Slinn and W.G.N. Slinn, Atmos. Environ., 14 (1980) 1013.
[32] G. Weichart, Ambio, 2 (1973) 99.
[33] J. Injuk, Ph. Otten, R. Laane, W. Maenhaut and R. Van Grieken, Atmos. Environ., 26A (1992) 2499.
[34] N.E.G. Lovestam, E. Swietlicki, U. Wätjen, E. Louwerix, A. Perujo and P. Rietveld, Nuclear Instrum. Meth., B69 (1992) 463.

ELSEVIER

The Science of the Total Environment 155 (1994) 131–149

the Science of the Total Environment

Elemental concentrations in atmospheric particulate matter sampled on the North Sea and the English Channel

Phillipe Otten, Jasna Injuk, René Van Grieken*

Department of Chemistry, University of Antwerpen (UIA), B-2610 Wilrijk-Antwerpen, Belgium

Received 8 November 1993; accepted 19 December 1993

Abstract

Air sampling on a series of 10 cruises, spanning the whole area of the North Sea, yielded detailed spatial distributions of atmospheric concentrations of Al, Si, S, Cl, P, K, Ca, Ti, V, Cr, Mn, Fe, Ni, Cu, Zn and Pb determined by EDXRF. A strong influence of the air mass history on the heavy metal concentrations was demonstrated for the whole sampling period of 5 years. Factor analysis performed on all samples collected with a stack filter unit resulted in the identification of three factors for the coarse particle fraction (sulphate particles with trace metals, sea salt particles and soil dust or metallurgic particles containing Fe) and four factors for the fine particle fraction (sea salt, sulphate with Pb and Zn), trace metal particles with Cu, Ni, Zn and fly-ash particles. The same statistics performed on all samples collected above the Southern Bight of the North Sea yielded three factors, namely: sea salt particles, particles enriched in Ni and V, originating from natural oil combustion and particles containing a variety of elements such as S, K, Ca, Fe, Pb, Cu and Zn. Compared with relevant measurements of trace elements in this area, a relatively good agreement can be found.

Keywords: Aerosols; Trace elements; North Sea; EDXRF

1. Introduction

In order to understand more about the North Sea aerosol constituents and their sources and their fate, an extensive sampling program, spanning more than 5 years, was set up with the Belgian oceanographic research vessel R/V Belgica. Aerosol samples were collected under different meteorological situations and from different regions, covering the complete North Sea and the English Channel. Particulate matter, collected on membrane-type filters, was analysed with energy-dispersive X-ray fluorescence (EDXRF) yielding atmospheric concentrations for Al, Si, P, S, Cl, K, Ca, Ti, V, Cr, Mn, Fe, Ni, Cu, Zn and Pb. The results of EDXRF measurements on 71 filter samples collected during these 10 different sampling campaigns are discussed. A multi-variate technique, factor analysis, was used for the determination of the underlying structure of the total data set.

* Corresponding author.

Elsevier Science BV.
SSDI 0048-9697(94)04146-E

2. Analytical procedure

2.1. Instrumentation

The analyses were performed by an EDXRF instrument Spectrace 5000 (Mountain View, CA, USA), which is completely controlled by and operated from an IBM-AT type microcomputer. The Spectrace 5000 uses a 17.5-watt power X-ray tube with Rh anode target. It operates within a range of 6–50 keV and with a maximum current of 0.35 mA. The exciting X-ray beam passes a 127-μm thick Be window, is collimated and finally passes through a filter system. The filter system allows the use of either no filter at all or a selection from five different filter types: a cellulose filter, a 127-μm Al filter, a 50-μm Rh filter, a 127-μm Rh filter or a 630-μm Cu filter.

At 90° relative to the incident X-ray beam, the characteristic X-rays from the sample and the scattered X-rays are detected by an energy-dispersive Si(Li) detector. Data acquisition and display is done by a PC.

2.2. Calibration

In the calibration procedure followed, a series of thin film reference standards, composed of pure elements or simple inorganic compounds evaporated on a 4-μm thick Mylar foil (Micromatter, Seattle, WA), were used. Low Z element standards were analysed with an accelerating voltage of 15 kV, using a current of 0.35 mA and an irradiation time of 1000 s. No collimator was used. Because of overlap between the Rh-L lines and the Cl-K and S-K lines, a cellulose filter was used for filtration of the incident polychromatic X-ray beam. For high Z element standards, irradiation was done during 1000 s with a 35-kV beam using a 0.35-mA current and a thin Rh-filter. For Pb, the L lines are used for calibration.

X-ray spectra were analysed with the AXIL software (Van Espen et al., 1986). The calibration procedure was evaluated by analysing two NBS reference standards consisting of a Nuclepore membrane with a deposited glass layer.

Table 1 lists the detection limits for airborne particulate matter samples, assuming 10 m^3 of air was drawn through a 47-mm diameter Nuclepore filter. Detection limits are calculated as three times the standard deviation on the peak surfaces, obtained by analysis of a blank filter. The high Cl detection limit is due to the interference of incompletely filtered Rh-L lines that coincide with the Cl-K lines.

Table 1
Detection limits assuming a sample volume of 10 m^3 and a filter diameter of 47 mm

Element	Detection limit (ng/m^3)
Al	200
Si	140
P	70
S	80
Cl	600
K	9
Ca	6
Ti	2.5
V	2.0
Cr	1.5
Mn	0.9
Fe	0.4
Ni	0.5
Cu	0.4
Zn	0.4
Pb	8

2.3. Sampling strategy

Total airborne particulate matter was collected from the R/V Belgica on 47-mm diameter, 0.4-μm pore-size polycarbonate membrane-type filters (Nuclepore, aerosol grade). In some cases, a dual filter unit was used, consisting of a 8.0-μm pore-size filter, followed by a 0.4-μm pore-size one. This double filter sampler allows separation of the coarse particle fraction (> 2 μm) from the fine particle fraction during sampling. The Plexiglass filter holder has a hat-type cover to protect the filters from contamination by seawater droplets. Table 2 shows the results of electron microscope measurements on five dual samples, with and without hat, taken on the North Sea. From the particle size distributions, the number of particles with a diameter > 2 μm was calculated. There is no systematic difference between the sampler with hat and the sampler without hat. The percentage of mass (calculated from the numerical size distribution by assuming the same

Table 2
Sampling efficiency of hat-type fitter system for 5 different dual samples

Percentage of particles > 2 μm		Percentage of mass represented by particles > 2 μm	
With hat	Without hat	With hat	Without hat
2.4	7.9	66	72
3.0	2.3	63	75
1.5	2.7	66	68
5.8	2.3	88	80
9.1	8.6	89	90

density and shape for all particles), represented by particles with a diameter larger than 2 μm, is nearly the same with the two setups used.

The filter holder was placed at the front end of the ship at a height of ~ 10 m above sea level. A 20-m plastic hose connects the filter unit to a vacuum pump (Becker type VT 6) and a dry gas meter which are placed at the upper deck near the bridge.

The pump is operated at a flow rate of ~ 35 l/min for 4–12 h for each sample in order to collect 10 m^3. Sampling was discontinued whenever the relative wind direction to the ship was $< -45°$ or $> 45°$ for reasons of possible contamination by the diesel engine exhaust of the ship itself. Therefore, although the sampling volume is nearly the same for all samples, they may be collected over a wide range of total sampling times.

Filter samples were immediately transferred to a flow hood inside the chemical laboratory on the ship and placed in a plastic box until analysis by EDXRF in the University laboratory.

3. Results

Here, an overview is given of all results concerning atmospheric concentrations of trace elements in the North Sea atmosphere. When no data are given for an element in campaign, all EDXRF results were below the detection limit during that campaign.

3.1. Campaign 1

General sampling data and meteorological information. During campaign 1, four aerosol samples were collected in the Southern Bight of the North Sea, more specifically on the Belgian Continental Shelf.

Two-dimensional, 96-h backward air mass trajectories were calculated by the Belgian weather service, KMI. Corresponding back trajectories for all four filters are shown in Fig. 1. These air mass trajectories indicate the origin and the history of the collected airborne particulate material. They often include more useful information than wind speed and wind direction data at the sampling site, since two samples collected at the same

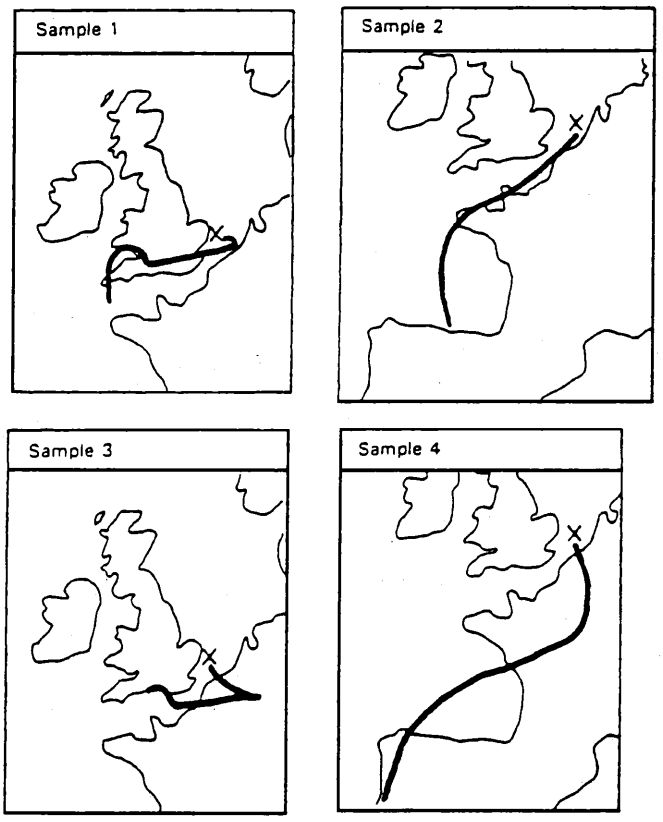

Fig. 1. The 96-h backward air mass trajectories for samples of campaign 1 (sample location indicated by an ×).

location under similar local meteorological conditions may have a completely different air mass history due to differences in the large-scale meteorological situation, i.e. the distribution of high and low pressure areas and the presence of cold and warm fronts.

EDXRF results. Table 3 lists the atmospheric concentrations obtained. In sample 1, the highest S, K, V, Ni, Cu, Zn and Pb concentrations are determined. From the air mass history (Fig. 1), the collected airborne material originated from the London area and the southern part of the UK. Sample 2 was collected under continental (French) influences (Fig. 1). Most concentrations are lower than in sample 1. The third sample was collected at higher wind speeds, up to 15 m/s. This is reflected in a higher Cl concentration, while the concentrations of all other elements are much lower than in samples 1 and 2. The fourth sample was also collected under more continental influence and at lower wind speeds, resulting in higher concentrations for anthropogenic elements and a lower Cl concentration compared with the previous sample. Although there is only an interval of 12 h between the third and the fourth sample, concentrations differ significantly; the Pb concentration goes up by a factor of 3.5 from 40 to 140 ng/m^3. Rapid changes in the meteorological situation are reflected without delay in the atmospheric concentrations of trace elements.

3.2. Campaign 2

General sampling data and meteorological information. During the first part of a 3-week campaign, between Zeebrugge (Belgium) and Bergen (Norway), 8 aerosol samples were collected on 0.4-μm pore-size Nuclepore filters. During the second part of the campaign, between Bergen and Zeebrugge, another 7 samples were collected, this time by using a stacked filter unit consisting of a 8.0-μm pore-size Nuclepore filter, followed by a 0.4-μm one.

Table 4 summarizes the available meteorological information for campaign 2: wind direction, wind speed and an indication of the air mass

Table 3
EDXRF results in ng/m^3 — Campaign 1

Element	Sample			
	1	2	3	4
S	4600	1650	600	1510
Cl	800	620	1350	< 600
K	310	310	190	270
Ca	250	450	120	140
V	70	32	18	30
Fe	470	720	300	740
Ni	15	7.0	< 0.5	< 0.5
Cu	33	8.0	< 0.4	< 0.4
Zn	180	180	32	80
Pb	210	150	40	140

Table 4
Meteorological information — Campaign 2

Sample	Wind sector	Wind speed (m/s, range)	Air mass history
1	NW–NE	1–9	North Sea
2	NE–N	2–9	North Sea
3	NE–NW	8–10	Norway, northern Atlantic, North Sea
4	NW	4–11	Northern Atlantic
5	NW	11–18	Northern Atlantic
6	W	2–9	Northern Atlantic
7	NE	15–22	Norway, north Atlantic
8	NE	4–15	Norway, northern Atlantic
9	NE–N	6–11	Norway, northern Atlantic
10	N–W	2–11	Northern Atlantic
11	Variable	4–6	Norway, North Sea
12	SE–E	10–13	North Sea, Germany, Denmark
13	Variable	4–6	North Sea, Denmark
14	N–NE	5–8	Norway, North Sea
15	NW	5–8	UK, North Sea

history. Fig. 2 shows the track followed by the R/V Belgica during campaign 2 and the 15 sampling locations.

EDXRF results. Table 5 lists the EDXRF results for samples 1–8 of campaign 2. Sample 1 shows an extremely high Cu concentration (420 ng/m^3), probably due to contamination, although the source for this contamination is not clear. Sample 5 has high concentrations for marine elements, most likely due to contamination by sea spray droplets from breaking waves at the bow of the ship. Generally speaking, concentrations are reduced rapidly after the first sample and then remain low.

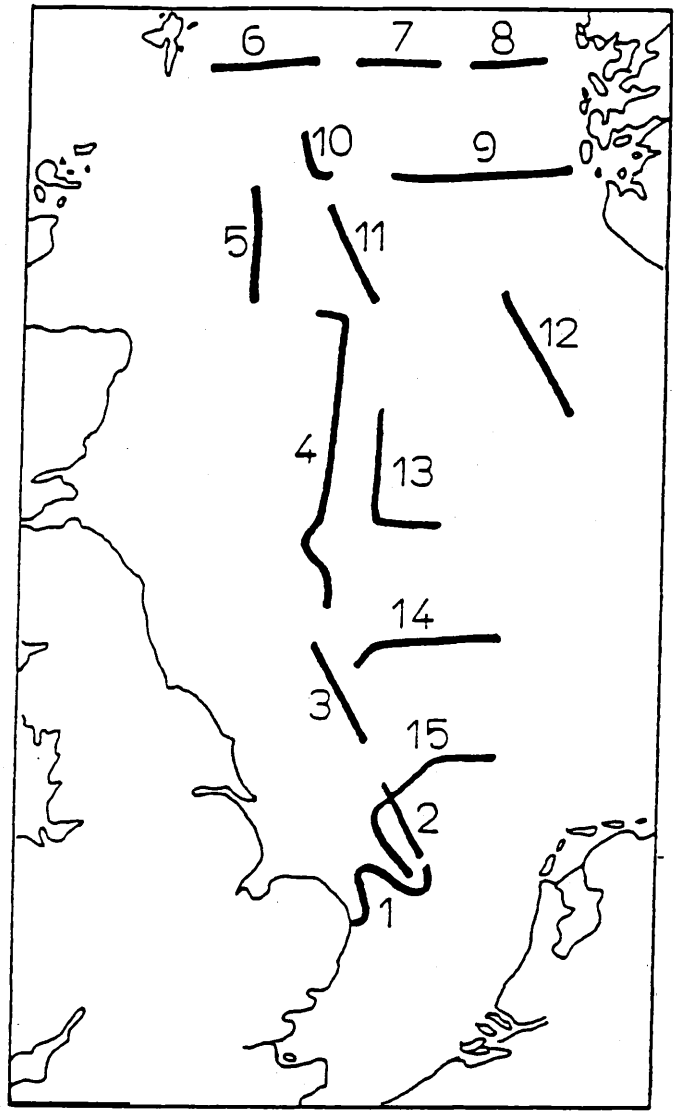

Fig. 2. Track of campaign 2 (the numbers refer to the sample numbers).

The air mass history indicates that the first sample was collected under partial influence of emissions from the UK, while samples 2–8 were collected under a predominantly northern wind with very little continental influence.

Table 6 lists the EDXRF results for the second part of campaign 2, for the coarse particle fraction. The highest wind speed, measured during collection of sample 12, is reflected in a Cl concentration of 17200 ng/m^3. During the time samples 9–11 were being collected, the wind direction was mainly north and sampled air masses had very little continental influence, resulting in low concentrations for all elements except Cl. As the wind direction changed and the sampled air mass passed over Germany and UK, concentrations started to increase. In the fine fraction results (Table 7), this is even more clearly the case. Pb concentrations in the fine fraction increase from below the detection limit (< 8 ng/m^3) in samples 9–11 to 18–27 ng/m^3 in samples 12–15. Zn concentrations increase from 1–4 ng/m^3 to 14–19 ng/m^3 and S concentrations from 460–940 ng/m^3 to 1580–2550 ng/m^3.

3.3. Campaign 3

General sampling data and meteorological information. The track followed during campaign 3 is shown in Fig. 3. Three filter samples were collected on the way north from Zeebrugge (Belgium) to Hull (UK), while three others were collected on the way back to Zeebrugge. Wind speed and wind direction data are listed in Table 8.

EDXRF results. The relatively high wind speed during the first part of the track is reflected in high Cl concentrations for samples 1–3. Sample 3, taken at the northern part of the track, shows the lowest heavy metal (Cu, Zn and Pb) concentrations (Table 9).

During the second part of the campaign, the wind direction changed from southwest, over north to east and finally to southeast while the wind speed decreased steadily from 10–15 ms to 0–5 m/s. Similar to the results of campaign 1, we

Table 5
DXRF results in ng/m³ — Campaign 2: first part of campaign 2, single filter used for particle collection

Element	Sample							
	1	2	3	4	5	6	7	8
	< 70	89	< 70	120	< 70	89	< 70	< 70
	2400	900	650	500	14 100	620	630	100
l	20 700	2490	5050	3140	99 600	2600	3040	910
	560	110	140	80	4100	100	110	24
a	440	120	130	99	3100	82	94	31
n	< 0.9	2.0	1	1	< 0.9	< 0.9	< 0.9	< 0.9
e	30	19	12	23	17	< 0.4	10	2.0
i	3	< 0.5	1.0	1.0	< 0.5	< 0.5	1	< 0.5
u	420	1	2	1	14	1	1	0.5
n	12	3	5	3	35	5	< 0.4	2
)	14	< 8	< 8	< 8	< 8	< 8	< 8	< 8

Table 6
DXRF results in ng/m³ — Campaign 2: second part of campaign 2, coarse particle fraction (> 2 μm)

Element	Sample						
	9	10	11	12	13	14	15
	740	180	120	1300	365	640	860
	6200	1370	665	17 200	3020	2500	4000
	170	40	26	300	110	200	250
a	230	31	26	380	93	370	450
	< 2.5	< 2.5	7	< 2.5	< 2.5	25	< 2.5
e	24	5	15	19	35	145	110
i	2	1	< 0.4	< 0.4	< 0.4	< 0.4	< 0.4
n	6	< 0.4	< 0.4	3	3	10	13
)	13	< 8	< 8	10	10	9	16

Table 7
DXRF results in ng/m³ — Campaign 2: second part of campaign 2, fine particle fraction (< 2 μm)

Element	Sample						
	9	10	11	12	13	14	15
	940	660	460	1580	2550	640	1660
	< 600	< 600	< 600	< 600	< 600	2500	< 600
	34	21	8	38	85	200	81
i	28	12	10	23	23	370	29
	< 2.5	< 2.5	< 2.5	< 2.5	< 2.5	25	< 2.5
	< 2.0	< 2.0	< 2.0	10	5	< 2.0	11
n	< 0.9	3	< 0.9	2	3	< 0.9	7
e	11	4	4	26	30	145	28
	1	1	1	2	2	< 0.5	6
i	4	1	< 0.4	2	2	< 0.4	4
n	4	2	1	14	19	10	19
)	< 8	< 8	< 8	19	18	9	27

see that Mn, Zn and Pb concentrations increase relatively more than other trace metal concentrations, when the wind turns to the south.

3.4. Campaign 4

General sampling data and meteorological information. Fig. 4 shows the track during this campaign. The first 6 samples were collected with easterly wind. During samples 7 and 8, the wind direction changed slightly to the southeast. The wind speed never exceeded 7 m/s and was most of the time lower than 5 m/s.

EDXRF results. Table 10 shows the EDXRF results. Cl was not detected in a single sample. At very low wind speeds, the sea produces little sea spray droplets. In addition, high acid pollution concentrations will react with the few NaCl aerosols in the marine atmosphere, resulting in a release of HCl.

All anthropogenic elemental concentrations measured during this campaign are very high. Pb concentrations vary from 46 to 280 ng/m^3, Zn concentrations from 110 to 790 ng/m^3 and S concentrations from 6400 to 15 200 ng/m^3. It is well known that, during the meteorological conditions present during this campaign, pollutant concentrations tend to rise rapidly. A combination of a low inversion height and low wind speeds limits natural dispersion of pollutants. Furthermore, the absence of any form of precipitation restricts the possibilities of concentration decrease through wet deposition processes.

At the end of campaign 4, the wind direction gradually shifted from east to southeast, resulting in the highest concentrations for all elements.

Fig. 3. Track of campaign 3 (the numbers refer to the sample numbers).

3.5. Campaign 5

General sampling data and meteorological information. Campaign 5 was performed in the English Channel, between Zeebrugge (Belgium) and the border of open Atlantic Ocean at 5°W. The track followed during this sampling campaign is shown in Fig. 5.

During the first half of the sampling campaign, a moderate wind speed of 10 m/s increased gradually to 15 m/s, while the wind direction was southwest to west. During the second half of campaign 5, the wind speed rapidly decreased to below 5 m/s and the wind direction changed to east to southeast (Table 11).

EDXRF results. As the R/V Belgica passed through the English Channel and the wind speed increased, the origin of the sampled air mass became more and more marine. This was reflected in a steady decrease in the S concentration from samples 1 to 5. While the wind direction changed from southwest to southeast and the

Table 8
Meteorological data — Campaign 3

Sample	Wind sector	Wind speed (m/s, range)
1	SW	7–10
2	SW	4–6
3	SW	7–9
4	S–SW	3–6
5	NE–E	2–4
6	E–SE	5–10

Table 9
EDXRF results in ng/m^3 — Campaign 3

Element	Sample					
	1	2	3	4	5	6
Si	< 140	260	< 140	680	190	870
P	120	< 70	< 70	< 70	< 70	< 70
S	1630	870	640	2740	4510	4960
Cl	6060	3960	5070	910	730	730
K	420	230	340	840	420	700
Ca	360	360	210	170	170	700
Ti	< 2.5	26	< 2.5	23	< 2.5	< 2.5
V	< 2.0	< 2.0	< 2.0	29	74	20
Cr	31	6.0	55	11	97	46
Mn	< 0.9	< 0.9	< 0.9	22	15	68
Fe	130	180	110	320	610	840
Ni	4.0	5.0	8.0	14	30	11
Cu	6.1	4	< 0.4	6.8	5.0	8.5
Zn	53	34	23	86	4.2	86
Pb	34	31	< 8	53	18	69

Table 10
EDXRF results in ng/m^3 — Campaign 4

Element	Sample							
	1	2	3	4	5	6	7	8
Si	840	1130	1120	940	1200	1860	2490	4820
P	290	420	370	380	380	600	690	690
S	6360	9600	8250	8790	8740	12900	14500	15200
K	300	340	330	420	400	560	740	1560
Ca	180	150	250	160	240	520	980	1970
Ti	11	20	31	15	26	69	100	180
V	14	18	13	11	17	33	42	46
Cr	2.3	4	8	21	7	8	14	27
Mn	17	17	19	23	21	33	46	180
Fe	370	360	410	400	530	980	1170	2760
Ni	8	8	6	7	7	15	21	24
Cu	11	10	15	16	14	22	21	39
Zn	140	150	110	200	150	200	220	790
Pb	120	76	46	84	73	140	170	280

Table 11
Meteorological data — Campaign 5

Sample	Wind sector	Wind speed (m/s, range)
1	SW	5–10
2	S–SW	10–15
3	S–SW	10–15
4	NW	10–15
5	W–NW	5–10
6	Variable	5–10
7	Variable	0–5

wind speed decreased at the end of the campaign, concentrations for most elements went up again (Table 12). The continental influence and the very low wind speed in sample 7 is illustrated by the low Cl concentration: < 600 ng/m^3 versus 3190 ng/m^3 in the previous sample.

3.6. Campaign 6

General sampling data and meteorological information. Campaign 6 was organized through the

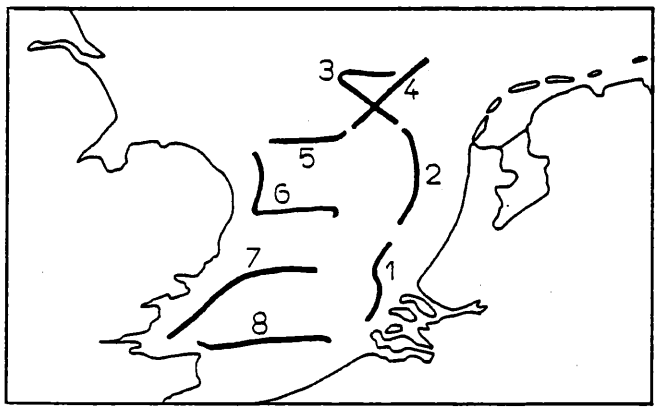

Fig. 4. Track of campaign 4 (the numbers refer to the sample numbers).

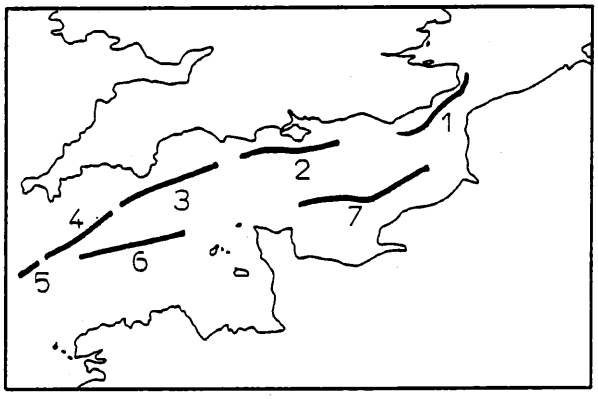

Fig. 5. Track of campaign 5 (the numbers refer to the sample numbers).

English Channel and seven filter samples were collected between Zeebrugge (Belgium) and the most westerly point of the followed track. Some 96 h backward air mass trajectories are shown in Fig. 6.

EDXRF Results. Table 13 lists the EDXRF results for sampling campaign 6. Analogous to campaign 5, the concentrations of most elements go down steadily, as the R/V Belgica passed through the English Channel and the origin of the collected air mass is mostly marine.

3.7. Campaign 7

General sampling data and meteorological information. Fig. 7 shows the track followed during campaign 7. The 96-h backward air mass trajectories for the four samples collected are shown in Fig. 8. A stacked filter unit was used for collection of the airborne particulate material.

EDXRF results. The coarse and fine particle concentrations are listed in Tables 14 and 15. respectively.

The air mass collected during samples 3 and 4

Table 12
EDXRF results in ng/m^3 — Campaign 5

Element	Sample						
	1	2	3	4	5	6	7
Al	< 200	230	< 200	230	< 200	< 200	< 200
Si	180	270	150	220	< 140	< 140	< 140
P	140	300	200	260	78	82	< 70
S	1360	1530	870	860	410	590	1200
Cl	3270	10400	7190	9990	3560	3190	< 600
K	150	280	150	180	69	95	89
Ca	180	230	150	170	80	93	160
Ti	< 2	< 2	< 2	< 2	< 2	< 2	17
V	12	9	< 2	< 2.0	2	6	18
Cr	7	7	< 1.5	< 1.5	< 1.5	< 1.5	< 1.5
Mn	2	< 0.9	< 0.9	< 0.9	< 0.9	< 0.9	3
Fe	48	5	4.1	3.7	7.3	16	105
Ni	5	5	< 0.4	< 0.4	< 0.4	< 0.4	5
Cu	< 0.4	< 0.4	< 0.4	< 0.4	< 0.4	< 0.4	2
Zn	6	2	< 0.4	< 0.4	< 0.4	2	27
Pb	10	< 8	< 8	< 8	< 8	< 8	< 8

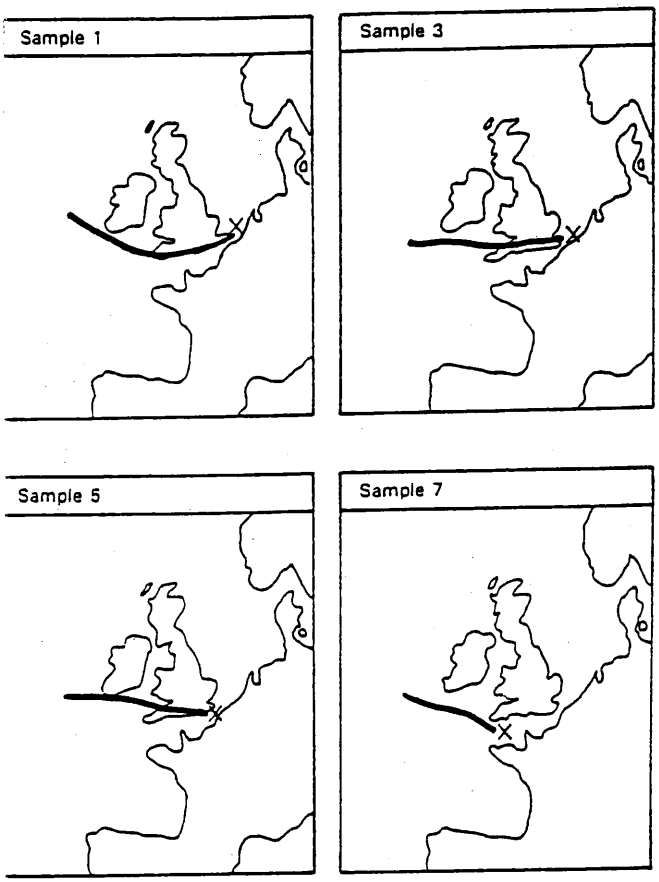

Fig. 6. Some 96-h back trajectories for campaign 6 (sampling location indicated by an ×).

has an important influence from emissions in France, while samples 1 and 2 are influenced by emissions in the UK.

3.8. Campaign 8

General sampling data and meteorological information. The track followed during campaign 8 is shown in Fig. 9. The 96-h backward trajectories are shown in Fig. 10 for samples 1–5; they indicate continental air masses. Samples 7 and 8 were collected by a stacked filter unit when the wind direction changed to the southwest and the wind speed rapidly increased up to 10–11 on the Beaufort scale.

EDXRF results. Table 16 shows the coarse particle fraction results for samples 1–8. Cl concentrations are reduced until sample 6, then a sudden increase due to a violent change in wind direction and wind speed results in a Cl concentration of 5000–6000 ng/m^3, while Fe, Zn and Pb concentrations decrease abruptly at sample 7.

Table 17 lists the fine particle fraction results for campaign 8. S, K, Fe, V, Zn and Pb all show the same profile: an abrupt decrease as the meteorological situation changes rapidly.

Table 13
EDXRF results in ng/m^3 — Campaign 6

Element	Sample						
	1	2	3	4	5	6	7
Al	250	< 200	< 200	< 200	< 200	< 200	< 200
Si	510	190	210	170	140	140	300
P	220	79	110	< 70	< 70	< 70	85
S	1890	1310	1080	1010	410	570	1040
Cl	5440	< 600	2470	< 600	< 600	< 600	1910
K	480	72	84	49	10	< 9	< 9
Ca	320	62	86	48	10	6.6	< 6
Ti	8	3	< 2	3	2.0	< 2.0	< 2.0
Mn	1.0	< 0.9	0.9	< 0.9	< 0.9	< 0.9	< 0.9
Fe	28	12	6	15	3	1.0	3
Ni	3.0	0.6	< 0.5	1.1	< 0.5	< 0.5	0.7
Cu	1.0	< 0.4	< 0.4	0.7	< 0.4	0.4	0.5
Zn	6.7	0.4	0.6	< 0.4	< 0.4	0.5	< 0.4
Pb	< 8	10	< 8	< 8	< 8	< 8	< 8

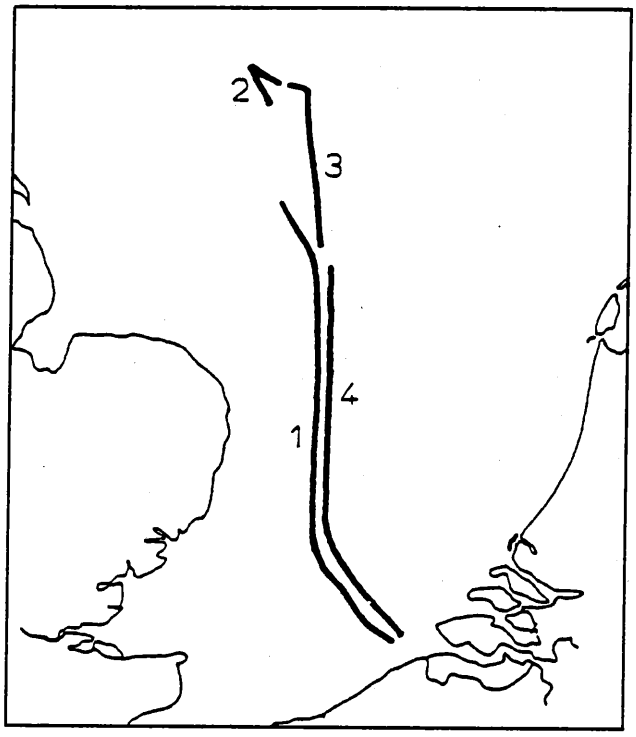

Fig. 7. Track of campaign 7 (the numbers refer to the sample numbers).

3.9. Campaign 9

General sampling data and meteorological information. Six samples were collected when crossing the Southern Bight of the North Sea, between Zeebrugge and London. The wind direction was stable during the sampling period and remained between 280 and 320. Samples 5 and 6 were collected during entrance of the Thames estuary in the direction of London.

EDXRF results. Table 18 shows the EDXRF results for campaign 9. The very high Mn concentrations in sample 1 is probably due to an unknown source of contamination. Samples 1–4 have comparable concentrations for most elements. The 10-fold increase in Fe and Zn concentrations is clearly associated with emissions from the London area and the industry in southern England. Cu and Ni concentrations go up by a factor of 5.

3.10. Campaign 10

General sampling data and meteorological information. Fig. 11 shows the track followed during campaign 10. All samples were collected under

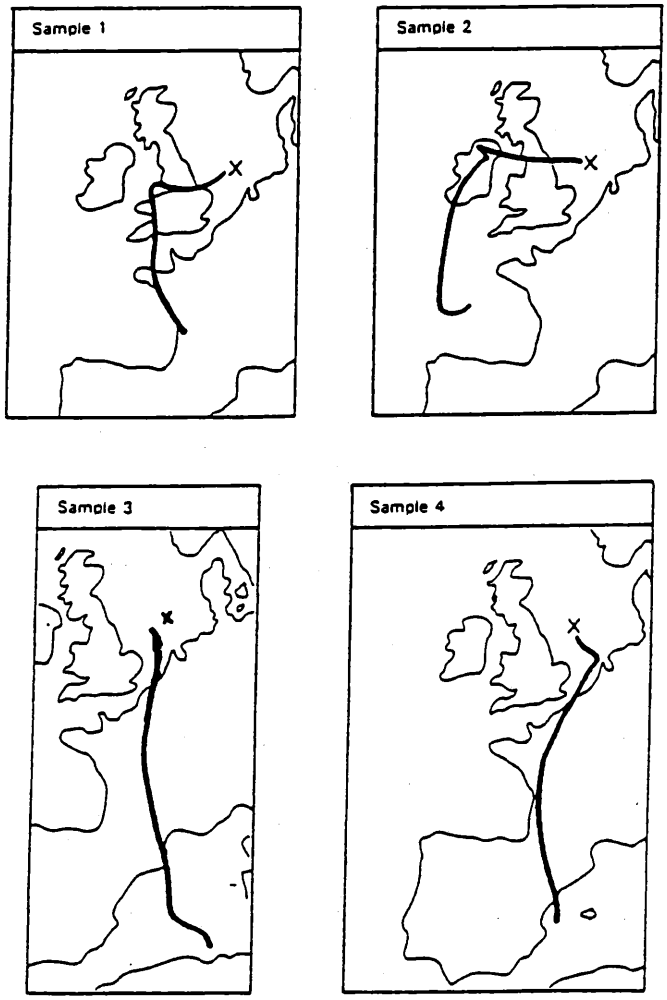

Fig. 8. The 96-h backward trajectories for campaign 7 (sampling location indicated with an ×).

similar meteorological conditions. The wind direction stayed within the northern sector, between 320° and 30°.

EDXRF results. Table 19 lists the EDXRF results of campaign 10. All elemental concentrations in all eight samples are quite low. Not much variation is found as a function of time, which is in agreement with the constant wind direction and thus the fairly constant air mass history.

4. Average concentrations

Statistical data on the complete data set of aerosol samples are listed in Table 20: average, median, first quartile and fourth quartile concentration. These averages were calculated by leaving

Table 14
EDXRF results in ng/m³ — Campaign 7, coarse particle fraction (> 2 μm)

lement	Sample			
	1	2	3	4
l	300	< 200	< 200	< 200
i	750	150	< 140	< 140
	< 70	81	120	< 70
	400	400	590	460
l	1930	4140	4890	2300
	150	93	110	77
a	46	91	110	68
i	20	< 2.5	< 2.5	< 2.5
	< 2.0	< 2.0	< 2.0	5
fn	5	< 0.9	< 0.9	< 0.9
e	260	57	34	180
i	4	1.2	1.0	6
u	2	1.0	1.2	3
n	15	3	1.1	6
b	< 8	< 8	9	< 8

ut two contaminated samples of campaign 2. hese numbers can be considered as average oncentrations for the total North Sea, including ie English Channel.

Table 21 lists separately the average concentraon for the total North Sea, the Southern Bight f the North Sea (defined as the area of the lorth Sea south of latitude 54°N), and the northrn part of the North Sea. Altogether 35 samples were collected between 51° and 54°N. These are considered to be representative for the atmosphere above the Southern Bight of the North Sea.

It is obvious from Table 21 that concentrations in the northern part of the North Sea are much lower than in the Southern Bight. Mn, Zn, Pb and Fe all show concentrations that are more than 10 times higher in the southern part of the North

Table 15
EDXRF results in ng/m³ — Campaign 7, fine particle fraction (< 2 μm)

lement	Sample			
	1	2	3	4
l	240	< 200	< 200	< 200
i	150	< 140	< 140	< 140
	190	< 70	130	< 70
	1150	660	740	1480
l	6540	1610	5300	< 600
	150	59	24	77
a	35	18	14	12
	3	< 2.0	< 2.0	< 2.0
r	< 1.5	5	< 15	< 1.5
fn	3	1	< 0.9	< 0.9
e	40	5	7	42
i	2	< 0.5	1	4
u	< 0.4	< 0.4	1.2	1.0
n	11	3	3	11
b	13	< 8	9	9

Table 16
EDXRF results in ng/m^3 — Campaign 8, coarse particle fraction (2 μm)

Element	Sample							
	1	2	3	4	5	6	7	8
Al	310	230	< 200	< 200	< 200	< 200	< 200	< 200
Si	520	510	150	220	190	140	< 140	< 140
P	130	100	< 70	< 70	< 70	< 70	120	130
S	1720	1300	550	880	760	1060	510	670
Cl	1450	710	< 600	< 600	< 600	< 600	5080	5900
K	110	160	51	100	79	62	110	300
Ca	280	400	90	120	110	71	110	260
Ti	48	21	4	6	< 2.5	4	< 2.5	< 2.5
V	2	3	< 2.0	< 2.0	< 2.0	< 2.0	< 2.0	< 2.0
Mn	11	71	2	2	3	2	< 0.9	< 0.9
Fe	490	290	67	96	73	57	4	3
Ni	3	2	2	< 0.5	1.2	1.0	1.0	2
Cu	3	4	1.0	1.3	1.2	1.0	< 0.4	1.1
Zn	51	48	17	20	16	18	2	3
Pb	24	32	9	17	< 8	15	13	< 8

Sea compared with the northern part. Si, S, Ti and Cu concentrations are 4–6 times higher in the south. K. Ca, V and Ni have very similar 'southern part to northern part' concentration ratios: 3.6–3.9. Al, P and Cr show the least difference between the northern part concentrations and southern part. This is merely a result of the large number of observations that were below the detection limit of the analytical technique used. Average Cl concentrations are identical to within 5%.

5. Factor analysis

The main goal of applying factor analysis is to try to reduce a large number of variables (in our

Table 17
EDXRF results in ng/m^3 — Campaign 8, fine particle fraction (< 2 μm)

Element	Sample							
	1	2	3	4	5	6	7	8
Al	210	< 200	< 200	< 200	200	< 200	< 200	< 200
Si	160	180	160	< 140	< 140	< 140	< 140	< 140
P	220	200	130	190	180	170	< 70	< 70
S	3930	3470	2660	3780	3680	3200	92	< 80
Cl	610	< 600	< 600	< 600	< 600	< 600	< 600	< 600
K	200	320	190	240	140	110	10	< 9
Ca	15	33	< 6	7	< 6	7	< 6	< 6
Ti	7	3	< 2.5	3	< 2.5	4	< 2.5	5
V	20	16	10	10	8	6	2	6
Cr	6	3	2	2	< 1.5	< 1.5	4	6
Mn	13	18	10	6	5	4	< 0.9	< 0.9
Fe	197	159	25	18	9	5	< 0.4	< 0.4
Ni	3	5	2	2	1.2	1.2	< 0.5	< 0.5
Cu	3	8	3	1.3	< 0.4	< 0.4	< 0.4	< 0.4
Zn	68	107	43	32	23	20	< 0.4	< 0.4
Pb	66	135	58	52	31	31	< 8	< 8

Table 18
EDXRF results in ng/m^3 — Campaign 9

Element	Sample					
	1	2	3	4	5	6
Si	< 140	< 140	< 140	< 140	250	550
S	900	1970	1480	1070	4830	7940
Cl	4520	6200	9840	6440	< 600	970
K	280	270	640	230	330	530
Ca	330	290	1090	290	210	820
Ti	20	< 2.5	20	13	17	48
V	20	11	12	< 2.0	10	17
Cr	15	40	26	17	19	48
Mn	170	< 0.9	7.9	< 0.9	14	20
Fe	87	68	110	41	280	550
Ni	10	4.7	6.0	1.5	4.9	8.2
Cu	8	8	15	3	7	15
Zn	74	13	64	10	72	140
Pb	19	13	18	< 8	65	120

case, 16 elemental concentrations) measured in a system (in our case, the North Sea atmosphere) to a limited number of independent factors that explain the variation of the observed system.

Factor analysis was performed using STATGRAPHICS version 2.6 software that runs on an AT-type PC.

5.1. Coarse fraction versus fine fraction

Factor analysis was performed on a limited sample set of 19 aerosol samples, collected with a stacked filter unit, in order to evaluate any difference in inter-element correlations between the coarse and the fine particle fraction. The results for the coarse fraction aerosol samples are presented in Table 22. Since, in a significant number of samples, several elements are not detected, only seven variables were selected: S, Cl, K, Ca, Fe, Zn and Pb. Some 90% of the total variance can be explained by the first three independent factors. The first factor is heavily loaded with Pb (0.94), S (0.79) and Zn (0.72) and represents sulphate particles that are rich in trace metals. The second factor with K (0.96), Cl (0.83) and Ca

Table 19
EDXRF results in ng/m^3 — Campaign 10

Element	Sample							
	1	2	3	4	5	6	7	8
S	290	220	230	220	130	340	140	300
Cl	1030	670	950	< 600	< 600	2400	< 600	< 600
K	49	35	88	17	16	100	34	17
Ca	60	52	28	25	49	110	20	< 6
Ti	23	< 2	7	15	20	13	9	11
V	12	6	5	< 2.0	6	< 2.0	< 2.0	8
Cr	30	18	12	19	21	16	12	22
Fe	43	38	16	51	35	23	22	28
Ni	3	2	1.5	< 0.5	3	< 0.5	3	3
Cu	6	4	3	4	5	4	4	5
Zn	7	4	3	4	2	2	3	4

Table 20
Average, median, first and fourth quartile concentrations in ng/m^3, for all analysed samples

Element	Average	Median	First quartile–fourth quartile
Si	399	< 140	< 140–270
P	174	< 70	< 70–200
S	2750	1400	630–3900
Cl	2890	1400	< 600–4500
K	254	200	88–340
Ca	239	150	78–320
Ti	14.0	0.7	< 2.5–17
V	12.4	5.9	< 2.0–17
Cr	12.1	2.6	< 1.5–15
Mn	13.6	< 0.9	< 0.9–10
Fe	229	48	16–320
Ni	4.7	2.7	0.7–7.0
Cu	5.5	3.1	0.6–8.0
Zn	54.9	12	2.7–74
Pb	40.6	13	< 8–53

(0.77) is associated with sea salt particles. The third factor is heavily loaded with Fe (0.90) and can be associated with soil dust particles.

Factor analysis on the fine particle fraction (Table 23) yields four factors that explain 91.9% of the observed variance. Factor 1 with S (0.91), K (0.85), Pb (0.76) and Zn (0.75) is again identified with trace metal rich sulphate particles. Factor 2 is loaded with Cu (0.88), Ni (0.86) and Zn (0.62) and is also pollution related. Factor 3 with Ca (0.95) and Fe (0.67) is associated with $CaSO_4$ and fly-ash emissions. The fourth factor, with Cl (0.98), is typical for the marine aerosol.

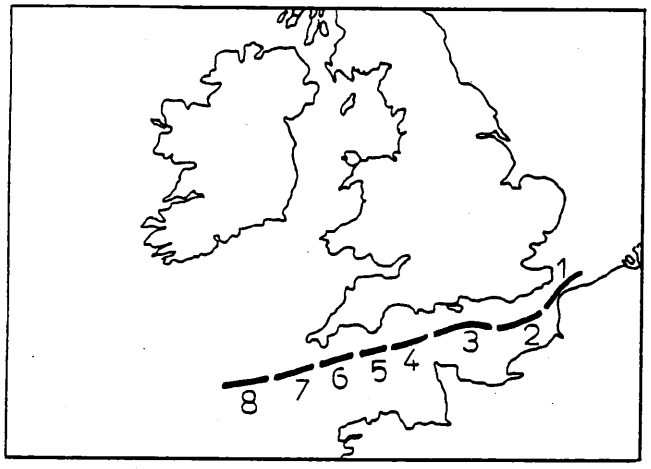

Fig. 9. Track of campaign 8 (the numbers refer to the sample numbers).

5.2. Samples collected on the Southern Bight of the North Sea

Thirty-five samples were collected when the R/V Belgica was in the Southern Bight of the North Sea, between 51° and 54°N. Factor analysis was performed on this data set using the fol-

Table 21
Average atmospheric concentrations in ng/m^3

Element	Southern Bight	Northern North Sea
Si	725	119
P	249	97
S	4780	778
Cl	2960	2830
K	401	110
Ca	382	100
Ti	24.9	4.6
V	18.8	4.9
Cr	14.2	10.1
Mn	28.5	0.8
Fe	432	31.3
Ni	7.5	2.0
Cu	9.2	1.9
Zn	107	4.7
Pb	77	5.0

lowing variables: S, Cl, K, Ca, V, Fe, Ni, Cu, Zn and Pb.

Table 24 shows that 91.5% of the observed variance can be explained by three factors. Sea salt particles are identified by the third factor with a high loading for Cl (0.92). Factor 2 is heavily loaded with V (0.92) and Ni (0.91), two elements that are typical for oil burning residue. The first factor contains all other elements: Zn (0.91), Ca (0.89), Cu (0.87), K (0.85), Fe (0.84), Pb (0.83) and S (0.69).

Factor analysis applied to our data is only able to reveal a limited number of aerosol particle sources: sea salt particles, oil burning residue and trace metal rich particles. Although there may be a larger number of particle sources and thus different particle types, the emission occurs mainly on land. After dispersion and transport, the continental aerosol will reach the marine atmosphere as a well mixed aerosol. In this way, factor analysis on bulk results can not reveal the original sources. The fact that emissions from oil burning

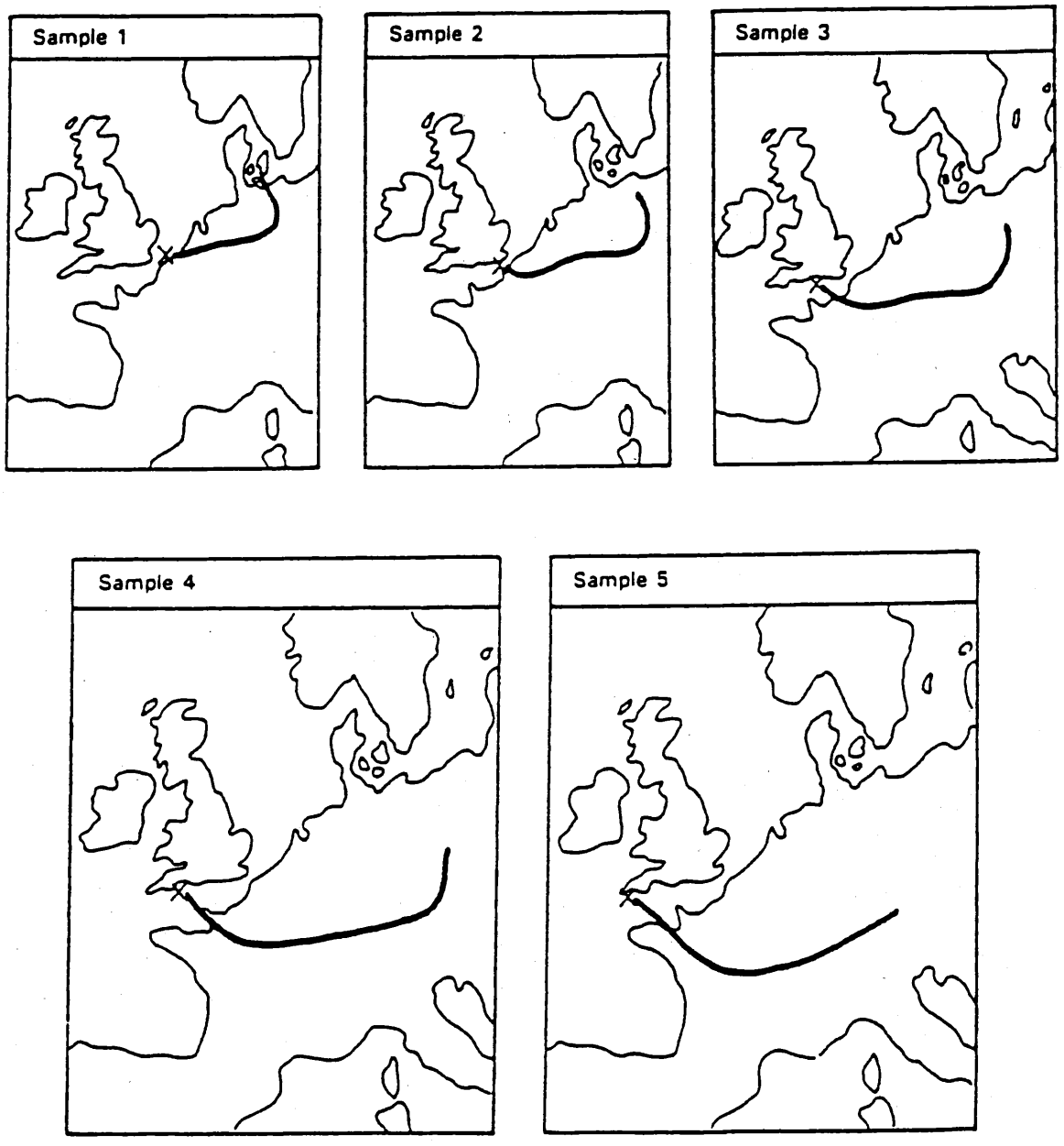

Fig. 10. Some 96-h backward air mass trajectories for campaign 8 (sampling location indicated with an ×).

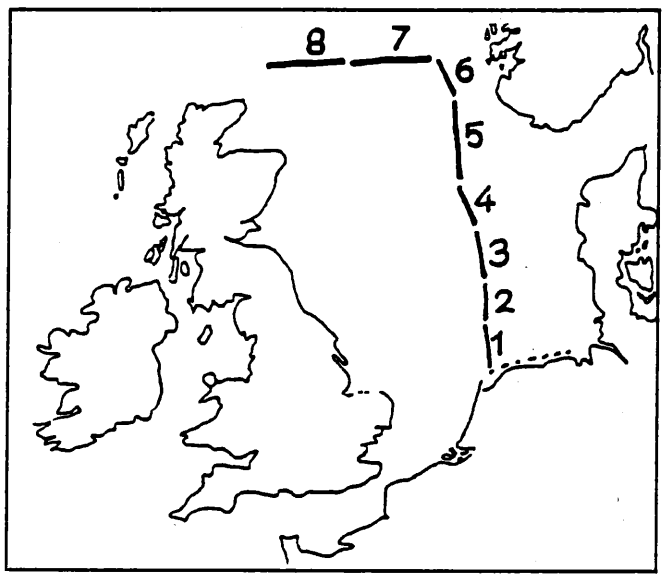

Fig. 11. Track of campaign 10 (the numbers refer to the sample numbers).

are often recognized as an independent source above the sea, suggests that this source has a somewhat different behaviour than other pollution sources. This might be explained by the emission of Ni and V through diesel engine exhaust of the numerous ships, present on the North Sea.

In order to differentiate the various continental aerosol sources, other analysis techniques should be used; single particle techniques such as electron microprobe can offer more information here (Van Grieken and Xhoffer, 1992).

6. Conclusions

Atmospheric concentrations of different elements in the lower troposphere above the North Sea are highly variable as a function of both time and location. Rapid changes in the meteorological situation are reflected without delay in the atmospheric concentrations of trace elements.

Average Cl concentration above the northern part of the North Sea are approximately the same as above the Southern Bight of the North Sea. Mn, Zn, Pb and Fe concentrations are 10–30 times lower in the northern North Sea atmosphere than in the southern part. Si, S, Ti, Cr, K,

Table 22a
Factor analysis results, coarse particle fraction

Factor	Eigenvalue %	Variance	Cumulative variance
1	3.6	51.7	51.7
2	2.3	32.9	84.5
3	0.4	6.3	90.9
4	0.4	5.6	96.4
5	0.1	1.9	98.4
6	0.1	1.2	99.6
7	0.0	0.4	100.0

Table 22b
Estimated communality

Variable	Estimated communality
S	0.871
Cl	0.826
K	0.931
Ca	0.861
Fe	0.952
Zn	0.975
Pb	0.943

Table 22c
Varimax rotated factor loading matrix

Variable	Factor		
	1	2	3
S	0.79	0.37	0.33
Cl	0.05	0.83	0.38
K	0.05	0.96	0.04
Ca	0.48	0.77	0.21
Fe	0.37	0.03	0.90
Zn	0.72	0.13	0.66
Pb	0.94	0.05	0.22

Table 23a
Factor analysis results, fine particle fraction

Factor	Eigenvalue %	Variance	Cumulative variance
1	4.97	55.2	55.2
2	1.68	18.6	73.8
3	0.85	9.4	83.3
4	0.78	8.7	91.9
5	0.38	4.2	96.1
6	0.23	2.6	98.7
7	0.87	1.0	99.7
8	0.28	0.3	100.0
9	0.02	0.0	100.0

Table 23b
Estimated communality

Variable	Estimated communality
S	0.925
Cl	0.997
K	0.933
Ca	0.949
Fe	0.863
Ni	0.790
Cu	0.899
Zn	0.972
Pb	0.946

Table 23c
Varimax rotated factor loading matrix

Variable	Factor			
	1	2	3	4
S	0.91	0.14	0.17	0.21
Cl	0.10	0.12	0.10	0.98
K	0.85	0.29	0.35	0.10
Ca	0.07	0.17	0.95	0.10
Fe	0.46	0.45	0.67	0.05
Ni	0.20	0.86	0.11	0.06
Cu	0.32	0.88	0.07	0.13
Zn	0.75	0.62	0.11	0.09
Pb	0.76	0.59	0.04	0.09

Ca, V, Ni and Cu concentrations are on the average 3–6 times lower above the northern North Sea, compared with the Southern Bight atmosphere.

Factor analysis performed on all samples distinguished several particle types, predominantly the sea-salt particles and anthropogenic particles.

Table 25 compiles some published aerosol concentration data relevant to the study area. Compared with similar results reported very recently by Ottley and Harrison (1993) ours are in relatively good agreement. However, for example, compared with the ship-based measurements performed by Dedeurwarder (1988) and Xhoffer et al. (1991), our results for the Southern Bight of the North Sea are up to 50% lower. This difference can most likely be attributed to the fact that these aerosol samples were collected in the very southern part of the North Sea, whereas our

Table 24a
Factor analysis results, Southern Bight samples

Factor	Eigenvalue	% variance	Cumulative variance
1	6.86	68.7	68.7
2	1.30	13.0	81.7
3	0.98	9.8	91.5
4	0.29	2.9	94.4
5	0.17	1.7	96.2
6	0.12	1.2	97.3
7	0.11	1.1	98.4
8	0.09	0.9	99.3
9	0.05	0.5	99.8
10	0.02	0.2	100.0

Table 24b
Estimated communality

Variable	Estimated communality
S	0.854
Cl	0.899
K	0.889
Ca	0.915
V	0.960
Fe	0.937
Ni	0.973
Cu	0.903
Zn	0.932
Pb	0.890

Table 24c
Varimax rotated factor loading matrix

Variable	Factor		
	1	2	3
S	0.69	0.26	0.56
Cl	0.08	0.21	0.92
K	0.85	0.41	0.03
Ca	0.89	0.24	0.25
V	0.25	0.92	0.24
Fe	0.84	0.43	0.21
Ni	0.36	0.91	0.15
Cu	0.87	0.26	0.27
Zn	0.91	0.20	0.25
Pb	0.83	0.16	0.41

Table 25
Comparison with some published aerosol concentration data (ng/m^3) relevant to the study area

Element	This work	Ottley and Harrison (1993)		Xhoffer et al. (1991)	Dedeurwaerder (1988)	Van Jaarsveld et al. (1986)
		North Sea	Marine*			
K	254	1239	357	—	—	—
Ca	239	467	269	—	—	—
Mn	13.6	—	—	—	58	—
Fe	229	184	156	—	560	—
Cu	5.5	6.9	1.8	9.2	17	1.9
Zn	54.9	74.6	24.1	110	150	17
Pb	40.6	29.1	3.5	77	150	33

* Marine indicates north air mass source region

samples are covering the whole area of the Southern Bight of the North Sea (south of 54°N). Model calculations by Van Jaarsveld et al. (1986) in the case of Pb show a good agreement with our observed Pb concentrations.

Acknowledgement

This work was partially prepared in the framework of the Impulse Programme in Marine Sciences, supported by the Belgian State Prime Minister's Service, Science Policy Office (contract MS/06/050).

References

Dedeurwaerder, H.L., 1988. Study of the Dynamic Transport and of the Fall-out of Some Ecotoxicological Heavy Metals in the Troposphere of the Southern Bight of the North Sea. Ph.D. Dissertation, Vrije Universiteit Brussel, Brussels, Belgium.

Ottley, C.J. and R.M. Harrison, 1993. Atmospheric dry deposition flux of metallic species to the North Sea. Atmos. Environ., 27A: 685–695.

Van Espen, P., K. Janssens, and J. Nobels, 1986. AXIL-PC, Software for the analysis of complex X-ray spectra. Chemometr. Intell. Lab. Syst., 1: 109–114.

Van Grieken, R. and C. Xhoffer, 1992. Microanalysis of individual environmental particles. J. Anal. Atom. Spectrom., 7: 81–88.

Van Jaarsveld, J.A., R.M. Van Aalst, and D. Onderlinden, 1986. Deposition of Metals from the Atmosphere into the North Sea: Model calculations, Report 842015002, RIVM, Bilthoven.

Xhoffer, C., P. Bernard, R. Van Grieken, and L. Van der Auwera, 1991. Chemical characterization and source apportionment of individual aerosol particles over the North Sea and the English Channel using multivariate techniques. Envir. Sci. Technol., 25: 1470–1478.

Journal of Atmospheric Chemistry **20:** 179–212, 1995.

Atmospheric Concentrations and Deposition of Heavy Metals over the North Sea: A Literature Review

JASNA INJUK and RENÉ VAN GRIEKEN
University of Antwerp (U.I.A.), Department of Chemistry, B-2610 Antwerpen-Wilrijk, Belgium

(Received: 4 January 1994; in final form: 24 May 1994)

Abstract. A literature review of the atmospheric concentration rates and dry and wet deposition fluxes of particulate Cd, Cr, Cu, Pb and Zn to the North Sea and adjacent areas is given. The results of direct measurements of dry and wet deposition fluxes are compared to indirect estimates and to modelling values. This work points out the large uncertainties in results of different studies on atmospheric input of trace elements into the North Sea. The current knowledge about the dependence of the deposition velocity upon the particle size and about the processes controlling wet deposition fluxes, and the quality and completeness of the emission data are still inadequate for describing the environmental cycle and impact of heavy metals in the North Sea.

Key words: Heavy metals, concentration, deposition, North Sea, troposphere.

1. Introduction

At present, there is much discussion on the sources and abatement policies of pollution to the sea. Atmospheric transport and deposition of pollutants over long distances have received much attention, particularly in connection with the acid rain problem, the formation of photochemical oxidants and ozone, and the global climatic effects. It is only relatively recently that it has become possible to estimate the amounts of material entering the oceans via the atmosphere. Though the pollution of the oceans is not a new phenomenon, the question of how important a role the atmosphere plays in this was addressed only a decade ago (NAS, 1978). As the calculations have become less crude, the atmospheric route seems to have gained in importance relative to the other paths, like those borne by rivers and direct discharges.

Still, quantitative data on heavy metal emissions, their concentration levels in air and their accumulation and transfer in the North Sea ecosystem have not been systematically gathered and intercompared hitherto. There are various sources which emit trace metals into the atmosphere, i.e. man-made pollution, aerosol formation from sea-spray, volcanic activity, vegetation and soil erosion. The concentrations of anthropogenic pollutants in the atmosphere are mainly due to the volatility of these elements at the high temperatures of fossil fuel combustion, and many other high-temperature industrial processes, particularly the extraction of non-ferrous metals

TABLE I. Comparison of the 1982 survey of trace element emission by Pacyna (1987) with national emission data (tons y^{-1}) for countries bordering the North Sea

Country	Cd	As	Pb	Zn	Reference
U.K.	31	117	8610	2230	Pacyna, 1987
	14	315	7590	–	Hutton and Symon, 1986
Belgium	12	85	2100	700	Pacyna, 1987
	22	–	2380	1090	Van Jaarsveld *et al.*, 1986
The Netherlands	5.5	34	2200	290	Pacyna, 1987
	3.8	–	–	–	Kendall *et al.*, 1985
Germany	80	350	5560	6660	Pacyna, 1987
	79*	500	7590	10000	*Schladot and Nürnberg, 1982 Braun *et al.*, 1984
Denmark	6.3	7	650	130	Pacyna, 1987
	5	–	–	–	Murkherje, 1986
Sweden	16	183	1053	426	Pacyna, 1987
	12	130	950	1200	Naturvardsverket, 1982
Norway	2.1	41	730	120	Pacyna, 1987
	1.7–2.7	–	–	–	Naturvardsverket, 1982

from sulphides. Among other industrial sources, waste incineration is becoming increasingly important, particularly in Western Europe, because of the emissions of Cd, Pb and other trace elements and a need to incinerate increasing amounts of wastes. A first preliminary review of the atmospheric emissions of various trace elements from anthropogenic sources in Europe, for 1979/1980, was provided by Pacyna (1983). The earlier surveys were concerned with either a single metal (van Enk, 1980; Hutton, 1982) or certain types of emission sources, e.g. fossil fuel combustion. As such, they were very valuable for control strategies, but less applicable for modelling of the long-range transport of air pollutants and their migration. The survey of Pacyna has more recently been updated and improved. In Table I, the estimates of Pacyna (1987) of trace element emissions from all sources in countries bordering the North Sea are compared with the countries' own estimates. The former estimates are based on emission factors, calculated separately for each of the countries, on statistics on the consumption of raw materials and on the production of various industrial goods in 1982.

2. Data on Trace Metal Concentrations in Air

There is quite a detailed data base of concentration measurements for trace metals in aerosols over the European regional seas (GESAMP, 1989). Table II gives an overview of literature values for the particulate Cd, Cr, Cu, Pb and Zn concentrations in the marine troposphere over the North Sea and adjacent areas. The data set covers a relatively long time period, of about 20 years. The oldest data, supplied by Peirson *et al.* (1973), Kretzschmar and Cosemans (1979) and Van Aalst *et al.* (1983) (who give a list of concentrations measured between 1974 and 1981 at coastal stations in Great Britain, Belgium and The Netherlands), are generally higher than the other reported values in Table II. The less accurate collection procedures and the precision of measurements in those days may be one reason, but these values were also obtained from coastal or even inland measurements, i.e. closer to the emission sources. Van Daalen (1991) measured the concentrations over the province of South-Holland in the Netherlands and although his sampling sites were not very far removed from the North Sea coast, his data show clearly high concentrations. The rest of the coastal values in Table II seem to agree very well with the exception of the Belgian ones from Ostende, due to very high concentrations measured in the continental air masses (factor 2 to 5 higher compared to the values for the eastern and western air-masses). Although not explicitly North Sea coastal measurements, the data collected by Flament *et al.* (1987) at the French coast in the Channel and those reported by Schneider (1987) in the Kiel Bight offer a good basis for intercomparison of results.

In contrast with measurements performed at coastal stations around the North Sea, much less data are available for samples taken on the North Sea itself. Results from the West Hinder light-ship station (51°23′ N, 2°21′ W) located off the Belgian coast were reported by Baeyens and Dedeurwaerder (1991), Dedeurwaerder (1988) and ATMOS (1984). The West-Hinder results are generally higher than comparable ones for the southern North Sea. One possible explanation is that ship West-Hinder is only separated from the coastline by a relatively small distance and is located at a very dense traffic channel (100 ships per day) on the North Sea. Values reported by Ottley and Harrison (1993) are broadly comparable to previously published values for metal concentrations in the North Sea atmosphere. The aircraft-measured values (Injuk *et al.*, 1992) agree well with those of cruises with the R/V Belgica (Otten *et al.*, 1989). Values reported by Otten *et al.* (1989), predominantly based on measurements done in the northern part of the North Sea, during north-westerly winds, can be considered as background values for the North Sea area. A concentration gradient from the southern North Sea (high concentrations) to the northern part (low concentrations) is observed.

Under the Paris Convention, an international commission (PARCOM-ATMOS) has been established to assess the state of the marine environment and formulate the policy to eliminate or reduce existing pollution. With regard to atmospheric pollution, a dual approach has been proposed: A monitoring programme at a num-

TABLE II. Measured airborne concentrations over the North Sea and adjacent areas in ng m^{-3} (s- or n-preceding an area means southern or northern, respectively)

Area	Period	Cd	Cr	Cu	Pb	Zn	Remarks	References
United Kingdom (coast)	'72	<4–<18	1.0–14	<1–55	35–380	64–415	range for 7 sites	Peirson *et al.* (1973)
United Kingdom (coast)	'75	4–6	–	13–15	20–120	15–300	range for 2 sites	Cawse (1974)
The Netherlands (coast)	'84–'88	0.3–2	1.7–14	3.7–23	36–178	18–200	–	van Daalen (1991)
North Sea (coast)	'72–'81	0.5–2.5	0.5–5	<5–25	20–200	10–100	–	van Aalst *et al.* (1983)
The Netherlands (coast)	'87	0.8	–	5.5	45	59	Hage	Cambray *et al.* (1975)
The Netherlands (coast)	'84–'85	0.7	1.3	3.3	39	40	Pellworm	Steiger (1991)
The Netherlands (coast)	'83	0.6	1.6	3.0	41	30	Tange	Kemp (1984)
Belgium (coast)	'72–'77	8	–	19	278	300	Ostende	Kretzschmar and Cosemans (1979)
Belgium (coast)	'81–'84	3.4	–	12.8	77	174	–	ATMOS (1984)
Norway (coast)	'78–'79	0.3	1	7	19	–	–	Pacyna *et al.* (1984)
Norway (coast)	'85–'86	0.14	1.1	1.6	18	15	Birkenes	Amundsen *et al.* (1992)
England (coast)	'87–'88	1.1	–	–	34	41	–	Yaaqub *et al.* (1991)
England (coast)	'72–'73	–	7.0	–	168	155	Leiston	Cambray *et al.* (1975)
German Bight	'86	1.9	1.9	4.7	52.6	46	island	Kersten *et al.* (1991)
Kiel Bight	'81–'83	–	–	40	53	57	lighthouse	Schneider (1987)
East Channel	'87	3	–	20	56	100	–	Flament *et al.* (1987)
North Sea	'86–'90	1.6	1.5	3.5	20.2	38	Helgoland	Kriews (1992)
North Sea	'87	0.9	–	3.9	28.5	42	FPN	Steiger (1991)
North Sea	'71–'73	–	4.8	–	155	161	Gasplatform	Cambray *et al.* (1975)
North Sea	'88–'89	1.4	–	11	55	67	flights	Injuk *et al.* (1992)
North Sea	'88–'89	1.3	–	6.9	29	75	cruise	Ottley and Harrison (1993)
North Sea	'84–'88	–	–	11	39	54	cruise	Otten *et al.* (1989)
sNorth Sea	'81–'84	2.9	–	9	104	94	West-Hinder	ATMOS (1984)
sNorth Sea	'84–'85	0.7	–	3	39	41	–	Stoeßel (1987)
sNorth Sea	'80–'85	4	–	17	150	150	West-Hinder	Dedeurwaerder (1988)
sNorth Sea	'84–'88	–	–	17	62	86	cruise	Otten *et al.* (1989)
sNorth Sea	'80–'85	2.8	–	14.7	96	67	West-Hinder & cruises	Baeyens and Dedeurwaerder (1991)
nNorth Sea	'72–'73	–	1.4	20	21	32	Collafirth	Cambray *et al.* (1975)
nNorth Sea	'84–'88	–	–	2	2	2	cruise	Otten *et al.* (1989)
North Sea	'91	0.2	2.0	1.9	4.5	30	Gullfaks 'C'	Dannecker *et al.* (1992)

ber of coastal stations and a modelling programme for which an emission database is being set up. The monitoring programme of PARCOM-ATMOS includes measuring concentrations in precipitation of Pb, Cd, Cu, Zn, Cr, Hg, Ni, NH_4^+ and NO_3^- and some of these species in air. In Tables III and IV, the basic description of the stations monitoring heavy metals in air and in precipitation and annual mean aerosol concentration values are given. From the summarized results in Table IV, it is obvious that only data from the Belgian stations (B1 and B2b) are not comparable with the others, due to high values for Cu, Ni, Pb and Zn. But these results agree well with reported ones for the same region by Kretzschmar and Cosemans (1979), indicating a high level of pollution for this region, or unrepresentative sampling. In Figure 1, the North Sea area with the stations which take part in the PARCOM-ATMOS monitoring program is given.

3. The Atmospheric Input of Trace Elements to the North Sea

For many years, research on pollution of the North Sea marine environment has focused on the most obvious inputs, those borne by rivers and direct discharges of wastes. In the work of Goldberg (1973) and Cambray *et al.* (1975), a first indication can be found that the atmospheric input might also be a significant contributor of trace elements to the North Sea. The first major studies of the deposition of heavy metals from the atmosphere started in the United Kingdom in the beginning of the 1970's (Cawse, 1974). The concentrations of some 40 elements were determined in dry and wet deposition at seven non-urban sites, while the water soluble and insoluble fractions of the total deposition were analyzed separately. At the same time, analyses of the deposition of heavy metals were made in Norway (Breekke, 1976), in the USA (Andren *et al.*, 1975; Feely *et al.*, 1976) and in the FRG (Ruppert, 1975). The routine monitoring of trace elements in precipitation began in Sweden in 1983 (Ross, 1987) with the aim to determine the atmospheric wet deposition of Cd, Cu, Fe, Mn, Pb and Zn.

Van Aalst *et al.* (1983) employed a simple model to assess the long-term average concentrations of various elements in the sea, and to determine the atmospheric input of a large group of contaminants into the North Sea. They have compared their results with information on the other inputs into the North Sea and concluded that atmospheric deposition was a relatively important source of contamination with Cu, Pb, Ni and Zn, and to a lesser extent with Cd and Cr. A first international attempt to estimate the input of various elements to the sea by atmospheric deposition and via other pathways was made by a European group of experts on behalf of the International Council for the Exploration of the Sea (ICES, 1978).

Since trace elements are removed from the atmosphere by dry deposition (sedimentation, interception and impaction) and by wet deposition (rainout, washout), the literature overview concerning both processes is given separately below.

TABLE III. Coastal measuring stations participating in Paris Commission Comprehensive Atmospheric Monitoring Programme (CAMP)

Number country	Name	Latitude longitude	Elevation	Distance from the sea	Parameters measured
B1 Belgium	Houtem	51°01′ N 2°35′ E	sea level	9 km	Pb, Zn in air
B2b Belgium	Bredene	51°14′ N 2°57′ E	≪ 10 m	2 km	Cu, Ni, Pb, Zn in air
B3a Belgium	Brugge	51°15′ N 3°11′ E	≪ 10 m	8 km	Cd, Cu, Pb, Zn in precipitation
GB1 Great Britain	East Ruston	52°48′ N 1°28′ E	5 m	8 km	Cd, Cr, Cu, Ni, Pb, Zn in air Cd, As, Cr, Cu, Ni, Pb, Zn in precipitation
GB2 Great Britain	Staxton Wold	54°11′ N 0°26′ W	170 m	10 km	Cd, Cr, Cu, Ni, Pb, Zn in air Cd, As, Cr, Cu, Ni, Pb, Zn in precipitation
GB3 Great Britain	Banchory	57°5′ N 2°32′ W	120 m	26.5 km	Cd, Cr, Cu, Ni, Pb, Zn in air Cd, As, Cr, Cu, Ni, Pb, Zn in precipitation
DK1 Denmark	Ulborg	56°17′ N 8°26′ E	40 m	20 km	Cd, As, Cr, Cu, Ni, Pb, Zn in air Cd, Cu, Pb, Zn in precipitation
D1 Germany	Westerland	54°53′ N 8°19′ E	5 m	2 km	Cd, Cu, Pb in air Cd, As, Cr, Cu, Ni, Pb, Zn in precipitation
NL3 The Netherlands	Kollumerwaard	53°20′ N 6°16′ E	0–5 m	10 km	Cd, As, Pb, Zn in air Cd, Cu, Ni, Pb, Zn in precipitation
NL2 The Netherlands	Leiduin	52°20′ N 4°35′ E	0–5 m	6.3 km	Cd, Cr, Cu, Ni, Pb, Zn in precipitation
N1 Norway	Birkenes	58°23′ N 8°15′ E	190 m	20 km	Cd, Pb, Zn in precipitation
N3 Norway	Lista	58°06′ N 6°34′ E	13 m	–	Cd, Cr, Cu, Ni, Pb, Zn in precipitation

TABLE IV. An overview of the data submitted to PARCOM-ATMOS as regards elemental concentrations (ng m^{-3}) in aerosols for 1988, 1989, 1990 and 1991, measured at 'CAMP' stations (ATMOS, 1990; ATMOS, 1991; ATMOS, 1992)

Station	Period	Cd	As	Cr	Cu	Ni	Pb	Zn
B1	'90	–	–	–	–	–	104	351
B2b	'89	–	–	–	–	–	112	150
	'91	–	–	–	23	15	86	222
DK1	'88	0.3	1.6	2.3	1.2	1.9	19.2	23.7
	'89	0.3	–	1.0	2.29	1.66	21.8	25.8
	'90	–	–	1.48	1.6	1.7	17	24
	'91	–	–	2.5	2.3	2	17	23
D1	'88	0.4	–	–	3.4	–	23.3	–
	'89	0.42	–	–	2.69	–	20.4	–
	'90	0.30	–	–	3.10	–	17.3	–
	'91	0.36	–	–	1.5	–	18	–
NL3	'90	0.33	0.78	–	–	–	27	52
	'91	0.4	1.48	–	–	–	30.2	51
GB1	'88	0.5	–	0.7	3.7	2.0	35.4	27.7
	'89	0.43	–	0.82	3.85	2.30	31.3	27.5
	'90	0.33	–	0.65	2.77	1.75	21	23
	'91	0.66	–	0.72	3.36	3.27	26.1	73.9
GB2	'88	0.5	–	1.2	4.6	3.1	22.3	111.3
	'89	0.64	–	1.33	3.62	2.5	27.2	59
	'91	1.9	–	0.79	3.06	2.36	17	50.7
GB3	'88	0.1	–	0.2	0.9	0.5	7.9	8.3
	'89	0.12	–	0.31	1.24	0.74	7.6	7.3
	'90	0.13	–	1.19	1.97	2.60	6.8	16.2
	'91	0.12	–	0.3	1.58	0.81	7.02	10.5

3.1. DRY DEPOSITION FLUXES TO THE NORTH SEA

Dry deposition of particles to the sea surface is the sum of all physical removal processes that take place when there is no form of precipitation (rain, snow or hail), such as gravitational settling, turbulent diffusion, Brownian diffusion or impaction. In general terms it can be stated that small particles (< 0.1 μm) are removed mainly by Brownian diffusion and large particles (> 10 μm) by gravitational settling. In the intermediate size range, impaction and interception are important. The loss of particles to the sea surface is frequently described in terms of a dry deposition velocity, which is the ratio between the deposition rate per unit area, and the ambient concentration. The dry deposition velocity of particles is strongly dependent on particle size, wind velocity and surface characteristics. Both theoretical considera-

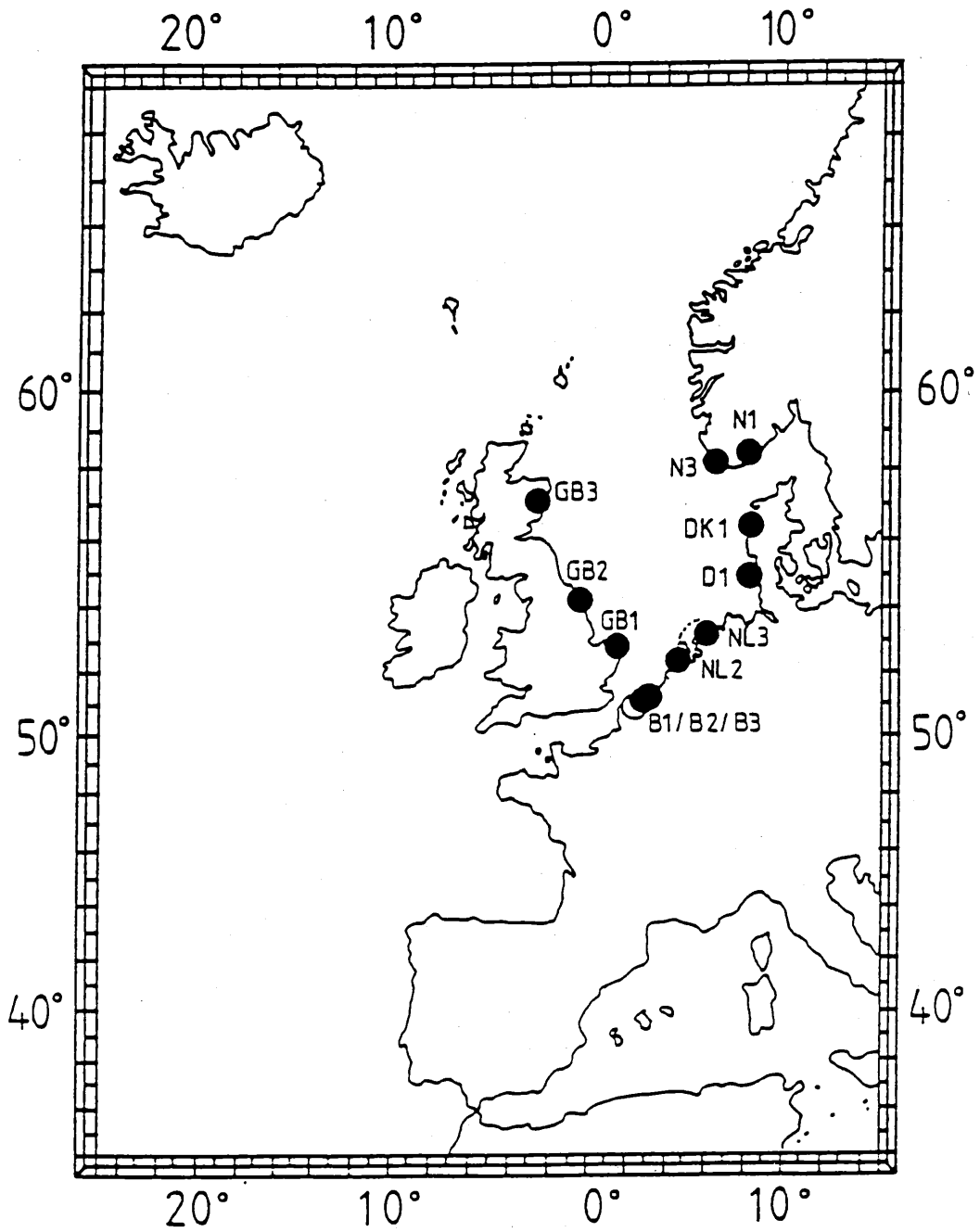

Fig. 1. The North Sea area with the stations which take part in the PARCOM Comprehensive Atmospheric Monitoring Programme (CAMP) – so called 'Central North Sea Stations'.

tions and field experiments show that the deposition velocity is small for particles with aerodynamic diameter less than 1 μm, typically of the order of 0.1 cm s^{-1}, while for the large particles it reaches a value of a few cm s^{-1}.

Transport fluxes across the air-sea interface can be determined by theoretical or semi-empirical relations (Sehmel and Hodgson, 1978; Slinn and Slinn, 1980; Williams, 1982; Friedlander *et al.*, 1986; Main and Friedlander, 1990). Dry depo-

sition velocities can also be evaluated by direct measurements of actual dry fluxes and particle concentrations in the air. Although the performance characteristics of air sampling equipment is quite well known, the properties of dry deposition collectors, as well as the structure of the laminar boundary layer above the collector and the collection efficiency still remain uncertain. It is still not clear how comparable the deposition to the surrogate surface is with the deposition to the natural sea surface. Another practical limitation, in case the deposited mass is measured, is that the results are strongly affected by the deposition of only a few large particles. Since the gravitational settling velocity is roughly proportional to the square of the particle diameter and the particle mass is proportional to the cube of the particle diameter, the deposited mass is a function of diameter to the 5th power. As a first approximation, a single 10 μm particle will therefore contribute as much to the total deposited mass as 100,000 particles of 1 μm. This makes direct measurements of the dry deposition velocity extremely difficult.

Only a few experimentalists have tried to measure directly the dry deposition of trace metals to the North Sea. Cambray *et al.* (1975) used a Whatman 541 cellulose filter, which was placed on a gas platform (53°5′ N, 2°21′ E). Samples were collected on a monthly basis. The high values found were explained by the authors as due to the possible contamination by resuspended sea water or by the platform itself.

Baeyens *et al.* (1990) measured dry deposition fluxes in a direct way with vasilinated plexiglass plates, in 14-days exposed intervals. Sampling was carried out throughout one year, at the West-Hinder lightvessel and during several cruises on the North Sea with the R/V Mechelen and the R/V Belgica. The collector plates were used horizontally and vertically. Directly measured dry deposition values were compared with the fluxes calculated by the adopted model of Slinn and Slinn (1980) and from a large set of *in situ* measured particle size distributions and their elemental concentrations. Despite the large uncertainties on the calculated dry deposition fluxes, results generally agree fairly well for both methods. The collection surfaces provide higher values, except for Mn and K, while the largest difference between both methods was observed for Pb (by a factor of 2.3).

Estimated dry deposition fluxes at the west coast of Sweden by Selin *et al.* (1992) were derived from trace element concentrations in the air in the winter of 1990 and from experimentally obtained deposition velocities.

Aircraft-based aerosol sampling in the lower troposphere was performed between September 1988 and October 1989 (Rojas *et al.*, 1993), above the Southern Bight of the North Sea. The dry deposition fluxes of Cd, Cu, Pb and Zn were calculated from size-differentiated atmospheric concentrations as a function of wind direction and dry deposition velocities obtained with the Slinn and Slinn model.

The dry deposition fluxes reported by Kriews (1992) are based on arithmetic mean values of atmospheric elemental concentrations, measured at Helgoland while for Cu, Pb and Zn, this percentage corresponds to 95, 96 and 97%, respectively.

For the same North Sea area, Baeyens *et al.* (1990) concluded that the first stages of their cascade impactor, i.e. particles larger than 4 μm, were responsible for 82% of the deposition of Pb. In the Mediterranean Sea, Dulac *et al.* (1989) reported that only 20% of the total deposition of Cd and Pb is accounted for by particles with sizes larger than 7 μm.

3.2. WET DEPOSITION FLUXES TO THE NORTH SEA

Wet deposition is the combination of rainout (in-cloud scavenging of particles) and washout (below-cloud scavenging of particles). Capture of particles by cloud droplets does not automatically lead to removal of the particles from the atmosphere, since cloud droplets may evaporate on their way to the earth's surface. This merely results in redistribution of the aerosol.

The amount of micropollutants which is deposited to the oceans over a certain period of time can be determined either directly or indirectly (Struyf and Van Grieken, 1993). In the direct way the wet atmospheric fluxes are determined by collecting rainwater in rain collectors over a certain period of time and measuring the concentrations of the substances involved. For particles, the annual wet flux F_w can be calculated with the following formula:

$$F_w = \sum_i C_i P_i,$$

or the flux F_w is the sum over all individual rain events i of the product of the concentrations in rainwater (C_i) times the amount of precipitation per unit area and time (P_i). The above equation is usually approximated as follows:

$$F_w = \overline{C} P,$$

where $\overline{C}$ is the average rainwater concentration and P the yearly precipitation rate. However, there are some major difficulties arising from determination of the wet deposition to the sea surface directly. Practically, collection of atmospheric material by rain water samplers should be avoided during dry periods (Ruijgrok *et al.*, 1990), (54°10′ N, 7°53′ E) in the period from 1986–1990, and deposition velocities following from the Slinn and Slinn model.

Atmospheric fluxes reported by ATMOS (1992) are based on mean aerosol concentration values measured at all the CAMP stations monitoring heavy metals in air during '88, '89, '90 and '91 and dry deposition velocities of 0.1 cm s^{-1} (Table V). However, the latter value is far from being generally accepted.

Estimated dry deposition fluxes by Ottley and Harrison (1993) are based upon data collected on 10 research cruises in 1988–89. A cascade impactor designed to collect efficiently size segregated aerosols, has produced detailed size distributions from which mass weighted deposition velocities were derived, followed by dry deposition flux estimates.

As seen in Table VI, published dry deposition fluxes of heavy metals to the North Sea show significant variations. In Table VII the dry deposition velocities,

TABLE V. The annual mean aerosol concentration (ng m^{-3}) and estimated dry deposition fluxes (kg km^{-2} y^{-1}) based on measurements at 'CAMP' stations (ATMOS, 1992)

Period	Param.	Cd	As	Cr	Cu	Ni	Pb	Zn
'88	conc.	0.36	1.6	1.1	2.76	1.87	21.6	42.7
	flux	0.01	0.05	0.04	0.09	0.06	0.73	1.45
'89	conc.	0.38	–	0.87	2.7	1.8	21.6	29.9
	flux	0.01	–	0.03	0.09	0.06	0.68	0.95
'90	conc.	0.27	0.78	1.1	2.4	2.0	32.2	93.2
	flux	0.01	0.03	0.03	0.07	0.06	1.0	3.0
'91	conc.	0.58	1.14	1.24	5.09	4.01	25.5	62.2
	flux	0.02	0.04	0.04	0.16	0.13	0.80	1.96

used by different authors for estimation of the dry deposition fluxes above the North Sea, are given. Considering the complex interaction of processes involved in particle deposition it is, perhaps, not surprising that inconsistencies have been evident in the reported research. Some of these inconsistencies are likely to indicate a real variability in environmental influences since an important number of factors influence the dry deposition processes. Meteorological data such as friction velocity, the aerodynamic surface roughness and the atmospheric stability are related to the deposition of particles. Humidity gradients and rainfall characteristics all affect the deposition of particles too. Furthermore, pollutant properties which vary with temperature, humidity and electrostatic gradients at the sea surface will result in a variation of the deposition characteristics of particles.

The main subject of discrepancy in the results concerning dry deposition velocities is due to the size distribution of the collected aerosols. Indeed, Van Aalst (1988) states that dry deposition velocities might vary in the range between 0.1 to 1 cm s^{-1}, and that most of this spread is caused by the lack of knowledge of the atmospheric particulate matter size distribution. Even though elements like Pb are more abundant in the sub-micrometer size range, these particles can coagulate with sea salt aerosols and reach super-micrometer dimensions. In order to give a quantitative idea on how important relatively large particles can be in the whole deposition process, Table VIII shows the percentage of the dry deposition flux accounted for by a given particle size class. Here only particle diameters larger than 1 μm are tabulated since the contribution of the sub-micrometer particles can be considered as negligible (Rojas *et al.*, 1993). It is seen from this table that 98% of the measured dry deposition velocity for Cd is accounted for by particles larger than 4 μm so wet-only samplers need to be used. Additional problems include sea-spray and contamination or deterioration of the samples prior to or during analysis by material sampling and handling, particularly if one deals with trace amounts (Ross, 1984; Buijsman *et al.*, 1991). Also, the statistical relevance

TABLE VI. Dry deposition fluxes (kg km^{-2} y^{-1}) to the North Sea – comparison of the literature data

	Cambray *et al.* (1975) Gas-platform	Stoßel (1987) Pellworm	Bayens *et al.* (1990) West-Hinder & ship		Selin *et al.* (1992) Sweden-west coast	Rojas *et al.* (1993) aircraft	ATMOS (1991) CAMP-stations	Kriews (1992) Helgo-land	Ottley and Harrison (1993) North Sea
			model	exp.					
S	–	–	–	–	275	–	–	–	–
Cr	–	–	–	–	–	–	0.04	0.34	–
Mn	6.8	–	3.5	3.0	–	–	–	1.68	–
Fe	290	155	82	180	–	–	–	76	–
Ni	–	–	–	–	0.5	–	0.13	0.23	–
Cu	30	1.1	2.8	3.5	–	1.9	0.16	0.29	0.7
Zn	420	6.8	6.2	13	1.9	10.3	1.96	3.69	4.9
As	–	–	–	–	–	–	0.04	0.11	–
Pb	24	4.3	3.3	7.5	0.4	4.23	0.80	1.06	0.7
Cd	–	0.3	–	–	–	0.28	0.02	–	0.06

TABLE VII. Dry deposition velocities (cm s^{-1}), used by different authors for estimation of dry deposition fluxes

	Van Jaarsveld and Onderlinden (1986)	Krell and Roeckner (1988)	Dulac *et al.* (1989)	Baeyens *et al.* (1990)	Selin *et al.* (1992)	Rojas *et al.* (1993)	ATMOS (1992)	Kriews (1992)	Ottley and Harrison (1993)
S	–	–	–	–	1.0	–	–	–	–
Cr	–	–	–	–	–	–	0.1	0.69	–
Mn	–	–	–	0.49	–	–	–	0.75	–
Fe	–	–	–	0.56	–	–	–	1.0	0.30
Ni	–	–	–	–	1.3	–	0.1	0.28	–
Cu	0.22	–	–	0.53	–	0.48	0.1	0.26	0.44
Zn	0.22	–	–	0.41	0.34	0.35	0.1	0.31	0.30
As	–	–	–	–	–	–	0.1	0.19	–
Pb	0.22	0.2	0.04	1.35	0.14	0.25	0.1	0.17	0.13
Cd	0.22	0.2	0.05	0.53	–	0.39	0.1	–	0.24

TABLE VIII. Relative contribution of the particle size classes in the determination of dry deposition fluxes for the Southern Bight of the North Sea (Rojas *et al.*, 1993)

Contribution to the dry deposition in %				
Diameter (μm)	Cd	Cu	Pb	Zn
1–2	1.1	1.5	1.1	0.4
2–4	0.4	3.1	1.4	1.7
4–8	2.2	6.3	14	11
8–16	50	5.7	39	27
>16	46	83	43	59

of such direct measurements is doubtful. Firstly, precipitation is a discontinuous process and secondly, there is a natural variability of the concentrations of trace substances in precipitation. This means that a large number of rain events must be covered before meaningful average wet fluxes can be obtained, which is expensive and time-consuming. Also, these measurements are very much determined by the sampling location and time, which is problematic if one wants to investigate the deposition over a larger area and over a considerable period of time (Smith, 1991). For this reason, indirect approaches are often preferred. The limited amount of directly measured data is then used to check the results of these indirect approaches. For indirect measurements, the wet deposition flux of material to the ocean surface can be written as:

$$F_w = WPC_a,$$

where C_a is the concentration of the substance in air, P is the yearly precipitation rate and W is the washout ratio – also called scavenging ratio – which is the ratio of the concentration of a substance in rainwater to the concentration of the same substance in air (both concentrations measured in the same volume units, e.g. μg m^{-3}).

This equation can be modified in a number of ways. Some authors for instance, add the density of air ρ as an extra factor (GESAMP, 1989):

$$F_w = WPC_a\rho^{-1}.$$

In this case the resulting washout ratios are temperature and pressure dependent and about a factor of 1200–1300 smaller. An alternative method to calculate the wet flux is the use of scavenging rates. This subject was extensively described by Slinn (1983).

3.2.1. *Data on Precipitation*

The existing estimates of surface precipitation (rain, snow, hail, ...) over the seas and oceans are based on a very limited data set. A serious problem with the

measurement of precipitation, both on the ground and aloft, is its great variability in time and space. Moreover, the total amount of rainfall at any location can be a combination of a small number of very intense showers (of convective origin) together with comparatively extended periods of light rainfall from stratiform clouds. The overall contributions of these two kinds of precipitation are often comparable (Browning, 1990). Even for a relatively small area such as the North Sea, an accurate value for annual average rainfall is not available at present. It is, however, generally recognized that less rain falls over sea than over land (see e.g. Cambray *et al.*, 1979; Baeyens *et al.*, 1990). By measurements on a gas platform, the rainfall there was observed to be about 55% of that at land-based stations at similar latitude on either side of the North Sea (Cambray *et al.*, 1975). Taking this observation into account, a mean rainfall value of 438 mm per year was calculated for the North Sea on the basis of measurements of seventeen stations situated on adjacent land. This value was seen as a kind of 'standard' value. However, this value was adjusted to 475 mm annually on the basis of measurements at seven stations surrounding the North Sea (Cambray *et al.*, 1979). Van Aalst *et al.* (1983) disagree with Cambray's value, claiming that the difference between the amount of precipitation on land and at sea is lower than assumed before. Baeyens *et al.* (1990) measured the yearly precipitation volume at the West-Hinder light vessel; the mean value, based on a period of two years, amounts to 430 mm per year. They also indicated that, in general, there is less precipitation above the sea. They found an average ratio West-Hinder/De Blankaert (a Belgian coastal station) of 0.72 and a ratio of 0.60 for West-Hinder/all Belgian meteorological stations. Krell and Roeckner (1988) used a model to simulate the atmospheric input of Pb and Cd into the North Sea, and used yet another annual precipitation rate, namely 558 mm.

According to Balls (1989), the uncertainty in the amount of rainfall is the most important single error source in flux estimations. It is obvious that more reliable values are urgently needed in order to be able to calculate more accurate wet deposition fluxes. In the future, space-based techniques for measuring global rainfall will provide us with data with a good resolution and accuracy. Radars and/or radiometers, installed on satellites, will be able to measure the instantaneous intensity of the rain or hail that is falling, from which an estimation can be made of how much rain has fallen in a particular area over a certain amount of time, and all of this will happen on a routine basis (Bowler, 1990; Kedem *et al.*, 1990; Scofield, 1991).

3.2.2. *Concentrations in Precipitation*

In Table IX an overview of data concerning measured precipitation concentrations over the North Sea and adjacent areas is given. It is obvious that the Swedish concentrations measured by Ross (1987 and 1990) are lower than those reported for The Netherlands (van Jaarsveld and Onderlinden, 1986; van Daalen, 1991).

The coastal values listed by van Aalst *et al.* (1983) show rather large variations, probably because they were obtained by different operators using other sampling methods at different sites and over other time intervals. However, the lowest values of these ranges agree very well with the concentrations measured at the North Sea coasts of Norway (Pacyna *et al.*, 1984; S & TWG, 1987) and in Scotland (Balls, 1989). Ross (1987) observed that the concentrations in southern Sweden were higher and that the wet deposition fluxes were higher than the Swedish anthropogenic emissions, so a long range transport of the pollutants was postulated. Clearly, the southern North Sea concentration values included in Table IX are very high compared to the other values. The inconsistency of those mentioned in the GESAMP report (1989) is ascribed to sampling problems (e.g. not all measurements were wet-only) and difficult analysis associated with this kind of measurements. The concentration values reported for the rainwater collected at the West-Hinder station and during several cruises at the Southern Bight (Dedeurwaerder *et al.*, 1985; Baeyens *et al.*, 1990) are very high compared to other values, although the sampling was done only when precipitation occurred and precautions were taken to avoid contamination. The results of the ATMOS report (1984) point out that the heavy metal concentrations in rainwater above the sea are higher than above land. Cambray (1975) thought that this so-called 'maritime effect' was caused by bubble bursting processes, which bring aerosols coming from an enriched sea surface layer into the atmosphere. However, Balls (1989) concluded on the basis of measurements of the enrichment factor in surface water that this process is not a significant contributor to the 'maritime effect'. Possible alternative processes are thought to be enhanced solubility of the metals above the sea due to ageing of the aerosols emitted by land based sources (ATMOS, 1984).

Trace metal concentrations in precipitation collected from 'CAMP' stations, around the North Sea (Table X) are quite variable from year to year, probably due to orographic effects. Also, they show much less consistency, undoubtedly because of the greater sampling and analytical problems associated with such measurements.

3.2.3. *Estimated Wet Deposition Fluxes to the North Sea*

As explained above the wet flux of trace metals can be estimated either directly or indirectly. In Table XI wet and total fluxes to the North Sea and its coasts are given. The results will depend on the area considered to constitute the North Sea and the value used for the annual precipitation rate are included, as well as on the method used (direct or indirect measurement).

It is very difficult to compare any data in the Table XI, because the authors used different rainfall rates and methods, and because both total fluxes and wet fluxes are listed. The estimated fluxes to the coast of southern Norway (S & TWG, 1987) and of Scotland (Balls, 1989) are reported to be lower than the other coastal values. And for the North Sea itself, the West-Hinder values are either relatively

TABLE IX. Measured precipitation concentrations ($\mu g\ l^{-1}$) over the North Sea and adjacent areas (s- preceding an area means southern)

Area	Period	Cd	Cr	Cu	Pb	Zn	Remarks	References
The Netherlands (coast)	'82–'83	0.26–0.36	0.21–0.8	1.8–4.9	8.9–20	18–32	bulk	van Jaarsveld and Onderdelinden (1986)
The Netherlands (coast)	'86–'88	0.5–0.9	1.4–1.8	6.7–8.0	13–20	21–31	wet-only	van Daalen (1991)
Sweden (coast)	'84–'85	0.033–0.15	–	0.46–1.5	2–9	4.2–16	bulk	Ross (1987)
Sweden (coast)	'87–'88	0.04–0.12	0.06–0.16	0.85–2.32	1.84–3.75	4.1–10.2	wet-only	Ross (1990)
North Sea (coast)	'72–'81	0.3–1.2	0.2–4	4–30	10–35	20–160	literature range	van Aalst *et al.* (1983)
Norway (coast)	'78–'79	0.27	–	–	11	15	weekly bulk	Pacyna *et al.* (1984)
Norway (coast)	'80–'84	0.37	–	–	7.1	9.2	–	S & TWG (1987)
Scotland (coast)	'87–'88	0.68	–	2.3	4	13	wet-only	Balls (1989)
sNorth Sea	'81	3	–	39.5	13	194	wet-only	Dedeurwaerder *et al.* (1985)
sNorth Sea	'74–'85	0.5–9.5	–	2.5–77	10–29	26–490	literature range	GESAMP (1989)
sNorth Sea	'84–'87	10	–	77	29	500	wet-only	Baeyens *et al.* (1990)
German Bight (platform)	'88–'91	0.26	1.88	17.8	12	275	wet-only	Schulz (1993)

TABLE X. An overview of the data submitted to ATMOS as regards elemental concentrations ($\mu g\ l^{-1}$) in precipitation for 1988, 1989, 1990 and 1991, measured at 'CAMP' stations

Station	Period	Cd	As	Cr	Cu	Ni	Pb	Zn
B3A	'91	0.1	–	–	1.26	–	2.7	8.16
DK1	'88	0.08	–	–	1.4	–	4.2	12.1
	'89	0.10	0.45	0.46	1.1	0.45	3.93	15.58
	'90	0.10	–	0.28	0.99	0.50	2.73	9.10
	'91	–	–	0.17	1.42	0.35	2.72	1350
D1	'89	0.25	0.21	0.52	2.89	3.34	4.24	11.39
	'90	0.15	0.31	0.49	1.05	0.71	2.43	11.47
NL2	'88	0.19	–	–	2.9	–	6.4	–
	'89	0.12	–	–	2.62	0.35	10.18	14.95
	'90	0.16	–	–	2.45	–	5.91	11.26
	'91	0.16	–	0.40	2.97	0.51	6.41	14.52
NL3	'90	0.16	–	–	2.53	–	2.78	12.56
	'91	0.13	–	–	3.36	0.77	6.84	13.82
GB1	'88	0.28	–	–	3	–	8.7	16.1
	'89	0.23	0.78	1.93	4.65	1.42	7.67	25.08
	'90	0.40	0.70	0.75	2.00	1.46	4.93	16.8
	'91	0.16	0.42	0.50	6.50	1.70	7.70	18.70
GB2	'88	0.58	–	–	6.5	–	22.7	46.1
	'89	0.57	1.11	1.68	7.85	3.28	22.79	61.33
	'90	0.36	1.10	1.04	3.52	2.66	10.65	33.45
	'91	0.46	1.18	0.90	7.60	5.50	19.00	49.50
GB3	'88	0.20	–	–	2.4	–	7.5	8.3
	'89	0.13	0.59	0.68	3.06	1.31	5.25	9.66
	'90	0.13	–	0.25	1.94	0.74	3.04	8.98
	'91	0.14	0.26	0.30	4.30	0.70	4.00	8.10
N1	'88	0.11	–	–	–	–	7.4	14.1
	'89	0.11	–	–	–	–	5.45	11.43
N3	'91	0.06	–	0.60	2.50	0.10	7.00	14.20

high (Baeyens *et al.* 1990) or very low (Dedeurwaerder *et al.*, 1985). Baeyens *et al.* (1990) reported that the wet flux to the North Sea is clearly higher than that at a Belgian coastal station. It should be noted that the input values reported by Rojas *et al.* (1993) are based on sampling flights and that they were calculated using scavenging rates.

As far as wet fluxes are concerned, the uncertainties are far from being known. The theoretical approach to wet deposition is rather crude in the sense that the

TABLE XI. Total (dry + wet) or wet flux to the North Sea in kg km^{-2} y^{-1} (s- preceding an area means southern)

Area	Rain [mm y^{-1}]	Cd	Cr	Cu	Pb	Zn	Method	Remarks	References
Coastal stations	438	–	1.4	10.5	11	31	direct	wet	Cambray *et al.* (1979)
Coastal stations	778–1028	0.3–1.4	–	6.1–16.2	5.6–13.5	20.6–55.6	direct	total	Flament *et al.* (1984)
Coastal stations	–	0.09–1.7	0.58	0.8–27	5.1–14	9.3–156	–	total	PARCOM (1987)
Scotland (coast)	–	0.39	–	1.3	2.3	7.6	direct	wet	Balls (1989)
sNorway (coast)	1399	0.48	–	–	9.2	12	direct	total	S & TWG (1987)
Dutch Continental Shelf	–	0.06–0.11	0.15–0.30	0.28–0.55	4.8–9.6	2.4–4.8	–	total	S & TWG (1987)
North Sea	680	0.1–0.5	–	1–4.4	4–23	5–23	indirect	total	GESAMP (1989)
North Sea	430	2.9	–	25	7	170	direct	wet (dissolved)	Bayens *et al.* (1990)
North Sea	500	0.35	–	2.68	6.5	15.1	indirect	total	Rojas *et al.* (1993)
sNorth Sea	–	1.6	–	24.9	9.4	143	–	wet	ATMOS (1984)
Southern Bight	458	0.0002	–	0.0026	0.0014	0.015	direct	total	Dedeurwaerder *et al.* (1985)
Southern Bight	500	0.43	–	2.5	8.8	19.7	indirect	wet	Rojas *et al.* (1993)
Southern Bight	500	0.71	–	5.36	12.9	30.2	indirect	total	Rojas *et al.* (1993)
German Bight	677	–	0.43	1	5.7	4.3	indirect	wet	Kriews (1992)
German Bight	–	0.34	0.95	14.4	9.2	–	direct	wet	Schulz (1993)
Sweden (west coast)	–	–	–	3	2.6	9	direct	total	Selin *et al.* (1992)

mechanisms by which atmospheric particulate matter is scavenged by rain, are not yet fully understood. For indirect estimations of the wet flux, the washout ratio used in the calculations is of considerable importance. In Table XII some relatively recent values for trace metals are listed. They are again, very difficult to compare. The values used in the GESAMP (1989) report and by Rojas *et al.* (1993) are 'best estimates' based on published washout ratios for trace metals above the North Sea. In the ATMOS report (1984), it is stated that values for Cu, Zn and Cd above the sea are up to 5 times larger than above land.

To assess the environmental effect of the atmospheric input of heavy metals into the North Sea, it is important to know whether a distinction can be made between the amount of a certain trace metal that reaches the surface of the earth in a dissolved or in a particulate form. For instance, dissolved metals are much more readily available to be incorporated by organisms. Flament *et al.* (1984) investigated the metal distribution over the solid and liquid phases in rain at some French coastal sites. They found the following percentages of dissolved material: Pb (21–31%), Cd (53–78%), Cu (63–94%) and Zn (68–87%). Losno *et al.* (1988) observed that Zn partitioning is governed by adsorption/desorption processes on existing particles, which are pH dependent. Nevertheless, Colin *et al.* (1990) state that the nature of the particles is also important. Jickells *et al.* (1992) conclude that the solubility of an element is the result of the complex interplay of several factors and cannot be simply assigned to one factor such as pH.

3.3. TOTAL DEPOSITION FLUXES TO THE NORTH SEA

The total amount of heavy metals deposited to the North Sea (5.25×10^5 km^2) as reported by several authors, is given in Table XIII. The atmospheric flux reported in the ATMOS (1984) report is significantly higher than the other values, except for Pb. The range calculated by van Aalst *et al.* (1983) is also relatively high but the other total flux values agree fairly well. They were assessed at totally different points in time, with other methods and concentration measurements to start from (coastal precipitation vs. airborne concentrations), and even the area taken into consideration was different. The annual estimation of atmospheric fluxes reported by ATMOS are based on measurements during '88, '89, '90 and '91 at the so-called 'Central North Sea stations', but taking into account concentration gradients from land to sea due to removal processes or due to dilution. For each station a bulk gradient correction factor (defined as the ratio of the average deposition at a certain station to the average deposition over the total North Sea area) was derived from model calculations developed by RIVM (van Jaarsveld *et al.*, 1986; van Jaarsveld *et al.*, 1991). It is evident that, for a number of elements, the estimated depositions reported for '91 (ATMOS, 1992) are higher than those calculated for '90 (ATMOS, 1991). The estimated increases in Pb (30%) and Cu (40%) are due to high concentrations at UK stations.

TABLE XII. Washout ratios for trace metals

Cd	Cr	Cu	Pb	Zn	Remarks	References
125–500	150	140–751	76–169	179–1000	literature range	Schroeder *et al.* (1987)
–	–	–	–	1226	value measured	Jaffrezo and Colin (1988)
200–1000	–	200–1000	200–1000	200–1000	range used	GESAMP (1989)
150	–	150	150	150	value used	Rojas *et al.* (1993)
–	200–1280	60–3800	20–1350	280–11500	value measured (snow)	Cadle *et al.* (1990)

TABLE XIII. Total (dry + wet) atmospheric input of trace metals into the North Sea, in tons y^{-1}

Rain [mm y^{-1}]	Cd	Cr	Cu	Pb	As	Zn	Method	References
–	–	740	5600	5800	460	1600	indirect	Cambray *et al.* (1979)
685	110–430	70–1400	1400–10000	3600–13000	220–720	7200–58000	direct	van Aalst *et al.* (1983)
–	–	100–530	380–1600	1800–6400	150–510	3900–12000	indirect	Stößel
–	45–240	300–900	400–1600	2600–7400	40–120	4900–11000	direct	PARCOM (1987)
–	900	–	13542	7367	–	77566	–	ATMOS (1984)
500	47	205	620	1900	95	4600	indirect	ATMOS (1990)
520	32	88	321	958	95	2740	indirect	ATMOS (1991)
650	27	94	610	1241	83	3099	indirect	ATMOS (1992)
680	50–250	–	500–2300	2300–12000	130–580	2700–12000	indirect	GESAMP (1989)
600	158	–	1348	3670	–	7409	indirect	Injuk *et al.* (1992)
677	–	–	–	3500	160	–	indirect	Dannecker *et al.* (1992)
677	–	530	5100	3200	160	–	direct	Dannecker *et al.* (1994)
677	–	400	670	3500	160	4200	indirect	Kriews (1992)

If deposition to the total North Sea area is estimated from observations at coastal stations, one has to deal with the problem of how representative those observations are for larger areas, with respect to both precipitation amounts and measured concentrations. The first problem can be solved reasonably by using a precipitation which varies from year to year, i.e. by taking a precipitation amount which is 70% of the median precipitation of all the coastal stations. The second problem can be solved only when knowledge about atmospheric residence times is included in the method. A combined method based on observations and model calculations can therefore be expected to give the most realistic results.

As far as the relative importance of dry and wet deposition goes, most authors seem to agree on the fact that, for the trace metals, the wet flux is more important than the dry flux, except perhaps for Pb, where they may be of the same magnitude. However, on the extent of this difference, opinions vary very widely (Galloway *et al.*, 1982; ATMOS, 1984; Schroeder *et al.*, 1987; GESAMP, 1989; Martin *et al.*, 1989; Baeyens *et al.*, 1990; Remoudaki *et al.*, 1991). Martin *et al.* (1989) remark that the ratio of wet to dry deposition is controlled by many meteorological factors and also by the distance between the sampling site and the emission source (see also Migon *et al.*, 1991; Remoudaki *et al.*, 1991).

Whenever the deposition of micropollutants to a water surface is estimated, attention should be paid to the reverse fluxes (from the water to the atmosphere) as well. According to the ATMOS report (1984), for which the heavy metal content in the sea surface microlayer was determined, the maximum water-to-air fluxes are at least 30 times smaller than the total input fluxes. The authors of the GESAMP (1989) report state that, although the atmospheric concentrations of trace metals associated with large (resuspended) sea salt particles constitute only a minor fraction of the total atmospheric concentration, this fraction may well account for a significant part of the gross dry deposition flux. This complicates the assessment of the 'real' deposition fluxes to the sea.

3.4. DEPOSITION FLUXES BASED ON MODEL CALCULATIONS

An alternative way of determining the deposition of micropollutants from the atmosphere to the sea involves atmospheric transport models. Basically, one uses emission data for a certain source area (e.g. Europe) in combination with a long range transport model (which requires a number of input data) to simulate the dispersion and deposition of a substance for a determined receptor area (e.g. the North Sea). Model calculations can provide independent estimates for atmospheric inputs which can be compared to input estimates from measurements. Moreover, the calculations may indicate the spatial variation of the deposition, and allow the evaluation of the representativeness of measurements at coastal stations. In this section the results of calculations performed using relatively recent models, which have been applied to the calculation of the total deposition of heavy metals to

the North Sea, will be discussed and compared to the values obtained from field measurements.

3.4.1. *Literature Data on the Deposition Fluxes Based on Model Calculations*

In the 1980's, van Aalst *et al.* (1983) employed a simple model to compare the long-term (ca. 1 year) average concentrations of various elements, and wet and dry deposition for an area of 1000 × 1000 km^2 of the North Sea. The total air concentrations at the receptor site were calculated as the sum of the contributions from the different emission areas (the 'cells' of the emission grid) weighted by the probability that the air masses would be carried down from that emission cell. Based on the mass-median diameters, a value of 0.1 to 1 cms^{-1} for the deposition velocities was used. The results showed good agreement between measurements and calculations. The data from this and other works (PARCOM, 1985) were reviewed by van Aalst and Pacyna (PARCOM, 1986) in order to assess the atmospheric inputs of trace elements to the North Sea.

A more advanced 3-dimensional trajectory model based on the Monte Carlo method has been employed to estimate the long range transport and deposition of Pb to the North Sea (Krell *et al.*, 1986). The emission data used were the numbers from Pacyna (1985). In 1988, Krell and Roeckner used a more sophisticated trajectory model to estimate the dry and wet deposition of Pb and Cd into the North Sea, via a long range transport model using gridded data of the respective anthropogenic emissions in Europe and the relevant meteorological data. The authors considered aerosols only in the size range from 0.2 to 1 μm and a deposition velocity of 0.2 cm s^{-1} was used for all heavy metals. This model is particularly designed for episode studies. The model of Graßl *et al.* (1989) is very similar to the model of Krell and Roeckner.

The total annual atmospheric input of Pb to the North Sea was determined for all the months of 1980 to be ca. 1440 tons by Petersen (1987). A relatively large contribution on the order of 50% was estimated for the UK. The Netherlands, France and Germany contributed about 12% each, Belgium 5%, Sweden 1.5%, Denmark 1% and Norway even less. However, conclusions from this work should be taken with caution. The results are based only on a one year period, which shows a significant month-to-month variability of the deposition. More recently the same author estimated the annual input of Pb to be 2300 tons (Petersen *et al.*, 1988).

The TREND model was developed at the Dutch National Institute of Public Health and Environmental Protection in order to calculate long term averaged concentrations and depositions (van Jaarsveld *et al.*, 1986). It is a statistical long-range version of the Gaussian plume model, what means that the dispersion from a source is assumed to follow the prevailing wind direction and wind speed within a sector of 30% in the horizontal plane. The vertical dispersion is limited by the earth surface and the top of a mixing layer. Due to wet and dry deposition and chemical reactions, atmospheric concentrations decrease during the transport; this

process is also taken into account. The model assumes homogeneous climatology and boundary characteristics over whole Europe. The occurring meteorological situations are grouped in a limited number of classes and the calculations are carried out separately for 5 size classes from < 0.95 μm to > 20 μm particles, each of which has its own deposition characteristics. For all heavy metals a deposition velocity of 0.22 cms^{-1} was implemented. This model has been applied successfully to a period of a month, but even shorter periods yielded reasonable results.

The model of Warmenhoven *et al.* (1989) is, in fact, an elaborated version of the van Jaarsveld model, but instead of applying it to trace metals solely, a number of organic compounds like PAHs, PCBs, pesticides, etc. were also taken into consideration. The model assumes the same meteorology, surface characteristics and mass-averaged deposition velocities over the whole surface area.

The main problem concerning model based calculations is in estimating the emissions. Though, for some countries, there were explicit data on emissions of pollutants, generally the annual emissions from all countries have been estimated on the basis of industrial and agricultural activities within the countries. All the models used similar emission data as input to their model.

The total atmospheric input of some pollutants into the North Sea given by the above models is listed in Table XIV. Included is also the 'best' estimate defined as the value obtained when emissions are multiplied with the average ratio of measured/modelled air concentration. It can be seen that there is a general agreement between the results of the different models. Taking into account that all models use more or less the same emission data, this agreement confirms the idea that the influence of the different model assumptions is not very large, at least not in the case of the total deposition into the North Sea.

For the reported trace elements, the model values are consistently lower than the values obtained from field measurement data in Table XIII. Krell and Roeckner (1988) claim that this discrepancy can be explained as follows: the extrapolation of coastal measurements, on which most deposition estimates up until 1988 were based, cannot be justified, because there is no reason to believe that the high precipitation intensities/volumes measured along the southern and western coasts are representative for the whole of the North Sea. The authors find a strong argument in the life-time of clouds which is not more than a few hours for the precipitating one: in this way, most of the pollutant material is likely to be washed out within about 100 km from the coast. Their model simulations (and those by van Jaarsveld *et al.* (1986)) reveal a substantial decrease of the deposition across the southern and western coasts. Van Jaarsveld *et al.* (1986) state that the discrepancy might partly be due to less accurate sampling and analysis of rainwater as well.

3.4.2. *Validation of the Models*

Van Jaarsveld *et al.* (1986) note that there are some assumptions inherent to their model, which do not agree very well with reality. For instance, it is not correct to

TABLE XIV. Comparison of the total deposition (tons y^{-1}) to the North Sea calculated with different models

Reference	Cd	Cr	Cu	Pb	Zn	As
Earlier estimates reviewed in PARCOM (1985)	110–430	70–1400	1400–10000	3600–13000	7200–58000	220–720
PARCOM (1986)	14	70	130	2600	1200	42
Van Jaarsveld *et al.* (1986)	11	58	100	2000	940	–
Petersen (1987)	–	–	–	1440	–	–
Petersen *et al.* (1988)	–	–	–	2300	–	–
Krell and Roeckner (1988)	11	–	–	1200	–	–
Graßl *et al.* (1989)	–	–	–	2300	–	–
Warmenhoven *et al.* (1989)	15	72	110	1900	930	–
Van Jaarsveld (1991)	10	–	–	960	600	–
ATMOS (1990) – 'best' estimates (model/measurements)	13	–	–	870	1800	–

assume that transport and dispersion over sea are analogous to those over land. The stability over sea is mainly determined by the temperature difference between the air and the seawater, and shows hardly any diurnal variation. Also, in the coastal zone complicated transition phenomena occur, which are not accounted for in the model. However, the authors do not think that a more realistic model would yield largely different results.

Krell and Roeckner (1988) had difficulties in validating their model because of the lack of comparison material for the North Sea. Therefore, they were obliged to simulate air and precipitation concentrations at certain sites and for certain periods (e.g. a month) for which measurements were made, and their results agreed fairly well with the measured values.

Warmenhoven *et al.* (1989) estimate that the results concerning the heavy metal deposition are the most reliable ones. In general, the validity of this model is mainly governed by the quality of the emission data and the choice of the emission grid (because some materials are so stable in the atmosphere, that a much larger emission area should be taken into consideration). As a result of this, the real deposition of these elements should be higher than predicted by the model. Finally, the assumption that the North Sea is a well-mixed tank, without any inflow or outflow except from rivers (and the atmosphere), has an influence on the deposition estimates. In this concept it would be more realistic to include the dynamics of the North Sea in the model.

4. Relative Contribution of Atmospheric Deposition of Trace Metals to the Total Input into the North Sea

Apart from atmospheric pollution, the North Sea is subject to a number of other sources of pollution as well: e.g. input via rivers, direct discharges from industries into the estuaries, dumping of industrial wastes and drainage of sewage (van Aalst *et al.*, 1983). It is very difficult to evaluate the relative importance of the various input sources as most input estimates are subject to considerable uncertainty arising from analytical and sampling problems. Moreover, the actual quantity of pollutants entering the North Sea varies from year to year, depending on factors like natural variations in river flows and water exchange with adjacent sea areas, economic variations (industrial expansion and reorganization, large strikes), changing legislation (emission and dumping restrictions), atmospheric conditions (wind flow patterns, rainfall intensity) and unforeseen circumstances (accidents).

Although, in a number of publications, estimates of the non-atmospheric input are given (e.g. Cambray *et al.*, 1979; van Aalst *et al.*, 1983; ATMOS, 1984), we chose to use the recent data as given by Warmenhoven *et al.* (1989). They use the figures reported during the Second International Conference on the Protection of the North Sea in 1987, which are based on information obtained from the countries concerned. For the contaminants which are not included in the report of the Conference, the total fluxes are estimated on the basis of data on the total

TABLE XV. Relative contribution of atmospheric deposition to the total loading of the North Sea, in percent

Element	Atmospheric-measured ATMOS (1992)	Atmospheric-modelled Warmenhoven *et al.* (1989)
Cd	22	14
Cr	2	2
Cu	18	4
Pb	26	35
Zn	15	5

loading through the Rhine and the Meuse (Folkertsma, 1989). This author points out, however, that the values calculated in this way can only serve as in indication of the order of magnitude. Also, the contamination and natural heavy metal load of the water entering the North Sea from the English Channel, the Baltic Sea and the North Atlantic is not included in the estimates. And the river catchment areas are also subject to atmospheric deposition (Warmenhoven *et al.*, 1989). According to Warmenhoven *et al.*, 1989, the yearly estimates for non-atmospheric deposition of metals in tonnes are: 95 (Cd), 4000 (Cr), 2800 (Cu), 3500 (Pb) and 1700 (Zn). By comparing the non-atmospheric input to the atmospheric input fluxes discussed earlier, it is possible to get an idea of the relative importance of both pathways for the input of pollutants to the North Sea. In Table XV, the non-atmospheric values are compared with the measured and modeled atmospheric data. We used the values calculated by the model of Warmenhoven *et al.* (1989) and flux values reported by ATMOS (1992). The most important pathway for each compound seems the same for measurements and model. Based on this data, non-atmospheric input is more important for all the elements. GESAMP (1989) notes that, for particulate trace elements, the major source is usually the rivers. However, particulate riverine material is likely to be deposited close to the source regions, while atmospheric input can more easily occur in remote oceanic areas. Still according to the GESAMP report, the global atmospheric and riverine inputs are comparable for dissolved Cu, while for Zn and Cd atmospheric inputs appear to dominate. The atmospheric input of Pb is expected to decrease over the next decade, due to the growing use of unleaded gasoline. Martin *et al.* (1989) state that the atmospheric input to the Mediterranean Sea is predominant over the river input, either dissolved or particulate. For organic contaminants as well, the riverine flux may influence only the nearshore areas, while atmospheric input is supposed to have a much wider impact over regional seas (GESAMP, 1989).

However, it must be emphasized that the accuracy of the estimations of both the atmospheric and non-atmospheric input sources is still very poor.

5. Conclusions

From this literature review several important gaps in the knowledge of the atmospheric deposition to the North Sea have become apparent.

For aerosols, the presently available concentration data need to be improved by more accurate determinations of the size distribution of airborne particulate matter since this is directly controlling the deposition rates. The dependence of the deposition velocity upon the particle size requires further investigation and better knowledge of the kinetic parameters as deposition/transfer velocity.

It is obvious that current knowledge about the wet deposition of trace elements to the North Sea is insufficient. For the trace metals, which were dealt with in this review, a number of specific problems like the lack of accurate washout ratios for the North Sea area or the contribution of resuspension from the sea surface to the observed pollutant concentrations still have to be solved. Reported washout or scavenging ratios for a particular element vary substantially. Part of the problem is in the method by which scavenging ratios are determined; usually they are computed from rain and air concentrations measured on samples that were not collected contemporary. Therefore, it is absolutely necessary to work out a 'global' measurement strategy for the North Sea area which would include precipitation and air sampling, preferably simultaneously at a large number of sites (ship cruises, islands, platforms, coastal stations) and over a considerable period of time, in order to be able to calculate the scavenging rates from really paired rain and air samples. The considerable expansion of the geographical coverage of rain sampling programmes should eliminate the uncertainties on the temporal distributions of precipitations events for the North Sea area.

The results of different studies on the atmospheric input of trace elements into the North Sea are still indicating large uncertainties. A combined model and monitoring approach seems to be most useful for the determination of atmospheric fluxes to large surface waters. Model studies give much lower values than the studies based on measurements. The major uncertainty in model studies is the quality and completeness of the emission data and the different size distributions used in the models. Furthermore, none of the models takes into account particle growth due to high relative humidities. Emission estimates for Cd and Zn currently in use are most probably too low. Cd emissions in 1982–1989 over a whole region, should be at least 30% higher. For Zn, the general underestimating is at least a factor of 3. Therefore, research on emission processes and identification of unknown emission categories is urgently needed for heavy metals (Van Jaarsveld, 1991).

Acknowledgements

This work was partially financed by the Belgian State Prime Minister's Service – Science Policy Office, in the framework of the EUROTRAC program (contract EU

7/08) and the Impulse Programme in Marine Sciences, supported by the Belgian State – Prime Minister's Service – Science Policy Office (Contract MS/06/050).

References

Amundsen, C. E., Hanssen, J. E., Semb, A., and Steinnes, E., 1992, Long-range atmospheric transport of trace elements to Southern Norway, *Atmos. Environ.* **26A**, 1309–1324.

Andren, A. W., Lindberg, S. E., and Bate, L. C., 1975, Atmospheric input and geochemical cycling of selected trace elements in Walker Branch Watershed, Oak Ridge, TN, Oak Ridge National Laboratory, ORNL Report NSF-EATC-13.

ATMOS, 1984, Working group on the atmospheric input of pollutants to convection waters. Heavy metal input from the atmosphere into the North Sea, *ATMOS report* 4/4-E.

ATMOS, 1990, Working group on the atmospheric input of pollutants to convention waters, *ATMOS report* 8/12/1-E.

ATMOS, 1991, Working group on the atmospheric input of pollutants to convention waters, *ATMOS report* 9/18/1-E.

ATMOS, 1992, Working group on the atmospheric input of pollutants to convention waters, *ATMOS report* 10/4/2-E.

Baeyens, W., Dehairs, F., and Dedeurwaerder, H., 1990, Wet and dry deposition fluxes above the North Sea, *Atmos. Environ.* **24A**, 1693–1703.

Baeyens, W. and Dedeurwaerder, H., 1991, Particulate trace metals above the Southern Bight of the North Sea – I. Analytical procedures and average aerosol concentrations, *Atmos. Environ.* **25A**, 293–304.

Balls, P. W., 1989, Trace metal and major ion composition of precipitation at a North Sea coastal site, *Atmos. Environ.* **23**, 2751–2759.

Barrie, L. A., Lindberg, S. E., Chan, W. H., Ross, H. B., Arimoto, R., and Church, T. M., 1987, On the concentration of trace metals in precipitation, *Atmos. Environ.* **21**, 1133–1135.

Bowler, S., 1990, Radar network watches where the wind blows, *New Scientist* **24**, 30–31.

Braun, H., Vogg, H., Halbritter, G., Bräutigam, K. R., and Katzer, H., 1984, Comparison of the stack emissions from waste incineration facilities and coal fired heating power stations, *Recycling International* **1**, 1–2.

Breekke, F. H., 1976, Impact of acid precipitation forest and fresh-water ecosystems in Norway. SNSF Project Research Report, Phase 1, 1972–75. Norwegian Institute for Forest Research, Oslo.

Browning, K. A., 1990, Rain, rainclouds and climate, *Q.J.R. Meteorol. Soc.* **116**, 1025–1051.

Buijsman, E., Jonker, P. J., Asman, W. A. H., and Ridder, T. B., 1991, Chemical composition of precipitation collected on a weathership on the North Atlantic, *Atmos. Environ.* **25A**, 873–883.

Cadle, S. H., VandeKopple, R., Mulawa, P. A., and Muhlbaier Dasch, J., 1990, Ambient concentrations, scavenging ratios, and source regions of acid related compounds and trace metals during winter in northern Michigan, *Atmos. Environ.* **24A**, 2981–2989.

Cambray, R. S., Jefferies, D. F., and Topping, G., 1975, An estimate of the input of atmospheric trace elements into the North Sea at Clyde sea (1972–73), AERE Harwell, England (AERE Report R 7733).

Cambray, R. S., Jefferies, D. F., and Topping, G., 1979, The atmospheric input of trace elements to the North Sea, *Mar. Sci. Comm.* **5**, 175–194.

Cawse, P. A., 1974, A survey of atmospheric trace elements in the U.K. (1972–73), AERE, Harwell, England (AERE Report R 7669).

Colin, J. L., Jaffrezo, J. L., and Gros, J. M., 1990, Solubility of major species in precipitation: Factors of variations, *Atmos. Environ.* **24A**, 537–544.

Dannecker, W., Bredthauer, U., Kriews, M., Rebers, A., Selke, K., and Schultz, M., 1992, Preliminary Report of Atmospheric Pollutant Measurements in the Norther North Sea Region. University of Hamburg, Germany.

Dannecker, W., Hinzpeter, H., Kriews, M., Naumann, K., Schulz, M., Schwikowski, M., Steiger, M., and Terzenbach, U., 1994, Atmospheric transport of contaminants, their concentrations and input into the North Sea, in J. Sündermann (ed.), *Circulation and Contaminant Fluxes in the North Sea*, Springer Verlag Berlin, Heidelberg, New York (in press).

Dedeurwaerder, H., Dehairs, F., Xian, Q., and Nemery, B., 1985, Heavy metals transfer from the atmosphere to the sea in the Southern Bight of the North Sea, in R. Van Grieken and R. Wollast (eds.), *Proceedings 'Progress in Belgian Oceanographic Research'*, pp. 170–177, University of Antwerp (UIA), Belgium.

Dedeurwaerder, H. L., 1988, Study of the dynamic transport and the fall-out of some ecotoxicological heavy metals in the troposphere of the Southern Bight of the North Sea. Ph.D. thesis, University of Brussels (VUB), Belgium.

Dulac, F., Buat-Ménard, P., Ezat, U., Melki, S., and Bergametti, G., 1989, Atmospheric input of trace metals to the Western Mediterranean: Uncertainties in modelling dry deposition from cascade impactor data, *Tellus* **41B**, 362–378.

Flament, P., Noël, S., Auger, Y., Leman, G., Puskaric, E., and Wartel, M., 1984, Les retombées atmosphériques sur le littoral Nord-Pas-de-Calais, *Pollution atmosphérique oct.–déc. 1984*, 262–270.

Flament, P., Lepretre, A., Noël, S., and Auger, Y., 1987, Aerosols cotiers dans le nord de la Manche, *Ocean. Acta* **10**, 49–61.

Folkertsma, F., 1989, Nationale rapportage Noordzee-Aktieprogramma deel A: inventarisatie van emissies van geselecteerde stoffen in Nederland in 1985, Dienst Binnenwateren, RIZA, Lelystad, The Netherlands.

Friedlander, S. K., Turner, J. R., and Hering, S. V., 1986, A new method for estimating dry deposition velocities for atmospheric aerosols, *Atmos. Environ.* **17**, 240–244.

Galloway, J. N., Thornton, J. D., Norton, S. A., Volchok, H. L., and McLean, R. A. N., 1982, Trace metals in atmospheric deposition: A review and assessment, *Atmos. Environ.* **16**, 1677–1700.

GESAMP, 1989, IMO/FAO/UNESCO/WMO/WHO/IAEA/UN/UNEP Joint Group of Experts on the Scientific Aspects of Marine Pollution. The atmospheric input of trace species to the world ocean. Reports and Studies GESAMP-WMO 38.

Goldberg, E. D., 1973, North Sea Science, MIT Press, Cambridge, MS.

Graßl, H., Eppel, D., Pettersen, G., Schneider, B., Weber, H., Gandraß, J. G., Reinhardt, K. H., Wodarg, D., and Fließ, J., 1989, Stofeintrag in Nord- und Ostsee über die Atmosphäre. GKSS-Forschungszentrum, GKSS-89/E/8, Geesthacht, Germany.

Hutton, M. and Symon, C., 1986, The quantities of cadmium, lead, mercury and arsenic entering the U.K. environment from human activities, *Sci. Total Environ.* **57**, 129–150.

Hutton, M., 1982, Cadmium in the European Community. Monitoring and Assessment Research Centre, London (MARC Report 26).

ICES, 1978, Input of pollutants to the Oslo Commission area, Cooperative Research 77, Charlottenlund, Denmark, Int. Council for the Exploration of the Sea.

Injuk, J., Otten, Ph., Laane, R., Maenhaut, W., and Van Grieken, R., 1992, Atmospheric concentrations and size distributions of aircraft-sampled Cd, Cu, Pb and Zn over the Southern Bight of the North Sea, *Atmos. Environ.* **26A**, 2499–2508.

Jaffrezo, J. L. and Collin, J. L., 1988, Rain-aerosol coupling in urban area: Scavenging ratio measurement and identification of some transfer processes, *Atmos. Environ.* **5**, 929–935.

Jickells, T. D., Davies, T. D., Tranter, M., Landsberger, S., and Jarvis, K., 1992, Trace elements in snow samples from the Scottish Highlands: Sources and dissolved/particulate distributions, *Atmos. Environ.* **26A**, 393–401.

Kedem, B., Chiu, L. S., and North, G. R., 1990, Estimation of mean rain rate: Application to satellite observations, *J. Geophys. Res.* **95**, 1965–1972.

Kemp, K., 1984, Long term analysis of marine and nonmarine transported aerosols, *Nucl. Inst. Methods* **B3**, 470, 860–871.

Kersten, M., Kriews, M., and Förstner, U., 1991, Partitioning of trace metals released from polluted marine aerosols in coastal seawater, *Mar. Chem.* **36**, 165–182.

Kendall, P. M. H., Bevington, C. F. P., and Pearse, D. J., 1985, Atmospheric cadmium emission and deposition in the Netherlands. Metra Consulting B.V., Kockengen.

Krell, U., Lehmhaus, J., and Roeckner, E., 1986, Atmospheric input of heavy metals into the North Sea: First results of a 3-dimensional trajectory model. In: Proc. WMO Conf. on Air Pollution Modelling and Its Application, Leningrad, USSR, 18–24 May.

Krell, U. and Roeckner, E., 1988, Model simulation of the atmospheric input of lead and cadmium into the North Sea, *Atmos. Environ.* **22**, 375–381.

Kretzschmar, J. G. and Cosemans, G., 1979, A five year survey of some heavy metal levels in the air at the Belgian North Sea coast, *Atmos. Environ.* **13**, 267–277.

Kriews, M., 1992, Charakterisierung mariner Aerosole in der Deutschen Bucht sowie Prozesstudien zum Verhalten von Spurenmetallen beim Übergang Atmosphäre/Meerwasser. Ph.D. Thesis, University of Hamburg, Germany.

Losno, R., Bergametti, G., and Buat-Menard, P., 1988, Zinc partitioning in Mediterranean rainwater, *Geophys. Res. Lett.* **15**, 1389–1392.

Main, H. H. and Friedlander, S. K., 1990, Dry deposition of atmospheric aerosols by dual tracer method-I. Area source, *Atmos. Environ.* **24A**, 103–108.

Martin, J.-M., Elbaz-Poulichet, F., Guieu, C., Loije-Pilot, M.-D., and Han, G., 1989, River versus atmospheric input of material to the Mediterranean Sea: An overview, *Mar. Chem.* **28**, 159–182.

Migon, C., Morelli, J., Nicolas, E., and Copin-Montegut, G., 1991, Evaluation of total atmospheric deposition of Pb, Cd, Cu and Zn to the Ligurian Sea, *Sci. Total Environ.* **105**, 135–148.

Mukherje, A. B., 1986, The discharge of lead, cadmium and mercury into the ecosystem in relation to Finnish industry. Helsinki University of Technology (SF-02150).

Naturvardsverket, 1982, Monitor 1982. Tungmetaller och organiska miljögifter i svensk natur.

NAS, 1978, The Tropospheric Transport of Pollutants and Other Substances to the Oceans. National Academy of Sciences Press, Washington, D.C., 194 pp.

Ottley, C. J. and Harrison, R. M., 1993, Atmospheric dry deposition flux of metallic species to the North Sea, *Atmos. Environ.* **27A**, 685–685.

Otten, P., Storms, H., Xhoffer, C., and Van Grieken, R., 1989, Chemical composition, source identification and quantification of the atmospheric input into the North Sea. In Progress in Belgian Oceanographic Research (edited by G. Pichot), pp. 413–422. Prime Minister's Services of Science Policy Office & Ministry of Public Health and Environment, Brussels.

Pacyna, J. M., 1983, Trace element emission from anthropogenic sources in Europe. Report of the Norwegian Institute for Air Research. Lillestrøm (NILU TR 10/82).

Pacyna, J. M., Semb, A., and Hanssen, J. E., 1984, Emission and long-range transport of trace elements in Europe, *Tellus* **36B**, 163–178.

Pacyna, J. M., 1985, Spatial distribution of the As, Cd, Cu, Pb, V and Zn emissions in Europe within a 1.5 grid net. Norwegian Institute for Air Research. Lillestrøm (NILU OR 60/85).

Pacyna, J. M., 1987, Atmospheric emissions of arsenic, cadmium, mercury and zinc in Europe in 1982. Norwegian Institute for Air Research. Lillestrøm (EMEP/CCC-Rept. 3/86).

PARCOM, 1985, Sixth Annual Report of the Paris Commission, Annex 6, London.

PARCOM, 1986, Report from the Fourth Meeting of the Working Group on the Atmospheric Input of Pollutants to Convention Waters, Oslo 28–30 October.

PARCOM, 1987, Current estimates of atmospheric inputs to the North Sea. Ninth Annual Report on the Activities of the Paris Commission, Annex pp. 38–42.

Peirson, D. H., Cawse, P. A., Salmon, L., and Cambray, R. S., 1973, Trace elements in the atmospheric environment, *Nature* **241**, 252–256.

Petersen, G., 1987, Methodology for model calculations of the atmospheric input of trace metals into the North Sea and Baltic Sea. In: Proc. PARCOM Meeting, ATMOS-5, Berlin, 10–12 November.

Petersen, G., Weber, H., and Grassl, H., 1988, Modelling the Transport of Trace Metals from Europe to the North Sea and Baltic Sea, in J. M. Pacyna and B. Ottar (eds.), *Control and Fate of Atmospheric Trace Metals*, NATO ASI Series, Kluwer Academic Publishers, Dordrecht, The Netherlands.

Remoudaki, E., Bergametti, G., and Losno, R., 1991, On the dynamic of the atmospheric input of copper and manganese into the western Mediterranean Sea, *Atmos. Environ.* **25A**, 733–744.

Rojas, C. M., Injuk, J., Laane, R. W., and Van Grieken, R., 1993, Dry and wet deposition fluxes of Cd, Cu, Pb and Zn into the Southern Bight of the North Sea, *Atmos. Environ.* **27A**, 251–259.

Ross, H. B., 1984, Methodology for the collection and analysis of trace metals in atmospheric precipitation. Report CM-67, International Meteorological Institute in Stockholm/Dept. of Met., University of Stockholm, Sweden.

Ross, H. B., 1987, Trace metals in precipitation in Sweden, *Water, Air, and Soil Poll.* **36**, 349–363.

Ross, H. B., 1990, Trace metal wet deposition in Sweden: Insight gained from daily wet only collection, *Atmos. Environ.* **24A**, 1929–1938.

Ruijgrok, W., Visser, H., and Römer, F. G., 1990, Comparison of bulk and wet-only samplers for trend detection in wet deposition, *Proceedings International Workshop on Cloud Chemistry and Wet Deposition, Utrecht, The Netherlands*, April 1990, pp. 34–40.

Rupper, J., 1975, Geochemical investigations on atmospheric precipitation in a medium-sized city (Göttingen, FRG), *Water, Air and Soil Poll.* **4**, 447–455.

Schladot, J. D. and Nürnberg, H. W., 1982, Report Jülich, Nuclear Research Center.

Schneider, B., 1987, Source characterization for atmospheric trace metals over Kiel Bight, *Atmos. Environ.* **21**, 1275–1283.

Schroeder, W. H., Dobson, M., Kane, D. M., and Johnson, N. D., 1987, Toxic trace elements associated with airborne particulate matter: A review, *J. Air Poll. Control Ass.* **37**, 1267–1284.

Schulz, M., 1993, Räumliche und zeitliche Verteilung atmosphärischer Einträge von Spurenelementen in die Nordsee. Ph.D. thesis, University of Hamburg, Germany.

Scofield, R. A., 1991, Operational estimation of precipitation from satellite data, *Palaeogeography, Palaeoclimatology, Palaeoecology (Global and Planetary Change Section)* **90**, 79–86.

Sehmel, G. A. and Hodgson, W. J., 1978, A Model for Predicting Dry Deposition of Particles and Gases to Environmental Surfaces. Battelle, Pacific Northwest Laboratory, Richland, WA., PNL-SA-6721.

Selin, E., Mnubi, A., Isakson, J., Foltescu, V. L., and Djupström, M., 1992, Transport and Deposition of Particulate Pollution to the East Coast of Sweden. Environment, Lifestyle and Health FRN-Report 92:3, Swedish Council for Planning and Coordination of Research, 56–71.

Semb, A. and Pacyna, J. M., 1988, Toxic trace elements and chlorinated hydrocarbons: Sources, atmospheric transport and deposition. Environmental Report 1988:10. Nordic Council of Ministers, Copenhagen, ISBN Denmark.

Slinn, S. A. and Slinn, W. G. N., 1980, Predictions for particle deposition on natural waters, *Atmos. Environ.* **16**, 1785–1794.

Slinn, W. G. N., 1983, Air-to-sea transfer of particles. In Liss, P. S. and Slinn, W. G. N. (eds.): Air-sea Exchange of Gases and Particles. D. Reidel Dordrecht, pp. 299–405.

Smith, F. B., 1991, Deposition processes for airborne pollutants, *The Meteorological Magazine* **120**, 173–182.

S & TWG Scientific and Technical Working Group, 1987, Quality status of the North Sea. Second International Conference on the Protection of the North Sea, London, November 1987, Vol. 5, p. T8 and Vol. 6, pp. 6–10.

Steiger, M., Schulz, M., Schwikowski, M., Naumann, K., and Dannecker, W., 1989, Variability of aerosol size distribution above the North Sea and its implication to the dry deposition estimates, *J. Aerosol. Sci.* **20**, 1229–1232.

Steiger, M., 1991, Die anthropogenen und naturlichen Quellen urbaner und mariner Aerosole charakterisiert und quantifiziert durch Multielementanalyse und chemische Receptormodelle. Ph.D. Thesis, University of Hamburg, Germany.

Stöeßel, R., 1987, Untersuchungen zu Naß- und Trockendeposition von Schwermetallen auf der Insel Pellworm. Ph.D. Thesis, University of Hamburg, Germany.

Struyf, H. and Van Grieken, R., 1993, An overview of wet deposition of micropollutants to the North Sea, *Atmos. Environ.* **27A**, 2669–2687.

van Aalst, R. M., van Ardenne, R. A. M., de Kreuk, J. F., and Lems, Th., 1993, Pollution of the North Sea from the Atmosphere. TNO report CL 82/152, Delft, The Netherlands.

van Aalst, R. M., 1988, Input from the atmosphere. In Salomons, W., *et al.* (eds.): Pollution of the North Sea: An Assessment. Springer-Verlag, Berlin/Heidelberg, Germany.

van Daalen, J., 1991, Air quality and deposition of trace elements in the province of South-Holland, *Atmos. Environ.* **25A**, 691–698.

van Enk, R. H., 1980, The pathway of cadmium in the European Community, *European Appl. Res. Rept. Environ. and Nat. Res. Sec.*, 1:1.

Van Jaarsveld, J. A., van Aalst, R. M., and Onderdelinden, D., 1986, Deposition of metals from the atmosphere into the North Sea: Model calculations, RIVM, Bilthoven, Report 842015002.

Van Jaarsveld, J. A. and Onderdelinden, D., 1986, Modelmatige beschrijving van concentratie en depositie van kolen relevante componenten in Nederland, veroorzaakt door emissies in Europa. Nationaal Onderzoeksprogramma Kolen (NOK), deelrapport 4, April 1986, PEO, Utrecht, The Netherlands.

Van Jaarsveld, J. A., 1991, Estimating Atmospheric inputs of trace constituents to the North Sea: Methods and results. 19th NATO/CCMS-ITM on Air Pollution Modelling and its Application. 29 September–4 October 1991, Ierapetra, Greece.

Warmenhoven, J. P., Duiser, J. A., de Leu, L. Th., and Veldt, C., 1989, The contribution of the input from the atmosphere to the contamination of the North Sea and the Dutch Wadden Sea. TNO Report R 89/349A, Delft, The Netherlands.

Williams, R. M., 1982, A model for the dry deposition of particles to natural water surfaces, *Atmos. Environ.* **16**, 1933–1938.

Yaaqub, R. R., Davies, T. D., Jickells, T. D., and Miller, J. M., 1991, Trace element in daily collected aerosols at a site in southeast England, *Atmos. Environ.* **25A**, 985–996.

Recent Advances in the Analysis of Individual Environmental Particles*

A Review

Wendy Jambers, Lieve De Bock and René Van Grieken†

Micro and Trace Analysis Centre (MiTAC), Department of Chemistry, University of Antwerp (UIA), Universiteitsplein 1, B-2610 Antwerpen-Wilrijk, Belgium

Summary of Contents

Keywords: Microanalytical beam technique; environmental particle analysis; aerosol; electron microscopy; mass spectrometry; review

Introduction

Although microanalytical and surface analysis techniques are frequently used in material sciences, corrosion studies, microelectronics and earth research, applications to individual environmental particles are still rare. The importance of particulate matter in the environment is well understood: particles are the major material carriers in water and in air, atmospheric aerosols influence visibility and the global climate and many components of environmental particles are toxic. Individual particle analysis can provide detailed information concerning the origin, formation, transport, reactivity, transformation reactions and environmental impact of particles and it is therefore valuable as a complement to conventional bulk analysis.

However, microanalytical techniques have specific problems which are often related to the extremely small sizes of the sample. Quantitative results are difficult to obtain because of the uncertainties in determining the interaction volume and because of the absence of suitable standards. The interaction volume is defined as the volume of the sample in which the incident electrons or ions interact with the solid, depositing energy and producing those forms of secondary phenomena which are measured. This volume is the result of several elastic and inelastic scatterings and it cannot be well defined. The size and the geometry of the particles determine the volume in which scattering can occur, and thus regulate, together with the energy of the incident beam and the effective density of the sample, the shape and diameter of the interaction volume. This interaction volume is important in quantitative analysis because it represents the volume (and thus the mass) of the sample in which the measured signals are produced.

Another obstacle is the need to analyse large numbers of particles to ensure the statistical relevance of the information and this may render individual particle analysis very time consuming. Much effort has been invested in automation and computerization, and computer-controlled electron probe X-ray microanalysis (EPXMA) is the most advanced example of this development. However, the major drawback of most microbeam techniques is the need to operate under vacuum. This can cause loss and transformation of volatile and unstable compounds. Techniques such as Fourier transform infrared (FTIR) microscopy and micro-Raman spectrometry, which work under atmospheric pressure, and on-line laser microprobe mass spectrometry (on-line LMMS), which reduces losses by the small time interval between sampling and analysis, are expected to gain importance in the near future. Moreover, all techniques have their own specific limitations and they can complement each other with respect to lateral resolution, detection limits, detectable elements, *etc*. Hence, analysis using several microbeam techniques in combination with bulk analysis will give an optimum characterization of the sample. As most microanalytical techniques require expensive equipment, co-operation with other research centres will normally be a necessity.

This paper discusses the most recent advances in the field; it is based on a computer search of the literature on individual environmental particle analysis with microbeam techniques published exclusively during the period January 1990–April 1994. The most relevant techniques are briefly discussed and

* Presented at The Second International Symposium on Speciation of Elements in Toxicology and in Environmental and Biological Sciences, Loen, Norway, June 15–18, 1994.

† To whom correspondence should be addressed.

their latest applications are reported. For reviews on earlier applications, reference is made to articles by Grasserbauer[1] and Van Grieken and co-workers.[2–4]

Electron Beam Techniques

At present different types of electron microscopes are available. All these instruments use an electron beam to generate various signals. The difference is located in the signals analysed. In electron probe X-ray microanalysis (EPXMA) and scanning electron microscopy coupled with energy-dispersive or wavelength-dispersive X-ray detection (SEM–EDX and SEM–WDX), X-rays are detected in addition to back-scattered and secondary electrons, whereas in transmission electron microscopy (TEM) and electron energy loss spectroscopy (EELS) transmitted and diffracted electrons are used. The combination of a scanning device with TEM is called scanning transmission electron microscopy (STEM). Another expression frequently used is the analytical microscope (AEM). This is an electron microscope equipped with microdiffraction and microanalytical techniques such as EELS and energy-dispersive spectroscopy (EDS). This combination of image capabilities and small area sensitive techniques provides an expansion of the amount of information gain of a small area of the sample.[5]

Electron Probe X-ray Microanalysis and Scanning Electron Microscopy

Instrumentation

In EPXMA and SEM, the nanometre-sized electron probe generates various signals on sample interaction. In addition to possible morphological studies, based on the detection of secondary and backscattered electrons, compositional information can be acquired by the wavelength- or energy-dispersive detection of emitted characteristic X-rays and *via* the compositional backscattered electron image. Although originally SEM was mainly used to obtain high-resolution images and the chemical sample analysis was performed by EPXMA, the differences between the two techniques have been reduced over the years to only a difference in instrumental set-up and practical arrangement of the present detectors. To some extent chemical and morphological studies can now be performed by both techniques. More theoretical aspects on EPXMA and SEM–EDX analysis can be found in recent textbooks.[6,7]

At MiTAC, the Micro and Trace Analysis Centre at the University of Antwerp, several hundred individual particles can be analysed in a few hours with a JEOL Superprobe JXA-733 EPXMA unit, which is equipped with a Tracor Northern TN-2000 X-ray detection and analysis system and a system for automated particle recognition and characterization. The localization of a particle is performed by successive horizontal line scans with the electron beam. The contour pixels of the particle are saved and the area, perimeter and diameter of the particle are calculated. Then an X-ray spectrum is accumulated. All the information is stored on disk for off-line data processing on a UNIX computer. In spite of its unfavourable detection limits (0.1%), automated EPXMA, in combination with multivariate techniques and/or cluster analysis, is a powerful method for discriminating different particle types and for source apportion.

Recently a new JEOL JSM-6300 scanning electron microscope was installed at MiTAC. The instrument is equipped with a PGT (Princeton Gamma Tech) energy-dispersive X-ray detector. The IMIX software, available for X-ray collection and image processing, runs on a SUN workstation. Compared with the JEOL JXA-733 EPXMA, several interesting new applications are possible. Image processing and element mapping are more efficient owing to the new data system. Further, the windowless X-ray detector offers the possibility of detecting light elements such as C, N and O. The analyses are expected to be even faster and more reliable than before.

Application to Aerosols

EPXMA and SEM have been used successfully for the identification, classification and source characterization of aerosol particles originating from remote, marine, continental and urban regions.

Owing to its remote character, the Antarctic continent shows low anthropogenic pollution and is considered to be an ideal study site for background aerosols. The EPXMA study, in combination with hierarchical and non-hierarchical cluster techniques,[8] of coastal Antarctic aerosols by Van Grieken and co-workers[9–11] identified marine components as the dominant particle type in both the fine and coarse mode fraction. Additionally, small amounts of sulfur were detected in a significant number of NaCl and $MgCl_2$ particles, indicating possible reactions with gaseous sulfur compounds. Internal mixtures could be observed for silicates and marine aerosol particles and most of the sulfur in particles larger than 0.1 μm was present as $CaSO_4$. The abundance of the latter particles showed a seasonal variability with a maximum in the summer.

Compared with the Antarctic region, Siberia is characterized by both very remote and strongly polluted areas. Recently, EPXMA aerosol studies were performed[12] to investigate processes responsible for aerosol production, transport and fate in the Siberian region of both natural and pollution atmospheric aerosols at local, regional and long-range levels. Estimations both of heavy metal deposition from the atmosphere in polluted areas and over Lake Baikal and of the impact of aerosols on the Arctic region and the global climate should be possible.

To clarify chemical mechanisms occurring in the Amazon Basin atmosphere and to study processes involving aerosol and gas emission, individual background aerosol particles sampled over the Amazon Basin were analysed by EPXMA. Most of the particles could be related to two local sources, soil dust and biologically derived material. Aerosol particles produced by vegetation contained mainly S, K and P.[11]

Successful EPXMA of individual stack fly ash particles originating from a Hungarian power station,[13] by which two unexpected particle groups in the size fraction below 2 μm (particles with a high barium content and $CaSO_4$ particles with a high arsenic content) were identified, was followed by a study on Hungarian background aerosols.[14] Most of the Hungarian background aerosol in the 0.3–20 μm size range appeared to be of anthropogenic origin. Correlation of the identified particle types with the corresponding air back trajectories showed that source identification is reasonable for anthropogenic sources. To obtain the exact distinction between particle groups of similar composition, both morphological parameters and trace elements should be identified.

New evidence of long-range transport of particles was found in volcanic loess on the island of Hawaii.[15] Quartz grains, virtually unknown in the basalts of the Hawaiian Islands, were detected in late Quaternary loess deposits of the Pahala Formation at Pu'u o Mahana, by a combination of X-ray diffraction studies of bulk samples, SEM-EDS analyses of single mineral grains and X-ray mapping of particles in grain mounts. The numerous quartz particles with sizes ranging from 1 to 10 μm and a few as large as 60 μm were probably transported more than 10000 km from Asia by late Quaternary windstorms and they make up as much as 1–3% of the deposit.

To investigate the potential effect of the Kuwait oil fire plumes on the local and global environment, aerosol samples were collected on board an aircraft at different altitudes in the plumes. Morphology, concentration, size distribution and chemical composition of the samples were determined by EM (transmission and scanning).[16] It appeared that during transport of the plume more small sulfate particles were produced, probably as result of SO_2 oxidation followed by homogeneous nucleation. In those areas where the oil fire plumes became more dispersed, large soot, salt and dust particles contained a sulfur coating which turned them into active cloud condensation nuclei (CCN). These CCN can initiate haze, smog, fog or cloud droplets. Long-range transport of the aerosols depended on air flow and aerosol wet and dry deposition rates. Black carbon particles have the tendency, in the absence of rain, to remain airborne for a long time and travel long distances. Air trajectory analysis indicated that there were periods when aerosol particles generated by the fires could have reached China. To explain the severe rainfall in China at the end of May and the beginning of June as a result of the events in Kuwait, more research is needed.

Rojas *et al.*[17] showed in an aerosol study, using principal factor analysis (PFA) and absolute principal factor analysis (APFA) as receptor models with X-ray fluorescence (XRF) and single particle analysis, that compared with these models, the EPXMA technique provided a better resolution of the different sources affecting the monitoring site. The aerosol particles were collected 4 km west of downtown Santiago de Chile and they could be classified into eight different particle types in both the fine and coarse aerosol mode. Soil dust and particles from anthropogenic origin seemed to be the most abundant particle types present in the coarse and fine particle mode, respectively. Sulfur-bearing particles did not explicitly appear as an independent group of particles. They were present in six out of eight different particle types.

The composition of aerosols collected at Khartoum, Sudan, was obtained by a combination of different analytical techniques: XRF and particle-induced X-ray emission (PIXE) for bulk analysis and automated EPXMA for individual particle analysis.[18] Most of the Khartoum aerosol particles were identified as soil dust. The enrichment of sulfur, chlorine, zinc, bromine and lead present in the aerosols appeared to be among the lowest urban values yet recorded in the literature. The diurnal variations of airborne levels of bromine, lead and crustal elements indicate that they are controlled by traffic emissions. Differentiation of soil dust particles into aluminosilicates and lesser amounts of quartz and $CaCO_3$ particles was obtained by EPXMA. All the combustion particles consisted of sulfates. Bromine- and lead-containing particles were not detected by EPXMA.

An element that has received much attention both outdoors and indoors, owing to its threatening effect on the environment and human health, is lead. An EPXMA–PIXE–LAMMA (laser microprobe mass analysis) study[19] on lead-containing particles collected near the city of Antwerp, Belgium, showed that most of the particles were found in the fine particle mode with diameters <1 μm. Car exhaust products seemed to be responsible for lead sulfates and lead halides, accounting for 67 and 28% by mass of the total lead-containing particles, respectively. Additionally, it was observed that sulfation for many lead-rich particles occurs only partially, and bromine and chlorine were found to be completely removed from those particles. Lead halide particles were abundant; they exhibited varying concentrations of bromine and chlorine, but with an average bromine-to-lead ratio of 0.386. Ammonium sulfate was present as a surface coating on the lead-rich particles.

Indoor lead-containing particles were studied by Hunt *et al.*[20] using SEM–EDX. Based on a classification scheme[21] obtained by the analysis of different types of lead source particles, paint, road dust and garden soil with diameters in the size range 0–64 μm were suggested to be the major contributors of particulate lead to the floor dust of 16 residences situated in the London borough of Richmond, UK. Lead-containing dust particles in the 64–100 μm size range were identified as paint. The age of the homes appeared to be unrelated to variations in the contributions made by the major sources.

Qian and Ishizaka[22] used both SEM and TEM techniques together with thin-film chemical tests to study the nature and morphology of methanesulfonic acid (MSA) particles, sampled over the Sakushima Island, Japan. MSA and SO_2 are the major components formed during the oxidation of dimethyl sulfate, after its transfer from the sea's surface into the atmosphere. MSA-containing particles appeared to be dominant in the coarse particle fraction under very humid conditions and they seemed to be produced through heterogeneous nucleation reactions of gaseous MSA with sea salt or soil particles, leading to mixed particles. MSA particles were absent in the submicrometre size range, which was dominated by sulfate. Nitrate was found in both size ranges. Morphological information alone was shown to be insufficient for differentiating between sulfuric acid and MSA particles.

Recently, a method has been developed by Pardess *et al.*[23] for measuring the mass of sulfur in single aerosol particles using SEM analysis. Calibration graphs, acquired by laboratory-generated particles of known composition, offer the possibility of determining with reasonable accuracy the sulfur mass content in particles larger than 0.4 μm diameter and with a minimum of 10^{-13} g of sulfur. Quantitative estimations of sulfur in heterogeneous aerosol particles can also be obtained according to this method.

EPXMA in combination with an automated image analysis system has been used for the characterization of individual North Sea aerosols for several years.[24] More than 25 000 particles, sampled during a period of 4 years on-board a research vessel over the North Sea and the English Channel, were sized, chemically analysed and classified.[25] By combining single particle analysis and hierarchical clustering, North Sea aerosols were found to be predominantly composed of sea salt, sulfur-rich particles, silicates and calcium sulfate particles. The abundance of the different particle types depends on both meteorological conditions and sampling locations. Principle component analysis (PCA) was performed to investigate the differences between all samples, based on variations in abundance. The different components could be identified: the first contained marine-derived aerosol particles and became more important with increasing wind speeds or when sampling at more remote locations. The second component was characterized by anthropogenically derived $CaSO_4$ particles which seemed to be more abundant in air masses originating from the South of England. The samples of third cluster were related to high silicate and sulfur abundances. Source apportionment of the last group was obtained by a second PCA. Two clusters were differentiated: mixed marine/continental samples and pure continent-derived silicate and sulfur-rich samples.

The characterization of individual particles in the North Sea surface microlayer and the underlying sea-water was compared with the atmospheric and riverine particle data by Xhoffer *et al.*[26] More details are discussed below.

The aerosol composition at six different altitudes above the North Sea was studied by Rojas and Van Grieken.[27] The results of the EPXMA, in combination with hierarchical cluster analysis on 50 000 individual particles, showed that aluminosilicates, $CaSO_4$ and Fe-rich particles are the most abundant particle types present in continental air masses. Owing to the mixed nature of the atmosphere, no composi-

tional changes in the main particle types originating from western and marine air masses were recognized. By performing non-hierarchical cluster analysis the most abundant particle types in these air masses were identified as aluminosilicates, Fe-rich sea salt enriched with lead and organic material. About 60% of the analysed particles seemed to be related to combustion or energy-generation processes. The novel approach introduced in this study to reduce the data set by performing principal factor analysis (PFA) on the elemental frequency matrix revealed comparable results with PFA used in combination with cluster analysis.

Aerosol particles with diameters above 1 μm are called giant particles and, although the number of these particles in the lower troposphere is very small compared with the condensation mode particles, their contribution to the atmospheric deposition is of extreme importance.[28–30] Owing to the slow realization of the importance of giant aerosol particles in the atmosphere and to sampling difficulties and measurement errors, many questions regarding giant particles still remain unanswered. To investigate the importance of these giant particles, aerosol sampling was carried out using an impaction rod on top of an aircraft, which flew at different altitudes over the Southern Bight of the North Sea.[31] The analysis and classification of the collected samples was performed by EPXMA in combination with multivariate techniques. PFA revealed four different giant aerosol sources: aluminosilicate dispersal, combustion processes and an industrial and a marine source. The distinction between flights for which the associated air masses were marine and continental was found by hierarchical and non-hierarchical cluster analysis. The size distributions of the main particle types (sea salts, sea salts enriched with sulfur, organic particles, $CaSO_4$ and Fe-rich particles), were fitted well by a log-normal size distribution and the average diameters were found to be around 3 μm. Only aluminosilicates showed a bimodal size distribution with average size maxima at 4 and 15 μm.

To study the variations in composition of air masses crossing the North Sea due to air–sea exchange processes in the lower troposphere, aerosol and rainwater samples were collected on two research vessels positioned 200 km apart downwind from each other, in the central area of the North Sea.[32] Single particle analysis was achieved by EPXMA and a total of three to eight different particle types could be distinguished using hierarchical cluster analysis. The differences in composition between the two research vessels could be recognized as a decrease in the abundance of aluminosilicate particles and a relative increase for NaCl and sea-water crystallization products as the air masses crossed the North Sea. No significant decrease in particle diameter was observed. Both compositional and size differences appeared in the collected rainwater samples of both research vessels. Four different aerosol sources were obtained by PFA. Manual EPXMA was used to investigate the relationships between particle composition, origin and shape. For most of the particle types a characterization based on their shape was achieved.

Applications to suspensions and sediments

Johnson *et al.*[33] analysed suspended matter from Onondaga Lake, NY, USA, with a computer-controlled SEM (CCSEM). In this lake the size and composition of the particles are directly related to biological production and chemical precipitation in the water column and to the physical transport of suspended material by the lake tributaries. Strong temporal variations were found for the total amount of particulate matter and the relative contributions of the different particle types. These dynamics were regulated largely by (*a*) the composition and level of phytoplankton growth, (*b*) tributary loading of particles, particularly after run-off events, and (*c*) the precipitation of calcium carbonate.

By staining the suspended samples with ruthenium tetraoxide, organic particles can also be included in the automated SEM–EDX analysis. The only problem with ruthenium is a serious interference of the X-ray peak with that of chlorine. However, during aquatic sample preparation chlorine is usually removed, leaving no problems for the use of ruthenium. This preparation was used on samples collected in the Sargasso Sea. The organic fraction predominates in all samples (approximately 70%) and the major components of the inorganic fraction are iron-, calcium-, sulfur- and silicon-rich particles.[34]

Eisma *et al.*[35] used EPXMA and SEM for the characterization of suspension collected around Sumbawa Island, Indonesia. Samples collected from the north of the island are characterized by a high abundance of iron-rich particles, presumably of volcanic origin. In Saleh Bay, an enormous bay in the centre of the island, a relatively high content of tin-rich particles has been found. During earlier research in the Flores Sea and the Makasar Strait, tin-rich particles were also found in many samples.[36,37] Possible sources for these particles are present in the region but others cannot be excluded. SEM has been used for the morphological characterization of especially aggregates. These aggregates were found when biogenic material, *e.g.*, diatoms and coccolithophorids, is also present. A correlation between aggregates and the presence of diatoms has been observed previously.[36–38] It is likely that diatoms produce an organic material that acts as a glue between the flocculated particles.[35]

Samples collected during a small flood event in the Magela Creek, northern Australia, were investigated with automated EPXMA to give additional information on the nature of the mineral particulate and colloidal fraction transported by the river.[39] Surprisingly, there was little difference in the composition of the mineral fractions of suspended particulate matter (SPM) and coarse colloidal matter (CCM). Both are dominated by iron-rich aluminosilicates (70–80%) and quartz (10%), both of which are weathering products. The iron-rich aluminosilicates probably consist mainly of aluminosilicates coated with iron oxide.

Sediment samples from a longitudinal profile and suspended matter samples from a maximum peak flow were collected from the Elbe river in Germany.[40] Based on the particle types of the sediment samples, a clear distinction could be made between the marine and the fluvial end-member components. The variation in relative abundance of calcium carbonate could be accounted for by the mixing ratio of the fluvial and marine fraction. Automated EPXMA also revealed that the suspended particulate matter transported during the peak event originated mainly from the load transport characteristic for these discharge events and from erosion of settled mud particles.

By using EPXMA in combination with LMMS, North Sea bulk water and corresponding surface microlayer samples have been characterized.[26] Only a small variation was observed between the particle types and abundances in the sea surface microlayer and the underlying bulk sea-water samples. This could be explained by the roughness of the sea during sampling which causes mixture of the water layers. Organic particulate matter was more abundant in the microlayer and showed very good correlation with the metal-rich fraction. By comparison with aerosol samples collected above the North Sea, it was found that calcium-rich particles have to be of aquatic origin, as no chemical analogues were observed above the North Sea. However, a good similarity was found for the titanium-rich marine and atmospheric fractions.

A combination of EPXMA with conventional bulk techniques was used to analyse silty and clayey sediment samples

of the Baltic Sea.[41] Automated single particle analysis resulted in the identification of nine different particle types which could be identified as different mineral species. The most abundant types are quartz and aluminosilicates (often more than 95%), but they are not very useful for characterizing the geochemistry of the Baltic sediments. Reduced species such as iron sulfides and rhodochrosite are typical for anoxic sediment environments (*e.g.*, Gotland Deep), whereas oxides/hydroxides of iron and manganese indicate an oxic environment (*e.g.*, Kattegat). In regions with periodic changes in redox conditions, sulfides and oxides/hydroxides are detected side by side. The abundances of other particle types such as calcium- and titanium-rich particles depend on the geographical position. Calcium-rich particles are found in the transition area between the Baltic Sea and the North Sea, with a clean gradient from the North to the Baltic Sea: calcium-rich particles reach the Baltic Sea by inflow of North Sea water.[42] Titanium-rich particles have high abundances near the coastlines of Germany and southern Poland and may be the result of abrasion–erosion products of the German coast, or they may be of anthropogenic origin.[41]

Suspended samples collected in the Scotia Sea–Weddell Sea Confluence were used to confirm the correlation between the occurrence of suspended and sedimented barite and the intensity of past biological activity.[43] In the surface waters barite is mainly contained within large bio-aggregates. In the subsurface zone these aggregates are dispersed, possibly by bacterial activity, and the barite crystals become free discrete particles. As no association of barite with phytoplankton individuals was found, the formation of pelagic barite is probably a passive precipitation in saturated micro-environments.

SEM is often used for the morphological characterization of environmental particles. Examples of this usage were given by Eisma *et al.*,[35] Tucan and Pamukcu,[44] Tipping *et al.*[45] and Oades and Waters.[46]

Scanning Transmission Electron Microscopy–Energy-dispersive X-ray Analysis

Instrumentation

The STEM can be operated as an conventional TEM in which the whole imaged specimen area (thin section) is illuminated simultaneously and the magnified image is displayed on a fluorescent screen. The different imaging modes for TEM are bright-field (or conventional TEM), dark-field and electron diffraction. Bright- and dark-field images give morphological information, while electron diffraction is used to identify crystalline specimens by their crystal structure.

In the scanning mode, the specimen is scanned with a small electron probe which has a diameter of the order of 2–5 nm. Signals produced during this scanning are recorded with electronic detectors and displayed on an observation cathode-ray tube (CRT). The transmitted electrons can be recorded in bright- and dark-field mode, while the scattered electrons can be backscattered (BSE) or secondary electrons (SE). Detailed descriptions of TEM and STEM can be found in the literature.[47,48]

By assimilation of the STEM with an energy-dispersive X-ray analyser (EDX), X-ray microanalyses of small areas of thin and semi-thin specimens are possible. As the images in the scanning mode are recorded as serial electrical signals, flexible on-line image evaluation and processing are possible, and also analogue and digital recording for subsequent refining with an image-processing system.

The main advantages of STEM are in the production and positioning of small electron probes for imaging and X-ray analysis of small specimen areas. Using thin specimens minimizes the interaction volume and thus improves the lateral resolution for X-ray microanalysis.

Applications

Publications on STEM–EDX analysis for the characterization of environmental particles are limited. To our knowledge, nothing has been published on aerosol research. Leppard[49] reported on the analysis of aquatic colloids using electron microscopy. STEM–EDX was used to characterize the mineral and mineral–organic colloids. As the preparation of aquatic samples for STEM analysis is a crucial point in reducing artifacts, simple and powerful preparation techniques have been developed. For a description of these methods, see Leppard[49] and Perret *et al.*[50]

Fortin *et al.*[51] used this new Nanoplast preparation technique for the determination of iron oxyhydroxides in the sediments of eight lakes. By combining STEM–EDX with electron diffraction and X-ray diffraction, they found that the only forms of crystalline Fe^{III} oxyhydroxides present were poorly ordered ferrihydrite and lepidocrocite. Deposition of iron oxyhydroxide in the lake sediments also appears to occur on bacterial cells and on their exopolymers. This explains the presence of significant amounts of organic carbon in the diagenetic Fe^{III} oxyhydroxides. Silicon, sulfate, chloride, phosphate, manganese, calcium and aluminium are present as minor components and are probably sorbed onto the iron oxyhydroxides.

STEM–EDX has also been used to analyse the inorganic content of aquatic natural organic matter and the growth of natural organo-mineral associations implicated in the sedimentation phenomena.[52]

By combining STEM–EDX with selected area electron diffraction (SAED), identification of the mineral structure is possible. The first tests on inorganic North Sea suspension with micrometre dimensions have been performed and the possibilities of this combination are promising.[53]

In an effort to identify the aerosol particles responsible for the staining of paintings in the Correr museum in Venice, a study has recently been started to determine the composition of submicrometre indoor aerosol particles using STEM–EDX.[54] By cooling the sample holder with liquid nitrogen it is possible to analyse particles down to 100 nm in size. In this way the evaporation of the particles on the Formvar Cu grids can be prevented. Preliminary results identify the different particle types: silica- and sulfur-rich particles, Ti-rich particles and aluminosilicates. Further research on this topic will be performed.

Electron Energy Loss Spectrometry

Instrumentation

In 1986, Zeiss developed the first dedicated EELS instrument (Zeiss EM 902) by integrating a magnetic prism spectrometer in the optical column of a conventional TEM. This energy filter has two operation modes, namely a spectrum mode and an image mode. By selecting an aperture the final image becomes an energy-selected (or filtered) image. The energy loss spectrum is sequentially recorded by scanning the spectrum over a small slit and is analysed by using a personal computer as multichannel analyser.[55,56] By using a silicon-intensified target (SIT) vidicon camera, the energy-filtered images can be transferred to an image-processing system. For more details about the theory, instrumentation and application of the EELS technique, reference is made to the book by Egerton.[57]

EELS provides a way to identify and quantify elements not only by means of the spectra, but also by element specific

images (ESI). The main advantages of this technique are the high sensitivity for elements of low atomic number, the low detectable mass[58] (EELS is based on primary interaction effects, *i.e.*, the initial electrons give rise to the signal), and the electronic state and chemical bonding information which are included in a spectrum. To benefit from these advantages the samples need to be very thin in order to transmit enough signal and to prevent multiple scattering effects.[57]

The sequential recording of the spectra leads to an unacceptably long collection time for environmental particles.[59] In particular, volatile elements suffer under this long radiation, which results in frequent large mass losses.[60] However, by applying a parallel spectrum recording system the collection time can be reduced by a factor of 400. Parallel EELS (PEELS) is thus feasible for the analysis of ultra-fine environmental particles.[59]

Applications

As the EELS technique has only recently been commercialized, it still has an experimental status concerning environmental applications. The few applications on individual environmental particles published are discussed here.

Xhoffer[60] reported on the analysis of standard test aerosols of inorganic salts with serial and parallel EELS. He found that even at cryogenic temperatures preferential losses and structure reorganization cannot be avoided and analysis of beam-sensitive samples such as inorganic salts should be carried out using PEELS and only used for qualitative purposes.

Maynard and Brown[59] investigated atmospheric particles with PEELS and found that the majority of the ultra-fine particles consist of carbon. The carbonaceous aerosol particles collected in Phoenix, AZ, USA, are smaller than 2 μm and consist of 10–100 aggregated spherules.[61,62] By using the electronic state information included in the carbon edge, both researchers[61,62] found a mixture of amorphous and graphitic carbon within and among individual aggregate particles. The graphitic structures are interpreted as part of the primary soot spherules and the amorphous areas as hydrocarbons condensed during aggregation. In the summer a coating of sulfates and nitrates, deposited from the atmosphere as end-products of photochemical reactions, was found on some of the particles. ESI was used to provide visual evidence of sulfur coating of the carbonaceous particle surfaces.[62] The structural variations of the coated aggregates are similar to those found for uncoated aggregates, suggesting the same pre-emission sources.

EELS in combination with ESI is a very suitable method for studying the inhomogenous composition of nanometre-range surface-modified asbestos fibres.[63] Carbon maps of organosilane-coated chrysotile asbestos fibres reveal that the coating is not homogeneously distributed over the fibres. Some fibres even seem to be unaffected by the treatment. This means that the surface modification, necessary for reducing the cytotoxic and long-term hemolytic activity of the asbestos fibres, is only partially effective. The pre-edge of the oxygen peak in the spectra of $TiCl_3$-modified fibres reveals the bond between oxygen and titanium, which indicates that the titanium chloride has chemically reacted with the chrysotile fibres.[63] Lateral elemental titanium maps show that titanium forms an encapsulation around the material and thus covers the fibres completely.

Micro-particle-induced X-ray Emission

Instrumentation

The analysis of individual particles with a collimated micrometre-size ion beam can be performed by scanning proton microprobe analysis (SPM). This technique uses a proton beam with an energy of 1–3 MeV, which is well focused to a diameter of 0.5–10 μm with magnetic quadrupoles and/or electrostatic lenses. This high-energy proton beam is obtained by means of a cyclotron or nuclear electrostatic accelerator. A scanning system controls the beam position and a powerful computer system is needed to collect the data received from the different detectors positioned around the sample. To avoid specimen damage during the analysis, the proton beam current should be limited to 100 pA. As with EPXMA and LAMMA, some of the organic components could be lost owing to the high vacuum in the sample compartment.

In proton- or particle-induced X-ray emission (PIXE), an Si(Li) detector collects X-rays, produced at each beam position, while the beam scans over the sample and an on-line sorting process offers the possibility of obtaining real-time X-ray intensity imaging.[64] The acquired elemental maps are composed by a computer on a graphic terminal, and they are very similar to EPXMA mappings, but with much better detection limits (1–10 ppm) and inferior spatial resolution (0.5–10 μm). Images of, occasionally, up to 20 pre-selected elements can be displayed simultaneously during an analysis. Point analysis is accomplished with the X-ray spectra stored for off-line quantitative analysis.

During the interaction of the proton beam with the sample, several other signals are generated. In Rutherford backscattering (RBS) analysis,[65] the elastically backscattered protons are usually collected by a semiconductor surface barrier detector, to obtain quantitative analysis of light elements such as C, N and O. This technique is frequently performed simultaneously with PIXE. Gamma rays from F, Na and other elements, generated from nuclear reactions due to proton beam–sample interactions are measured with a Ge(Li) detector in particle-induced gamma emission (PIGE).[66] The depth profiles of light elements are evaluated with the elastic recoil detection technique (ERD) and the forward angle scattering technique (FAST) reveals information on the quantitative analysis of hydrogen. Scanning transmission ion microscopy (STIM)[67] is used to study local density variations in particles analysed by a proton microbeam.

In some microanalytical research groups such as the Microanalysis Research Centre in Melbourne, Australia, and in the Institute for Reference Materials and Measurements (IRMM) in Geel, Belgium, a new way of data acquisition and processing, named total quantitative scanning analysis (TSQA),[68] has been performed. In this system, all the incoming data are recorded in the original time sequence of events for simultaneous or later analysis, without any restriction on the amount of data taken up due to predefined energy regions. Next the data from each detector are sorted into a three-dimensional block, which can be cut and processed by the computer to obtain all information available for each technique described above. More information on data handling in SPM experiments can be found elsewhere.[11,69,70]

Applications

The use of focused MeV ion microprobes in material sciences, biology, archaeology and geology has increased rapidly during the last decade. Environmental SPM applications concerning individual particle analysis are still limited. Artaxo and co-workers[11,71,72] showed (using the SPM facilities at Oxford) the possibility of obtaining a better source apportionment and more clarity in atmospheric processes by performing single particle analysis, instead of bulk analysis, using SPM in combination with automated EPXMA and LAMMA. The aerosol particles were collected at the Brazilian Antarctic Station and at several biomass burning sites in the Amazon

region. Stoichiometric information on the different aerosol compounds is provided by RBS mapping of C, N and O simultaneously with elemental mapping for the trace elements.

Injuk and co-workers[73,74] studied the composition of giant North Sea aerosol particles on the SPM unit of IRMM in Belgium and that at the Lund Institute of Technology in Sweden. Major, minor and trace elements were determined by micro-PIXE and the quantitative evaluation of the acquired spectra revealed elemental compositions down to absolute masses of 50 fg for some metals. The heterogeneity of the individual giant particles, composed of agglomerates of several large particles, could be visualized by elemental maps.

The spatial distribution of trace elements in individual coal fly ash particles was investigated by Jakšić *et al.*[75] using the Oxford SPM. By performing simultaneously PIXE and RBS analyses, minor and trace elements could be detected and the matrix composition and target thickness could be assessed. In addition to areal maps radial line scans were also examined, which occasionally revealed trace element enrichment at the particle surface. The analysis of the aluminosilicate fly ash fraction was found to be very complex owing to the inhomogeneity of most of the analysed particles.

To acquire a better understanding of particle formation on coal combustion and of the collection mechanism during the precipitation, fly ash particles (diameters about 1 μm), collected at the inlet and outlet ports of the electrostatic precipitator of a coal-fired power station, were analysed using the Oxford SPM system by Caridi *et al.*[76] The particle composition was obtained after quantization of the simultaneously collected PIXE and RBS spectra. The different number of particle types determined in the inlet and outlet aerosol samples suggests the importance of the chemical composition effect on the electrostatic precipitation.

Recently, the influence of variations in areal density on the analysis results for individual particles by micro-PIXE was investigated by comparing the theoretically obtained X-ray yield maps from spherical fly ash particles with the experimental PIXE and STIM intensity maps.[77] For irregularly shaped fly ash particles, comparison with the theoretical X-ray yields seemed to be more difficult. STIM analysis of individual particles resulted in a better understanding of the micro-PIXE elemental intensity images. The only main qualitative information needed for the correct data interpretation are the particle shape and density distribution. When the density distribution is obtained by energy loss, the conversion from PIXE intensity maps into maps of concentration distributions is possible if local variations in areal density are known and a background reduction is performed.

Laser Microprobe Mass Spectrometry

The laser microprobe technique is referred to by various acronyms such as LAMMA (laser microprobe mass analysis) and LIMA (laser ionization mass analysis)), both of which are registed trademarks, LAMMS (laser microprobe mass spectrometry), LIMS (laser-induced mass spectrometry) or LMMS (laser microprobe mass spectrometry). Here the last notation is used in combination with TOF (time-of-flight) or FT (Fourier transform), which indicates the type of mass spectrometer used. Sometimes other mass spectrometers are used[78] but these will not be discussed further, as no applications to environmental particles have been reported.

Time-of-flight Laser Microprobe Mass Spectrometry

Instrumentation

In laser microprobe mass spectrometry, a high power density pulsed laser beam is used to evaporate and ionize a small area of the sample. The ionized part of the evaporated material consists of positive and negative elemental and molecular ions. The TOF mass spectrometer separates the ions with different mass-to-charge (m/z) ratios according to their flight times.[79] Depending on the polarity of the electric field, either positive or negative ions are recorded. More details of TOF-MS are given by Cotter.[79] Commercial TOF-LMMS achieves a mass resolution which decreases from 850 in the low-m/z range (m/z 208) to a unit mass separation around m/z 500.[80–82]

To overcome some of the limitations of the commercially available laser microprobe, the original LAMMA concept has recently been redesigned. The applications of resonant positioning has led to improvements in the mass resolution and the sensitivity and to a linear detection response over more orders of magnitude.[83,84]

For the processing of enormous amounts of individual particle spectra, computer-aided methods are recommended. Two different approaches have been published, namely pattern recognition[85,86] and library search.[87,88]

Applications

The compositions of some background aerosols have been defined by analysing remote aerosol particles collected at King George Island, Antarctica, and in the Amazon Basin. As sampling at Antarctica took place in a coastal environment, sea salt and transformed sea salt are the most abundant particle types. The remainder of the aerosols consists of sulfate-rich, aluminosilicate, iron-rich, organic, potassium-rich and zinc-rich particles. The sulfate-rich particles are most likely highly transformed sea salt whereas the aluminosilicates and iron-rich particles seem to be earth crustal dust. Potassium-rich and zinc-rich particles have a very low abundance (less than 1%) and might be derived from local contamination. Typical ions found in LMMS spectra of marine aerosols in less remote regions (*e.g.*, ammonium, nitrate and some trace element ions), are not detected in coastal Antarctic aerosols.[89] Aerosols from the Amazon Basin were analysed with EPXMA, LMMS and PIXE. EPXMA showed three major sources of aerosol particles: biogenic fraction, soil dust and sea salt particles. LMMS was used for further characterization of the biogenic fraction. In this fraction, potassium- and phosphorus-rich particles are the most abundant group. Spectra with a large number of mass peaks have also been reported, but these spectra are so complex that interpretation is not possible.[11]

An aircraft was used to collect samples at different heights above the North Sea. By LMMS analysis the aerosols could be defined into various well-separated particle types. Many of these particles appeared to occur as internal mixtures. Source identification was possible by interpreting the particle type abundances as a function of wind direction and particle size. Apart from a decrease in relative sea salt concentration above the inversion layer, no pronounced differences could be found in particle abundances as a function of height.[90]

Aerosols collected in the city of Santiago de Chile were analysed with bulk X-ray analysis, EPXMA and LMMS. EPXMA results show that soil dust and marine aerosols are the major particle types. LMMS results indicate that sea spray is transported into the city airshed, suffering several transformations and a sulfur enrichment. It also gives an indication of the abundance of carbon-rich particles, probably formed during fossil-fuel combustion, which cannot be detected by either bulk or single-particle X-ray analysis.[17]

The health hazards arising from coal mine dust are thought to depend mainly upon the quartz content of such materials. From a toxicological point of view, however, the detection of

potentially active particles or particle surfaces is much more relevant than the analysis of the total composition of the material. Tourmann and Kaufmann[91,92] used LMSS to reveal the heterogeneous distribution of potentially toxic constituents such as silica or siderite. A set of three quartz-rich coal mine dusts exhibiting significant differences in their toxicity but no correlations with conventional data have been investigated. LMMS provides, in contrast to bulk analysis, data that are in agreement with the toxicological information.[91–93]

The iron and steel industry is a major source of dust emissions that contain metal oxides. The toxicity of these metals sometimes depends on their oxidation state. LMMS is used to determine the chromium valency in particles emitted as dust by the steel industry. The oxidation of chromium depends on the particle size and the over-all composition of the particle. Small particles (diameter less than 1.1 μm) are basically composed of potassium and sodium matrices and contain hexavalent chromium, whereas large particles (diameter greater than 6 μm) are mainly calcium rich and contain trivalent chromium.[93,94]

Lead-containing aerosols collected near the city of Antwerp, Belgium, were analysed using LMMS and EPXMA. In this study, LMMS was used for further examination of the lead sulfate particles. An ammonium sulfate coating was found on all of these lead sulfate particles.[19] Lead was also detected in aerosols collected in a city and near a highway in The Netherlands.[95] Most of these particles were found to be a mixture of ammonium nitrate and ammonium sulfate and they had a variable content of metals (especially vanadium and lead).

On-line Laser Microprobe Mass Spectrometry

Instrumentation

In on-line laser microprobe mass spectrometry (on-line LMMS) or rapid single-particle mass spectrometry (RSMS), the size and chemical composition of individual particles are analysed *in situ* on a continuous and real-time basis. Different experimental set-ups have been reported,[96–103] all based on the same principle of laser desorption/ionization and analysis using mass spectrometry. Aerosols are sampled directly into the mass spectrometer through a nozzle. The resulting aerosol beam intercepts with a helium–neon laser beam. The scattered radiation from each particle can be measured to give an indication of the particle size. Additionally, the scattered signal triggers an excimer laser that vaporizes the particle and ionizes the fragments. A complete mass spectrum of the particle is subsequently recorded with a TOF mass spectrometer. Each mass spectrum corresponds to a single particle ablated by a single laser pulse.

This analytical method preserves the characteristics of the sample in two important ways. First, sample contamination and/or decomposition are reduced because of the elimination of sample–surface interactions. Second, a decrease in volatile component losses is accomplished because the particles spend less than 1 ms under vacuum conditions before ionization.[98] The analytical performances of on-line LMMS are comparable to those of TOF-LMMS.[102] The capability of this technique could be greatly improved by increased mass resolution,[98] better stray light rejection[98] and expansion of the data storage capacity.[102]

Applications

The first tests of on-line TOF-LMMS on artificially generated aerosols were reported by McKeown *et al.*[98] and Kievit *et al.*[99] By using oleic acid particles and different salt mixtures, McKeown *et al.*[98] concluded that the spectra were similar to those obtained by conventional LMMS but that a significant time shift of the ion peaks may be observed, depending upon the source configuration. Kievit *et al.*[99] compared the spectra of sodium chloride from on-line and conventional LMMS and found two extra peaks in the on-line spectrum. These probably represented hydrated sodium ions. This can be justified when the droplets from the nebulizer are not completely dried before entering the mass spectrometer. The water that is still present in the particles will flash freeze and inhibit the evaporation of the aerosols.

Mansoori *et al.*[102] used single glycerol droplets containing several dissolved metal salts and droplets containing sodium chloride to evaluate the accuracy and precision of on-line LMMS. The liquid solvent provides a reproducible local environment around the analyte and the droplet morphology is well defined. Therefore, preparation of calibration standards is straightfoward and absolute calibration can be achieved without an internal standard. A high precision can be obtained by spectral averaging over more particles. This, unfortunately, is not possible with an inhomogeneous particle mass. Nevertheless, with a mixed aerosol mass containing distinct groups of chemically and morphologically comparable particles,[104,105] it should be possible to average the spectra within one group. It was also noticed that, to a first approximation, the signal intensity of the atomic metal ion in the mass spectrum is independent of the presence of other ions in solution. Hence on-line LMMS could become a general method for determining ionic components in aerosol droplets. The results obtained with these glycerol droplets show that on-line laser desorption/ionization is capable of making quantitative measurements at concentration levels typically present in atmospheric aerosols.

Carson *et al.*[103] reported the application of RSMS for the speciation of semi-volatile and non-volatile sulfur compounds, the measurement of isotopic ratios and the detection of thin coatings on particles produced by condensation of reactive gases.

Fourier Transform Laser Microprobe Mass Spectrometry

Instrumentation

Although laser ionization offers unique possibilities for the analysis of organic ions, LMMS has been used mainly for the determination of elements. The determination of these organic compounds is largely restricted by the limited mass resolution of the TOF mass spectrometer.[81] Recently, LMMS has been adapted with a Fourier transform (FT) ion cyclotron resonance (ICR) mass spectrometer, which has a high resolving power and high mass accuracy. Several research groups have been working on this concept, resulting in completely different set-ups.[106–109] The ionization of the sample can take place in the ICR cell or in an external ion source, whereafter the ions are transferred to the cell for detection. In the ICR spectrometer, ions are brought into resonance with the frequency of an oscillating field, they then pick up energy and become coherent ion packets, which can be detected. Fourier transformation of the time-dependent signals result in a frequency spectrum that can be scaled into an m/z spectrum by calibration.[109] Marshall and Verdun[110] gave an excellent description of the principles of FTMS.

FT-LMMS with external ion source has comparable analytical performance to TOF-LMMS.[109] FT-LMMS allows the routine achievement of mass resolutions exceeding 10^6 below m/z 100 and 10^5 at m/z 1000 and gives an accuracy of m/z determination of approximately 1 ppm. This results in an increased specificity of the given signal by several orders of magnitude. The detection limit for elemental ions is about 10^8 atoms within the evaporated microvolume, but the minimum

spatial resolution is 5 μm instead of 1 μm for TOF-LMMS.[82,109]

Applications

FT-LMMS has only been available for a few years, and no papers on research on environmental particles using FT-LMMS could be found in the literature. Still, this technique is mentioned because in the near future the first tests on giant aerosols will be performed at the University of Antwerp and the expectations for analyses for especially organic compounds are high.

Secondary-ion Mass Spectrometry

Instrumentation

Secondary-ion mass spectrometry (SIMS) is based on the bombardment of a sample surface by a primary-ion beam. A small fraction of the sputtered atoms are charged. These secondary ions are analysed in a mass spectrometer. Two types of mass spectrometers are available, one based on electric/magnetic deflection fields and another on the quadrupole/time-of-flight principle. The first has a better mass resolution, but is more expensive and has a longer recording time. A detailed description of the theoretical aspects of SIMS was given by Benninghoven *et al.*[111] and Wilson *et al.*[112] gave a more practical overview of the SIMS technique.

As the analysed surface is sputtered away, observation of the distribution of the constituents with depth in a particle and the compositional heterogeneities within a particle are possible. The depth resolution of SIMS is about 1–2 nm. Other important advantages for single-particle analysis are the capability for the detection of all elements, fingerprinting of compounds, isotope ratio measurements and component imaging.[113]

Applications

Goschnick *et al.*[114] analysed sub-micrometre aerosol particles collected near a busy highway in Karlsruhe, Germany, with a combination of SIMS and secondary netural mass spectrometry (SNMS). Depth-resolved analysis revealed that most of the collected particles have an inorganic core which is coated with a 200 nm organic layer. The major component in the core is ammonium sulfate formed by reaction of ammonia with sulfuric acid in the atmosphere. The aromatic organic coating is probably formed by agglomeration of soot from car exhaust emissions onto the surface of the particles. Depth profiling on test salt samples that occur frequently in environmental materials (*e.g.*, chlorides, carbonates, nitrates and sulfates) has also been reported.[115]

Another study on urban aerosols was carried out by Van Grieken *et al.*[116] In this study, aerosols with a mean diameter of 5 μm were collected near the city of Antwerp, Belgium, and analysed with a caesium primary-ion beam. Depth profiles showed that the majority of the analysed aluminosilicates have a vanadium and chromium coating that is probably due to adsorption. This heavy metal coating suggests that these aluminosilicates are fly ash particles.

Chrysotile asbestos fibres coated with titanium chloride were also examined by SIMS[63] after analysis with EELS. On the Ti and TiO images, it can be seen that Ti has reacted fairly uniformly over the selected area of the chrysotile surface. The absence of titanium chloride ions is another indication of a full reaction of the titanium chloride with the chrysotile structure. Microstructures on the fibres cannot be seen with the caesium primary-ion beam used, as the resolution is about ten times the dimension of these microstructures.

By using a gallium focused ion beam (Ga-FIB), which has a better spatial resolution (beam diameter of less than 0.1 μm) than the oxygen and caesium types, analysis of sub-micrometre particles is possible. Nihei *et al.*[117] reported the analysis of fine particles in a thin-film multi-layer device and of a silicon oxide microcapsule filled with titanium oxide. No analyses of environmental particles with the Ga-FIB have been reported, but applciations in this domain will follow in the near future.[118]

Fourier Transform Infrared Spectrometry

Instrumentation

Infrared spectrometry is a very precise and specific method that has been used over several decades for the identification, characterization and quantification of various materials. The analyses are limited to compounds in which the dipole momentum changes during a normal molecular vibration or molecular rotation. Most of the problems involved with this technique were solved in the 1960s, owing to the development of FTIR spectrometry. FTIR spectrometers consist basically of a polychromatic IR radiation source, an interferometer, a sample compartment and a detector. In recent years some advanced components such as the helium–neon laser, pyroelectric detectors (TGS) and microcomputers were introduced to improve the quality of the measurements. To acquire chemical information on the sample composition, a background spectrum, which presents the IR radiation source characteristics, is subtracted from the spectrum obtained from the absorbing sample. Spectral analysis is performed by the Cooley–Tuckey fast Fourier transform algorithm. Coupling of FTIR spectrometry to other analytical techniques such as gas chromatography, high-performance liquid chromatography and thermogravimetric analysis provides information only on the bulk sample composition. FTIR microscopy, on the other hand, offers the possibility of analysing, in the reflection or transmission mode, individual particles with diameters >5 μm. Smaller particles can only be analysed as particle clusters. To isolate the areas of the sample of interest, knife-blade apertures are used. This image masking technique on the FTIR microscope is both quick and accurate. More information on FTIR microscopy can be found elsewhere.[119,120]

Applications

To our knowledge, no new publications have appeared on the topic of individual particle analysis with FTIR spectrometry since the review by Xhoffer *et al.*[4] The most recent results were published by Dangler *et al.*[121] and Kellner and Malissa,[122] who claimed that the FTIR technique can be used successfully to study single aerosol particles owing to three major advantages: (1) the amount of sample needed is very small, (2) sample dilution is unnecessary and (3) direct analysis of the aerosol particles as deposited on the impactor surface stage is possible.

In 1993, an evaluation of the possibilities of applying micro-FTIR spectrometry to giant marine aerosol particles, in combination with EPXMA, was carried out at MiTAC.[123] The first results were not very promising. Most of the particles were inorganic salts, which absorb only partly in the mid-IR region, and the percentage of organic material in the collected giant aerosol particles was very low. In addition, most marine particles are mixtures of several compounds. These mixtures led to strongly overlapping peaks in the spectra, which complicate spectral interpretation. Analysis of these particles in the far-IR region would probably improve spectral interpretation. In this region it is impossible, however, to analyse

individual micrometre-sized particles. Moreover, the additional information obtained by EPXMA is limited to elements with $z > 11$. Probably it will be more promising in the future to study particles with higher contents of organic material and to compare the results of analysis by micro-FTIR spectrometry with those obtained with a windowless JEOL 6300 scanning electron microscope.

Other Microanalytical Techniques

Although several other microanalytical beam techniques exist that are used in various research fields, their application to environmental particle samples is still scarce or non-existent. This includes scanning Auger microscopy (SAM) and X-ray photoelectron spectroscopy (XPS or ESCA).

SAM is difficult to use for the analysis of environmental particles. The major problems are the charging of non-conductive particles, which most environmental particles are, and the low detection power of the technique. SAM is a surface-sensitive technique and would be very useful in the analysis of coatings on the particles; however, the charging effect makes its use very limited. Another drawback is the particularly low sensitivity to high-Z elements. From the environmental and toxicological point of view, coatings with high-Z elements, and in particular heavy metals, are more important. This all indicates that SAM cannot be used very advantageously for most environmental analyses.

XPS is, like SAM, a surface-sensitive technique, but can be applied also to heavy metal coatings. At the moment, most environmental applications found in the literature are restricted to bulk analysis. The reason for this is the spatial resolution, which approaches 10 μm. Considerable improvements in the spatial resolution and the sensitivity of XPS are expected in the near future. Single-particle analysis in the environmental research area will become one of the new applications of XPS.

Micro-Raman spectroscopy is a very slow analytical method with great potential for the analysis of environmental particles. As the technique and its possibilities are largely unknown to environmental researchers, only a few applications have been reported.[3,94] The principle of this technique can be found in earlier reviews.[3,4]

Secondary neutral mass spectrometry (SNMS) has been discussed for environmental applications in combination with SIMS.[114,115]

This work was partially prepared in the framework of the Impulse Programme in Marine Sciences, supported by the Belgian State–Prime Minister's Service–Science Policy Office (contract MS/06/050). L. D. B. acknowledges the Instituut tot Aanmoediging van het Wetenschappelijk Onderzoek in Nijverheid en Landbouw (IWONL) for financial support.

References

1 Grasserbauer, M., *Mikrochim. Acta*, **Part III**, 1983, 415.
2 Van Grieken, R., Artaxo, P., Bernard, P., Leysen, L., Otten, P., Storms, H., Van Put, A., Wouters, L., and Xhoffer, C., *Chem. Anal.* (Warsaw), 1990, **35**, 75.
3 Van Grieken, R., and Xhoffer, C., *J. Anal. At. Spectrom.*, 1992, **7**, 81.
4 Xhoffer, C., Wouters, L., Artaxo, P., Van Put, A., and Van Grieken, R., in *Environmental Particles*, ed. Buffle, J., and Van Leeuwen, H. P., Lewis, Chelsea, MI, 1992, vol. 1, pp. 107–143.
5 Cowley, J. M., in *Principle of Analytical Electron Microscopy*, ed. Joy, D. C., Romig, A. D., Jr., and Goldstein, J. I., Plenum Press, New York, 1986, pp. 77–122.
6 Reimer, L., in *Scanning Electron Microscopy*, ed. Hawkes, P. W., Springer, Berlin, 1985.
7 Goldstein, J. I., Newbury, D. E., Echlin, P., Joy, D. C., Romig, A. D., Jr., Lyman, C. E., Fiori, C., and Lifshin, E., *Scanning Electron Microscopy and X-Ray Microanalysis*, Plenum Press, New York, 1992.
8 Bernard, P. C., Van Grieken, R. E., and Eisma, D., *Environ. Sci. Technol.*, 1986, **20**, 467.
9 Artaxo, P., Rabello, M. L. C., Maenhaut, W., and Van Grieken, R., *Tellus*, 1992, **44B**, 318.
10 Van Grieken, R. E., Artaxo, P., and Xhoffer, C., in *Proceedings of the 50th Annual Meeting of the Electron Microscopy Society of America*, ed. Bailey, G. W., Bentley, J., and Small, J. A., San Francisco Press, San Francisco, 1992, pp. 1482–1483.
11 Artaxo, P., Van Grieken, R., Watt, F., and Jakšić, M., in *Proceedings of the Second World Congress on Particle Technology*, Society of Powder Technology, Kyoto, 1990, pp. 421–426.
12 Van Malderen, H., and Van Grieken, R., *Ocean Atmos. Opt.*, in the press.
13 Sándor, S., Török, S., Xhoffer, C., and Van Grieken, R., in *Proceedings of the Twelfth International Congress on Electron Microscopy*, ed. Peachy, L. D., and Williams, P. B., San Francisco Press, San Francisco, 1990, pp. 245–255.
14 Török, Sz., Sándor, Sz., Xhoffer, C., Van Grieken, R., Mészáros, E., and Molnar, A., *Idojaras*, 1993, **96**, 223.
15 Begét, E. J., Keskinen, M., and Severin, K., *Sediment. Geol.*, 1993, **84**, 189.
16 Parungo, F., Kopcewicz, B., Nagamoto, C., Schnell, R., Sheridan, P., Zhu, C., and Harris, J., *J. Geophys. Res.*, 1992, **97**, 15867.
17 Rojas, C. M., Artaxo, P., and Van Grieken, R., *Atmos. Environ.*, 1990, **24B**, 227.
18 Eltayeb, M. A. H., Xhoffer, C. F., Van Espen, P. J., and Van Grieken, R. E., *Atmos. Environ.*, 1993, **27B**, 67.
19 Van Borm, W., Wouters, L., Van Grieken, R., and Adams, F., *Sci. Total Environ.*, 1990, **90**, 55.
20 Hunt, A., Johnson, D. L., Thornton, I., and Watt, J. M., *Sci. Total Environ.*, 1993, **138**, 183.
21 Hunt, A., Johnson, D. L., Watt, J. M., and Thornton, I., *Environ. Sci. Technol.*, 1992, **26**, 1513.
22 Qian, G.-W., and Ishizaka, Y., *J. Geophys. Res. Oceans*, 1993, **98**, 8459.
23 Pardess, D., Levin, Z., and Ganor, E., *Atmos. Environ.*, 1992, **26A**, 675.
24 Van Malderen, H., De Bock, L., Injuk, I., Xhoffer, C., and Van Grieken, R., in *Progress in Belgian Oceanographic Research*, Royal Academy of Belgium, Brussels, 1993, pp. 119–135.
25 Xhoffer, C., Bernard, P., and Van Grieken, R., *Environ. Sci. Technol.*, 1991, **25**, 1470.
26 Xhoffer, C., Wouters, L., and Van Grieken, R., *Environ. Sci. Technol.*, 1992, **26**, 2151.
27 Rojas, C. M., and Van Grieken, R., *Atmos. Environ.*, 1992, **26A**, 1231.
28 Jaenicke, R., *Ann. N.Y. Acad. Sci.*, 1980, **338**, 317.
29 Jaenicke, R., in *Chemistry of the Unpolluted and Polluted Troposphere*, ed. Georgii, W., and Jaeschke, W., Reidel, Dordrecht, 1st edn., 1982, pp. 341–374.
30 Dedeurwaerder, H. L., *PhD Thesis*, Free University of Brussels, 1988.
31 Van Malderen, H., Rojas, C., and Van Grieken, R., *Environ. Sci. Technol.*, 1992, **26**, 750.
32 De Bock, L. A., Van Malderen, H., and Van Grieken, R., *Environ. Sci. Technol.*, 1994, **28**, 1513.
33 Johnson, D. L., Jiao, J., DosSantos, S. G., and Effler, S. W., *Environ. Sci. Technol.*, 1991, **25**, 736.
34 Lavoie, D. M., *Deep-Sea Res.*, 1992, **39**, 1655.
35 Eisma, D., Van Put, A., and Van Grieken, R., *Mitt. Geol.-Paläont. Inst. Univ. Hamburg*, 1992, **70**, 137.
36 Eisma, D., Kalf, J., Karmini, M., Mook, W. G., Van Put, A., Bernard, P., and Van Grieken, R., *Neth. J. Sea Res.*, 1989, **24**, 383.
37 Van Put, A., Eisma, D., and Van Grieken, R., unpublished work.
38 Eisma, D., in *Facets of Modern Biogeochemistry*, ed. Ittekkot, V., Kempe, S., Michaelis, W., and Spitzy, A., Springer, Heidelberg, 1990, pp. 127–146.

39 Hart, B. T., Douglas, G. B., Beckett, R., Van Put, A., and Van Grieken, R. E., *Hydrol. Proc.*, 1993, **7**, 105.
40 Van Put, A., Van Grieken, R., Wilken, R.-D., and Hudec, B., *Water Res.*, 1994, **28**, 643.
41 Belmans, F., Van Grieken, R., and Brügmann, L., *Mar. Chem.*, 1993, **42**, 223.
42 Bernard, P. C., Van Grieken, R. E., and Brügmann, L., *Mar. Chem.*, 1989, **26**, 155.
43 Stroobants, N., Dehairs, F., Goeyens, L., Vanderheijden, N., and Van Grieken, R., *Mar. Chem.*, 1991, **35**, 411.
44 Tucan, A., and Pamukcu, S., in *Proceedings of the Mediterranean Conference on Environmental Geotechnology*, ed. Usmen and Acer, Balkema, Rotterdam, 1992, pp. 109–121.
45 Tipping, E., Woof, C., and Clarke, K., *Hydrol. Proc.*, 1993, **7**, 263.
46 Oades, J. M., and Waters, A. G., *Aust. J. Soil Res.*, 1991, **29**, 815.
47 Reimer, L., *Transmission Electron Microscopy: Physics of Image Formation and Microanalysis*, Springer, Berlin, 2nd edn., 1989.
48 *Principles of Analytical Electron Microscopy*, ed. Joy, D. C., Roming, A. D., Jr., and Goldstein, J. I., Plenum Press, New York, 1986.
49 Leppard, G. G., in *Environmental Particles*, ed. Buffle, J., and Van Leeuwen, H. P., Lewis, Chelsea MI, 1992, vol. 1, pp. 231–289.
50 Perret, D., Leppard, G. G., Müller, M., Belzile, N., De Vitre, R., and Buffle, J., *Water Res.*, 1991, **25**, 1333.
51 Fortin, D., Leppard, G. G., and Tessier, A., *Geochim. Cosmochim. Acta*, 1993, **57**, 4391.
52 Leppard, G. G., Burnison, B. K., and Buffle, J., *Anal. Chim. Acta*, 1990, **232**, 107.
53 Jambers, W., unpublished work.
54 De Bock, L. A., and Van Grieken, R. E., unpublished work.
55 Van Puymbroeck, J., Van Espen, P., and Jacob, W., *Micron Microsc. Acta*, 1989, **20**, 155.
56 Van Puymbroeck, J., *PhD Thesis*, University of Antwerp, 1992.
57 Egerton, R. F., *Electron Energy Loss Spectrometry in the Electron Microscope*, Plenum Press, New York, 1986.
58 Jeanguillaume, C., Tencé, M., Trebbia, P., and Colliex, C., *Scanning Electron Microsc.*, 1983, **11**, 745.
59 Maynard, A. D., and Brown, L. M., *J. Aerosol Sci.*, 1992, **23**, S433.
60 Xhoffer, C., *PhD Thesis*, University of Antwerp, 1993, pp. 189–204.
61 Xhoffer, C., *PhD Thesis*, University of Antwerp, 1993, pp. 205–233.
62 Katrinak, K. A., Rez, P., and Buseck, P. R., *Environ. Sci. Technol.*, 1992, **26**, 1967.
63 Berghmans, P., Injuk, J., Van Grieken, R., and Adams, F., *Anal. Chim. Acta*, 1994, **297**, 27.
64 Johansson, S. A. E., and Campbell, J. L., *PIXE—A Novel Technique for Elemental Analysis*, Wiley, New York, 1988.
65 Finstad, T. G., and Chu, W. K., in *Analytical Techniques for Thin Films*, ed. Tu, K. N., and Rosenberg, R., Academic Press, Boston, 1988, pp. 391–447.
66 Bird, J. R., in *Ion Beams for Material Analysis*, ed. Williams, J. S., Academic Press, Sydney, 1989.
67 Lefevre, H. W., Schofield, R. M. S., Overley, J. C., and MacDonald, J. D., *Scanning Microsc.*, 1987, **1**, 879.
68 Legge, G. J. F., and Hammond, I., *J. Microsc.*, 1979, **117**, 201.
69 Legge, G. J. F., in *Ion Beams for Material Analysis*, ed. Williams, J. S., and Bird, J. R., Academic Press, Sydney, 1989, pp. 445–513.
70 Lövenstam, N. E. G., and Swietlicki, E., *Scanning Microsc.*, 1992, **6**, 607.
71 Artaxo, P., Rabello, M. L. C., Watt, F., Grime, G., and Swietlicki, E., *Nucl. Instrum. Methods B*, 1993, **75**, 521.
72 Artaxo, P., Rabello, M. L. C., Watt, F., Grime, G., Swietlicki, E., Knox, J., and Hansson, H.-C., *J. Aerosol Sci.*, 1992, **23**, 373.
73 Injuk, J., Van Malderen, H., Van Grieken, R., Swietlicki, E., Knox, J. M., and Schofield, R., *X-Ray Spectrometry*, 1993, **22**, 220.
74 Injuk, J., Breitenbach, L., Van Grieken, R., and Wätjen, U., *Mikrochim. Acta*, 1994, **114/115**, 313.
75 Jakšić, M., Watt, F., and Grime, G. W., *Nucl. Instrum. Methods B*, 1991, **56/57**, 699.
76 Caridi, A., Cerede, E., Grime, G. W., Jakšić, M., Braga Marcazzan, G. M., Valković, V., and Watt, F., *Nucl. Instrum. Methods B*, 1993, **77**, 524.
77 Bogdanović, I., Fazinić, S., Jakšić, M., Grime, G. W., and Valković, V., *Nucl. Instrum. Methods B*, 1994, **85**, 732.
78 Davis, R., and Frearson, M., *Mass Spectrometry*, ed. Prichard, F. E., Wiley, Chichester, 1987.
79 Cotter, R. J., *Biomed. Environ. Mass Spectrom.*, 1989, **18**, 512.
80 Kaufmann, R., in *Microbeam Analysis 1982*, ed. Heinrich, K. F. J., San Francisco Press, San Francisco, 1982, pp. 341–358.
81 Van Vaeck, L., Van Roy, W., Gijbels, R., and Adams, F., in *Laser Ionization Mass Analysis*, ed. Vertes, A., Gijbels, R., and Adams, F., Wiley, Chichester, 1993, pp. 7–126.
82 Eeckhaoudt, S., Gijbels, R., and Van Grieken, R., *Scanning Microsc.*, in the press.
83 Kaufmann, R., and Spengler, B., in *Proceedings of the 50th Annual Meeting of the Electron Microscopy Society of America*, ed. Bailey, G. W., Bentley, J., and Small, J. A., San Francisco Press, San Francisco, 1992, pp. 1558–1559.
84 Kaufmann, R., and Spengler, B., in *Proceedings of the 50th Annual Meeting of the Electron Microscopy Society of America*, ed. Bailey, G. W., Bentley, J., and Small, J. A., San Francisco Press, San Francisco, 1992, pp. 1598–1599.
85 Harrington, P., Street, T., Voorhees, K., Radicati di Brozolo, F., and Odom, R. W., *Anal. Chem.*, 1989, **61**, 715.
86 Lindner, B., and Seydel, U., in *Microbeam Analysis 1989*, ed. Russell, P. E., San Francisco Press, San Francisco, 1989, pp. 286–292.
87 Wouters, L., *PhD Thesis*, University of Antwerp, 1991, sect. 5.1–5.12.
88 Wouters, L., Michaud, D., and Van Grieken, R., *Mikrochim. Acta*, 1993, **110**, 31.
89 Wouters, L., Artaxo, P., and Van Grieken, R., *Int. J. Environ. Anal. Chem.*, 1990, **38**, 427.
90 Dierck, I., Michaud, D., Wouters, L., and Van Grieken, R., *Environ. Sci. Technol.*, 1992, **26**, 802.
91 Tourmann, J. L., and Kaufmann, R., *Int. J. Environ. Anal. Chem.*, 1993, **52**, 215.
92 Tourmann, J. L., and Kaufmann, R., *Analusis*, 1992, **20**, 65S.
93 Poitevin, E., Krier, G., and Muller, J. F., and Kaufmann, R., *Analusis*, 1992, **20**, M36.
94 Hachimi, A., Poitevin, E., Krier, G., Muller, J. F., Pironon, J., and Klein, F., *Analusis*, 1993, **21**, 77.
95 Wonders, J. H. A. M., Houweling, S., De Bont, F. A. J., Van Leeuwen, H. P., Eeckhaoudt, S. E., and Van Grieken, R. E., *Int. J. Environ. Anal. Chem.*, 1994, **56**, 193.
96 Sinha, M. P., *Rev. Sci. Instrum.*, 1984, **55**, 886.
97 Marijnissen, J., Scarlett, B., and Verheijen, P., *J. Aerosol Sci.*, 1988, **19**, 1307.
98 McKeown, P. J., Johnston, M. V., and Murphy, D. M., *Anal. Chem.*, 1991, **63**, 2069.
99 Kievit, O., Marijnissen, J. C. M., Verheijen, P. J. T., and Scarlett, B., *J. Aerosol Sci.*, 1992, **23**, S301.
100 Thomson, D. S., and Murphy, D. M., *Appl. Opt.*, 1993, **32**, 6818.
101 Murray, K. K., and Russel, D. H., *J. Am. Soc. Mass Spectrom.*, 1994, **5**, 1.
102 Mansoori, B. A., Johnston, M. V., and Wexler, A. S., *Anal. Chem.*, 1994, **66**, 3681.
103 Carson, P. G., Neubauer, K. R., Johnston, M. V., and Wexler, A. S., *J. Aerosol Sci.*, submitted for publication.
104 Ro, C.-U., Musselman, I. H., and Linton, R. W., *Anal. Chim. Acta*, 1991, **243**, 139.
105 Shattuck, T. W., Germani, M. S., and Buseck, P. R., *Anal. Chem.*, 1991, **63**, 2646.
106 Brenna, J. T., Creasy, W. R., McBain, W., and Soria, C., *Rev. Sci. Instrum.*, 1988, **59**, 873.
107 Brenna, J. T., in *Microbeam Analysis 1989*, ed. Russel, P. E., San Francisco Press, San Francisco, 1989, pp. 306–310.
108 Muller, J. F., Pelletier, M., Krier, G., Weil, D., and Campana, J., in *Microbeam Analysis 1989*, ed. Russel, P. E., San Francisco Press, San Francisco, 1989, pp. 311–316.
109 Van Vaeck, L., Van Roy, W., Struyf, H., Adams, F., and Caravatti, P., *Rapid Commun. Mass Spectrom.*, 1993, **7**, 323.
110 Marshall, A. G., and Verdun, F. R., *Fourier Transform in NMR, Optical and Mass Spectrometry*, Elsevier, Amsterdam, 1990, pp. 225–278.

111 Benninghoven, A., Rüdenauer, F. G., and Werner, H. W., *Secondary Ion Mass Spectrometry: Basic Concept, Instrumental Aspects, Applications and Trends*, Wiley, New York, 1987.
112 Wilson, R. G., Stevie, F. A., and Magee, C. W., *Secondary Ion Mass Spectrometry*, Wiley, New York, 1987.
113 Newbury, D. E., in *Proceedings of the Particle Analysis Session of the 13th Annual Conference of the Microbeam Analysis Society, Ann Arbor, MI, June 22, 1978, NBS Special Publication No. 533*, ed. Heinrich, K. F. J., National Bureau of Standards, Gaithersburg, MD, 1980, p. 139.
114 Goschnick, J., Fichtner, M., Lipp, M., Schuricht, J., and Ache, H. J., *Appl. Surf. Sci.*, 1993, **70/71**, 63.
115 Fichtner, M., Lipp, M., Goschnick, J., and Ache, H. J., *Surf. Interface Anal.*, 1991, **17**, 151.
116 Van Gricken, R., Injuk, J., Owari, M., and Van Espen, P., *Abstracts of the Fourth International Aerosol Conference*, ed. Flagan, R. C., American Association for Aerosol Research, 1994, vol. 1, pp. 10–11.
117 Nihei, Y., Satoh, H., Tomiyasu, B., and Owari, M., *Anal. Sci.*, 1991, **7** Suppl., 527.
118 Owari, M., personal communication.
119 Griffiths, P. R., and de Haseth, J. A., *Fourier Transform Infrared Spectrometry*, ed. Elving, P. J., Winefordner, J. D., and Kolthoff, I. M., Wiley, New York, 1986.
120 Vansant, E. F., Gillis-D'Hamers, I., Molinard, A., and Vanhoof, C., *Textbook FTIR*, Infra Red Education Centre, University of Antwerp, Antwerp, 1992.
121 Dangler, M., Bruke, S., Hering, S. V., and Allen, D. T., *Atmos. Environ.*, 1987, **21**, 1001.
122 Kellner, R., and Malissa, H., *Aerosol Sci. Technol.*, 1989, **10**, 397.
123 De Bock, L. A., and Van Grieken, R., unpublished work.

Paper 4/04936E
Received August 8, 1994
Accepted October 28, 1994

ELSEVIER

Spectrochimica Acta Part B 50 (1995) 1281–1292

SPECTROCHIMICA ACTA
PART B

Problems in quantitatively analyzing individual salt aerosol particles using electron energy loss spectroscopy

C. Xhoffer[a], W. Jacob[b], P. R. Buseck[c], R. Van Grieken[a,*]

[a]*Department of Chemistry, University of Antwerp, B-2610 Antwerp, Belgium*
[b]*Department of Medicine, University of Antwerp, B-2610 Antwerp, Belgium*
[c]*Arizona State University, Departments of Chemistry and Geology, Tempe, AZ 85287, USA*

Received 19 August 1994; accepted 17 March 1995

Abstract

Polydisperse standard aerosols of NaCl, $(NH_4)_2SO_4$ and KNO_3 have been generated from their solutions by pneumatic nebulization. These aerosol particles are electron beam sensitive and therefore special precautions are necessary. A methodology is proposed for serially recording electron energy loss spectra (EELS) from sub-micrometer salt particles. The results of quantification are compared with those obtained by parallel electron energy loss spectroscopy (PEELS).

Experimental conditions such as the intensity of the primary beam, time of radiation and temperature are responsible for large deviations from the theoretical values. These deviations arise because heavy mass losses occur, especially during the serial spectrum acquisition. The more time consuming serial EELS is therefore at a disadvantage relative to the parallel method.

The best results are obtained for NaCl because the halogen loss can be reduced more efficiently than nitrogen and oxygen losses. The results show that nitrogen loss occurs within the first few seconds of the experiment at normal radiation doses. Even at cryogenic temperatures, losses of volatile elements cannot be avoided.

Keywords: Aerosol; EELS; PEELS; sodium chloride

1. Introduction

Various electron-beam techniques such as scanning electron microscopy (SEM), (scanning) transmission electron microscopy ((S)TEM) and electron probe X-ray microanalysis (EPXMA) have proven their success in fields such as physics, biology, medicine, geology and chemistry. Also, the number of studies of environmental particles has expanded rapidly during the last 20 years. All this is mainly the result of technological advances in instrumentation and improved knowledge of electron optics and electronics. However each of the above techniques is limited by either poor resolution, detection possibilities (high detection limits, or poor low-Z elemental detection) or lack of quantization. From a theoretical viewpoint, electron energy loss spectroscopy (EELS) does not have these shortcomings.

* Corresponding author.

SSDI 0584-8547(95)01338-5

EELS utilizes changes in energy resulting from interactions between primary bombarding electrons and electrons from the sample. The signal is obtained by plotting the loss in energy of the transmitted primary electrons versus their intensity. The features observed in an energy loss spectrum are characteristic for the atoms present in the interaction volume, and the number of atoms can be deduced from the integrated intensity. For more details on EELS, the reader is referred to published books and review papers [1–3].

We report here a study of individual particles of NaCl, $(NH_4)_2SO_4$ and KNO_3 analyzed using Zeiss EM 902 and JEOL 2000 FX instruments. These aerosols can be prepared easily as standards in the laboratory. Moreover, there is clear need for low-Z element determination in environmental aerosol research. Additionally, there is a growing interest in small particles in environmental studies because these might be initiators or catalysts for secondary reactions, act as condensation nuclei and easily undergo further chemical transformation reactions. These environmental particles are mainly composed of elements such as carbon, nitrogen and oxygen, that are difficult to detect with conventional X-ray analysis techniques. Thus the high spatial resolution combined with low-Z elemental analysis should favor EELS analysis over other electron-beam techniques. However, only a few EELS publications in the broad field of aerosol research have been reported hitherto [4–7].

2. Experimental

2.1. Sample preparation

Standard test aerosols of NaCl, $(NH_4)SO_4$ and KNO_3 were generated by nebulization of their respective aqueous solutions. The generation and sampling equipment for the preparation of standard particulate salt material is shown schematically in Fig. 1. The average aerosol diameter can be controlled by either changing the concentration of the solution or by varying the collection distance above the solution [8]. To prevent the collection of droplets, the generated aerosol was passed through a diffusion dryer during the upward trajectory before impaction. Experiments showed that a reproducible aerosol particle fraction was formed from an approximately 0.1 M solution. The exhaust aerosols were collected on either 700 mesh amorphous carbon coated grids or on 400 mesh grids covered by a perforated Formvar foil and coated with a thin carbon layer. These microscope grids were mounted in a Battelle DCI-5 single-jet cascade impactor for the collection step. To preserve the grids from contamination, the impactor was placed just above the diffusion dryer and operated at a reduced input flow relative to the diffusion dryer output. This nebulizing mechanism produced polydisperse aerosols (i.e. particles with various diameters). Only the last impactor stage, with a cut-off diameter of 0.25 μm,

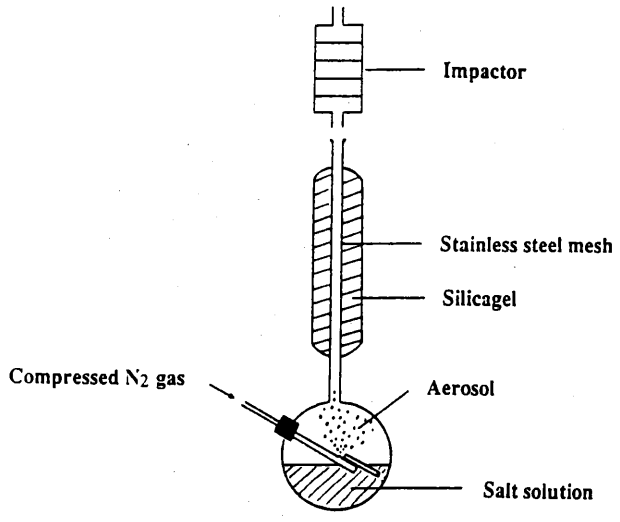

Fig. 1. Apparatus used to generate standard test aerosols.

was used for EELS analysis. This aerosol generation method allowed us to control the size of the collected particles, which was not possible by directly placing a suspension on the grid. By using this procedure, aggregation of the particles was greatly reduced, and a homogeneous distribution was obtained over the entire collection area.

2.2. Procedure

The Zeiss EM 902 (TEM) instrument uses a magnetic-prism spectrometer of the Henry-Castaing type [9,10] and collects spectra during serial scans. The acceleration voltage is limited to 80 kV. The intensity of the transmitted electron loss signal is converted into a voltage and integrated by a PREMA 4000 digital voltmeter. The digital read-out is transferred to and stored in an IBM-compatible personal computer (PC/AT) acting as a multichannel analyzer [11]. The energy loss intensity per channel is an average of three individual recordings of one second. Typical acquisition times are then of the order of 10 min for an energy span of 400 eV in steps of 2 eV. Recording times can be reduced at the expense of the statistical reliability of the data.

The JEOL 2000 FX (STEM) unit is equipped with a Gatan 666 magnetic-sector spectrometer coupled to a Kevex data storage and processing unit for parallel spectrum recording. Here an array of diodes, that are position sensitive [12–14] and placed in the dispersion plane of the analyzer, are used for single-electron counting. By using a low-noise scintillator and photomultiplier tube, shot noise that results from Poisson statistics of the arriving electrons [15] is then the main noise component in the spectrum. The microscope is operated at a 200 kV acceleration voltage because Blake et al. [16] observed that structural damage is reduced, at least in the case of fluorite (CaF_2) by using high voltages compared to lower voltages. The parallel spectra are acquired into 1024 channels, where each channel corresponds to an energy increment of 1 eV. A useful range of about 1000 eV may be achieved during one spectrum acquisition and only takes about 3 s. Thus, for comparable spectrum acquisition parameters (energy span of 2000 eV in steps of 2 eV) the parallel collection system is about 1000 times more efficient than the serial system of the Zeiss instrument. However, this factor is significantly reduced when smaller energy loss spans are of interest, as is usually the case. This efficiency factor does not affect the obtained results significantly as we will show, unless time is a critical factor in spectrum acquisition.

For both instruments, a nitrogen-cooled cold stage is used because this can reduce the rate of mass losses of certain elements under electron beam radiation [17–20]. The energy resolution in spectrum mode varies between 1.3 and 1.7 eV for both instruments as measured separately on the zero-loss signal.

2.3. Data handling

All spectra obtained with the Zeiss EM 902 are recorded at a magnification of 30 000 times. The spectrometer acceptance angle is then limited by an objective aperture of 60 μm (β = 6 mrad) and the analyzed area has a dimension of 0.26 μm. Higher magnifications reduce the transmission signal and so statistically reliable data cannot be obtained. For the JEOL 2000 FX instrument, magnifications of 30 000 to 50 000 times are used. The analyzed area is dependent on the probe size and can be reduced to 50–100 nm.

If the carbon signal from the supporting foil does not interfere with the characteristic peak positions of other elements of interest, one should analyze particles supported by the carbon foil instead of those lying over the holes. Substrate conductivity can help protect the interaction volume from radiation damage during low-temperature electron microscopy [21,22]. Therefore, analyses on the amorphous-C supporting foil were preferred because heat is more efficiently conducted away from the sample and out-diffusion of volatile species is thereby reduced [20,23,24]. The electron dose received by the specimen was calculated for the Zeiss instrument by measuring the transmitted beam current using a Faraday cup located at the screen level (this is the object plane for the spectrometer). Table 1 gives an overview of the differences between the Zeiss EM 902 and the JEOL 2000 FX instruments, together with the conditions used for recording and processing the spectra.

Table 1
Instrumental parameters and spectrum recording and processing conditions of the EEL spectra

Parameter	Zeiss EM 902	JEOL 2000 FX
Acceleration voltage/kV	50–80	80–200
Filament	W	LaB_6
Spectrometer	Prism spectrometer	Magnetic sector
Electron detector	PMT	YAG scint. + photodiode array
Spectrum recording	Serial scans	Parallel mode
E-range/eV	0–2000	0–4000
Step size/eV per channel	2	1 or 2
Acquisition time/channel	3 × 1 s	3 × 1 s
Total acquisition time	ca. 3 to 10 min	3 s
Magnification	30 000 times	30 000–80 000 times
Background fitting region (Γ)/eV	70	70
Background extrapolation (Δ)/eV	70	70
Fitting strategy	Unweighted least squares	Weighted least squares

The modelled background fit was judged visually by superimposing the fit over its experimental spectrum [1]. However, several authors have recently demonstrated that the quality of the fit can also be calculated by a "goodness of fit" criterion [25–27]. Lack of a fit of good quality may indicate the presence of scattering artifacts in the spectrum [28].

Modelling of the background in the pre-ionization edge region and extrapolation below the ionization edge was done by an inverse power law of the form

$$I_i = A_0 E_i^{-R} \tag{1}$$

After a logarithmic transformation, the coefficients A_0 and R can be calculated by linear regression. Variance calculations of the intensity output of each channel strongly depend on the way electron energy loss signals are recorded, and these differ for the Zeiss EM 902 and the JEOL FX 2000 instruments.

In most literature about EELs, the intensity Y_i represents the number of electrons which reached the detector during a specified time interval at the specific energy loss channels. These data are Poisson distributed (electron counting). The mean is equal to the variance and is estimated by the number of events ($\mu = \sigma^2 = Y_i$). The Poisson distribution can be approximated by a Gaussian distribution if the number of counts is large ($\mu = Y_i$ and $\sigma_i^2 = Y_i$).

This procedure is applied to the JEOL data. Because σ_i^2 differs from channel to channel because it equals the intensity Y_i (different for every channel), a weighted least squares estimation is required to calculate the power law coefficients of the background in the JEOL data.

For the Zeiss instrument, the output signal has lost some discreteness of electron counting. A photomultiplier tube (PMT) that operates in analog mode finally converts electrons into a voltage pulse. The voltage differences between the dynodes are further converted to current pulses that are related to the initial charge of electrons. The intensity data of Y_i of the Zeiss instrument are proportional representations of the measured number of electrons. In practice, if a spectrum is recorded for n measurements Y_{ij} at an energy loss E_i, the average intensity Y_i and a sample variance s_i^2 are approximated by a normal distribution [29] and determined by

$$Y_i = \frac{1}{n} \sum_{j=1}^{n} Y_{ij} \tag{2}$$

$$s_i^2 = \frac{1}{n-1} \sum_{j=1}^{n} (Y_{ij} - Y_i)^2 \tag{3}$$

The average intensity Y_i and the variances s_i^2 remain normally distributed after logarithmic transformation necessary for the background parameter calculations [29].

It can be proven that weighting will not drastically affect the accuracy of the least squares estimation but will rather influence the precision of the estimated coefficients [30].

Fig. 2 shows parameters that are to be selected prior to spectrum processing. The integration window Δ must be large enough to cover all fine structures in the cross section calculations but, in order to fulfil the power law, it should not be too large. A Δ value of 70 eV was selected as it is best that it is less than or equal to the region over which the background fit is performed. For most experiments, the background fitting region Γ was consistently set at 70 eV. However, for nitrogen determinations, both a Γ value and a Δ value of 50 eV were used, because problems can arise as the fitting region will interfere with the broad C *K* edge or the K $L_{2,3}$ edge. The net edge integral I_k is calculated by integrating the total edge intensity I_t over the pre-set energy window ($\Delta = 70$ eV) and subtracting the extrapolated background I_b values for the corresponding channels within Δ. The standard deviation of the characteristic edge signal is based on the error propagation and calculated as proposed by Van Puymbroeck [30]. Only statistical errors are taken into account rather than (a) errors of the measurement itself (incorrectly measured values for the electron-collection angle β, or lens aberration errors), (b) errors resulting from plural (elastic and inelastic) scattering, and (c) errors in the inelastic cross sections used. Statistical errors can occur in the measurement of the characteristic edge intensity I_k arising from the limited number of core-loss electrons included within the integration window Δ [31]. However, this error is normally small in comparison with extrapolation errors inherent in the background fitting procedure. The extrapolation error is partly statistical being related to the number of electrons recorded within the background fitting region and related to the range of the extrapolation [15,32].

From a recorded EEL spectrum, one can get the elemental concentration N of a particular element, expressed as the number of atoms per area, using the equation

$$N = \frac{I_k(\beta,\Delta)}{I_l(\beta,\Delta)\,\sigma_k(\beta,\Delta)\,G} \tag{4}$$

where $I_l(\beta,\Delta)$ represents the integrated intensity from the low-loss region, $I_k(\beta,\Delta)$ is the area above the background and beyond the k-shell ionization edge (k = *K*, *L*, *M* ...) as integrated for an energy window equal to Δ and a scattering angle less than β, $\sigma_k(\beta,\Delta)$ is the corresponding partial cross section for inelastic scattering from a particular shell of an element, and G accounts for the gain change of the detector between low- and high-energy regions of the spectrum.

The net integrated energy intensities are determined from the experiment while the hydrogenic "SIGMAK2" and modified hydrogenic "SIGMAL2" cross sections are used for the calculation of the partial cross sections of the *K*- and *L*-edges, respectively [2].

For serial recording, a detector gain change is introduced to expand the dynamic range, if the characteristic features are separated by an energy increment of more than 300 eV. For quantification, one needs to determine this gain factor G accurately. This determination can be done by calculating the amplification ratio from the intensities between overlapping channels for the two regions [30].

The ratio N^X/N^Y for two elements X and Y in the same particle, giving rise to the characteristic edges, can then be calculated from the relation

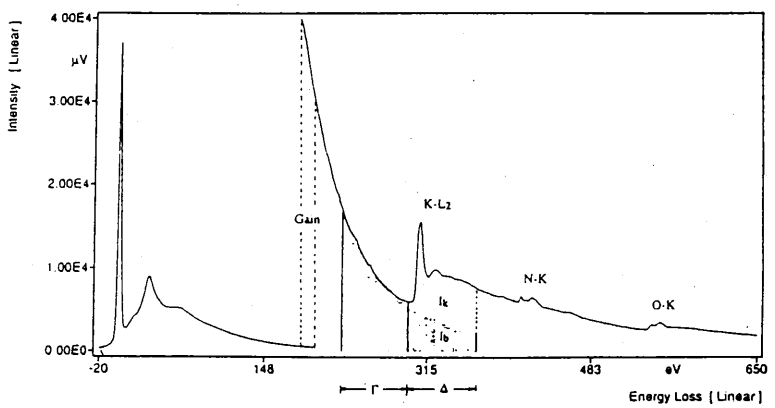

Fig. 2. Energy loss spectrum of a KNO_3 particle showing the spectrum processing parameters needed for quantization.

$$\frac{N^X}{N^Y} = \frac{I^X(\beta,\Delta)}{I^Y(\beta,\Delta)} \frac{\sigma^X(\beta,\Delta)}{\sigma^Y(\beta,\Delta)\, G'} \tag{5}$$

where G' refers to the gain change between the regions of the two elements of interest. Note that Eq. (5) can be used for elements of different edge types. For this equation, the assumption is that no mass losses occur during the acquisition of one spectrum so that the low-loss region remains the same for all elements and thus cancels out. This assumption is almost true for the fast parallel detection method but is not quite applicable for the more time consuming serial recordings at medium to high electron doses. However, applying this equation enables us to study the effect of mass losses in EELS analyses of salt particles.

For NaCl, serial recording needed special attention. The NaCl spectra were collected in three partial scans over different energy regions. The first and third regions correspond to the energy loss regions of chlorine and sodium, respectively. An approximately two-fold electron radiation dose and a maximum detector gain were necessary for the collection of sodium edges at about 1080 eV loss. The chlorine and sodium regions were matched by an energy loss region extending from 250 to 1020 eV. This region of 780 eV was recorded by integrating the signal per channel for only 3×0.1 s in order to reduce the total acquisition time.

For monitoring mass losses of one specific element as a function of time or electron dose, the relative concentration of a particular element $N(\mathrm{R})$ can be defined as the ratio of the initial concentration of that element $N(0)$ to the concentration at higher dose $N(\mathrm{D})$ or after a specific time $N(t)$

$$N(\mathrm{R}) = \frac{N(\mathrm{D})}{N(0)} = \frac{I_k^D(\beta,\Delta)}{I_l^D(\beta,\Delta)} \frac{I_l^0(\beta,\Delta)}{I_k^0(\beta,\Delta)} \frac{G^0}{G^D} \tag{6}$$

The superscripts 0 and D represent the initial values and their values at an electron dose D, respectively. It is possible that the thickness of the analyzed area changes as elemental losses occur. For this, the net areas under the characteristic edges are normalized by dividing them by the areas under the zero-loss peak. Dark-current corrections were performed on all spectra in order to reduce the effect of electronic noise.

Some 20 to 30 spectra were recorded for each standard particle type. Only those that have a characteristic signal-to-noise ratio exceeding three were selected for quantification. The reason some spectra show bad statistics is mainly that, at very low electron doses, an insufficient number of transmitted electrons reached the detector.

3. Results and discussion

For all standards, severe electron-beam-induced radiation damage was observed within less than 1 min at normal exposure (electron doses of approximately 0.5 to 5 C cm^{-2}). The residual structure of NaCl was observed to mature into a stable configuration after 1–2 min and applying a higher electron dose had no subsequent effect. The structural damage, as visible with the TEM, reflects the sputtering of the halogen atoms [33–35] rather than out-diffusion processes [36]. Different phenomena seem to occur for KNO_3 and $(NH_4)_2SO_4$ as they partly or totally sublime and disappear. When liquid nitrogen temperatures are used and the beam current is reduced by a factor of 10 to 50 (to about 0.01 to 0.5 C cm^{-2}), the visual damage did not appear in NaCl within the first 5 min of viewing time. For KNO_3 and $(NH4)_2SO_4$, only slow morphological changes occurred. The highest electron doses which still leave the analyzed sample volume unchanged, were used to collect electron energy loss spectra.

The mean element ratios determined from the quantitative EELS analyses are given in Table 2, as are the minimum and maximum determined ratios.

3.1. NaCl

Fig. 3 shows a typical EEL spectrum of a sub-micrometer NaCl particle. It is important to start spectrum collection from chlorine towards the higher electron energy losses of sodium. Fig. 4 demonstrates that chlorine losses are greater than sodium losses, even when the latter

Table 2
The mean elemental atomic ratios determined by serial and parallel EELS of three different inorganic standard salt particles; the minimum and maximum observed elemental ratios are also given

Sample	Instrument	Ratio			Min–max observed ratio		
		Na/Cl			Na/Cl		
NaCl	Zeiss	1.2 ± 0.8			0.8–1.4		
	JEOL	1.1 ± 0.6			0.9–1.3		
		O/S	N/S	O/N	O/S	N/S	O/N
$(NH_4)_2SO_4$	Zeiss	2.1 ± 0.8	1.1 ± 1.2	2.9 ± 0.9	1.4–3.4	0.4–1.8	1.0–6.1
	JEOL	3.9 ± 0.9	1.2 ± 0.6	2.5 ± 0.7	1.5–7.7	0.6–2.1	2.2–3.6
		O/K	N/K	O/N	O/K	N/K	O/N
KNO_3	Zeiss	2.4 ± 0.5	0.7 ± 0.6	3.9 ± 2.9	1.9–2.6	0.2–1.2	2.1–8.8
	JEOL	3.5 ± 0.7	1.0 ± 0.4	3.7 ± 2.1	2.1–4.6	0.3–1.9	2.4–6.4

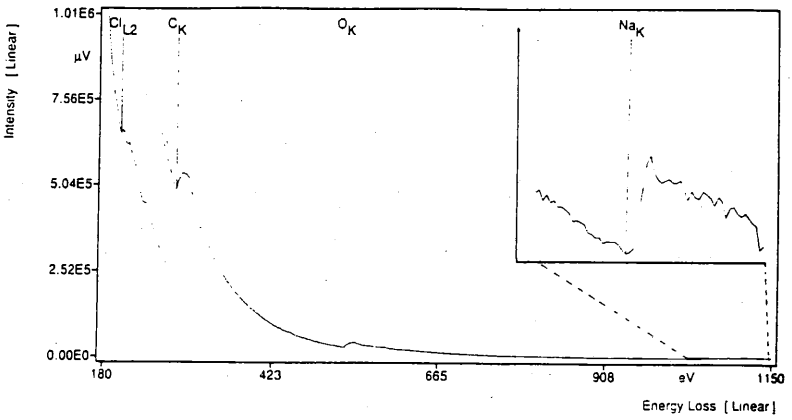

Fig. 3. EEL spectrum of a NaCl particle showing the Cl L_2 ionization edge and the Na K ionization edge (enlarged view in the upper right corner). A C K edge from the supporting foil and an O K edge as a result of an oxidation process are also shown.

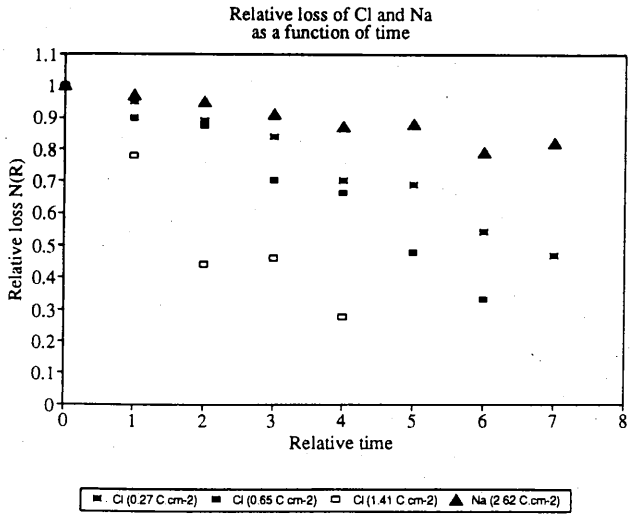

Fig. 4. Relative loss N(R) of chlorine and sodium from NaCl as a function of time, collected at a constant electron irradiation flux. The relative loss is the ratio of the measured element intensity at constant time intervals (relative time in units of 5 min) to the initially measured element intensity (t = 0).

are collected at electron doses that are ten times greater. There is a good agreement between the element ratios determined for NaCl by parallel and serial EELS.

For the relative loss measurements of specific elements, characteristic features were collected over an energy range of 160 eV for 5×0.1 s and per energy increment of 2 eV. The zero-loss region (1 eV per channel) and the intermediate region (2 eV per channel) were recorded for 3×0.1 s. This all corresponds to a total acquisition time of about 2.5 min. One minute intervals were used between the end and the start of a new spectrum to correspond with the time needed to store all information and to control all instrument settings.

The signal-to-noise ratio of the chlorine ionization edge above the extrapolated background did not exceed the value of unity after a relative time interval of 4 min at a dose of 1.41 C cm^{-2}.

Collection of serial spectra in reverse order, starting from the high energy loss towards the low-loss region, results in a mean Na/Cl ratio of 1.8, which is far above the theoretical value of unity. The reason for this difference is that chlorine losses had occurred before the signal was acquired. From Fig. 5, it can be seen that chlorine losses occur more rapidly as the electron doses increase. Under much higher electron doses, the halogen atoms can be removed totally, but also removal of the metallic component can occur either by diffusion or, in the case of alkali metal, by thermal desorption [37,38].

There is evidence that radiation damage arises from inelastic scattering of the incident electrons resulting in excitation, decay and reformation mechanisms [39]. The remaining alkali atoms may segregate into a metallic phase that will be oxidized in a TEM [24]. The oxidation is shown in the NaCl spectrum (Fig. 3) by the appearance of the O *K* edge at 545 eV.

3.2. $(NH_4)_2SO_4$

A typical serially recorded $(NH_4)_2SO_4$ spectrum is shown in Fig. 6. First the N *K* and O *K* signals were collected and then the S ionization edge was recorded at a reduced PMT gain. The sulfur energy-loss region was rescaled according to the gain setting used.

Just as for NaCl, element losses determine the success of analysis, but for $(NH_4)_2SO_4$, degradation occurs more readily. Fig. 7 shows the time dependency of nitrogen, oxygen and sulfur losses in $(NH_4)_2SO_4$. After only one spectrum acquisition, the relative nitrogen intensity dropped by a factor of three. After four relative time intervals, the signal-to-noise ratio for nitrogen did not even exceed the one sigma criterion. Oxygen losses seemed to be less severe, whereas for sulfur only a small relative loss in concentration was observed. Fig. 8 shows the relative nitrogen, oxygen and sulfur concentrations as a function of electron dose. For nitrogen, the net intensity decreases rapidly with time. The effect of electron radiation on the nitrogen losses can be seen from the N/S and O/N ratios. The results of the PEELS experiments show that nitrogen losses occurred within the first few seconds of recording (mean N/S ratio of 1.2 for $(NH_4)_2SO_4$). Oxygen loss is slower than nitrogen loss, and therefore O/N element ratios

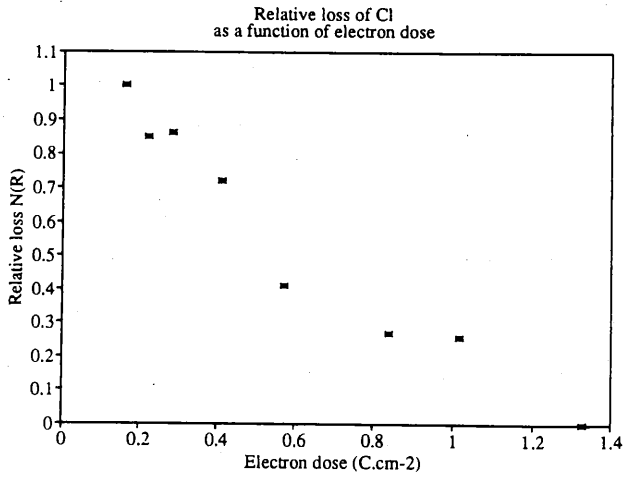

Fig. 5. Relative loss of chlorine from NaCl as a function of electron radiation dose.

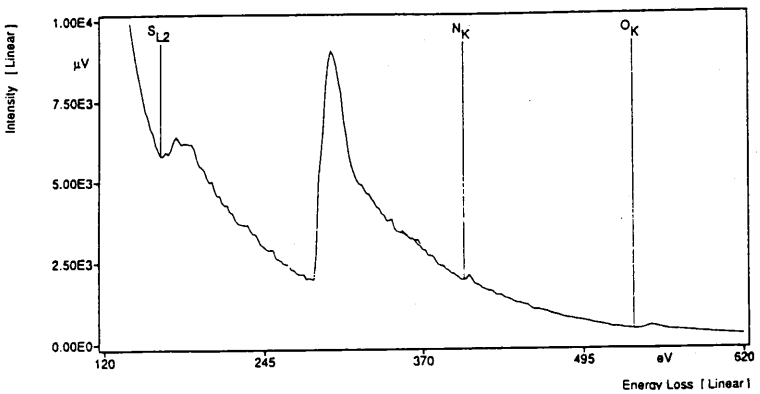

Fig. 6. EEL spectrum of an $(NH_4)_2SO_4$ aerosol particle that was collected in two scans; the first scan went from nitrogen, the most beam-sensitive element, to oxygen, while the second scan extended from sulfur to an energy loss region overlapping with the first scan. The spectrum was constructed by increasing the intensities of the first region by the corresponding gain change.

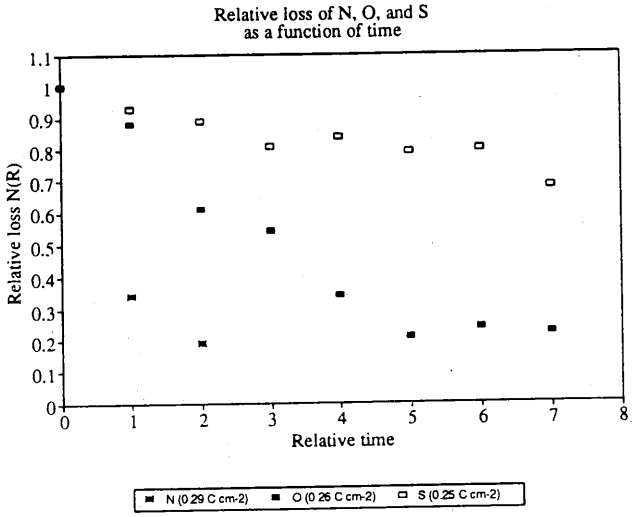

Fig. 7. Relative loss of nitrogen, oxygen and sulfur from $(NH_4)_2SO_4$ as a function of time (relative time in units of 5 min) and collected at a nearly constant electron dose.

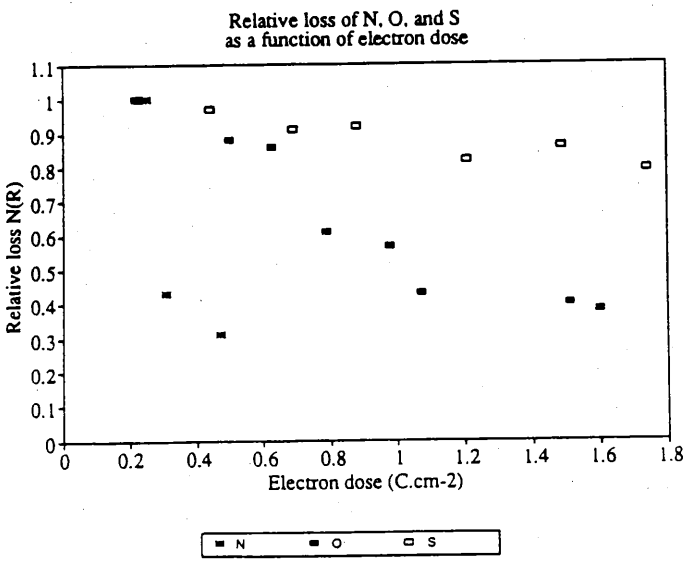

Fig. 8. Relative loss of nitrogen, oxygen, and sulfur from $(NH_4)_2SO_4$ as a function of electron irradiation dose.

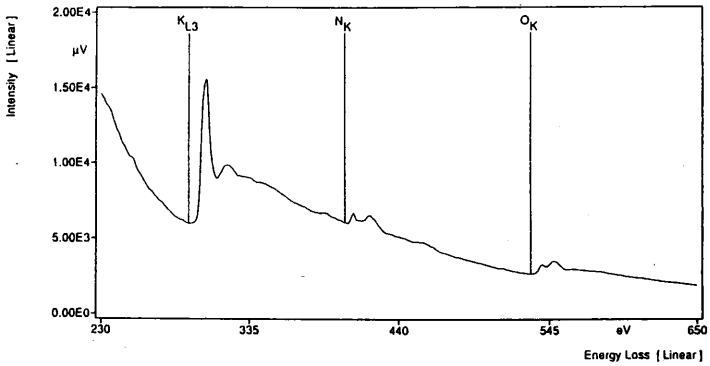

Fig. 9. EEL spectrum of a standard KNO_3 particle showing the K $L_{2,3}$, N K and O K ionization edges.

above the theoretically predicted values are found. However, oxygen mass losses occur as a function of time, and this also results in lower O/S ratio for the more time consuming serial recording. The small decrease in relative sulfur concentration as a function of time and radiation dose is probably the result of hydrogen sulfide formation, a phenomenon also observed in sulfur-containing amino acids [40].

3.3. KNO_3

Fig. 9 shows a PEELS spectrum of a KNO_3 particle. Because the broad C K feature (C K at 283 eV loss) of the carbon foil overlaps with the K $L_{2,3}$ edge (K $L_{2,3}$ at 294 eV loss), it is necessary to select and analyze particles that lie over holes in the supporting foil. For the serially recorded KNO_3 spectra, the gain does not need to be changed because all characteristic edges lie within an energy span of less than 300 eV. As nitrogen seems to be the most beam sensitive, it is advisable to start serial spectrum collection from nitrogen towards oxygen as a separately defined region from potassium. Fig. 10 shows that the electron dose affects the relative loss in the order: N > O > K.

For KNO_3, the elemental ratio differences between the serial and parallel recorded spectra are less extreme than for $(NH_4)_2SO_4$, but, just as for $(NH_4)_2SO_4$, nitrogen and oxygen losses limit the success of EELS analyses.

4. Conclusions

Preferential element losses and structure reorganization occur frequently in the electron microscope. These changes can lead to poor or even unsuccessful analyses. From the elemental

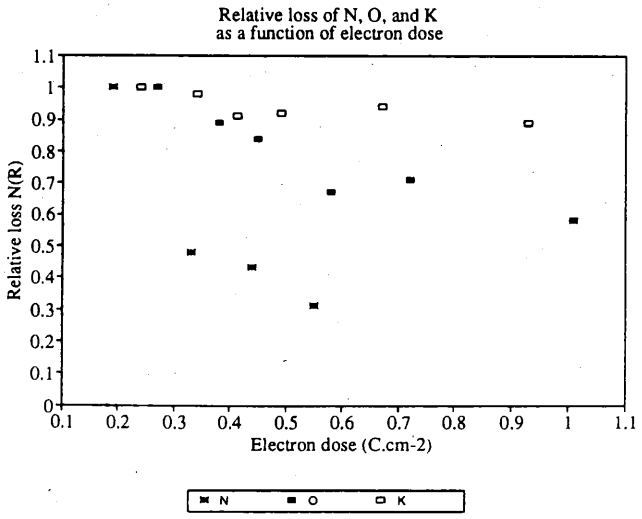

Fig. 10. Relative loss of nitrogen, oxygen and potassium from KNO_3 as a function of electron dose.

ratios, we conclude that the volatile elements are released more rapidly than the others, resulting in a sequence of nitrogen before oxygen before chlorine, potassium, sodium and sulfur. Even at cryogenic temperatures, preferential losses and structure reorganization cannot be avoided.

The quality of the analyses is limited by counting statistics. High relative standard deviations were observed, ranging from 15% to 100%. Large counting times and high electron doses (lower detector gain necessary) favor good statistics because the signal-to-noise ratio is increased, but mass losses also become more important. A compromise should be made by using the lowest electron doses that still fulfil the signal-to-noise ratio requirements and that preserve the object as much as possible from structural changes. This can be done by analyzing some particles and directly processing the energy loss spectra. Minor changes of electron dose or acquisition times can be made according to the statistics required.

Element ratios closer to the theoretical values are observed when EEL spectra are recorded in the parallel mode, indicating that the acquisition time is important. For analyzing beam sensitive samples such as inorganic salt particles, a parallel recording device is therefore advantageous.

In general, EELS is only of limited use for quantitative particle determination. Analysis of inorganic salt particles such as KNO_3 and $(NH_4)_2SO_4$, is best restricted to qualitative purposes.

Acknowledgements

This work was partially supported by the Belgian Government-Prime Minister's Office-Services for Scientific, Cultural and Scientific Affairs (under Contract EU7/08 in the framework of EUROTRAC and contract MS/06/050 in the framework of the Impulse Programme Marine Sciences) and by the Belgian Nationaal Fonds voor Wetenschappelijk Onderzoek (NFWO). C. X. acknowledges a research fellowship from the Belgian Instituut ter Aanmoediging van Wetenschappelijk Onderzoek in Nijverheid en Landbouw (IWONL). Support was provided by a grant from Atmospheric Chemistry division of the US National Science Foundation to PRB. Electron microscopy was performed at Center for High Resolution Electron Microscopy at Arizona State University, with support from NSF (grant DMR-6913384).

References

[1] C.C. Ahn and O.L. Krivanek, EELS Atlas, Arizona State University, 1983.
[2] R.F. Egerton, Electron Energy Loss Spectroscopy in the Electron Microscope, Plenum Press, New York, 1986.
[3] P.R. Buseck and P.G. Self, in P.R. Buseck (Ed.), Minerals and Reactions at the Atomic Scale: Transmission Electron Microscopy, Reviews in Mineralogy, Vol. 27, Mineral Soc. Amer., Washington DC, 1992, p. 141.
[4] B. Wolf, Z. Naturforsch. Teil C, 43 (1988) 155.
[5] C. Xhoffer, W. Jacob and R. Van Grieken, J. Aerosol Sci., 20 (1989) 1617.
[6] K. Katrinak, P. Rez and P.R. Buseck. Environ. Sci. Technol., 26 (1992) 1967.
[7] C. Xhoffer, C. Lathen, W. Van Borm, J.A.C. Broekaert, W. Jacob and R. Van Grieken, Spectrochimica Acta Part B, 47 (1992) 155.
[8] P. Otten, F. Bruynseels and R. Van Grieken, Bull. Soc. Chim. Belg., 95 (1986) 447.
[9] H. Castaing and L. Henry, C. R. Acad. Sci. Ser. B, 255 (1962) 76.
[10] R.M. Henkelmann and F.P. Ottensmeyer, J. Microsc. 102 (1974) 79.
[11] J. Van Puymbroeck, P. Van Espen and W. Jacob, Micron Microsc. Acta, 20 (1989) 155.
[12] B.L. Jones, D.G. Jenkins and G.R. Booker, Inst. Phys. Conf. Ser., 36 (1977) 73.
[13] J.N. Chapman, P.T.E. Roberts, A.M. MacLeod and F.P. Ferrier, Inst. Phys. Conf. Ser., 52 (1980) 77.
[14] D.G. Jenkins, C.J. Rossow, G.R. Booker and P.W. Fry, Inst. Phys. Conf. Ser., 52 (1980) 73.
[15] R.F. Egerton, in K.F.J. Heinrich (Ed.), Microbeam Analysis, San Francisco Press, San Francisco, 1982, p. 43.
[16] D.F. Blake, L.F. Allard, C.J. Echer and F. Freund, in D.E. Newbury (Ed.) Microbeam Analysis, San Francisco Press, San Francisco, 1988, p. 129.
[17] T.A. Hall and B.L. Gupta, J. Microsc., 109 (1974) 1193.
[18] H. Shuman, A.V. Somlyo and A.P. Somlyo, Ultramicroscopy, 1 (1976) 317.
[19] A.P. Somlyo, A.V. Somlyo and H. Shuman, J. Cell. Biol., 81 (1979) 316.
[20] R.F. Egerton, Ultramicroscopy, 5 (1980) 521.
[21] E.H. Jacobsen, J.G. King, M.G.R. Thomson and J.C. Weaver, Sciene, 173 (1971) 751.
[22] M.K. Lamvik, S.D. Davilla and L.L. Klatte, Ultramicroscopy, 29 (1989) 241.
[23] J.R. Fryer and F. Holland, Ultramicroscopy, 11 (1984) 67.

[24] R.F. Egerton, P.A. Crozier and P. Rice, Ultramicroscopy, 23 (1987) 305.
[25] M. Unser, J.R. Ellis, T. Pun and M. Eden, J. Microsc., 145 (1987) 245.
[26] P. Trebbia, Ultramicroscopy, 24 (1988) 399.
[27] P. Trebbia and T. Manoubi, Ultramicroscopy, 28 (1989) 266.
[28] D.C. Joy and D.M. Maher, in O. Johari (Ed.) Scanning Electron Microscopy 1980, Vol. 1, SEM Inc., Chicago, 1980, p. 25.
[29] D.G. Rees, J. Am. Stat. Assoc., 65 (1970) 161.
[30] J. Van Puymbroeck, Ph.D. Thesis, University of Antwerp (UIA), 1992.
[31] R.F. Egerton, in G.M. Roomans (Ed.), Scanning Electron Microscopy 1984, Vol II, SEM Inc., Chicago, 1984, p. 505.
[32] P. Rez, in R. Gooley (Ed.), Microbeam Analysis, San Francisco Press, San Francisco, 1983, p. 153.
[33] M. Szymonski and A.E. de Vries, in N.H. Talk, M.M. Traum, J.C. Tully and T.E. Madey (Eds.), Desorption Induced by Electronic Transitions (DIET I), Springer, Berlin, 1983, p. 216.
[34] M. Szymonski, J. Ruthowski, A. Poradzisz and Z. Postawa, in W. Brenig and D. Menzel (Eds.), Desorption Induced by Electronic Transitions (DIET II), Springer, Berlin, 1985, p. 160.
[35] T. Nakayama and N. Itoh, in W. Brenig and D. Menzel (Eds.), Desorption Induced by Electronic Transitions (DIET II), Springer, Berlin, 1985, p. 237.
[36] Y.Al Jammal, D. Pooley and P.D. Townsend, J. Phys. C., 6 (1973) 247.
[37] A. Muray, M. Isaacson and I. Adesida, Appl. Phys. Lett., 45 (1984) 589.
[38] P.M. Mankiewich, H.G. Craighead, T.R. Harrison and A.H. Dayem, Appl. Phys. Lett., 44 (1984) 468.
[39] L.W. Hobbs, J. Am. Ceram. Soc., 62 (1979) 267.
[40] M. Misra and R.F. Egerton, J. Phys. D., 13 (1980) L71.

:LSEVIER

Analytica Chimica Acta 317 (1995) 33–51

ANALYTICA
CHIMICA
ACTA

Elucidating the composition of atmospheric aerosols through the combined hierarchical, non-hierarchical and fuzzy clustering of large electron probe microanalysis data sets

B. Treiger, I. Bondarenko, H. Van Malderen, R. Van Grieken *

Department of Chemistry, University of Antwerp (UIA), Universiteitsplein 1, B-2610 Antwerp (Wilrijk), Belgium

Received 3 January 1995; revised 25 July 1995; accepted 9 August 1995

bstract

Combined utilization of hierarchical, non-hierarchical and fuzzy clustering is introduced to find the intrinsic structure of rge analytical data sets. Modified algorithms for nonhierarchical and fuzzy clustering are used. The interpretation of the sults of clustering is based on the extensive use of different types of graphs. New approaches to the graphical presentation of the results of fuzzy clustering are proposed. The method is applied to data of electron probe X-ray icroanalysis of individual aerosol particles. The advantages of the method are shown.

eywords: Chemometrics; Cluster analysis; Aerosols; Environmental analysis; Electron probe microanalysis

. Introduction

Cluster analysis belongs to the well-developed nultivariate statistical techniques which have been sed for a long time for the processing of data sets, .g. those containing the chemical compositions of ndividual aerosol particles (see, e.g. [1]). The deter-nination of the composition of individual aerosol articles based on electron probe X-ray microanaly-is (EPXMA) is the source of very useful environ-nental and scientific information.

In order to derive knowledge about the type and bundance of the different particle types in an aerosol ample from the measured composition of the indi-vidual aerosol particles cluster analysis can be applied, besides other multivariate statistical techniques. Hierarchical cluster analysis (HCA) is widely used for this purpose (see, e.g. [2]) although sometimes it is stated that conventional hierarchical clustering techniques are no longer valid if they deal with large data sets (> 100 objects) [3]. Their main advantages are the relative simplicity and ability to visually represent the results in the form of dendrograms. Their main disadvantage lies in the fact that, according to the logic of hierarchical clustering, a kind of hierarchical structure is necessarily superimposed on the data, even in spite of the fact that data may not possess this structure at all. Obviously, this can lead to the misclassification of the particles.

Nonhierarchical cluster analysis (NHCA), also frequently used for the processing of EPXMA data of individual aerosol particles [1,4,5], is free from this disadvantage. Instead, the problem here lies in

* Corresponding author.

SSDI 0003-2670(95)00405-X

the dependence of the results of NHCA on the choice of seed points. In addition, such visual form of representation of clustering results as dendrogram is impossible in NHCA.

Both clustering techniques are referred to as hard clustering schemes, where each object (here: aerosol particle) is assumed to belong to one and only one cluster. In the case of touching or overlapped clusters, this assumption is apparently invalid, leading to misclassification.

Fuzzy cluster analysis (FCA), first introduced by Ruspini [6] and further developed by Bezdek [7], overcomes this disadvantage. Its main idea is to replace the procedure of the splitting of the multivariate data for M objects into c clusters by a procedure of determining the probability of belonging (membership coefficient) of each object to each cluster. From the fuzzy point of view, hard clustering can be considered as a particular case of fuzzy clustering, namely when all but one membership coefficients are equal to zero. Although it is yet another mathematical model that not necessary describes the real data structure, it seems a priori that such an approach should lead to more appropriate results. It should be noted, however, that in spite of the fact that one can find in the literature many successful applications of the fuzzy approach for clustering, to the authors' knowledge there are still only a few papers dealing with the comparison of fuzzy and hard methods of cluster analysis (see, e.g. [8,9]) as applied to real data sets. Maybe this is due to the fact that the term 'fuzzy clustering' is to some extent contradictory because 'clustering' implies an attempt to reveal some structure initially inherent to the experimental data, whereas 'fuzzy' is based on the idea that this structure is weak (when the data are completely fuzzy there is no underlying structure and the clustering is meaningless). So, the advantages of FCA over conventional hard clustering methods are not completely evident. Furthermore, the results of FCA cannot be visualized easily, which is a disadvantage and sometimes strong.

Common to all three above clustering techniques is the problem how to choose correctly or in the most suitable sense the number of clusters (so called clustering criterion). It is clear that this problem is a crucial one for the interpretation of clustering of large analytical dataset.

A few conclusions can be drawn from all mentioned above:

1. Only combined use of these three clustering techniques can reveal the actual structure of large data-set.
2. The uncertainty related with the problem of the clustering criterion should be understood. The researcher should be provided with all information he may need to make the most founded decision.
3. New visualization approaches are of need for representation of clustering results.

Therefore, the main objectives of the present paper are to investigate the combined application of HCA, NHCA and FCA to large EPXMA data sets of aerosol particles, to find a reasonable choice for the number of clusters and to demonstrate new visualization means for the representation of clustering results. As an example, the developed technique of clustering is applied to the processing of a set of EPXMA data for typical Siberian aerosols. The impact of Siberia in global environmental processes is important, in view of its area. Being previously closed for Western researchers, Siberia is an interesting region to study the long range transport of atmospheric particles which might contribute significantly to the Arctic Haze. The composition of Siberian aerosols is determined and their source apportionment is made.

2. Brief theory

The details of the clustering techniques used in the present study and the description of the developed Windows software IDAS are provided elsewhere [10]. Now we will only briefly state the most important points.

2.1. Hierarchical cluster analysis

HCA is a well-established technique [11]. In the present study we have chosen Ward's strategy which is proven to give the most reliable results with experimental data [2]. The metric of data space is Euclidean without any scaling of analytical data. This should provide the classification of data where major details will be seen.

As is mentioned above, the most difficult problem in HCA is the problem of cutting the dendrogram at a certain level to terminate the further growth of clusters, i.e. the correct choice of the clustering criterion (also called stopping rule). The problem has been extensively discussed in the literature (see the recent book by Jain [12]). We are deeply convinced that the most fruitful approach implies knowledge of the application field of each criterion. Therefore we propose to use not one clustering criterion but a set of criteria providing the analyst with all information he may need.

The following types of criteria are proposed for use with HCA on analytical data sets:

(1) *Akaike Information Criterion (AIC)* [13]. It implies minimization of the function:

$$AIC = M * N * (1 + \ln(2\pi)) + \sum_{m=1}^{c} n_m * \ln|S_m| + 4 * c * N \quad (1)$$

where c is the number of clusters, M is the number of particles in the dataset, N is the dimension of the data space (number of the analysed elements), n_m is the number of particles in mth cluster, and $|S_m|$ is the determinant of the matrix $\mathbf{S}_m$ which is the unbiased maximum likelihood estimate of the covariance matrix for cluster m. It is calculated as:

$$\mathbf{S}_m = \frac{1}{\mathbf{n}_m - 1} * \mathbf{X}_m^T * \mathbf{X}_m \quad (2)$$

where $\mathbf{X}_m$ is the submatrix of data matrix $\mathbf{X}$, containing the data of all particles in cluster m.

AIC was successfully applied in our laboratory for the classification of Siberian aerosol particles based on clustering of EPXMA data [14]. However, sometimes, especially in case of diffused clusters, it cuts the dendrogram at a very low level providing the analyst with too detailed information. This is a known drawback of *AIC* [13].

As a heuristic rule, we recommend to consider not only the global minimum of AIC (if it exists) but its 'knees' and local minima because they are indicative for the changes of the behaviour of the graph AIC vs. number of clusters c. This will be exemplified in Section IV.

(2) *Davies-Bouldin index (DB)* [12]. It is based on the following measure of within-to-between cluster spread for clusters i and m:

$$R_{i,m} = \frac{e_i + e_m}{d_{im}} \quad (3)$$

where e_i is within-cluster variation (error sum of squares) for the ith cluster and d_{im} is the distance between the centers of the clusters. Within-cluster variation is calculated as

$$e_i^2 = \sum_{k=1}^{N} \sum_{j=1}^{n_i} \left(x_{jk}^{(i)} - \bar{x}_k\right)^2 \quad (4)$$

where $x_j^{(i)}$ denotes the jth particle belonging to ith cluster and $\bar{x}^{(i)}$ stands for the center of the cluster. Then the index for each cluster is

$$R_i = \max_{i \neq m} \{R_{i,m}\} \quad (5)$$

and

$$DB(c) = \frac{1}{c} \sum_{i=1}^{c} R_i \quad (6)$$

The smaller the criterion the better clustering is reached.

When one observes the graph *DB* vs. c, one should look either for a pronounced local minimum or for, at least, a 'knee' because with increasing number of clusters (and decreasing of their population) *DB* approaches zero. Therefore, this criterion may have disadvantages in the region of large c values.

(3) *Total error sum of squares criterion.* The criterion value is calculated as:

$$E(c) = \sum_{i=1}^{c} e_i \quad (7)$$

The minimum of this criterion indicates the formation of the most compact cluster structure.

Comparison of all three criteria exhibits that, although they have a common statistical nature, their mathematical form apparently differs. Therefore they may indicate different clustering as the most suitable, thus providing the analyst with the necessary freedom of choice. This allows the analyst to make a decision based on the different grounds and on his experience as well.

2.2. Nonhierarchical cluster analysis

NHCA is also a well-established multivariate statistical analysis procedure commonly used in processing of large dataset containing the results of EPXMA of individual aerosol particles [1,2]. It can be considered as an intermediate case between hierarchical and fuzzy clustering. The common feature with fuzzy clustering is that it does not impose any hierarchical structure on the data set. Its common feature with hierarchical clustering is that it is also a hard clustering approach.

In the present study we modified [10] MacQueen's algorithm, considered as one of the most widespread [12] in order to provide the possibility for the combined use of NHCA and HCA and to improve the performance and speed of NHCA. Joint application of HCA and NHCA allows to refine the results of the clustering of a data set. The final furnishing is to be done with fuzzy clustering.

2.3. Fuzzy cluster analysis

Usually fuzziness is inherent to large data sets because of the presence of objects with intermediate properties, intermediate position in data space, etc. However, as it was mentioned in the Introduction, it is not so easy to combine the fuzzy approach with clustering.

One of the most widespread algorithms for fuzzy clustering is the fuzzy c-means algorithm [15,16] (FCM). We modernised this algorithm to allow the joint application of hierarchical and fuzzy clustering as it was in the case of NHCA [10] and to improve the performance and interpretation of fuzzy clustering itself.

2.4. Combined use of hierarchical, non-hierarchical and fuzzy clustering

So, the procedure of classification of large analytical data sets based on the combined use of HCA, NHCA and FCA consists of the following stages:

1. Hierarchical clustering of a data set. The suitable number of clusters is determined as described in Section 2.1.
2. Redetermination (adjusting) of composition and number population of clusters with nonhierarchical clustering.
3. Studying of the internal structure of clusters and their interrelationships with fuzzy clustering.

Hence, this procedure is developed in general terms. It will be illustrated by specific applications in Section IV. However, there is still one problem, mentioned in the Introduction, which is not solved yet, i.e. the problem which can facilitate significantly the interpretation of the results, the most important step of cluster analysis: the problem of the most advantageously representing the clustering results.

2.5. Visualization of the results of cluster analysis

The detailed description of the graphical part of our Windows software can be found elsewhere [10]. Here we give the overview of the visualization means. The graphical representation of HCA and NHCA results is done with the help of the following graphs:

1. Average composition of a cluster (the concentrations of the chemical elements are given for a cluster).
2. Mean concentration of a chemical element in all clusters. It allows the comparison of the composition of the clusters element by element.
3. Mean concentration of the chemical elements in a set of clusters. It allows the comparison of the concentration of certain elements in a number of clusters.
4. Distribution of the elements in a cluster. It shows a number of non-zero occurrences of the chemical elements in the individual aerosol particles which belong to a cluster.
5. Pie chart of cluster populations.
6. Graphs of different clustering criteria discussed in Section 2.1.

The results of HCA are also depicted in the form of a dendrogram. A dendrogram gives the analyst a personal impression about the hierarchical structure of a dataset.

The most difficult problem is the representation of the results of fuzzy clustering. It is the permanent subject of the attention of chemometricians. The last proposition was to use principal components plot of the membership coefficients [17]. However, up to now there was no efficient way of representing just that part of information which is due to the fuzzy nature of clustering. From the point of view of analytical chemists, it is interesting to get informa-

tion about interrelationships between clusters (e.g. are they compact or diffuse?), and about the number populations of clusters under different probability levels. Therefore, visualization of the results of FCA is provided with the help of graphs representing the following information:

1. Distribution of the probability within a cluster, showing the histogram of membership coefficients of objects for a cluster.
2. Distribution of the probability in the set of clusters, showing the number of objects belonging to each of clusters from the specified set, together with their probabilities (starting with certain prespecified level).
3. Linkage probability bar for a cluster, showing how many particles considered as belonging to a present cluster belong at the same time to other clusters (along with their membership coefficients).These three types of graphs represent the fuzzy part of information in the most evident form. Besides these, three other types of graphs are also intended to visualize the results of fuzzy clustering.
4. Average composition of the clusters.
5. Mean concentration of a chemical element in all clusters.
6. Mean concentrations of the chemical elements in the set of clusters.

The information the last three graphs provide is mostly the same as of their hard clustering counterparts. The only difference is that they are calculated in accordance with the membership coefficients of the aerosol particles belonging to a cluster.

3. Experimental

3.1. Sampling

The sampling took place at two stations in Siberia, near the city of Novosibirsk ('Klyuchi' station), and in Karasuk, some 400 km west of Novosibirsk ('Karasuk' station), considered to represent well the average Siberian industrial aerosol.

Aerosol samples were acquired during February (winter) and during August (summer) 1992 at the 'Karasuk' station and during August, 1992 at the 'Klyuchi' station. Total airborne particulate matter was collected on 47 mm diameter, 0.4 μm pore size Nuclepore polycarbonate membrane filters (aerosol grade). The filter was placed in a plexiglas filter holder with a hat-type cover to protect it from vertical deposition and rain. The filter holder was connected to a vacuum pump, which was operated at a flow rate of approximately 12 l min^{-1} for 4 h. In this way over one hundred samples were collected for single particle analysis. The environmental significance of the results is discussed in more detail elsewhere [18].

3.2. Electron probe X-ray microanalysis

The analysis of individual aerosol particles was performed on a JEOL JXA-733 Superprobe equipped with an energy-dispersive Si(Li) detector under the control of a Tracor TN-2000 system. The accelerating voltage was 25 kV and the beam current ca. 1 nA. An energy-dispersive X-ray spectrum was collected during 20 s at the particle centroid. Usually the total X-ray count rate was between 1000 and 2000 counts/s. Under these conditions, detection limits are of the order of 2%. The peak intensities of the K X-ray lines of Na, Mg, Al, Si, P, S, Cl, K, Ca, Ti, Mn, Zn and Fe and the L X-ray lines of Ba and Pb were integrated after subtracting linearly interpolated background contributions from the total counts in the spectral regions of interest. After normalizing to 100% the relative peak intensities were used as input data for clustering (when the net peak intensity was below 1000 counts the particle was not taken into account due to the impossibility of reliably interpreting the relative X-ray intensities). Then the average values for clusters were converted into compositions with ZAF correction procedures.

For the automatic analysis of single particles we developed in-house software running on the TN-2000 system (PDP-11/23). The details of the computer-controlled EPXMA implemented in our laboratory have been published elsewhere [19].

For each of the nearly 100 aerosol samples collected at stations 'Klyuchi' and 'Karasuk' for single particle analysis, EPXMA of typically 400 particles was conducted.

In this work, clustering techniques were applied to separate aerosol samples collected as described above and to three average samples considered as

characteristic samples for a sampling campaign. The average samples were composed of the EPXMA data of 20 to 25 individual aerosol particles randomly taken from each sample from the campaign. The total size of an average sample was ca. 600 particles.

4. Results and discussion

We will start with the average sample 'kar-win', composed of EPXMA data from the samples collected during the winter campaign at the 'Karasuk'

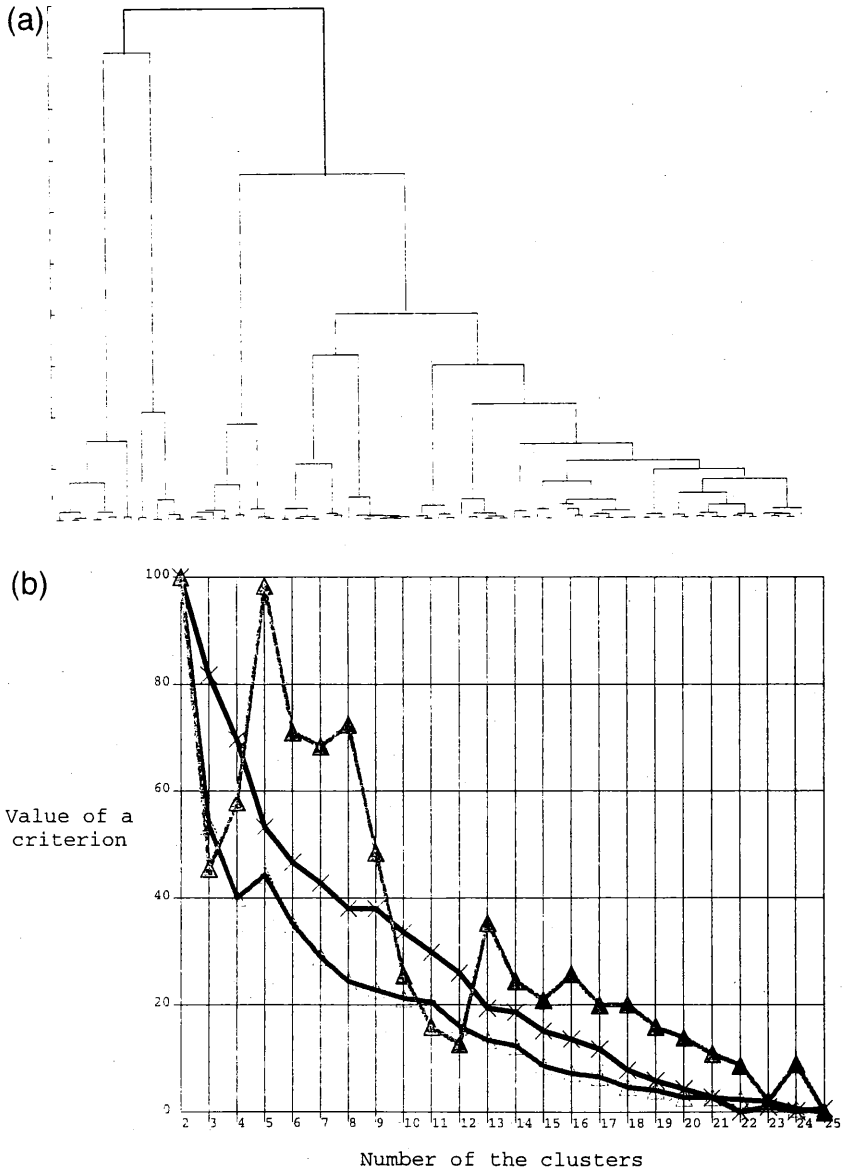

Fig. 1. Dendrogram (a) and the graphs of the clustering criteria (b) for HCA of the sample 'kar-win'. Key: × = *AIC*, △ = *DB*, ▲ = *E*.

station. The main reason is that the soil was covered with snow and one can expect less variety in the different types of aerosol particles. The dendrogram, representing the results of HCA, and the graphs of three different criteria for cutting the dendrogram are given in Fig. 1. The dendrogram shows that the internal structure of this sample is not well-pronounced. One can hardly say at what level the dendrogram can be cut. The observation of Fig. 1b displays evidently that the behaviour of AIC and DB criteria differs essentially from that of E criterion. The E criterion exhibits a local minimum at $c = 3$, whereas two other criteria have pronounced peculiarities at $c = 5$. The compositions of the corresponding

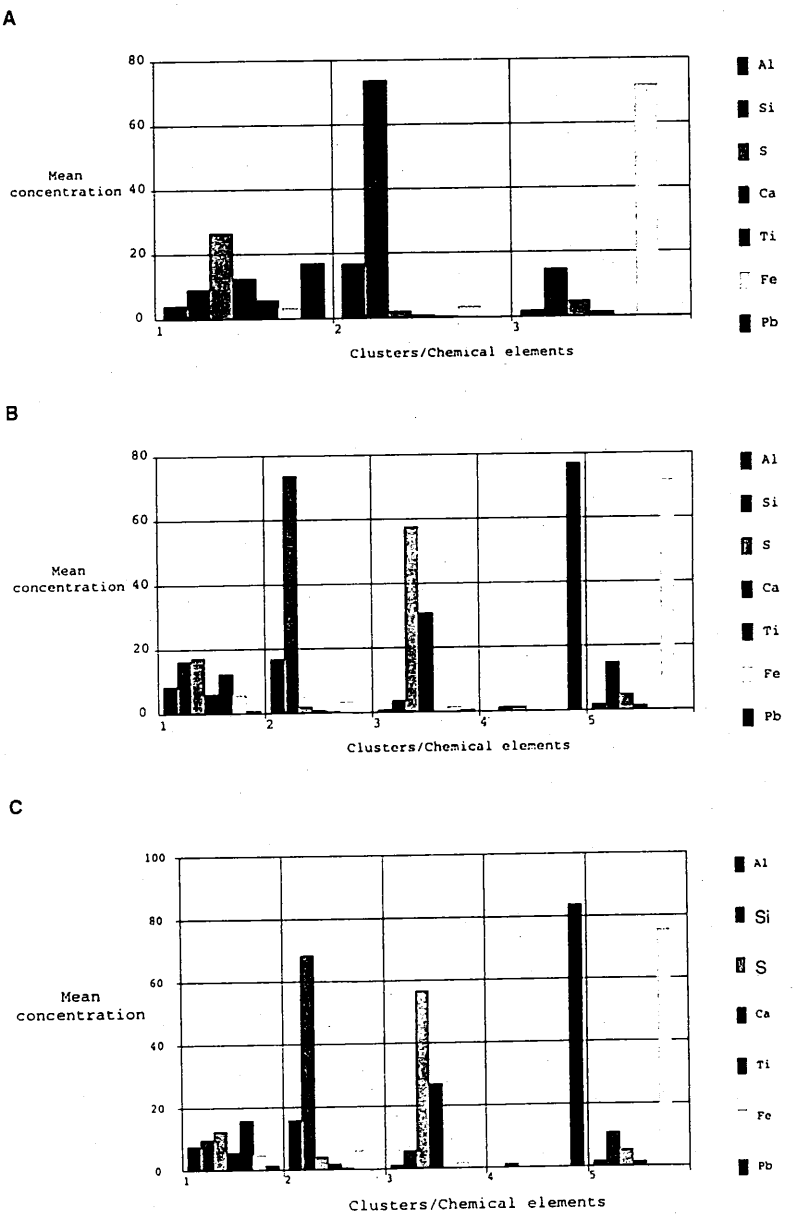

Fig. 2. Composition of the sample 'kar-win' obtained with (a) $c = 3$ clusters, HCA; (b) $c = 5$ clusters, HCA; (c) $c = 5$ clusters, NHCA.

clusters and pie charts of their populations are given in Fig. 2a and b and Fig. 3a and b. From the point of view of the analytical chemist, Fig. 2a underestimates the number of clusters whereas Fig. 2b gives a more realistic estimation. Indeed, only two clusters (2 and 3), with evidently different compositions, are seen in Fig. 2a, while cluster 1 which contains unclassified and mixed particles (very low values of the concentrations of all chemical elements indicate the large scattering of composition from particle to particle), encompasses more than 70% of all aerosol particles from the sample. On the contrary, Fig. 2b points out the existence of four clusters with essentially different compositions (aluminosilicates, Ca- and S-rich particles, Fe- and Pb-rich particles) and one cluster of mixed nature with population of less than 30% of all aerosol particles from the sample. Of course, it is possible to divide this mixed cluster further on. This process will result in the appearance of clusters, containing different types of aluminosili-

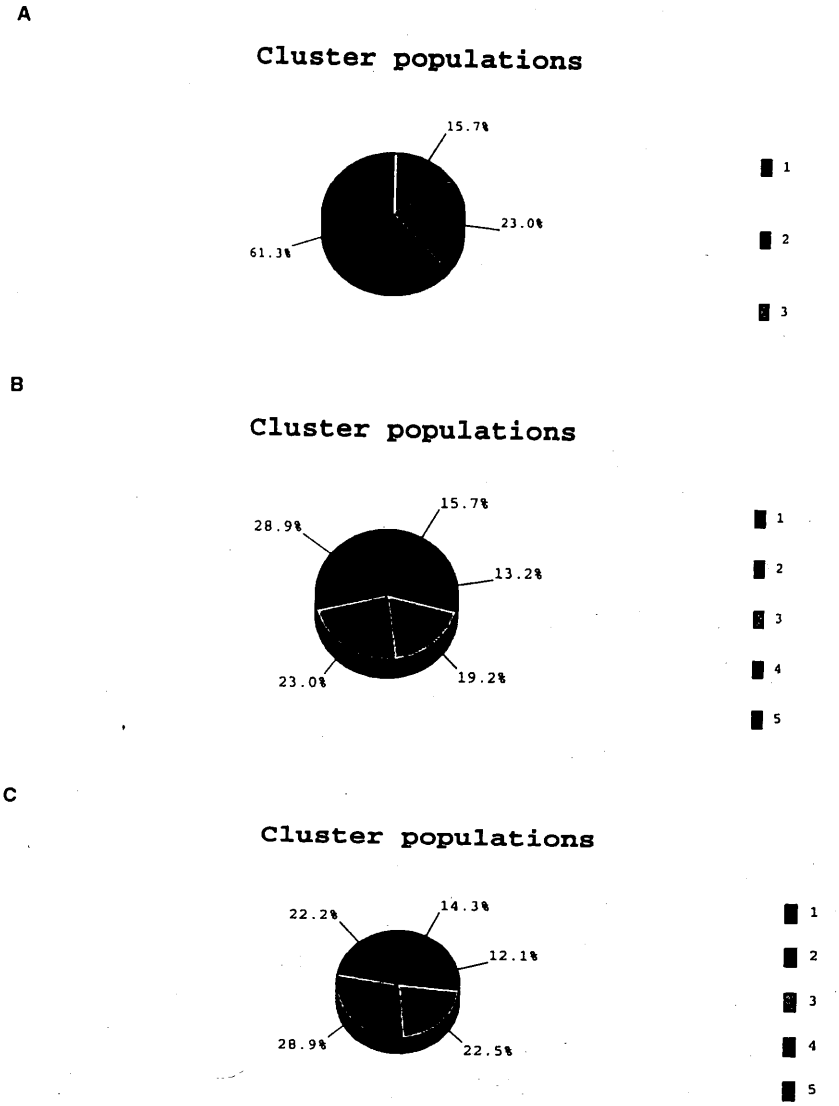

Fig. 3. Pie charts of the number populations of the sample 'kar-win' corresponding to clustering in Fig. 2.

cates, sulphur-containing particles, a cluster of titanium-rich particles, etc. But this process obviously will not provide us with any other cluster of qualitatively new composition. Therefore, we can draw the conclusion that, on a qualitative level, cutting of the dendrogram at $c = 5$ as predicted by AIC and DB seems reasonable.

As regards the quantitative information (the more

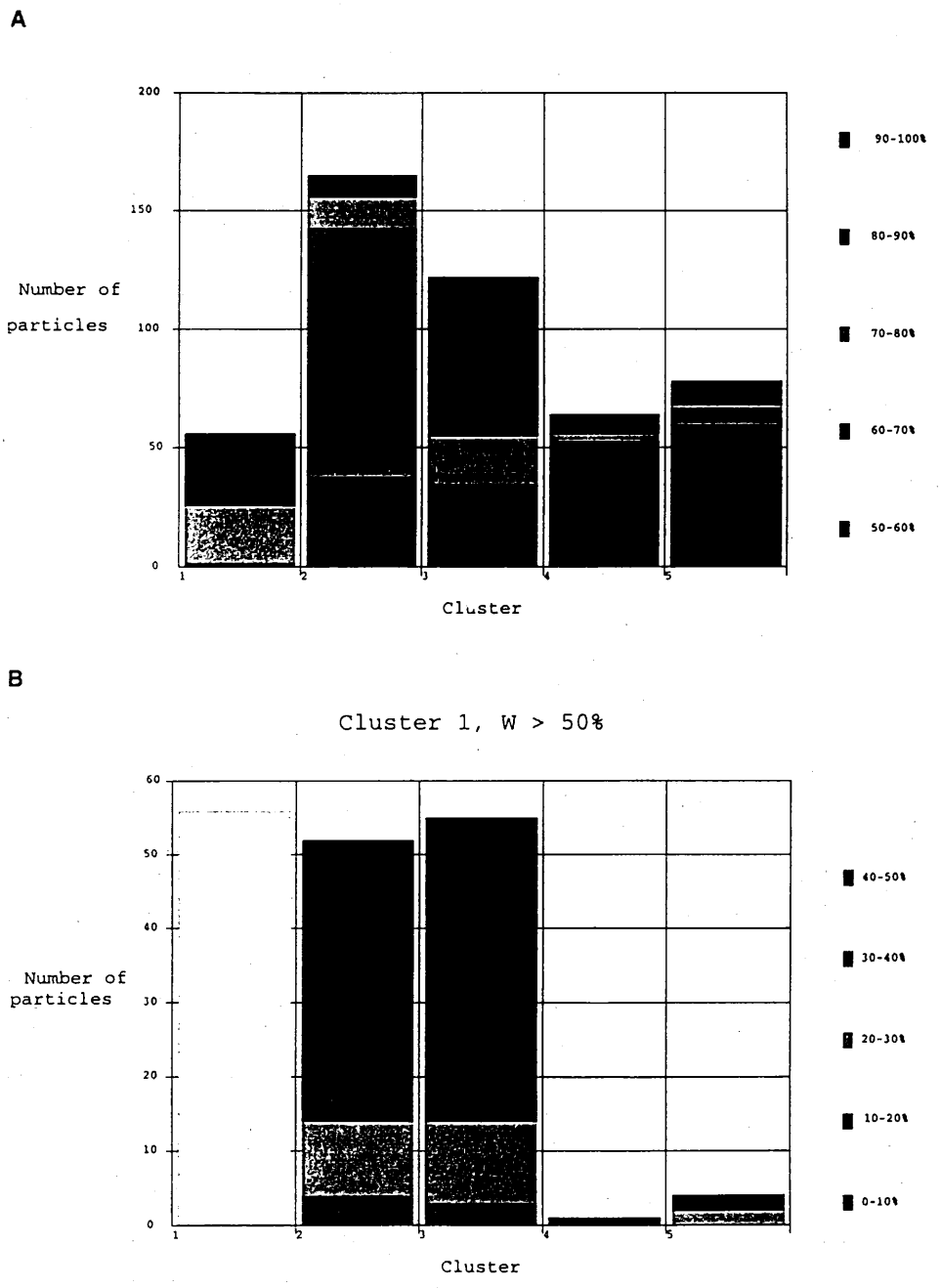

Fig. 4. The results of FCA of the sample 'kar-win' with $c = 5$. (a) Distribution of probability within clusters. (b) Linkage probability bar for cluster 1.

precise cluster compositions and number populations) we refer to NHCA and FCA. The results of NHCA are presented in Fig. 2c and 3c. The comparison with the corresponding results of HCA (Fig. 2b and 3b) shows that the differences are not essential. However, the overall improvement is evident; NHCA decreases the population of the mixed cluster 1 to ca. 22%.

The distribution of the probability for these five clusters is given in Fig. 4a. As it can be expected, cluster 1 is diffuse because the majority of its particles have a low membership coefficients. The degree

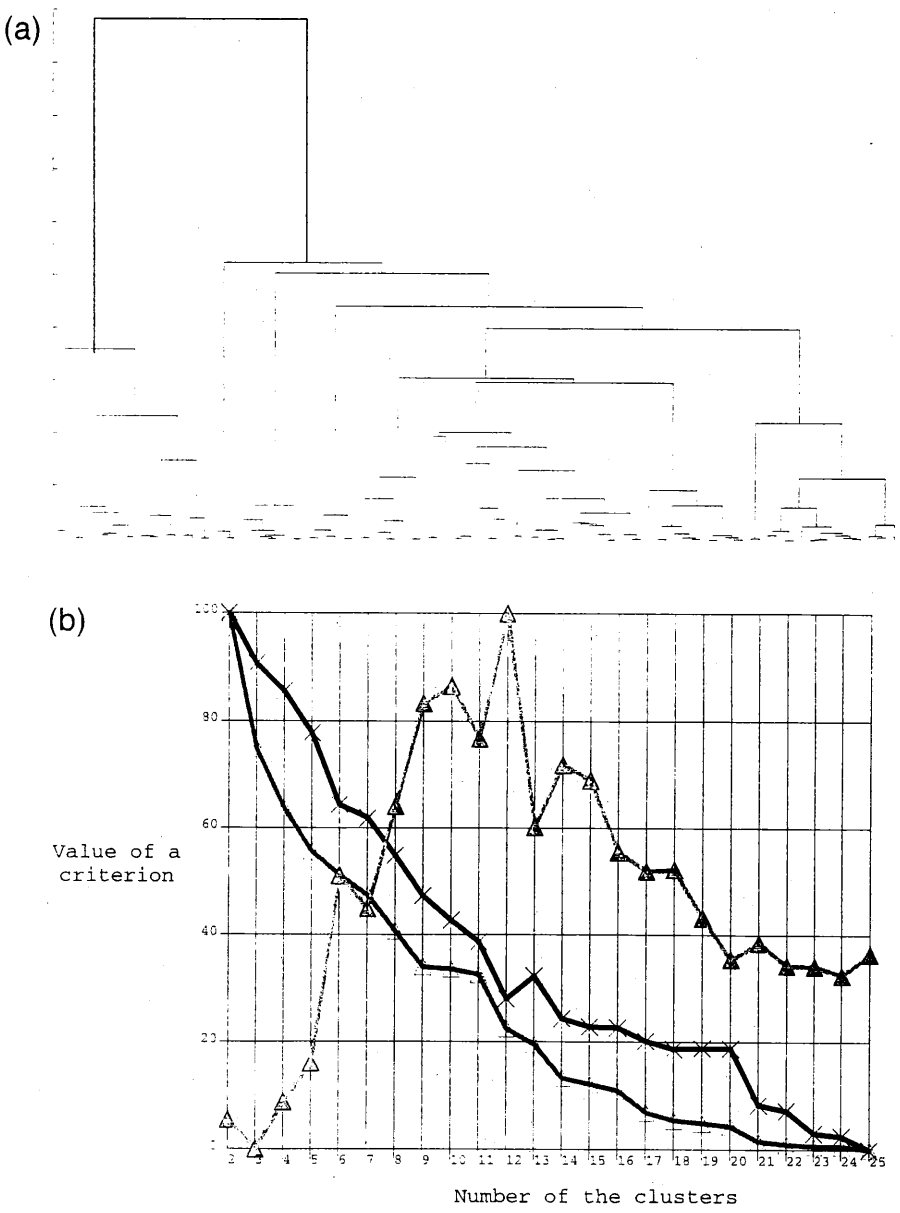

Fig. 5. Dendrogram (a) and the graphs of the clustering criteria (b) for HCA of the sample 'kar-sum'. For key to symbols, see Fig. 1b.

of compactness of the cluster, containing S- and Ca-rich particles and the cluster, containing aluminosilicates, is evidently higher. The clusters, containing the Fe- and the Pb-rich particles are compact ones.

The fact that the cluster 1 is diffuse, has a mixed

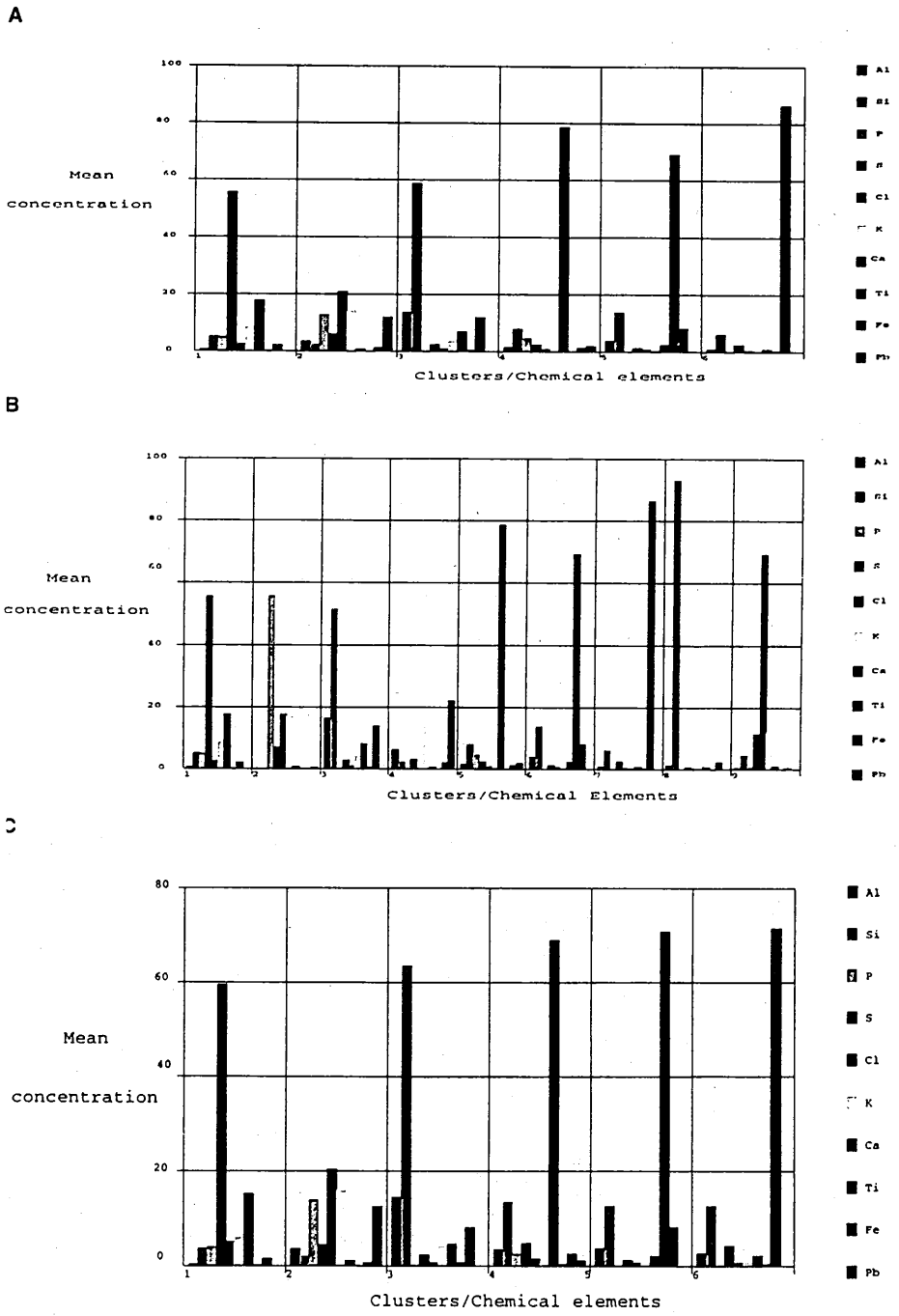

Fig. 6. Composition of the sample 'kar-sum' obtained with (a) $c = 6$ clusters, HCA; (b) $c = 9$ clusters, HCA; (c) $c = 6$ clusters, NHCA.

nature and is a strongly overlapping with the others, is further on confirmed by Fig. 4b, where the linkage probability bar for the cluster is presented. The lower level for the membership coefficients for the particles belonging to the cluster 1 is taken at 50%. The figure shows that nearly all particles which belong to the cluster 1 with a probability above 50% (the bar corresponding to cluster 1) belong at the same time to the aluminosilicates and/or to gypsum clusters. The overlapping with the two other clusters is much less.

The results of cluster analyses allow us to draw the conclusion that aerosol samples collected during the winter campaign at the 'Karasuk' station consist of ca. 29% of aluminosilicates, ca. 22% of particles enriched with S and Ca (mainly gypsum), ca. 12% of particles with very high concentration of lead, ca. 14% of Fe-containing particles. The rest (ca. 22%)

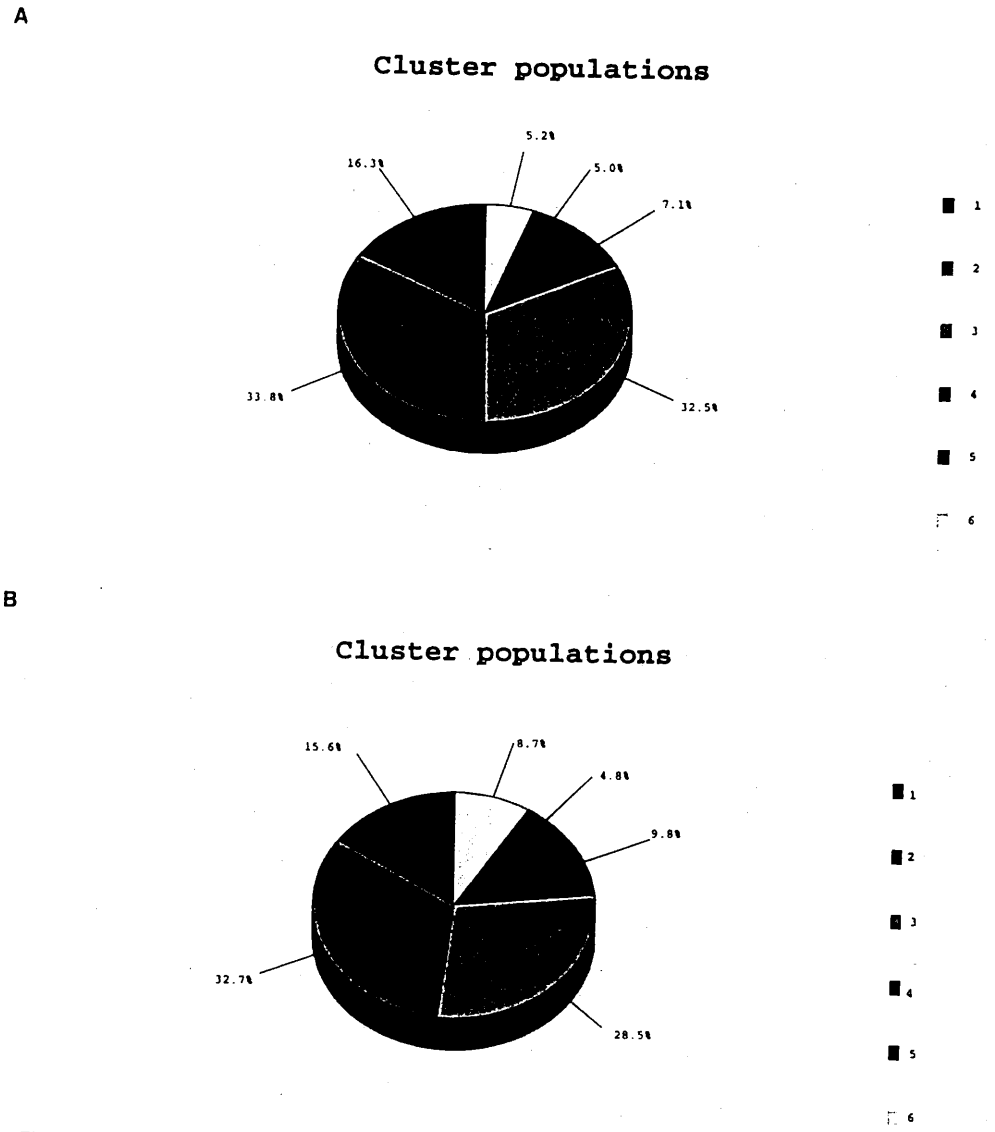

Fig. 7. Pie charts of the number populations of the sample 'kar-sum' corresponding to clusterings in Fig. 6.

are unclassified particles containing some sulphur, calcium, silicon, aluminium and titanium which do not form a certain specific group.

The presence of gypsum is typical for atmospheric aerosols both in remote [20,21] and polluted [22,23] environments. The source of Pb in winter samples can be naturally ascribed to combustion products of anthropogenic origin (mainly coal).

Now let us proceed with the average sample 'kar-sum', composed of EPXMA data from the samples collected during the summer campaign at the same station.

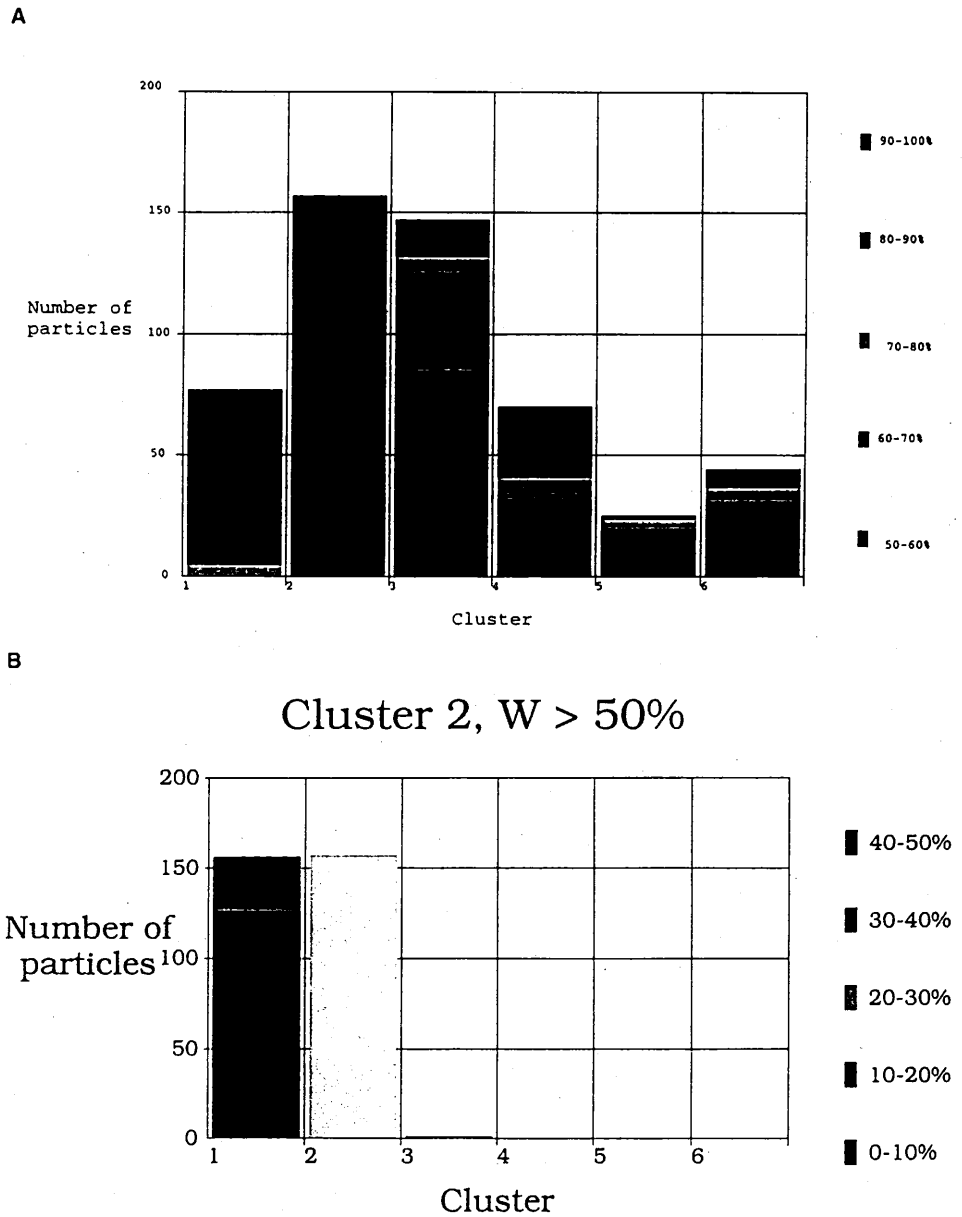

Fig. 8. The results of FCA of the sample 'kar-sum' with $c = 6$. (a) Distribution of probability within clusters. (b) Linkage probability bar for cluster 2.

The dendrogram, representing the hierarchical clustering, and graphs of the clustering criteria are given in Fig. 5. As in the previous case, we may note that the behaviour of AIC and DB criteria, on the one hand, and that of the E criterion, on the other hand, are different. The E criterion has a minimum at $c = 3$ which is, from the point of view of interpretation, an underestimation. AIC has a 'knee' at $c = 6$ clusters, whereas DB has knee at $c = 9$. Let us check which of the possibilities gives the most suitable classification. Comparison of the composition of the clusters obtained for these two clustering (see Fig. 6a and b) shows that clustering with c = 9 is too detailed. Clusters 9 and 2, containing vegetation particles (rich in S, Cl, K and P) are separated; cluster 8, consisting mainly of quartz, is separated from cluster 3, containing aluminosilicates. On the contrary, clustering according to $c = 6$, gives clusters containing mainly gypsum (1), aluminosilicates (3), limestone (4), Ti-rich and Fe-rich particles (5 and 6, correspondingly). Cluster 2 has a mixed nature, encompassing unclassified particles, primarily those from vegetation and of lead. The impossibility to separate a certain part of the Pb-containing particles (encompassed by the cluster 2) which is evidently seen in Fig. 6a, is due to the mixed nature of these particles.

Hence we can conclude that clustering with c = 6 pointed out by AIC fits the experimental data the best. The number populations of the obtained clusters is shown in Fig. 7a.

To get more precise results, let us now proceed with NHCA and FCA. The compositions and number populations of the clusters are given in Fig. 6c and 7b. There are certain changes as compared with the results of HCA, but they are insignificant. The coincidence between the compositions and populations of the clusters obtained by HCA and NHCA is quite good.

FCA shows, on the one hand (see Fig. 8a), that cluster 2 is the most diffuse among the six clusters and, on the other hand (see Fig. 8b), that there is strong overlapping between clusters 2 and 1. The reason for this overlapping is the presence of the common elements: P, S, Cl and K, although in different concentrations. Such an overlapping implies that further division of this cluster will not provide us with a cluster of definitely different composition. Therefore, the conclusions are that (a) cutting of dendrogram at $c = 6$ clusters fits the data structure best, and (b) the sample 'kar-sum', collected at the Karasuk station during the summer campaign in 1992, consists primarily of aluminosilicates (ca.

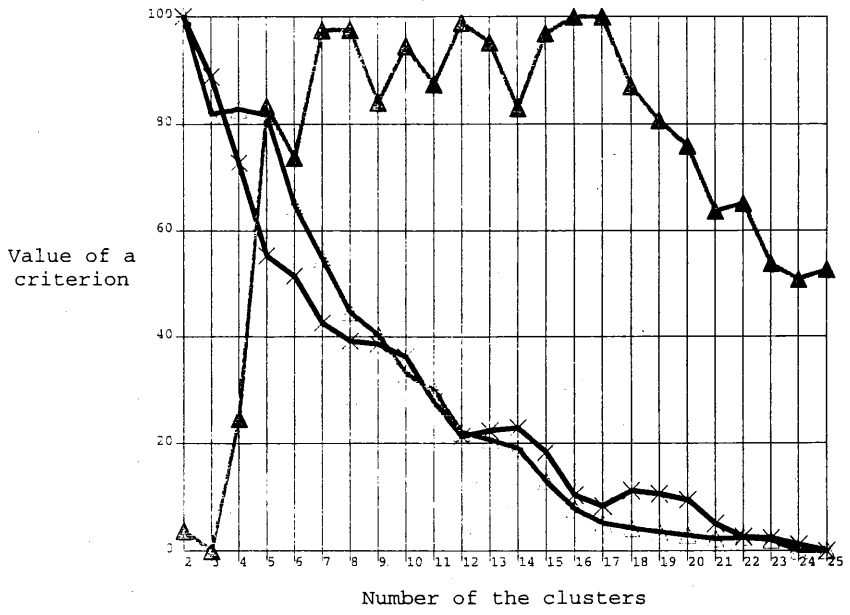

Fig. 9. Graphs of the clustering criteria for HCA of the sample 'klyuchi'. For key to symbols, see Fig. 1b.

28%), S- and Ca-containing particles mostly gypsum (ca. 16%), limestone (ca. 10%), Fe-rich particles (ca. 9%), Ti-rich particles (ca. 5%) and of ca. 33% of unclassified particles (principally, vegetation products and Pb-containing particles).

The last sample to be discussed in the present

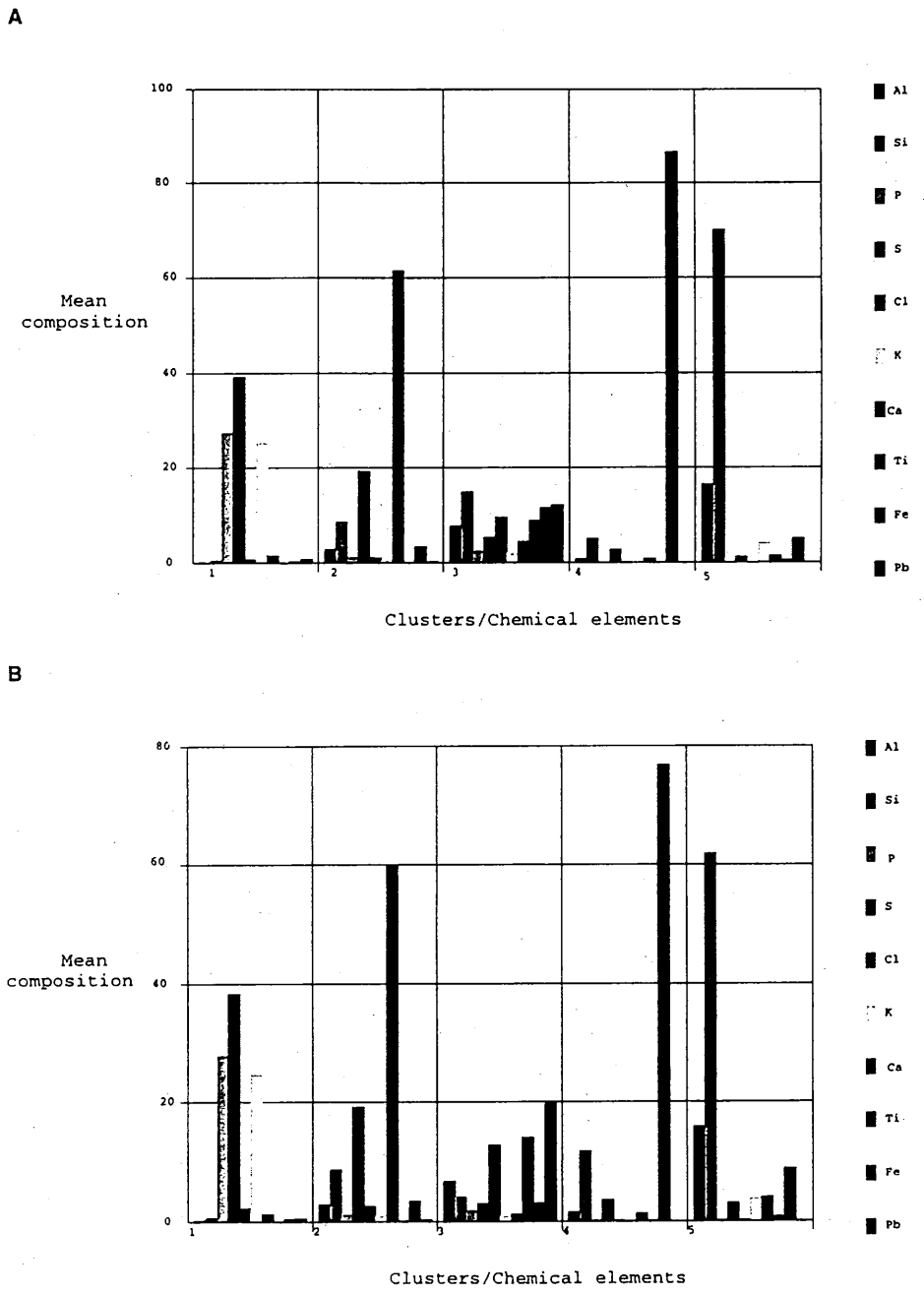

Fig. 10. Composition of the sample 'klyuchi' obtained with (a) $c = 5$ clusters, HCA; (b) $c = 5$ clusters, NHCA.

paper is the average sample 'klyuchi', composed of EPXMA data from the samples collected during the summer campaign at the 'Klyuchi' station.

The graphs of the clustering criteria are given in Fig. 9 (we do not give the dendrogram because it has the same complicated appearance as earlier). As in the previous cases, we may note that the behaviour of AIC and DB criteria, on one hand, and that of the E criterion are different, but now some new features appeared. All three criteria change their behaviour at $c = 5$. The E criterion reaches its local maximum and starts oscillating around this value. Both AIC

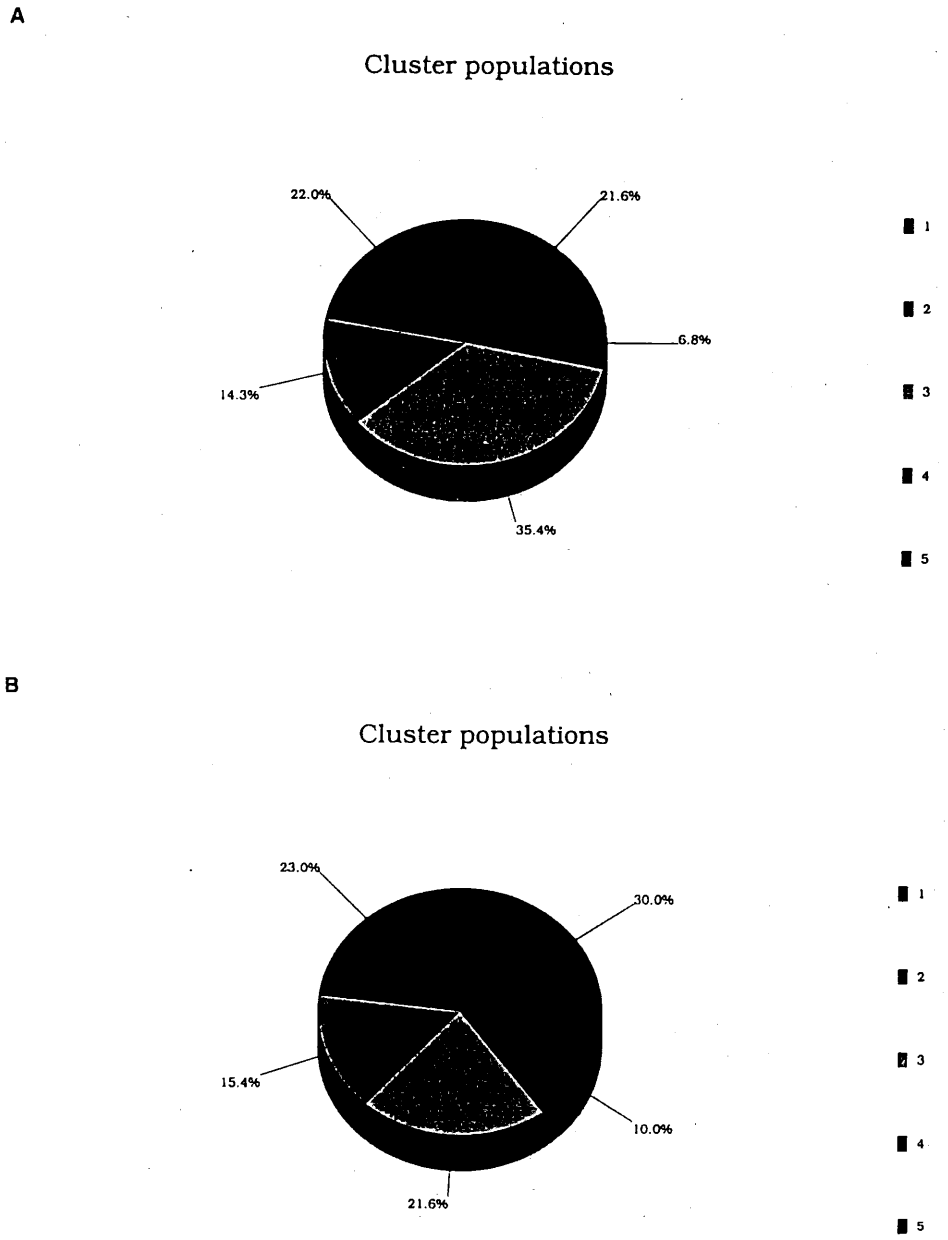

Fig. 11. Pie charts of the number populations of the sample 'klyuchi' corresponding to the clusterings in Fig. 10.

and DB have here 'points of inflection'. The shapes of the curves of these two criteria were essentially different prior to this point and became similar after it. All this denotes that clustering at $c = 5$ fits the experimental data the best. The composition of the correspondent clusters and the pie chart of their

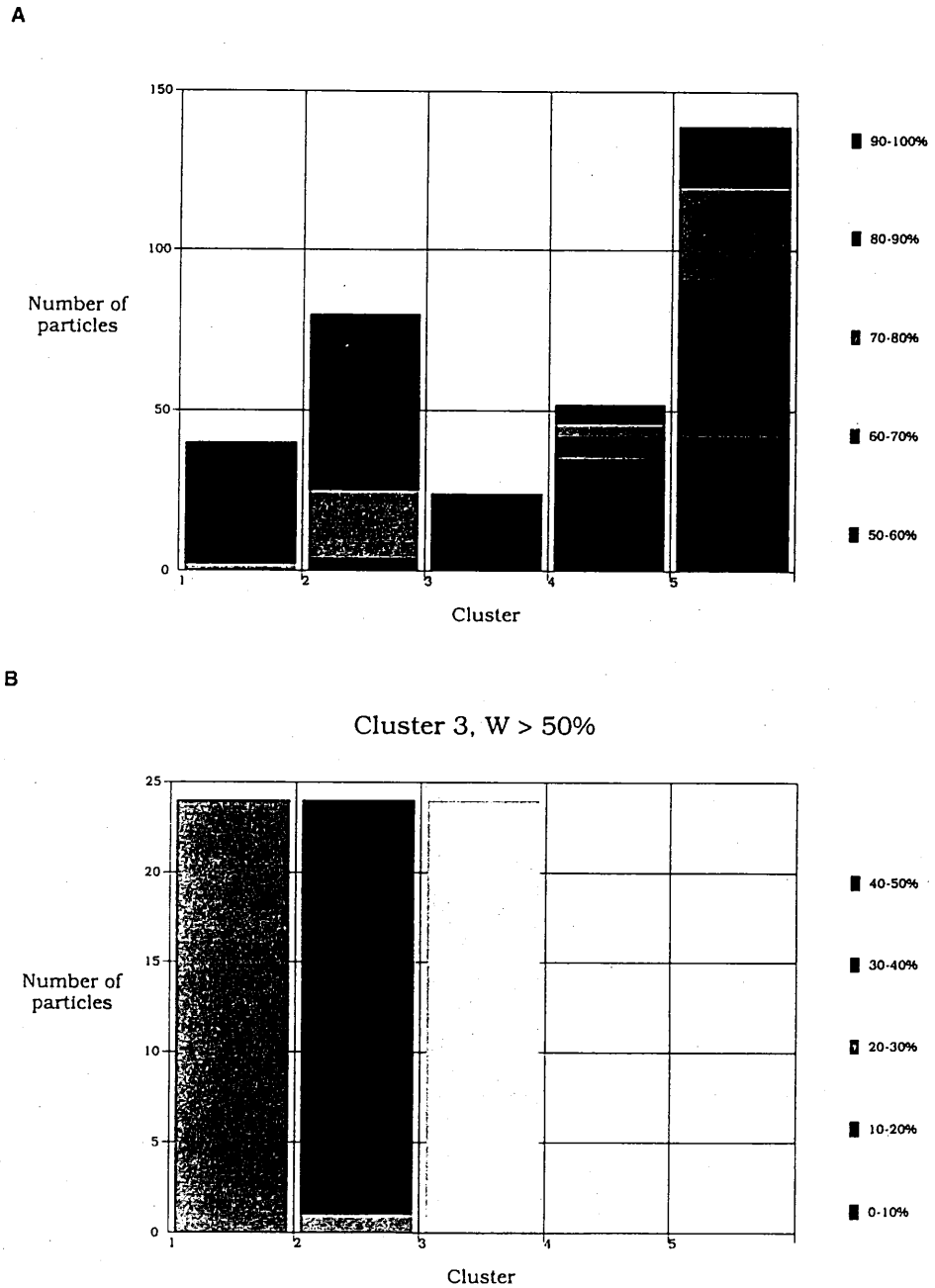

Fig. 12. The results of FCA of the sample 'klyuchi' with $c = 5$. (a) Distribution of probability within clusters. (b) Linkage probability bar for cluster 3.

number populations are shown in Figs. 10 and 11a. The main constituents of the aerosol at the Klyuchi station in summer are vegetation products (cluster 1), gypsum and limestone (cluster 2), aluminosilicates (cluster 5), Fe-rich particles (cluster 4) and mixed and unclassified particles (cluster 3), containing all four above-mentioned classes plus Pb and some minor elements.

NHCA leads to a significant improvement of the classification (see Fig. 10b and 11b). The number population of the cluster 3 (unclassified and mixed particles) decreased from more than 35% for HCA to less than 22% for NHCA, due to the redistribution of the particles among the other four clusters. At the same time, the qualitative and quantitative composition of the clusters did not change significantly, except for cluster 3 where now the presence of Pb, Zn, Ti and Cl became obvious.

The internal structure and interrelationships between the clusters are revealed with FCA (Fig. 12). As in all previous cases we see that a cluster with unclassified and mixed particles (here cluster 3) is the most diffuse one (Fig. 12a) and it overlaps essentially with clusters 1 and 2 (Fig. 12b). Therefore, the further division of this cluster will not lead to the appearance of a cluster with the principally new composition.

Summarising, we can note that the sample 'klyuchi' consists of aluminosilicates (ca. 30%), vegetation products (ca. 23%), particles, enriched with Ca and S, mainly gypsum and limestone (ca. 15%), Fe-rich particles (ca. 10%) and unclassified particles, enriched with Pb, Zn, Ti and Cl (ca. 22%). The large amount of vegetation products, as in the case of the sample 'kar-sum' is due to the season (summer).

The common features among all three samples under investigation is the presence of ca. 30% of aluminosilicates, ca. 15% of S and Ca containing particles (gypsum and/or limestone) and ca. 10% of Fe-rich particles. The seasonal changes lead to the increasing of number of Pb-containing particles and to the appearance of the vegetation products.

5. Conclusions

A method for finding the intrinsic structure of large analytical data sets, based on the combined application of hierarchical, nonhierarchical and fuzzy clustering has been developed.

All mathematical techniques are realized in the form of PC software running under Windows.

The advantages of the method are:

1. simplicity;
2. use of competitive means for revealing the clustering structure, including the incorporation of the experience of the analyst;
3. visual presentation of clustering results.

The utilization of the method is shown on the example of EPXMA data of individual aerosol particles collected during winter and summer campaigns of 1992 in Siberia. The composition of Siberia aerosol is determined.

Acknowledgements

This work was partially supported by the Belgian NFWO and by the Belgian State – Prime Minister's Service – Services for Scientific, Technical and Cultural Affairs (contract MS/06/050). The sampling was carried out in collaboration with of K.P. Koutsenogii and N.S. Bufetov of the Institute of Chemical Kinetics and Combustion, Russian Academy of Sciences, Novosibirsk, Russia.

References

[1] T.W. Shattuck, M.S. Germani and P.R. Buseck, Anal. Chem., 63 (1991) 2646.
[2] P.C. Bernard and R.E. Van Grieken, Anal. Chim. Acta, 267 (1992) 81.
[3] C.B. Lucasius, A.D. Dane and G. Kateman, Anal. Chim Acta, 282 (1993) 647.
[4] T.W. Shattuck, M.S. Germani and P.R. Buseck, in J.J. Bree and P.E. Robinson (Eds.), Environmental Applications of Chemometrics; ACS Symposium Series No. 292; ACS, Washington, DC, 1985, Chap. 9.
[5] P.C. Bernard, R.E. Van Grieken and D. Eisma, Environ. Sci. Technol., 20 (1986) 467.
[6] E. Ruspini, Inf. Control., 15 (1969) 22.
[7] J.C. Bezdek, Pattern Recognition with Fuzzy Objective Function Algorithms, Plenum Press, New York, 1981.
[8] S. Marsili-Libelli, in E. Feoli and L. Orloci (Eds.), Computer Assisted Vegetation Analysis, Kluwer, Amsterdam, 1991, p. 173.
[9] F. Ehrentreich, M. Nofz and H.-G. Bartel, J. Chemom. Intell. Lab. Syst., 15 (1992) 61.

[10] I. Bondarenko, B. Treiger, R. Van Grieken and P. Van Espen, Spectrochimica Acta Electronica, submitted for publication.
[11] D.L. Massart and L. Kaufman, The Interpretation of Analytical Data by the Use of Cluster Analysis, Wiley, New York, 1983.
[12] A.K. Jain, Algorithms for Clustering Data, Prentice Hall, New York, 1991.
[13] Y. Sakamoto, M. Ishiguro and G. Kitagawa, Akaike Information Criterion Statistics, KTK Scientific Publishers, Tokyo, 1986.
[14] I. Bondarenko, H. Van Malderen, B. Treiger, P. Van Espen and R. Van Grieken, Chemom. Intell. Lab. Syst., 22 (1994) 87.
[15] J.C. Bezdek, R. Ehrlich and W. Full, Comput. Geosci., 10 (1984) 191.
[16] S.Z. Selim and M.A. Ismail, Pattern Recogn., 17 (1984) 559.
[17] P.J. Rousseeuw, M.-P. Derde and L. Kaufman, Trends Anal. Chem., 8 (1989) 249.
[18] H. Van Malderen and R. Van Grieken, unpublished results, Antwerpen, 1994.
[19] B. Raeymaekers, Ph.D. Thesis, UIA, Antwerpen, 1986.
[20] P. Artaxo, H. Storms, F. Bruynseels, R. Van Grieken and W. Maenhaut, J. Geophys. Res., 93 (1988) 1605.
[21] M.O. Andreae, R.L. Charlson, F. Bruynseels, H. Storms, R. Van Grieken and W. Maenhaut, Science, 232 (1986) 1620.
[22] C. Xhoffer, P. Bernard, R. Van Grieken and L. Van der Auwera, Environ. Sci. Technol., 25 (1991) 1470.
[23] H. Van Malderen, C. Rojas and R. Van Grieken, Environ. Sci. Technol., 26 (1992) 750.

ELSEVIER

Spectrochimica Acta Part B 50 (1995) 1787–1803

SPECTROCHIMICA ACTA PART B

Optimisation of total-reflection X-ray fluorescence for aerosol analysis

Jasna Injuk, René Van Grieken*

Department of Chemistry, University of Antwerp (UIA), B-2610 Antwerp, Belgium

Received 18 March 1995; accepted 2 June 1995

Abstract

The capabilities of total-reflection X-ray fluorescence (TXRF) analysis were investigated to develop an efficient, simple, rapid and low cost analytical method for aerosols. The technique involves direct impaction of airborne particulate matter on the quartz sample-reflector discs for TXRF. Special attention was paid to bounce-off effects, and hence the aerosol size distributions for the impactor stages; influence of siliconizing the quartz discs on the adhesion of particles; choice of the internal standard; local distribution of the material deposited on the quartz disc; and alternative materials for aerosol collection. Moreover, the proposed method could be used in combination with a one-stage impactor for total aerosol mass collection and analysis.

Keywords: Aerosol; Air analysis; Total-reflection X-ray fluorescence

1. Introduction

Experimentally, total reflection of X-rays was first discovered by Compton in 1923, when the reflection of X-rays at angles of some milliradiants on a polished silver or glass mirror was demonstrated [1]. Fifty years later total-reflection X-ray fluorescence was initially suggested as an analytical method by Yoneda and Horiuchi [2] in 1971, when they implied a pattern for the background reduction by depositing samples on an optically flat surface. Subsequently, Wobrauschek and Aiginger applied the method and clarified the physical principles [3]. In the 1970s Knoth and Schwenke succeeded in developing a compact, stable and easily adjustable total-reflection module, which was the decisive step towards introduction of the method into analytical practice and commercialization [4]. This was superseded by an updated version with several mirrors for multiple reflection, resulting in further reduction of spectral background and hence further improvements of the detection limits [5]. Since then, developments of TXRF have been very rapid and have led to the development of commercially available units with detection limits in the picogram range [6]. Various excitation techniques were employed, such as X-ray tubes with a rotating anode and with various anode materials [7]. In order to gain access to even lower concentration levels with regard to all elements, polarized X-ray radiation was utilised as an excitation source. Because of its outstanding features like brilliance and

* Corresponding author.

SSDI 0584-8547(95)01375-X

polarization, synchrotron radiation is obviously the best source of polarized X-rays, but these setups are seldom available [8].

All this resulted in advanced applications of TXRF today. Currently, approximately 30 laboratories are working with commercial TXRF instruments on a variety of analytical applications. These cover the areas of estuarine and marine water quality management and research, chemical oceanography, air pollution studies, mineralogical investigations, chemical oceanography, medicine, wafer materials in the semiconductor industry and layer structures in materials technology [9].

The use of TXRF in the analysis of aerosol samples deposited on a filter support was first reported by Ketelsen and Knöchel in 1984 [10]. Wet decomposition of the sample material with HNO_3 in a closed system and subsequent evaporation of an aliquot of the solution on the sample carrier yielded detection limits down to 0.3 ng cm^{-2}. The reproducibilities for all detected elements were between 5% and 25%. Similar results were obtained when a low-temperature oxygen plasma was employed for direct ashing of the filters. The systematic losses of the elements, for both methods, were investigated with radiotracers as well as with inactive techniques and a good agreement was achieved in most cases. In all the other similar studies, the airborne particles collected for a long sampling time, were usually removed from the sampling support, brought into solution and transferred to reflector holders.

A new method for the determination of size-segregated atmospheric trace metal concentrations in small air volumes (0.5 m^3; 1 h sampling time) was proposed by Schneider in 1989 [11]. The TXRF sample carrier plates were mounted in a six-stages cascade impactor. In that way a stream of particle-laden air was directed at the sample holders for TXRF. Then a drop of solution with Y as an internal standard was pipetted upon the spot and allowed to dry. Elements like S, K, Ca, Ti, V, Cr, Mn, Fe, Ni, Cu, Zn, Hg, Pb, Se, Br and Rb were detected with concentrations of e.g. 2.7 ng V m^{-3} and 1 ng Pb m^{-3}. The same procedure, was followed by Salvà et al. [12], but the results were hampered by erosion of the stainless steel cascade impactor itself (sampling time was between 3 and 4 h).

When multi-staged impactors are used to achieve size-fractionated collection of particles, a particle impacting on a surface experiences a complex process of losing and recovering energy. This process has been studied by several investigators to understand and describe the phenomena of particle reentrainment and bounce-off from impaction surfaces [13]. Reentrainment is the resuspension of a previously collected particle from the surface into the gas flow due either to the motion of the air over the surface or to impact of an incoming particle. When a particle strikes a surface, its kinetic energy is partitioned into energy lost in plastic deformation and energy stored in elastic deformation. The overall effects for the particle which does not stick are: it can bounce off back into the gas stream, break into fragments, or cause a previously adsorbed particle to be knocked off into the gas stream. In all three cases the collection efficiency is lowered and the net effect is referred to as bounce-off. To minimize these problems, the surface of the impactor is often coated with soft, energy-absorbing substance such as oil, grease, plastic film, water, resin, parafin or paper. A summary of the types of agents

Table 1
Review of TXRF analysis application for atmospheric particles

Preconcentration step	Type of sample	Reported detection limits	Ref.
Spraying	Aerosols	10–100 ppm	[17]
			[18]
Aqueous suspension	Aerosols on Al foil	0.1–3 ppm	[19]
Pressure digestion	Aerosols on filter	0.2–6 ng cm^{-2}	[20]
Pressure digestion	Aerosols on filter	1 ng/filter	[16]
Ashing	Aerosols on filter	0.3 ng cm^{-2}	[10]
Tetrahydrofurane suspension	Aerosols on filter	0.5–10 ng/filter	[12]
Open digestion	Aerosols on filter	0.3 ng cm^{-2}	[10]
Open digestion	Aerosols on filter	10–100 pg m^{-3}	[21]
None	Aerosols on TXRF sample holder	1 ng m^{-3}	[11]
None	Aerosols on TXRF sample holder	0.5–10 ng/filter	[12]

used to minimize bounce-off and reentrainment is given by Marple and Willeke [14] and Cahill [15].

In this work, we have applied the concept introduced by Schneider [11] for the aerosol impaction and analysis, but a further evaluation of the method is achieved with respect to: bounce-off effects of the aerosols particles during the collection and, consequently, the collection efficiency of the TXRF holders for airborne particles, the influence of silicone solution on the adhesion of the particles, the choice of an internal standard, the local distribution of the material deposited on the quartz disc and alternative materials for aerosol collection. Correct measurements of the size distributions in impactors is of a great importance in all atmospheric deposition studies since the deposition velocity, used for calculation of dry deposition fluxes, is particle size dependent [16].

The literature review given in Table 1 illustrates the capability of TXRF for aerosols and the different analytical approaches that have been used. It also shows that, hitherto, direct analysis of impaction surfaces has only been discussed in two papers.

2. Experimental section

2.1. Instrumentation

The spectrometer used is a slight modification of the TXRF module prototype developed in the Atominstitut in Vienna [22]. It consists of an Al base plate (100 mm × 500 mm), mounted on top of the high voltage generator housing. On the Al base, at first a brass collimator with two 10 mm long collimating slits was mounted and adjusted. In our case, the 2 kW Philips Mo tube used has a fine focus, 8×0.04 mm^2, so the separation of the slits was set at 0.05 mm. As a precaution against stray radiation scattered from the first collimating slit, one end of the collimator was modified in a way that it fitted right into the X-ray tube window. In the primary beam path, a cut-off reflector (a brass piece that holds a polished quartz Synsil block of $50 \times 20 \times 5$ mm^3) was installed permitting it to alter the spectral distribution of the excitation radiation. High-energy photons contribute to an increased low-energy background in the detector crystal. This undesired noise contribution can be suppressed by filtering out the high energy photons when the total reflection conditions are established. In our case, for a Mo anode with characteristic radiation energies of Kα = 17.48 keV and Kβ = 19.60 keV, a cut off energy of 20 keV is convenient. Therefore, the corresponding cut off angle below which total reflection occurs is 1.6 mrad. After correct adjustment of the cut off angle, the passing beam with its original spectral distribution was absorbed by a Pb-beam stopper attachment on the unit, so that only the reflected beam was propagated versus the sample. The intensity losses are negligible as total reflection offers a high degree of reflectivity of up to 90% or more. The sample support is mounted in a special Al-plate, which is precisely adjustable by three micrometer screws to allow perfect realization of the total reflection conditions. Here, the beam separation was arranged to be less than 2 mrad. To have a better defined plane, three steel balls (∅ 0.5 mm) served as a three-point support for the sample reflector discs. Through a hole in the Al-base plate, a Kevex Si(Li) detector, with a resolution of 165 eV at the Mn Kα line was positioned with the Be-window looking upward, at a distance of about 4 mm from the sample on the polished quartz disc. The detector is equipped with an ion getter pump and interfaced to a PC via a multichannel analysis card (Canberra System 100). The equipment is designed to give a mechanically stable unit together with the X-ray tube, the TXRF unit and the detector. Once the adjustments were completed, the measurements in series were free of any instrumental problems. All samples were irradiated for 500 s, at 20 mA and 40 kV. X-ray spectrum evaluation was done with the computer programme AXIL [23].

Electron-probe micro-analysis (EPMA) with a JEOL Superprobe JXA-733 unit was used to determine the size of the aerosol particles deposited on each impactor stage and to investigate the spatial distribution of the internal standard within the sample spot.

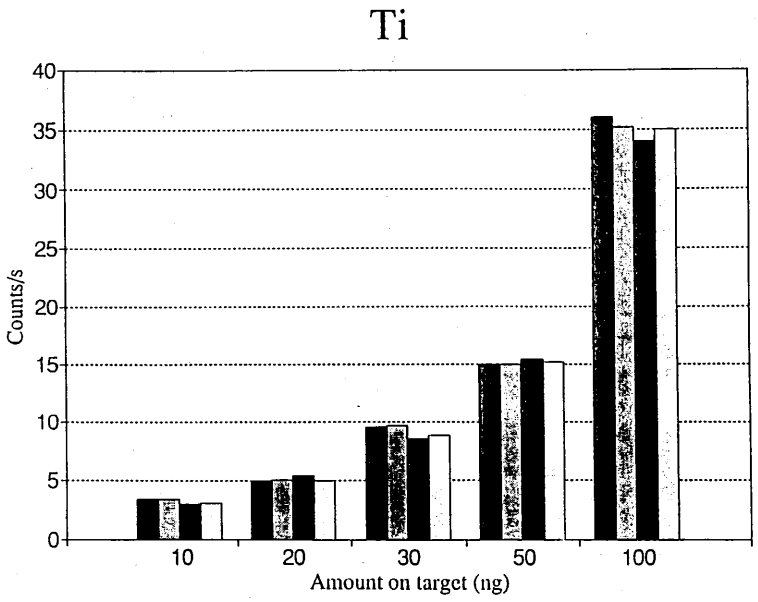

Fig. 1. Four individual measurements of five Ti solutions; drop volume 5 μl. Working conditions: 40 kV, 20 mA, 500 s.

2.2. Standardization

To determine the linearity of the technique and the sensitivity factors, multielement standards (Merck) were used.

2.3. Sample collection and preparation

More than 200 mass-segregated airborne samples were collected at a station located approximately 100 m from the Belgian coastal line in Blankenberge. An improved sampling scheme, which allows quantitative collection of large particles without problems of a variable cut-off with the wind direction and wind speed, was achieved by taking samples in a continuous forced air flow inside a wind tunnel positioned always in a windward orientation [24]. The

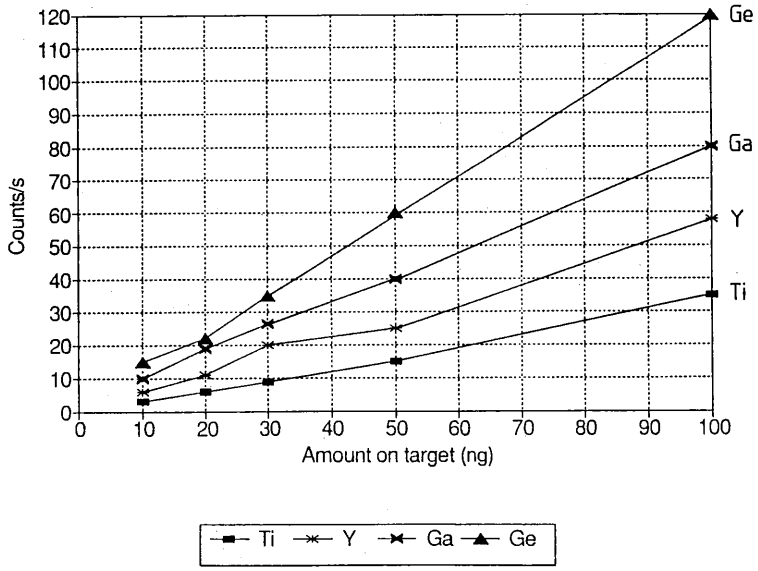

Fig. 2. Calibration curve for Ti, Ge, Y and Ga; mean values of the six analyses. Drop volume 5 μl. Working conditions: 40 kV, 20 mA, 500 s.

use of seven stages Battelle cascade-impactor (cut-off diameters: 0.25, 0.5, 1, 2, 4, 8, 16 μm; flow-rate: 1.2 l min^{-1}) provided information of the mass-size distribution on the aerosols collected during each sampling period. As a sample support for the direct impaction of airborne-matter, TXRF reflector holders were used (Synsil, 30 mm diameter, 3 mm thickness). Only small mechanical changes were necessary to fit them in the cascade impactor. Prior to the collection, siliconizing of the quartz discs was achieved by dispersing a 5 μl drop of silicone solution (SERVA, Polylab). The aerosol deposits were concentrated right in the middle of the discs. Subsequently, the aerosol deposit was supplied with a 5 μl droplet containing 25 ng of Ga as an internal standard and the drop was evaporated in an exsiccator under reduced pressure. All handling was done manually and in a laminar flow clean bench; no Latex gloves were used, because they led to remarkable Zn contamination.

The following cleaning procedure for the quartz discs was applied prior to all aerosol collections.

(a) Removal of the spot with a soft tissue moistened with detergent solution (RBS 50).

(b) Rinsing of the discs with Milli-Q water.

(c) Gentle boiling for 30 min in a mixture (1:1) of Milli-Q water and sub-boiling concentrated HNO_3 in specially constructed teflon racks.

(d) Further rinsing with Milli-Q water.

(e) Rinsing with acetone and coating with silicone solution.

Plexiglass discs were used only for one sampling campaign and thrown away after analysis.

For aerosol samples, collected on Nuclepore filters, microwave acid digestion was used. Three heating cycles of 10 min, with supra pure concentrated (70%) HNO_3 (3 ml) and HF (1 ml) acids in a high-pressure digestion vessel were followed by evaporation for 30 min. Then, the sample residue was supplied with 1 ml Milli-Q water, ultrasonically treated for 10 min and finally an aliquot of 5 μl was transferred to a quartz carrier, vacuum dried and measured. A Ga internal standard was added prior to the digestion procedure.

2.4. Quality control

To ensure a good accuracy and precision of measurements, as a rule a home-made standard for Cr, Co, Zn and Ga was measured before and after every series of aerosol samples.

3. Results and discussion

3.1. Linearity check of the system

Quantitative analysis by TXRF is feasible if the system reflects the linear increase in analyte concentration also as a linear increase in the observed intensity. Thus, five sample solutions

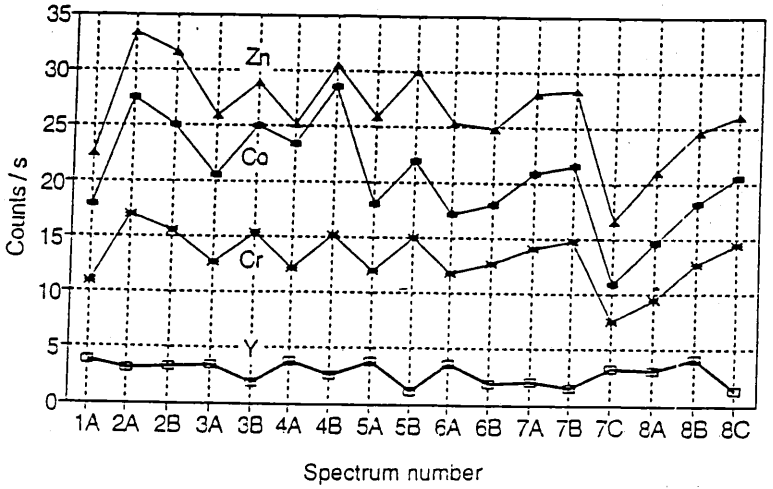

Fig. 3. Variations in count rates for eight samples each containing 25 ng of Cr, Co, Zn and Y; drop 5 μl. A, B, C indicate different positions of the quartz disc in sample holder.

in the concentration range from 2 to 20 ppm were prepared for the elements Ti, Ge, Y and Ga. At least four spectra were recorded for each elemental concentration. In Fig. 1 an example for individual measurements of five Ti solutions is given. Then, the set of counts for each element was averaged, as it is displayed in Fig. 2. Based on regression analysis, the linearity for Y was found to be very poor; the observed count rates were quite variable and lower than expected.

3.2. Selection of the internal standard

The variations in Y count rates were not only observed for different samples; even the same sample spot gave widely varying results after turning the disc in the sample holder support

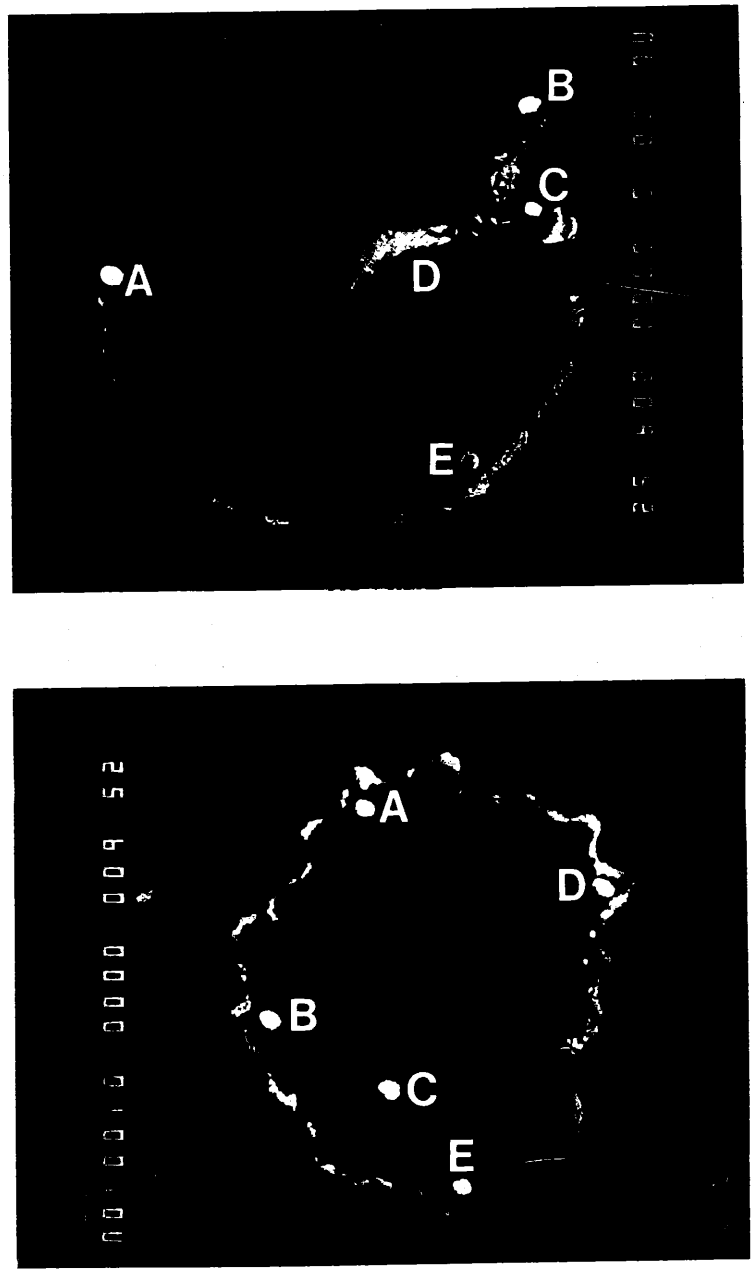

Fig. 4. Backscattered electron images of the two 5 μl drops. (a) Drop I: 5 ppm of Ti, Co, Ni, Y; (b) Drop II: 5 ppm of Ti, Co, Ni, Ga. Investigated spots are indicated with A, B, C, D, E.

Table 2
EPMA results of the elemental distribution in the two 5 μl drops presented in Figs. 4a and 4b; 5 ppm of Ti, Co, Ni, Y (drop I) and 5 ppm of Ti, Co, Ni, Ga (drop II); the given numbers correspond to the X-ray intensity ratios; investigated spots are indicated with A, B, C, D, E

Drop I	Ti/Y	Co/Y	Ni/Y	Drop II	Ti/Ga	Co/Ga	Ni/Ga
A	13.6	11.9	11.3	A	1.7	1.9	1.5
B	3.1	0.1	ND	B	2.1	1.8	1.5
C	15.8	17.7	17.1	C	1.9	1.1	1.0
D	12.7	12.9	12.8	D	1.7	1.0	0.9
E	63.6	80.3	69.2	E	1.8	1.3	1.1
Mean	21.8	24.6	27.6		1.8	1.4	1.2
St.dev.	21.4	28.4	24.1		0.1	0.4	0.2

for about 180°. Fig. 3 displays the measurements of eight samples of a same standard solution containing 25 ng of Cr, Co, Zn and Y in a 5 μl drop. Characters A, B and C stand for different rotations of the same sample. Between the individual spectra the observed variations for the intensities of the elements Cr, Co and Zn mostly followed the same trend, whereas Y showed the opposite trend in count variations.

Although a data set of four samples is not representative enough for a statistical assessment of count rate reproducibilities, one has to consider it as a realistic estimate of standard working procedures. Routine analysis in a laboratory hardly comprises more than four measurements of one sample. Thus an inhomogeneous distribution of Y relative to the other elements on the spot was assumed.

In view of the non-linearity and irreproducibility of Y, the elements Ge and Ga were examined as possible internal standards. Ge seemed to be appropriate at first, but anomalities in the relative sensitivity curve (defined as the ratio of the counts per second per nanogram to those of an arbitrarily selected reference element) were related to the fact that some Ge halides have a very high volatility (e.g. $GeCl_4$ has a boiling point of only 84°C). This was reflected in the extraordinarily high relative efficiency values for Cr, Co and Zn when Ge was used, because the standard solution of these three elements also contained Cl as counterion. As a consequence, Ge was lost during evaporation of the drop in the exsiccator. Because of this observation, Ge was rejected and the properties of Ga were investigated. Boiling points were found to be high

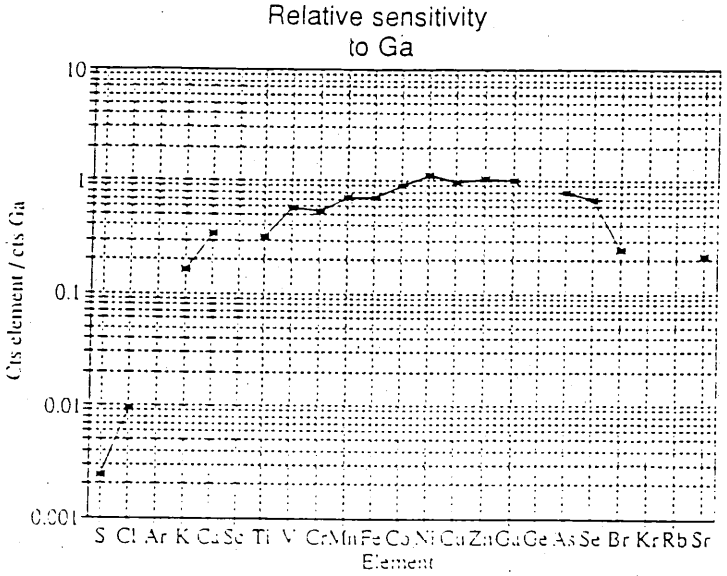

Fig. 5. Relative sensitivities of elements to Ga for excitation with a Mo-tube. Working conditions 40 kV, 25 mA, 500 s.

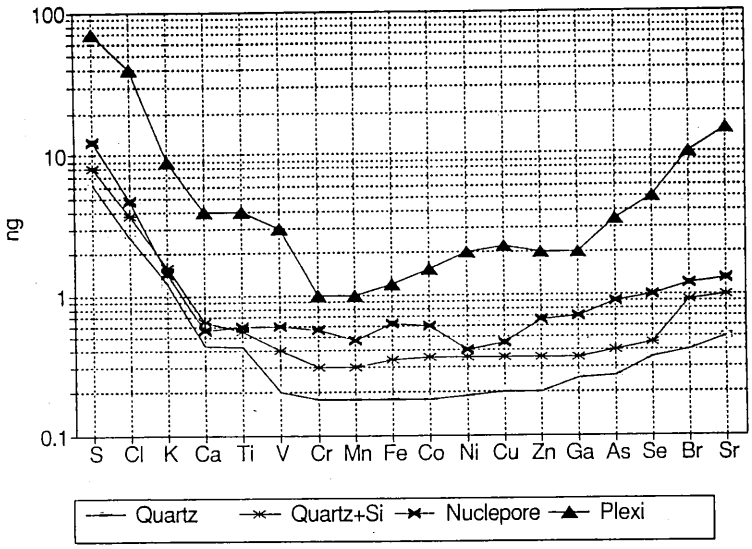

Fig. 6. Limits of detection (*DL*) for aerosol samples collected on different substrates: Quartz, clean disc; Quartz + Si, siliconized quartz disc; Plexi, plexiglass disc; Nuclepore, digested. Working conditions: 40 kV, 20 mA, 500 s.

enough not to cause losses during sample preparation. However a certain drawback was the partial overlap of the Zn Kβ peak with Ga Kα, but since Zn was detected almost always in minor amounts, this was tolerable. Multiple analysis of several Ga solutions showed sufficient linearity and reproducibility.

For the non-linear behaviour of Y, our presumption was that a certain spatial separation of Y from the other elements occurred because of fractionated crystallization during the drop evaporation resulting in heterogeneous excitation/detection in the geometry of the used Atominstitut TXRF unit. Because the Y Kα line is close to the cutoff energy of our system, only small changes of the cutoff angle (owing to mechanical instability of the system) can introduce significant differences in the fluorescence signal. In order to investigate this phenomenon, the elemental distributions within one sample drop were analyzed by EPMA. Of standard solutions of Ti, Co, Ni, Ga and Y, two 5 μl drops were spotted on plastic discs (PE) commonly used for EPMA. Drop I consisted of a 5 ppm solution of Ti, Co, Ni and Y and its backscattered electron image is given in Fig. 4a. Drop II was a 5 ppm solution of Ti, Co, Ni and Ga, and it is presented in Fig. 4b. The results of selective measurements of elemental X-ray intensities at five different random places (A, B, C, D, E) within the deposits of the two drops are summarized in Table 2. The Y distribution was found to be quite inhomogeneous, that has resulted in large standard deviations, while results involving Ga as an internal standard were satisfactory.

3.3. Acquisition of the sensitivity curve

To determine the relative sensitivity factors R_{ef} required for quantification, multielement standard solutions were prepared. Starting from a 20-fold diluted standard solution of 100 ppm, an aliquot of 5 μl was deposited on a clean quartz disc, dried and measured. Each spot was analyzed a second time after the disc had been rotated for about 180°. The values for R_{ef} were averaged and displayed in Fig. 5.

3.4. Determination of limits of detection

The limits of detection (*DL*) were calculated using the spectral data of the measured multielement standard solution. With the help of the AXIL program, the channel values of the peak limits (CH_1, CH_2), their corresponding counts (*a*, *b*) and the peak area of the Kα peaks were obtained. The background was calculated as the trapezoid area below the Kα signal peak

$$BG = \frac{a + b}{2}(CH_2 - CH_1) \quad (1)$$

The limits of detection of our system were obtained, after IUPAC definition as

$$DL = \frac{3\sqrt{BG}}{E_f} \quad (2)$$

where E_f is expressed in counts per 1 ng of analyte. The limits of detection of our TXRF unit with the Atominstitute module, for standard solutions, were in the range 0.2–0.5 ng for most heavy metals.

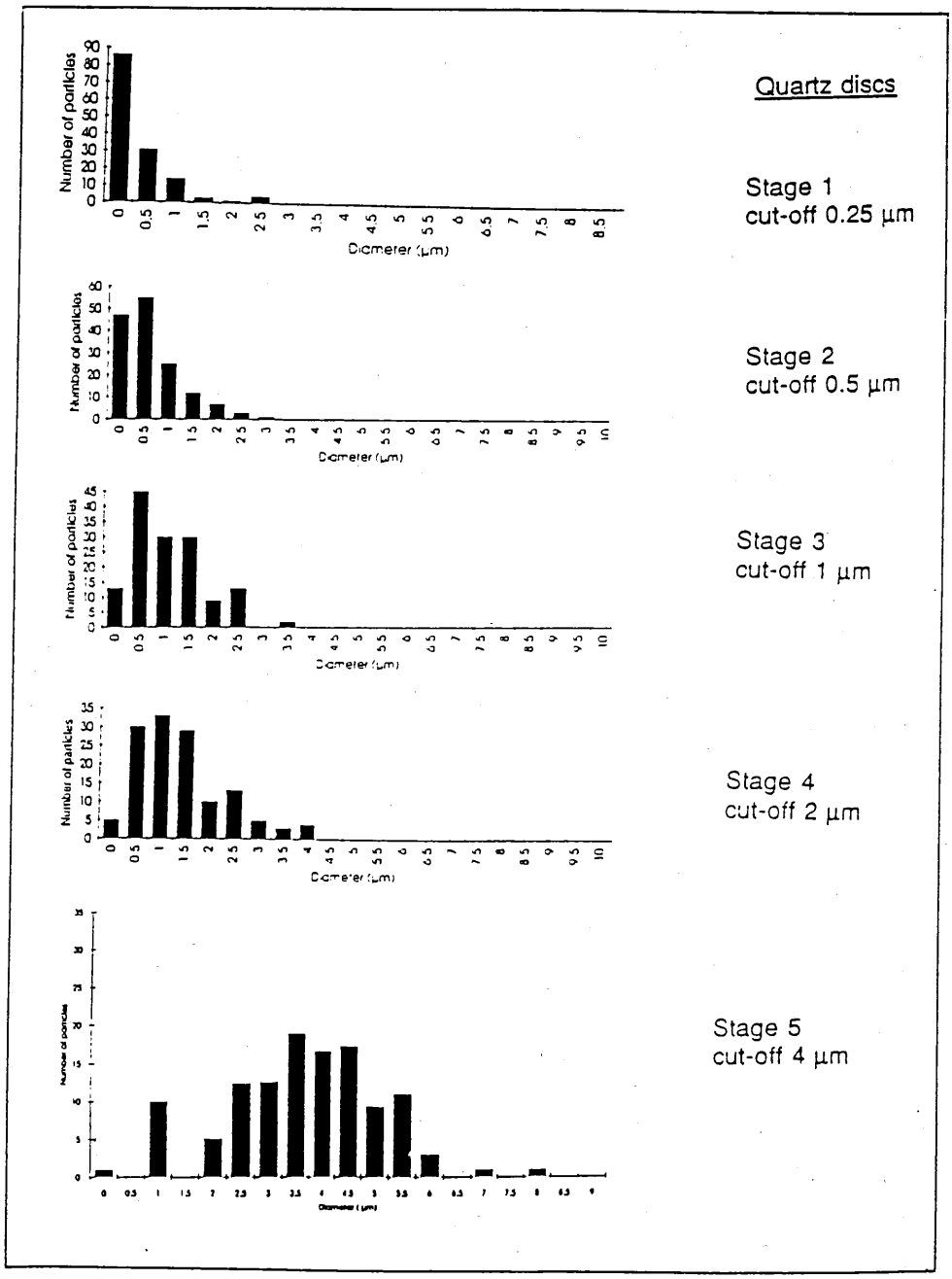

Fig. 7. Size distributions of aerosol particles collected directly on quartz discs for TXRF.

Table 3
EPMA results for the size distributions of aerosol particles collected directly on the quartz discs by means of a Battelle cascade impactor

Stage	Cut-off diameter (μm)-ad	Mean particle diameter and st. dev. (μm)	Analysed area (mm^2)
1	0.25	0.28 ± 0.20	0.050
2	0.5	0.81 ± 0.68	0.034
3	1	1.18 ± 0.91	0.064
4	2	1.36 ± 1.46	0.058
5	4	3.52 ± 2.84	0.068

Key: ad means aerodynamic diameter.

3.5. Choice of sample support

The properties of different supports for airborne particles with respect to the detection performance of TXRF, have been investigated. The aerosols were collected on different substrates: quartz discs with and without silicone solution, plexiglass discs and supported Nuclepore filters. The aerosols loaded Nuclepore filters were digested prior to analysis as it is described in section 3.3. while the polished quartz and plexiglass discs were analyzed directly. Fig. 6 shows the calculated detection limits, for different backing materials used, as a function of the atomic number. The detection limits are given in terms of masses, because this appears to be the most explicit measure. However, if concentrations are required instead of amounts, the mass expressed in ng should be divided by the sample volume of 5 μl placed on the sample carrier (e.g. in the case of Zn on a quartz disc the *DL* is 40 ppb). As follows from Fig. 6, quartz discs, without silicone solution, appear to have the best detection properties, while the *DL* values involving siliconized quartz discs are slightly higher due to the disturbed surface flatness of the disc. And compared with digested Nuclepore filters and plexiglass discs, detection limits are lower by a factor of about 2.5 and 12 in favour of quartz discs. These results are according to the well known relation of the "energy transfer" into various materials; for incident X-rays of 17.5 keV and an angle of incidence of approximately 5 mrad, the energy transfer into quartz is about eight times lower than into the plexiglass [5]. In contrast, to the typical aerosol investigations using filters and their digestion, the sample preparation step involving direct aerosol collection on the siliconized quartz disc is reduced considerably, from a few hours to a few minutes. Also, the low costs of the proposed method should be recognized.

3.6. Bounce-off effect investigations

As was already mentioned in the Introduction, two of the fundamental limitations of cascade impactors are that particles are prone to bounce and that particle clusters and droplets may fracture upon impaction. When the impacted particle is reentrained into the air stream, it pro-

Table 4
EPMA results on a size distributions of aerosol particles collected on coated Nuclepore filters by means of a Battelle cascade impactor. Measurements on the first stage were not possible due to over-collection of the particles

Stage	Cut-off diameter (μm)-ad	Mean particle diameter and st. dev. (μm)	Analysed area (mm^2)
1	0.25	–	–
2	0.5	0.54 ± 0.40	0.132
3	1	0.94 ± 0.66	0.421
4	2	1.65 ± 1.11	0.903
5	4	3.70 ± 2.09	2.690

Key: ad means aerodynamic diameter.

duces a lower collection efficiency, particularly for the larger aerodynamic size classes. The overall effect is one of producing a positive bias in small aerosol concentrations relative to the large aerosol, and possibly an incomplete particle collection. Additionally, when aerosols are sampled by direct impaction on quartz discs, the possible shrinking of the particles from the optically flat and smooth sample carriers is a major restrainment. For direct analysis of submicron particles by TXRF a new particle sampling technique, involving electrostatic precipitator (ESP), was developed by Dixkens et al. in 1993 [26]. The designed ESP was able to concentrate submicron particles homogeneously on a spot of the TXRF sample support with the 100% collection efficiency for particles smaller than 1 μm at a flow rate of 1.3 l min^{-1}. But, disadvantages of such electrostatic precipitation include the lack of size information, particle reentrainment due to sparking, and practical costs such as high costs and shock hazards [27].

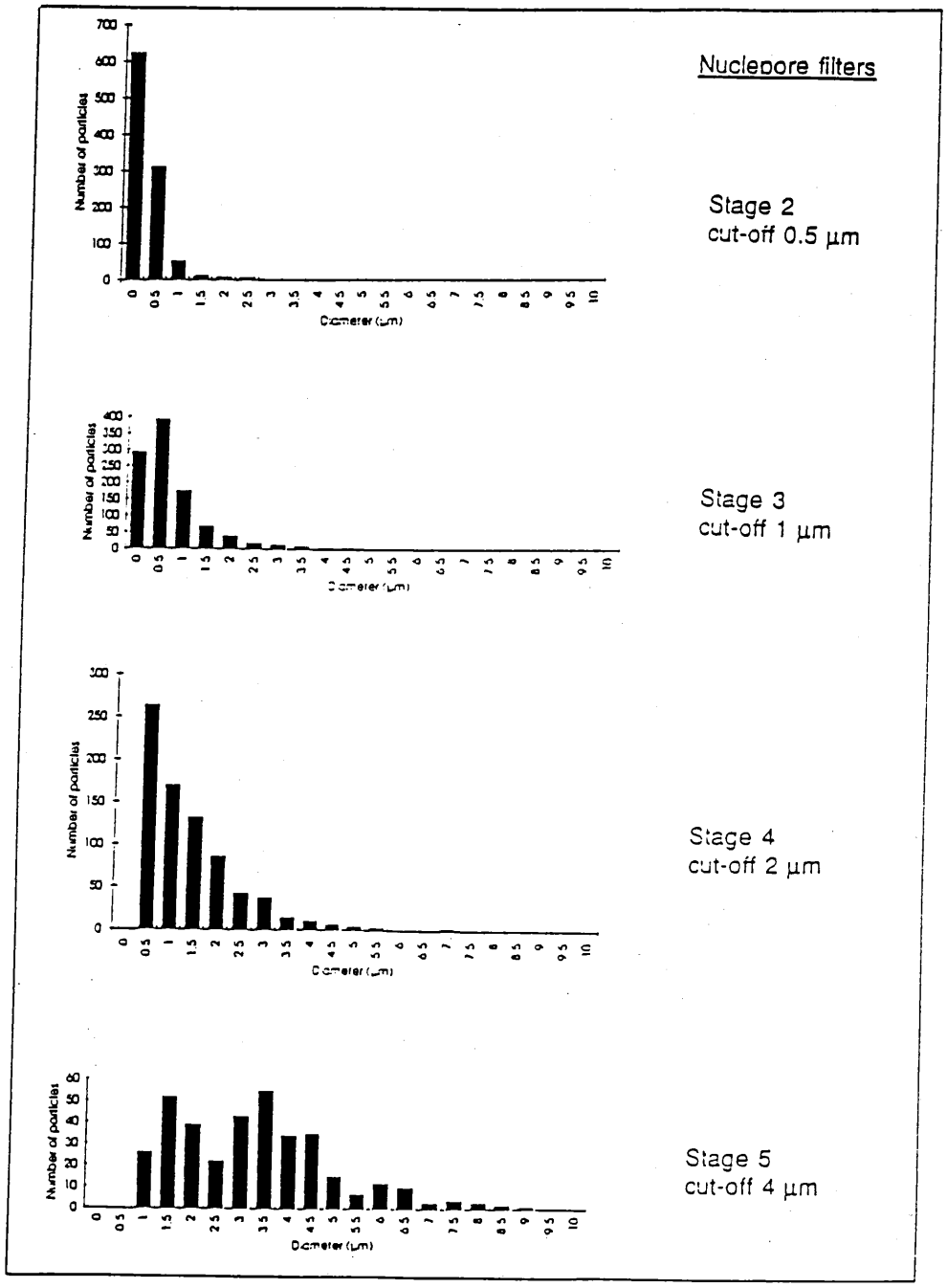

Fig. 8. Size distributions of aerosol particles collected on Nuclepore filters.

Stage 1

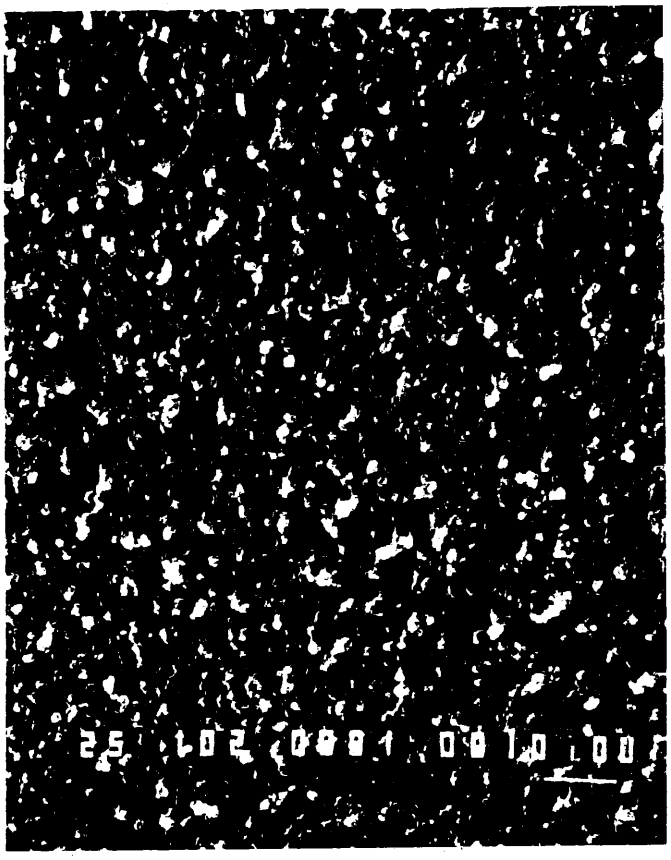

Stage 2

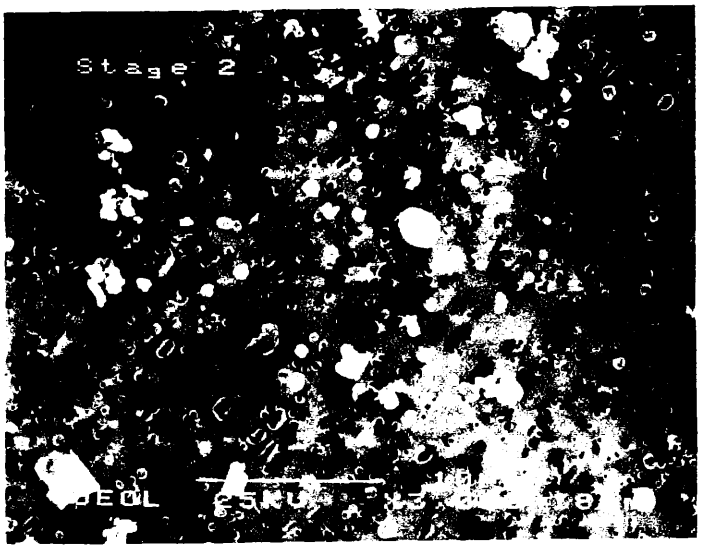

Fig. 9. Backscattered electron images of aerosol particles collected by the means of Battelle cascade impactor. The bars correspond to 10 μm length.

Stage 3

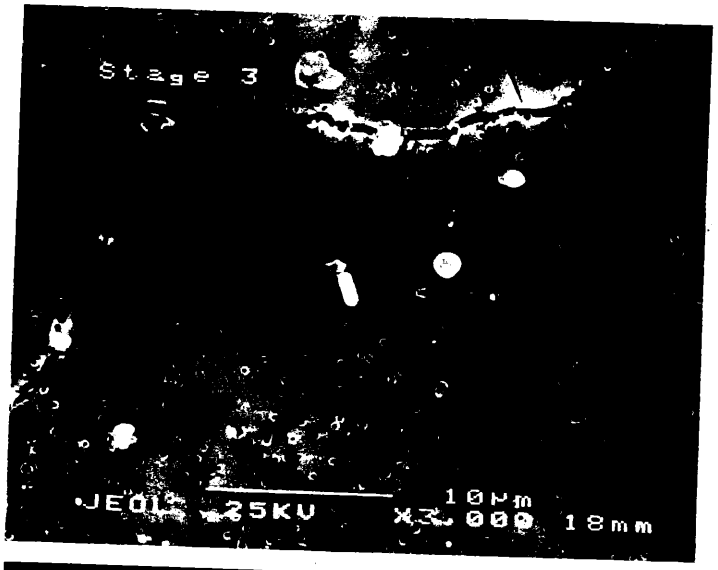

Stage 4

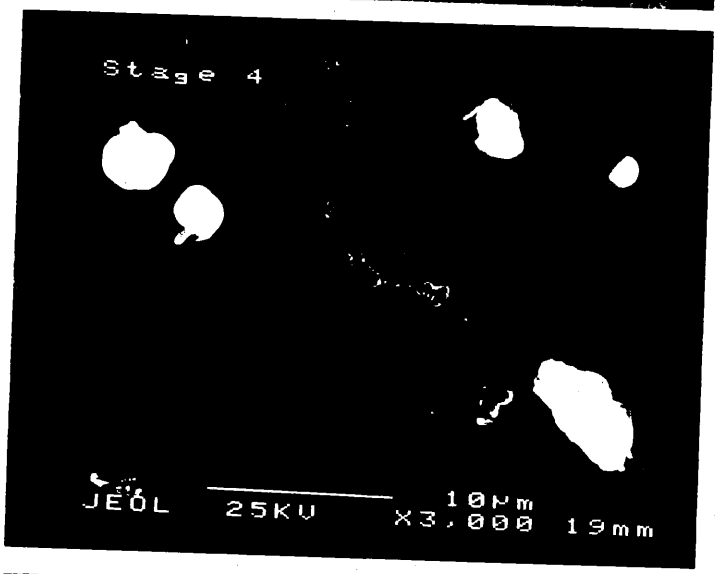

Stage 5

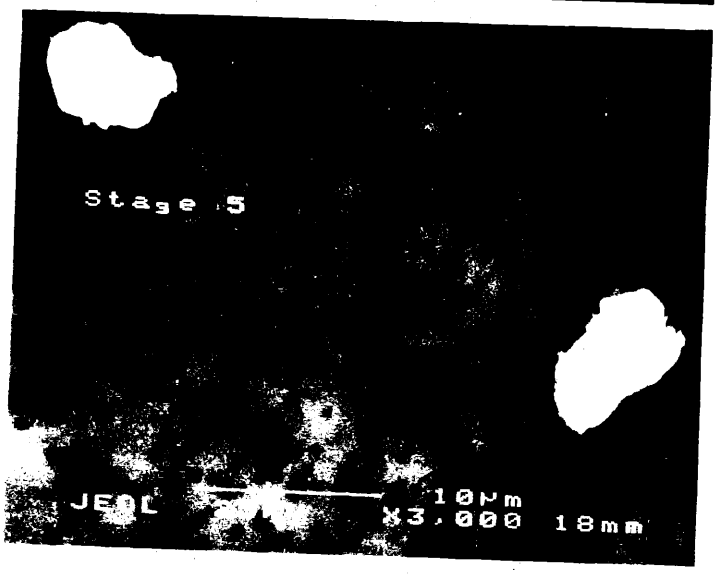

Fig. 9. Continued.

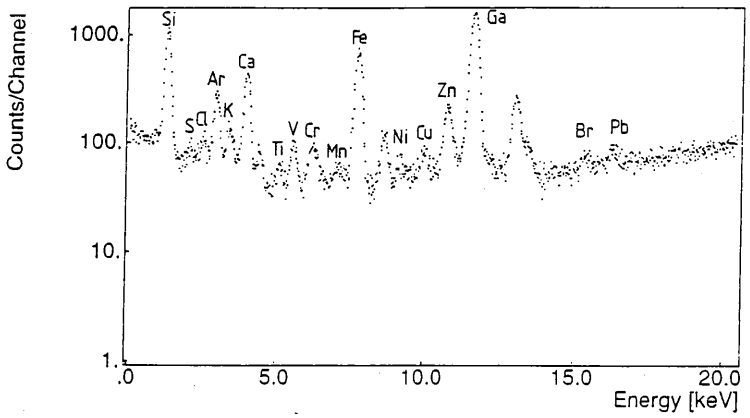

Fig. 10. TXRF spectrum of an aerosol sample, representative for the marine troposphere of the North Sea.

In this work, the bounce-off phenomena have been investigated in detail, by means of EPMA. The diameter of more than 100 particles, deposited on a clean non-siliconized quartz discs, was measured (when measurements were performed on siliconized discs, the coating has surrounded some of the particles and thus interfered with the results). The discs were placed in a five-stage Battelle cascade impactor with cut-off diameters of <0.25, 0.5, 1, 2 and >4 μm. Sampling was done at the campus of UIA and it was restricted to a few minutes only, to avoid overloading of the particles. The results are given in Table 3, while in Fig. 7 the particle size distributions for each class size are shown. A point that should be stressed here is that, by cascade impactors, particles are separated according to their inertia; cascade impactors do not actually measure the particle size directly and hence, the cut-off diameter is the aerodynamic diameter of a spherical particle of unit density, whose collection efficiency is 50% on the given stage. Contrary, by EPMA, the linear diameters of the collected particles were measured (the density is approximately 1.5 g cm^{-3}) and the mean particle size cannot be associated directly with the cut-off point. For example, for the fifth impactor stage, the collected particulate matter should have an equivalent size greater than the 50% cut-off of the fifth stage nozzle. For the fourth impactor stage, the linear size of the collected particle matter should be greater than the fourth stage 50% cut-off but less than for the fifth stage 50% cut-off point, etc. For comparison, identically the same investigation was done for the aerosols collected on Nuclepore filters as is commonly done. These results are given in Table 4 and the graphical presentation of the whole data set is given in Fig. 8.

It follows from Figs. 7 and 8 that the collection performance of the impactors loaded with both quartz discs and with Nuclepore filters is quite similar. On average, 50% of the total amount of the measured particles in both cases impact on the appropriate stage according to their linear diameter. And, in spite of some observed deviations, the discrepancies due to the surface properties (Nuclepore and quartz) can not be considered as significant. The differences between the results of two methods were investigated by *t*- and *z*-test (Microsoft Excel); in both cases the discrepancies among the mean values and variances were found to be statistically insignificant.

In Fig. 9 the EPMA images of aerosol particles collected directly on the quartz discs by means of five-stages Battelle cascade impactor are given. The separation of particles according to their inertial properties (size and density) is evident. Also, EPMA measurements were performed of a backup filter, in case the impactor was loaded with quartz discs and no particles above the 0.2 μm (what is a detection limit of the automated EPMA method) were found. The same results for a backup filter were obtained when impactor stages were loaded with Nuclepore filters.

In summary, the results of the investigation of the bounce-off effects when quartz discs were used for aerosol collection by means of Battelle cascade impactor were quite reassuring; when compared with the commonly accepted collection on Nuclepore filters as a sample support, no significant differences were found.

Table 5
TXRF results for major and trace elements and st. dev. in different size fractions of one representative aerosol sample collected at the Belgian North Sea coast (all values are in ng m^{-3}, dl = limits of detection)

	0.25 μm	0.5 μm	1 μm	2 μm	4 μm	8 μm	16 μm	Total
S	44 ± 2	<dl	120 ± 3	180 ± 4	91 ± 2	<dl	<dl	440 ± 12
Cl	<dl	60 ± 2	270 ± 3	430 ± 5	210 ± 3	66 ± 2	<dl	1030 ± 10
K	3.3 ± 0.3	1.3 ± 0.6	9.9 ± 0.3	12.9 ± 0.5	10.4 ± 7.4	3.3 ± 2.7	1.7 ± 6.8	42 ± 3
Ca	1.2 ± 0.1	3.3 ± 0.3	12.4 ± 0.2	22.7 ± 0.4	12.9 ± 0.3	7.9 ± 0.2	1.8 ± 0.1	62 ± 2
Ti	0.29 ± 0.14	2.1 ± 0.4	0.28 ± 0.13	0.53 ± 0.20	0.40 ± 0.13	0.77 ± 0.22	<dl	4.4 ± 1.2
V	0.37 ± 0.07	0.42 ± 0.17	0.09 ± 0.01	0.09 ± 0.01	<dl	0.33 ± 0.01	0.02 ± 0.01	1.2 ± 0.35
Cr	0.17 ± 0.01	0.51 ± 0.04	0.19 ± 0.01	0.17 ± 0.01	0.49 ± 0.03	0.43 ± 0.02	0.61 ± 0.05	2.58 ± 0.36
Mn	0.21 ± 0.04	1.45 ± 0.12	0.35 ± 0.04	0.75 ± 0.07	0.29 ± 0.04	0.82 ± 0.07	<dl	3.87 ± 0.40
Fe	1.9 ± 0.1	16.9 ± 0.4	5.6 ± 0.1	12.2 ± 0.2	7.9 ± 0.1	10.7 ± 0.2	1.11 ± 0.04	56.4 ± 1.1
Ni	0.29 ± 0.03	1.29 ± 0.08	0.08 ± 0.01	0.26 ± 0.04	0.08 ± 0.01	0.57 ± 0.05	<dl	2.56 ± 0.20
Cu	0.39 ± 0.04	0.40 ± 0.08	0.41 ± 0.04	0.45 ± 0.05	0.27 ± 0.03	0.28 ± 0.05	0.23 ± 0.03	2.44 ± 0.31
Zn	4.86 ± 0.04	2.35 ± 0.08	0.78 ± 0.04	0.81 ± 0.05	2.61 ± 0.04	0.47 ± 0.05	0.26 ± 0.03	12.1 ± 0.3
As	0.25 ± 0.02	<dl	<dl	0.04 ± 0.01	<dl	<dl	<dl	0.29 ± 0.03
Br	5.7 ± 0.6	1.5 ± 0.2	4.1 ± 0.3	6.6 ± 0.7	7.7 ± 0.8	1.6 ± 0.2	0.15 ± 0.02	27.2 ± 1.7
Sr	<dl	<dl	0.73 ± 0.05	1.7 ± 0.2	1.4 ± 0.2	0.46 ± 0.03	<dl	4.2 ± 0.5
Pb	5.4 ± 0.4	2.6 ± 0.3	1.2 ± 0.1	2.2 ± 0.3	0.33 ± 0.04	0.23 ± 0.03	0.18 ± 0.02	12.1 ± 1.2

3.7. Some results of TXRF analysis of aerosol samples

As an illustration, Table 5 shows the results of the analysis of aerosol samples collected at the Belgian North Sea coast. Here, the concentration data in the seven size classes and the total elemental concentrations are given to demonstrate the potential of the TXRF method for the determination of major and trace elements in the size-segregated airborne particles. And, in case only bulk aerosol analysis is required, collection can be done by using only the last impactor stage, provided with a quartz disc and analyzing the deposit directly by TXRF. As an example, a TXRF spectrum of aerosol sample is given in Fig. 10. The reproducibility of the measurement was found to be about 10%.

4. Conclusions

The principal advantages of TXRF were explored to develop an efficient, simple, rapid and low cost method for the routine analysis of atmospheric aerosols, collected directly on TXRF reflectors from small air volumes (0.2 m^3) and with short sampling times (3 h). The majority of elements detectable by TXRF exhibited detection limits below 1 ng per disc. Compared to typical aerosol investigations using filters and/or digestion of particle loaded filters, the sampling and analysis time and the detection limits are reduced considerably.

Acknowledgements

We thank P. Wobrauschek (Atominstitut, Vienna) and R. Klockenkämper (ISAS, Dortmund) for their valuable suggestions at the initial stage of this work and W. Dorrinė (University of Antwerpen) for carrying out the EPMA measurements. This work was supported by the Belgian State, Prime Minister's Service, Science Policy Office, Impulse Programme in Marine Sciences (contract MS/06/050).

References

[1] A.H. Compton, Phil. Mag., 45 (1923) 1121.
[2] Y. Yoneda and T. Horiuchi, Rev. Sci. Instrum., 42 (1971) 1069.
[3] H. Aiginger and P. Wobrauschek, Nucl. Instr. Meth., 114 (1974) 157.
[4] J. Knoth and H. Schwenke, Fresenius' Z. Anal. Chem., 291 (1978) 200.
[5] H. Schwenke and J. Knoth, In: Handbook of X-Ray Spectrometry, R. Van Grieken and A. Markowicz (Eds.), Marcel Dekker, New York, 1993, pp. 453–488.
[6] R. Klockenkämper, J. Knoth, A. Prange and H. Schwenke, Anal. Chem. 64 (1992) 1115A.
[7] W. Ladisch, R. Rieder, P. Wobrauschek and H. Aiginger, Nucl. Instr. Meth. Phys. Res. A330 (1993) 501.
[8] A. Iida, Adv. X-Ray Anal. 35B (1992) 795.
[9] S. Török and R. Van Grieken, Anal. Chem. 66 (1994) 186R.
[10] P. Ketelsen and A. Knöchel, Fresenius J. Anal. Chem. 317 (1984) 333.
[11] B. Schneider, Spectrochim. Acta. 44B (1989) 519.
[12] A. Salvá, A. von Bohlen, R. Klockenkämper and D. Klockow, Quimica Analitica 12 (1993) 57.
[13] M. Xu and K. Willeke, J. Aerosol Sci., 24 (1993) 19.
[14] V.A. Marple and K. Willeke, In: Fine Particles: Aerosol Generation, Measurement, Sampling and Analysis, B.Y.H. Liu (Ed.), Academic Press, New York, 1976, pp. 411–446.
[15] T.A. Cahill, In: Aerosol Measurement, D.A. Lundgren, F.S. Harris, Jr., W.H. Marlow, M. Lippmann, W.E. Clark and M.D. Durham (Eds.), University Press of Florida, Florida, 1979, pp. 131–134.
[16] K.E. Noll, P.F. Yuen and K.Y.P. Fang, Atmos. Environm., 24A (1990) 903.
[17] A. von Bohlen, R. Eller, R. Klockenkämper and G. Tölg, Anal. Chem. 59 (1987) 2551.
[18] W. Michaelis, J. Knoth, A. Prange and H. Schwenke, Adv. X-Ray Anal. 28 (1985) 75.
[19] D.J. Leland, D.B. Bilbrey, D.E. Leyden, P. Wobrauschek and H. Aiginger, Anal. Chem., 59 (1987) 1911.
[20] B.T. Eddy, Analytical Science Division, The National Association of Clean Air Symposium, Durban, 14–15 November 1991.
[21] R. Pepelnik, B. Erbslöh, W. Michaelis and A. Prange, Spectrochim. Acta Part B, 48 (1993) 223.
[22] H. Aiginger, P. Wobrauschek and C. Streli, "Totalreflexions-Röntgenfluoreszenzanalyse", First Workshop, GKSS/E/61 (1986) 693.

[23] P. Van Espen, K. Janssens and J. Nobels, Chemom. Intell. Lab. System., 1 (1986) 109.
[24] Y. Vawda, I. Colbeck, R.M. Harrison and K.W. Nicholson, J. Aerosol Sci., 23, (1992) 233.
[25] J.R. Turner and S.V. Hering, J. Aerosol Sci., 18 (1987) 215.
[26] J. Dixkens, H. Fissan and T. Dose, Spectrochim. Acat Part B, 48 (1993) 231.
[27] T.T. Mercer, Aerosol Technology in Hazard Evaluation, Academic Press, New York, 1973.

Mikrochim. Acta 120, 121–137 (1995)

Mikrochimica Acta

Assessment of Local Analysis by Fourier Transform Laser Microprobe Mass Spectrometry with External Ion Source

Wim Van Roy[1], Herbert Struyf[1], Paul Kennis[1], Luc Van Vaeck[1,*], René Van Grieken[1], and Claudia Andrle[2]

[1] Department of Chemistry, University of Antwerp (UIA), Universiteitsplein 1, B-2610 Wilrijk, Belgium

[2] Department of Chemistry, University of Dortmund, P. O. Box 500500, D-442277 Dortmund 50, Federal Republic of Germany

Abstract. Laser microprobe mass spectrometry (LMMS) is a technique for local analysis of inorganic and organic constituents in the μm range. This paper will focus on selected applications. First of all, element detection is illustrated by data from a 50-nm TiW layer on silicon and by the detection of residual Cr on HPLC column packing material. Speciation capabilities of LMMS are demonstrated on pure substances and on a coated neo-ceramic. Finally, the feasibility of organic analysis is shown in the case of a biologically active compound and dyed cloth fibres.

Key words: laser microprobe mass spectrometry, local analysis, elemental analysis, inorganic speciation, organic analysis.

Laser microprobe mass spectrometry (LMMS) uses focused UV laser pulses to evaporate and ionize a microvolume of a solid sample. The application of laser mass spectrometry (LMS) has been increasingly appreciated to ionize and detect inorganic and organic materials. Sample requirements are minimal and essentially restricted to stability of the specimen in vacuum. No special precautions are needed for non-conducting samples. Traditionally, developments in LMS have been aimed at the quantitative determination of elements or alternatively at the structural analysis of thermolabile high molecular weight organic compounds [1, 2]. Laser ionization capabilities are strikingly illustrated by the generation of giant ions up to 230 kDA using the matrix-assisted laser desorption-ionization technique (MALDI) [3].

LMMS was developed in the late seventies to perform local analysis. Initial instruments used time-of-flight (TOF) mass spectrometers, providing full panoramic registration for each ionization event. Their low-resolution MS features complicate

* To whom correspondence should be addressed

the structural assignment of the detected ions. Nevertheless, TOF LMMS demonstrated the potential of focused laser ionization for local analysis in selected problem-solving applications [4, 5]. In contrast to LMS, quantitation in LMMS is not straightforward, for reasons extensively discussed elsewhere [6]. The interest in LMMS stems from its ability to perform element localization, speciation of inorganic compounds and structural characterization of organic compounds with the same instrument. This motivated the development of Fourier transform laser microprobe mass spectrometers (FT LMMS) [7–9]. In this way the well-known high mass-resolution capabilities of FTMS become available in microprobe experiments to separate isobaric ions and to determine the mass-over-charge (m/z) ratio of an ion with an accuracy in the ppm range. The latter feature allows one to deduce the elemental composition of a detected ion unambiguously.

The physics of the mass analyser inherently determine which fraction of the generated ion population will be detected. This is not only a question of transmission and, hence, sensitivity, but also of initial kinetic energy distribution, the emission angles of the ions from the sample and the time domain from which the ions can be collected by a given mass spectrometer [6]. The main question, however, is not how FT LMMS data compare with TOF LMMS, but to what extent the obtained information is adequate for the qualitative characterization of local constituents.

The purpose of this paper is to present the application of FT LMMS with external ion source in each of the main analytical tasks. First of all, element detection is addressed. A preliminary assessment of the information depth is reported. The comparative analysis of chromatographic column-packing material by FT LMMS and analytical electron microscopy is discussed. Secondly, speciation is considered. Selected data from a systematic study illustrate how the molecular structure is deduced from the spectrum. As an application, the analysis of a coating on neo-ceramic materials is presented. Finally, the use of FT LMMS for the analysis of organic compounds is highlighted by the results from a polyfunctional molecule. Dyed cotton fibers are used as a model system to assess the sensitivity. Note that the local analysis of organic compounds practically excludes the use of MALDI. As a result, the typical molecular weight molecular weight range is confined to a few kDa.

Experimental

The FT LMMS used in our laboratory is based on a Spectrospin CMS 47X (Spectrospin AG, Fällanden, Switzerland) and is now commercialized as the MicroFocus™ version [9]. The instrument is equipped with the Infinity Cell™ [10]. TOF LMMS measurements were performed on a LAMMA-500 instrument (Leybold-Hereaus, Köln, Germany) [11]. Table 1 gives the experimental parameters for both LMMS instruments. A Jeol JXA-733 Superprobe (Tokyo, Japan) with energy and wavelength dispersive spectrometers was used for EPXMA measurements. Scanning transmission electron microscope (STEM) experiments were carried out on a Jeol JSM-6300 (Tokyo, Japan) with energy dispersive X-ray (EDX) detection.

Powder samples of flusperilene, $NaNO_3$ and $NaNO_2$ were simply ground to 10-μm particles and then attached to the sample holder by double-sided tape. Vacuum deposition was applied to obtain a 50-nm TiW layer on silicon (in collaboration with the Interuniversity Micro-Electronics Center, Leuven, Belgium). The neo-ceramic materials were provided by the Institut für Spektrochemie und Angewandte Spektroskopie (Dortmund, Germany). The boron carbides were prepared by adding B_4C

Table 1. Comparison of experimental parameters for TOF and FT LMMS instruments used in this study

	LAMMA 500	MicroFocus
Mass resolution	< 850	10^5–10^6
Lateral resolution	1–3 μm	5 μm
Mass accuracy	0.5 *m/z*	1 ppm
Laser irradiation	transmission	reflection
Detection range	H-unlimited	15–15 000
Laser power density	10^6–10^{11} W cm^{-2}	10^6–10^{10} W cm^{-2}
Laser energy per pulse	2 mJ per 15 ns pulse	20 mJ per 5 ns pulse
Laser wavelength	266 nm	266 nm

powder to a 20 mole% solution of Si_2H_6 in tetrahydrofuran. After evaporation and calcination at 1000 °C in an inert gas, an SiC-coated powder was obtained (SiC/B_4C) with the following composition: 72.3 mole% B, 21.4 mole% C and 4.2 mole% Si.

Dyed cotton samples were prepared by soaking a tissue in a methanol solution of the dye at different concentrations. The averave surface coverage of dye ranged from 17 to 1.3 μg cm^{-2}.

Results and Discussion

To facilitate the discussion of the results, the so-called TOF effect in FT LMMS with external ion source is dealt with first. The transport of ions from the external ion source to the FTMS cell by means of electrical fields induces a mass-dependent velocity of the ions. Hence, time separation of ions with different *m/z* occurs over the distance of about 1 m between source and cell. Ions with low *m/z* arrive earlier at the entrance of the FTMS cell than those with higher *m/z*. Injection of ions into the cell implies that the potential barrier in the orifice of the front plate is electrically eliminated. Once inside the cell, the ions are reflected by the back trapping plate and arrive again at the entrance of the cell after the so-called reflect time. Obviously, when the front trap plate still allows free transmission, higher *m/z* ions with longer flight times can enter while low *m/z* ions can leave the cell. As a result, the reflect time of the lowest *m/z* ions determines the ultimate difference in flight time with the highest *m/z* ions, which can be trapped simultaneously with the lowest *m/z* ions. The *m/z* range for panoramic registration of a mass spectrum is limited to a factor of about five [9]. The parameter $T_{\text{open gate}}$ refers to the time between the laser pulse and the disabling of the external ion injection into the cell.

Element Detection

The positive ion mass spectra, recorded by FT LMMS from a 50-nm thick TiW layer on silicon, essentially contain the signals from the elemental ions. Figure 1 surveys the results for different instrument settings. The upper data in Fig. 1a are taken with a power density of 4×10^{10} W cm^{-2} and show the detection of intense signals from Ti^+ and W^+, stemming from the surface layer. The $T_{\text{open gate}}$ is adequate to trap elemental ions of Ti^+ and W^+ simultaneously, but Si^+ ions have already escaped the

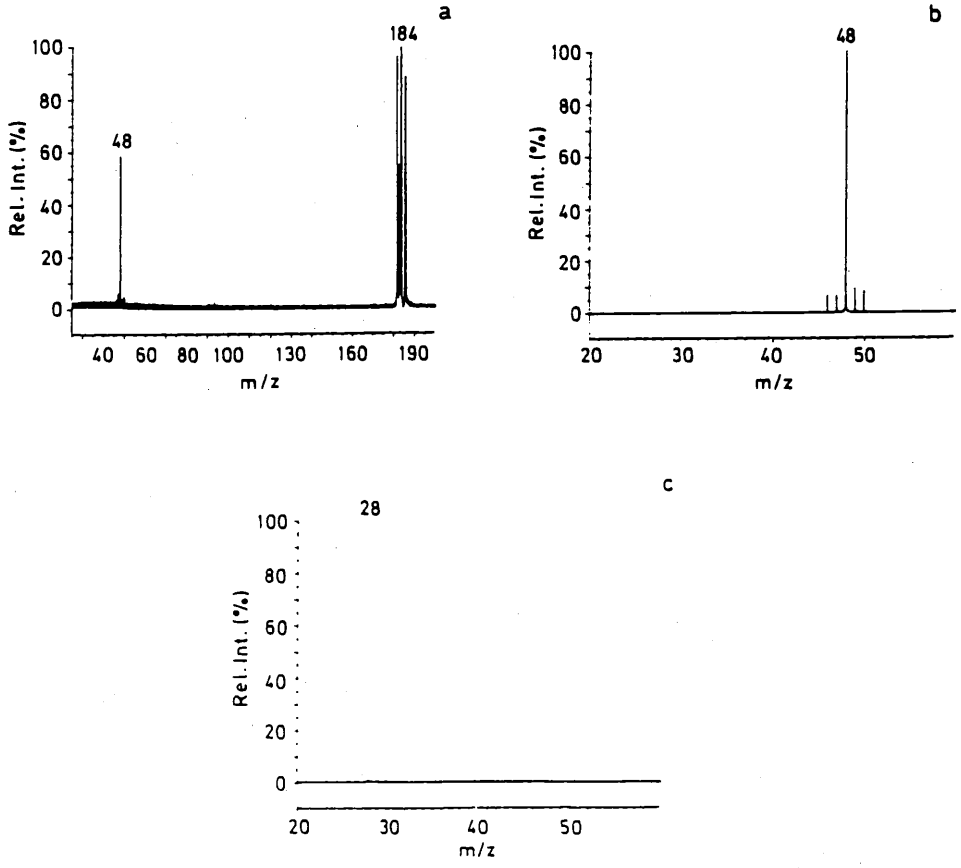

Fig. 1. FT LMMS analysis of a 50-nm thick TiW layer on silicon (**a**, **b**) and from the uncoated substrate (**c**). The positive ion mass spectra are recorded under the following laser conditions of power density and $T_{\text{open gate}}$ (**a**) 4×10^{10} W cm^{-2}, $T_{\text{open gate}}$ 300 μs, (**b**) and (**c**) 10^{11} W cm^{-2}, $T_{\text{open gate}}$ 175 μs

cell. Therefore a $T_{\text{open gate}}$ of 175 μs was taken for Fig. 1b, so that Ti^+ could be trapped together with Si^+ ions if they were generated. Although the power was raised even to 10^{11} W cm^{-2}, no ions from the silicon substrate could be detected. For reference purposes Fig. 1c illustrates the Si^+ signals recorded under exactly the same instrumental conditions as Fig. 1b from the substrate without TiW surface coating. The signal/noise (S/N) ratios for $^{28}Si^+$ and $^{48}Ti^+$ are 220 and 460, respectively. The relative element sensitivity factor ratio of Ti over Si elemental ions is about two so that the absence of the Si^+ signals in Fig. 1b strongly suggests that the information depth in LMMS does not exceed the surface layer thickness of 50 nm.

The accurate measurement of isotopic abundance distributions in FTMS strongly depends on the careful optimization of the instrumental conditions. Space charge effects, coupling of trapping and radiofrequency fields during fast excitation and the digitization of the transient signal affect the isotope ratios unless special precautions are taken. Routine data acquisition of panoramic or broadband spectra by FT LMMS typically yields deviations of the order of 10% for isotopes with relative intensities within a factor of 5 or less. The deviations on isotope ratios for W^+ in Fig. 1 remain between 7 and 11% but rise to 20–24% for Ti^+, involving ratios

of about 10. Note the systematic deviation of the lower isotopes $^{46}Ti^+$ and $^{47}Ti^+$, which are underestimated, against the overestimated $^{49}Ti^+$ and $^{50}Ti^+$. For one or another reason this tendency only occurs with the lower m/z ions, close to the limit where the excitation power must be lowered. Neither of the two effects is yet understood, nor the existence of a significant relationship between the two observations. The accurate measurement of isotope patterns under routine conditions is in practice not crucial for the use of FT LMMS in most problem-solving applications. Qualitative identification with minimal sample preparation is the main task of the technique. Detection of ions in the high resolution mode offers high specificity because of the resolving power exceeding 100 000 and the mass accuracy within 1 ppm. The use of isotope patterns for identification of the ions is especially helpful in low-resolution mass spectrometry, but less essential to FT LMMS applications.

Note that the mass resolution in Fig. 1 is only 5000 on W^+, i.e. substantially lower than the typically claimed values of more than 100 000. The reason is that the FTMS performance with respect to sensitivity and mass resolution is best in the narrow-band mode, where the signal is electronically converted to a low-frequency signal. The sampling and digitization can then be performed under the best conditions. The mass resolution on the W^+ signal, measured in single-shot and narrow-band, exceeds 1.5×10^6. To obtain a full mass spectrum in FT LMMS, the transient signal is digitized as such at a rate determined by the lowest m/z. The length of the sampled transient and hence the number of low frequency (high m/z) periods is inevitably limited by the memory size.

The high mass resolution capabilities offered by FT LMMS frequently exceed the resolving power required to separate isobaric ions in practical applications. Figure 2 shows the separation of several isotopes in the $SnO{\cdot}SnCl^+$ cluster ions at m/z 291. Without special optimization of the cell potentials, a mass resolution of 150 000 is achieved.

Although further research is necessary, these preliminary results already show that, even under high power density conditions, the information depth of FT LMMS remains lower than 50 nm while the crater depth easily extends to 100 nm. Otherwise stated, the information in the mass spectra stems from the upper and near surface layers, although the erosion goes much deeper. As a result, FT LMMS holds an intermediate position between methods such as EPXMA, generating chemical

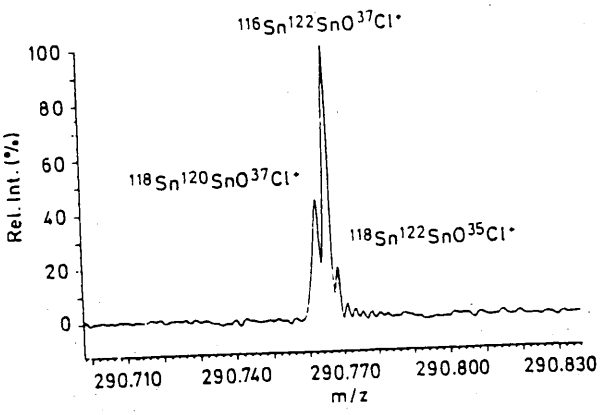

Fig. 2. Separation of $SnO{\cdot}SnCl^+$ ions by FT LMMS in the narrow band mode. The mass resolution is 150 000. The laser power density is 3.8×10^8 W cm^{-2}

information from a microvolume extending up to 1 μm deep in the sample, and real surface techniques such as Auger electron spectroscopy, X-ray photoelectron spectroscopy and static secondary ion mass spectrometry (SIMS), which provide chemical information on atomic or molecular monolayers at the surface. The discrepancy between information and crater depth implies that FT LMMS is incapable of real depth-profiling experiments, as in, for instance, dynamic SIMS. The limited information depth for elemental ions of FT LMMS in the reflection geometry contrasts with the data reported by Linton et al. [12] for TOF LMMS. A multilayer sample consisting of pure Ni and S, separated by an intermediate gold layer was analysed in the transmission mode with maximum laser power density. The total sample thickness was about 1 μm. In spite of preferential ion formation from the layer facing the mass spectrometer, strong signals from the elemental ions stemming from the underlying layers were detected. The cluster ions observed contained both S and Ni. These data indicate that the components within the entire evaporated microvolume contribute significantly to the detected ions. In spite of some surface selectivity, the information depth is clearly superior to that in FT LMMS. Note that the information depth in transmission TOF LMMS is also quite confined in the case of structural ions from organic products [13]. Virtually no detectable ions originate from deeper than 50 nm in a sandwich sample.

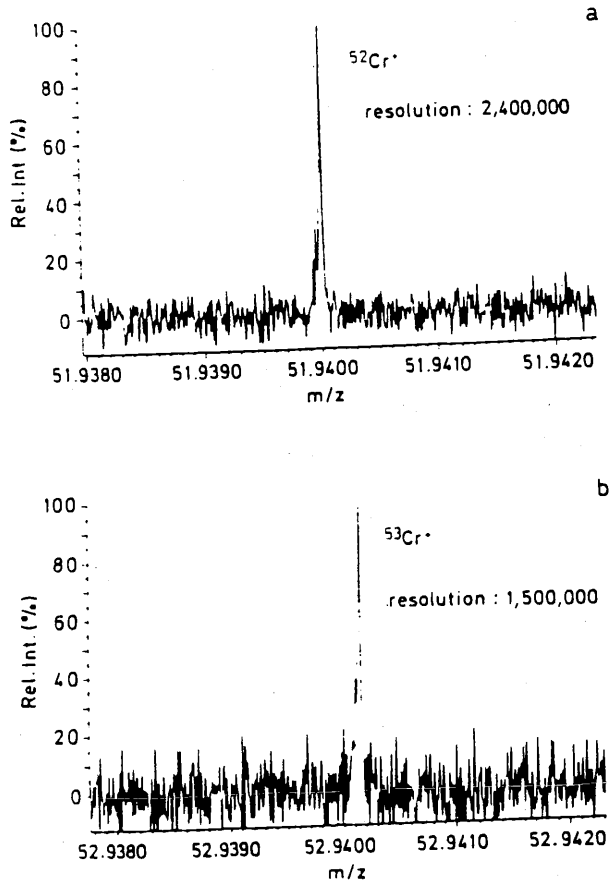

Fig. 3. Analysis of a chromium complex adsorbed on HPLC column-packing material. Positive ion signals recorded upon a single laser shot by FT LMMS from $^{52}Cr^+$ (a) and $^{53}Cr^+$ (b). The laser power density is 2×10^{10} W cm^{-2} in the high resolution mode upon a single shot

The limited information depth does not necessarily contradict reasonable detection limits for surface components. This was evidenced by a practical application, stemming from an analytical study on the chromatographic separation process involving the Cr^{3+}-pyrrolidine-dithiocarbamate complex. The detection of the residual Cr on different HPLC column-packings was required. The adsorption of Cr on the column particles amounted to 2×10^{-16} g Cr per particle of 5-μm diameter. The Cr-levels were below the detection limit in STEM EDX. Figure 3 shows the high-resolution mode signals recorded by FT LMMS for the elemental ions $^{52}Cr^+$ and $^{53}Cr^+$. Each isotope was recorded in separate single laser interactions. The detection of the major isotope occurred with the best mass resolution and S/N of 2 400 000 and 10.5, respectively, but for the less abundant $^{53}Cr^+$ still reasonable values like 1 500 000 mass resolution and an S/N ratio of 5.1 were obtained. Shot-to-shot reproducibility on different particles showed a homogeneous distribution of the element. As a result, the total number of available ^{52}Cr and ^{53}Cr atoms can be assessed in the order of 10^6 and 10^5, respectively. This is consistent with previous estimates for the detection limit of FT LMMS on gold layers [9].

Chemical Structure Sensitivity – Inorganics

A systematic study of about forty compounds from different groups such as binary salts, oxysalts, oxides and sulfides has been undertaken to assess the speciation capabilities of FTLMMS [14–16]. The combination of positive and negative spectra provides intense signals from which the original molecular composition of the substance can be deduced. Figure 4a shows the negative ion mass spectrum of sodium nitrate. In the positive ion mode data, the presence of a sodium oxysalt is evident from the Na^+ signal while the higher m/z peaks result from the combination of a number of Na_2O building blocks and the charged species Na^+ and NaO^+. To identify the counter-ion, the negative ion mass spectrum is required. The peaks at m/z 46 and 64 refer to a nitrate or a nitrite. The distinction between $NaNO_3$ and $NaNO_2$ is not clear from the positive ion mass spectrum alone. However, the base peak at m/z 147 in the negative mode refers to $NaNO_3 \cdot NO_3^-$. These ions do not occur in the corresponding $NaNO_2$ negative ion mass spectrum and permit identification of the analyte as sodium nitrate.

Figure 4b contains the wavelength dispersive X-ray spectrum obtained from sodium nitrate. The problems with the detection of oxygen in sodium salts and of the low-Z elements in general, result in poor estimates of the relative element compositions. The comparison shows the strength of FTLMMS. Speciation is based on the detection of the analyte as an entire entity, combined with a stable charged species. As a result, identification of the analyte can be performed by quite straightforward guidelines. For instance, binary salts (MX_n) essentially yield ions of the type $(MX_n)_mM^+$ or $(MX_n)_mX^-$. Also the spectra from oxysalts (MOX) are readily interpreted on the condition that MO and X instead of M^+ and OX^- are considered as building-blocks. The cationization of neutral entities by element oxide ions and the anionization by oxygen-deficient counter-ions is tentatively related to the formation of gas-phase species, which are different from the original counter-ions. As a result, the main peaks in FT LMMS simply refer to $(MO)_n(X)_m \cdot M(O)^+$ and $(MO)_nX_m \cdot X^-$. This means that, looking to the usually unambiguous low-mass

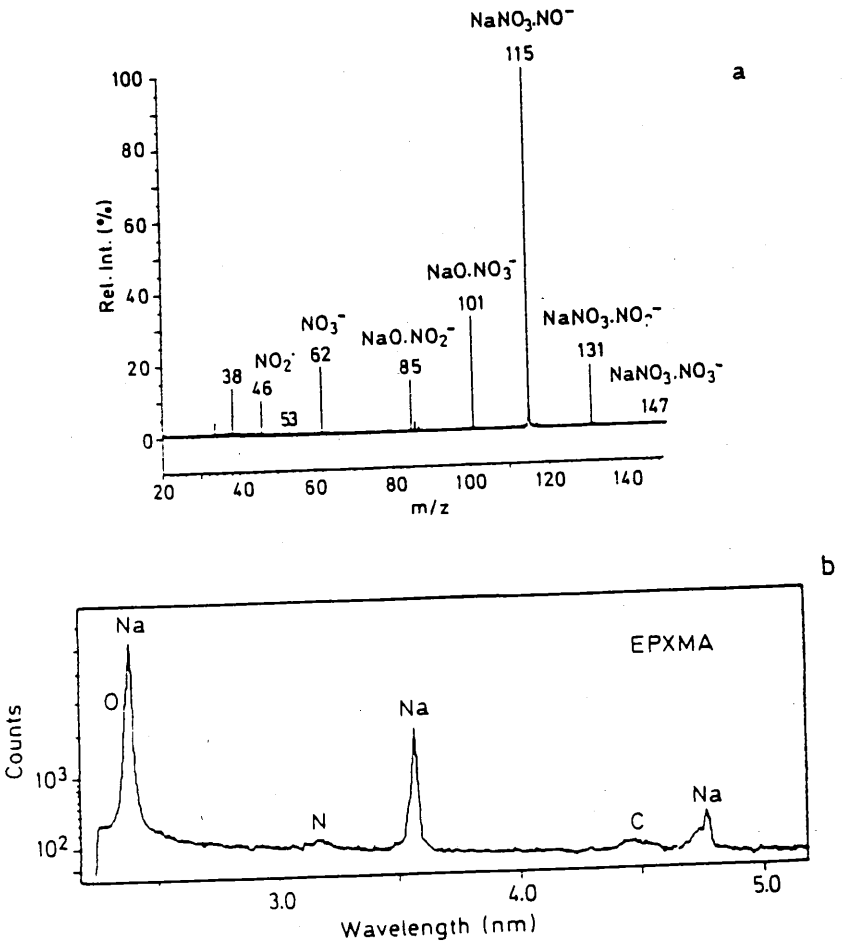

Fig. 4. Speciation of sodium nitrate. (**a**) Negative ion mass spectrum recorded by FT LMMS at a $T_{\text{open gate}}$ of 250 μs and a laser power density of 7.4×10^8 W cm^{-2}. The signal around m/z 78 is due to electronic noise. (**b**) Wavelength dispersive spectrum by EPXMA

signals from M^+ and X^-, the composition of the ions corresponding to the main signals can be readily derived.

The limitations to the detection of low-mass elements does not only apply to EPXMA. For practical reasons, most commercial FTMS instruments have a lower cut-off at m/z 15. As a result, the elemental ions below cannot be monitored directly by our FT LMMS instrument. However, using the systematics described above, LiCl can still be characterized by the specific $LiCl{\cdot}Li^+$ and $LiCl{\cdot}Cl^-$ signals [16]. Since EPXMA relies on the detection of elements with $Z > 4$ in recent instruments, no information is obtained on this compound, except that it contains chlorine.

FT LMMS can be considered as a second-generation laser microprobe, intended to increase the specificity of the information obtained in comparison with former TOF LMMS instruments. As a test case to evaluate the current capability of FT LMMS, the characterisation of a coating on neo-ceramics was selected. Figure 5 shows the positive ion mass spectra for SiC/B_4C, as recorded by TOF and FT

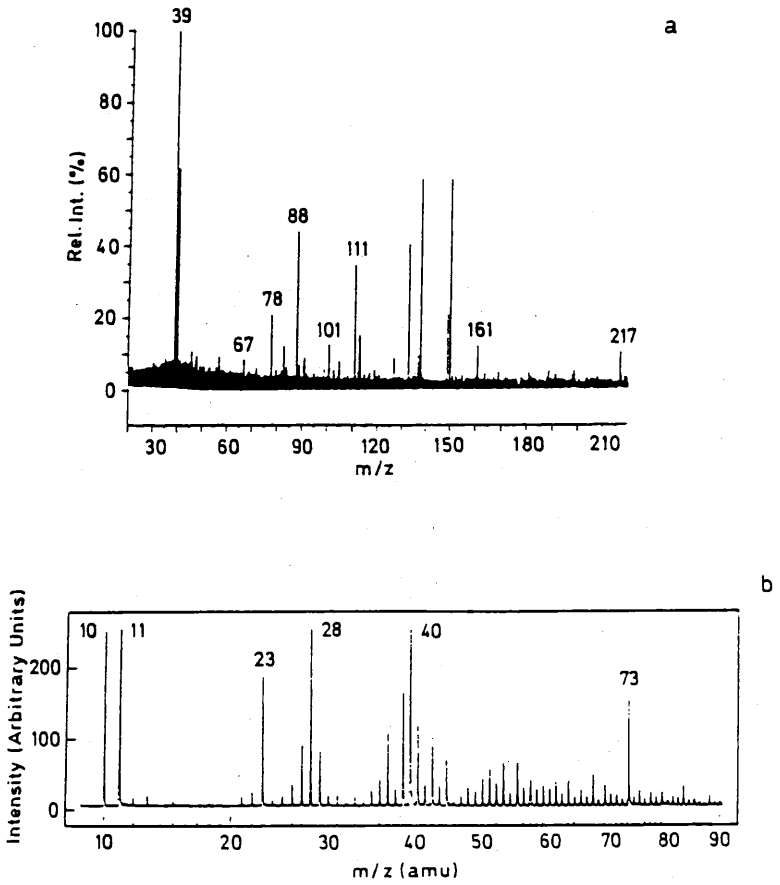

Fig. 5. Analysis of SiC/B_4C neo-ceramic material. Positive ion mass spectrum recorded by (**a**) FT LMMS at $T_{\text{open gate}}$ of 350 µs and a laser power density 7.4×10^8 W cm^{-2} and (**b**) TOF LMMS at the same laser power density. The signal around *m/z* 78 is due to electronic noise

LMMS. In contrast to FT LMMS, no peaks are detected above *m/z* 100 in TOF LMMS. The signal around *m/z* 78 in FT LMMS is due to electronic noise. This peak originates from a radiofrequency emitting source in the environment and not from ions, as can be proven when the excitation step is omitted.

A selection of diagnostic positive ions from the represented spectra is given in Table 2. TOF LMMS provides nominal mass resolution and *m/z* accuracy. As a result, the use of isotopic abundances in nature is necessary to derive the assignment. This can be less obvious for complex peak patterns, due to the superposition of several species. Furthermore, the accuracy of the peak intensities is about 10–20% under routine conditions [17]. Hence, several possible assignments must still be considered. In contrast, the high-mass resolution and ppm mass accuracy of the FT LMMS technique permits the assignment of peaks in the spectra even without the use of isotope patterns. As a result, and as can be seen in Table 2, FT LMMS permits us to rule out several ions proposed on the basis of TOF results or to come up with new ion compositions. Specifically, unexpected elements such as Ti^+ and Sr^+ are identified. Especially the identification of such species is not obvious in

Table 2. Assignment of the selected diagnostic positively charged ions detected by TOF and FT LMMS from SiC coating on B_4C

TOF LMMS		FT LMMS		
m/z	Mass assignment	*m/z*	Elemental composition	Error of mass measurement (ppm)
39	K^-, BCO^+ or $C_3H_3^+$	38.9632	K^+	0.2
		39.0053	LiO_2^+	0.5
40	Ca^- or SiC^+	39.9621	Ca^+	0.5
41	$^{41}K^-$, $^{29}SiC^-$ or $CHSi^+$	40.9613	$^{41}K^+$	1.5
48	C_4^-	47.9474	Ti^+	0.9
53	C_3OH^-, $BC_2 \cdot H_2O^-$, $^{29}SiC_2^-$ or SiC_2H^-	52.9843	SiC_2H^+	1.0
57	$SiOCH^-$, $CaOH^-$, B_3C^- or $C_4H_9^-$	56.9648	$CaOH^+$	1.0
65	SiC_3H^-, $^{65}Cu^-$ or $^{29}SiC_3^-$	64.9699	CaC_2H^+	1.1
67	$NaSiO^-$, $SiCBO^-$ or $C_2BO_2^-$	66.9611	$NaSiO^+$	1.2
		66.9663	$CaBO^+$	1.2
73	C_6H^-, B_3SiC^- or B_3Ca^-		not detected	
83	$SiCBO_2^-$, $NaSiO_2^-$ or BC_6^-	82.9351	$KSiO^+$	0.9
		82.9612	$CaBO_2^+$	0.7
88	$SiOB_2^-$ or $SiO \cdot SiO^-$	87.9052	Sr^-	0.9

the complex peak patterns of TOF LMMS. The corresponding negative ion mass spectra are shown in Fig. 6, while the assignments of relevant peaks are given in Table 3. The same features as for the positive spectra can be observed. Similarly to the case of LiCl, structural information on the SiC/B_4C material can be obtained from FT LMMS measurements, although boron and carbon have *m/z* values too low to be detected directly. Note that LMMS results in the positive ion detection mode show virtually no structurally relevant ions, but primarily ions due to contamination of the sample. This however, is largely compensated by the information gained from the negative ions, where clusters of boron, carbon and oxygen are visible. Contrary to TOF LMMS, silicon-containing ions were detected in the negative ion spectrum by FT LMMS, albeit only for *m/z* 75. Similarly to TOF LMMS, however, only the negative ion clusters BC_2^-, $C_2 \cdot BC_2^-$ and $C_4 \cdot BC_2^-$ were detected.

In conclusion, it can be stated that FT LMMS fulfils the need in laser micropobe applications to determine the element composition accurately and routinely. The aspect of ion assignment becomes especially critical in LMMS because of the lack of insight into the ion formation, which is in turn a consequence of the problems of performing quantitative experiments.

Table 3. Assignment of the selected diagnostic negatively charged ions detected by TOF and FT LMMS from SiC coating on B_4C

TOF LMMS		FT LMMS		
m/z	Mass assignment	*m/z*	Elemental composition	Error of mass measurement (ppm)
24	BHC^- or C_2^-		not detected	
25	$BH_2{\cdot}BH^-$ or BH_2C^-		not detected	
26	CN^- or BH_3C^-	26.0036	CN^-	0.5
		26.0084	$^{10}BO^-$	0.6
27	BO^-	27.0048	BO^-	0.5
35	BC_2^-	35.0098	BC_2^-	0.2
43	BO_2^- or $BH_2C{\cdot}H_2O^-$	42.9997	BO_2^-	0.9
51	$C_2{\cdot}BO^-$ or $B_3H_2O^-$	51.0048	$C_2{\cdot}BO^-$	0.4
59	$C_2{\cdot}BC_2^-$	59.0099	$C_2{\cdot}BC_2^-$	0.3
75	$C_4{\cdot}BO^-$	74.9867	$SiC{\cdot}BC_2^-$	0.7
		75.0047	$C_4{\cdot}BO^-$	0.8
83	$C_4{\cdot}BC_2^-$	83.0098	$C_4{\cdot}BC_2^-$	0.3
85	$C_2{\cdot}H_2O.BO_2^-$	85.0233	$B_2C_3{\cdot}BO^-$	1.3
93	not detected	93.0131	$B_2CO{\cdot}BO_2^-$	1.0
100	not detected	100.0218	$^{10}BBC_3{\cdot}BO_2^-$	1.2
101	not detected	101.0182	$B_2C_3{\cdot}BO_2^-$	0.9
108	not detected	108.0270	$^{10}BBC_5{\cdot}BO^-$	0.1
109	not detected	109.0232	$B_2C_5{\cdot}BO^-$	1.2

Chemical Structure Sensitivity – Organics

To show the detailed nature of the structural information which can be obtained from organic compounds by FT LMMS, Figs. 7 and 8 provide the positive and negative ion mass spectra of the biologically active compound flusperilene. Because of the TOF effect in FT LMMS with external ion source, partial data from m/z 20 to 100 and 100 to 500 are represented. The results exhibit the features one expects from LMMS on organic products [18]. Molecular weight information is available from the $[M + H]^+$ and $[M - H]^-$ ions and there are intense fragment signals detected in both the positive and negative ion modes. Accurate mass measurement (within 1 ppm) permits reliable assignment of the signals to the expected structures, as can be seen from Tables 4 and 5. Figure 9 gives a survey of suggested structures for the fragment ions of flusperilene. Fragments issue from well-known cleavages and rearrangements. Further discussion of the different fragmentation routes for poly-functional molecules lies beyond the scope of this paper and will be published elsewhere [19]. The point of interest is that FT LMMS provides parent ions to determine the molecular weight and fragment ions to deduce the functionalities in the compound studied.

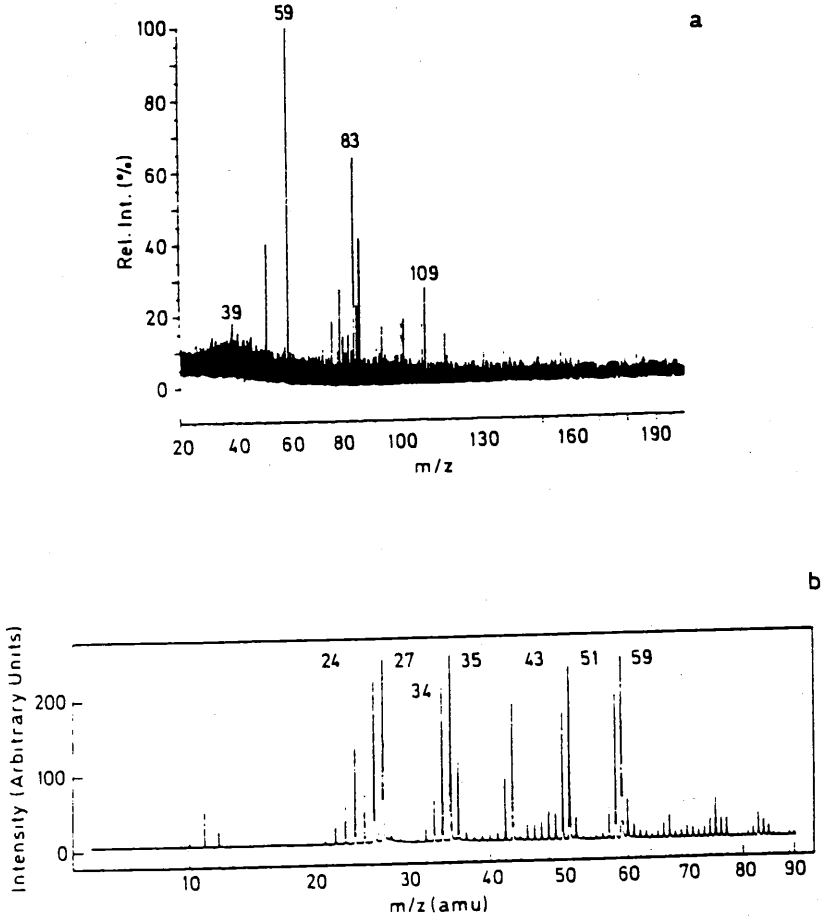

Fig. 6. Analysis of SiC B_4C neo-ceramic material. Negative ion mass spectrum recorded by (**a**) FT LMMS with a $T_{open\ gate}$ of 300 µs and a laser power density of 7.4×10^8 W cm^{-2} and (**b**) TOF LMMS with the same power density. The signal around *m/z* 78 is due to electronic noise

The analysis of dyed cloth fibres represents a micro-analytical test case with a practical application in, for instance, forensic research [20]. Micro-analysis experiments require optimisation of the instrumental parameters by means of representative model systems. Cotton dyed with methylene blue is used because the molecule exhibits almost no fragmentation. As a result, the total ion current is almost carried by a single peak. Molecules that exhibit fragmentation have proportionally poorer detection limits.

Figure 10 represents the main results from the model system of dyed cotton. The detection limit was determined as the lowest concentration, where one shot out of two yielded a detectable signal for methylene blue. Hence, the single shot result in Fig. 10b refers within a factor of 2 to a total sampled amount of 0.3 pg per area of 5-µm diameter. The broadband spectrum in Fig. 10c contains, apart from the methylene blue cation, a few small peaks in the lower mass range associated with calcium-containing residues of washing powders and water softeners in the

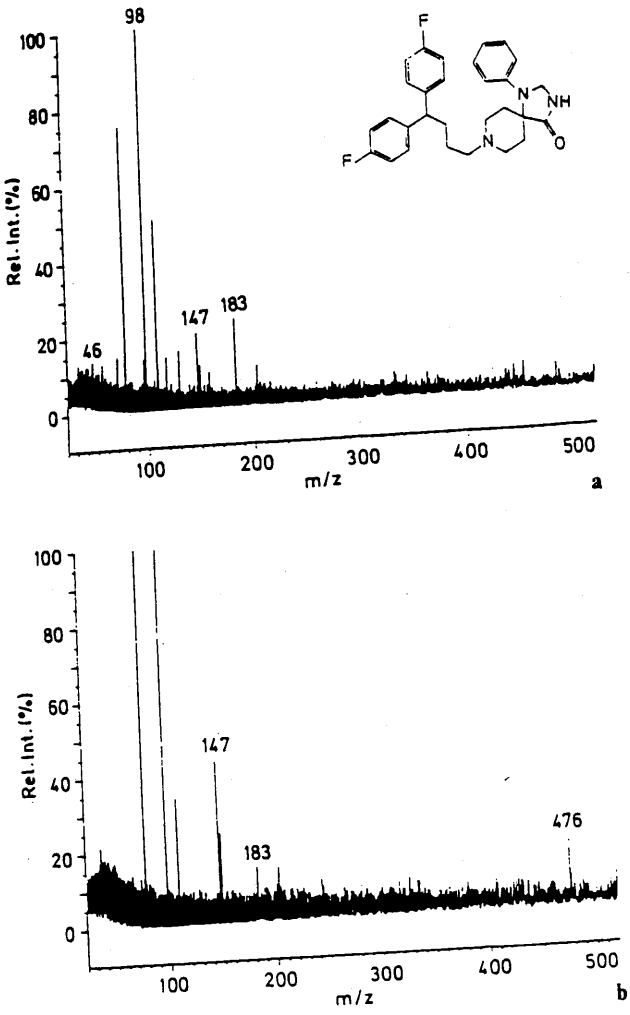

Fig. 7. Analysis of flusperilene (MW 475). Positive ion mass spectra recorded by FT LMMS with a $T_{open\ gate}$ of 300 (**a**) and 500 (**b**) μs. The laser power density is 6.1×10^8 W cm^{-2}. The signal around $m = 78$ is due to electronic noise

textile. The spectrum demonstrates the selectivity one can achieve, by careful optimization of the laser irradiation, depending on the structure of the target and the matrix.

Using this experience, preliminary experiments have been carried out on commercial jeans tissues. The adduct ion of indigo was detected in the single-shot mode using a 5-μm diameter spot for irradiation of the cloth tissue [21]. The feasibility of FT LMMS as an organic microprobe has also been investigated recently by the study of the localization of pigment modecules in plant specimens at the μm level by means of structural ions [22].

Conclusions

The application of FT LMMS in different analytical fields has been presented. The capability of element detection was demonstrated by the analysis of a 50-nm TiW

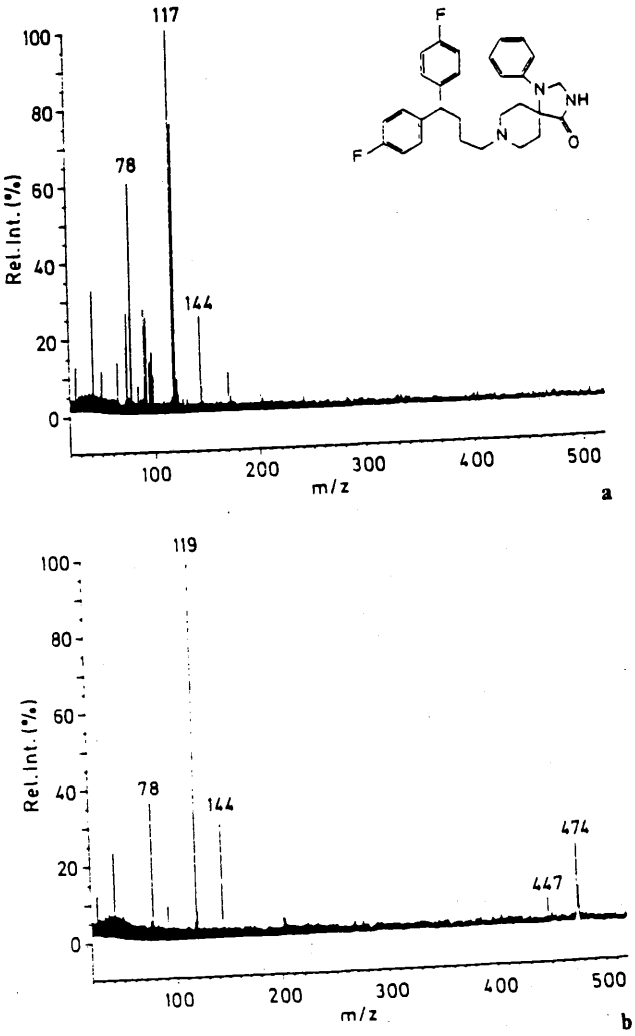

Fig. 8. Analysis of flusperilene (MW 475). Negative ion mass spectra recorded by FT LMMS at a $T_{open\ gate}$ of 200 µs (**a**) and 400 µs (**b**) and a laser power density of 4.3×10^8 W cm^{-2}. The signal around *m/z* 78 is due to electronic noise

Table 4. Mass measurement of the ions in the positive ion mass spectrum of flusperilene, recorded by FT LMMS

m/z	Elemental composition	Absolute error of mass measurement (ppm)
476.250	$C_{29}H_{32}F_2N_3O$	0.9
203.067	$C_{13}H_9F_2$	0.6
183.061	$C_{13}H_8F$	0.6
149.076	$C_{10}H_{10}F$	0.9
147.060	$C_{10}H_8F$	0.7
109.045	C_7H_6F	1.0
98.0602	C_5H_8NO	1.3

Table 5. Mass measurement of the ions in the negative ion mass spectrum of fluspirilene, recorded by FT LMMS

m/z	Elemental composition	Absolute error of mass measurement (ppm)
474.235	$C_{29}H_{30}F_2N_3O$	1.7
447.226	$C_{28}H_{29}F_2N_2O$	1.1
201.052	$C_{13}H_7F_2$	0.9
144.082	$C_{10}H_{10}N$	0.9
119.061	$C_7H_7N_2$	0.2
117.046	$C_7H_5N_2$	0.2
95.0251	$C_4H_3N_2O$	0.3
92.0506	C_6H_6N	0.3
90.0349	C_6H_4N	0.7
74.0036	C_5N	0.2
73.0084	C_6H	0.3
41.9986	CNO	0.9
26.0036	CN	0.8

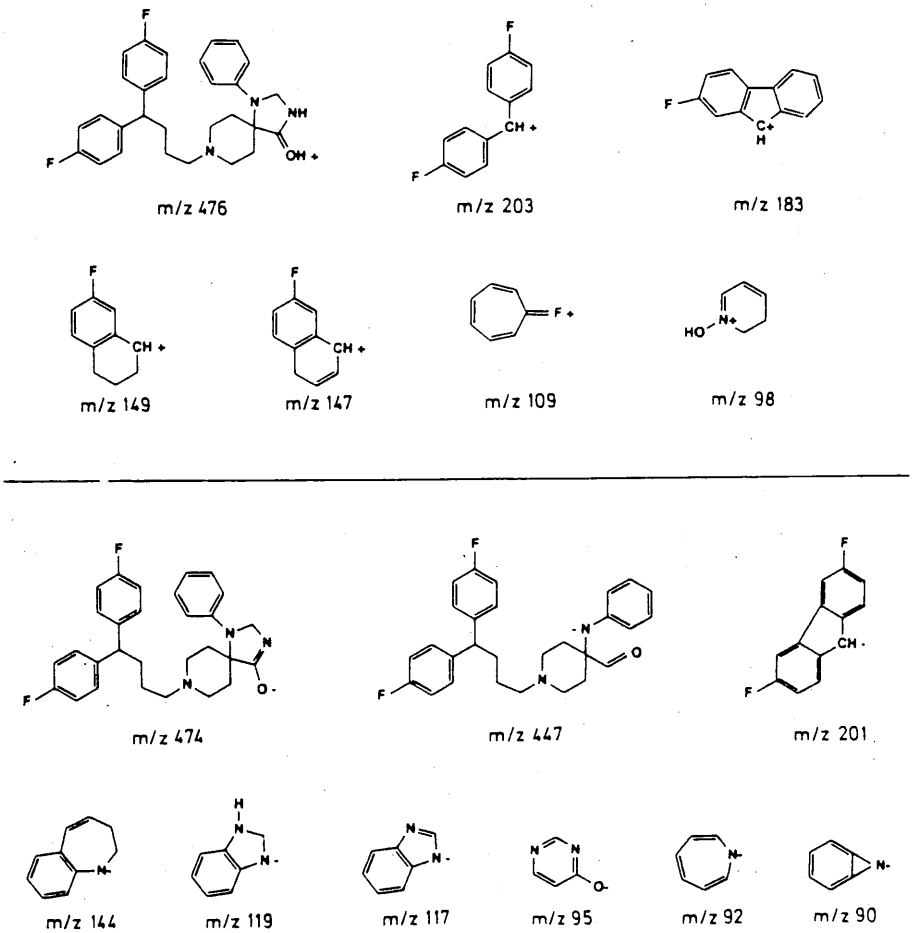

Fig. 9. Survey of structures for the main fragment ions from flusperilene detected by FT LMMS

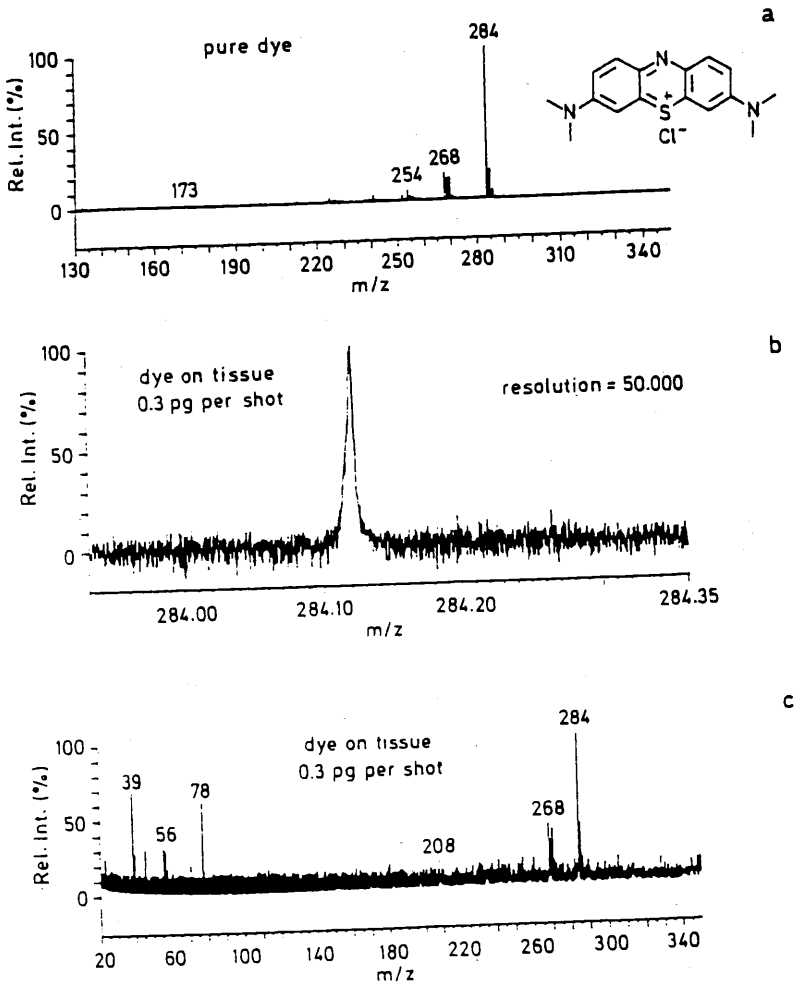

Fig. 10. Positive ion mass spectra recorded by FT LIMMS at a laser power density of 8.6×10^8 W cm^{-2} and $T_{\text{open gate}}$ of 500 μs from methylene blue as a pure dye (**a**) and adsorbed on tissue (**c**). The high resolution signal at m/z 284 is recorded from the dyed tissue (**b**)

layer on a silicon substrate. This was exploited in the practical case of Cr on HPLC column-packing material where detection by analytical electron microscopy was not possible. It was demonstrated that the identification of the molecular structure represents the strength of the method. Also, qualitative information is often sufficient for practical problem-solving. Furthermore, FT LMMS has the advantage that the same sample can be investigated for organic and inorganic constituents. The speciation of inorganic compounds occurs by the direct characterization of the structural fragments. The systematics of cluster ion formation permitted the characterization of LiCl, even though the instrument cannot detect ions under m/z 15. The analysis of a neo-ceramic material sample allowed the comparison of FT with TOF LMMS for speciation purposes. FT LMMS was proved to increase the specificity of the information by its high mass resolution and mass accuracy. Finally, the results of the analysis of flusperilene and dyed cotton fibers demonstrated that FT LMMS gives access to organic analysis. In conclusion, FT LMMS has the potential to

become a method of choice in applications where qualitative information on organic and/or inorganic compounds is needed on a local scale.

Acknowledgements. Wim Van Roy and Luc Van Vaeck are indebted to the National Science Foundation, Belgium (NFWO) as research assistant and research director, respectively. Herbert Struyf acknowledges the 'Impulse Programme in Marine Sciences', supported by the Belgian State – Prime Minister's Services – Science Policy Office (contract MS/06/050). W. Vandervorst (IMEC) is thanked for providing the metal-coated silicon samples.

References

[1] D. Lubman, *Mass Spectrom. Rev.* **1988**, 7, 535 and 559.
[2] L. Van Vaeck, W. Van Roy, R. Gijbels, F. Adams, in: *Laser Ionization Mass Analysis* (A. Vertes, R. Gijbels, F. Adams, eds.), Wiley, New York, 1993, p. 7.
[3] M. Karas, U. Bahr, U. Giessman, *Mass Spectrom Rev.* **1991**, *10*, 335.
[4] D. Holtkamp, G. Bayer, R. Holm, *Mikrochim. Acta* **1991**, *I*, 245.
[5] L. Van Vaeck, H. Struyf, W. Van Roy, F. Adams, *Mass Spectrom. Rev.* **1994**, *13*, 209.
[6] L. Van Vaeck, H. Struyf, W. Van Roy, F. Adams, *Mass Spectrom. Rev.* **1994**, *13*, 189.
[7] M. Pelletier, G. Krier, J. F. Muller, D. Weil, M. Johnston, *Rapid Commun. Mass Spectrom.* **1987**, *3*, 146.
[8] J. T. Brenna, W. R. Creasy, W. McBain, C. Soria, *Rev. Sci. Instrum.* **1988**, *59*, 873.
[9] L. Van Vaeck, W. Van Roy, H. Struyf, F. Adams, P. Caravatti, *Rapid Commun. Mass Spectrom.* **1993**, *7*, 323.
[10] P. Caravatti, M. Alleman, *Org. Mass Spectrom.* **1991**, *26*, 514.
[11] H. Vogt, H. J. Heinen, S. Meier, R. Wechsung, *Fresenius Z. Anal. Chem.* **1981**, *308*, 195.
[12] R. W. Linton, I. H. Musselman, F. Bruynseels, D. S. Simons, *Microbeam Analysis-1987* (R. H. Geiss, ed.), San Francisco Press, San Francisco, 1987, p. 365.
[13] L. Van Vaeck, P. Van Espen, E. Jacob, R. Gijbels, W. Cautreels, *Biomed. Environ. Mass Spectrom.* **1988**, *16*, 113.
[14] H. Struyf, L. Van Vaeck, R. Nulens, R. Van Grieken, *Rapid Commun. Mass Spectrom.* Submitted.
[15] H. Struyf, W. Van Roy, L. Van Vaeck, R. Van Grieken, R. Gijbels, P. Caravatti, *Anal. Chim. Acta* **1993**, *283*, 139.
[16] H. Struyf, W. Van Roy, L. Van Vaeck, R. Van Grieken, P. Caravatti, *Rapid Commun. Mass Spectrom.* **1994**, *8*, 32.
[17] L. Van Vaeck, R. Gijbels, *Fresenius' J. Anal. Chem.* **1990**, *337*, 743, 755.
[18] W. Van Roy, H. Struyf, L. Van Vaeck, R. Gijbels, P. Caravatti, *Rapid Commun. Mass Spectrom.* **1994**, *8*, 40.
[19] W. Van Roy, L. Van Vaeck, H. Struyf, R. Gijbels, *J. Mass Spectrom.* submitted.
[20] P. F. Schmidt, B. Brinkmann, in: *Microbeam Analysis-1989* (P. E. Russell, ed.), San Franciso Press, San Francisco, 1989, p. 330.
[21] W. Van Roy, H. Struyf, L. Van Vaeck, R. Gijbels, SIMS IX Proc, *Yokohama, Nov. 7-12, 1993*, A. Bennighoven, Y. Nihei, R. Shimizu, H. W. Werner (eds.), p. 463.
[22] A. Mathey, W. Van Roy, L. Van Vaeck, G. Eckhardt, W. Steglich, *Rapid Commun. Mass Spectrom.* **1994**, *8*, 46.

Received July 22, 1994. Revision June 1, 1995.

trends

Present and future applications of beam techniques in environmental microanalysis

Wendy Jambers, René Van Grieken *
Antwerp, Belgium

This article describes the recent applications of electron-probe X-ray microanalysis (EPXMA), laser microprobe mass spectrometry (LMMS), including on-line LMMS, and microparticle-induced X-ray emission (μ-PIXE) in environmental single particle analysis. The microbeam techniques which are in development and potentially interesting for environmental analysis are briefly discussed.

1. Introduction

The analysis of gaseous pollutants originally dominated the environmental analytical research area. Soon, however, it was confirmed that particles play a much larger role in the environment than was believed earlier. It is now well understood that particles are the major transport form of material in water and in air, that environmental particles frequently contain toxic components and that aerosols influence the global climate and the visibility of the atmosphere. During the last decade, bulk and single particle techniques have been used together to characterize these particles. This review will only discuss microbeam techniques which can be used for single particle analysis. These techniques are very valuable as a complement to the more conventional bulk analysis, because they provide detailed information concerning the origin, formation, transport, reactivity, transformation reactions and environmental impact of particulate matter.

The small sizes of the particles result in specific problems in single particle analysis. The uncertainty in the determination of the interaction volume and the absence of suitable particle standards make quantitative analysis difficult. To ensure the statistical relevance of the results, a large number of particles need to be analysed and this makes individual particle analysis time consuming. Computer-controlled electron-probe X-ray microanalysis (EPXMA) is the most advanced example of automation and computerization which reduce the long analysing times. Another problem with most microbeam techniques is the need to operate in

* Corresponding author.

0165-9936/96/$15.00
SSDI 0165-9936(95)00098-4

Table 1
Overview of the study areas where atmospheric and indoor aerosols have been analysed with microanalytical techniques

Study area	Microanalytical technique				
	EPXMA	LMMS	μ-PIXE	EELS	SIMS
Atmospheric aerosols					
Alaska	+				
Amazon Basin	+	+	+		
Antarctic	+	+	+		
Antwerp, Belgium	+	+	+		
Bahamas		+			
Bolivia		+			
Brazil		+			
Cape Grime, Tasmania	+	+			
Coal mines		+	+		
Hawaii	+				
Hungary	+				
Karlsruhe, Germany					+
Khartoum, Sudan	+				
Kuwait	+				
North Sea	+	+	+		
Pacific Ocean	+				
Phoenix, AZ, USA	+			+	
Sakushima Island, Japan	+				
Santiago, Chile	+	+			
Sargasso Sea		+			
Siberia	+				
Indoor aerosols					
Asbestos fibres		+		+	+
House dust	+				
Industrial aerosols	+	+	+		

vacuum. This can cause serious losses and transformations of volatile and unstable compounds. In on-line laser microprobe mass spectrometry (on-line LMMS), these losses are reduced by using a very small time interval between ambient sampling and analysis. Since all microanalytical beam techniques have their own characteristic limitations, several techniques should be combined with conventional bulk analysis to characterize the sample fully.

The applications of microanalytical techniques to different environmental problems over the period 1984–94 are summarized in Table 1 and Table 2 (using information from earlier reviews by Van Grieken and Xhoffer [1] and Jambers et al. [2]). These tables show that EPXMA, LMMS and microparticle-induced X-ray emission (μ-PIXE) are the microbeam techniques which are most used for environmental analysis. Their most recent applications, published during 1993–94, will be discussed in more detail in this review. For descriptions of the microanalytical techniques involved and for applications of scanning transmission electron microscopy (STEM), electron energy loss spectrometry (EELS), secondary ion mass spectrometry (SIMS) and micro-Raman spectroscopy, reference is made to earlier reviews [1–4]. Microscopic X-ray fluorescence (μ-XRF) and synchrotron radiation μ-XRF (μ-SRXRF) are techniques which have recently been developed and will undergo major improvements in the near future. Since these techniques will become very useful for single particle environmental analysis, they are briefly discussed at the end of this review.

Table 2
Overview of the study areas where aqueous suspension and sediments have been analysed with microanalytical techniques

Study area	Microanalytical technique		
	EPXMA	LMMS	STEM
Suspensions			
Atlantic Ocean	+		
Elbe estuary, Germany	+		
Ems estuary, Germany	+		
Flores Sea, Indonesia	+		
Garonne estuary, France	+		
Magela Creek, Australia	+		
Makasar Strait, Indonesia	+		
North Sea	+	+	
Onondaga Lake, NY, USA	+		
Rhône estuary, France	+		
Sargasso Sea	+		
Scheldt estuary, Belgium		+	
Scotia Sea-Weddel Sea	+		
Sumbawa Island, Indonesia	+		
Sediments			
Baltic Sea	+		
Eight lakes in Ontario			+

2. Electron-probe X-ray microanalysis and scanning electron microscopy

The fundamental differences between EPXMA and scanning electron microscopy with energy-dispersive X-ray detection (SEM–EDX) have been minimized over the years to a slight difference in instrumental set-up. Both techniques can now be used for both chemical and morphological studies and their applications to environmental particles are therefore discussed together.

2.1. Applications to aerosols

A primary characterization of remote aerosols from Eastern Europe was applied to samples which were collected in the middle of the Great Hungarian Plain [5]. From the EPXMA results it could be concluded that anthropogenic emissions are important sources of these background aerosols. Industrial sources contributed 59% of the total particle abundance. The largest group of anthropogenic particles were fly ashes consisting of silicates and produced by power plants and metallurgy. For gypsum particles various sources are possible, but since some Hungarian power plants use lime to reduce the sulphur dioxide emission, these are certainly responsible for some of the gypsum. The last industrial particle groups were the iron-rich and the iron sulphate aerosols which may originate from different sources.

New evidence of long-range transportation of aerosols has been given by the analysis of volcanic loess on the island of Hawaii [6]. Particles from late Quaternary volcanic loess deposits of the Pahala formation were characterized by combining bulk X-ray powder diffraction with SEM–EDX of single particles and SEM–EDX X-ray mappings of grain mount slides of 0.25 mm^2. In this volcanic loess evidence was found of sustained long-range transport, deposition and preservation of Asian dust. The Hawaiian lava and Pahala silts have a very restricted mineralogy (they consist only of basalt) and the discovered quartz grains thus must have an exotic, distance source. Since the annual dust storms from the Asian deserts can still be measured at the Mauna Loa Observatory, the source of these quartz particles was easily traced. Still surprising is that these particles contributed 1–3% to the deposition and that numerous grains had a diameter between 1 and 10 μm, some even 60 μm.

Aerosols from the city of Khartoum, Sudan, have been characterized by combining different bulk techniques with automated EPXMA measurements [7]. EPXMA confirmed the bulk results and allowed the differentiation of the dominant soil dust group into different particle types. The majority of these particles could be identified as aluminosilicates, while quartz and calcium carbonate formed the minor fractions. The few combustion particles found (on average 5%) all consisted of sulphates.

The decrease in the use of leaded gasoline is visible in the reduction of lead-containing particles in aerosols collected over the last decade in Phoenix, Arizona [8]. Automated SEM–EDX also revealed the dominance of 'zero count' particles; these are organic particles which do not have any elements heavier than sodium, in the size fraction smaller than 2 μm. These organic aerosols are most likely carbonaceous particles produced by anthropogenic sources such as motor vehicles. Sulphur-containing particles were also common in the fine fraction but their abundance has decreased from 30% to 17% over the last decade. The coarse fraction, on the other hand, was dominated by silicon- and calcium-rich mineral particles.

Methanesulphonic acid (MSA) can be used as a tracer for oceanic emissions and atmospheric reaction pathways of organosulphur because no other source but the ocean is known for MSA. Dimethyl sulphide (DMS) is the most abundant reduced sulphur compound transferred from the sea into the atmosphere, where it is oxidized to MSA and sulphur dioxide. The nature and morphology of MSA particles, collected over Sakushima Island, located in central Japan near the Pacific Ocean, were determined by combining SEM and transmission electron microscopy (TEM) with thin-film chemical tests [9]. MSA particles dominated the micrometre size range under very humid conditions. They are apparently formed through heterogeneous nucleation reactions of gaseous MSA with sea salt and/or soil particles. The sub-micrometre range was characterized by huge amounts of sulphate particles and a complete absence of MSA.

Air masses which cross a marine area in the lower troposphere are subject to air–sea exchange processes which can modify their composition. This variation in composition was studied through EPXMA of aerosol and rain water samples collected on-board two research vessels which were constantly positioned 200 km down-wind from each other in the central part of the North Sea [10].

This research was focused on giant aerosols, i.e., aerosols with a diameter larger than 1 μm. Earlier work indicated that these giant aerosols, although their abundances are very low compared with the smaller aerosols, play an extremely important role in the total atmospheric deposition. Principal factor analysis (PFA) of the data set showed that these giant aerosols could be related to four sources while hierarchical clustering revealed a total of eight different particle types. During the crossing over the sea, no significant decrease in particle diameter was observed, although the amount of aluminosilicates was reduced and replaced by sea salt and sea water crystallization products. The particles collected from rain water showed significant differences in diameter and in composition. During a travel distance of 200 km larger particles are more prone to undergo dry and wet deposition and the air mass is also diluted, which can explain the absence of large and anthropogenic particles in samples collected on-board the second vessel. The correlation between the particle composition, origin and shape was studied by manual EPXMA. Characterization on basis of the shape was possible for most particle types.

Siberia is characterized by some very remote areas, without any industry and with a very low population density, and other regions with serious heavy metal pollution. Since western and central Siberia are probably the most important source of pollutants for the air of the Arctic region, it is necessary to characterize single particles from these regions. Van Malderen et al. [11] published some preliminary results of EPXMA measurements of aerosols collected in Karasuk and Klyuchi and above Lake Baikal. Aluminosilicates dominate in all samples from the two cities. For the summer samples, this can be explained by soil dust, but during winter when the ground is completely covered with snow, the only possible source of aluminosilicates is fly ash. The pollution in the lower basin of lake Baikal is clearly visible in the aerosol samples although a constant but small (less than 3%) amount of heavy metal aerosols was found in all Baikal samples.

SEM–EDX has also been used to study particulate lead in floor dust in houses located in the London Borough of Richmond, UK [12]. The results were classified using a scheme which was obtained by analysing different types of lead source particles. For particles in the size range 64–1000 μm the major source of lead-containing house dust seems to be paint, whereas for the 0–64 μm size fraction, paint, road dust and garden soil are the major contributors. The variations in these major particle types could not be related to the age of the houses.

2.2. Applications to suspensions and sediments

Sediment samples collected from a longitudinal profile in the Elbe estuary were analysed with automated EPXMA to determine their composition and source and to estimate the extent to which marine solids are transported upstream [13]. Silicon-rich particles, i.e., quartz and aluminosilicates, dominate these samples. Calcium-rich, iron-rich and titanium-rich particles are also present in all samples but in much lower abundances. The calcium-rich particles are identified as calcite, which can be used to determine the mixing ratio of marine and fluvial sediments. This mixing ratio showed the transportation of marine sediments across the salt wedge. Suspended matter transported during a maximum peak flow on the Elbe was also analysed with automated EPXMA. This suspended matter originates mainly from the load transported by the peak flow and from erosion of settles mud particles.

Suspended matter collected during a small flood event in the Magela Creek, tropical northern Australia, has been separated into suspended particulate matter (SPM) with a diameter larger than 1 μm and coarse and fine colloidal matter (CCM with a size of 0.1–1 μm and FCM with diameters of 0.015–0.1 μm) [14]. SPM was predominantly inorganic while the two colloidal fractions were characterized by high abundances of organic matter. Individual particle analysis with automated EPXMA was used to characterize the inorganic fractions of SPM and CCM (the FCM is too small to be analysed and contributed only 10% of the total colloidal matter). Both SPM and CCM were dominated by iron-rich aluminosilicates and quartz particles.

A combination of automated EPXMA and bulk techniques was used to characterize silty and clayey sediments collected in the Baltic Sea [15]. Clustering resulted in nine particle types which could be identified as different minerals. All samples were dominated by quartz and aluminosilicates, but these are not very useful for characterizing the geochemistry of the Baltic sediments. Reduced species, such as iron sulphides and rhodochrosite characterize anoxic sediments, e.g., those found in the Gotland Deep, whereas more oxygen-rich areas such as the Kattegat are characterized by iron and

manganese oxides/hydroxides. Sulphides and oxides/hydroxides are both present in regions with changeable redox conditions. Erosion and anthropogenic deposition are the most probable sources of the large amounts of titanium-rich particles which were detected near the coast of Germany and southern Poland. Calcium-rich sediments were only present in the transition zone between the Baltic and the North Sea. The gradient shows clearly that there is an inflow of calcium-rich particles from the North Sea into the Baltic Sea.

3. Microparticle induced X-ray emission

Aerosols collected above the North Sea in the air–sea exchange study were next to their characterization with EPXMA [10] also studied with μ-PIXE [16]. The giant aerosols with a diameter larger than 5 μm could be divided into three basic particle types: sea salt, sea salt combined with large amounts of sulphur, potassium and calcium and metal-rich particles. The heterogeneous structure of these giant marine aerosols could be demonstrated with elemental maps of these particles. Especially agglomerates showed distinct differences in local elemental composition. Fig. 1 illustrates the local differences in the chlorine, potassium, calcium and titanium maps of one aggregated particle. It was seen that in the presence of huge amounts of sea salt particles, large fractions of heavy metal-rich particles, which are normally restricted to the sub-micrometre size range, coagulate with sea salt and form particles with diameters larger than 5 μm.

μ-Pixe and RBS (Rutherford back-scattering) analysis have been used to characterize 1 μm fly-ash particles collected at the inlet and outlet of the electrostatic precipitator of a coal-fired power plant [17]. By sampling both inlet and outlet a better understanding can be acquired of the collection mechanism during the precipitation, but the inlet samples can also be used to study particle formation during coal combustion. The difference in particle types found at the inlet and outlet suggest the importance of the chemical composition effect on the electrostatic precipitation.

Elemental maps recorded by μ-PIXE are usually presented as elemental intensity maps. Local changes in areal density and topology of the analysed particles result in differences between the actual concentration distribution and the elemental intensities recorded in the μ-PIXE maps. The local

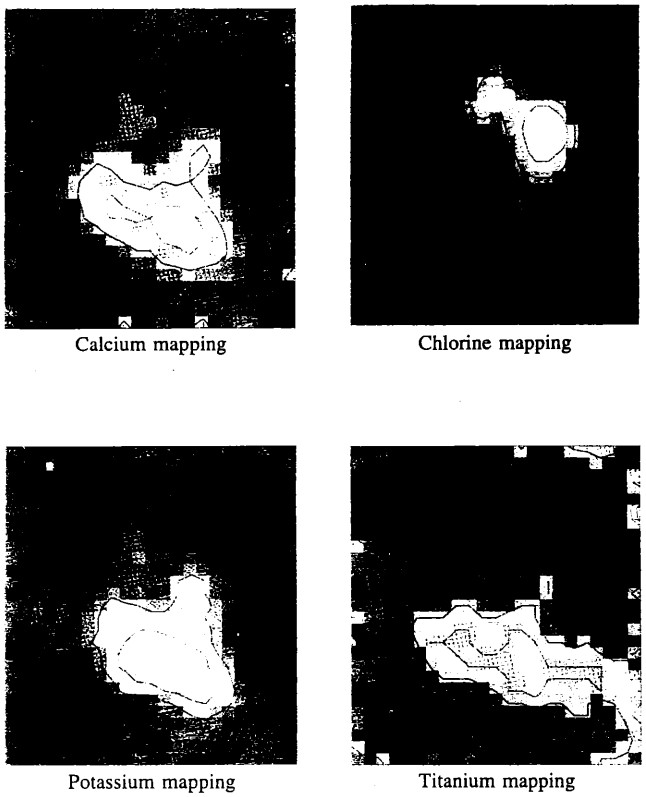

Fig. 1. Elemental distribution of a 16 μm North Sea aerosol agglomerate. These maps were collected with a 2.5 MeV proton microbeam with spot size 2.5 μm. The total area is 44 by 52 μm and the radiation time was 45 min. This figure is similar to that given in Ref. [16]. (This Figure is available in full colour on the Internet at: http://www.elsevier.nl/locate/trac under Supplementary material.)

density variation in the analysed particles can be determined by scanning transmission ion microscopy (STIM) [18]. Comparison of theoretically obtained X-ray maps of spherical coal fly ash aerosols with experimental μ-PIXE and STIM maps showed that STIM is very useful for the determination of the areal concentration maps of the particles. A combination of μ-PIXE, RBS and STIM was also used to characterize aerosols collected in the city of Singapore [19].

4. Laser microprobe mass spectrometry

It is thought that mainly the quartz content is responsible for the health risk produced by coal mine dust. A set of three quartz-rich coal mine dust samples with significant toxicological differences were analysed with conventional bulk methods and LMMS [20]. No correlation could be found

between the toxicity and the bulk results, while LMMS provided data which were in agreement with the toxicological knowledge. LMMS revealed heterogeneous distributions of potentially toxic components such as silica and siderite. This confirms that from toxicological point of view information about the potentially active particles or particle surfaces is much more important than the total composition of the sample.

Dusts containing metal oxides are mainly produced in the iron and steel industries. The oxidation state of these metals can influence their toxic and carcinogenic effects. LMMS, in combination with Raman spectrometry, was used to determine the chromium valency in dust emitted by steel factories [21]. The valency and type of chromium depends on the size and the overall composition of the particles. The smallest (<1.1 μm) and the largest particles (>6 μm) contain hexavalent chromium, whereas the intermediate size fraction mainly encloses trivalent chromium. The hexavalent chromium is present as calcium chromate in the largest particles and possibly as sodium and potassium chromate in the smallest size fraction.

A combination of bulk techniques and LMMS was used to determine lead in standard particles and in particles collected in a city and near a highway in The Netherlands [22]. Both LMMS and differential pulse anodic stripping voltammetry (DPASV) were able to discriminate between lead-coated and lead-coprecipitated calcium carbonate standard particles. For the much more complex natural aerosols, no surface-related information could be deduced with LMMS, although this technique was still useful for determining the single particle composition. Most aerosols were mixed salts of ammonium nitrate and ammonium sulphate and contained variable metal concentrations (especially lead and vanadium).

Recently, on-line LMMS or rapid single particle mass spectrometry (RSMS) has been developed. This technique can determine the chemical composition and size of individual particles in situ on a continuous and real-time basis. Particles are sampled directly into the mass spectrometer; they are located though interception with continuous lasers and vaporized and ionized by excimer lasers. For a more detailed description of the instrument, reference is made to Prather et al. [23], Carson et al. [24] and Jambers et al. [2]. Until now, only descriptions of instrumentation and tests on artificial aerosols have been reported in the literature. The most recent publication describes the application of RSMS for the speciation of non-volatile and semi-volatile sulphur compounds, the measurement of isotopic ratios and the detection of thin coatings on particles produced by condensation of reactive gases [24]. Prather et al. [23] reported on the use of an instrument in which the particle localization is done by dual-beam light scattering. This modification makes it possible to obtain simultaneously the size and the composition of a particle in real time. Another advantage is that this two-laser system is independent of the way in which the particle passes though the beam. This implies that no prior knowledge of the refractive index of the particles is necessary.

LMMS has recently been adapted with a Fourier transform (FT) ion cyclotron resonance (ICR) mass spectrometer, which has a high resolving power and high mass accuracy [25]. The analytical performance of FT-LMMS with an external source is comparable to that of time of flight (TOF) LMMS, but it has a better mass resolution (about 1 000 000 compared with about 1000) and has a better accuracy in the m/z determination. The lateral resolution of FT-LMMS is 5 μm instead of 1 μm for TOF-LMMS. Since FT-LMMS has only been available for a few years, no papers have been published on environmental applications of this technique.

5. Microscopic X-ray fluorescence and microscopic synchrotron radiation X-ray fluorescence

The development of relatively simple focusing devices for X-rays has made microscopic X-ray fluorescence (μ-XRF) interesting for single particle analysis [26]. Conical or tapered capillaries make it possible to focus the X-ray beam to a 10 μm spot with a minimum loss of photon flux. The major advantages of this technique are the good detection limits for heavy elements, simple sample preparation and the possibility of working under atmospheric pressure. The main limitation at present is the relatively large beam diameter (<10 μm).

The conventional X-ray source can be replaced by synchrotron radiation to obtain microscopic synchrotron radiation X-ray fluorescence (μ-SRXRF). The high intensity and natural collimation make this kind of radiation ideal for the formation of X-ray microbeams. At present microbeams with a lateral resolution of 5–10 μm are

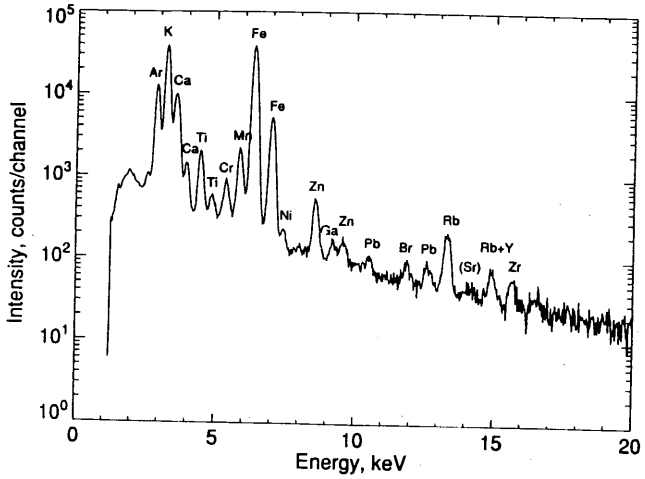

Fig. 2. X-ray spectrum of a 15 μm diameter Antarctic ice core particle. This figure is similar to that given in Ref. [26].

available in second-generation synchrotrons. The low emittance of the synchrotron source makes it possible to use, next to conical capillaries, Bragg-reflecting or totally reflecting curved mirrors to create X-ray beams of sub-micrometre dimensions. This sophisticated X-ray optics will be used, e.g., in the μ-SRXRF dedicated beamline of the European Synchrotron Radiation Facility (ESRF) at Grenoble, France, which is now under development and will be operational in 1997. In this beamline a high-flux 5–10 μm spot will be combined with a lower flux sub-micrometre spot. This sub-micrometre spot will be very useful for the determination of trace metals in single environmental particles.

Antarctic ice core particles have already been analysed using μ-SRXRF in the second-generation synchrotron at Brookhaven, New York [27]. The spectrum and the metal concentrations of such a particle are given in Fig. 2 and Table 3. The concentrations have been calculated on the total mass of this particle, which was 1300 pg, with the iron peak as a reference. These concentrations in the femtogram range illustrate the good detection limit.

Table 3
Heavy metal content calculated from the X-ray spectrum shown in Fig. 2

Heavy metal	Content (fg)
Cr	150
Mn	640
Ni	30
Zn	200
Ga	35
Pb	88
Br	48
Rb	340
Sr	35
Y	34
Zr	110

Fly ash particles taken from different types of power plants and incinerators have also been analysed with the μ-SRXRF-module at Brookhaven [28]. It was possible to measure the elemental composition of individual fly ash particles with sizes down to a few micrometres and to obtain two-dimensional maps of the elemental distributions in 10 μm sections of large particles. Micrometre and sub-micrometre analysis and mappings of individual particles, however, will only be possible in the third-generation synchrotrons.

6. Conclusion

Although the importance of single particle analysis to environmental research is widely recognized, the applications are still limited. EPXMA, LMMS and μ-PIXE seem to have found their position in the laboratories of environmental aerosol scientists. These techniques are able to give fast and reliable results and are mostly used in combination with conventional bulk methods. Other microanalytical techniques have only recently been discovered by environmental scientists and their application in this domain are now being refined. The more complex sample preparation has resulted in a limited number of applications on aquatic suspensions and sediments. In the last few years, simple and powerful techniques for the preparation of electron microscopy samples have become available and the first applications are being published. Some of these preparations are also useful for other techniques and we expect that the number of applications will increase dramatically in the near future. At the moment new μ-SRXRF beamlines are in development which will make it possible to analyse environmental particles with a beam spot smaller than 1 μm.

7. Glossary

CCM	coarse colloidal matter
DMS	dimethyl sulphide

DPASV	differential pulse anodic stripping voltammetry
EELS	electron energy loss spectrometry
EPXMA	electron-probe X-ray microanalysis
FCM	fine colloidal matter
FT-ICR-MS	Fourier transform ion cyclotron resonance mass spectrometry
FT-LMMS	Fourier transform laser microprobe mass spectrometry
LMMS	laser microprobe mass spectrometry
MSA	methanesulphonic acid
μ-PIXE	microparticle-induced x-ray emission
μ-SRXRF	microscopic synchrotron radiation X-ray fluorescence
μ-XRF	microscopic X-ray fluorescence
PFA	principal factor analysis
RBS	Rutherford back-scattering analysis
RSMS	rapid single particle mass spectrometry
SEM	scanning electron microscopy
SEM–EDX	scanning electron microscopy–energy dispersive X-ray analysis
SIMS	secondary ion mass spectrometry
SPM	suspended particulate matter
STEM	scanning transmission electron microscopy
STIM	scanning transmission ion microscopy
TEM	transmission electron microscopy
TOF-LMMS	time-of-flight laser microprobe mass spectrometry

Acknowledgements

We thank Dr. J. Injuk and Dr. K. Janssens for the figures of μ-PIXE and μ-SRXRF. This work was partially prepared in the framework of the Impulse Programme in Marine Sciences, supported by the Belgian State-Prime Minister's Service-Services for Scientific, Technical and Cultural Affairs (contract MS/06/050).

References

[1] R. Van Grieken and C. Xhoffer, J. Anal. At. Spectrom., 7 (1992) 81.
[2] W. Jambers, L. De Bock and R. Van Grieken, Analyst, 120 (1995) 681.
[3] M. Grasserbauer, Mikrochim. Acta, III (1983) 415.
[4] C. Xhoffer, L. Wouters, P. Artaxo, A. Van Put and R. Van Grieken, in J. Buffle and H.P. Van Leeuwen (Editors), Environmental Particles, Vol. 1, Lewis, Chelsea, MI, 1992, p. 107.
[5] S. Török, S. Sándor, C. Xhoffer, R. Van Grieken, E. Mészáros and A. Molnar, Időjárás, 96 (1993) 223.
[6] E.J. Bejét, M. Keskinen and K. Severin, Sediment. Geol., 84 (1993) 189.
[7] M.A.H. Eltayeb, C.F. Xhoffer, P.J. Van Espen and R.E. Van Grieken, Atmos. Environ., 27B (1993) 67.
[8] K.A. Katrinak, J.R. Anderson and P.R. Buseck, Environ. Sci. Technol., 29 (1995) 321.
[9] G.-W. Qian and Y. Ishizaka, J. Geophys. Res. Oceans, 98 (1993) 8459.
[10] L.A. De Bock, H. Van Malderen and R. Van Grieken, Environ. Sci. Technol., 28 (1994) 1513.
[11] H. Van Malderen, R. Van Grieken, T. Khodzher, M. Grachev, V. Bufetov and K.P. Koutzenogii, in P. Hoffmann (Editor), Proceedings of 2nd Russian–Ukrainian–Austrian–German Analytical Symposium, Technische Hochschule Darmstadt, 1993, p. 241.
[12] A. Hunt, D.L. Johnson, I. Thornton and J.M. Watt, Sci. Total Environ.,138 (1993) 183.
[13] A. Van Put, R. Van Grieken, R.-D. Wilken and B. Hudec, Water Res., 28 (1994) 643.
[14] B.T. Hart, G.B. Douglas, R. Beckett, A. Van Put and R.E. Van Grieken, Hydrol. Proc., 7 (1993) 105.
[15] F. Belmans, R. Van Grieken and L. Brügmann, Mar. Chem., 42 (1993) 223.
[16] J. Injuk, L. Breitenbach, R. Van Grieken and U. Wätjen, Mikrochim. Acta, 114/115 (1994) 313.
[17] A. Caridi, E. Cerede, G.W. Grime, M. Jakšić, G.M. Braga Marcazzan, V. Valković and F. Watt, Nucl. Instrum. and Methods B, 77 (1993) 524.
[18] I. Bogdanović, S. Fazinić, M. Jakšić, G.W. Grime and V. Valković, Nucl. Instrum. Methods B, 85 (1994) 732.

[19] I. Orlic, F. Watt, K.K. Loh and S.M. Tang, Nucl. Instrum. Methods B, 85 (1994) 840.
[20] J.L. Tourmann and R. Kaufmann, Int. J. Environ. Anal. Chem., 52 (1993) 215.
[21] A. Hachimi, E. Poitevin, G. Krier, J.F. Muller, J. Pironon and F. Klein, Analusis, 21 (1993) 77.
[22] J.H.A.M. Wonders, S. Houweling, F.A.J. De Bont, H.P. Van Leeuwen, S.E. Eeckhaoudt and R.E. Van Grieken, Int. J. Environ. Anal. Chem., 56 (1994) 193.
[23] K.A. Prather, T. Nordmeyer and K. Salt, Anal. Chem., 66 (1994) 1403.
[24] P.G. Carson, K.R. Neubauer, M.V. Johnston and A.S. Wexler, J. Aerosol Sci., 26 (1995) 535.
[25] L. Van Vaeck, W. Van Roy, H. Struyf, F. Adams and P. Caravatti, Rapid Commun. Mass Spectrom., 7 (1993) 323.
[26] K. Janssens, L. Vincze, J. Rubio, F. Adams and G. Bernasconi, J. Anal. At. Spectrom., 9 (1994) 151.
[27] K. Janssens, personal communication.
[28] C. Tuniz, K.W. Jones, M.L. Rivers, S.R. Sutton and S. Török, Environ. Sci. Technol., in press.

Wendy Jambers is graduated in 1992 as chemist at the University of Antwerp in Belgium, with a dissertation on microanalysis. She is now working as a PhD student at the Micro- and Trace Analysis Centre of the University of Antwerp. Her research is focused on the analysis of aquatic environmental particles with microanalytical techniques.
René Van Grieken is at the Micro and Trace Analysis Centre (MiTAC), Department of Chemistry, University of Antwerp (UIA). Universiteitsplein 1, B-2610 Antwerp, Belgium. He received his MSc and PhD degrees in chemistry at the University of Gent in Belgium. Since 1974, he has been Professor of Analytical and Environmental Chemistry at the University of Antwerp in Belgium. He is co-director of the Micro- and Trace Analysis Centre, which involves approximately 60 researchers, studying the methodology of the various micro- and trace analysis techniques and their applications in environmental chemistry and material science.

RAPID COMMUNICATIONS IN MASS SPECTROMETRY, VOL. 10, 551–561 (1996)

Desorption/Ionization of Inorganic Compounds in Fourier Transform Laser Microprobe Mass Spectrometry with External Ion Source†

Herbert Struyf, Luc Van Vaeck* and René Van Grieken
Department of Chemistry, University of Antwerp, Universiteitsplein 1, B-2610 Wilrijk-Antwerpen, Belgium

Application of FT LMMS to inorganic compounds offers the advantage of direct speciation. This means that signals which refer to intact analyte molecules are detected. Current concepts of desorption and ionization in LMMS are mainly based on time-of-flight data and hence on ions formed during the laser pulse. This paper focuses on indications about the desorption and ionization mechanisms for inorganic compounds that can be deduced from the mass spectra in our FT LMMS database. Specifically, the occurrence of continuing ion formation during several hundreds of microseconds is demonstrated. These data are relevant to the possible role of selvedge ionization versus direct ion emission from the solid state.

Laser microprobe mass spectrometry (LMMS) is an analytical tool for local surface analysis, i.e. the characterization of the main components in a microscopic volume.[1–3] A 1–5 μm laser spot diameter allows LMMS to link micromorphological information directly to the chemical composition. The possibility of obtaining information on both organic and inorganic compounds is a major asset in practical problem solving. Therefore, LMMS is especially useful in applied material research. Current microprobes essentially provide element ratios for the identification of molecules. In contrast, LMMS yields refined qualitative information. Specifically, LMMS generates signals referring to the intact analytes as well as to specific fragments from which the functionalities and composition of the original molecules can be deduced.[3,4] This applies to organic as well as inorganic analytes. The term 'direct speciation' denotes identification of inorganic analytes in the same way as organic compounds are structurally characterized. Quantitation in heterogeneous samples is, however, not yet routinely feasible.

Progress in LMMS methodology and applicability depends on complete control over the parameters governing the ion current as a function of the local concentration. Therefore, understanding the desorption and ionization (DI) mechanisms becomes a prerequisite. The first generation of LMMS instruments, equipped with a time-of-flight (TOF) mass spectrometer, permitted an exploration of the analytical capabilities of laser microbeam irradiation but did not provide extensive experimental possibilities for a detailed study of inorganic DI. More specifically, TOF LMMS signals relate almost exclusively to ions generated during the laser pulse, i.e. the so-called 'prompt' ions.[1]

However, from earlier laser desorption (LD) experiments in a defocused mode it could be anticipated that DI in LMMS would continue long after the laser pulse, i.e. the so-called 'post-laser DI' phenomenon.[6,7] Moreover, the TOF LMMS design inherently favours the detection of direct ion emission from the solid state, while it discriminates against the possible contribution of ion–molecule reactions in the selvedge, i.e. the high-density plume just above the sample.[1] As a result, the concepts of inorganic DI in the literature are inherently biased by TOF LMMS' instrumental features.

† Presented at the 3rd European Workshop on ICR, 4–6 September 1995, Bremen, Germany

* Author for correspondence.

CCC 0951–4198/96/050551–11

A second generation of laser microprobe, the Fourier transform laser microprobe mass spectrometer (FT LMMS), has been developed to permit local analysis with high resolution MS features.[8–10] Although laser ionization is performed in the same way as in TOF LMMS, the spectra look different. The reason is that FT LMMS detects a different fraction of the initial ion population. For instance, FT LMMS registers prompt ions together with the ones from post-laser DI. The external source in our FT LMMS instrument allows ion–molecule interactions during a residence time in the cell of about 1 μs, compared to less than 100 ns in TOF LMMS. As an ion trap instrument, FT LMMS can only store ions with an energy spread of less than 1/3 of the trapping potential values, typically 1.5 eV, while prompt laser ions are believed to show broad energy spreads.[11,12] Additionally, the ion transfer system in our instrument with external ion source only transmits ions with an emission angle of up to 3° to the normal on the sample while TOF LMMS tyically accepts emission angles up to 10°.[13]

A systematic study of inorganic compounds has been undertaken. The selection of compounds served to assess systematic relationships between the signals in the spectrum and the analysed substance so that identification of unknown analytes without reference spectra is made possible.[14] However, through careful evaluation of both the instrumental features and the spectra in the database interesting indications were found about the DI of inorganic compounds. Note that for the very first time FT LMMS data give access to the ions formed during *and* after the laser pulse. The purpose of this paper is to survey the clues the mass spectra offer with respect to the moment of ion formation. This becomes a key feature in the assessment of the relative importance of ion–molecule reactions in the selvedge versus direct ion emission from the solid state.

EXPERIMENTAL

Instrumentation

The FT LMMS instrumentation was developed from a Spectrospin CMS 47X FTMS[15] (Bruker Spectrospin, Billerica, MA, USA). The system uses an Infinity Cell™,[16] a 4.7 T magnet and an external ion source. Static electrical fields transport the ions from the source into the cell.

Received 28 October 1995
Accepted (revised) 29 January 1996

Differential pumping of the transfer line permits the maintenance of a pressure of 10^{-8} Torr in the source, while the cell pressure is 5×10^{-10} Torr. Samples are irradiated under 45° in the reflection mode. Ionization uses a frequency-quadrupled Nd:YAG laser (Quanta-Ray DCR 2-10, Spectra Physics, Mountain View, CA, USA) with fill-in optics for a Gaussian beam profile. The beam is focused to a 5 μm spot. The sample holder can be moved with a precision of 1 μm, allowing the area of interest to be positioned exactly in the waist of the beam. The sample can be viewed under 700× magnification. Additional information on the instrument specifications can be found elsewhere.[10]

Sample preparation

Small quantities of the substances were ground using a mortar and subsequently attached to a wetted sample holder. In cases of poor adhesion double-sided tape was used.

The following compounds were analytical grade reagents from Merck (Darmstadt, Germany): sodium phosphate, calcium nitrate, indium(III) oxide and bismuth(III) oxide. Lead(II) oxide and molybdenum(VI) oxide were purchased from UCB (Brussels, Belgium), cerium(IV) oxide from Fluka (Buchs, Switzerland) and caesium iodide from Janssen Chimica (Beerse, Belgium).

RESULTS AND DISCUSSION

To facilitate the discussion of the results a survey of the concepts of DI of inorganic compounds in LMMS will be presented first. One of the most relevant instrumental parameters, T_{gate}, will be explained in detail.

Concepts of DI in LMMS

Up to now, virtually all concepts of DI induced by focused laser irradiation of solids have been based on TOF results. However, the TOF mass analysers used have no gate in front of the drift tube, which means that the detection of ions is confined to those generated during the laser pulse.

Most authors adhere to the direct ion emission idea. Hillenkamp[17] stressed the non-thermal aspect of microbeam laser DI, which was considered to be a collective non-equilibrium process. This would be sustained by the broad initial kinetic energy distributions of elemental ions, more than 10 eV wide, and the generation of large cluster ions, considered incompatible with thermal evaporation processes. The term 'true laser desorption' was used to denote an ill-defined whole of processes which would emit ions directly from the solid essentially during the laser pulse. Novak *et al.*[18] distinguished physically separated regions in the solid around the point of laser impact. In the centre atomization would take place while molecules and large inorganic clusters would be ejected at the edge. This direct laser ionization would occur during the duration of the laser pulse. The creation of plasma-like conditions under high power density irradiation of solids would allow ion–molecule interactions in a zone very close to the solid surface. This secondary ionization and surface ionization would occur mainly after the laser pulse. There are however, no direct experimental data sustaining these rather vague concepts. Additionally, from systematic studies on alkali halides by TOF LMMS it was concluded that cluster ions would be directly generated from the solid phase by disruption of the lattice.[19–23] The role of gas-phase ionization would be negligible. The energy transfer from the laser beam to the lattice would not happen through heating but via multiphoton absorption, leading to the generation of highly excited free electrons.

In contrast, the possibility of the ion formation through ion–molecule interactions in the selvedge was suggested by Dennemont and Landry[24] on the basis of TOF LMMS data from a variety of inorganic materials. Similarly, measurement of the kinetic energy distributions on carbon and titanium oxide clusters in a transmission mode TOF LMMS showed that the median of the distribution lies at a negative value.[11,12] This means that the ions are produced in the extraction field at some distance from the sample surface. The recombination of ^{12}C and ^{13}C clusters from physically separated carbon foils upon laser ionization pointed in the same direction.[25] Another early publication mentioned the possibility of post-laser-generated elemental ions in TOF LMMS but did not include extensive experimental evidence.[26]

In conclusion, the discussion about the role of the selvedge DI as opposed to the predominance of direct ion emission continues. In our opinion this could be related to the fact that TOF LMMS data primarily refer to the promptly-formed ions.

Instrumental evaluation of the ion formation moment

From the discussion above it is clear that the moment of ion formation is a key element for the distinction between direct ion emission from the solid and DI through ion–molecule interactions in the selvedge. In the latter case, thermal processes are expected to play a prominent role in the ionization of the released neutrals. It is known that the thermionic emission of, for instance, Na^+ continues over up to several hundreds of μs after the laser pulse.[27,28]

The FT LMMS instrument with external ion source gives indirect access to the moment of ion formation, during or after the laser pulse by the so-called gate time or T_{gate}. Ion transfer by electrostatic fields induces a time-of-flight (TOF) effect: low m/z ions arrive at the cell sooner than high m/z ions. The entrance electrodes of the cell are deactivated to permit injection of ions. Once inside the cell ions are reflected from the second trapping-plate electrode. The first electrode must be reactivated to keep them in the cell, which obviously prevents the heavier ions from entering the cell. Assuming that all ions are formed at the same time and place in the source, the reflection time of the lighter ions determines the TOF difference with higher mass ions, that can still be trapped simultaneously.

Ion trajectories were simulated using the SIMION program (Idaho National Engineering Laboratory, Idaho Falls, ID, USA).[29] The inhomogeneous fringing field of the superconducting 4.7 tesla magnet was taken into account. The time spent by ions of a given m/z to get from source to cell is denoted as T_{flight} and that for return to the cell entrance after reflection from the second trapping-plate inside the cell as T_{refl}. In a first approximation for the voltages applied in the Spectrospin transfer system, T_{flight} and T_{refl} can be derived from the following equations (in μs):

$$T_{flight}=24.381\sqrt{m/z}$$

$$T_{refl}=10.436\sqrt{m/z}$$

The instrumental parameter T_{gate} refers to the length of the period, starting with the laser pulse, during which the electrodes in front of the cell are biased to enable free passage of ions in and out of the cell. Neglecting the effects of the ion kinetic energy distribution, T_{gate} should be chosen to be between T_{flight} and $T_{flight}+T_{refl}$ on the assumption that the

ions are generated during the laser pulse (prompt ions). Whenever ost-laser DI occurs over a period T_{pld} (in μs), T_{pld} must be added to T_{flight} when T_{gate} is calculated. As long as T_{pld} remains small compared to T_{refl}, T_{gate} can be kept constant without affecting the signal intensity significantly. However, whenever T_{pld} exceeds T_{refl} by Δt, T_{gate} must be increased accordingly. In that case, post-laser DI occurring from a time Δt up to a time $\Delta t + T_{refl}$ is detected.

FT LMMS of binary salts

A series of common binary salts MX_n was systematically studied. The FT LMMS results on NaCl, KCl, $SnCl_2$, $InCl_3$, $CaCl_2$, etc. display major signals from the elemental ions M^+ and X^- as well as from the cationized or anionized salts $(MX_n)M^+$ or $(MX_n)X^-$, depending on the analog. Apart from CsI, no polymeric clusters $(MX_n)_mM^+$ or $(MX_n)_mX^-$ were detected as opposed to in TOF LMMS.[30] In both instruments, laser irradiation is performed at the same wavelength and with comparable pulse length and power density. Highly polymeric ions are more likely to issue from lattice disruption than from high-order ion–molecule interactions in the selvedge. Directly emitted ions should be detected in both TOF and FT LMMS. However, this does not apply to gas-phase ionization. Hence the FT LMMS data suggest that there is an additional ion contribution, superimposed on the directly emitted one, and most likely related to selvedge DI. First-order type ions will represent the major fraction in the latter contribution. Furthermore, the contribution of selvedge over prompt-ions will be relatively increased in FT LMMS by the integration of the ion current over T_{refl} as opposed to 10–20 ns in TOF LMMS.

Sustaining evidence for the selvedge processes is available from the experimental T_{gate} values. Salts such as NaCl and KCl obviously give rise to a significant Na^+ and K^+ signal at a Δt exceeding the length of the laser pulse by hundreds of μs. Moreover, significant post-laser DI continuing over a time T_{pld} which exceeded T_{refl} was observed for Sn^+ ions as well as for In^+ and $InCl.In^+$ from $SnCl_2$ and $InCl_3$, respectively. More specifically, In^+ and Sn^+ ions were detected at a T_{gate} value which exceeded the sum of the corresponding T_{refl} and T_{flight} values (225 μs and 120 μs respectively), while the $InCl.In^+$ ions arrived between 30 and 220 μs late in the cell. The intensity of the corresponding signals corresponds to at least 40% of the signal detected at the 'minimal' T_{gate}, calculated for prompt ions. Note that the ion formation for salts where the signal detection was confined to the minimal T_{gate} does not exclude the occurrence of post-laser DI. The FT LMMS instrument inherently integrates the ions formed within T_{refl}, which typically ranges over more than 50 μs and therefore exceeds the time period for prompt DI by three orders of magnitude.

FT LMMS analysis of caesium iodide revealed a few remarkable features, not seen for other binary salts. Figures 1 and 2 show the positive and negative mass spectra as a function of increasing T_{gate}. The spectra (a–d) of Figure 1 illustrate the expected influence of the T_{gate} on the relative peak intensities. At a T_{gate} of 300 μs only Cs^+ reaches the cell while at a T_{gate} of 500 μs of $CsI.Cs^+$ is trapped as well, together with a smaller number of Cs^+ ions. Note that $CsI.Cs^+$ in spectrum (b) is generated during the laser pulse or within one T_{refl} period while Cs^+ is produced over at least 100 μs after the laser pulse. This means that the same spectrum displays peaks from ions formed at different moments in the source. As a result, assessment of the relative ion currents generated in the source must be achieved using the S/N ratio of individual peaks, not by relative peak intensities in a given mass spectrum. Later on, higher cluster ions up to $(CsI)_4.Cs^+$ are detected. The relative importance clearly decreases when more molecules are incorporated, which is consistent with the selvedge DI concept. The spectra (e–h) demonstrate that Cs^+ also results from extensive post-laser desorption. The S/N of the signal remains strikingly constant from a T_{gate} of 900 μs up to a T_{gate} of 3.2×10^5 μs.

In the negative-ion mode, similar observations apply. The first spectra (a–c) illustrate the generation of $(CsI)_nI^-$ with $n=0$, 1 and 2. The signals in these three spectra show the expected TOF effect, but from (d–h) it is clear that the I^- signal continues to appear with almost no decay in intensity up to 0.5 seconds after the laser pulse.

In conclusion, CsI—although quite an exceptional case within our FT LMMS database—shows two features which may point to the predominance of selvedge DI. Apart from the extended post-laser generation of Cs^+, the spectra do show higher-order clusters with 3 to 4 neutral molecules. The generation of trimeric and tetrameric forms in FT LMMS from CsI—as opposed to other binary salts—is readily understood in view of the extremely low power density needed to generate the CsI spectrum. Easy desorption logically leads to a dense selvedge with an increased probability of higher order interactions. However, the clusters remain smaller than the stable 'giant' clusters, which are commonly generated in condensed phase ionization methods and expected to occur when lattice disruption prevails.[30] Furthermore, the extended formation of Cs^+ in FT LMMS shows the importance of post-laser DI for laser microbeam irradiation of solids.

FT LMMS of oxysalts

The FT LMMS results on pure oxysalts $M_n(XO_y)_m$ can be described as follows. First of all, the constituents M and XO_y are easily recognised from the low m/z signals in the positive- and negative-ion detection mode, respectively. Note that the main anions XO_t^- do not always correspond to the chemical form in the analyte. For instance, PO_2^- and PO_3^- occur in the case of phosphates, CO_3^- for carbonates. Still, the distinction between the major classes can readily be made. Secondly, a major signal in the higher m/z range of the positive- and/or negative-ion spectra corresponds to the adducts of the analyte molecules with M^+ or the stable XO_t^- species. These ions are the ones of interest for direct speciation. Finally, the remaining peaks in the mass spectra can be assigned to combinations of the stable entities with M^+, MO^+ or YO_t^- as charge carriers. Often these stable moieties can be found by considering the oxysalt as a combination of the metal oxide M_pO_q in its chemically stable form and the remaining $(M_n(XO_y)_m - M_pO_q)$ moiety. Of course, mass spectra of given analytes may exhibit additional features depending on the structure and the properties of the sample.

Figure 3 illustrates the positive-ion mass spectra of sodium phosphate. The main signals clearly fit into the systematic trends outlined above. Note that the signal intensity of the ions with m/z values less than 40 is severely underestimated because of the z-axis ejection occurring during excitation in the Infinity Cell. Special attention should be given to the detection of the peak at m/z 351, which corresponds to a neutral analyte dimer combined with

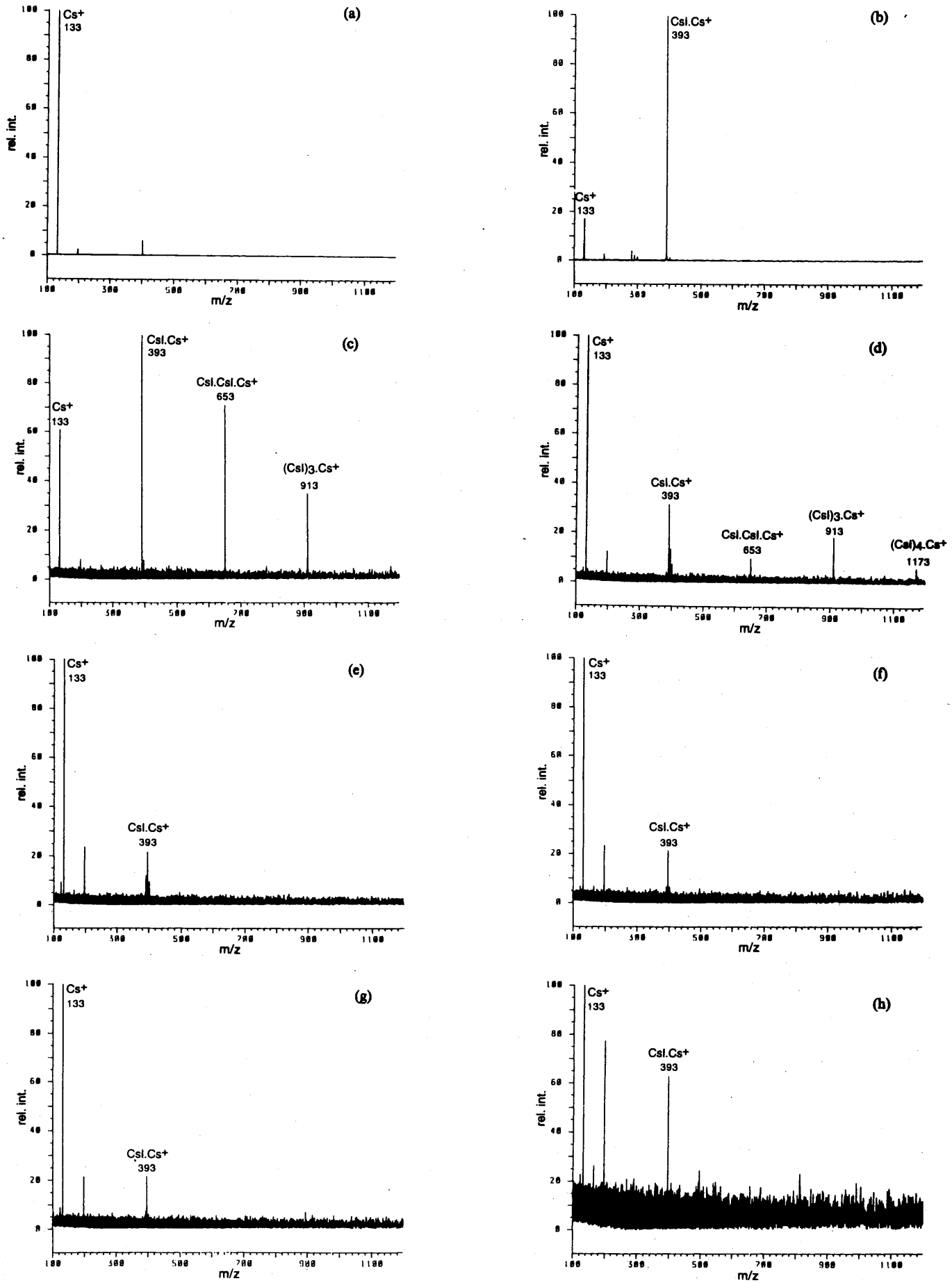

Figure 1. Positive-ion mass spectra of caesium iodide recorded at a T_{gate} of 300 μs (a), 500 μs (b), 900 μs (c), 1300 μs (d), 80 000 μs (e), 160 000 μs (f), 320 000 μs (g) and 640 000 μs (h). The number of scans was 10 (a), 20 (b–c), 70 (d), 160 (e) and 125 (f–h).

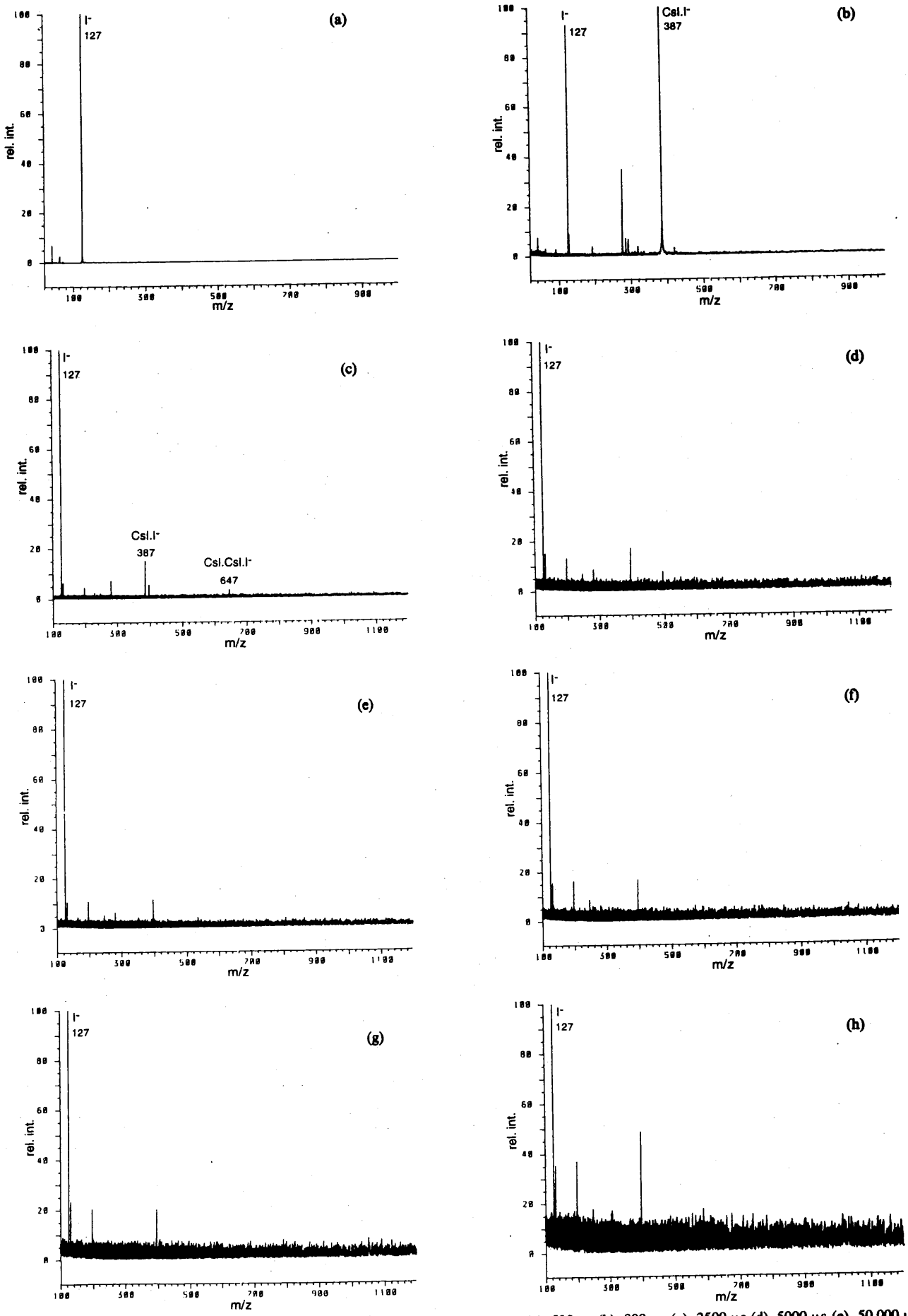

Figure 2. Negative-ion mass spectra of caesium iodide recorded at a T_{gate} of 300 μs (a), 500 μs (b), 800 μs (c), 2500 μs (d), 5000 μs (e), 50 000 μs (f), 500 000 μs (g) and 1 000 000 μs (h). The number of scans was 20 (a), 40 (b), 80 (c–d) and 60 (e–h).

Na^+. The occurrence of such dimeric ions is limited to the analytes exhibiting a low laser power density threshold. This feature is reminiscent of organic mass spectra[31] and may point towards the role of selvedge ionization. This view is sustained by the effect of T_{gate} shown in spectrum (c) of Figure 3. The $Na_3PO_4.Na_3PO_4.Na^+$ ions indeed show post-laser DI since they are still generated between 120 and 290 μs after the laser pulse. From the S/N, it can be deduced that a significant fraction of the *m/z* 351 ions is formed 'too late'. Post-laser DI over a period greater than T_{refl} is also observed for the ions at *m/z* 187 and 23. The latter is readily linked to thermionic emission while the $Na_3PO_4.Na^+$ ion is again a straightforward result of an ion–molecule interaction in the selvedge. Consistent with this reasoning, the generation of ions involving smaller fragments of the analyte molecule, such as Na_2OH^+, $NaPO_2.Na^+$ and $Na_2PO_3^+$, seems to be confined to the length of the laser pulse and possibly T_{refl}.

As to the negative ions, Figure 4 shows that the main ions, PO_2^- and PO_3^-, exhibit a formation process which continues for a long time after the laser pulse. Considering the S/N and the T_{gate} values, it is easily deduced that at least 25% of the maximum peak current for the PO_2^- and PO_3^- ions is produced between about 200 and 300 μs after the laser pulse. Note that the ion signal detected with the minimal T_{gate} in FT LMMS already corresponds to the sum of the prompt and the post-laser DI contribution, generated within the T_{refl} of about 85 μs.

Although the time resolution could be improved, this does not affect the main conclusion. For the positive- as well as for the negative-ion detection mode, our results show for the very first time that a substantial fraction of the diagnostic ions is produced long after the laser pulse. Note that our current results represent a minimal estimate of the relative importance of the post-laser DI against the prompt ionization. This is an important consideration in the assessment of how well TOF LMMS, which detects the prompt contribution solely, exploits the available ion population. Our results show that a substantial amount of the available ion population is not used for signal detection in TOF LMMS.

Positive-ion mass spectra from calcium phosphate confirm the previous observations. The clusters at lower *m/z*, primarily containing fragments of the analyte, are only formed within one T_{refl} period after the laser pulse, while diagnostic species such as $Ca_2PO_3^+$, $Ca_2PO_4^+$ and $CaO.Ca_2PO_4^+$ exhibit post-laser DI. This feature is certainly not compatible with direct ion emission from the solid lattice but is associated with selvedge DI.

The positive ion mass spectra of calcium nitrate in Figure 5 show a series of clusters consisting of up to six CaO neutrals with H^+, Ca^+, CaO^+ and FeO^+. The latter clusters probably refer to the presence of impurities, while the incorporation of H^+ logically results from the well-known

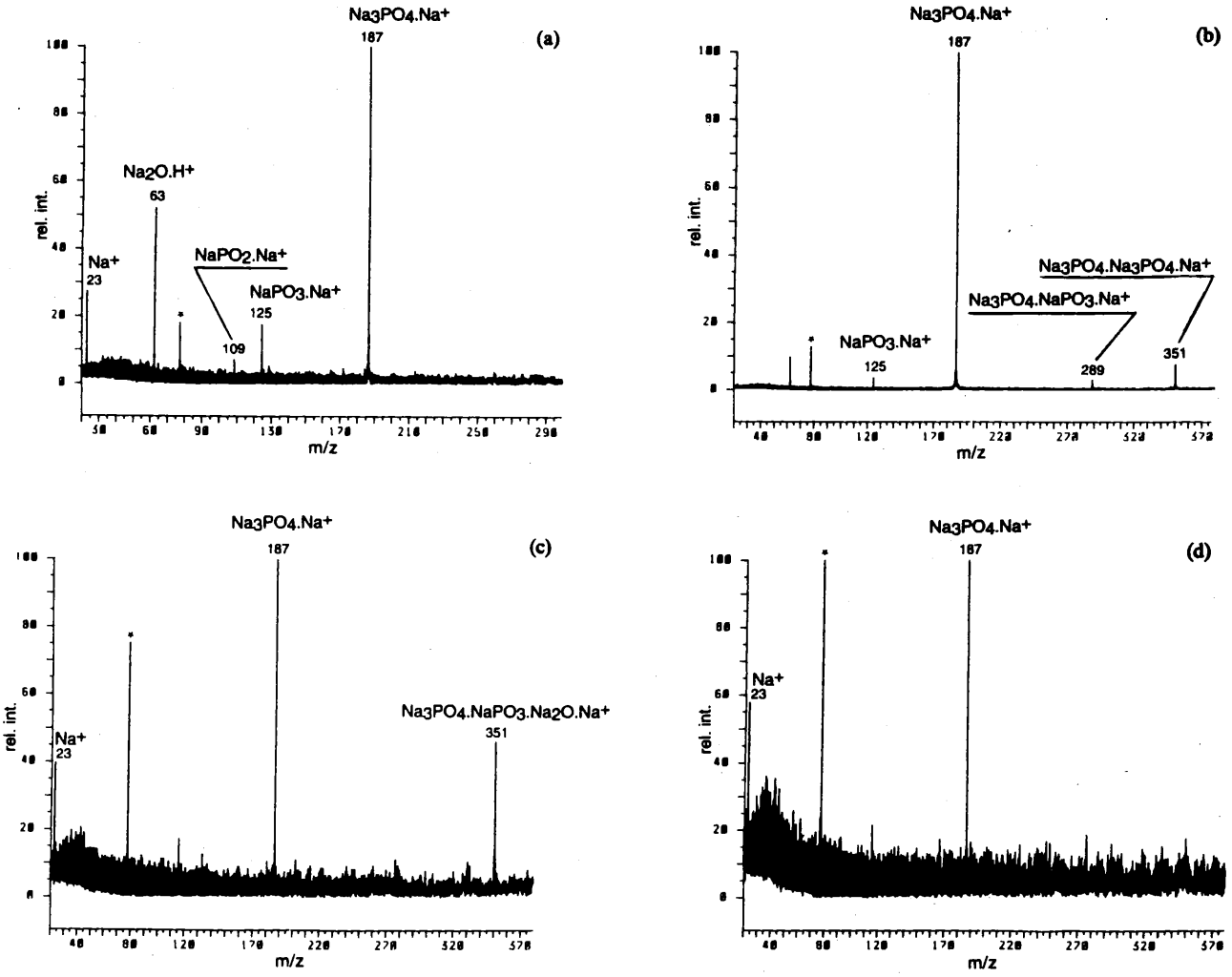

Figure 3. Positive-ion mass spectra of sodium phosphate recorded at a T_{gate} of 300 μs (a), 500 μs (b), 800 μs (c) and 1000 μs (d). The number of scans was 200 (a, c, d) and 100 (b).

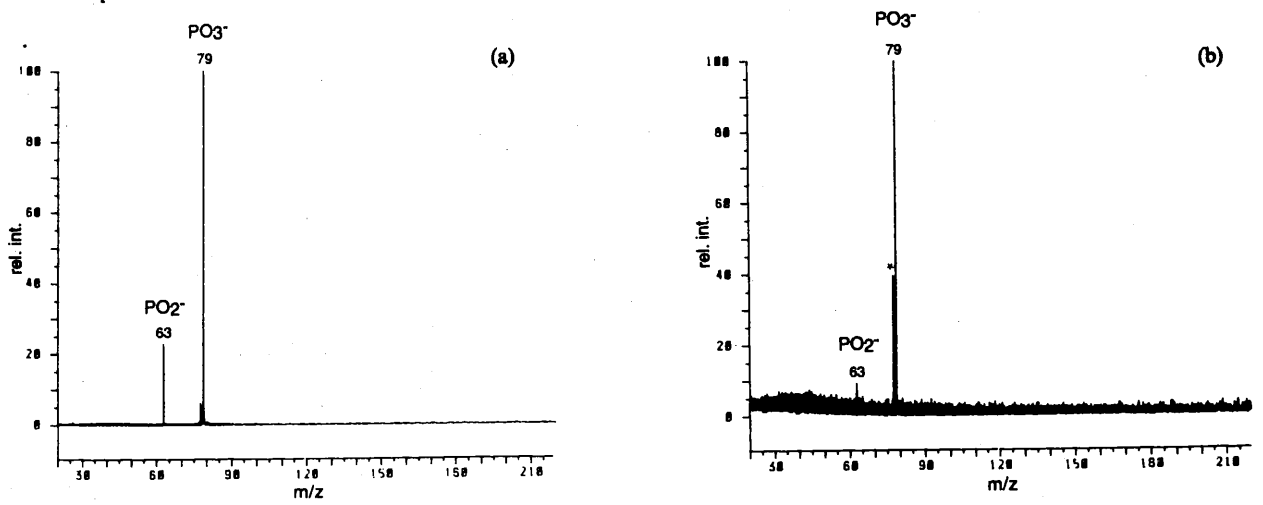

Figure 4. Negative-ion mass spectra of sodium phosphate recorded at a T_{gate} of 200 μs (a) and 500 μs (b).

process of water adsorption at the surface of hygroscopic analytes. The intensity ratio of the $(CaO)_2.CaO^+$ vs. $(CaO)_3.H^+$ ions at m/z 168 and 169 changes from 0.6 to 0.1, when the T_{gate} is lengthened from 300 to 600 μs. The small m/z difference excludes the possible influence of a TOF effect on the peak intensities. Clearly, the $(CaO)_3H^+$ ions are still formed between 150 and 290 μs after the laser pulse, and more abundantly than $(CaO)_2.CaO^+$. This observation generally applies to the clusters containing 3 or more CaO. The signals from the protonated signals appear with more intensity than the ones with Ca^+ or CaO^+ as charged species. Moreover, the $(CaO)_n.H^+$ ions show post-laser DI as opposed to the Ca^+- or CaO^+-cationized neutrals. This observation is tentatively explained by the preferential involvement of H^+ ions from surface moisture in the ion–molecule processes in the selvedge, while the Ca^+ and CaO^+ containing clusters are primarily associated with direct ion emission.

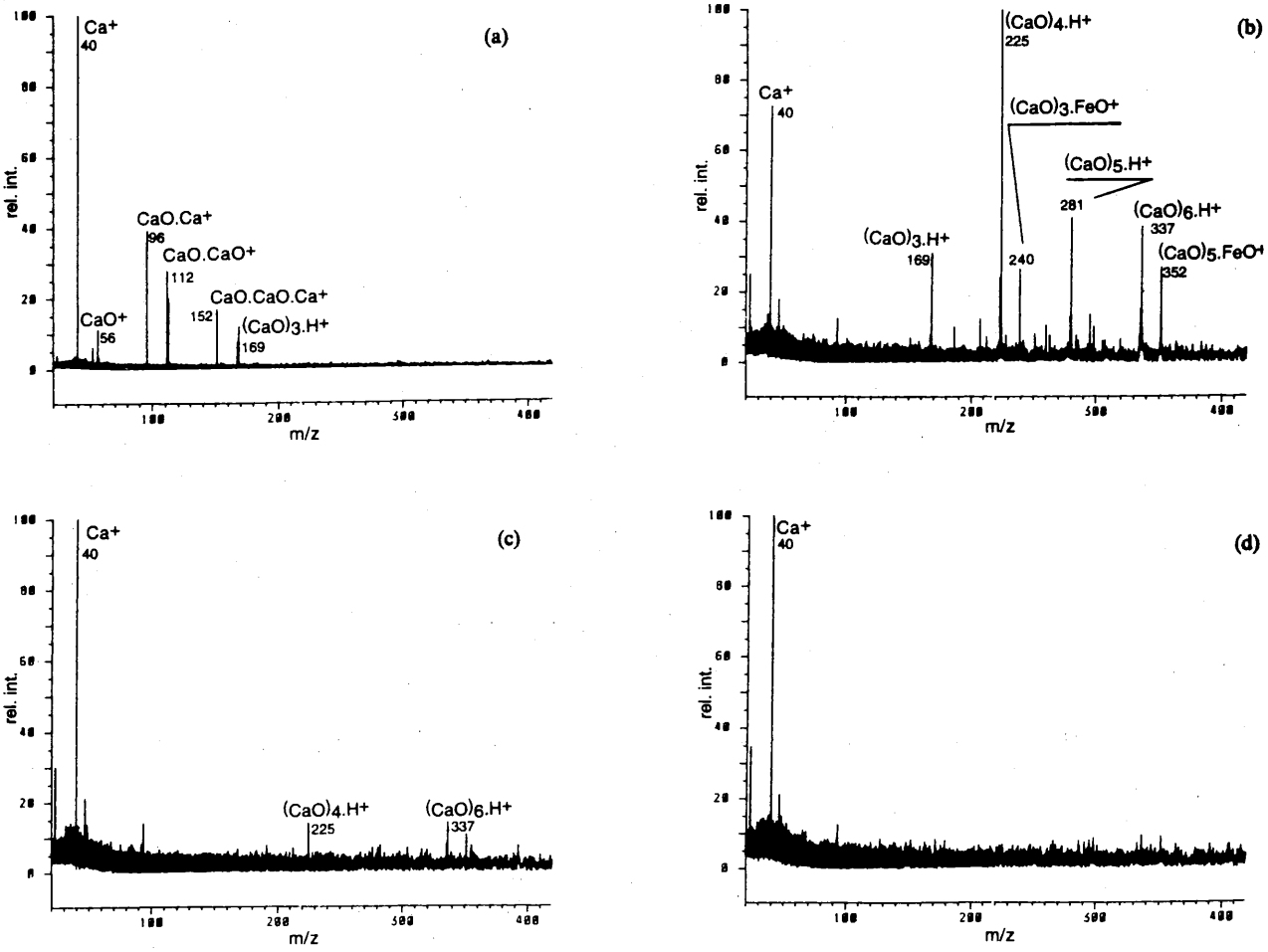

Figure 5. Positive-ion mass spectra of calcium nitrate recorded at a T_{gate} of 300 μs (a), 600 μs (b), 700 μs (c) and 800 μs (d). The number of scans was 50 (a) and 150 (b–d).

FT LMMS of oxides

The mass spectra of oxides (M_mO_n compounds) are relatively straightforward to interpret. The major signals in the positive-ion detection mode refer to the elemental ions M^+, while the clusters at higher m/z consist of combinations of the neutral oxide with M^+ and MO^+. In additon, $M_p.M^+$ ($p=1-3$, depending on the analyte) peaks occur. In the negative-ion mass spectra, MO_p^- ($p=1-n$, depending on the analyte) type ions are detected. Combinations of MO_p^- with a neutral analyte occur when the analyte is analyzed under threshold conditions.

Figure 6 shows the positive-ion mass spectra of lead oxide. The base peak is due to Pb^+ while $PbO.Pb^+$ clusters yield only a minor signal. It is also seen that both Pb^+ and $PbO.Pb^+$ are still detected as significant signals at a T_{gate} of 900 μs. Taking into account the number of scans and the S/N, it can be deduced that more than 15% of the maximum ion current is generated between 400 and 550 μs for Pb^+ and 175 and 400 μs for $PbO.Pb^+$. The analyte exhibits a transition energy corresponding to the wavelength used. This is believed to favour the generation of elemental ions. Nevertheless, significant post-laser DI still occurs.

The FT LMMS mass spectra of bismuth oxide in Figure 7 exhibit the features one expects from oxides. All diagnostic signals mentioned before are present. Post-laser desorption is observed for the majority of signals but to a different extent. For instance, $Bi.Bi^+$, $BiO.Bi^+$ and $BiO.BiO^+$ are shown to be generated up to at least 50–80 μs and, considering the effect of T_{refl}, up to about 250–280 μs after the laser pulse. However, Bi^+ and $Bi_2O_3.BiO^+$ exhibit continuing DI, lasting up to at least 700 and 300 μs after the laser pulse, respectively. Again ion currents are at least 15% of the maximum values at minimal T_{gate}. The Bi^+ signal remains fairly intense up to a T_{gate} of 1400 μs. In conclusion, the data prove that direct ion emission is not the sole process, as was always implicitly assumed in TOF LMMS. Furthermore, the results strongly suggest that the combination of the intact analyte with a stable charged species, i.e. the diagnostically most relevant ions, is likely to occur in the selvedge.

The positive ion mass spectra of molybdenum oxide in Figure 8 appear to be especially interesting because of the continuing generation of ions such as MoO^+ and MoO_2^+ long after the laser pulse. The data for a T_{gate} of 200 μs incorporate the prompt-ion contribution, so the elemental ions prevail as expected. Later on, the relative abundance of MoO^+ and MoO_2^+ strongly increases in comparison with Mo^+. It is unlikely that the former two ions originate from recombinations in the selvedge. Therefore, it is proposed that the emission of these species must be due to the thermal heating of the solid after the laser pulse. A similar tendency is observed for CeO_2. Although the generation of Ce^+ and CeO^+ does not extend beyond the time T_{refl}, the signal-intensity ratio for Ce^+ to CeO^+ decreases from 35 to 10 when T_{gate} is increased from 200 to 400 μs. This suggests that MO^+ is formed for a longer time than M^+ after the laser pulse.

Tentative model for DI of inorganic compounds

The data presented deonstrate the persistent nature of some major ions originating from inorganic compounds under focused laser microbeam irradiation of solids. In our opinion, the experimental assessment of the importance of the post-laser processes may constitute an important argument in the continuing speculations about inorganic DI.

Post-laser DI applies to all elemental ions as well as to some cluster ions at higher m/z values. Continuing emission was expected for the alkali ions, but was also proven to occur for elements like Pb^+, Bi^+, In^+, Sn^+, etc. Ions such as BiO^+, InO^+, etc. exhibit the same long-lasting DI when generated from covalent oxides. Combinations of neutral analytes with the most likely small ion(s) are generated up to 200–300 μs after the laser pulse for several binary salts, oxysalts and oxides. Apart from the time aspect, the incorporation of the intact analyte molecules into the higher-mass clusters represents a characteristic feature in FT LMMS, which was less evident in TOF LMMS results. Finally, the generation of the so-called polymeric clusters seems more dependent on the threshold power density than on the composition of the analyte. The more easily an analyte can be analysed at a low power density, the more polymeric ions are detected.

Figure 9 shows, in schematic form, a tentative model for DI which we propose in order to rationalize these observations. While the TOF LMMS literature usually makes a distinction between inorganic and organic ion formation, our approach unifies the DI concepts. To explain the features of the LMMS results, the whole event is rationalized in terms of three basic parameters in mass spectrometry.

First of all, the energy-related effects of DI are considered. Laser impact is assumed to generate an energy gradient which results in physically separated regions, mainly along the surface, each with a different local energy regime. This may give rise to complete destruction of the

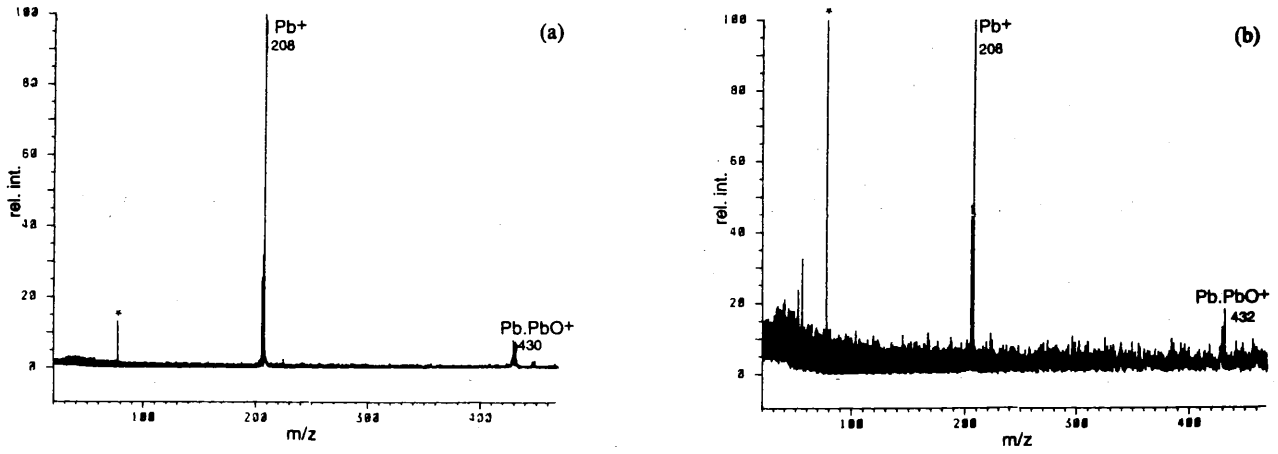

Figure 6. Positive-ion mass spectra of lead oxide recorded at a T_{gate} of 600 μs (a) and 900 μs (b). The number of scans was 150 (a) and 300 (b).

analyte or 'atomization' in the hot spots, while direct ion emission of small and larger cluster ions from the solid lattice may occur under the milder conditions next to the hot spot. Furthermore, the thermal component of the DI process is given an important role, which involves the generation of neutrals, thermionic emission and perhaps direct emission of smaller fragments such as MO^+ from oxides. All of these species are released from the sample into a kind of microcloud or selvedge, just above the sample surface. Here, processes such as electron and adduct ionization and charge transfer can occur.

Local pressure is the second factor to consider. The probability of second-order interactions depends on the density of this selvedge. This parameter directly depends on the balance between the power density applied to the solid and the 'volatility' of the analyte, i.e. its readiness to desorb under minimum power density conditions. This explains why volatile analytes give rise to polymeric cluster ions. The selvedge concept makes the observed generation of cationized and anionized analytes, long after the laser pulse, plausible. Note that the relative importance of such 'chemical ionization' reactions compared with DI where no such interaction occurs depends on the volatility of the sample, but also on the initial kinetic energy of the initially

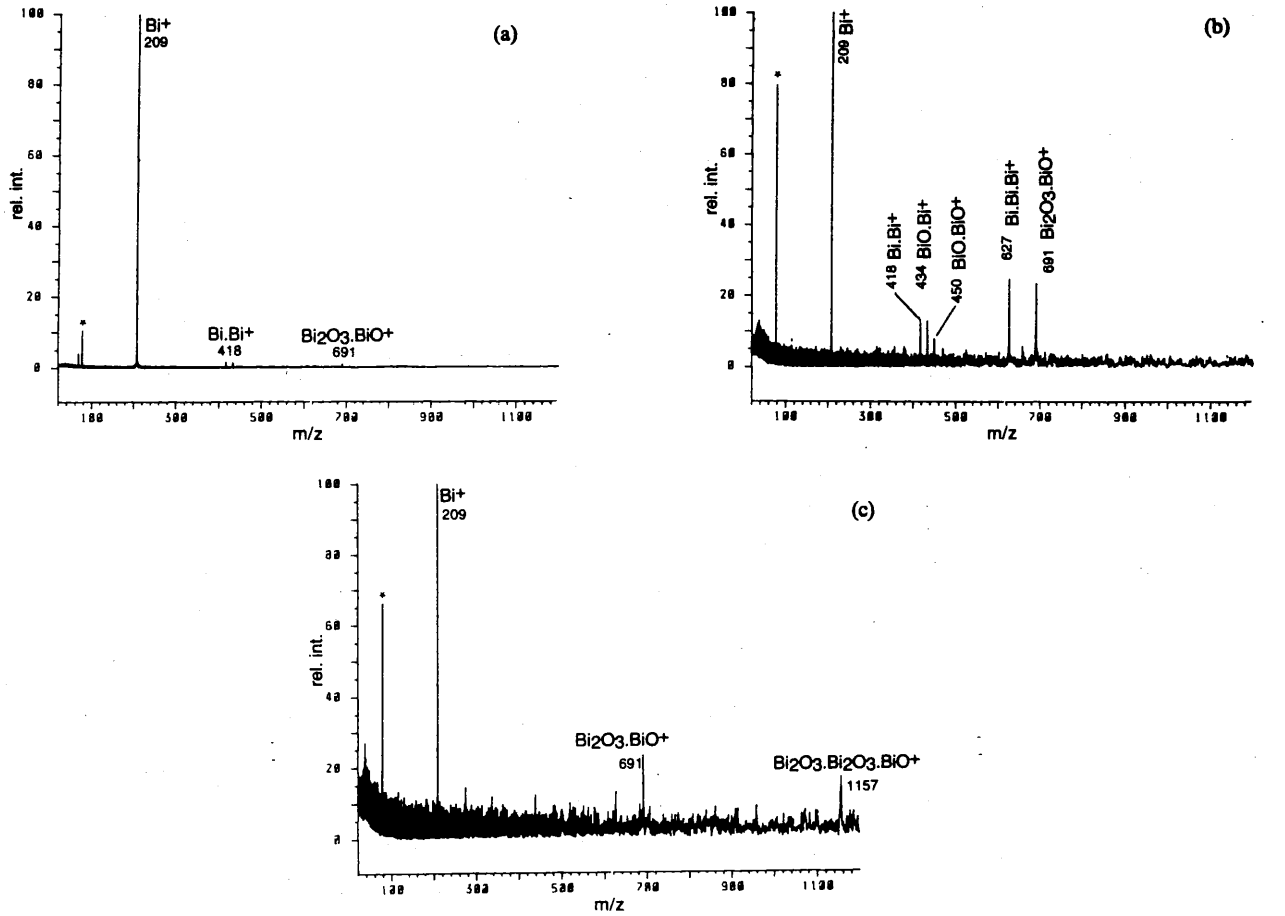

Figure 7. Positive-ion mass spectra of bismuth oxide recorded at a T_{gate} of 400 μs (a), 800 μs (b) and 1200 μs (c). The number of scans was 150 (a,b) and 400 (c).

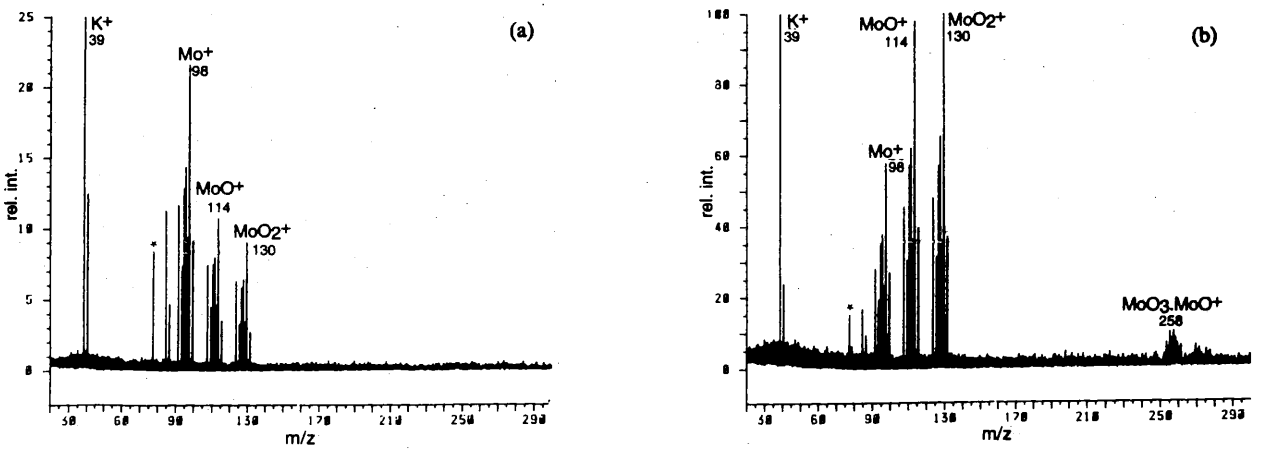

Figure 8. Positive-ion mass spectra of molybdenum oxide recorded at a T_{gate} of 200 μs (a) and 600 μs (b). The number of scans was 150 (a) and 200 (b).

released species and the extraction field applied in the source. The latter is low in FT LMMS and therefore explains the contribution from ion–molecule interactions. Promptly formed ions with high kinetic energy are less likely to be subjected to recombination with neutrals than the slowly released thermal species which follow the laser pulse.

Finally, the time component constitutes an intrinsic part of our DI approach. It serves to link the observations in TOF and FT LMMS, especially concerning the increased contribution of the cationized or anionized analytes in the latter technique. Considering the instrumental design it is probable that TOF LMMS and FT LMMS detect different fractions of the ion populations generated by laser irradiation of solids. More specifically, TOF LMMS is confined to prompt ions. In contrast to the general notion in the literature, however, they do not constitute the only ion type. Our data show that significant post-laser DI occurs, which should be taken into account whenever spectra are interpreted.

CONCLUSION

Selected results from our FT LMMS database on inorganic compounds have been presented. Up to now it was a common notion that inorganic ions are essentially formed during the laser pulse. Our data demonstrate that the formation of a substantial fraction of the detected ions continues for several hundreds of microseconds after the laser pulse. This applies to virtually all elemental ions analysed as well as to many higher m/z clusters. It is shown that specifically the clusters corresponding to a combination of the neutral analyte with a charged species tend to be formed later on. The number of neutral molecules incorporated in the cluster ions depends on the 'volatility' of the analyte. As a result, a DI model was proposed which closely relates to the previous approach for organic compounds. Further investigations will be needed to refine the time resolution in the source so that the relative importance of prompt and delayed ion formation processes can be determined more precisely. This is necessary to assess whether an integrating type of MS is really needed in LMMS.

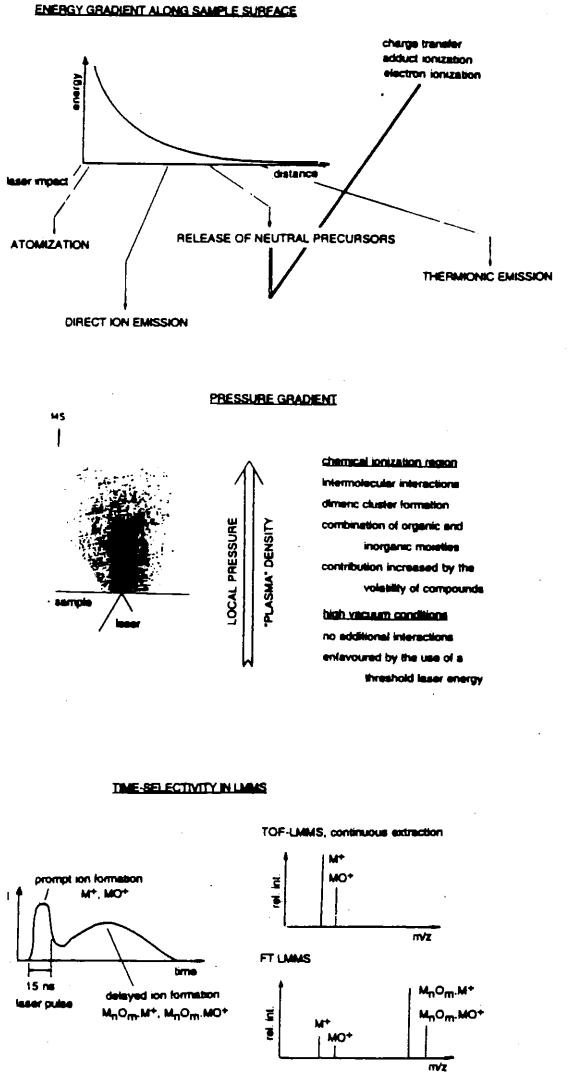

Figure 9. Tentative model for inorganic desorption-ionization (DI) in LMMS.

Acknowledgements

Luc Van Vaeck is indebted to the National Science Foundation of Belgium (NFWO) as research director. Herbert Struyf acknowledges the "Impulse Programme in Marine Sciences", supported by the Belgian State—Prime Minister's Services—Science Policy Office (contract MS/06/050).

REFERENCES

1. L. Van Vaeck, H. Struyf, W. Van Roy and F. Adams, *Mass Spectrom. Rev.* **13**, 189 (1994).
2. L. Van Vaeck, H. Struyf, W. Van Roy and F. Adams, *Mass Spectrom. Rev.* **13**, 209 (1994).
3. D. S. Simons, *Applied Surf. Sci.* **31**, 103 (1988).
4. J. Dennemont, J.-Cl. Landry, J.-Y. Chevalley and J. Jaccard, *Analusis* **17**, 139 (1989).
5. F. Bruynseels, Ph. Otten and R. Van Grieken, *J. Anal. Atomic Spectrom.* **3**, 237 (1988).
6. R. J. Cotter, *Anal. Chim. Acta* **195**, 45 (1987).
7. G. J. Q. Van der Peyl, J. Haverkamp and P. G. Kistemaker, *Int. J. Mass Spectrom. Ion Physics* **42**, 125 (1982).
8. M. Pelletier, G. Krier, J.-F. Muller, D. Weil and M. Johnston, *Rapid Commun. Mass Spectrom.* **2**, 146 (1988).
9. J. T. Brenna, W. R. Creasy, W. McBain and C. Soria, *Rev. Sci. Instrum.* **59**, 873 (1988).
10. L. Van Vaeck, W. Van Roy, H. Struyf, F. Adams and P. Caravatti, *Rapid Commun. Mass Spectrom.* **7**, 323 (1993).
11. T. Mauney and F. Adams, *Int. J. Mass Spectrom. Ion Processes* **59**, 103 (1984).
12. E. Michiels, A. Celis and R. Gijbels, *Int. J. Mass Spectrom Ion Physics* **47**, 23 (1983).
13. M. Dewolfs, T. Mauney, E. Michiels and R. Gijbels, *Scanning Electron Microsc.* III, 799 (1986).
14. H. Struyf, L. Van Vaeck and R. Van Grieken, "Speciation of inorganic compounds by Fourier transform laser microprobe mass spectrometry with external ion source", *Anal. Chem.* submitted.
15. P. Grossmann, P. Caravatti, M. Allemann and H. P. Kellerhals, in *Proceedings of the 36th ASMS Conference on Mass Spectrometry and Allied Topics, San Francisco, CA*, ASMS, East Lansing, 1988, pp. 616–617.
16. P. Caravatti and M. Allemann, *Org. Mass Spectrom.* **26**, 514 (1991).
17. F. Hillenkamp, in *Proceedings of the Second Workshop on Ion Formation from Organic Solids, Münster, Germany*, ed. by A. Benninghoven, p. 190, Springer-Verlag, Berlin, 1983.
18. F. P. Novak, K. Balansanmugan, K. Visnawadham, C. D. Parker, Z. A. Wilk, D. Mattern and D. M. Hercules *Int. J. Mass Spectrom. Ion Physics* **53**, 135 (1983).
19. B. Schueler, F. R. Krueger and P. Feigl, *Int. J. Mass Spectrom. Ion Physics* **47**, 3 (1983).
20. B. Schueler, P. D. K. Feigl and F. R. Krueger, *Z. Naturforsch.* **38a**, 1078 (1983).
21. B. Jöst, B. Schueler and F. R. Krueger, *Z. Naturforsch.* **37a**, 18 (1982).
22. F.R. Krueger, *Appl. Surf. Sci.* **11/12**, 819 (1982).
23. F. R. Krueger, *Z. Naturforsch.* **38A**, 385 (1983).
24. J. Dennemont and J. C. Landry, in *Microbeam Analysis—1985*, ed. by J. T. Armstrong, p. 305, San Francisco Press, Inc., San Francisco, 1985.

25. F. Bruynseels and R. Van Grieken, *Int. J. Mass Spectrom. Ion Proc.* **74**, 161 (1986).
26. P. K. D. Feigl, F. R. Krueger and B. Schueler, *Mikrochim. Acta* **2**, 85 (1984).
27. G. J. Q. Van der Peyl, J. Haverkamp and P. G. Kistemaker, *Int. J. Mass Spectrom. Ion Physics* **42**, 125 (1982).
28. R. J. Cotter, *Anal. Chim. Acta* **195**, 45 (1987).
29. H. Struyf, W. Van Roy, L. Van Vaeck, R. Van Grieken and P. Caravatti, *Rapid Commun. Mass Spectrom.* **8**, 32 (1994).
30. C. B. Lebrilla, I. J. Amster and R. T. McIver, Jr., *Int. J. Mass Spectrom. Ion Proc.* **87**, R7 (1989).
31. L. Van Vaeck, P. Van Espen, F. Adams, R. Gijbels, W. Lauwers and E. Esmans, *Biomed. Environ. Mass Spectrom.* **18**, 581 (1989).

Reprinted from ENVIRONMENTAL SCIENCE & TECHNOLOGY, Vol. 30, 1996

Identification of Individual Aerosol Particles Containing Cr, Pb, and Zn above the North Sea

HANS VAN MALDEREN, STEFAAN HOORNAERT, AND RENÉ VAN GRIEKEN*

Department of Chemistry, University of Antwerp (UIA), Universiteitsplein 1, B-2610 Antwerp, Belgium

Aerosol samples have been collected over the southern bight of the North Sea from an aircraft. In this way, 96 samples were taken for single-particle analysis during 16 flights. Almost 45 000 individual particles were analyzed with electron probe X-ray microanalysis. More than 5000 of these were found to contain significant concentrations of one or more of the heavy metals Cr, Pb, and Zn. With the help of hierarchical, nonhierarchical, and fuzzy clustering techniques, various heavy metal-containing particle types could be identified. Significant differences in abundances were detected in the North Sea heavy metal aerosol, depending on the origin of the air masses. In samples with continental influence 50 times more Zn- and Pb-containing particles were found than in samples with a marine history. For Cr, on the other hand, we found abundances in the marine sector that were one-third of the values for continental sectors. This might point to a rather undefined marine source, which could be the recycling of previously deposited material by reinjection into the atmosphere by sea spray. The highest values for Cr-, Pb-, and Zn-containing particles were always detected under southeastern wind directions.

Introduction

During the past few decades, the input of heavy metals to the North Sea has increased significantly due to the growing industrial activity and car traffic in European countries. Despite the first positive signals of improvement, e.g., the reduction of atmospheric Pb levels as a result of the use of unleaded gasoline (*1*–*3*), the annual total toxicity of all heavy metals mobilized was reported to exceed the combined toxicity of all of the radioactive and organic wastes generated each year (*4*). The ever increasing dispersion of heavy metals through the atmosphere, water, and soil is a major concern due to their hazardous effect on human health, the possible changes they initiate in natural biochemical processes in all ecosystems, and their inevitable accumulation in the food chain.

* Corresponding author fax: +32-3-820-23-76; e-mail address: vgrieken@uia.ua.ac.be.

It has often been demonstrated that wet and dry deposition of pollutants from the atmosphere to the North Sea is a dominant transport system for a number of elements. For several years now, efforts have been made to assess heavy metal concentrations and size distributions over the North Sea and to quantify the deposition fluxes of these elements by using a wide variety of analytical bulk techniques (*5*). Microanalysis techniques, however, have not been widely used, despite their enormous potential to characterize the morphology and composition of micrometer-sized individual aerosol particles. Observation of particular elements allows the identification of specific particle types, characterization of their source, and investigation of their abundance as a function of physical parameters. Moreover, shorter sampling times (minutes rather than hours for bulk analysis) are needed for microanalysis, which allows one to study short time variations in atmospheric composition as a result of wind direction changes and to overcome some of the problems of airborne sampling from airplanes, where shorter sampling times evidently are needed than for ship-based measurements.

The present study is part of a large investigation regarding heavy metal deposition into the North Sea. Several articles have already been published in the framework of this study on the single-particle analysis of particulate atmospheric matter using electron probe X-ray microanalysis (EPXMA) (*6*), especially for giant aerosol particles (*7*), and using laser microprobe mass analysis (*8*). Besides single-particle analysis, bulk analysis by energy-dispersive X-ray spectrometry and proton-induced X-ray emission (*9*) and by differential pulse anodic stripping voltammetry (*10*) was performed in order to obtain atmospheric concentrations of different elements. With these data, several deposition models were tested (*11*, *12*), which in the end provided us with estimates for wet and dry deposition fluxes of heavy metals into the North Sea (*2*). The aim of the present article is the detailed identification and characterization of exactly the specific particle types that are responsible for the input of heavy metals Cr, Zn, and Pb.

Experimental Section

The samples were collected during several flights with a twin-engine aircraft, a Piper Chieftain PA 31-350 owned by Geosens B.V. (Rotterdam, The Netherlands), over a period of 13 months. All flights were performed under relatively cloudless and dry conditions. Wind speeds over the sampling campaign were between 2 and 13 m s^{-1}. After takeoff from Rotterdam airport, a spiral flight was initiated at the Goeree platform (51°55′30″ N, 3°40′ E) in order to localize the inversion layer. Once this was done, the aircraft flew tracks of ca. 110 km at six different heights more or less evenly spaced between sea level and the inversion layer. The lowest track, only 10–30 m above sea level, was intended to assess particle resuspension by sea spray. During these tracks, airborne particulate matter was collected on 0.4-μm-pore-size Nuclepore membrane filters using an isokinetic inlet (*13*). The flow rate was approximately 1 m^3 h^{-1}. All tracks were flown parallel with the wind direction to allow later calculation of backward trajectories. These 36-h isobaric back trajectories were provided by the Royal Dutch Meteorological Institute

0013-936X/96/0930-0489$12.00/0

(KNMI) and are shown in Figure 1. More detailed information about the sampling campaign can be found elsewhere (*14*).

In this way, 96 samples were collected during 16 flights. The analysis of almost 48 000 individual particles (500 in each sample) was done by EPXMA on a JXA-733 Superprobe of JEOL (Tokyo, Japan). For the analysis, an accelerating voltage of 20 kV and a beam current of 1 nA were used. The minimal detection limit for elemental concentration is around 1000 ppm, whereas the minimum detectable particle size is 0.2 μm. EPXMA permits one to obtain morphological parameters such as the diameter and shape factor of a particle, while the chemical composition is derived from an energy-dispersive (ED) X-ray spectrum. More detailed information on this method can be found elsewhere (*6*). The resulting data set contained both morphological and chemical information for almost 48 000 particles.

It is not difficult to imagine that, when working with such large data sets, some method of data reduction is needed. We chose a combined approach of several multivariate cluster techniques. A home-written Windows-based program, called IDAS, was used. More information about the program can be found elsewhere (*15*). Cluster analysis is a well-developed multivariate method, which has been used regularly in connection with single-particle analysis (*16*–*19*). Most of these publications dealt with hierarchical clustering methods. In our case, we applied a combination of hierarchical, nonhierarchical, and fuzzy clustering to our data set.

The clustering was performed on the X-ray elemental intensities emitted by each aerosol particle, and no normalization was done prior to the statistical treatment. Hierarchical cluster analysis (HCA) is the most simple of the three and therefore most frequently used. It has also the advantage of easy visual interpretation with the help of so-called dendrograms. Its main disadvantage lies in the fact that some hierarchical structure is presumed, and this is not always the case when working with atmospheric data sets. This might lead to the misclassification of some particles. Nonhierarchical clustering methods (NHCA) do not have these problems; however, they require prior knowledge about the data structure. This is solved by using the results of the hierarchical clustering as centroids for the nonhierarchical clustering. Both HCA and NHCA are so-called hard clustering methods: this means that one particle belongs to only one cluster after the clustering. In some cases, when dealing with overlapping clusters, this can lead to mistakes in the clustering. This problem is overcome by fuzzy clustering analysis (FCA). The main idea is to replace the procedure of splitting the multivariate data into a certain number of clusters by a procedure of determining the probability of belonging for each object to each cluster. Hard clustering therefore can be considered as a special case of fuzzy clustering, namely, when all membership coefficients but one are equal to 0. More detailed information can be found in a publication by Treiger et al. (*20*). The results of all three types of clustering very much depend on the correct choice of the number of clusters. Previously, this was done on the basis of the personal experience of the analyst rather than on the basis of statistical criteria. This problem was overcome by implementing Akaike's information criterion (AIC), which is based on the relation between entropy and ordering in an isolated system: if there is full ordering in the system, the entropy is minimal. Further information and examples of AIC are found elsewhere (*21*).

Results and Discussion

To investigate the aerosol composition dependence on wind direction, we divided the 16 flights into five sectors according to the air mass history obtained from 36-h backward trajectories. Chester and Bradshaw (*22*) stressed the immense importance of the air mass origin for the aerosol composition compared to the position of the sampling location. Therefore, much care was given to the division of the samples over the five sectors, which are shown in Figure 1. Only particles containing Cr, Zn, or Pb were selected. In this way we obtained all Cr-, Zn-, or Pb-containing particles divided per sector. The distribution of the flights over the different sectors and the number of particles containing one or more of these metals in each flight are shown in Table 1. Figures 2–4 show the percentage of metal-containing particles per sector.

From these figures, it is clear that the lowest occurrences of Cr-, Pb-, and Zn-rich particles were always found in sector 1. This sector is characterized by unpolluted air masses of pure marine origin and can be considered an indicator of North Sea background values. Main sources of pollution in this sector should be ships as well as gas and oil drilling platforms, which are positioned over the central area of the North Sea, but their influence seems to be rather small. Only the percentage of Cr-containing particles is significant compared with values from sectors with continental influence (ca. one-third of pure continental values), which might support the assumption of a marine source of Cr-containing particles. The reinjection by sea spray of previously deposited particles has been proposed (*23*) as a possible source for marine-derived trace metal-containing particles, but the reality and quantification of this possible recycled marine component are still controversial (*24*). Pb and Zn values are more than 50 times lower than continental values. Sector 2 has intermediate values for Cr (1.4%) and Pb (3.0%), but the amount of Zn-rich particles is rather high (7.8%). This sector accounts for emissions from the Netherlands, the northern part of Germany, eastern Europe, and all Scandinavian countries. The highest number of heavy metal-containing particles was always encountered in sector 3. This sector is identified by air masses with pure continental history, which carry emissions from Belgium, central and southern Germany, and the eastern part of France. These high numbers are not totally unexpected, since industrial sources of heavy metals alone are thought to be 10 times higher on a global scale than all natural sources combined (*25*). Sector 4 is affected by air masses from the northwestern part of France (including the industrial centers of Dunkerque, Cherbourg, and Lille) and by emissions from the United Kingdom, but also has some influence from air masses coming from the Atlantic ocean and the English Channel. Percentages in this sector are approximately half of those in sector 3. Only Cr (2.2%) abundances are on the same level as that for sector 3 (2.1%). Samples collected on flights 4, 9, and 14 were taken under low wind speeds and variable wind conditions. Therefore, they are grouped in sector 5, called "local". The values found in this sector are also quite high.

To investigate the true chemical composition of the particles containing Cr, Zn, or Pb, we needed to identify the different particle groups and determine their abundance variations over the five sectors. This was done only for

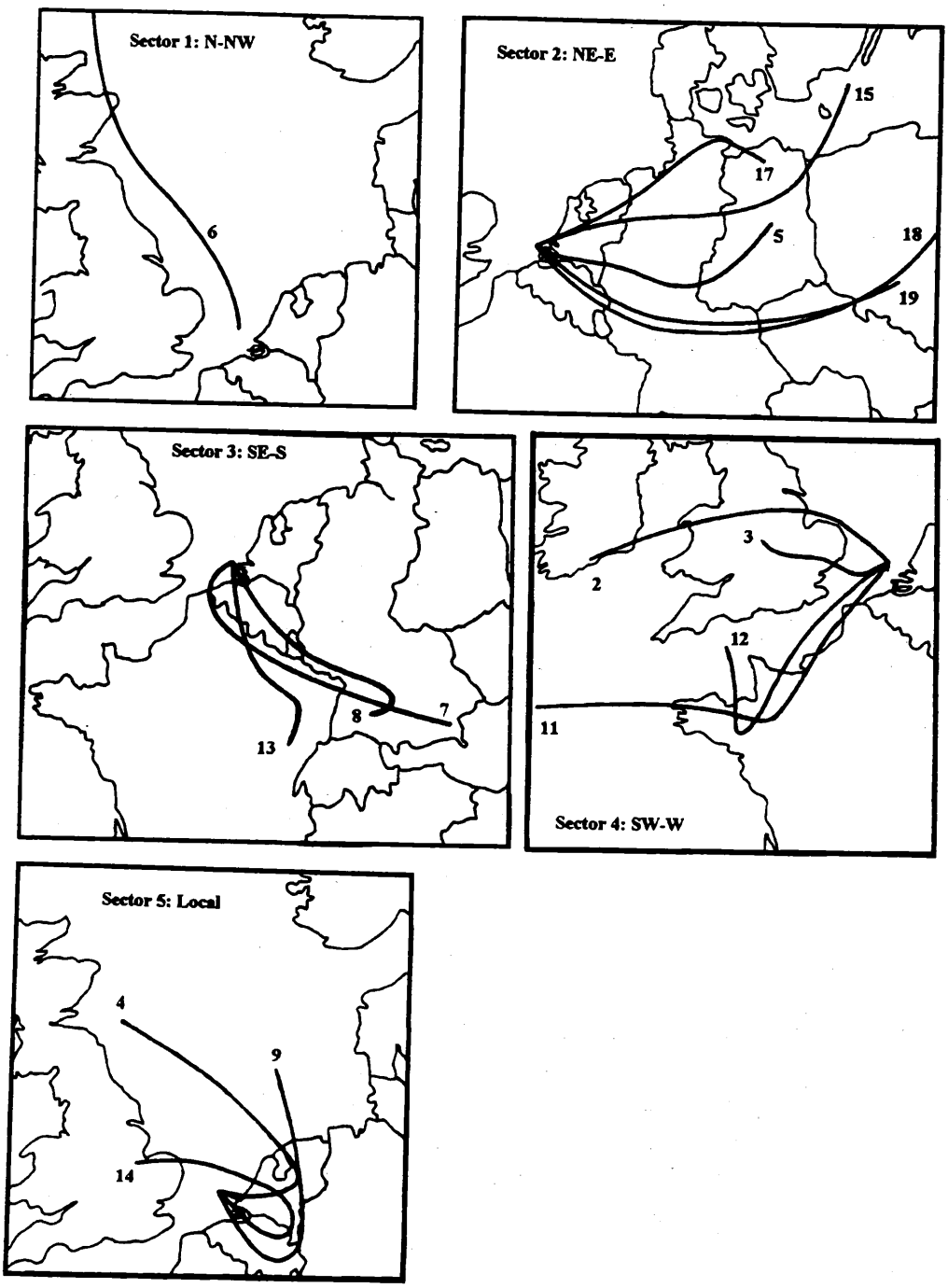

FIGURE 1. 1000-hp, 36-h air mass back trajectories at our sampling site for the five different sectors. The numbers indicate flight numbers.

particles containing one or more of the elements Cr, Zn, and Pb. Other heavy elements such as Ni, V, Sn, Cd, and Cu were not investigated, because the number of particles containing one or more of these elements was too small to obtain statistically significant information. For each of the three elements we performed hierarchical, nonhierarchical, and fuzzy clustering for each of the five sectors. The results of the hierarchical clustering were used as centroids for the nonhierarchical and fuzzy clustering. The number of groups was chosen after careful evaluation of Akaike's criterion. The fuzzy clustering was employed for studying the internal overlap between the different groups. The final interpretation was carried out on the basis of the combination of the information obtained for the three clustering techniques. The results for Cr-, Zn-, and Pb-containing particles for each of the five sectors are given in Tables 2–4.

Chromium-Containing Particles. In total, 750 particles were found containing Cr, which is 1.7% of the entire number of particles analyzed. After the clustering, several different Cr-containing particle types were detected, embodying a variety of compositions, but some frequently occurring types could be identified. The results of the clustering for the five sectors are shown in Table 2. All sectors are dominated by the appearance of Fe–Cr particles, sometimes in combination with other elements. Pure Cr particles (these are most likely Cr oxides, but since only elements with Z above 11 are detected with energy-dispersive EPXMA, O is not measured) were only encountered in sectors 2 and 4. In most sectors Cr was also detected

TABLE 1

Number of Particles Containing Cr, Pb, and Zn as a Function of the Total Number of Particles Analyzed per Flight and per Sector

flight no.	particles analyzed per flight	Cr-containing particles	Pb-containing particles	Zn-containing particles
		Sector 1: North/Northwest		
6	2922	21	4	0
total (sector 1)	2922	21 (0.7%)	4 (0.1%)	0 (0.0%)
		Sector 2: Northeast/East		
5	3401	36	88	305
15	2851	52	25	141
17	3000	39	106	234
18	1980	31	119	260
19	3000	40	87	163
total (sector 2)	14232	198 (1.4%)	425 (3.0%)	1103 (7.8%)
		Sector 3: Southeast/South		
7	3000	50	244	414
8	3000	52	176	243
13	3000	83	130	216
total (sector 3)	9000	185 (2.1%)	550 (6.1%)	873 (9.7%)
		Sector 4: Southwest/West		
2	1573	28	101	69
3	2844	41	135	164
11	2655	25	13	35
12	2880	127	38	104
total (sector 4)	9952	221 (2.2%)	287 (2.9%)	372 (3.7%)
		Sector 5: Local		
4	1764	28	156	100
9	2455	74	68	264
14	3000	50	80	103
total (sector 5)	7219	152 (2.1%)	304 (4.2%)	467 (6.5%)
total (all sectors)	43325	750 (1.7%)	1570 (3.6%)	2815 (6.5%)

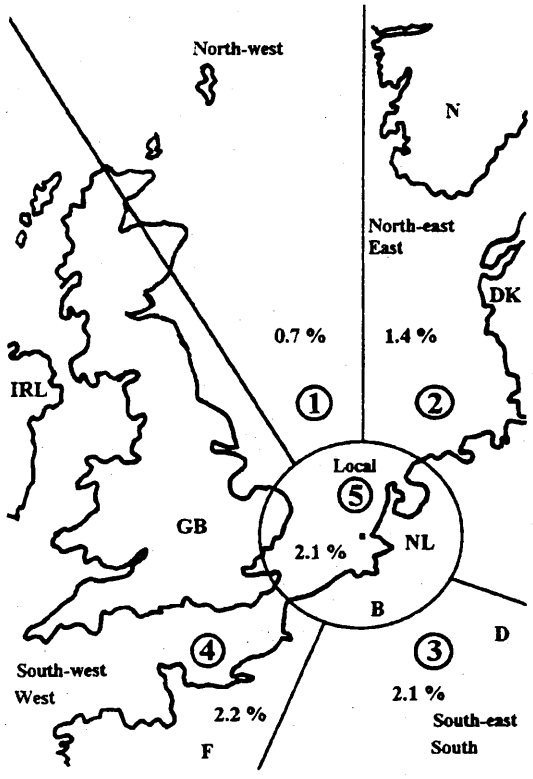

FIGURE 2. Percentage of Cr-containing particles per sector. The encircled numbers indicate the sector number.

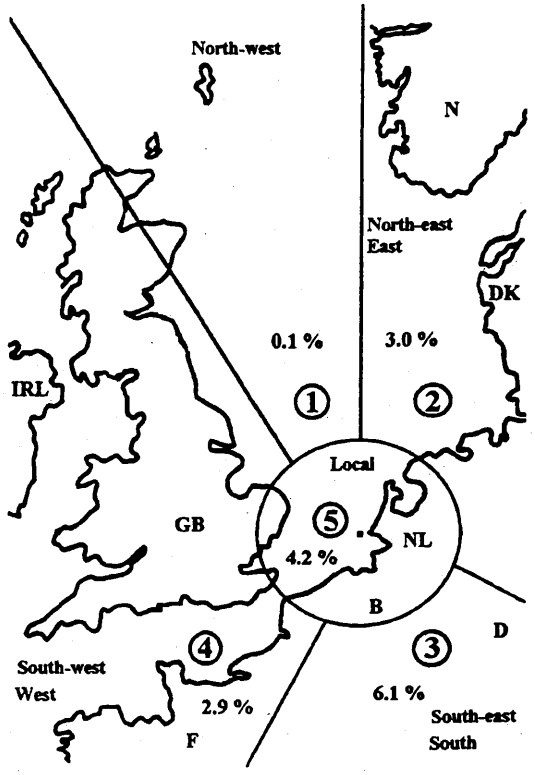

FIGURE 3. Percentage of Pb-containing particles per sector. The encircled numbers indicate the sector number.

in combination with the elements S, Ca, Cl, and K. In Table 2 they are indicated as Cr/medium-*Z*. In some sectors Cr was associated with high-*Z* elements such as Ni, Zn, Cu, and Pb. Another frequently occurring particle type is Cr associated with Si. In Table 2 these particles are noted as Si/Cr. The size of the different particle types varies between

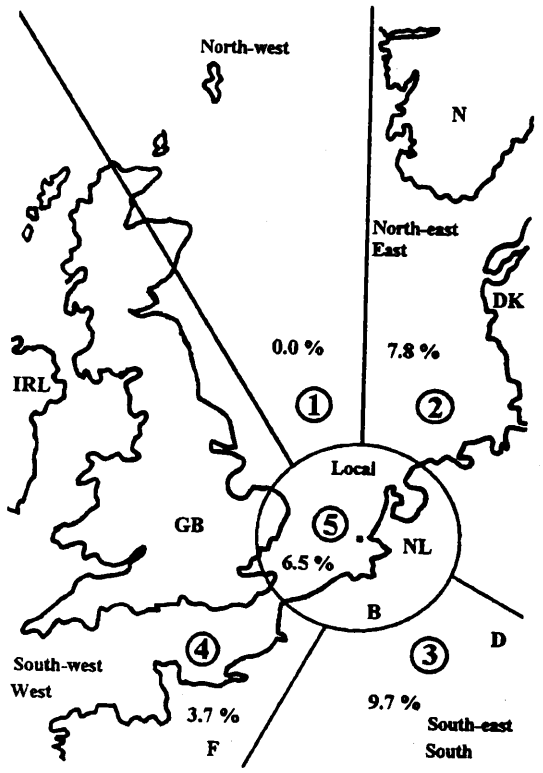

FIGURE 4. Percentage of Zn-containing particles per sector. The encircled numbers indicate the sector number.

0.3 and 2.5 μm. This variation is larger than that for Pb- and Zn-rich materials. This might point to a natural source of Cr, which is not present for Zn and Pb.

More than 10 million tons of chromite ($FeOCr_2O_3$), the only economically important Cr mineral, is used globally each year, divided over three main industries: 76% for metallurgical, 13% for refractory, and 11% for chemical applications (*26*). The different industrial applications call for different forms of Cr, such as chromite, ferrochromium, Cr metal, and several other Cr compounds. Each of these industries emits Cr in one form or another. The closest Cr-emitting industries are probably the steel factories in Boulogne, Dunkerque, Lille, and Roubaix, approximately 300 km distant from the sampling location. The industrial center of the Ruhr area, with many steel factories, lies ca. 500 km east. The source identification of all of these particles types is quite complex, considering the relatively small differences between some of the particle groups. Moreover, due to the high boiling point, Cr vapors from chromium steel production and coal combustion rapidly condense as oxides on the surface of different sorts of airborne particles (*27*). During the combustion of fuels, the volatile species in coal evaporate in the furnace and subsequently condense as submicrometer-sized particles or on ash particles. Cr was found to be significantly concentrated on the surface of combustion particles (*28*). These processes give rise to a wide variety of Cr-containing particles and complicate source identification. Several particle groups with low Cr content are probably created in this way. The influence of particle size on the occurrence of this particle type is rather unclear: sizes vary between 0.5 and 1.5 μm.

The differences in abundances between the various particle groups shown in Table 2 are not to be interpreted as final, since classification of some of the clusters was difficult and subject to personal interpretation. They do, however, give a good indication of the occurrence of the various groups.

Fe–Cr clusters are the most abundant in all of the sectors. The values vary between 39% (sector 3) and 57% (sector 1). Several publications (*4, 27, 29*) suggest metallurgical industries, which are the main consumers of chromite for the production of iron, steel, and stainless steel (Cr improves corrosion resistance), as the primary source of Fe–Cr-rich particles. Pacyna (*30*) also pinpoints the steel industry as the major emitter of Cr in Europe (15 000 tons $year^{-1}$). The mineralogical composition of dusts released in the different phases of iron and steel production has been identified as consisting of a significant part of Fe minerals as hematite (Fe_2O_3) and magnetite (Fe_3O_4), which sometimes contain very high concentrations (on the order of 100–1000 ppm) of heavy metals including Cr (*31*).

Cr-rich groups, which are correlated with Si and sometimes Al, were found in all sectors as well. They could be natural windblown soil dust particles. Some Saharan dusts are known to contain high levels of Cr, up to 3000 ppm. Long-range transport of such soils was expected to contribute to Cr release, even in Europe (*32*). On the other hand, they might also be the result of Cr condensation on airborne soil dust. Evidently, this Cr-containing particle type is rather large in size, often larger than 1.0 μm. This might point to a natural origin for this group. Another, and probably important, possibility is quartz (SiO_2) particles released in the steel production process, which may contain high Cr concentrations (*31*).

The main medium-*Z* elements that are found in combination with Cr are Ca, S, Cl, and K. Here again the emission from the metallurgical industry is probably the main contributor to this type of particles. Significant quantities of Ca minerals such as calcite ($CaCO_3$), dolomite ($CaMg(CO_3)_2$), and gypsum ($CaSO_4 \cdot 2H_2O$) enriched with Cr are released during the production process. Calcite is known to react with SO_2 and results in gypsum. The cement industry is another potential source of atmospheric Cr. Manufacture of cement is a high-temperature process using more than 30 raw materials, with limestone, which contains Cr concentrations in the ppm range, as a major ingredient (*32*).

Pure Cr particles were only found in the northeastern and southwestern wind directions, and not in the southeastern direction. It is possible that this is partly an artifact of the clustering, which incorporated pure Cr particles into groups with high Cr content. Metallic Cr is used primarily in nonferrous alloys, where the use of less expensive ferrochromium alloys can introduce undesirable amounts of Fe (*26*). Cr particles associated with heavy metals are also likely to originate from this source. Presumably this is also the reason why they are found in higher quantities in sectors 2 and 4. The closest important nonferrous industry in the southeastern direction is much more distant than in the other directions. The occurrence of Cl in some groups is most likely explained by the coagulation of anthropogenic Cr particles and sea salt. The size of these particles is very small (around 0.4 μm).

Lead-Containing Particles. Over the five sectors together, 1570 particles were found containing Pb. This is 3.6% of the total number of particles analyzed. Again, we tried to discover the various particle types by means of a combined clustering approach. This resulted in the identification of five major Pb-containing particle types, shown in Table 3. Approximately 50% of the particles were

TABLE 2

Abundances, Diameters, and Composition of Cr-Containing Particle Groups According to Their Different Source Sectors as Found by Statistical Clustering

particle type	total abun	abundance (%)	diameter (μm)	relative concentration (weight %) of main elements detected by EPXMA
			Sector 1: North/Northwest	
Fe/Cr	57.0	57.0	0.8	**Cr**(20), Fe(73), Ni (7)
Cr/high-*Z*	28.6	28.6	1.2	S(10), Cl(26), Ca(18), **Cr**(15), Cu(23)
Si/Cr	14.3	14.3	2.5	Si(16), **Cr**(84)
			Sector 2: Northeast/East	
Fe/Cr	45.6	14.6	0.5	**Cr**(17), Fe(80)
		14.0	0.6	Si(6), **Cr**(18), Mn (6), Fe(62)
		12.3	1.4	Si(21), S(6), Cl(6), **Cr**(14), Fe(43)
		4.7	0.4	Si(11), **Cr**(48), Fe(29)
pure Cr	31.0	31.0	0.4	**Cr**(100)
Cr/high-*Z*	11.1	6.4	0.5	S(12), Cl(10), **Cr** (10), Fe(57), Zn (7)
		4.7	0.6	S(24), K(7), Ca(11), **Cr**(20), Fe(17), Zn (10)
Cr/medium-*Z*	9.3	5.8	0.3	S(14), **Cr**(81)
		3.5	0.3	S(26), Ca(53), **Cr**(7)
Si/Cr	2.9	2.9	0.4	Mg(7), Al(6), Si(58), S(9), **Cr**(12)
			Sector 3: Southeast/South	
Fe/Cr	40.0	23.8	0.6	**Cr**(25), Fe(65)
		10.3	0.9	**Cr**(11), Fe(85)
		5.9	0.7	Si(7), S(6), **Cr**(11), Mn(32), Fe(34), Zn(7)
Cr/high-*Z*	30.2	15.1	0.4	Si(5), **Cr**(39), Fe(34), Ni(4), Zn(12)
		15.1	0.7	Si(4), **Cr**(11), Fe(60), Zn(12)
Si/Cr	16.2	9.2	0.9	Si(7), **Cr**(81), Fe(6)
		7.0	0.6	Si(47), S(6), **Cr**(25), Fe(14)
Cr/medium-*Z*	13.5	9.2	1.7	Al(6), Si(10), S(12), Cl(16), K(5), Ca(6), Ti(6), **Cr**(17), Fe(21)
		4.3	0.9	S(48), Ca(37), **Cr**(10)
			Sector 4: Southwest/West	
Fe/Cr	39.0	18.1	1.5	**Cr**(18), Fe(73), Ni (4)
		10.9	0.5	**Cr**(46), Fe(40)
		10.0	0.9	Si(14), **Cr**(14), Fe(51), S(5), Cl(3)
pure Cr	24.0	24.0	0.4	**Cr**(100)
Cr/medium-*Z*	23.9	14.9	1.4	Cl(64), **Cr**(28)
		9.0	0.4	Ca(9), **Cr**(64), Fe(8)
Cr/high-*Z*	7.7	5.0	0.9	S(20), Cl(7), Ca(19), Ti(7), V(7), **Cr**(15), Fe(9), Cu(14)
		2.7	0.4	S(52), **Cr**(43), Cu(5)
Si/Cr	5.4	5.4	1.0	Si(83), **Cr**(6)
			Sector 5: Local	
Fe/Cr	53.3	23.0	0.9	**Cr**(25), Fe(68), Ni(6)
		12.5	0.6	**Cr**(49), Fe(42)
		9.2	0.6	**Cr**(13), Fe(84)
		8.6	0.7	Cl(9), S(7), Si(5), Fe(52), **Cr**(17)
Si/Cr	20.7	11.8	1.0	Si(11), **Cr**(85)
		7.9	1.1	Si(87), **Cr**(13)
Cr/medium-*Z*	17.8	12.5	0.7	S(42), Ca(45), **Cr**(12)
		5.3	0.5	S(50), K(11), **Cr**(25)
Cr/high-*Z*	9.2	5.9	1.0	Si(7), Cl(15), **Cr**(20), Pb(4)
		3.3	1.4	Cl(4), **Cr**(17), Cu(76)

found to be "pure" Pb particles, most likely metallic Pb and Pb oxides. Other groups with high abundances were Pb chlorides, Pb associated with medium-*Z* elements such as P, Ca, and K, and Pb-containing particles with high-*Z* elements (mostly Zn, sometimes Cu and Sn). Pb correlated with Si, identified as Si/Pb in Table 3, accounted for only a few percent in most sectors.

Pb is an element that is used very extensively in a wide variety of applications. The average emission for all sources was estimated to be around 123 000 tons year^{-1} in Europe (*30*). The total deposition flux of Pb in the southern bight of the North Sea was estimated to be 13.8 kg km^{-2} year^{-1}, which is 2200 tons year^{-1} (*2*). Gasoline combustion accounts for more than 50% of the Pb emission, but the introduction of unleaded gasoline should have reduced this number dramatically. Other major emitters are coal combustion, Pb production, Cu–Ni production, Zn–Cd production, the steel industry, and cement factories (*4*). The size of Pb-containing particles varies between 0.3 and 0.8 μm and seems to be generally smaller than for Cr-containing particles.

Table 3 shows the high abundance of "pure" Pb particles (45% in sector 5, up to 54% in sector 2). The results for sector 1 are only based on four particles, so no statistical conclusions can be made. According to Fergusson (*33*), metallic Pb, $PbCO_3$, or Pb oxides (all of which could be the so-called "pure" Pb, because only elements with $Z > 11$ are detected in ED EPXMA) are created in various processes: emissions of coal-fired power stations, cement and fertilizer production, base metal smelting, and even automotive exhaust can eventually result in such species. The main components in aged vehicle aerosols are oxylead species: $PbCO_3$, $(PbO)_2{\cdot}PbCO_3$, $PbSO_4$, and PbO (*34*). Therefore, it is rather complicated to assign these "pure" Pb particles to one particular source. The size of these particles is rather small (0.4 μm).

TABLE 3

Abundances, Diameters, and Composition of Pb-Containing Particle Groups According to Their Different Source Sectors as Found by Statistical Clustering

particle type	total abun	abundance (%)	diameter (μm)	relative concentration (weight %) of main elements detected by EPXMA
		Sector 1: North/Northwest		
pure Pb	75	75	0.4	**Pb**(100)
Al/Pb	25	25	0.6	Al(60), **Pb**(40)
		Sector 2: Northeast/East		
pure Pb	53.6	53.6	0.4	**Pb**(100)
Pb/high-*Z*	24.1	8.7	0.5	K(4), Zn(64), **Pb**(27)
		5.6	0.5	Zn(46), **Pb**(52)
		4.7	0.7	Fe(56), Zn(19), **Pb**(12)
		3.5	0.5	Cu(54), Zn(5), **Pb**(38)
		1.6	0.8	Si(5), Cl(3), Sn(66), **Pb**(23)
Pb chlorides	12.3	9.9	0.7	Cl(58), **Pb**(39)
		2.4	0.6	Cl(40), K(11), Zn(22), **Pb**(27)
Pb/medium-*Z*	6.6	3.8	0.6	P(4), Ca(47), **Pb**(34)
		2.8	0.4	K(63), Zn(4), **Pb**(33)
Si/Pb	3.3	3.3	0.5	Al(5), Si(56), Fe(6), Zn(4), **Pb**(22)
		Sector 3: Southeast/South		
pure Pb	48.4	48.4	0.4	**Pb**(100)
Pb chlorides	32.7	9.6	0.4	Cl(73), **Pb**(27)
		9.5	0.7	Cl(60), **Pb**(40)
		6.5	0.8	Cl(49), **Pb**(51)
		4.2	0.6	Cl(54), **Pb**(23)
		2.9	0.7	Cl(40), **Pb**(18), P(4), Ca(5), Fe(10), Zn(25)
Pb/medium-*Z*	10.9	3.8	0.3	P(40), Cl(5), **Pb**(53)
		3.3	0.8	Ca(55), Zn(8), **Pb**(35)
		2.0	0.5	Al(27), P(13), Ti(4), Cr(8), Sn(3), **Pb**(40)
		1.8	0.4	Cl(15), K(40), Ca(6), **Pb**(38)
Pb/high-*Z*	6.9	4.2	0.7	Fe(56), Zn(13), **Pb**(19)
		2.7	0.4	Zn(55), **Pb**(43)
Si/Pb	1.1	1.1	1.0	Al(6), Si(47), K(4), Fe(7), Zn(14), **Pb**(20)
		Sector 4: Southwest/West		
pure Pb	49.8	49.8	0.5	**Pb**(100)
Pb chlorides	23.3	23.3	0.7	Cl(52), Zn(3), Br(4), **Pb**(38)
Pb/high-*Z*	18.1	10.5	0.5	Fe(3), Zn(46), **Pb**(48)
		6.6	0.5	P(13), Ca(11), Cu(16), **Pb**(47)
		1.0	0.7	Ca(11), Sn(59), **Pb**(31)
Si/Pb	6.3	6.3	0.6	Si(38), Ca(3), Fe(29), Zn(8), **Pb**(20)
Pb/medium-*Z*	2.4	2.4	0.7	Cl(4), K(62), **Pb**(35)
		Sector 5: Local		
pure Pb	44.7	44.7	0.4	**Pb**(100)
Pb chlorides	34.9	21.1	0.6	Cl(68), **Pb**(28)
		13.8	0.7	Cl(48), Zn(3), Br(3), **Pb**(38)
Si/Pb	11.2	11.2	0.5	Al (1), Si(8), P(5), Mn(2), Fe(13), Zn(24), **Pb**(36)
Pb/medium-*Z*	6.2	3.9	0.3	P(6), Ca(50), **Pb**(38)
		2.3	0.3	K(60), Zn(2), **Pb**(37)
Pb/high-*Z*	3.0	3.0	0.4	Cl(6), Cu(54), **Pb**(38)

The second most abundant particle type was Pb chlorides. These particles originate from car exhaust emissions and have been studied extensively (*35*, *36*). The primary material from the exhaust of cars is PbClBr. However, PbO, Pb(OH)Cl, Pb(OH)Br, and sometimes $PbSO_4$ and Pb may occur. PbClBr reacts in the atmosphere with many products, all resulting in the loss of halides and finally producing Pb sulfates, nitrates, and oxides (*33*). The detected percentages of traffic-related particles in the different sectors correlate quite well with the amount of car traffic in these sectors: sector 5 (35%) and sector 3 (33%) had air masses passing over densely populated areas in Belgium, The Netherlands, and Germany. Sector 4 (23%) also has a lot of traffic, but it is much more distant from the sampling area. Therefore, the particles had much more time to react with atmospheric compounds. No Pb halides were found in sector 1 (marine sector).

Another detected particle type was Pb associated with P, Ca, or K. Particles containing P and/or Ca are probably linked to emissions by cement manufacturing or fertilizer production. Zn and Cl were sometimes found in association with Pb particles holding K. They might be connected to emissions from refuse incineration, which is known to be a major source of airborne heavy metals (*37*). Pb was found together with Zn in a lot of particles classified as Pb/high-*Z*, but also with other heavy metals such as Sn and Cu. Ferroalloy production is probably the main emitter of these types of particles. Their abundances varied between 3.0% in sector 5 and 24% in sector 2. Pb particles in correlation with Si can be associated with soil. This might be partly true since windblown soil dust is known to bring 20 000 tons of Pb into the atmosphere globally every year (*30*), but they could also be fly ash particles, containing high amounts of heavy metals (*38*). These particles sometimes constitute up to 50% of the particle abundance in the North Sea atmosphere (*6*). Other possibilities for Pb silicates are base metal smelting and refining (*33*).

TABLE 4

Abundances, Diameters, and Composition of Zn-Containing Particle Groups According to Their Different Source Sectors as Found by Statistical Clustering

particle type	total abun	abundance (%)	diameter (μm)	relative concentration (weight %) of main elements detected by EPXMA
		Sector 1: North/Northwest		
no Zn-containing particles encountered				
		Sector 2: Northeast/East		
Fe/Zn	48.5	30.9	0.5	Fe(72), **Zn**(18)
		17.6	0.5	S(19), Fe(41), **Zn**(27)
Zn sulfides	25.8	13.5	0.4	S(38), **Zn**(58)
		12.3	0.5	S(60), **Zn**(26)
pure Zn	8.7	8.7	0.4	**Zn**(100)
Si/Zn	7.8	7.8	0.8	Al(6), Si(23), S(12), K(10), **Zn**(90), Sn(4)
Zn/high-*Z*	5.7	5.7	0.5	Cl(4), **Zn**(51), Pb(38)
Zn/medium-*Z*	3.4	3.4	0.5	Cl(12), Ca(59), **Zn**(11)
		Sector 3: Southeast/South		
Fe/Zn	59.6	59.6	0.5	S(4), Fe(65), **Zn**(20)
Zn chlorides	16.0	16.0	0.6	Cl(28), **Zn**(48), Pb(9)
Zn sulfides	15.6	15.6	0.5	S(48), Cl(5), Fe(7), **Zn**(26)
Si/Zn	8.8	8.8	0.5	Si(42), Mn(6), Fe(17), **Zn**(18)
		Sector 4: Southwest/West		
Fe/Zn	45.5	29.6	0.6	Fe(73), **Zn**(14)
		15.9	0.6	Si(6), S(10), Fe(45), **Zn**(22)
Zn sulfides	18.8	11.0	0.5	S(59), Ca(6), **Zn**(20)
		7.8	0.4	S(40), **Zn**(57)
Zn/high-*Z*	15.1	6.2	0.7	P(8), Cu(5), **Zn**(58), Sn(9), Pb(10)
		6.2	0.5	**Zn**(38), Pb(59)
		2.7	0.4	Cr(58), Fe(28), **Zn**(8)
Si/Zn	10.5	10.5	0.9	Al(13), Si(50), S(7), Fe(8), **Zn**(11)
Zn chlorides	10.2	10.2	0.7	Si(7), S(12), Cl(49), **Zn**(20), Pb(5)
		Sector 5: Local		
Fe/Zn	39.8	16.7	0.5	Fe(63), **Zn**(28)
		15.8	0.6	Fe(83), **Zn**(10)
		7.3	0.6	Si(2), S(9), Ca(3), Mn(26), Fe(40), **Zn**(18)
Zn sulfides	32.1	11.1	0.5	S(34), Cl(30), **Zn**(32)
		9.2	0.4	S(65), **Zn**(28), As(4)
		6.0	0.4	S(44), **Zn**(51)
		5.8	0.6	S(29), Fe(37), **Zn**(26)
Si/Zn	8.1	4.9	0.7	Al(16), Si(19), S(9), Fe(25), **Zn**(13)
		3.2	0.7	Al(8), Si(54), S(6), Fe(6), **Zn**(16)
pure Zn	7.3	7.3	0.3	**Zn**(100)
Zn chlorides	6.9	6.9	0.7	Cl(53), **Zn**(30), Pb(7)
Zn/high-*Z*	3.6	3.6	0.4	P(7), K(7), **Zn**(44), Pb(34)
Zn/medium-*Z*	2.1	2.1	0.9	P(12), S(13), Ca(55), **Zn**(16)

Zinc-Containing Particles. Except for sector 1, particles containing Zn were found in all sectors. This clearly points to the fact that a marine source for Zn is very unlikely. In the other sectors together, 2815 Zn-rich particles were detected, what is almost twice as much as Pb-containing particles. As for Cr and Pb, we performed hierarchical, nonhierarchical, and fuzzy clustering on the combined Zn-rich particles for the five different sectors. This again resulted in the identification of seven major Zn-containing particle types (Table 4). The most important group is the Fe–Zn particles, which constitute up to 60% of the particle abundance (sector 3). Dependent on the wind direction, Zn sulfides make up between 16% and 32% of the Zn particles. Zn chlorides, often in the presence of Pb, were found to account for approximately 5–16% of the detected particles. Less abundant groups were "pure" Zn particles, Zn correlated with medium-*Z* elements such as Ca and P, high-*Z* elements such as Pb and Sn, and Zn particles with significant concentrations of Si. The particle size of Zn-containing particles seems to vary between 0.3 and 1.0 μm. These rather small variations make size-related interpretation of the data difficult.

Worldwide, most Zn production originates from ZnS minerals, which are converted into metallic Zn in a series of processes. The main use of Zn is in galvanizing iron and steel products, which are coated with a layer of Zn in order to increase the corrosion resistance. Zn is also used in numerous Zn–base alloys, which are utilized in a wide variety of applications such as Ni–Zn batteries. Other applications of Zn are in plumbing materials, as a catalyst in vulcanization processes (Zn oxides), in paints (ZnS), and in cosmetic and pharmaceutical products. Natural Zn emissions (43.5×10^6 kg year^{-1}), with windblown dust as a major contributor, are estimated to be almost 10 times lower than the combined industrial emissions (314×10^6 kg year^{-1}). Here the main sources are primary Zn production, iron and steel industries, industrial applications, coal and wood combustion, and waste incineration (*4*, *39*). The yearly total deposition flux of Zn into the southern bight of the North Sea was calculated to be 28 kg km^{-2} year^{-1}, which is approximately 4432 tons per year for the total area of the southern bight (*2*).

As for Cr, the most abundant group of Zn particles is particles containing high amounts of Fe. Sometimes these

particles held small concentrations of S and Si. Rybicka (*31*) found significant concentrations of Zn (200–2500 ppm) in mineral dusts containing Fe (magnetite and hematite) emitted by the different stages of the metallurgical production processes by knowing that the iron and steel industries are the second most important source of atmospheric Zn (*4*), and considering the large amount of metallurgical complexes in a rather short distance to our sampling area (northern France, Ruhr area, Gent area, and Manchester area), this might explain the large amount of Zn-containing Fe-rich particles. Strong correlations for Fe, Zn, and Mn above the North Sea (sector 5) have been reported before by Baeyens and Dedeurwaerder (*40*). They recognized metallurgical emissions from Dunkerque, Gravelines, and Boulogne as point sources for these elements.

Zn sulfides are the second most abundant group in three out of four sectors. They might be partly related to windblown Zn ores, which are mostly stored uncovered and therefore easily taken up by the wind, and which easily react to yield a number of secondary minerals. These minerals, such as $ZnCO_3$, can be partly responsible for the detected "pure" Zn particles (again, low-*Z* elements are not detected by our method). The reaction between Zn oxides and sulfuric acid, during release in metallurgical processes, might also yield a fraction of the detected Zn–S particles.

In sectors 3–5, 7–16% of the particles were Zn chlorides. The major part is probably linked to emissions of refuse incineration. The vaporization of volatile elements, among which are heavy metals, during combustion is followed by condensation of these elements on small particles present in the exhaust. The high concentrations of Cl species in the gas stream provides an excellent opportunity to form volatile metal chlorides (*37*). In the coarse fraction of incinerator particles, Mamane (*41*) found all particles to contain at least some Zn, K, and Cl. He stated that these particles were formed through the condensation of volatile Zn, K, and Cl on existing minerals. This type of particle was the only significant heavy metal-containing giant particle type found in the North Sea aerosol (*7*).

In most sectors, approximately 10% of the Zn-rich particles contained a significant percentage of Si. They might be partially related to windblown soil dust, since the average Zn concentration in soil is 100 ppm, but some contain more than 1000 ppm (*42*). On the other hand, these Zn-rich particles are probably for a significant fraction fly ash (just as Pb/Si particles), which is known to contain important concentrations of heavy metals (*38*, *43*). Also, the small average diameter of this group (0.5 μm) points to a significant anthropogenic fraction. Although the concentrations of heavy elements such as Cr, Pb, and Zn might not be high enough in most fly ash particles to be detected with our method, this does not mean that they do not contribute to the atmospheric input of trace metals to the North Sea.

Other less frequently occurring particle types were Zn in association with Pb, Cr, and Sn. Again, ferroalloy production is presumably the main source of these particles. Abundances were as high as 15% (sector 4). Zn associated with medium-*Z* elements such as Ca and P is likely derived from the manufacture of phosphate fertilizer or from cement production (*30*).

General Overview. The combined interpretation of the three cluster techniques produced 5–7 major particle types containing Cr, Pb, or Zn. Most of the particle types were directly or indirectly connected to emissions of the metallurgical industry, which is eminently present in the northern part of France, the German Ruhr area, and the industrial centers in the middle of the United Kingdom. A major part of Pb-rich particles was found to be associated with automotive exhaust. Less important sources were cement production and refuse incineration.

On top of this, we should not forget that concentrations lower than 1000 ppm cannot be detected with ED EPXMA. Thus, we must presume that at least a fraction of the particles containing lower concentrations of Cr, Pb, and Zn were not identified as heavy metal-containing, but indeed contribute to the atmospheric heavy metal inputs. An important example of such a particle type is fly ash, which constitutes a major part of North Sea particulate matter. Only a small fraction of these fly ash particles were found with heavy metal concentrations higher than 1000 pmm. This does not mean that they do not contribute to the heavy metal inputs, when considering the high amounts of fly ash particles in some sectors.

Our results provide ample evidence for the apparent existence of a heavy metal-containing North Sea aerosol. It was mainly overlooked in previous investigations using single-particle analysis, because these particles are "drowned" in an excess of other, more abundant, particle types such as sea salt and aluminosilicates. The enormous number of particles (48 000) obtained by our automated analysis method allows us to acquire much more statistically reliable results than by manual single-particle analysis, with which only a few hundred particles can be analyzed in a reasonable time. It is exactly this huge database that allowed us to focus on special, low-abundant particle types such as heavy metal-containing particles.

Acknowledgments

We acknowledge the financial support by Rijkswaterstaat, Dienst Getijdewateren (The Netherlands) under Grants NOMIVE*2 No DGW-920 and No DGW-217 and, at a later stage, by the Belgian State—Prime Minister's Office—Services for Scientific, Technicol and Cultural Affairs (Contract MS/06/050 of the Impulse Program in Marine Sciences).

Literature Cited

(1) Katrinak, K. A.; Anderson, J. A.; Buseck, P. R. *Environ. Sci. Technol.* **1995**, *29*, 321–329.
(2) Rojas, C. M.; Injuk, J.; Van Grieken, R. E.; Laane, R. W. *Atmos. Environ.* **1993**, *27A*, 251–259.
(3) Hooper, J. F.; Ross, H. B.; Sturges, W. T.; Barrie, L. A. *Tellus* **1991**, *43B*, 45–60.
(4) Nriagu, J. O.; Pacyna, J. M. *Nature* **1988**, *333*, 134–139.
(5) Ottley, C. J.; Harrison, R. M. *Sci. Total Environ.* **1991**, *100*, 301–318.
(6) Rojas, C. M.; Van Grieken, R. E. *Atmos. Environ.* **1992**, *26A*, 1231–1237.
(7) Van Malderen, H.; Rojas, C.; Van Grieken, R. *Environ. Sci. Technol.* **1992**, *26*, 750–756.
(8) Dierck, I.; Michaud, D.; Wouters, L.; Van Grieken, R. *Environ. Sci. Technol.* **1992**, *26*, 802–808.
(9) Rojas, C. M.; Van Grieken, R. E.; Maenhaut, W. *Air Soil Pollut.* **1993**, *71*, 391–404.
(10) Injuk, J.; Otten, Ph.; Laane, R.; Maenhaut, W.; Van Grieken R. *Atmos. Environ.* **1992**, *26A*, 2499–2508.
(11) Rojas, C. M.; Otten, Ph. M.; Van Grieken, R. E.; Laane, R. W. In *Air Pollution Modelling and Its Application*; van Dop, H., Steyn, D., Eds.; Plenum Press: New York, 1991.
(12) Rojas, C. M.; Van Grieken, R. E.; Laane, R. W. *Atmos. Environ.* **1993**, *27A*, 363–370.
(13) Pena, J. A.; Norman, J. M.; Thomson, D. W. *J. Air Pollut. Control Assoc.* **1977**, *27*, 337–340.
(14) Otten, Ph.; Rojas, C.; Wouters, L.; Van Grieken, R. Atmospheric Deposition of Heavy Metals (Cd, Cu, Pb and Zn) into the North

Sea. Report 2 to Rijkswaterstaat (The Hague, The Netherlands) on Project NOMIVE*2 DGW 920, University of Antwerp (UIA), Belgium.
(15) Bondarenko, I.; Treiger, B.; Van Grieken, R.; Van Espen, P. *Spectrochim. Acta Electron.*, submitted.
(16) Crutcher, H. L.; Rhodes, R. C.; Graves, M. E.; Fairbaim, B.; Nelson, A. C. *JAPCA* **1986**, *36*, 1116–1122.
(17) Saucy, D. A.; Anderson, J. R.; Buseck, P. R. *Atmos. Environ.* **1987**, *21*, 1649–1657.
(18) Shattuck, T. W.; Germani, M. S.; Buseck, P. R. *Anal. Chem.* **1991**, *63*, 2646–2656.
(19) Bernard, P. C.; Van Grieken, R. E. *Anal. Chim. Acta* **1992**, *267*, 81–93.
(20) Treiger, B.; Bondarenko, I.; Van Malderen, H.; Van Grieken, R. *Anal. Chim. Acta*, in press.
(21) Bondarenko, I.; Van Malderen, H.; Treiger, B.; Van Espen, P.; Van Grieken, R. *Chemom. Intell. Lab. Syst.* **1994**, *22*, 87–95.
(22) Chester, R.; Bradshaw, G. F. *Mar. Pollut. Bull.* **1991**, *22*, 30–36.
(23) Duce, R. A.; Liss, P. S.; Merrill, J. T.; Atlas, E. L.; Buat-Menard, P.; Hicks, B. B.; Miller, J. M.; Prospero, J. M.; Arimoto, R.; Church, T. M.; Ellis, W.; Galloway, J. N.; Hansen, L.; Jickels, T. D.; Knap, A. H.; Reinhard, K. H.; Schneider, B.; Soudine, A.; Tokas, J. J.; Tsunogai, S.; Wollast, R.; Zhou, M. *Global Biogeochem. Cycles* **1991**, *5*, 193–259.
(24) Ottley, C. J.; Harrison, R. M. *Atmos. Environ.* **1993**, *27A*, 685–695.
(25) *Toxic Metals in the Atmosphere*; Nriagu, J. O., Davidson, C. I., Eds.; Advances in Environmental Science and Technology 17; Wiley and Sons: New York, 1986.
(26) Nriagu, J. O. In *Chromium in the Natural and Human Environments*; Nriagu, J. O., Nieboer, E., Eds.; Advances in Environmental Science and Technology 20; Wiley and Sons: New York, 1988.
(27) Moore, J. W.; Ramamoorthy, S. *Heavy Metals in Natural Waters*; Springer-Verlag: New York, 1984.
(28) Natusch, D. F.; Wallace, J. R. *Science* **1974**, *86*, 695–699.
(29) Xhoffer, C.; Bernard, P.; Van Grieken, R.; Van der Auwera, L. *Environ. Sci. Technol.* **1992**, *25*, 1470–1478.
(30) Pacyna, J. M. In *Toxic Metals in the Atmosphere*; Nriagu, J. O., Davidson, C. I., Eds.; Advances in Environmental Science and Technology 17; Wiley and Sons: New York, 1986.
(31) Rybicka, E. H. *Environ. Technol. Lett.* **1989**, *10*, 921–928.
(32) Pacyna, J. M.; Nriagu, J. O. In *Chromium in the Natural and Human Environments*; Nriagu, J. O., Nieboer, E., Eds.; Advances in Environmental Science and Technology 20; Wiley and Sons: New York, 1988.
(33) Fergusson, J. E. *The Heavy Elements*; Pergamon Press: Oxford, 1990.
(34) Harrison, R. M. In *Toxic Metals in the Atmosphere*; Nriagu, J. O., Davidson, C. I., Eds.; Advances in Environmental Science and Technology 17; Wiley and Sons: New York, 1986.
(35) Harrison, R. M.; Sturges, W. T. *Atmos. Environ.* **1983**, *17*, 311–328.
(36) Hirschler, D. A.; Gilbert, L. F.; Lamb, F. W.; Niebylski, L. M. *Ind. Eng. Chem.* **1957**, *49*, 1131–1142.
(37) Greenberg, R. R.; Zoller, W. H.; Gordon, G. E. *Environ. Sci. Technol.* **1978**, *12*, 566–573.
(38) Norton, G. A.; Malaby, K. L.; Dekalb, E. L. *Environ. Sci. Technol.* **1988**, *22*, 1279–1283.
(39) Nriagu, J. O. *Nature* **1979**, *279*, 409–411.
(40) Baeyens, W.; Dedeurwaerder, H. *Atmos. Environ.* **1991**, *25A*, 1077–1092.
(41) Mamane, Y. *Atmos. Environ.* **1988**, *22*, 2411–2418.
(42) Aubert, H.; Pinta, M. *Trace Elements in Soils*; Elsevier Scientific Publishing: Amsterdam, 1977.
(43) Ondov, J. M.; Choquette, C. E.; Zoller, W. H.; Gordon, G. E.; Biermann, A. H.; Heft, R. E. *Atmos. Environ.* **1989**, *23*, 2193–2204.

Received for review March 24, 1995. Revised manuscript received September 11, 1995. Accepted September 12, 1995.[⊗]

ES950205L

[⊗] Abstract published in *Advance ACS Abstracts*, December 1, 1995.

Fresenius J Anal Chem (1996) ♥♥♥ : ♥♥♥–♥♥♥

LECTURE

Wendy Jambers · Lieve De Bock · René Van Grieken[1]

Applications of micro-analysis to individual environmental particles

Received: 25 September 1995 / Accepted: 30 November 1995

Abstract An overview is given of the recent applications of micro-analytical techniques to single particle environmental research performed at the University of Antwerp since 1990. Automated electron probe X-ray micro-analysis, laser microprobe mass spectrometry and micro-particle induced X-ray emission are the techniques most used for aerosol, aqueous suspension and sediment characterisation. Other techniques like scaning transmission electron microscopy, electron energy loss spectroscopy, Fourier transform infra red microscopy and secondary ion mass spectrometry have only recently been implemented into environmental research.

Introduction

Particles play an important role in the environment. It is now well understood that particles are the major transport form of material in water and in air, that environmental particles frequently contain toxic components and that aerosols influence the global climate and the visibility of the atmosphere. Hitherto particulate matter has mostly been characterized by bulk techniques. However, micro analyses of single particles are very valuable as a complement to the more conventional bulk analysis, because they provide detailed information concerning origin, formation, transport reactivity, transformation reactions and environmental impact of particulate matter. This article will give an overview of the micro-analytical applications to single environmental particles.

Specific problems of single particle analysis are related to the small sizes of the particles. The main problem is the difficulty to perform quantitative analysis, because of the uncertainty in the determination of the interaction volume and the absence of suitable particle standards. A second drawback is the necessity to analyze large numbers of particles as a base for statistically relevant results, which makes individual particle analysis time consuming. These long analysis times are reduced and partially compensated by automation and computerization, with computer controlled electron probe X-ray micro-analysis (EPXMA) as the most advanced example. Another obstacle most micro-beam techniques have to cope with, is the need to operative in vacuum. This can cause serious losses and transformations of volatile and unstable compounds. Since all micro-analytical beam techniques have their own characteristic limitations, a full characterisation of a sample can only be obtained by combining several of these techniques with conventional bulk analysis.

Earlier reviews have pointed out that EPXMA, laser microprobe mass analysis (LMMS) and micro-particle induced X-ray emission (μ-PIXE) are the techniques most used for environmental applications [1–4]. Other techniques like scanning transmission electron microscopy – energy dispersive X-ray detection (STEM-EDX), electron energy loss spectrometry (EELS), micro-Raman spectrometry, Fourier transform infra red microscopy (μ-FTIR) and secondary ion mass spectrometry (SIMS) have only found limited applications in environmental research or have only been recently discovered by environmental laboratories.

This article will give an overview of the micro-analytical applications on single particles performed in the Micro- and Trace Analysis Centre (MiTAC) of the University of Antwerp since 1990. For descriptions of the micro-analytical techniques involved and for other environmental applications, reference is made to Grasserbauer [1], Van Grieken and Xhoffer [2], Xhoffer et al. [3] and Jambers et al. [4].

Aerosols

Remote marine and continental aerosols

The increasing industrialization together with long range transport of pollutants has reduced the possibility to locate

W. Jambers · L. De Bock · R. van Grieken (✉)
Micro and Trace Analysis Centre (MiTAC),
Department of Chemistry, University of Antwerp (UIA),
Universiteitsplein 1, B-2610 Antwerpen, Belgium

Fresenius J Anal Chem
Artikel: **06579**
Schneider Druck GmbH, Rothenburg

Springer, Heidelberg
Seite(n): **1–7**
1. Korrektur:

Bearbeitung:
Schliwa / FV

and characterise the composition of "pure" aerosols in the absence of any pollution. The Antarctic continent is one of the few locations where the so-called background aerosols are still present. In the fine and coarse mode fraction of coastal Antarctic aerosols, marine components were identified by EPXMA as the dominant particle type and only a minor crustal component could be detected [5–8]. Evidence of possible reactions with gaseous sulphur compounds was found in the small amounts of sulphur present in several NaCl and $MgCl_2$ particles. In the majority of particles larger than 0.1 μm, sulphur is present as gypsum and these sulphate particles showed a seasonal variability with a maximum in number and in mass during the summer. Manual analysis revealed that some of the aerosols were internal mixtures of marine components and silicates.

The composition of background aerosols collected at King George Island, Antarctica was studied with LMMS by Wouters et al. [9]: the majority of particles could be identified as sea salt and transformed sea salt. Sulphate-rich, aluminosilicate, iron-rich, organic, potassium-rich and zinc-rich particles were also found, but in much smaller abundances. The sulphate particles detected in the size fraction 0.5–1 μm are suggested to be highly transformed sea salt in which little or no chloride was found. Earth crustal dust seemed to be responsible for the aluminosilicates and iron-rich particles in the coarse size fraction (2–4 μm). A very low abundance (< 1%) was obtained for the potassium-rich and zinc-rich particles, they may be related to local contamination events. Typical ions (ammonium, nitrate and some trace element ions) often identified in LMMS spectra of marine aerosol particles from less remote regions, were not present in the coastal Antarctic aerosols (see Fig. 1).

Siberia is characterised by some very remote areas, without any industry and with a very low population density, and other regions with serious heavy metal pollution.

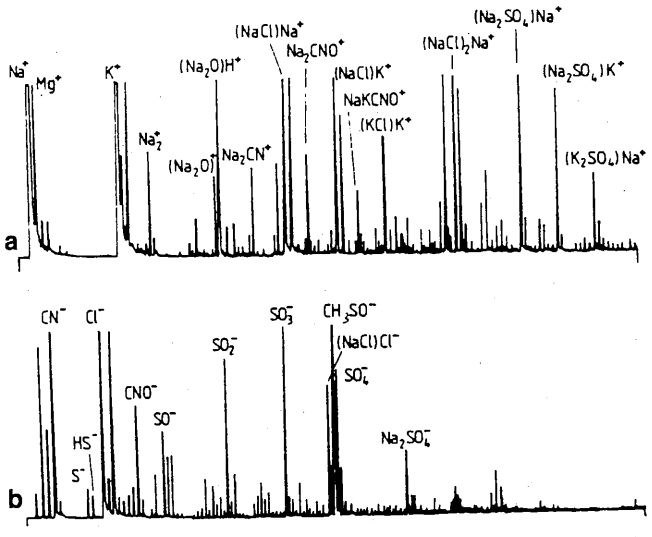

Fig. 1 a, b Positive mode (**a**) and negative mode (**b**) LMMS spectra of an Antarctic sea salt particle with a sulphate enrichment [9]. The figures are reproduced with permission of the International Publishers distributor

Since Western and Central Siberia are probably the most important source of pollutants for the air of the Arctic region, it is necessary to characterise single particles from these regions. EPXMA was used to characterize aerosols which were collected in Karasuk and Klyuchi and above Lake Baikal [10]. Aluminosilicates dominate in all samples from the two cities. For the summer samples, this can be explained by soil dust, but during winter when the ground is completely covered with snow, the only possible source of aluminosilicates is fly ash. The pollution in the lower basin of lake Baikal is clearly detectable in the aerosol samples, although a constant but small (less than 3%) amount of heavy metal aerosols was found in all Baikal samples.

A primary characterisation of rather remote aerosols from Eastern Europe was done on samples which were collected in the middle of the Great Hungarian Plain [11]. The EPXMA results in combination with the recorded air back trajectories reveal that anthropogenic emissions are important sources of these "background" aerosols. Industrial sources contributed 59% of the total particle abundance. The largest group of anthropogenic particles were fly ashes consisting of silicates and produced by power plants and metallurgy. For gypsum particles various sources are possible, but since some Hungarian power plants use line to reduce the sulphur dioxide emission, these are certainly responsible for some of the gypsum.

The combination of EPXMA, LMMS and PIXE was used to characterize individual aerosol particles from the Amazon basin [8]. The aim of this project was to investigate the chemical mechanisms occurring in this environment, to study the processes involving aerosol and gas emission of the forest and to determine the long range transport of pollution aerosols to the basin. The three major aerosol types detected with EPXMA are biogenic, soil dust and sea salt particles. The biogenic fraction was further identified by means of LMMS and could be divided into two major particles types: potassium-rich and phosophor-rich particles. Some LMMS spectra were too complex to interpret due to the superposition of many organic compounds.

North Sea aerosols

For several years EPXMA has been used for the characterisation of individual North Sea aerosols [12]. Over a period of 4 years more than 25,000 particles, sampled during successive campaigns on board of a research vessel over the North Sea and the English Channel, were characterised and classified based on their inorganic composition and size [13]. Hierarchical cluster analysis on the data revealed four different particle types: sea salt, sulphur-rich particles, silicates and calcium sulphate particles. Both meteorological conditions and sampling locations influence the abundance of these different particle types. The differences between all samples, based on variations in abundance, was studied by principal component analysis (PCA). Three different components were found

and apportioned to their source. Marine-derived aerosol particles could be identified as the first component which expands with increasing wind speed and/or increasing distance to the coast. The second component contains anthropogenically derived gypsum particles, while the third group was characterised by particles with high content of silicate and sulphur. A second PCA on the latter group differentiated between two sources, namely a mixed marine/continental source and a pure continental one.

Samples collected on board an aircraft at 6 different altitudes above the North Sea were used to study the difference in aerosol composition with height [14, 15]. The analysis of 50,000 individual particles with EPXMA in combination with hierarchical clustering, showed that for continental air masses the majority of particles could be classified into three types: aluminosilicates, gypsum and iron-rich particles [14]. Due to the turbulent nature of the troposphere, no compositional changes with altitude occurred in the main particles types from western and marine air masses. Non-hierarchical analysis revealed that aluminosilicates, iron-rich particles and sea salt enriched with lead and organic material could be identified as the major particle types in these air masses. Combustion or energy-generation processes seemed to be responsible for up to 60% of the analysed particles. LMMS-analysis confirmed the different particle types found with EPXMA, but many particles seemed to appear as internal mixtures [15].

Air-sea exchange processes in the lower troposphere can cause variations in compositions of air masses crossing the North Sea. This phenomenon was studied with aerosol and rain water samples which were collected on two research vessels which were positioned 200 km apart and downwind from each other for two weeks, in the central area of the North Sea [16]. By combining automated EPXMA, cluster analysis and principal factor analysis (PFA), three to eight different particle types could be distinguished, which were apportioned to found major sources. When the air masses cross the North Sea a decrease in aluminosilicate particles appeared associated with a relative increase for sea salt and sea water crystallisation products. No significant changes in particle diameter could be observed. Manual EPXMA was performed on several samples to study the relations between particle composition, origin and shape. The characterisation based on the particle shape was possible for most particle types. The particles collected from the rain water showed significant differences in diameter and in composition.

Aerosol particles with diameters above 1 μm are classified as giant aerosols. Although the number of these particles in the lower troposphere is small in comparison with the condensation mode particles, their contribution to the atmospheric deposition is of great importance. The slow realisation of the importance of these particles together with sampling difficulties and measurement errors, have made giant aerosol a hot topic in the field of aerosol research. Giant aerosol particles, collected using an impactor rod on top of an aircraft above the Southern Bight of the North Sea, were analysed by EPXMA and processed by multivariate techniques [17]. Four aerosol sources could be distinguished by PFA: aluminosilicate dispersal, combustion processes, industrial activity and a marine source. Cluster analysis enabled us to classify the analysed particles and revealed clear differences between marine and continental air masses. The size distributions of the main particles types could be well fitted by a log-normal distribution with an average diameter of 3 μm. A bimodal size distribution with average size maxima at 4 and 15 μm was only found in the case of aluminosilicate particles.

By using the scanning proton microprobe (SPM) facilities of the IRMM in Belgium and of the Lund Institute of Technology in Sweden, the major, minor and trace elements in individual giant North Sea aerosols were determined by μ-PIXE [18, 19]. Titanium, vanadium, and chromium could be detected down to concentrations of 50 fg. Three different aerosol types were distinguished: sea salt particles, sea salt combined with a high contents of sulphur, potassium and calcium and particles rich in titanium, chromium, iron and nickel. Elemental maps exposed the different large particles which had been agglomerated to individual giant aerosol particles. Figure 2 shows some elemental maps of metals (Ti, Cr, Mn, Zn, Fe, V) found in an agglomerated particle.

Recently the feasibility of using micro-FTIR spectrometry or FTIR microscopy (μ-FT-IR) in combination

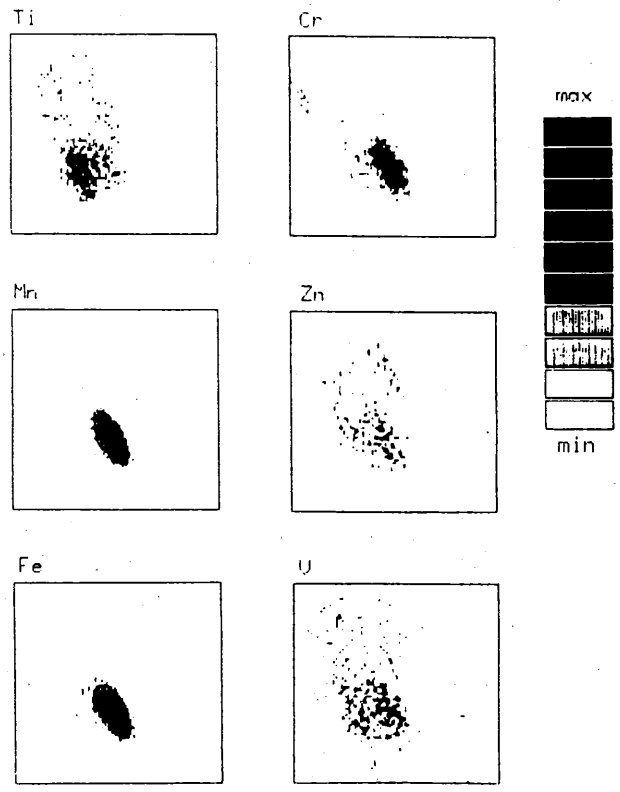

Fig. 2 Element maps of Ti, V, Cr, Fe and Zn in an agglomerated particle found in the North Sea air mass, obtained with the nuclear microprobe. Scan area: 25 μm × 25 μm [18]. The figures are reproduced with permission of John Wiley & Sons, Ltd.

EPXMA for the chemical analysis of giant marine aerosol particles has been tested [20]. One of the major difficulties during the particle analysis with μ-FTIR could be assigned to the composition of marine particles in the size class above 5 μm. These particles were mostly characterised by large amounts of inorganic salts, which absorb only partly in the mid-IR region, and by low percentages of organic material. Moreover the mixed particle composition produced strongly overlapping peaks in the FTIR spectra, which complicated the interpretation. Individual particle analysis in the far-IR region would provide a solution for these problems but is still impossible with the available equipment. Comparison with EPXMA results was limited to elements with $Z > 11$. More promising results should be obtained in the future by studying particles with higher organic content and by comparing the μ-FTIR analysis results with those acquired by a windowless scanning electron microscope.

Urban aerosols

Concerning the urban aerosol composition, numerous of studies have been focused on highly industrialised countries and only limited data are available from so-called developing countries. Aerosols from the city of Khartoum in the sub-Saharian region of Sudan were characterised by combining automated EPXMA with different bulk techniques [21]. Most of the Khartoum aerosol particles were identified as soil dust and could be differentiated into aluminosilicates and smaller amounts of quartz and calcite. In comparison with literature data on urban aerosol composition, the concentrations of sulphur, chlorine, zinc, bromine and lead in the Khartoum dust particles are the lowest values ever published. The airborne levels of bromine, lead and crustal elements seemed to be controlled by traffic emissions.

A combination of EPXMA, LMMS and X-ray fluorescence (XRF) was used to characterise aerosol which were sampled 4 km west of Santiago de Chile [22]. Automated EPXMA revealed eight different particle types in both the fine and coarse aerosol mode. The coarse mode was mainly dominated by soil dust while anthropogenic particles controlled the fine particle mode. Although a high amount of particles contain sulphur, they could not be classified into one particle type but are distributed over six groups. The LMMS results indicate that the sea spray particles undergo several transformations and a sulphur enrichment during their transportation to the city (about 100 km). Using LMMS also carbon-rich particles, probably produced by fossil-fuel combustion, could be identified.

Based on EPXMA, LMMS and PIXE analysis, most of the lead-containing particles, collected on top of a 15-m high building 5 km south of Antwerp, were identifed in the fine fraction < 1 μm [23]. The EPXMA results could be classified in five main classes. The lead sulphates and lead halides produced by car exhaust accounted up to 67% and 28% by mass of the total lead-containing particles, respectively. The obtained results suggested also that the individual lead particles are not completely converted to pure lead sulphate particles upon reaction with ammonium sulphate aerosols present in the urban atmosphere. Chlorine and bromine were found to be completely removed from the lead sulphate particles (see Fig. 3). LMMS was performed to detect elements with $Z < 11$, particularly ammonium compounds. Ammonium sulphate coatings were found to be present on nearly all lead particles.

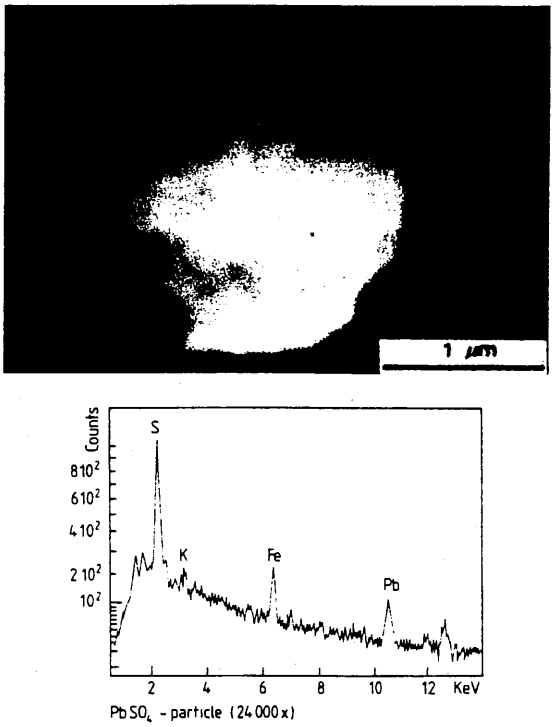

Fig. 3 Secondary electron image and X-ray spectrum of a lead sulphate particle in an urban atmosphere [23]. The figures are reproduced with permission of Elsevier Science Publishers B.V.

Wonders et al. [24] reported on the LMMS analysis of lead-containing aerosols collected both at the city Wageningen and at the downwind side of a highway at Ede, in The Netherlands. Most particles were identifed as mixed salts of ammonium nitrate and ammonium sulphate and showed a variable content of metals especially in the case of vanadium and lead.

Van Grieken et al. [25] reported on the depth analysis with SIMS of individual particles. Aerosols were collected near the city of Antwerp, Belgium onto a freshly sliced indium chip which was equipped with an electron microscopy index grid. This sample preparation enables a quick location of the particles of interest and prevent loss of surface information due to beam sputtering before the actual analysis. The depth profiles of the analysed aluminosilicate particles showed a vanadium-chromium enrichment in the surface layer. The existence of such coatings indicates that these aluminosilicates are fly ash particles.

EELS was used to characterise individual carbonaceous urban aerosol particles from Phoenix, AZ, USA

[26]. The particles incorporated ten to hundred aggregated spheres and showed diameters below 2 µm. The energy loss near edge fine structure (ELNEFS) of the C-K edge reflected the presence of a mixture of graphitic and amorphous carbon within and among the individual aggregate particles. The graphitic structures were assumed to be part of the primary spheres, while the amorphous regions were probably condensed hydrocarbons. Surface coatings containing sulphur and nitrogen appeared on the carbonaceous aggregates collected during the summer. The deposition of sulphates and nitrates from the atmosphere as end products of photochemical reactions could probably be responsible for these kind of coatings. Visual evidence of the sulphur coating was obtained by element specific imaging (ESI). The carbon structural variations were found to be similar for both the coated and uncoated carbonaceous particles, suggesting comparable pre-emission sources.

Industrial aerosols

Coal fly ash particles emitted by a Hungarian power station were characterised by single particle analysis using EPXMA [27]. Two unexpected particle groups were detected in the power plant aerosol fraction below 2 µm: barium-rich particles and arsenic-rich gypsum particles. The first group is probably produced by the cleaning process with barium-containing liquid to reduce the sulphur content of added slag. The arsenic coating on the second particle group results from the condensation in the cooled stack gas.

Indoor aerosols

Since it has been discovered that asbestos fibres can cause health problems, methods are being developed to modify the fibre but keep its fire-resistant characteristics. Surface modification, upon reaction with different products will result in thermally and chemically stable fibres. In this way their cytotoxic and haemolytic activity could be reduced or could even completely disappear. EELS in combination with ESI revealed some very interesting results in a study on the modification of the surface reactivity of chrysotile asbestos fibres [28]. Carbon maps obtained from the organosilane coated asbestos fibres showed an inhomogeneous distribution of the coating over the fibres and moreover some of the fibres seemed to be unaffected by the treatment. Better results were found for $TiCl_3$-modified fibres. Evidence for the chemical reaction between titanium chloride and thy chrysotile fibres was discovered in the pre-edge of the oxygen peak in the EEL spectrum, which indicates a bond between oxygen and titanium. Lateral elemental titanium maps of cross-sectioned treated fibres revealed the presence of titanium inside as well as on the external surface of the analyzed fibres, leading to a complete encapsulation of the material. SIMS analyses on these $TiCl_3$-coated fibres confirmed with Ti^+ and TiO^+ distribution images the uniform reaction of titanium with the chrysolite surface. A second indication of a full reaction of $TiCl_3$ with the asbestos fibres was found in the absence of $TiCl^-$ ions.

Recently a study has been started, using STEM-EDX to characterise the indoor submicrometer aerosol particles that might be responsible for the staining of famous paintings in the Correr museum at San Marco Square, Venice [29]. To prevent particle evaporation during analysis, the sample holder was cooled with liquid nitrogen. In this way it became possible to analyse individual aerosol particles > 100 nm. Further research on this topic will presumably provide a way to obtain compositional information on individual particles down to 50 nm.

Aqueous suspension and sediments

Oceans and seas

North Sea bulk water and corresponding surface micro layer samples have been characterised by a combination of EPXMA and LMMS [30]. Due to the roughness of the North Sea, only small differences in particle types and abundances could be noticed between the collected surface micro layer and the underlying bulk samples. Organic particular matter was more abundant in the micro layer and showed a correlation with the metal-rich fraction. These marine samples were also compared with their corresponding aerosol samples. Since no chemical analogues for calcium-rich aluminosilicates were observed above the North Sea, they must be of aquatic origin. Titanium-rich particles however, have a similar marine and atmospheric fraction and are thus deposited from the air.

The mineral structure of crystalline particles can be obtained by combining STEM-EDX with selected area electron diffraction (SAED). This combination has been tested on Nanoplast embedded micrometer suspended particles collected in the Southern Bight of the North Sea, and the results are promising [31].

Silty and clayey sediments collected in the Baltic Sea were characterised by combining automated EPXMA with bulk techniques [32]. Clustering resulted in nine particle types which could be identified as different minerals. All samples were dominated by quartz and aluminosilicates, but these are not very useful to characterise the geochemistry of the Baltic sediments. Reduced species, like iron sulphides and rhodochrosite characterise anoxic sediments, such as found in the Gotland Deep, while more oxygen-rich areas like Kattegat are characteristed by iron and manganese oxides/hydroxides. Sulphides and oxides/hydroxides are both present in regions with changeable redox conditions. The high amounts of titanium-rich particles, which were detected near the coast of Germany and Southern Poland, are probably the result of erosion and anthropogenic deposition. Calcium-rich sediments were only present in the transition zone between the Baltic and the North Sea. The gradient shows clearly that there is an inflow of calcium-rich particles from the North Sea into the Baltic Sea.

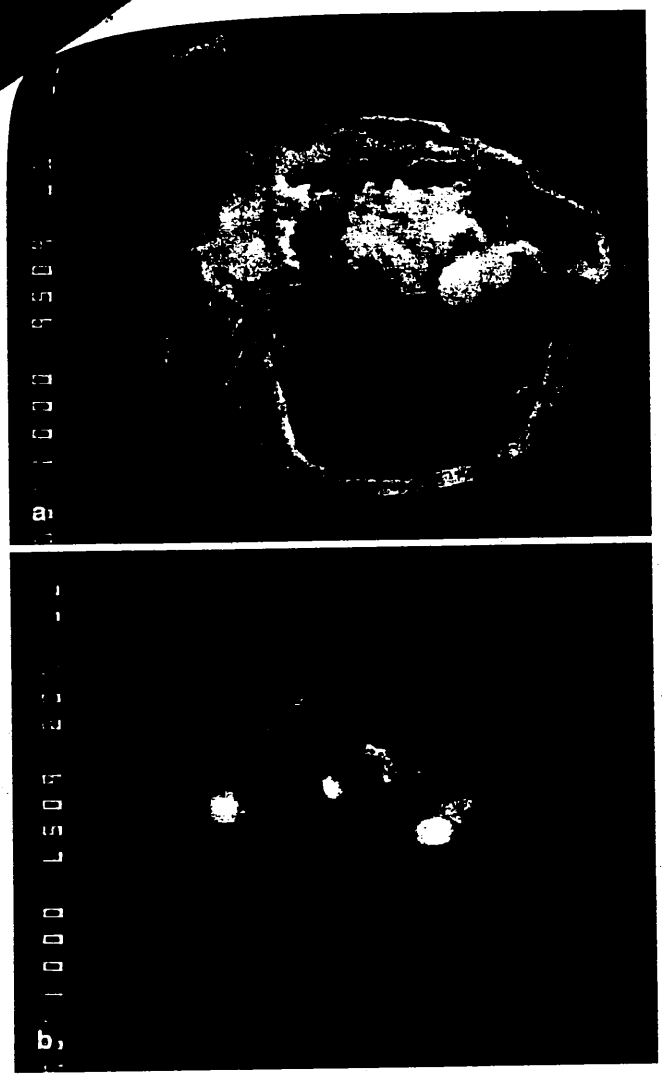

Fig. 4 a, b Secondary (**a**) and back-scatter (**b**) electron image (magnification: × 6000) of a micro-environment (organic matter) containing barite crystals, collected in the Southern Ocean near King George Island. The barite crystals are very bright (because of their high atomic number) in comparison with the surrounding organic matter [34]. The figures are reproduced with permission of Elsevier Science Publishers B.V.

EPXMA and SEM were used to identify the sources and study the lateral distribution of suspended matter collected around Sumbawa Island, Indonesia [33]. Samples collected at the northern side of the island are dominated by iron-rich particles, which are probably from volcanic origin. Suspended matter from Saleh Bay, a huge bay on the Sumbawa Island near the Tambora volcano, is characterised by a high content of tin-rich particles. Possible regional sources of tin are present, but others cannot be excluded. A morphological study of aggregates showed that these exist only in the presence of biogenic material such as diatoms and coccolithophorids. The flocculated particles are probably held together by a gummy organic material produced by the diatoms.

The correlation between the occurrence of suspended and sedimented barite and the intensity of previous biological activity was confirmed by manual EPXMA of suspended matter from the Scotia Sea-Weddel Sea Confluence [34]. In the surface waters, barite is mainly contained within large bio-aggregates. Figure 4 shows the secondary and backscattered electron image of barite crystals encapsulated in organic matter. In the sub-surface zone these aggregates disperse and the barite crystals become individual particles. No association of barite with phytoplankton was found. The pelagic barite is thus most likely formed through passive precipitation in a saturated micro-environment.

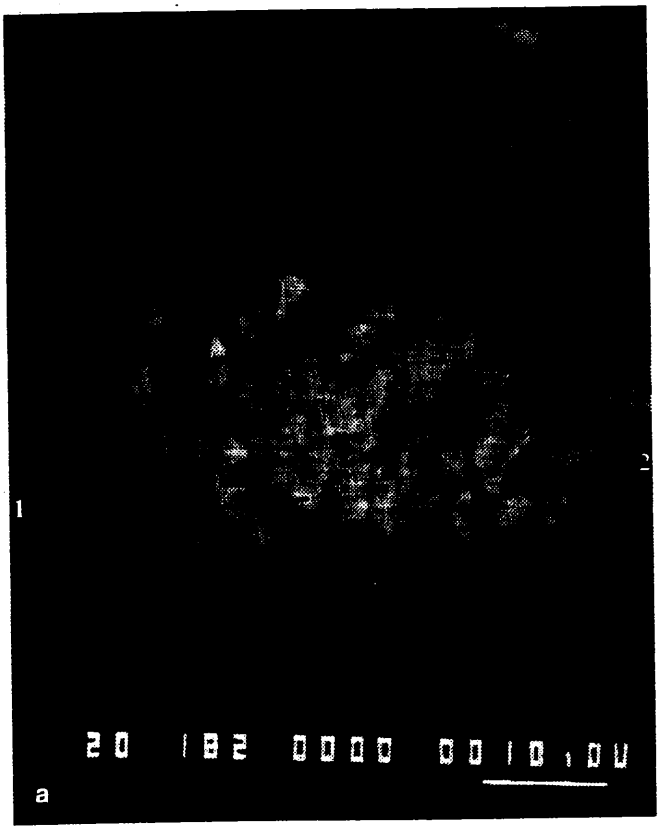

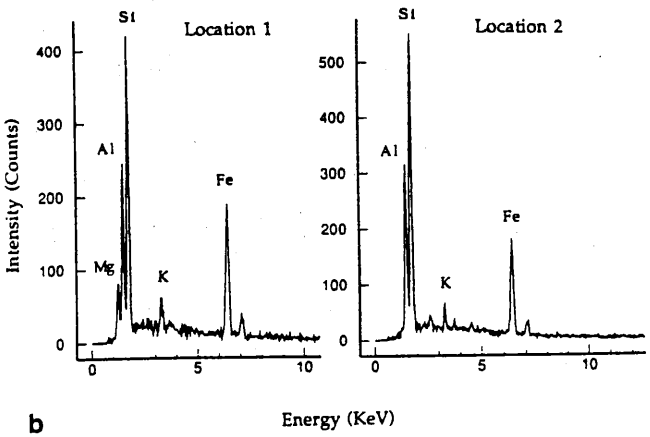

Fig. 5 a, b Secondary electron image (**a**) and X-ray spectra of two locations (**b**) of an aggregated iron-rich aluminosilicate, collected at the Magela Creek, Australia [39]. The figures are reproduced with permission of John Wiley & Sons, Ltd.

The deposition, remobilisation and mixing of materials from different origins in estuaries has been studied by automated EPXMA. Analysis of suspended matter from the Ems estuary (at the border of Germany and The Netherlands) revealed the mixing with marine material in the freshwater zone and the transport of marine suspension across the salt wedge [35]. However no net flux of marine suspended matter into the estuaries of the Garonne and Rhône (France) was found [36, 37]. This is probably due to the different nature of these estuaries. Sediment samples from a longitunal profile and suspended matter from a maximum peak flow were collected in the Elbe river (Germany) [38]. The variation in abundance of calcium carbonate was used to determine the mixing ratio of marine and fluvial sediments and the results are comparable with those found for the Ems river. Load transport, characteristic for discharge events, and erosion of settled mud particles are the major source of suspended matter transported during peak events in the Elbe.

Suspended matter collected during a small flood event in the Magela Creek, tropical northern Australia, has been separated into suspended particulate matter with a diameter larger than 1 μm and coarse and fine colloidal matter (with diameters of 0.1–1 μm and 0.015–0.1 μm respectively) [39]. The former was predominantly inorganic while the two colloidal fractions were characterised by high abundances of organic matter. Individual particle analysis with automated EPXMA was used to characterise the inorganic fractions of suspended and coarse colloidal material (the fine colloidal matter is too small to be analysed and contributed only 10% of the total colloidal matter). Both were dominated by iron-rich aluminosilicates and quartz particles. Figure 5 gives the secondary electron image and the X-ray spectra of spot analysis of an aggregated iron-rich aluminosilicate.

Acknowledgements This work was partially prepared in the framework of the Impulse Programme in Marine Sciences, supported by the Belgian State – Prime Minister's Service – Services for Scientific, Technical and Cultural Affairs (contract MS/06/050). Lieve De Bock acknowledges the "Vlaams Instituut voor de Bevordering van het Wetenschappelijk-Technologisch Onderzoek in de Industrie" (IWT) for financial support.

References

1. Grasserbauer M (1983) Mikrochim Acta Part III: 415–448
2. Van Grieken R, Xhoffer C (1992) J Anal At Spectrom 7: 81–88
3. Xhoffer C, Wouters L, Artaxo P, Van Put A, Van Grieken R (1992) In: Buffle J, Van Leeuwen HP (eds) Environmental particles, vol I, Lewis, Chelsea, MI, pp 107–143
4. Jambers W, De Bock L, Van Grieken R (1995), Analyst 120: 681–692
5. Bernard PC, Van Grieken RE, Eisma D (1986) Environ Sci Technol 20: 467–473
6. Artaxo P, Rabello MLC, Maenhaut W, Van Grieken R (1992) Tellus 44B: 318
7. Van Grieken RE, Artaxo P, Xhoffer C (1992) In: Bailey GW, Bentley J, Small JA (eds) Proceedings of the Fiftieth Annual Meeting by the Electron Microscopy Society of America, San Francisco Press, San Francisco, pp 1482–1483
8. Artaxo P, Van Grieken R, Watt F, Jakšic M (1990) In: Proceedings of the Second World Congress on Particle Technology, Society of Powder Technology, Kyoto, pp 421–426
9. Wouters L, Artaxo P, Van Grieken R (1990) Intern J Environ Anal Chem 38: 427–438
10. Van Malderen H, Van Grieken R (1996) Ocean and atmospheric optics. In press
11. Török Sz, Sándor Sz, Xhoffer C, Van Grieken R, Mészáros E, Molnar A (1993) Időjárás 96: 223–233
12. Van Malderen H, De Bock L, Injuk J, Xhoffer C, Van Grieken R (1993) In: Progress in Belgian oceanographic research. Royal Academy of Belgium, Brussels, pp 119–135
13. Xhoffer C, Bernard P, Van Grieken R (1991) Environ Sci Technol 25: 1470–1478
14. Rojas CM, Van Grieken R (1992) Atoms Environ 26A: 1231–1237
15. Dierck I, Michaud D, Wouters L, Van Grieken R (1992) Environ Sci Technol 26: 802–808
16. De Bock LA, Van Malderen H, Van Grieken R (1994) Environ Sci Technol 28: 1513–1520
17. Van Malderen H, Rojas C, Van Grieken R (1992) Environ Sci Technol 26: 750–756
18. Injuk J, Van Malderen H, Van Grieken R, Swietlicki E, Knox JM, Schofield R (1993) X-Ray Spectrom 22: 220–228
19. Injuk J, Breitenbach L, Van Grieken R, Wätjen U (1994) Microchim Acta 114/115: 313–321
20. De Bock LA, Van Grieken R, Unpublished work
21. Eltayeb MAH, Xhoffer CF, Van Espen PJ, Van Grieken RE (1993) Atoms Environ 27B: 67–76
22. Rojas CM, Artaxo P, Van Grieken R (1990) Atoms Environ 24B: 227–241
23. Van Borm W, Wouters L, Van Grieken R, Adams F (1990) Sci Total Environ 90: 55–66
24. Wonders JHAM, Houweling S, De Bont FAJ, Van Leeuwen HP, Eeckhaoudt SE, Van Grieken RE (1994) Internat J Environ Anal Chem 56: 193–205
25. Van Grieken R, Injuk J, Owari M, Van Espen P (1994) In: Flagan RC (ed) Abstracts of Fourth International Aerosol Conference, vol 1, American Association for Aerosol Research, Cincinnati, OH, pp 10–11
26. Xhoffer C (1993) PhD Thesis, University of Antwerp, pp 205–233
27. Sándor Sz, Török Sz, Xhoffer C, Van Grieken R (1990). In: Peachy LD, Williams PB (eds) Proceedings of the Twelfth International Congress for Electron Microscopy, San Francisco Press, San Francisco, pp 245–255
28. Berghmans P, Injuk J, Van Grieken R, Adams F (1994) Anal Chim Acta 297: 27–42
29. De Bock LA, Van Grieken RE, Camuffo D, Unpublished work
30. Xhoffer C, Wouters L, Van Grieken R (1992) Environ Sci Technol 26: 2151–2162
31. Jambers W, Van Grieken R, Unpublished work
32. Belmans F, Van Grieken R, Brügmann L (1993) Mar Chem 42: 223–236
33. Eisma D, Van Put A, Van Grieken R (1992) Mitt Geol-Paläont Inst Univ Hamburg 70: 137–147
34. Stroobants N, Dehairs F, Goeyens L, Vanderheijden N, Van Grieken R (1991) Mar Chem 35: 411–421
35. Bernard P, Van Grieken R, Eisma D, Hudec B (1986) Environ Sci Technol 20: 467–473
36. Eisma D, Bernard P, Boon J, Van Grieken R, Kalf J, Mook W (1985) Mitt Geol-Paläont Inst Univ Hamburg 58: 397–412
37. Eisma D, Bernard P, Cadee G, Ittekot V, Kalf J, Laane R, Martin J, Mook W, Van Put A, Schumacher T (1991) Neth J Sea Res 28: 193–214
38. Van Put A, Van Grieken R, Wilken R-D, Hudec B (1994) Wat Res 28: 643–655
39. Hart BT, Douglas GB, Beckett R, Van Put A, Van Grieken RE (1993) Hydrol Proc 7: 105–118

Gypsum and Other Calcium-Rich Aerosol Particles above the North Sea

STEFAAN HOORNAERT, HANS VAN MALDEREN, AND RENÉ VAN GRIEKEN*

Department of Chemistry, University of Antwerp (UIA), Universiteitsplein 1, B-2610 Antwerpen, Belgium

Ca-containing particles, especially $CaSO_4$ particles, have been encountered in several atmospheric aerosol studies. An overview is given of the different sources of airborne Ca-containing particles. The North Sea atmosphere is studied to identify the different Ca-containing particle types and to find the correlation between their occurrence and the source regions of the corresponding air masses. About 50 000 individual aerosol samples were collected above the Southern Bight of the North Sea for several wind directions and analyzed for their composition using electron probe X-ray microanalysis. Nonhierarchical cluster analysis is performed on the data to reveal the different particle types, their relative abundances and their sources. $CaSO_4$ in most cases constitutes the largest fraction of the Ca-containing particles. Extremely high numbers of $CaSO_4$ particles are found for northeastern winds, coming from the central part of Germany, suggesting that a great fraction is derived from anthropogenic sources located in this region. Among the other Ca-containing particle types are the aluminosilicates, $CaCO_3$, Fe–Ca-rich particles, and $CaSO_4$ or $CaCO_3$ in combination with NaCl.

Introduction

Prior studies have pointed out that atmospheric deposition is a major source for the input of some heavy metals into the Southern Bight of the North Sea (*1*, *2*). The presence of quite considerable amounts of $CaSO_4$ particles in several studies of the North Sea atmosphere, as well as the possible interaction of hygroscopic particles in cloud formation processes (*3*), resulted in a growing interest in this type of particulates and their emission sources (*4*–*7*). In this work, we therefore want to give an overview of the sources of airborne Ca-containing, especially $CaSO_4$, particles. Neither type of particle has ever been studied in more detail. Several sources have been reported by various authors, but they have never been gathered in one paper. We discuss the results of automated electron probe X-ray microanalysis of airborne particulate matter, collected in the North Sea atmosphere with the aid of an airplane. Single-particle analysis, combined with multivariate statistical approaches, like nonhierarchical cluster analysis, has proven to be a useful tool in air pollution studies and especially in the apportionment of the different aerosol sources (*7*–*11*).

Experimental Section

Sampling Strategy. The samples used were taken over the Southern Bight of the North Sea, using a twin-engine Piper Chieftain PA 31-350 call sign PH-ECO of Geosens B.V. Co. The aircraft is equipped with an isokinetic inlet for the sampling of particulate matter (*12*). In our experimental setup, a 47 mm diameter "aerosol-grade" Nuclepore filter with 0.4 μm pore size is used. Nineteen flights were made, of which 16 yielded useful sample sets. All sampling flights were performed in the same way. At the Goeree platform (position 51°55′ N, 03°40′ E), an upward spiral track was performed, during which the temperature inversion height is localized. Once this was achieved, tracks were flown at six different heights equally spaced under the inversion layer. Filter samples were collected on each track. All tracks were flown parallel to the wind direction. Thirty-six hour back-trajectories were calculated by the KNMI (De Bilt, the Netherlands) for four different levels (1000, 900, 850, and 700 mbar). More details on the sampling campaign can be found elsewhere (*13*).

Chemical Analysis. Single-particle analysis was done by electron probe X-ray microanalysis (EPXMA) using a JEOL JXA-733 superprobe (Tokyo, Japan) equipped with a TN-2000 energy-dispersive X-ray detection system (Tracor Northern, Middleton, USA). A modified particle recognition and characterization (PRC, Tracor Northern, Middleton, WI) software package, the 733B program, allowed us to perform automated individual particle analysis. Once the particles are localized, their diameter, area, and shape factor are computed, and finally an X-ray spectrum is accumulated. For each sample (one per flight track), up to 500 particles were analyzed.

Numerical Analysis. To allow a comparison between the results for different wind directions, all flights were classified into five wind sectors according to the origin of the air masses as inferred from the back-trajectories: northeast-east (NE-E), southeast-south (SE-S), southwest-west (SW-W), northwest (NW) (Figure 1), and a "local" sector (with variable wind drections). Data reduction and interpretation, in particular classification of particles with similar chemical composition into "particle groups", was done by cluster analysis. All elements that were detected in more than 1% of the particles were considered, i.e., Na, Mg, Al, Si, P, S, Cl, K, Ca, Ti, V, Cr, Mn, Fe, Ni, Cu, Zn, and Pb. Clustering was performed on the normalized elemental X-ray intensities using the software package DPP (*14*). Because of the great number of particles, hierarchical clustering requires an enormous amount of computer time for calculating the distances between the particles in each cycle of the hierarchical clustering. Therefore, we used the nearest centroid sorting method of Forgy, a nonhierarchical clustering procedure. The number of clusters (particle groups) is determined by the so-called consistent Akaike's information criterion (CAIC), a mathematical function based on the relation between order, entropy, and information of an isolated system. Its value reaches a minimum for the optimum number of clusters. The criterion is

0013-936X/96/0930-1515$12.00/0

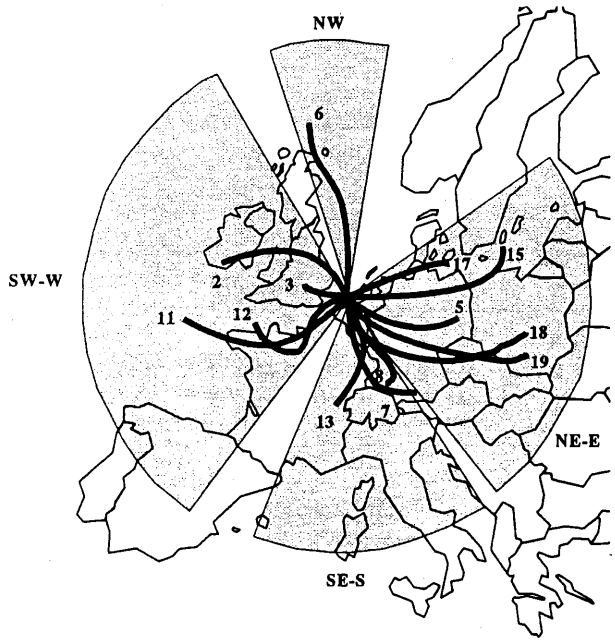

FIGURE 1. Classification of the different sampling flights into five sectors (the local sector is not shown). The indicated lines are the corresponding 1000 hPa air mass trajectories for air masses arriving at the sampling site.

discussed in more detail by Bondarenko et al. (*15*). The program for calculating the criterion forms part of the home-made integrated data analysis system (IDAS), which has recently become available (*16*). After the clustering, *ZAF* correction (a mathematical procedure to correct the observed X-ray intensities for differences in matrix composition between standards and unknown samples) was carried out in order to convert the relative peak intensities into elemental weight compositions.

Results and Discussion

Only the NW sector, which contains only flight 6, can be regarded as purely marine. The results of two sectors reflect the continental influence, natural as well as anthropogenic. These are the NE-E sector, including flights 5, 15, 17, 18, and 19, for which the air masses have passed over Belgium, the Netherlands, Germany, and some eastern European countries, and the SE-S sector, including flights 7, 8, and 13, influenced by Belgium, the southern part of Germany, and the northern and eastern parts of France. Samples collected during flights 2, 3, 11, and 12 characterize the SW-W sector and are related to the influences of the United Kingdom and the northwestern part of France, but also to some extent those of the north Atlantic Ocean and the English Channel. Finally, aerosols collected during flights 4, 9, and 14 were obtained under low wind speed and variable wind direction conditions; therefore, they are classified in the local sector.

(1) Investigation of the Ca-Containing Particles. Cluster analysis was performed on the EPXMA data in order to identify the different types of Ca-containing particles (these are particles with a Ca content >0%). Since we are mainly interested in those particles in which Ca is not just a minor element, we made a selection of all the particles having a relative Ca X-ray peak intensity >10% of that from all elements (hereafter these particles will be called "Ca-enriched" particles, not to be confused with Ca-rich particles, used in other studies, which are composed of mainly Ca). So, by using this threshold value, the clusters should be better separated, and therefore interpretation of them should be easier. Comparing the numbers of particles after selection with the original number of analyzed particles yields the "Ca > 10" fraction, which is reported for all flights and sectors in Table 1. The values shown for each flight are the averages over the six tracks.

TABLE 1

Ca > 10 Fraction for the Different Flights (Averaged over the Six Tracks) and Sectors

flight no.	Ca > 10 fraction (%)	flight no.	Ca > 10 fraction (%)
northwest		southwest-west	
6	1.6	2	16
northeast-east		3	12
5	39	11	7
15	31	12	15
17	24	average	12
18	18	local	
19	17	4	16
average	26	9	13
southeast-south		14	17
7	12	average	15
8	13		
13	16		
average	14		

(1.1) Fraction of Ca-Enriched Particles. We can see from these results that, in general, the value of the Ca > 10 fraction ranges from 7% to 18%. Four flights are exceptions to this rule: flight 6 with only 1.6%, flight 5 with 39%, flight 15 with 31%, and flight 17 with 24%. The lower fraction for flight 6 is due to the great contribution of seasalt particles in this sector as a result of the marine origin of the corresponding air masses and is probably also due to the sea being only a minor source of Ca-enriched particulates. The values of flight 17 and especially flights 5 and 15 are rather high. All three flights belong to the NE-E sector, and their respective air masses have passed over nearly the same regions, including Germany and the Netherlands, suggesting some very important sources of Ca in this region. We also found, by inspecting the Ca > 10 fractions for the different tracks separately, that Ca is distributed rather homogeneously over the six tracks for each flight (small or no decreasing or increasing trends), except again for flights 5 and 15, where higher fractions are found in the lower tracks (up to 49% and 39% for the sixth track of flights 5 and 15, respectively). These lower tracks correspond to air masses coming from even a smaller region, the central and northern parts of Germany and the Netherlands. The high values for these flights result in a high Ca fraction for the whole NE-E sector (26% in comparison to 15% for the local sector and even lower fractions in the other). The big difference between the two continental sectors (NE-E and SE-S) might suggest that mainly anthropogenic sources are responsible for the high values in the NE-E sector.

(1.2) Cluster Analysis for the Ca-Enriched Particles. The nonhierarchical cluster analysis of the Ca-enriched (Ca > 10) particles should provide us with the different particle types. The numbers of clusters, determined by the CAIC criterion, are slightly different for the five sectors. Except for the NW sector, for which four different clusters are found, the number of groups is six or seven. The results, after *ZAF* correction, are summarized in Table 2.

The results from enrichment factor (EF) and back-trajectory calculations show that the marine sources of

TABLE 2

Results of the Nonhierarchical Clustering of the Data after Selection of the Ca-Enriched Particles

cluster no.	elemental composition (wt %) (relative to all elements detectable by EPXMA)	classification	abundance (%)
	Northeast-East		
1	Ca(48) S(45)	$CaSO_4$	49
2	Si(43) Al(19) Ca(17) Fe(12)	aluminosilicates	14
3	Ca(30) Si(20) S(19) Al(12) Fe(8)		11
4	Fe(34) Ca(27) S(23)		9.1
5	Ca(58) S(10) P(5)		7.6
6	Fe(68) Ca(13)		5.6
7	Ca(96)	Ca-rich	4.3
	Southeast-South		
1	Ca(48) S(43)	$CaSO_4$	36
2	Si(43) Ca(20) Al(13) Fe(11)	aluminosilicates	17
3	Ca(26) S(26) Si(15) Fe(5)		16
4	Fe(43) Ca(19) S(13) Zn(10)		13
5	Ca(63) P(10) Pb(9)		10
6	Fe(79) Ca(10)		7.8
	Southwest-West		
1	Ca(46) S(42)	$CaSO_4$	33
2	Si(42) Al(17) Ca(17) Fe(13)	aluminosilicates	15
3	Cl(57) Na(22) Ca(15)	$NaCl-CaCO_3$	14
4	Ca(83)	Ca-rich	13
5	Ca(31) S(15) Si(14) Fe(13)		12
6	Cl(32) Ca(28) S(17) Na(11)	$NaCl-CaSO_4$	7.4
7	Fe(73) Ca(13)		6.4
	Northwest		
1	Cl(42) Na(36) Ca(12) S(8)	$NaCl-CaSO_4$	48
2	Ca(51) S(36)	$CaSO_4$	31
3	Ca(47) Fe(15) Si(14) Mg(8)		15
4	Si(47) Al(27) Ca(17) Fe(9)	aluminosilicates	6.3
	Local		
1	Ca(48) S(43)	$CaSO_4$	41
2	Si(42) Al(19) Ca(17) Fe(12)	aluminosilicates	18
3	Ca(21) S(20) Na(18) Cl(6)		14
4	Ca(51) P(11) Pb(6)		11
5	Ca(90)	Ca-rich	9.2
6	Fe(77) Ca(13)		7.7

atmospheric Ca compounds are less important than the land-based ones, natural or anthropogenic. Only about 25% of airborne Ca comes from the sea (*17*), and at least 60% of Ca is coming from nonsoil sources (*18*). So it seems that a considerable amount of the atmospheric Ca content is originating from anthropogenic sources.

With this information, we tried to relate the different particle types that resulted from our clustering with possible sources. From Table 2 it is clear that, in every case, $CaSO_4$ is the most abundant particle type, except for the NW sector. In the NE-E sector, these particles are even responsible for half of the Ca-enriched particles (49%) (expressed relative to all elements detectable by EPXMA, so excluding elements with $Z < 11$; this definition will be used systematically below), but also in the other sectors they constitute more than 30% of the total load of Ca-enriched particles (local, 41%; SE-S, 36%; SW-W, 33%; NW, 31%). The sources for these airborne particulates are discussed in part 2.2.

The aluminosilicates are the second most important Ca-enriched group for the continental sectors (NE-E and SE-S) the local and the SW-W sectors, but their abundance is much less than that of $CaSO_4$ (only 14−18%). For the marine sector, however, they constitute the least abundant group (6.3%). Considering the major elements, the composition of this cluster is nearly the same for every sector: 42−47 wt % Si, 13−27 wt % Al, 17−20 wt % Ca, and 9−12 wt % Fe. The sources for this airborne particulates are soil dust, transported into the air by the action of erosion and wind (*19*−*21*), stack emissions from coal-fired power plants and boilers (*22*), and probably also emissions from waste incinerators, which are characterized by the same elements in similar proportions (*23*).

Thus far, the results for the different sectors are very alike. Concerning the other groups, there is still a good resemblance between the main elemental compositions of most of the clusters, but there are some differences between the sectors in their relative importance. In all the air masses that have traveled over the sea to some extent, a cluster is found that is mainly composed of Cl, Na, Ca, and S. Examining the composition of the individual particles in these clusters revealed that we are dealing with mixed particles (all four elements present), so the combination of these elements is not the result of the classification of two different particle types, e.g., $CaSO_4$ and NaCl, in one and the same cluster. The high Na and Cl content can be attributed to the sea, the main source of atmospheric NaCl aerosols, which is confirmed by the absence of these particles in continental air masses. Also, the Ca component may originate from the sea under the form of $CaCO_3$ (coccoliths), as reported by Rojas and Van Grieken (*19*), which then might react with atmospheric sulfur compounds. However, one must not forget the possible coagulation between airborne $CaSO_4$ and NaCl particulates. These particles constitute nearly half of the Ca-enriched particles in the NW sector (48%), while in the local sector they are the third most abundant particle type (14%). In the SW-W sector, they are much less important (the second last group); however, here, there is a similar group that is much more important with a similar composition, except for the sulfur content, which is now much lower. This can

be interpreted as the coagulation between $CaCO_3$, which may be partly derived from the cliffs along the English Channel, situated in this sector (*7*), and NaCl or as the incomplete reaction between marine particles and atmospheric sulfur. In this sector, the role of the sea in the formation of this particle type is very clear if one considers the results for the different flights separately; the particles are much more abundant in the samples collected during flights 11 and 12, when the air was passing mainly over the English Channel, than during flights 2 and 3, when the air was coming from the UK.

The third most abundant Ca-enriched particles in both of the continental air masses (NE-E, 11%; SE-S, 16%) which are also present in the SW-W sector (12%), are composed of Ca (26–31 wt %), S (15–26 wt %), Si (14–20 wt %), and Fe (5–13 wt %) and sometimes also contain some Al. The combination of Ca, S, and Si can be thought of as being $CaSO_4$ particles with a silicate core and are most likely formed by combustion processes (*24*). This type of Ca-enriched particles is absent in the local and the marine sectors.

Except for the marine sector, Fe–Ca-rich particles are present everywhere. Two different Fe–Ca-rich particle types can be found. The first one, which is present in each of the four sectors, is composed of mainly Fe (68–79 wt %) and Ca (10–13 wt %) but is the least abundant cluster in almost every sector (5.6%–7.8%). The second type is present only in the continental air masses and is characterized by Fe (34–43 wt %), Ca (19–27 wt %), and also S (13–23 wt %) but with abundances that are somewhat higher (9.1% for the NE-E sector and 13% for the SE-S sector). According to Hopke (*23*), such Fe–Ca-rich emissions are characteristic for sewage sludge incineration and several ferrous metal-related sources. These assumptions are supported by the presence of some heavy metals like Pb and Zn (*25*).

Clusters containing only Ca are identified as $CaCO_3$ (*24*) (C and O cannot be detected by our method). In our clustering, these particles are present mainly in the SW-W sector (13%) but are also in the local (9.2%) and the NE-E sectors (4.3%). As mentioned earlier, airborne $CaCO_3$ can be of marine origin or from sources on the land. The latter include both natural and anthropogenic sources. An important natural source, which might explain the relatively higher abundance in the SW-W sector, is again the cliffs along the English Channel (*7*). Industrial sources with important Ca emissions are the production of construction materials like asphalt and concrete batch plants and limestone kilns (*20, 23*). Other important calcite-emitting industries are iron and steel plants, chemical plants, heat- and power-generating plants and cement plants (*20, 26–28*), agricultural liming (*20, 27, 28*), and the abrasion of streets and buildings (*28*).

The identification of the remaining particle types is less clear; however, the combination of Ca and P found mainly in the local and the SE-S sectors and also in the NE-E might suggest the cement industry (*23*).

(2) A Closer Look at the $CaSO_4$ Particles. (2.1) Fraction of CaSO4 Particles. From the above results, it is clear that the $CaSO_4$ particles are joined in a single cluster for each of the sectors, providing us with the number of $CaSO_4$ particles. In the following discussion, we use these numbers of $CaSO_4$ particles to make some comparisons. The selection of the particles with a relative Ca intensity greater than 10% should not have any influence on the number of $CaSO_4$ particles, since the latter by definition have a Ca content greater than 10%. In Table 3, a comparison is made for each flight between the $CaSO_4$ particles and the original number of particles (called the $CaSO_4$ fraction).

TABLE 3

Gypsum Fraction for the Different Flights (Averaged over the Six Tracks) and Sectors

flight no.	$CaSO_4$ fraction (%)	flight no.	$CaSO_4$ fraction (%)
northwest		southwest-west	
6	0.5	2	7
northeast-east		3	7
5	29	11	2
15	12	12	2
17	12	average	4
18	5	local	
19	4	4	5
average	13	9	6
southeast-south		14	7
7	5	average	6
8	5		
13	5		
average	5		

For the different flights, it can be said that as a general rule the value of the $CaSO_4$ fraction lies between 2% and 7%. Again, some outlying values are present for flights classified in the marine sector and the NE-E sector. Flight 6 contains only 0.5% of $CaSO_4$ particles, while flights 15, 17, and especially 5 contain much more of them (12%, 12%, and 29%, respectively). It is also clear again that, although flights 2, 3, 11, and 12 have been joined in one and the same cluster, there exists a difference between the composition of the air masses corresponding to them. The $CaSO_4$ fractions for flights 11 and 12, which are influenced mainly by the English Channel, are rather low (2%), while the fractions for flights 2 and 3, mainly influenced by the UK, are higher (7%). To get a better view on the dependence of the $CaSO_4$ fractions on the origin of the air masses for the two continental sectors, the back-trajectories for each track were compared and ordered geographically from north to south (Figure 2). Back-trajectories which were too variable and could not be assigned to a single direction were omitted. The corresponding $CaSO_4$ fractions for the ordered tracks are represented graphically in Figure 2. A remarkable trend is observed. High values (10% or more) are found for air masses passing over the northern part of Germany and the Netherlands and even much higher values (up to 40%) for the central part of Germany. For wind directions more to the south, the $CaSO_4$ fractions are much lower (less than 8%) and more uniformly distributed. Thus, it is apparent that some very important $CaSO_4$ sources are situated in Germany and its neighboring Eastern European countries.

(2.2) Sources of $CaSO_4$ Particles. *Marine Sources of $CaSO_4$.* The occurrence of pure $CaSO_4$ in the atmosphere can be the result of fractional crystallization of marine aerosols (*29, 30*). The evaporation of seawater is accompanied by sequential crystallization of several salts: as a first step, calcite ($CaCO_3$) and dolomite ($CaMg(CO_3)_2$) crystallize, next gypsum ($CaSO_4(aq)$), followed by halite (NaCl), and finally the Mg–K salts (*31*). In this way, loosely bound conglomerates of several particles are formed which are shattered during transport in the atmosphere or by impaction on the filter during sampling. This might result in the presence of one of these pure salts in the samples.

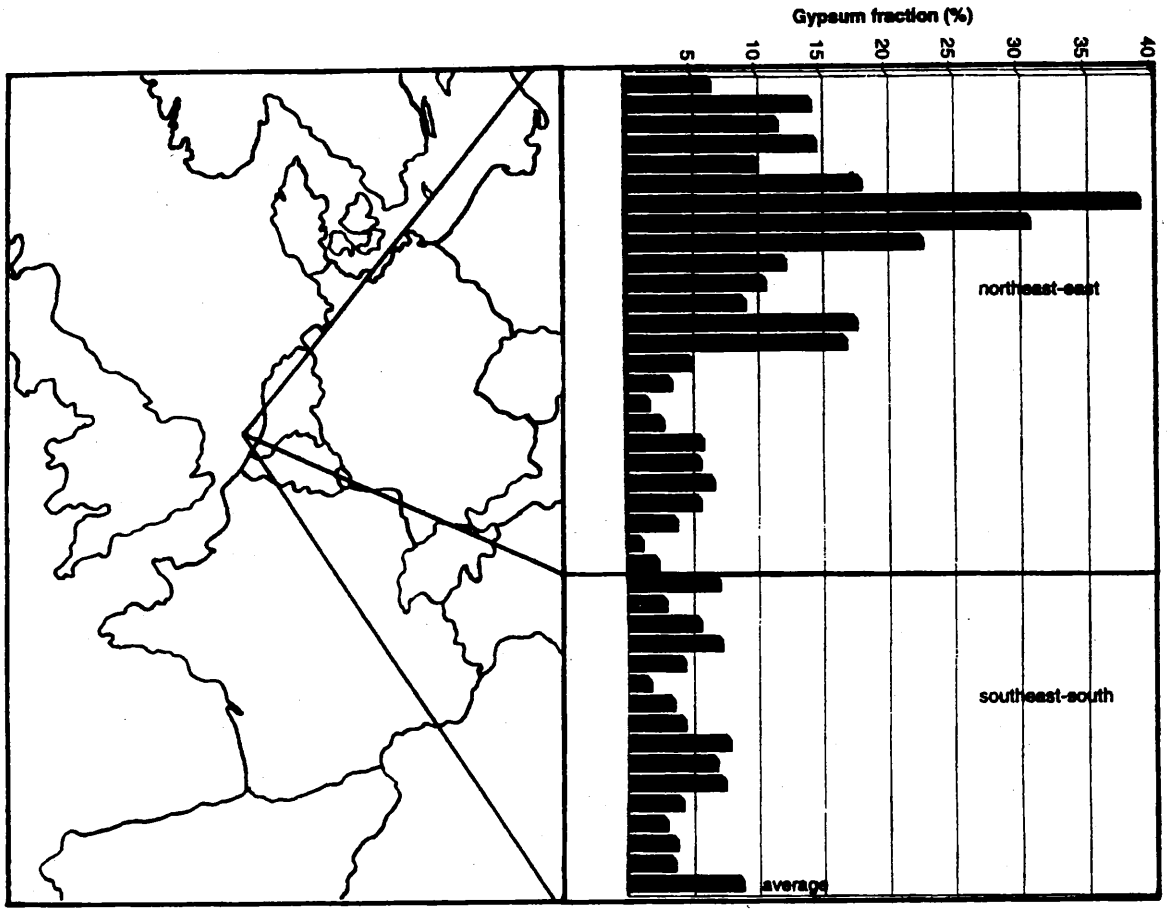

FIGURE 2. Fraction of gypsum particles of ordered geographically from north to south for both of the continental sectors.

Another marine source of $CaSO_4$, though indirect, is the reaction of marine $CaCO_3$ with atmospheric sulfur components, mainly H_2SO_4, formed by the oxidation of SO_2 (direct industrial emissions), H_2S (anaerobic decomposition), DMSO, or DMS (algae) (*4, 30, 32*). This reaction also takes place on the filters during and after sampling, resulting in a clean, fresh appearance of the crystals (*33, 34*). The marine $CaCO_3$, coming from the skeletons of pelagic organisms and coccoliths, which create a suitable chemical environment for this reaction because of their alkalinity, is introduced in the atmosphere by sea spray.

Land-Based Sources of $CaSO_4$. A variety of land-based sources of $CaSO_4$ have been suggested in the past by several authors. Van Borm et al. (*35*) indicated that primary atmospheric $CaSO_4$ particles are produced by the weathering of limestone buildings, covered by a crust of gypsum, which is formed by interaction with atmospheric sulfur compounds. Other sources of $CaSO_4$ are proposed by Biggins and Harrison (*36, 37*), like the attrition of building materials such as plaster and dusts from quarries, from which gypsum is extracted commercially. In the latter case, the particulates are derived from wind erosion, blasting, and transport of the quarried material. Still other sources are reported by Rybicka (*26*), who finds gypsum in dusts emitted by metallurgical plants, and by Bruynseels et al. (*4*), who suggested combustion processes and eolian transport from the continent as sources of $CaSO_4$. The former is also implied by Shattuck et al. (*24*), who associate this particle type with the combustion of coal. Del Monte and Sabbioni (*38*), who investigated the morphology and the mineralogy of fly ash from a coal-fueled power plant, discovered that the fly ash, when exposed to a high level of relative humidity, leads to the nucleation of gypsum crystals. The gypsum is thus confirmed not to be a crystalline phase of the fly ash emissions but to have an airborne origin on the fly ash particles. Also, carbonaceous particles emitted by oil combustion seem to behave in the same way. Similarly, Andreae et al. (*30*) find $CaSO_4$ particles on silicate aerosol particles. These are produced by the reaction between acid sulfates and silicate minerals brought together by in-cloud processes, and they are characterized by a low Ca content in the silicate component because of extraction of Ca from the minerals by H_2SO_4. Just as marine $CaCO_3$, land-derived $CaCO_3$ can react with atmospheric SO_2 or H_2SO_4 to form airborne $CaSO_4$. The $CaCO_3$ is present in dust from metallurgical plants, chemical plants, and cement plants (*26*) or is originating from soil dust and road wear (*35*). According to Ichikuni (*39*), it can also be the result of the world-wide spreading of desert dust, which contains $CaCO_3$ as a major constituent. Another source of airborne $CaSO_4$ is the desulfurization processes in thermal power plants that use limestone for SO_2 removal. Besides other sulfur emission control techniques, two limestone injection processes are applied. One is a dry process, in which limestone is injected into the high-temperature combustion zone as a mixture with the coal, where it is calcined as $CaCO_3 \rightarrow CO_2 + CaO$. Part of the produced CaO reacts in the furnace with SO_2 to produce $CaSO_4$ as $CaO + SO_2 + 0.5O_2 \rightarrow CaSO_4$. A second, more effective limestone injection process is the wet variant, which is initiated like the dry process, but, in addition, the combustion flue gas and unreacted limestone are scrubbed after the furnace with a lime slurry, which flows down through a marble bed in the scrubber

for further removal of SO_2 (*40–42*). The different flue gas desulfurization processes in Germany produce about 1 Mton of gypsum each year. Parungo et al. (*29*), who made a study of plume aerosols from a coal-fired power plant which uses such a lime slurry to scrub the SO_2 gases, found that about 10% of the particles in the plume consisted of crystalline or irregular $CaSO_4$ particles. Drops of the $CaSO_4$ solution, formed in the scrubber, escape along with the flue gas, are transformed in solid $CaSO_4$ particles after evaporation, and are released into the plume.

Acknowledgments

S.H. is supported by the Belgian National Fund for Scientific Research (NFWO). We acknowledge partial financial support by the Belgian Federal Office for Scientific, Technical and Cultural Affairs in the framework of the Impulse Programme in Marine Sciences (Contract MS/06/050) and, before, by Rijkswaterstaat, the Netherlands (Contracts NOMIVE*2 DGW-217 and -920).

Literature Cited

(1) Injuk, J.; Otten, Ph.; Laane, R.; Maenhaut, W.; Van Grieken R. *Atmos. Environ.* **1992**, *26A*, 2499–2508.
(2) Rojas, C. M.; Injuk, J.; Van Grieken, R.; Laane R. W. *Atmos. Environ.* **1993**, *27A*, 251–259.
(3) Charlson, R. J.; Schwartz, S. E.; Hales, J. M.; Cess, R. D.; Coakley, J. A., Jr.; Hansen, J. E.; Hofmann, D. J. *Science* **1992**, *255*, 423–430.
(4) Bruynseels, F.; Storms, H.; Van Grieken, R. *Atmos. Environ.* **1988**, *22*, 2593–2602.
(5) Injuk, J.; Van Malderen, H.; Van Grieken, R.; Swietlicki, E.; Knox, J. M.; Schofield, R. *X-Ray Spectrom.* **1993**, *22*, 220–228.
(6) Rojas, C. M.; Otten, P. M.; Van Grieken, R. *J. Aerosol Sci.* **1989**, *20*, 1257–1260.
(7) Xhoffer, C.; Bernard, P.; Van Grieken, R.; Van der Auwera, L. *Environ. Sci. Technol.* **1991**, *25*, 1470–1478.
(8) Van Malderen, H.; Rojas, C.; Van Grieken, R. *Environ. Sci. Technol.* **1992**, *26*, 750–756.
(9) Sanchez Gomez, M. L.; Ramos Martin, M. C. *Atmos. Environ.* **1987**, *21*, 1521–1527.
(10) Saucy, D. A.; Anderson, J. R.; Buseck, P. R. *J. Geophys. Res.* **1991**, *96*, 7407–7414.
(11) Casuccio, G. S.; Janocko, P. B.; Lee, R. J.; Kelly, J. F.; Dattner, S. L.; Mgebroff, J. S. *J. Air Pollut. Control Assoc.* **1983**, *33*, 937–943.
(12) Pena, J. A.; Norman, J. M.; Thomson, D. W. *J. Air Pollut. Control Assoc.* **1977**, *27*, 337–341.
(13) Otten, Ph.; Rojas, C.; Wouters, L.; Van Grieken, R. *Atmospheric Deposition of Heavy Metals (Cd, Cu, Pb and Zn) into the North Sea;* Second report to Rijkswaterstaat on Project NOMIVE* DGW-920; University of Antwerp (UIA), Belgium, 1989.
(14) Van Espen, P. *Anal. Chim. Acta* **1984**, *165*, 31–49.
(15) Bondarenko, I.; Van Malderen, H.; Treiger, B.; Van Espen, P.; Van Grieken, R. *Chemom. Intell. Lab. Syst.* **1994**, *22*, 87–95.
(16) Bondarenko, I.; Treiger, B.; Van Grieken, R.; Van Espen, P. *Spectrochim. Acta Electron.*, in press.
(17) Yaaqub, R. R.; Davies, T. D.; Jickells, T. D.; Miller, J. M. *Atmos. Environ.* **1991**, *25A*, 985–996.
(18) Losno, R.; Bergametti, G.; Carlier, P. *J. Atmos. Chem.* **1992**, *15*, 333–352.
(19) Rojas, C. M.; Van Grieken, R. *Atmos. Environ.* **1992**, *26A*, 1231–1237.
(20) Parekh, P. P.; Husain, L. *Atmos. Environ.* **1988**, *22*, 707–713.
(21) Sadasivan, S.; Negi, B. S. *Sci. Total Environ.* **1990**, *96*, 269–279.
(22) Bacci, P.; Caruso, E.; Braga Marcazzan, G. M.; Redaelli, P.; Sabbioni, C.; Ventura, A. *Nucl. Instrum. Methods Phys. Res.* **1984**, *B3*, 522–525.
(23) Hopke, P. K. *Receptor modeling in environmental chemistry;* John Wiley and Sons: New York, 1985; pp 267–314.
(24) Shattuck, T. W.; Germani, M. S.; Buseck, P. R. In *Environmental Applications of Chemometrics;* Breen, J. J., Robinson, P. E., Eds.; ACS Symposium Series 292; American Chemical Society: Washington, DC, 1985; pp 118–129.
(25) Usero, J.; Rosa, F.; Ternero, M.; Gracia, I. *Int. J. Environ. Anal. Chem.* **1988**, *33*, 233–244.
(26) Rybicka, E. H. *Environ. Technol. Lett.* **1989**, *10*, 921–928.
(27) Kowalczyk, G. S.; Choquette, C. E.; Gordon, G. E. *Atmos. Environ.* **1978**, *12*, 1143–1153.
(28) Kowalczyk, G. S.; Gordon, G. E.; Rheingrover, S. W. *Environ. Sci. Technol.* **1982**, *16*, 79–90.
(29) Parungo, F. P.; Nagamoto, C. T.; Harris, J. M. *Atmos. Res.* **1986**, *20*, 23–37.
(30) Andreae, M. O.; Charlson, R. J.; Bruynseels, F.; Storms, H.; Van Grieken, R.; Maenhaut, W. *Science* **1986**, *232*, 1620–23.
(31) Borchert, H. In *Chemical Oceanography;* Riley, J. P., Skirrow, G., Eds.; Academic: London, 1965; pp 205–276.
(32) Moharram, M. A.; Sowelim, M. A. *Atmos. Environ.* **1980**, *14*, 853–856.
(33) Savoie, D. L.; Prospero, J. M. *J. Geophys. Res.* **1980**, *85*, 385–392.
(34) Prodi, F.; Santachiara, G.; Oliosi, F. *J. Geophys. Res.* **1983**, *88*, 10957–10968.
(35) Van Borm, W. A.; Adams, F. C.; Maenhaut, W. *Atmos. Environ.* **1989**, *23*, 1139–1151.
(36) Biggins, P. D. E.; Harrison, R. M. *J. Air Pollut. Control Assoc.* **1979**, *29*, 838–840.
(37) Biggins, P. D. E.; Harrison, R. M. *Atmos. Environ.* **1979**, *13*, 1213–1216.
(38) Del Monte, M.; Sabbioni, C. *Arch. Meteorol. Geophys. Bioklimatol.* **1984**, *B35*, 93–104.
(39) Ichikuni, M. *J. Geophys. Res.* **1978**, *83*, 6249–6252.
(40) Perkins, H. C. *Air Pollution;* McGraw-Hill: New York, 1974; pp 273–283.
(41) Nishimura, H. *How to Conquer Air Pollution, a Japanese Experience;* Elsevier: Amsterdam, 1989; pp 150–153.
(42) Breihofer, D.; Mielenz, A.; Rentz, O. *Emission Control of SO_2, NO_x and VOC at Stationary Sources in the Federal Republic of Germany;* Report supported by the Bundesminister für Umwelt, Naturschutz und Reaktorsicherheit/Umweltbundesamt, Karlsruhe, 1991.

Received for review June 22, 1995. Revised manuscript received January 12, 1996. Accepted January 15, 1996.[⊗]

ES9504350

[⊗] Abstract published in *Advance ACS Abstracts,* March 15, 1996.

A message in the dust

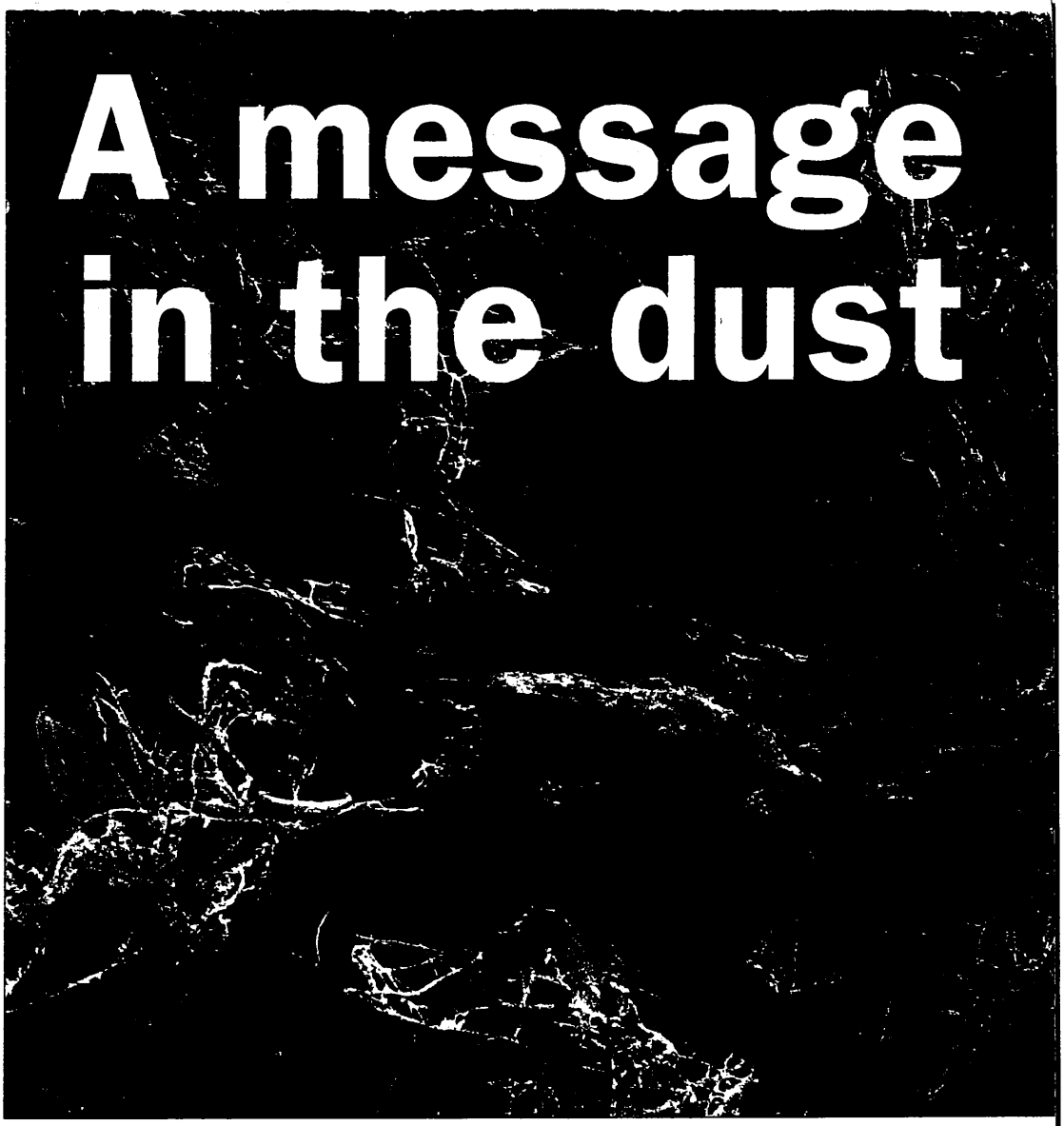

Il suffit d'un grain de poussière pour en dire long sur l'état de l'environment, mais les techniques permettant dévoiler l'origine et le destin de la matière particulaire ne sont que rarement utilisées. **Wendy Jambers** et **René Van Grieken** examinent pour vous ces techniques

Ein Staubkorn kann viel über den Zustand der Umwelt besagen, trotzdem finden Verfahren, die zur Aufklärung des Mysteriums über Ursprung und Schicksal partikularer Stoffe dienen, nur selten Anwendung. **Wendy Jambers** und **René Van Grieken** diskutieren einige dieser Techniken

A speck of dust can deliver valuable information about the state of the environment. **Wendy Jambers** and **René Van Grieken** describe some of the microanalytical techniques available for particle analysis and argue that they should be taken much more seriously

Heavy metals are constantly in the limelight as a danger to public health, which is why in the last ten years bulk techniques have become commonplace to determine environmental heavy metal concentrations.

However, microanalytical techniques can characterise the morphology and composition of individual micrometre-sized particles yet they are seldom used – even though they could be a valuable complement to bulk analysis. They may provide detailed information about the origin, formation, transport, reactivity, transformation reactions and environmental impact of particulate matter.

There are particular problems about analysing single particles. There is the difficulty of obtaining quantitative results in the absence of suitable standards and the uncertainty in determining the interaction volume. The need to analyze a large number of particles to ensure the statistical relevance of the data is also time-consuming, but for some methods this has already been compensated for by automation. Computer-controlled electron probe X-ray micro analysis (CC-EPXMA) is one advanced example. The biggest problem with most micro-analytical techniques is having to operate under vacuum: volatile and unstable compounds are often subject to serious losses and transformations.

The detection limits of most heavy metal micro-analytical techniques are poor but recently new methods with much improved detection limits, for example micro-particle induced X-ray emission (micro-PIXE) and microscopical X-ray fluorescence (micro-XRF), have become more commonplace. But the applications of these techniques are limited by their relatively large lateral resolution (1-10 μm). For micro-XRF this problem can be partly solved by replacing the conventional X-ray source by synchrotron radiation, which allows better focusing of the beam. Microscopic synchrotron radiation X-ray fluorescence (micro-SRXRF) is available using second generation synchrotrons with micro-beams of 5 μm. Sophisticated X-ray optics, which are being implemented in the micro-SRXRF dedicated beam-lines of the new

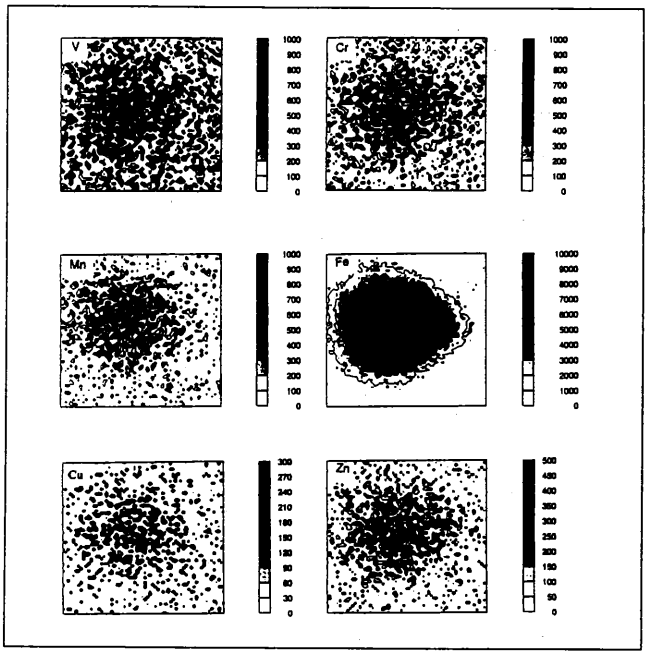

Figure 1 *Elemental maps of a fly-ash particle for vanadium, chromium, manganese, iron, copper and zinc, obtained with the nuclear microprobe. The scanning area was 12 by 11 μm.*

third generation synchrotrons,will, in principle, become sub-micrometer beams.

Siberian tales

Siberia is one of the most remote and sparsely-populated regions on Earth, with virtually no industry, so any aerosol material could reasonably be considered as a 'baseline' value. The western and central parts of the area are probably the main source of any pollution in the atmosphere above the Arctic.

A combination of EPXMA with micro-PIXE was used to characterise aerosols which were collected in two cities in South–Central Siberia and over Lake Baikal. Since micro-PIXE has much better detection limits, this technique was used to determine the heavy metal concentrations. The results of analysis of 124 particles were classified into seven groups by means of hierarchical cluster analysis. Some 75 per cent of the particles belonged to one of four major groups:

- gypsum particles containing traces of manganese and zinc, probably linked to the metalurgy industry
- fly-ash particles produced from power plant emissions
- calcium-rich particles with traces of zinc and strontium
- internally mixed particles containing equal amounts of silicon, sulfur, chlorine, potassium, calcium and iron.

The remaining particles were classified into three minor groups:

- iron/silicon rich particles with high concentrations of zinc, probably produced during ferrous manganese furnace processes
- iron-rich particles with a low trace metal content, linked to a natural source
- titanium-rich particles with very high copper, zinc and zirconium concentrations, probably from anthropogenic titanium emissions from coal fired boilers, asphalt production and power plants.

The homogeneity of some particles was studied by X-ray mappings. Figure 1 shows elemental maps of a fly-ash particle. Most elements are homogeneously distributed on this particular particle.

The second generation synchrotron at Brookhaven, New York, has been used for micro-SRXRF analyses of Antarctic ice core particles. Although the lateral resolution is not yet optimal, at only 5 μm, the detection limits for heavy metals are very impressive (down to the femtogram range). As an example the metal concentrations of a particle with a total mass of 1 300 pg were calculated with the iron peak as a reference. Table 1 shows the trace metal concentrations of this particle.

Heavy metals	Concentration (fg)
Cr	150
Mn	640
Ni	30
Zn	200
Ga	35
Pb	88
Br	48
Rb	340
Sr	35
Y	34
Zr	110

Table 1 *Heavy metal content of an Antarctic ice core particle, calculated from the SRXRF X-ray spectrum with iron as a reference.*

North Sea aerosols

Ninety-six aerosol samples collected from an aircraft above the Southern Bight of the North Sea have been analyzed with EPXMA. More than 5 000 of the 45 000 particles analyzed contained significant concentrations of chromium, lead and zinc. Depending on the origin of the air mass, significant differences in abundance of these heavy metal aerosols were found. Samples with a continental origin had 50 times more heavy metal containing aerosols than those from a marine source. The abundance of chromium-containing particles in air with a marine origin is, compared to lead and zinc, still quite high (about one third of the continental contribution).

The marine source of this chromium is probably the recycling of previously deposited material through re-injection into the atmosphere by sea-spray. A south-south eastern wind, originating from Belgium, central and southern Germany and the eastern part of France resulted in the highest values for lead, chromium and zinc-containing aerosol particles. Figure 2 gives the abundances of lead for

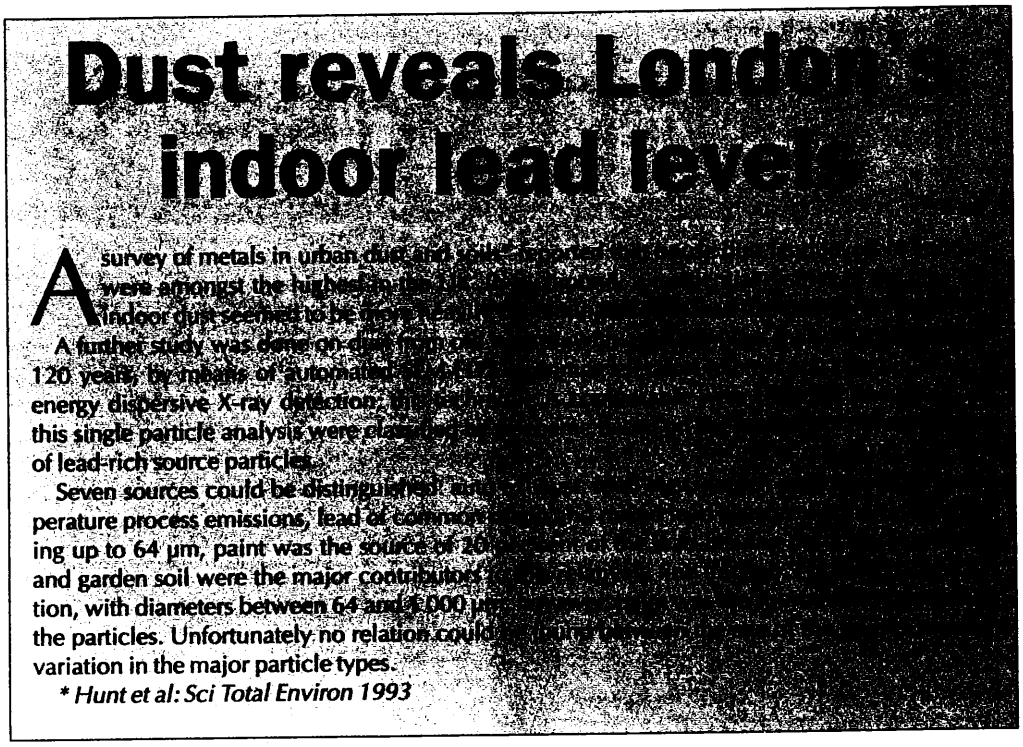

the different regions. Hierarchical, non-hierarchical and fuzzy clustering were combined to classify the particles into different particle types. Most were related to emissions from the metallurgical industry, which is concentrated in the northern part of France, the German Ruhr area and the industrial centres in the middle of the UK. Automobile exhausts were the major source of the lead-containing particles.

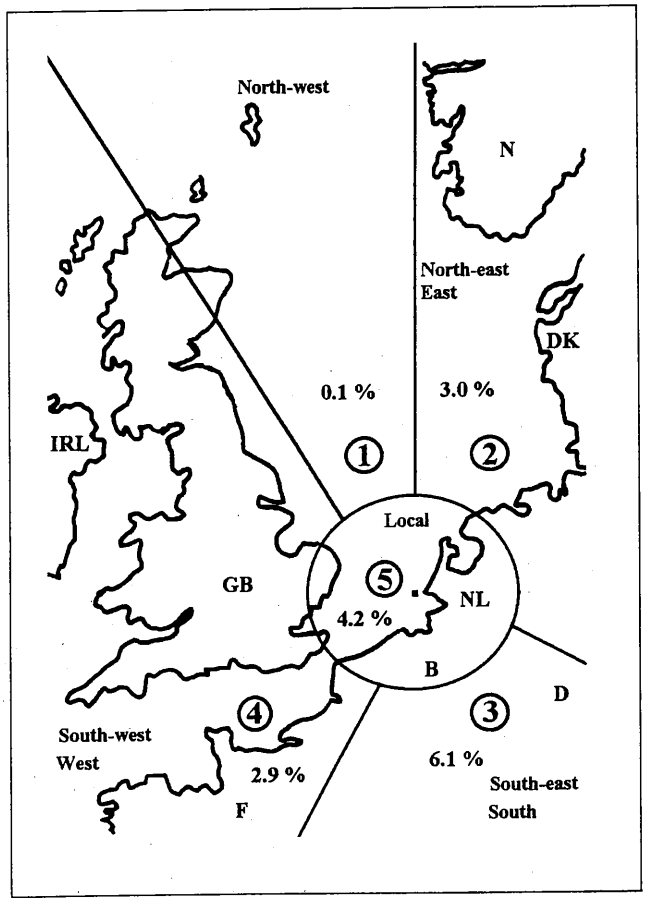

Figure 2 *The percentage of lead-containing aerosol particles per wind sector as detected by EPXMA. The figure is reproduced with the permission of the American Chemical Society.*

North Sea aerosol particles were also collected on the research platform *Nordsee* and on two research vessels. Micro-PIXE was used to determine the major and trace element concentrations in individual giant aerosols with a diameter larger than 5 µm. These aerosols could be classified into three particle types:

- sea salt
- sea salt with high amounts of sulfur, potassium and calcium
- metal-rich particles, mainly titanium, chromium, iron and nickel.

The heterogeneity of these giant aerosols was studied by elemental mapping. The differences in local elemental concentrations across these giant particles shows that they are made by agglomeration of different large particles. Due to the high wind speeds during collection, large amounts of sea salt were present: under these conditions large fractions of sub-micrometer heavy metal-rich particles coagulate with sea salt and form aggregates with diameters larger than 5 µm.

Urban types

About 1 500 lead-containing particles, which were collected on top of a fifteen metre high building in a suburban site of Antwerp, Belgium, were analyzed with EPXMA and laser microprobe mass analysis (LMMS). The particles were classified into five particle types based on the EPXMA results. Lead sulfates and lead halides are the major groups. They account for 67 per cent and 28 per cent of the lead particles and are produced by automobile exhaust. The lead sulfate particles are probably the result of a partial sulfation which occurs as a conversion of lead halide into lead sulfates through reaction with atmospheric ammonium sulfate aerosols. The sulfation seemed to be very efficient, because halides such as bromine and chlorine were completely absent. The lead halide particles, on the other hand, had variable concentrations of bromine

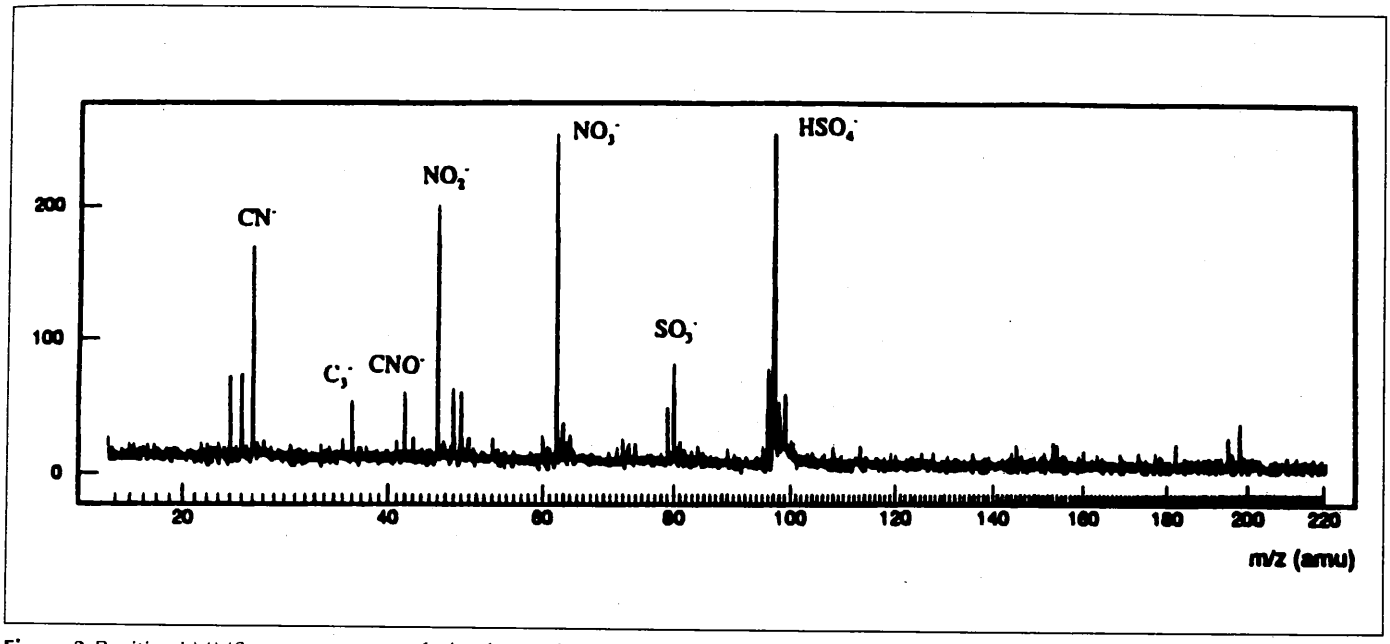

Figure 3 *Positive LMMS mass spectrum of a lead particle enriched with ammonium.*

and chlorine. The presence of ammonium compounds was tested with LMMS (this technique allows determination of low-Z elements). Ammonium sulfate was found in all lead particles and was presumably present as a coating.

Roadside lead

Lead-containing particles, collected in the Netherlands cities of Vlaardingen and Wageningen and near a highway at Ede, as well as lead/calcium carbonate standard particles have been analyzed by combining bulk techniques with LMMS. Both LMMS and the bulk techniques were able to discriminate between lead-coated calcium carbonate particles and those in which lead and calcium carbonate had been co-precipitated internally. LMMS was also used to identify single ambient aerosol particles. The amount of lead-containing particles was limited, except for collections near the highway. No surface-related information could be found for these more complex ambient aerosols. However, a great deal of information was recorded about the single particle composition. Most lead-rich particles had high concentrations of ammonium. These were mixed salts of ammonium nitrate and sulfate which contained variable metal concentrations, particularly lead and vanadium. Figure 3 shows the positive ion LMMS-spectrum of a lead-containing ammonium-rich particle.

Obstacles

Although it is important to understand the distribution of heavy metals in single particles, only a limited number of applications has been published. This can be explained by the high detection limits for heavy metals, which restrict the usage of most single-particle techniques for the analyses of trace compounds. Another obstacle is the poor lateral resolution of techniques such as micro-PIXE and micro-SRXRF in second generation synchrotrons. Now new techniques with very good detection limits for heavy metals and a sub-micrometer beam size, for instance micro-SRXRF in third generation synchrotrons, are being developed. These will give a new dimension to heavy metal analysis in single particles and will stimulate this important part of environmental research enormously.

Acknowledgements

This work was partially prepared in the framework of the Impulse Programme in Marine Sciences, supported by the Belgian State – Prime Minister's Service – Services for Scientific, Technical and Cultural Affairs. (Contract MS/06/050).

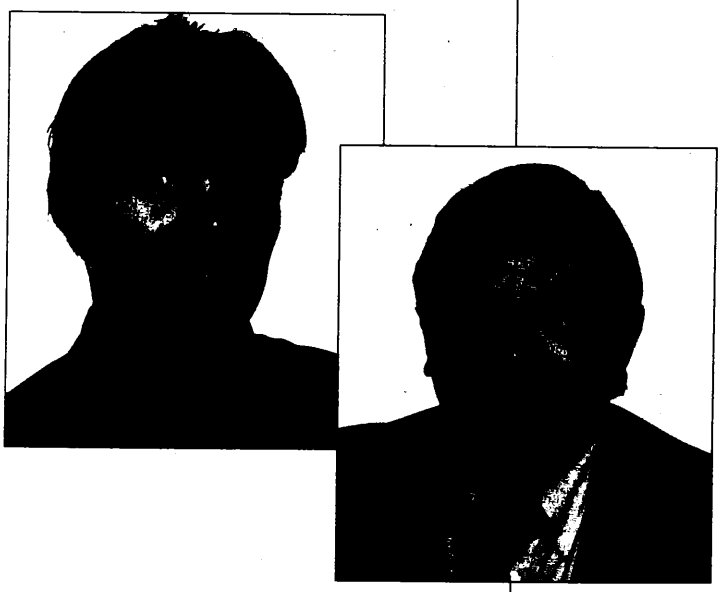

Wendy Jambers (top) and **René Van Grieken** work at the Micro and Trace Analysis Centre (MiTAC), Department of Chemistry, University of Antwerp (UIA), Universiteitsplein 1, B-2610 Antwerpen, Belgium

Anal. Chem. **1996**, *68*, 1136–1142

Glow Discharge Mass Spectrometric Analysis of Atmospheric Particulate Matter

Wim Schelles, Kris J. R. Maes, Stefan De Gendt, and René E. Van Grieken*

Department of Chemistry, University of Antwerp (UIA), Universiteitsplein 1, B-2610 Antwerpen, Belgium

A direct current (dc) glow discharge mass spectrometer has been used to analyze atmospheric particulate matter. The sample preparation used is simple and time-saving. The air is sucked by a pump through a single-orifice impactor stage, in which the aerosols are impacted on a metal support, forming a central spot. This metal plate is directly used as a cathode in a dc glow discharge mass spectrometer. Evaluation of the sample loading and of the discharge parameters allowed us to optimize the signal intensity and to minimize its decrease, the latter being a consequence of its consumption by continuous sputtering in the discharge. The available aerosol analysis time could be prolonged to more than 3 h, a time span necessary to perform a multielement analysis using a magnetic sector instrument and long integration times. A NIST reference aerosol was measured to evaluate the quantitative analysis potential. The internal reproducibility was better than 10% RSD, and the limits of detection were estimated to be in the low ppm or sub ppm region. Even without the use of any standards or correction factors, glow discharge mass spectrometry could offer good semiquantitative results, based only on the use of an internal standard.

Aerosols (or atmospheric particulate matter) are defined as suspended solid or liquid particles in a gaseous medium.[1,2] The particle size ranges from about 0.01 to more than 10 μm. Characterization of these particles has become of great interest in atmospheric chemistry, especially because of health concerns. Quantitative trace analysis of bulk aerosols is usually done by atomic absorption analysis, a single-element technique, or by multielemental inductively coupled plasma emission or mass spectrometry[3,4] and voltammetry.[5,6] These techniques require a solution sample; hence, they can only be used after (time-consuming) quantitative destruction of the aerosol sample. Alternatively, there are techniques, like X-ray fluorescence, particle-induced X-ray emission, and neutron activation analysis, that can handle solid samples but have other shortcomings: many elements cannot be measured with satisfactory sensitivity, or not at all, and the quantification may be difficult.[4,7]

In this study, the use of direct current glow discharge mass spectrometry (dc-GDMS) to analyze aerosols is investigated. GDMS has already proven to be a very powerful tool for analysis of conducting and semiconducting materials.[8–10] The most important advantages are the low limits of detection (even sub-ppb levels) and the good semiquantitative results obtained even without the use of an external standard. However, the main problem is the requirement that the sample be electrically conducting. Different ways have been investigated to overcome this problem. Substituting the common dc source to a radio frequency (rf) discharge is a very appealing method because nonconducting samples can be measured directly, without the use of an auxiliary conductor.[11,12] Promising results have been reported, and rf glow discharges have already been interfaced successfully with commercial mass spectrometers.[13,14] For dc-GDMS, however, nonconducting powder samples are mostly brought into a conducting host matrix (e.g., copper powder,[15,16] gallium,[17] tantalum,[18] etc.), and electrodes can be formed. Alternatively, flat, solid, nonconducting samples, e.g., glass plates, can be analyzed with dc-GDMS by means of the so-called secondary cathode technique. The sample is exposed to the discharge through an aperture of a conducting diaphragm, the secondary cathode. Due to the continuous in situ sputter-redeposition of the secondary cathode atoms, a thin conducting layer is formed on the nonconducting sample. This allows atomization of the nonconducting material as the bombarding ions can penetrate through the thin conducting layer. This concept has already been applied successfully to the analysis of several sample types with varying chemical and physical properties: glass, iron ore,

(1) Hinds, W. C. *Aerosol Technology, Properties, Behavior, and Measurement of Airborne Particles;* John Wiley & Sons: New York, 1982; Chapter 1.
(2) Götz, G.; Mészáros, E.; Vali, G. *Atmospheric Particles and Nuclei;* Akademiai Kiadó: Budapest, 1991; Chapter 2.
(3) Bettinelli, M.; Baroni, U.; Pastorelli, N. *J. Anal. At. Spectrom.* **1987**, *2*, 485–489.
(4) Krivan, V.; Franek, M.; Baumann, H.; Pavel J. *Fresnius J. Anal. Chem.* **1990**, *338*, 583–587.
(5) Khandekar, R. N.; Dhaneshwar, R. G.; Palrecha, M. M.; Zarapkar, L. R. *Fresenius J. Anal. Chem.* **1981**, *307*, 365–368.
(6) Nimmo, M.; Fones, G. *Anal. Chim. Acta* **1994**, *291*, 321–328.
(7) Quisefit, J. P.; de Chateaubourg, P.; Garivait, S.; Steiner, E. *X-Ray Spectrom.* **1994**, *23*, 59–64.
(8) Harrison, W. W.; Barshick, C. M.; Klinger, J. A.; Ratliff, P. H.; Mei, Y. *Anal. Chem.* **1990**, *62*, 943A–949A.
(9) Mykytiuk, A. P.; Semeniuk, P.; Berman, S. *Spectrochim. Acta Rev.* **1990**, *13*, 1–10.
(10) King, F. L.; Harrison, W. W. Glow discharge mass spectrometry. In *Glow Discharge Spectroscopies;* Marcus, R. K., Ed.; Plenum Press: New York, 1993; Chapter 5.
(11) Duckworth, D. C.; Marcus, R. K. *Anal. Chem.* **1989**, *61*, 1879–1986.
(12) Marcus, R. K.; Harville, T. R.; Mei, Y.; Shick, C. R., Jr. *Anal. Chem.* **1994**, *66*, 902A–911A.
(13) Duckworth, D. C.; Donohue, D. L.; Smith, D. H.; Lewis T. A.; Marcus, R. K. *Anal. Chem.* **1993**, *65*, 2478–2484.
(14) Shick, C. R., Jr.; Raith, A.; Marcus, R. K. *J. Anal. At. Spectrom.* **1993**, *8*, 1043–1048.
(15) Woo, J. C.; Jakubowski, N.; Stuewer, D. *J. Anal. At. Spectrom.* **1993**, *8*, 881–889.
(16) De Gendt, S.; Schelles, W.; Muller, V.; Van Grieken, R. *J. Anal. At. Spectrom.* **1995**, *10*, 681–687.
(17) Efimov, A. G.; Pavela, M.; Paulovicheva, E. Presented at 17th Arbeitstreffen Festkörpermassenspektrometrie, KFA, Jülich, Germany, 2–4 May, 1994.
(18) Tong, S. L.; Harrison, W. W. *Spectrochim. Acta* **1993**, *48B*, 1237–1245.

0003-2700/96/0368-1136$12.00/0

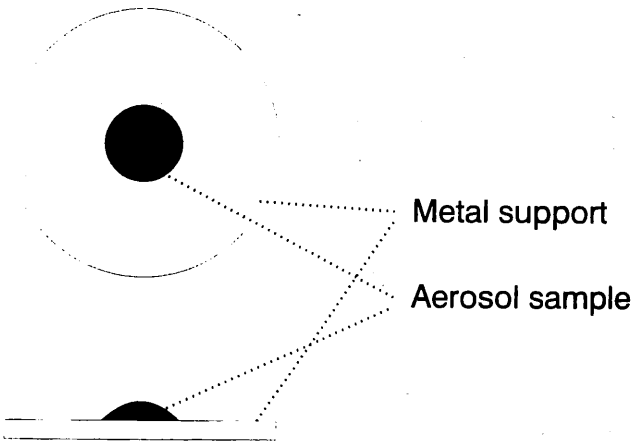

Figure 1. Aerosol sample spot, impacted on the metal support.

polycarbonate, marble, Teflon, aluminum oxide, and uranium oxide.[19-22]

Aerosols are, depending on the geographical origin, mainly composed of soil dust, sea salt, sulfates, etc.; therefore, they can generally be considered as "nonconducting". They have already been analyzed with dc-GDMS, using the above-described method for nonconducting powder analysis.[23] For this goal, a large amount of powder had to be collected; after it was pressed into an indium rod, an electrode was formed. We preferred, however, a much less time-consuming and more direct sample preparation method, which has not yet been used for dc-GDMS: the direct impaction technique. A similar concept has already been used for secondary ion mass spectrometry and sputtered neutrals mass spectrometry measurements,[24] but those studies aimed at depth profiling of the aerosols rather than bulk trace analysis. In our approach, the sampled atmospheric particles are directly impacted on a metal plate. The nonconducting central aerosol spot is surrounded by the underlying conducting support material (see Figure 1). This situation is comparable with the starting point of the secondary cathode concept, where also a conducting area surrounds a nonconducting one.

In this methodological study, the first results concerning this sample preparation method, combined with dc-GDMS analysis, are presented. It is investigated whether the secondary cathode concept also holds for the configuration used, i.e., whether the continuous in situ sputter-redeposition is necessary to create a stable discharge. Different parameters, like the required amount of aerosol, the nature of the support material, and the discharge conditions, are evaluated with regard to the intensity and stability of the aerosol signal. Finally, the quantitative possibilities are estimated by means of a standard reference aerosol analysis.

EXPERIMENTAL SECTION

Mass Spectrometer. All of the glow discharge work reported in this study was done with a VG9000 (Fisons Instruments Elemental Analysis, Winsford, Cheshire, UK). This double-focusing instrument of reversed Nier–Johnson geometry has already been described in detail elsewhere.[25] A typical working resolution (at 5% peak height) of 3500 was routinely used for these studies. The detection system consists of a combination of a Faraday cup and a Daly detector, providing a dynamic range of about 10 orders of magnitude (i.e., 1×10^{-19}–1×10^{-9} A). For all the measurements, the "new flat cell" was used, already described elsewhere.[26] The cell was cryogenically cooled to reduce the background due to residual gases. The glow discharge was supported by high-purity argon (Air Liquide, 99.9997%, 2 ppm H_2O as most important impurity).

Sample Preparation. Sampling was done at the campus of the University of Antwerp (UIA), Belgium. Air was sucked with an electrical pump at a rate of about 16 L/min into a single-orifice Battelle impactor. This device consists of consecutive funnel-shaped stages. The smaller the exit opening, the faster the air goes through and the smaller the size of the particles collected on impactor plates positioned behind the exit orifice. Therefore, impactors are able to separate sampled particles with different sizes on different supports.[27] In this study, only one stage of the impactor was used for the aerosol collection. This one stage was completed with two other stages (without impacting plates) to prevent rain from coming directly in the impactor. The collection stage had a 2 mm exit orifice, resulting in an aerosol spot size of about 3 mm on the support, positioned 0.5 mm behind the exit orifice. The theoretical cutoff diameter of the impactor stage used was 0.5 μm; this means that, in principle, all particles with a diameter larger than 0.5 μm are collected. The possible loss of the smallest particles (<0.5 μm) during collection is not considered in this methodological study.

The aerosols were collected on high-purity metal plates with a diameter of 25 mm. Three different foils were used as support materials: aluminum (Johnson Matthey, 99.999%, 1 mm thick), copper (Johnson Matthey, Puratronic, 99.999%, 0.25 mm thick), and tantalum (Aldrich, 99.9+%, 0.25 mm thick). No "sticky" coating on the plates (to prevent bounce-off of particles during impaction)[28] was applied. Between sampling and measurement, the loaded plates were kept in a desiccator. For analytical purposes, the amount of sample material collected on each plate had to be quantified. Weighing pointed out that the average amount was smaller than 0.5 mg. A mechanical profilometer (Dektak 3030, Veeco Instruments, Plainview, NY) was therefore used to characterize the aerosol deposit by its height and its broadness. An aerosol profile is depicted in Figure 2. The amount of collected sample was largely dependent on the weather conditions. Rain, for example, can wash the particulate matter out of the air, resulting in an important decrease of the aerosol concentration.[29] Sampling times were therefore varied from 3 h (dry weather) up to about 3 days (rainy weather). At regular intervals, the amount of aerosols was checked, until an appropriate loading was obtained (see Results and Discussion).

Standard reference atmospheric particulate matter in powdered form was also prepared for a GDMS analysis. The standard used

(19) Milton, D. M. P.; Hutton, R. C. *Spectrochim. Acta* **1993**, *48B*, 39–52.
(20) Schelles, W.; De Gendt, S.; Muller, V.; Van Grieken, R. *Appl. Spectrosc.* **1995**, *49*, 939–944.
(21) Schelles, W.; De Gendt, S.; Maes, K.; Van Grieken, R. *Fresenius J. Anal. Chem.*, in press.
(22) Betti, M. European Commission—Institute for Transuranium Elements—Annual Report. *EUR 16152 EN* **1995**, 188–193.
(23) Takahashi, T.; Takaku, Y.; Masuda, K.; Shimamura, T. *Bunseki Kagaku* **1994**, *43*, 1083–1086.
(24) Goschnick, J.; Schuricht, J.; Ache, H. J. *Fresenius J. Anal. Chem.* **1994**, *350*, 426–430.
(25) Robinson, K.; Nayler, R. *Eur. Spectrosc. News* **1986**, *68*, 18–22.
(26) van Straaten, M.; Gijbels, R.; Vertes, A. *Anal. Chem.* **1992**, *64*, 1855–1863.
(27) Finlayson-Pitts, B. I.; Pitts, J. N., Jr. *Atmospheric Chemistry: Fundamentals and Experimental Techniques;* John Wiley & Sons, New York, 1986; p 829.
(28) Lawson, D. R. *Atmos. Environ.* **1980**, *14*, 195–199.
(29) Caddle, R. D. Particulate matter in the lower atmosphere. In *Chemistry of the Lower Atmosphere;* Rasool, S. I., Ed.; Plenum Press: New York, 1973; Chapter 2, p 108.

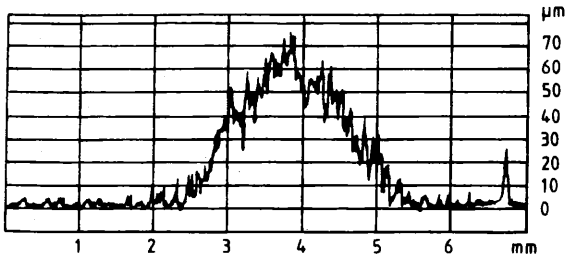

Figure 2. Section of the aerosol spot as measured by a mechanical profilometer.

in this study was NBS 1648, urban particulate matter. Its composition is listed later in this paper (Table 4). A suspension was made by mixing the reference sample with acetone (Merck, pro analysi), which was nebulized with an air brush in front of the impactor stage. The artificial aerosols were collected in the same manner as the natural aerosols.

RESULTS AND DISCUSSION

Evaluation of the Suitability of the Direct Impaction Sample Preparation Method. Analyses of poorly conducting or nonconducting samples with dc-GDMS using the secondary cathode technique have demonstrated that the electrical resistivity of the sample can largely affect the optimum measurement conditions.[20] Therefore, the electrical resistivity of the aerosols should be measured for a good understanding and optimization of the aerosol analysis. However, in practice, it was impossible to apply test leads to the small aerosol spot for the resistivity measurement. An indirect evaluation of the electrical resistivity can be obtained by exposing the sample to the glow discharge. The behavior of the sample in the discharge allows one to classify the "nonconductors" into different categories, according to the possibility of obtaining a stable discharge. This classification is of main importance for the dc-GDMS analysis of poorly conducting or nonconducting samples, especially when a secondary cathode is used. To evaluate this behavior, only the aerosol itself, and not the support material, was exposed to the plasma. A front plate with a 2 mm diameter opening was placed before the 3 mm diameter aerosol spot, thus preventing support material from being sputtered. With this configuration, and thus with only aerosols as cathode material, it was impossible to create a stable discharge, regardless of the discharge pressure or voltage used. This confirms that atmospheric particulate matter can be considered as "nonconducting" for the dc-GDMS analysis; the exposure of an auxiliary conductor to the plasma is absolutely necessary to create a stable glow discharge.

Because of the instabilities, caused by the use of a 2 mm opening in the front plate, the experiments were continued with a 5 mm opening, resulting in a conducting edge of about 1 mm on each side of the aerosol spot. As already mentioned, this conducting edge is also exposed to the discharge, a necessity to create a stable discharge. Initial experiments were performed with three different support materials: Al, Ta, and Cu. For these measurements, no effort was undertaken to quantify the amount of collected material on the support plate; the amount was simply visually estimated, i.e., air was sampled until a distinct, dark spot was obtained on the metal support. All these loaded plates were analyzed at 2 mA, 0.6 kV discharge conditions. These initial discharge conditions were chosen for convenience rather than as optimum conditions. None of the loaded support plates used

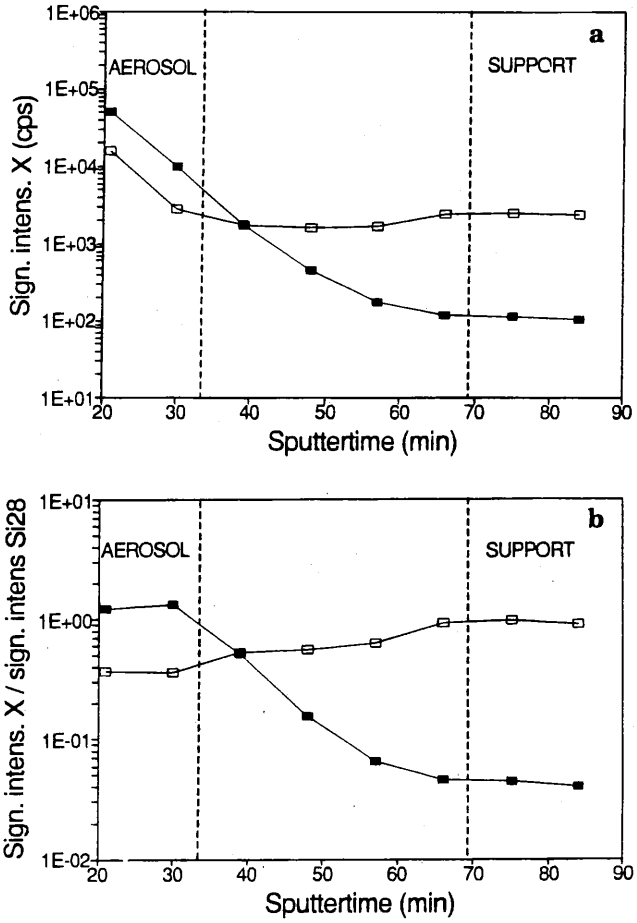

Figure 3. Course of the absolute signal intensities (a) and the signal intensity ratios relative to Si (b) of some matrix elements in the aerosol as a function of the sputter time. ■, Mg; □, Al.

gave rise to an unstable discharge. Typical in these measurements was the transient character of the signal intensities. For each element, the obtained signal is composed of the signal originating from the aerosol sample and the signal from the support material (and additionally of the signals of isobaric and molecular interferences). In the first minutes after the ignition of the discharge, the signals are mainly produced by the sputtering of the aerosols; after a certain sputter time, when all of the aerosol is sputter-consumed, the signal intensities represent, in principle, the blank values of the support material. The sputter time dependency of the absolute signal intensities of some selected elements in an aerosol (impacted on a tantalum support) are illustrated in Figure 3a. Figure 3b depicts the signal intensity of some isotopes relative to the signal intensity of ^{28}Si. It can be understood that this ratio of signal intensities (X versus ^{28}Si) is, in most cases, significantly different for the aerosol and for the support material. Consequently, this graph allows identification of the "aerosol region" and the "support region". In an ideal case, the aerosol signal intensity (the left-hand side of Figure 3a) should be high, to obtain low limits of detection, and decrease infinitely slowly, resulting in a long available time of analysis, making a time-consuming multielement analysis possible.

Based on these preliminary results, it can be concluded that the aerosols can, indeed, be analyzed with dc-GDMS after direct impaction on a support material. However, to obtain useful analytical information, the evaluation of different parameters,

Table 1. Blank Values (>0.5 ppm) in Different Support Materials

	Cu	Ta	Al		Cu	Ta	Al
B	0.07	0.02	0.5	Sb	0.025	<0.02	5
Na	1.2	30	50	Gd	0.02	<0.007	1.8
Mg	0.04	0.4	1.5	Fe	0.32	45	16
Al	1.0	20	10^6	Co	<0.003	0.1	3.3
Si	1.4	0.5	17	Ni	0.01	80	1.0
P	4.7	<0.2	<0.1	Cu	10^6	40	3
S	9.0	<5	1.5	Zn	<0.3	<1	44
Cl	0.2	2	2.4	As	0.06	<0.6	3.3
K	2.2	<0.1	14	Br	<0.03	<0.2	1.8
Ca	<0.1	<2	6	Zr	0.2	0.1	0.9
Ti	0.01	<0.1	18	Nb	0.003	80	0.03
Cr	<0.008	60	0.5	Mo	<0.06	5	0.15
Ag	3.6	<0.02	0.2	W	0.04	200	0.3
Cd	<0.05	<2	2.4	Au	0.5	5	2.5
Sn	<0.04	<0.07	40				

which are thought to influence the course of the (transient) signal, is of major importance.

Influence of Support Materials. According to the secondary cathode concept, the material of the diaphragm, and thus, in this study, of the support plate, can be extremely important. For the analysis of glass, for example, up to now only tantalum[19,20] and tungsten[30] were found to be useful; other materials like molybdenum and aluminum give rise to a coated sample, due to their higher sputter yields. For analogous reasons, a significant support material dependency was expected for the aerosol analysis, especially because sputtering of the conducting edge around the aerosol was found to be necessary to create a stable glow discharge. However, the preliminary measurements on the aerosols, mentioned above, did not reveal a distinct effect of the support material. For, e.g., tantalum (low sputter yield)[31] and copper (high sputter yield)[31] supports, neither unstable discharges nor coated aerosol samples were noticed upon varying the discharge conditions; only a very large aerosol loading caused some instabilities (see Influence of the Aerosol Loading, below). Consequently, one can conclude from these results that the sputter yield of the support material is of minor importance for the aerosol analysis with respect to the discharge stability. However, it was also noticed that the use of an aluminum support (with an intermediate sputter yield relative to tantalum and copper) was not preferable because it gave rise to a slightly unstable discharge, which lasted for 1 h or more. Even when no more sparks were noticed, the background was up to 10 times higher than that for a tantalum support ($\sim 10^{-17}$ A, 640 ms integration time, for the aluminum support). These instabilities are very likely to be caused by the naturally occurring oxidic layer on aluminum. The classical solutions to this problem, i.e., mechanical removal, chemical etching, or high-power presputtering, cannot be used, as the aerosol itself would be removed.

Another factor determining the choice of support material is the blank contribution, caused either by impurities in the support material or by potential clusters. Blank values were determined for 72 elements. In Table 1, the concentrations of the impurities that were found in a concentration of at least 0.5 ppm are listed for the different support materials. Also, interferences due to cluster formation can be prominent, especially because of the complexity of the aerosol matrix (oxides, sulfates, organic matter, etc.). A tantalum support, for example, can cause problems when traces of platinum have to be analyzed, due to the clusters of tantalum with residual gas species (e.g., $^{180}Ta^{14}N$ on ^{194}Pt, $^{181}Ta^{16}O^{1}H$ on ^{198}Pt). It will also be difficult to determine, for example, traces of the monoisotopic rhodium (^{103}Rh) on a copper support, regardless the blank concentration, because of the $^{63}Cu^{40}Ar$ interference. Not only the blank concentrations in the support material have to be considered, but, even more importantly, also their actual influence on the aerosol analysis, i.e., their "weight" in the measurement. This is represented by the ratio between the support signal intensity and the sample signal intensity. Due to the continuous decrease of the aerosol signal intensity, this weight factor will increase during the measurement. Multiplication of the blank values in the support material with this weight factor results in the "apparent blank values",[20] which is of main importance in the determination of the limits of detection.

Summarizing, it can be concluded that the sputter yield of the support material seems to be of minor importance, but that all factors affecting the background have to be taken into account. This includes the noise level, blank values, and interferences. Therefore, the optimum support material has to be chosen for each measurement, according to the required information.

Influence of the Aerosol Loading. The sample preparation method gives rise to an aerosol sample lying on top of a support. During a measurement, this sample will be sputter-consumed. Consequently, the thickness of the aerosol layer can largely affect the available measurement time. It is, for example, possible that the aerosol sample has been consumed completely, and thus that its signal has disappeared before the whole measurement has been completed. This problem especially holds for a magnetic sector instrument, where the scanning of the mass spectrum takes a relatively long time (e.g., when a long integration time or a multielement analysis is required). To characterize the different loadings, a Dektak 3030 profilometer is used to scan the aerosol spot mechanically over its diameter. These measurements reveal typical triangular profiles (see Figure 2); because the aerosol spot is circularly symmetrical, the loading is more or less cone-shaped. This means, in principle, that during sputtering the area of the aerosol spot and thus the sample signal intensity will decrease continuously, as already mentioned. The influence of the loading on the sample signal intensity and on the available analysis time is evaluated using four identical tantalum plates with varying aerosol loadings: 25, 35, 50, and 90 μm cone height, respectively.

All these samples were sputtered under the same discharge conditions (2 mA, 0.6 kV). We evaluated two features: (1) the "total aerosol signal" (TAS), based on the Mg^+, Al^+, and Fe^+ signal, as matrix elements in the aerosol (see the formula below), and (2) the ratio (S/A) between the total support signal (TSS) and the total aerosol signal (TAS). The ratio S/A represents the weight of the blanks in the support, as already discussed. The values are calculated as follows:

$$\mathrm{TAS} = \frac{[I(^{24}\mathrm{Mg})/A(^{24}\mathrm{Mg})] + [I(^{27}\mathrm{Al})/A(^{27}\mathrm{Al})] + [I(^{56}\mathrm{Fe})/A\,^{56}\mathrm{Fe})]}{\mathrm{RC(Mg)} + \mathrm{RC(Al)} + \mathrm{RC(Fe)}} \times 100\%$$

$$\mathrm{TSS} = \frac{I(^{x}\mathrm{support})/A(^{x}\mathrm{support})}{\mathrm{RC(support)}} \times 100\%$$

(30) Schelles, W., unpublished results.

(31) Chapman, B. *Glow Discharge Processes;* John Wiley & Sons: New York, 1980; pp 394–396.

$$S/A = TSS/TAS$$

where I stands for signal intensity, A for isotopic abundance, ^{x}support for the support isotope measured, and RC for a reference concentration (expressed as wt %). In these calculations, the added concentration of Mg, Al, and Fe is estimated at 2.6% (by weight, relative to the total aerosol mass), as determined with particle induced X-ray emission (PIXE) for urban Antwerp air.[32] In case of pure metals, like the support materials used, the reference concentration of the support material is 100%. For an ideal aerosol analysis, the TAS should be high and the S/A should be low. Figure 4 shows for different aerosol loadings the course of the TAS as a function of sputter time. The ratio S/A is listed in Table 2 as a function of the sputter time. Data for short sputtering times are not available for every measurement, because this time was used for the thorough optimization of the signal intensity. Both Figure 4 and Table 2 indicate that a high aerosol loading results in the most favorable TAS and S/A. However, this does not mean that very high aerosol loadings are preferable. The 90 μm aerosol loading gave rise to some instabilities in the discharge. Moreover, a higher loading requires a longer sampling time. On the other hand, when small loadings are used, the TAS and S/A values are significantly inferior in comparison with those for the 50 μm loading. In summary, an aerosol loading between 50 and 70 μm cone height can be considered as the optimum loading.

Influence of the Discharge Conditions. The discharge current and voltage determine two features which are of interest for these measurements: (1) the sample signal intensity and (2) the sputter rate of the sample, and thus the available measurement time. To evaluate these, five tantalum plates with approximately the same aerosol loading (50 ± 5 μm cone height) were measured under different discharge conditions. Each time the ion beam was optimized before the data acquisition to make a comparison of absolute sample signals possible. The course of the TAS (calculated as described in the previous section) for varying discharge conditions is depicted in Figure 5 as a function of the sputter time. Table 3 lists the corresponding S/A ratios, also calculated as in the previous section, as a function of the sputter time. It is clear that the discharge conditions largely affect the course and, therefore, the usefulness of the measurement. The discharge voltage in particular seems to be of major importance. Apparently, a relatively high voltage (0.75 kV) gives rise to a rapid signal intensity decrease and an inferior support-to-sample signal intensity ratio. Comparing the results obtained with 0.75 kV, 2 mA with those obtained with 0.5 kV, 3 mA (both 1.5 W discharge power) illustrates this clearly. The use of 0.75 kV produces a higher absolute signal during the first 90 min of sputtering; afterward, the situation is reversed, due to the rapid decrease of the aerosol signal. Also, the very high value of the S/A ratio for the 0.75 kV, 2 mA measurement is striking and not favorable. It should be noted that these data are obtained for a tantalum support. The use of another support material, with other sputter characteristics, will probably result in other figures, although it is believed that the same trends will hold for all support materials.

In any case, an important conclusion is that the "optimum" discharge conditions are determined on the basis of the required information. The measurement of trace elements requires a high absolute sample signal. If, however, the blank value of the element under investigation is rather high, the support-to-sample signal intensity ratio should be kept low. For a multielement analysis, a long analysis time will be required, and the decrease of the aerosol signal is of major interest. When all these requirements have to be combined, a good compromise has to

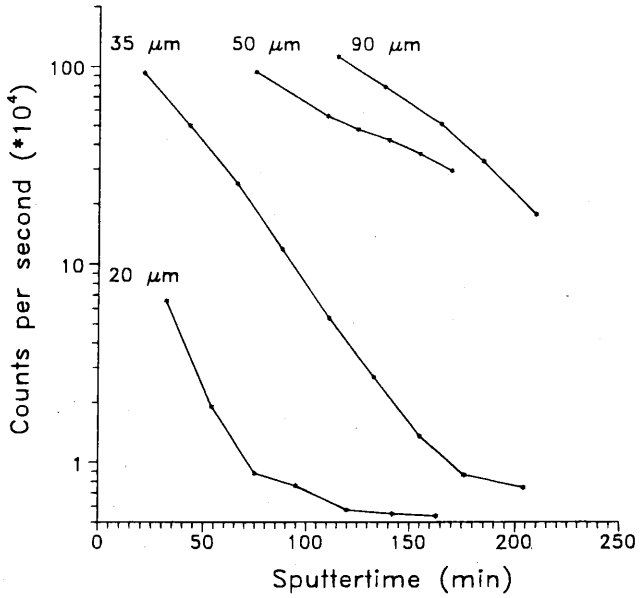

Figure 4. Absolute aerosol signal intensity for varying aerosol loadings as a function of the sputter time.

Table 2. Support Signal Intensity/Aerosol Signal Intensity Ratio, for Varying Aerosol Loadings as a Function of the Sputter Time

	aerosol loading (μm)			
sputter time (min)	20	35	50	90
75	170	14	2.5	
115	400	60	5	4
170		350	10	8

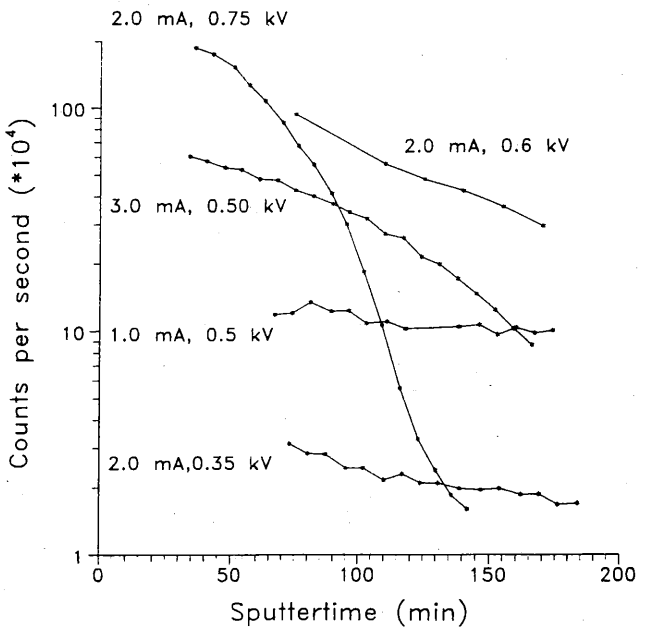

Figure 5. Absolute aerosol signal intensity for varying discharge conditions as a function of the sputter time.

(32) Van Borm, W. PhD. Thesis, University of Antwerp, Antwerpen, Belgium, 1987.

Table 3. Support Signal Intensity/Aerosol Signal Intensity Ratio for Varying Discharge Conditions as a Function of the Sputter Time

sputter time (min)	discharge conditions 0.5 kV, 1.0 mA	0.35 kV, 2.0 mA	0.6 kV, 2.0 mA	0.75 kV, 2.0 mA	0.5 kV, 3.0 mA
75	0.5	0.4	2.5	5	2.5
115	0.7	0.5	5	100	5
170	0.8	0.6	10		15

be found. In the case of the tantalum support, this is set at 2 mA, 0.6 kV.

Analytical Figures of Merit. To evaluate the quantitative possibilities of GDMS for the aerosol analysis, standard reference particulate matter was analyzed. The reference sample NBS 1648 was suspended in acetone. This suspension was nebulized with an air-brush in front of the impactor during pumping. The particulate matter was collected on a copper support in the same way that the natural aerosols were collected. Two samples were prepared and measured in a 2 mA, 0.6 kV discharge. Copper, rather than tantalum, was chosen as support material because of its blank values, e.g., for tungsten (see Table 1). The blank values, due to the sputtering of the support material, were for all measured elements less than 0.8% of the certified concentration. The support-to-sample signal intensity ratio was about 2.5. Therefore, the apparent blank values were for each element estimated to be, at maximum, 2% of the sample concentration (2.5 × 0.8%). For this reason, the blank correction was neglected. To obtain "raw" calculated concentrations, a uniform sensitivity for all the elements was considered, and the ^{56}Fe signal was used as an internal standard, according to

$$\text{concn(X)} = \text{concn(Fe)} \frac{I(\text{X})}{A(\text{X})} \frac{A(^{56}\text{Fe})}{I(^{56}\text{Fe})}$$

The signal intensities (I) are corrected for the natural abundance (A) of the measured isotope. The calculated concentrations of the selected elements are listed in Table 4. For these results, only one internal standard (^{56}Fe), and no external reference standards, was used. The average internal precision was 6.5% RSD ($\sigma = 1$, $n = 3$) over about 60 min of sputtering, after 30 min of presputtering to optimize the ion optics. As a measure for the external precision ($n = 2$), the difference between the concentration determined in each external run and the average concentration was calculated. This was found to be 18.5%, averaged over all the elements measured.

Probably the most interesting outcome is that the obtained data, which are based only on an internal standard, can be used as good semiquantitative results, without the use of any form of calibration. The measured concentrations differ for most elements by not more than a factor of 2–3 compared to the certified concentrations. Comparison of these calculated concentrations with the reference concentrations results in relative sensitivity factors (RSFs),[33]

$$\text{RSF} = \text{ref concn/calcd concn}$$

These RSFs, listed in Table 4, can be considered as correction factors for reproducible variations in elemental sensitivities. This type of calibration is generally used for GDMS analyses of conducting materials. RSFs are often considered as matrix-independent and generally applicable to various matrices, without loss of much accuracy.[33] However, studies in our laboratory[16] revealed that this concept may hold within a certain group of samples (e.g., pin-shaped metals) and for certain discharge conditions. This can be seen in Table 4, where three previously determined sets of RSFs are listed: RSFs obtained for (1) conducting matrices,[33,34] (2) powdered oxide-based samples, mixed with a silver binder,[16] and (3) glass plates, analyzed with the secondary cathode technique.[19] It is clear that the set of RSFs acquired for the aerosol analysis does not match any of the other sets. Therefore, specific RSFs for aerosol analysis seem to be required for an accurate quantitative measurement. In this context, it also has to be mentioned that the RSFs are likely to change with varying discharge conditions and with varying support materials. It has been demonstrated, for example, that the oxygen content in a nonconducting sample can largely influence the RSFs.[35] Therefore, the use of a tantalum or copper support (with a high and low reactivity toward oxygen)[36] will probably result in a different set of RSFs.

Limits of detection were estimated from an extrapolation of the counts per ppm ratio. It should be noticed that values might depend on the measured element, possible interferences, integration time, etc. Considering 10 counts (peak area) as detectable and using the high-resolution mode and an integration time of 160 ms, average limits of detection are in the low ppm to sub-ppm region. This is in agreement with the results obtained for the aerosol collected at the University of Antwerp (used for the parameter evaluation), where comparison of the aerosol signal intensities and the concentrations of the elements (as measured with PIXE)[32] also revealed sub-ppm limits of detection.

CONCLUSION

It has been demonstrated that dc-GDMS is suitable for the trace analysis of bulk atmospheric particulate matter that is directly impacted on a metal support. This sample preparation method is very easy and far less time-consuming than, for example, the destructive approach necessary for wet chemical analysis methods. In comparison to X-ray analysis techniques, the ability to measure all the elements and even isotopes can be an important feature for specific applications. Optimization of the aerosol loading and of the discharge conditions used allows measurements with a good internal reproducibility and limits of detection (under certain circumstances) of about 0.3 ppm (relative to the total aerosol mass), i.e., about 2×10^{-11} g of particulate matter per m^3 of sampled air. It is believed that this feature can be improved by optimization of the sample preparation. This can be done, for example, by creating a larger spot diameter (using an appropriate impactor stage) and by avoiding so-called bounce-off effects during

(33) Vieth, W.; Huneke, J. C. *Spectrochim. Acta* **1991**, *46B*, 137–153.

(34) *Fisons Instruments Elemental Analysis*, VG9000, software version 5.3; Fisons Instruments, Winsford, Cheshire, UK, 1990.

(35) Teng, J.; Barshick C. M.; Duckworth D. C.; Morton S. J.; Smith D. H.; King F. L. *Appl. Spectrosc.* **1995**, *49*, 1361–1366.

(36) Ohorodnik S. K.; De Gendt S.; Tong S. L.; Harrison W. W. *J. Anal. At. Spectrom.* **1993**, *8*, 859–865.

Table 4. Measurement of the Standard Reference Aerosol[a]

	measd concn							
	1	2	av concn (ppm)	ref concn (ppm)	RSF_{aero}	RSF_{stand}	RSF_{ox}	RSF_{glass}
Na	5560	7590	6580	4000	0.61	2.5	0.54	1.8
Mg	12100	14900	13500	8000	0.59	1.3	1.0	1.6
Al	64500	68900	66700	33000	0.49	1.4	0.57	1.1
Si	165000	176000	171000	125000	0.73	2.0	1.3	1.7
S	68200	94200	81200	51400	0.63	3.3		0.87
Cl	1370	2710	2040	4500	2.2	5.0		
K	8780	8780	8780	10000	1.1	1.21		1.6
Sc	15.8	7.1	11.4	7	0.61	0.39		
Ti	2620	1375	2000	4000	2.0	0.42	0.42	0.42
V	94	65	79	130	1.6	0.55	0.47	
Cr	348	371	359	403	1.1	2.2	1.4	
Mn	890	1030	961	860	0.89	1.5	1.0	1.5
Fe	39100	39100	39100	39100	1.0	1.0	1.0	1.0
Ni	348	320	334	82	0.25	1.5		1.6
Co	34	15	25	18	0.73	1.1		1.4
Zn	2030	3440	2740	4760	1.7	5.5		7.1
As	75	102	88	115	1.3	3.1		1.4
Cd	28	48	38	75	2.0		7.2	
Sb	29	38	34	45	1.3	3.9		
Ba	92	25	59	737	12.5	1.2		2.8
W	34	13	24	4.8	0.20	1.5		
Pb	2630	2530	2580	6550	2.5	2.2		3.2

[a] The measured concentrations (measd concn 1 and 2) are compared with the reference concentration (ref concn), resulting in relative sensitivity factors (RSF_{aero}).

sampling (using soft metal plates like indium or sticky coatings). An appealing advantage of the trace analysis of atmospheric particulate matter with GDMS, is the possibility of obtaining good semiquantitative results, based only on an internal standard and no external standard.

ACKNOWLEDGMENT

This work was partially prepared in the framework of the Impulse Program in Marine Sciences, supported by the Belgian State—Prime Minister's Service—Services for Scientific, Technical and Cultural Affairs (DWTC, Contract MS/06/050). W.S. acknowledges financial support by the Vlaams Instituut voor de bevordering van het Wetenschappelijk-technologisch Onderzoek in de Industrie (IWT). S.D.G. is financially supported by the Belgian Nationaal Fonds voor Wetenschappelijk Onderzoek (NFWO). The authors thank H. Van Malderen, L. De Bock, and J. Injuk for valuable information concerning the aerosol sampling and K. De Cauwsemaecker and R. Saelens for technical support.

Received for review September 28, 1995. Accepted January 9, 1996.[⊗]

AC9509768

[⊗] Abstract published in *Advance ACS Abstracts*, February 15, 1996.